METHODS AND APPLICATIONS IN RESPIRATORY PHYSIOLOGY

EDITED BY: Walter Araujo Zin, Mona Eskandari and Lorenzo Ball
PUBLISHED IN: Frontiers in Physiology

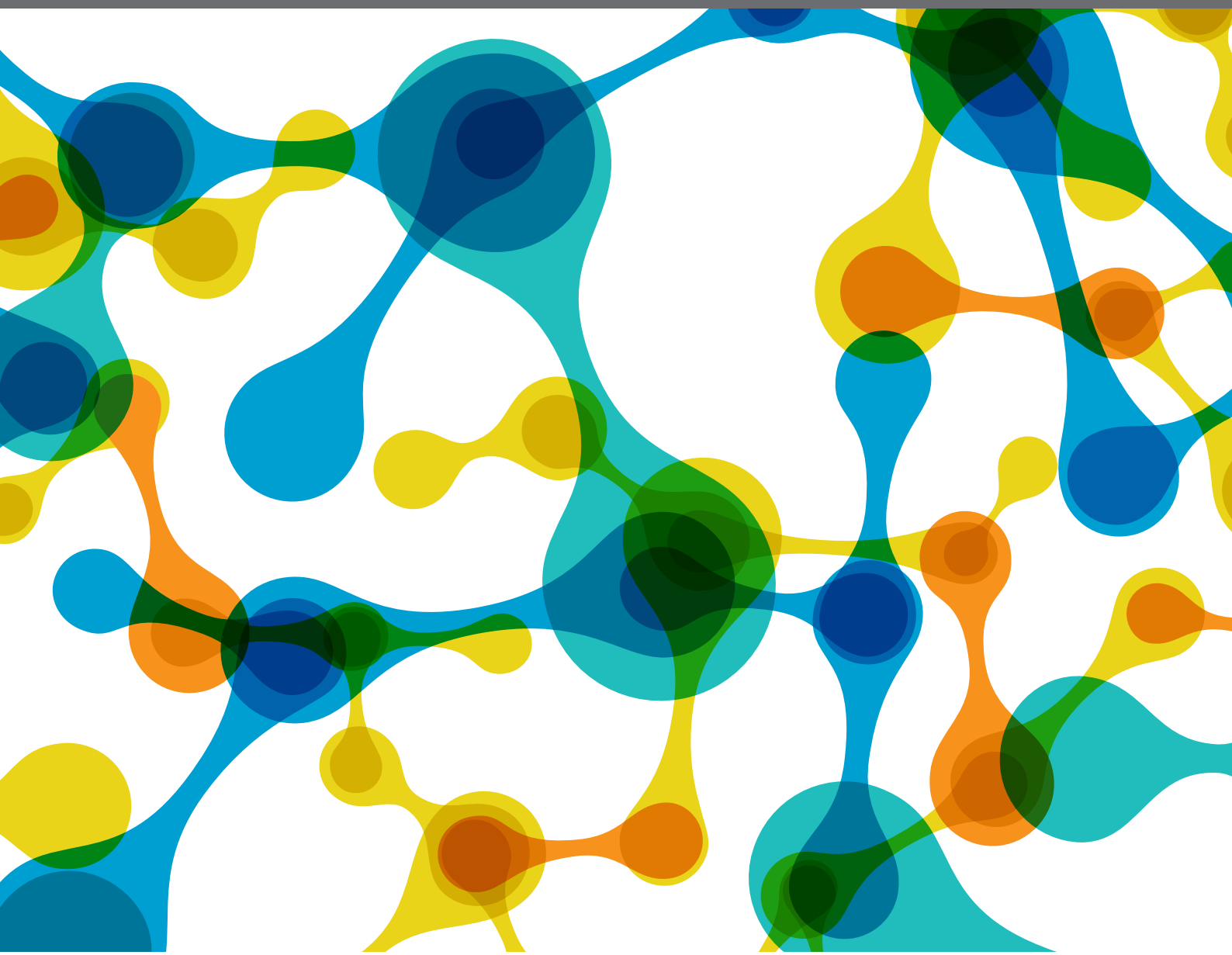

frontiers Research Topics

ISSN 1664-8714
ISBN 978-2-83250-542-7
DOI 10.3389/978-2-83250-542-7

About Frontiers

Frontiers is more than just an open-access publisher of scholarly articles: it is a pioneering approach to the world of academia, radically improving the way scholarly research is managed. The grand vision of Frontiers is a world where all people have an equal opportunity to seek, share and generate knowledge. Frontiers provides immediate and permanent online open access to all its publications, but this alone is not enough to realize our grand goals.

Frontiers Journal Series

The Frontiers Journal Series is a multi-tier and interdisciplinary set of open-access, online journals, promising a paradigm shift from the current review, selection and dissemination processes in academic publishing. All Frontiers journals are driven by researchers for researchers; therefore, they constitute a service to the scholarly community. At the same time, the Frontiers Journal Series operates on a revolutionary invention, the tiered publishing system, initially addressing specific communities of scholars, and gradually climbing up to broader public understanding, thus serving the interests of the lay society, too.

Dedication to Quality

Each Frontiers article is a landmark of the highest quality, thanks to genuinely collaborative interactions between authors and review editors, who include some of the world's best academicians. Research must be certified by peers before entering a stream of knowledge that may eventually reach the public - and shape society; therefore, Frontiers only applies the most rigorous and unbiased reviews.
Frontiers revolutionizes research publishing by freely delivering the most outstanding research, evaluated with no bias from both the academic and social point of view. By applying the most advanced information technologies, Frontiers is catapulting scholarly publishing into a new generation.

What are Frontiers Research Topics?

Frontiers Research Topics are very popular trademarks of the Frontiers Journals Series: they are collections of at least ten articles, all centered on a particular subject. With their unique mix of varied contributions from Original Research to Review Articles, Frontiers Research Topics unify the most influential researchers, the latest key findings and historical advances in a hot research area! Find out more on how to host your own Frontiers Research Topic or contribute to one as an author by contacting the Frontiers Editorial Office: frontiersin.org/about/contact

METHODS AND APPLICATIONS IN RESPIRATORY PHYSIOLOGY

Topic Editors:
Walter Araujo Zin, Federal University of Rio de Janeiro, Brazil
Mona Eskandari, University of California, Riverside, United States
Lorenzo Ball, University of Genoa, Italy

Citation: Zin, W. A., Eskandari, M., Ball, L., eds. (2022). Methods and Applications in Respiratory Physiology. Lausanne: Frontiers Media SA.
doi: 10.3389/978-2-83250-542-7

Table of Contents

frontiers | Frontiers in Physiology

TYPE Editorial
PUBLISHED 04 October 2022
DOI 10.3389/fphys.2022.1039039

OPEN ACCESS

EDITED AND REVIEWED BY
Andrew John Halayko,
University of Manitoba, Canada

*CORRESPONDENCE
Walter Araujo Zin,
walter_zin@hotmail.com

SPECIALTY SECTION
This article was submitted to Respiratory Physiology and Pathophysiology, a section of the journal Frontiers in Physiology

RECEIVED 07 September 2022
ACCEPTED 12 September 2022
PUBLISHED 04 October 2022

CITATION
Zin WA (2022), Editorial: Methods and applications in respiratory physiology. *Front. Physiol.* 13:1039039. doi: 10.3389/fphys.2022.1039039

Editorial: Methods and applications in respiratory physiology

Walter Araujo Zin*

Carlos Chagas Filho Institute of Biophysics, Universidade Federal do Rio de Janeiro, Rio de Janeiro, Brazil

KEYWORDS

respiratory physiology, pathophysiology, methods, lung, cell, organelle

Editorial on the Research Topic
Methods and applications in respiratory physiology

The Research Topic *Methods and Applications in Respiratory Physiology* focus on various methods and techniques applied to Respiratory Physiology. *Methods and Applications in Respiratory Physiology* welcomed contributions on new or existing methods and protocols that look at the respiratory system under organ, tissue, cellular, subcellular, and molecular lenses. The networking within the system and with other organs and functions of the organism was also highly appreciated. The overall type of contributions encompassed: (i) Methods: Including either existing methods that are significantly improved or adapted for specific purposes or new methods, which may also include primary (original) data; (ii) Protocols: Should provide a detailed description, with pitfalls and troubleshooting, and be of immediate use to the readers. The protocols must be proven to work. (iii) Perspective or General Commentaries on methods and protocols relevant for physiology research; and (iv) Reviews and mini-reviews of current methods and protocols highlighting the important future directions of the field. Hence, contributions based on biological, biochemical, biophysical, engineering, mathematical, behavioral and clinical approaches were encouraged. As a natural result, this Research Topic encompasses interesting topics from the whole lung down to the subcellular level, from biology to mathematics and physics, from models to new devices (Agrawal et al.; Aymerich et al.; Caldeira et al.; Gattarello et al.; Prisk; Krause-Sorio et al.; Sarabia-Vallejos et al.; Alapati and Shaffer; Barbas; Bayat et al.; Biselli et al.; Cao et al.; Choi et al.; Demoulin et al.; Godbole et al.; Guérin et al.; Kim et al.; Miserocchi et al.; Nof et al.; Patel et al.).

Aymerich et al. present a portable, low-cost and specific device for maximal inspiratory and expiratory pressures that could greatly facilitate monitoring of patients at point-of-care sites. Detailed technical information to easily reproduce the device is freely released and its design is available according to the open-source hardware approach. Considering that many lung models can be found in the literature, and pathophysiology and interactions between lungs and ventilators present challenges for

modeling efforts not yet thoroughly solved, Agrawal et al. developed a damaged-informed lung ventilator model relying in mathematizing ventilator pressure and volume waveforms. Their model has enough flexibility to reproduce commonly observed variability in clinical (human) and laboratory (mouse) waveform data, providing high fidelity estimates of pulmonary pathophysiological conditions. Demoulin et al. introduce a physical analog to assess surgical face mask airflow resistance during tidal ventilation. The physical analog was made of a plaster cast dummy head connected through a pneumotachograph to a series of bellows inflated/deflated by a ventilator. They measured the added respiratory mechanical load due to ten surgical masks tested in four different ways. Nof et al. describe a multicompartmental human airway on-chip platform to serve as a preclinical *in vitro* benchmark underlining regional lung crosstalk for viral infections pathways. The platform mimics key elements of the respiratory system including nasal passages that serve as the alleged origin of infections, the mid-bronchial airway region, and the peripheric acinar zone. The authors share detailed methodologies for fabricating, assembling, calibrating, and using the platform, including open-source fabrication files.

Sarabia-Vallejos et al. combine micro computed-tomography (micro-CT) and computational geometry algorithms to evaluate the regional distribution of key morphological parameters throughout the whole rat lung. They found that regional porosity, alveolar surface density and surface-to-volume ratio present a uniform distribution in normal lungs that is unaffected by gravitational effects. They also introduce a new dehydration protocol including methanol-PBS solution before dehydration that avoids the sample shrinking commonly found in ethanol-based protocols. Synchrotron radiation imaging methods are clearly described by Bayat et al. It offers unique properties of coherence, employed in phase-contrast imaging, and high flux as well as a wide energy spectrum. These properties allow the quantitative determination of lung morphology, and map regional lung ventilation, perfusion, inflammation, aerosol particle distribution and biomechanical properties with microscopic spatial resolution. Barbas discusses the use of thoracic-computed tomography (CT) in the assessment and treatment of patients with acute respiratory distress syndrome (ARDS) and COVID-19 pulmonary disease. Other than helping to correctly diagnose ARDS, CT can assist the adjustment of positive end-expiratory pressure, ideal tidal volume, and to position the patient during invasive mechanical ventilation. CT has been the most sensitive imaging technique to pinpoint pulmonary involvement in COVID-19 patients. Choi et al. applied CT image matching to assess the degree of pulmonary motion in idiopathic interstitial disease such as interstitial pneumonia (UIP) e nonspecific interstitial pneumonia (NUIP) patients. They report that lung motion quantified by image registration-based lower lobe dorsal-basal displacement may be used to assess the degree of motion reflecting limited motion owing to fibrosis in UIP and NUIP subjects.

Gattarello et al. studied pigs mechanically ventilated for 48 h and divided them into two groups: high or low pleural pressure. They assessed respiratory mechanics, hemodynamics, fluid, sodium, and osmotic balance at specific time points along the experimental duration. As a conclusion, the mechanical power and pleural pressure were positively associated with hemodynamic support maneuvers, increased sodium and fluid retention, and pulmonary edema. Interestingly, Miserocchi et al. report that the tendency to develop lung edema in edemagenic conditions, i.e., work in the face of hypoxia, is directly proportional to the ratio of lung capillary blood volume to the diffusion capacity of the alveolar membrane, as suggested by an estimate of the mechanical properties of the respiratory system with the forced oscillation technique. Cao et al. searched three online electronic databases, yielding seven studies, and report that elevated central venous pressure (CVP) and brain natriuretic peptide (BNP) levels are associated with extubation failure in critically ill patients and further suggest that BNP levels are more valuable than CVP levels in predicting extubation outcomes.

Efficiency of pulmonary gas exchange has long been assessed using the alveolar-arterial difference in partial pressure of oxygen ($A\text{-}aDO_2$). However, this measurement is invasive and unsuitable for serial measurements, since it requires arterial blood sample(s). According to Prisk, recent technological advances provide for portable and rapidly responding measurements of PO_2 and PCO_2 in expired gas, which combined with the usual determination of arterial oxygen saturation *via* pulse oximetry (SpO_2) make practical a non-invasive surrogate measurement of $A\text{-}aDO_2$. In fact, the approach shares the underlying basis of the measurement of gas exchange efficiency and simplifies the determination of the oxygen deficit. Godbole et al. advance that lung resection surgery carries significant risks of postoperative pulmonary complications (PPC). The authors prospectively determined the utility of resting measurements of physiologic dead space (VC) and physiologic dead space to tidal volume ratio (VD/VT) in predicting PPC in patients who underwent robotic-assisted lung resection and found that preoperative resting VD was significantly elevated in patients with PCC. They advance that the increase in resting VD may be a potentially useful predictor of PCC in patients under similar conditions.

Inspiratory muscle training (IMT) may improve respiratory and cardiovascular functions in obstructive sleep apnea (OSA). However, the available IMT protocols cannot be completed by some OSA patients. Hence, Krause-Sorio et al. describe a new 13-week OSA-friendly protocol for IMT and applied it to five sedentary OSA patients. The practice and subsequent 65% IMT resistance targets resulted in inspiratory strength gains that reached a steady-state by the end of 10 weeks of training and no report of adverse effects. Patel et al. present an extensive review concerning *methods and applications in respiratory physiology* and pathophysiology of neuromuscular and chest wall disorders. The authors cover respiratory muscles,

reduction in respiratory resistance and elastance, obesity, respiratory mechanical loads and reactional compensation, dyspnea, muscle fatigue, cough, respiratory muscle failure, evaluation of respiratory muscle function, airflow limitation, control of ventilation, sleep quality, oximetry and capnography, gene therapy, electrical and magnetic muscle stimulation, respiratory mechanics in neuro muscular diseases. Additionally, they present future promising research fields. Guérin et al. describe pathophysiological aspects of ARDS such as impairment of lung microvasculature, loss of alveolar aeration as a result of lesions to the small peripheral airways, as evidenced by high-resolution imaging techniques, atelectrauma, expiratory flow limitation, pattern of airway opening pressure disclosed in the inspiratory volume-pressure curve, functional interplay between airway opening pressure and expiratory flow limitation, and individualization of PEEP settings. Another review article by Biselli et al. addresses the use of respiratory mechanics in basic science to investigate asthma and chronic obstructive pulmonary disease (COPD), discusses the use of lung mechanics in clinical care and its role in the development of mechanical ventilators. Finally, they explore some or the difficult questions that intensive care personnel still face when managing respiratory failure.

The assessment of mitochondrial function in organs and tissues is essential to better understand their biochemistry, physiology, and pathophysiology. The evaluation of mitochondrial function is usually accomplished in isolated mitochondria, permeabilized fibers, or cells. These techniques are very well-defined in several types of tissue, e.g., heart, kidney, liver, adipose tissue, and brain. On the other hand, assessment of lung mitochondrial function presents difficulties associated with obtaining isolated, intact, coupled, and functional mitochondria. The methodological difficulty of obtaining viable lung mitochondria derives mainly from an elevated fatty acid content, low number of mitochondria in the cell, fibrous and air-filled tissue, and the required amount of tissue. To solve this issue, Caldeira et al. present an isolation protocol specific for lung tissue mitochondria and detail the mitochondrial function pertaining to several respiratory complexes.

Electrical impedance tomography (EIT) is an evolving technique that monitors physiological functions based on temporal changes in electrical conductivity in different tissues. Kim et al. measured tidal volumes by EIT in rabbit pups and compared the measurements to those provided by a mechanical ventilator. Three groups of animals were used: untreated (preterm), surfactant-treated (preterm) and control (term puppies). In all instances the results provided by EIT and mechanical ventilator were not different.

In a review article, Alapati and Shaffer address the use of inert liquids for respiratory support and as a vehicle to deliver biological agents to the respiratory system. They cover the respiratory support with inert liquids, clinical and non-clinical studies using inert liquids, and drug/gene product administration.

In conclusion, the studies published in this Research Topic confirm the broad range of methods and techniques used to address respiratory function in health and disease.

Author contributions

WZ wrote the Editorial.

Conflict of interest

The authors declare that the research was conducted in the absence of any commercial or financial relationships that could be construed as a potential conflict of interest.

Publisher's note

frontiers in Physiology

BRIEF RESEARCH REPORT
published: 26 August 2021
doi: 10.3389/fphys.2021.719372

Low-Cost Open-Source Device to Measure Maximal Inspiratory and Expiratory Pressures

Claudia Aymerich[1], *Miguel Rodríguez-Lázaro*[1], *Gorka Solana*[2], *Ramon Farré*[1,3,4] *and Jorge Otero*[1,3]*

[1] Unitat de Biofísica i Bioenginyeria, Facultat de Medicina i Ciències de la Salut, Universitat de Barcelona, Barcelona, Spain, [2] Faculdade de Engenharias e Tecnologias, Universidade Save – Moçambique, Maxixe, Mozambique, [3] Centro de Investigación Biomédica en Red de Enfermedades Respiratorias, Madrid, Spain, [4] Institut d'Investigacions Biomediques August Pi Sunyer, Barcelona, Spain

The measurement of maximal inspiratory (MIP) and maximal expiratory (MEP) pressures is a widely used technique to non-invasively evaluate respiratory muscle strength in clinical practice. The commercial devices that perform this test range from whole body plethysmographs to portable spirometers, both expensive and include a wide range of other respiratory tests. Given that a portable, low-cost, and specific option for MIP and MEP measuring device is not currently available in the market. A high-performance and easy-to-build prototype has been developed and the detailed technical information to easily reproduce it is freely released. A novel device is based on an Arduino microcontroller with a digital display, an integrated pressure transducer, and three-dimensional (3D) printed enclosure (total retail cost €80). The validation of the device was performed by comparison with a laboratory reference setting, and results showed accuracy within ±1%. As the device design is available according to the open-source hardware approach, measuring MIP/MEP can greatly facilitate easily available point-of-care devices for the monitoring of patients and, most important, for making this lung function measurement tool affordable to users in low- and middle-income countries.

Keywords: open-source hardware, measuring devices, respiratory monitoring, lung function, inspiratory and expiratory pressures, low cost devices, low and middle income countries, point-of-care

OPEN ACCESS

Edited by:
Lorenzo Ball,
University of Genoa, Italy

Reviewed by:
James Martin,
McGill University, Canada
Irene C. Solomon,
Stony Brook University, United States

***Correspondence:**
Jorge Otero
jorge.otero@ub.edu

Specialty section:
This article was submitted to Respiratory Physiology, a section of the journal Frontiers in Physiology

Received: *02 June 2021*
Accepted: *30 July 2021*
Published: *26 August 2021*

Citation:
Aymerich C, Rodríguez-Lázaro M, Solana G, Farré R and Otero J (2021) Low-Cost Open-Source Device to Measure Maximal Inspiratory and Expiratory Pressures. Front. Physiol. 12:719372. doi: 10.3389/fphys.2021.719372

INTRODUCTION

Measurement of maximal inspiratory (MIP) and maximal expiratory (MEP) pressures is an easy, non-invasive, and rapid test to assess the strength of the respiratory muscles (American Thoracic Society/European Respiratory Society, 2002; Caruso et al., 2015). MIP is the maximum negative pressure that can be generated by forced inspiration. It is generated by maximum contraction of the diaphragm and intercostal muscles which tend to increase the volume of the rib cage and consequently lung volume. MEP is the maximum positive pressure that can be generated on forced expiration when the abdominal muscles push the diaphragm and the internal intercostals up, thus tending to reduce the thorax and lung volumes. This test of breathing muscles is a routine procedure in the diagnosis of certain pulmonary diseases, specifically in patients with suspected respiratory muscle weakness. Some examples of very prevalent diseases which alter MIP/MEP values are chronic obstructive pulmonary disease (COPD), neuromuscular diseases, such as multiple sclerosis, or chronic heart failure (Laghi and Tobin, 2003; Kelley and Ferreira, 2017; Nambiar et al., 2018; Laveneziana et al., 2019).

Traditionally, the MIP/MEP test has been performed in lung function labs by means of whole-body plethysmography equipment, which is very expensive (>€50,000). In recent years, several companies have invested in the development of portable solutions, mainly regarding spirometry tests. Although the cost of these portable spirometers is significantly lower than the whole-body plethysmograph equipment, the devices are still too expensive (∼€2,000) for low- and middle-income countries (LMICs). Interestingly, affordable and easy-to-use open-source hardware electronics, such as Arduino, or distributed digital manufacturing strategies, such as three-dimensional (3D) printing, have become disruptive tools to design new research and medical devices in a cost-effective way without compromising the quality of the performance. Moreover, the development and commercialization of very accurate, easy-to-install, compensated, and/or amplified low-cost pressure sensors has also been a key fact for the expansion of this type of low-cost application. Accordingly, the objective of this work was to develop and test a portable, low-cost, and easy-to-build device to specifically measure MIP and MEP by using the technologies mentioned above. The aim was not to simply design a performance device but, following an open-source hardware approach (DePasse et al., 2016; Eslambolchilar and Thimbleby, 2016; Pearce, 2017), to freely release all the detailed technical information required to easily replicate the device. Hence, this new device is intended to expand the accessibility of a respiratory function test, applicable at the point of care (Beyette et al., 2011), that otherwise would require much more expensive equipment.

METHODS

The components and materials employed were chosen according to the rationale of developing a device very simple to replicate with easy-to-find components, mostly through e-commerce. The device consists of a development board with a microcontroller, a liquid crystal display (LCD) screen, a pressure transducer, a rechargeable 9 V battery block, a switch, a power supply base, and a customized enclosure produced by using any conventional 3D printer.

Electronic Components

The board chosen for this device is the Arduino Mega 2560 due to higher memory capacity to run the developed program than other Arduino boards (256 kB of FLASH memory and 8 kB of SRAM instead of 32 and 22 kB, respectively of the well-known Arduino UNO). The selected LCD touch screen (Open Smart 3.2-inch touch screen TFT LCD Shield) is compatible with the Arduino Mega 2560 and has a resolution of 240 × 400 pixels. The use of a touch screen avoids the need for buttons or any other external component to select the parameters for the measurement. The pressure transducer employed is a piezoresistive strain gauge. Considering that MIP and MEP values range from −100 cmH_2O to more than +140 cmH_2O, the SSCDRNN160MDAA5 (Honeywell pressure sensor, Charlotte, NC, US), with a differential pressure range of ±163 cmH_2O was chosen. This sensor is provided with in-factory calibration.

Driving Code

The operating code was developed with the Arduino Integrated Development Environment (Arduino IDE, Somerville, MA, US), which supports the C and C++ languages. The diagram of the developed code is shown in **Figure 1**. Briefly, a measuring session starts by asking the user to select running a MIP or MEP measurement, and then data acquisition starts immediately (see user manual in the **Supplementary File** "Technical_Description"). The acquisition lasts 5 s and is carried out with a sampling frequency of 70 Hz. After 5 s of data sampling (70 Hz), the device screen shows the corresponding pressure-time curve and the MIP/MEP value (computed as the maximum pressure sustained for 1 s) (Laveneziana et al., 2019), asking the user whether the maneuver should be accepted or not and whether a new maneuver will be carried out. After subsequent repeated maneuvers, the device shows all previously accepted maneuvers and indicates whether the quality control criterion to select the final result has been achieved: The maximum value of three maneuvers that vary by <10% (Laveneziana et al., 2019).

Three-Dimensional Enclosure

The device is designed to have two independent blocks. The first one is the hand-held framework (to be used by the MIP/MEP test technician) containing the electronics and digital display of the measurement process and results. The second one is a hand-held mouthpiece support to contain a disposable mouthpiece for the patient. Both blocks are connected through a 1-m length (3 mm ID) silicone tube. The mouthpiece framework incorporates two small holes. One of them communicates the airway opening (mouthpiece) to the pressure transducer through the silicon tube. The other orifice allows a small air-leak moving from/to the airway to the room air, which is required to prevent the closure of the glottis during forced inspiration and to decrease use of the oral muscles during forced expiration (Laveneziana et al., 2019).

Open Source Description

Detailed information of the circuits, electrical connections, driving code, and files for 3D printing are provided in **Supplementary File** "Technical_Description.zip."

Device Testing

The accuracy of the device was tested in a conventional way (Beyette et al., 2011) by comparing its performance with a reference laboratory setting based on a specifically calibrated and well-characterized pressure transducer. The signal of a reference transducer (Honeywell 26PC Series) was sampled with an AD/DA board and LabVIEW software, and stored for subsequently computing MIP/MEP with a Python 3 script of the same algorithm within the Arduino in the device under test. This allowed to precisely check all the measuring steps carried out by the Arduino setting in the device. For the performance test, the pressure outlet of the device mouthpiece framework was sensed simultaneously by the device sensor and the reference setting sensor. Two subjects from the technical staff who were familiar with the MIP/MEP measurements performed a series of 64 maneuvers with different intensities to mimic the ample range of values found in clinical practice. The degree of agreement

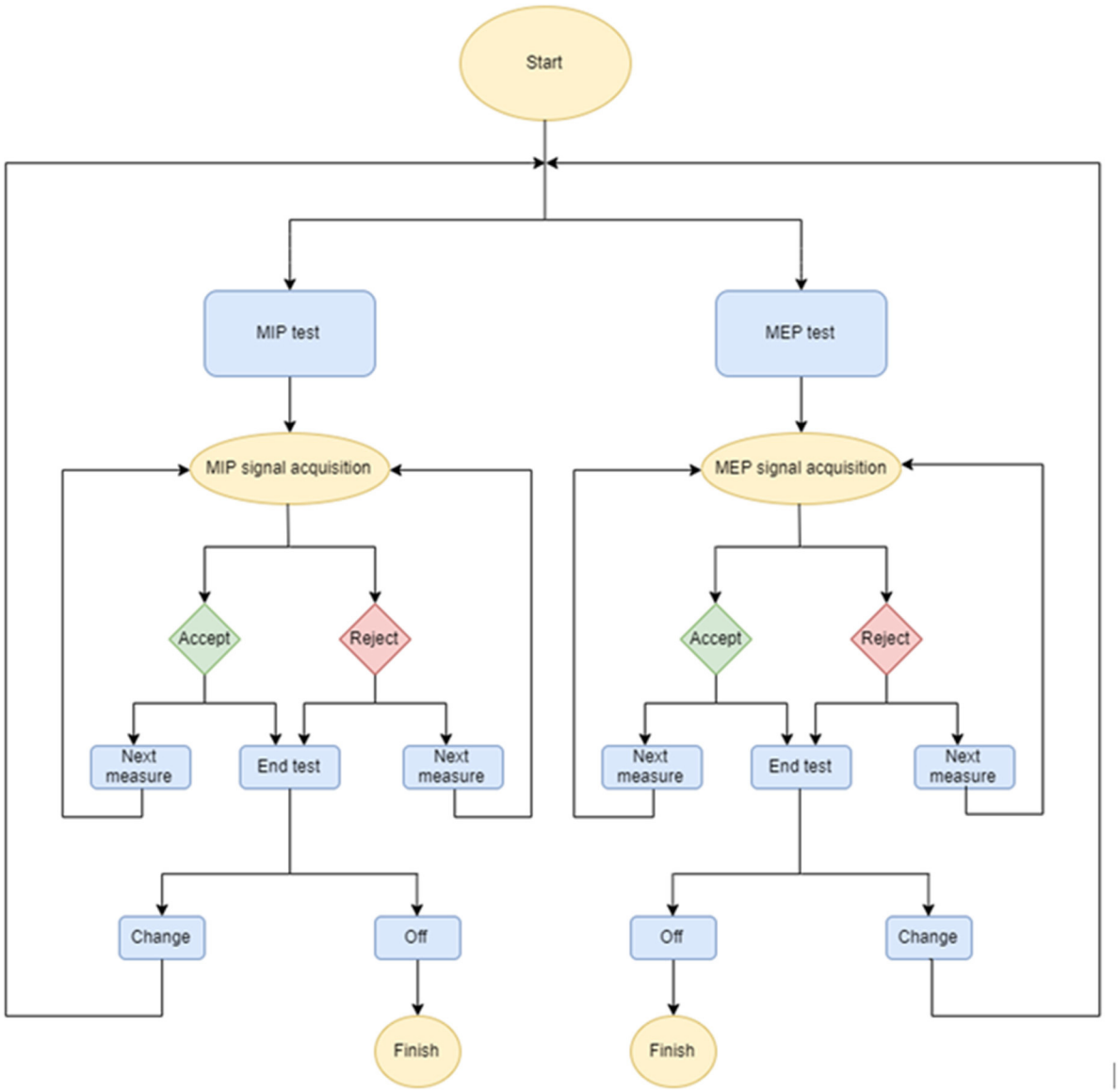

FIGURE 1 | Flow diagram of the maximal inspiratory (MIP) and maximal expiratory (MEP) pressures device.

between measures obtained by the designed device and reference equipment was carried out by Bland–Altman analysis. Moreover, a linear regression plot was carried out for evaluating the device vs. the reference equipment measurements.

RESULTS

An image of the assembled prototype is shown in **Figure 2**. This figure (bottom) also shows a view of one of the screens of the device appearing during the acquisition of an MEP signal. Importantly, **Table 1** summarizes the components cost of the prototype which amounted to €80.

The results obtained when the device was evaluated by comparison with a laboratory reference setting are presented in **Figure 3** by means of the Bland–Altman (top) and linear regression (bottom) plots. The obtained average difference in MIP/MEP values from the prototype and the lab reference setting was 0.13 cmH_2O (range of agreement from −0.86 to 1.12 cmH_2O), which corresponds to ±1% accuracy. Therefore, the developed device is fully suitable to perform MIP and MEP measurements within clinical ranges.

DISCUSSION

Following the aim of this methodological work, we have designed and tested a low-cost device for measuring MIP/MEP and provided full open-source technical details allowing any

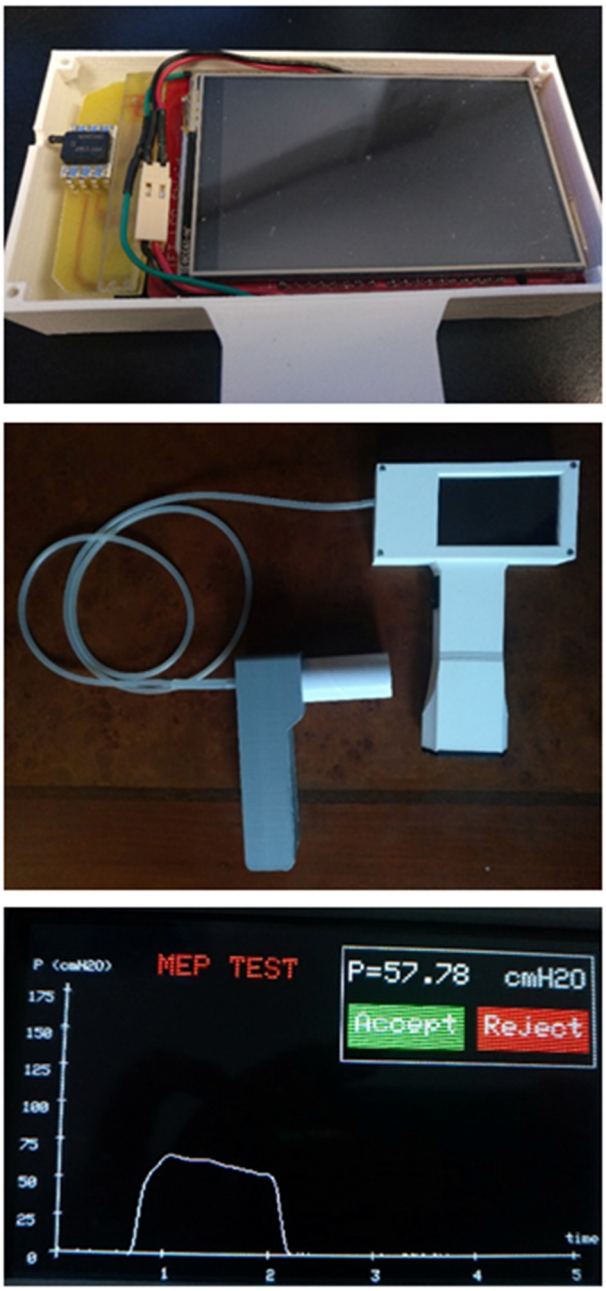

FIGURE 2 | (Top) Inside view of the MIP and MEP device prototype showing the operator enclosure, the pressure transducer, and the liquid crystal display (LCD) screen [on top of the Arduino controller (not visible)]. (Center) Complete external view of the device showing the operator hand-held block and the mouthpiece block for the patient, connected through a silicone flexible tube. (Bottom) Example of one of the screens during device operation, showing the result of an MEP maneuver test (time course of expiratory pressure, MEP result, and option to allow the user to accept or reject this specific maneuver).

TABLE 1 | Retail cost of components used in the device.

Component	Price	Units	Total
Arduino Mega 2560	35 €	1	35 €
LCD	20 €	1	20 €
Transducer	10.36 €	1	10.36 €
PCB copper sheet	4.57 €	1	4.57 €
PLA (for 3D printer)	20 €/kg	0.25 kg	5 €
Silicone tube	0.47 €/m	1 m	0.47 €
Switch	1.29 €	1	1.29 €
Power supply base	0.83 €	1	0.83 €
Total			77.52 €

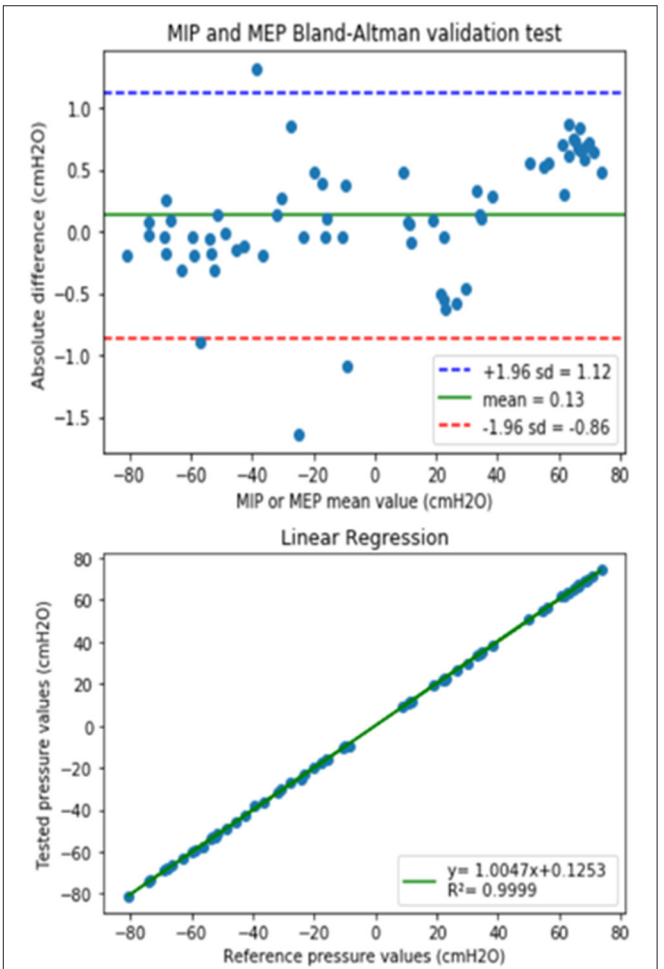

FIGURE 3 | (Top) The Bland–Altman plot showing the difference between values measured by the prototype and the reference equipment, as a function of the measured values for both MIP (negative values) and MEP (positive values). Green line is the prototype bias and blue-red lines indicate the limits of agreement. (Bottom) Linear regression of the values obtained with the developed device and the laboratory reference.

interested user to directly reproduce or modify it according to the specific requirements.

The standard MIP/MEP test is aimed at non-invasively and selectively assessing the strength of inspiratory and expiratory muscles. Correct performance of this technique requires following the indications published by medical societies, such

as the American Thoracic Society (ATS) and the European Respiratory Society (ERS) that agreed to establish a standard protocol, which was published in 2002 (American Thoracic Society/European Respiratory Society, 2002) and was updated by the ERS in 2019 (Laveneziana et al., 2019). In practice, MIP/MEP measurements are obtained in the seated position of patient. Maximum inspiratory (Mueller maneuver) and maximal expiratory (Valsalva maneuver) measurements should be supervised by a trained technician, who must ask the patient to exert his/her maximal effort. Both forced inspiratory and expiratory muscle efforts should ideally be maintained for at least 1.5 s, allowing that maximum pressure is measured for a 1-s period. The MIP/MEP device should give a visual feedback of the patient maneuver by displaying the pressure-time curve and the value of the 1-s average maximum pressure. After observing the pressure-time curve along the maneuver, the technician should determine whether it has been satisfactorily performed. Finally, the maximum value of three correctly performed maneuvers which vary by <10% is the retained figure (Laveneziana et al., 2019). The algorithm implemented in the designed device follows these recommendations and guides the technician along a clear and user-friendly procedure. Moreover, the low-cost device presented herein covers all the potential wide range of pressures that can be found in both healthy young people and in patients with severe dysfunction of respiratory muscles, with high accuracy (**Figure 3**).

The MIP/MEP measurement technique is in fact very simple from both conceptual and technical viewpoints. Indeed, it is based on recording pressures at the mouthpiece, computing the average of high pressures along a 1-s of stable inspiratory/expiratory effort, and providing the variability among values in subsequent maneuvers to select the maximum value among several representative muscle efforts. The design and construction of the device illustrate how fruitful could be a multidisciplinary approach. In fact, common projects carried out following a collaborative scheme have already produced several examples of low-cost open-source devices for both research and treatment (Farré et al., 2019a,b; Garmendia et al., 2020; Osuna et al., 2021).

The novelty of the device described here is that it is low-cost and easy-to-build from fully disclosed technical information. Indeed, other simple devices with a similar function were described but the technical details allowing their simple replication by other potential users were not provided (Smith and Royall, 1992; Hamnegård et al., 1994; Maruthy and Vaz, 1999; Torres-Castro et al., 2019). Accordingly, this device is of interest for two potential application scenarios. On the one hand, it may facilitate the affordable provision of a considerable number of devices to be used as point-of-care tools (Pearce, 2012). Indeed, MIP/MEP measurements have potential interest for monitoring respiratory muscle strength as a biomarker of progress/recovery in extremely prevalent diseases, such as COPD and heart failure. Having affordable MIP/MEP devices available for extended home monitoring of patients may allow for carrying out clinical studies that otherwise would not be possible. On the other hand, the device described in this work opens the opportunity to provide a low-cost tool to patients and doctors in low- and middle-income countries (LMICs). In this regard, it is interesting to mention that the low-tech components required to build the device make it possible that its construction and maintenance are performed by teams of engineers in LMICs (De Maria et al., 2014; Mackintosh et al., 2018). It is also noteworthy that the collaborative approach followed in this study, consisting of co-creation and design thinking (Ranger and Mantzavinou, 2018) by teams in Mozambique and Barcelona may help toward moving the design focus from the developed country perspective to that of the LMIC team and to potentially stimulate the development of local industry (Clifford and Zaman, 2016).

DATA AVAILABILITY STATEMENT

The original contributions presented in the study are included in the article/**Supplementary Material**, further inquiries can be directed to the corresponding author/s.

AUTHOR CONTRIBUTIONS

JO and RF: conception and supervision of the study. MR-L, CA, and GS: experimental design and implementation. CA, MR-L, and RF: draft preparation. RF and JO: manuscript edition. All authors final manuscript review and approval.

ACKNOWLEDGMENTS

Design and construction of the device was the work presented as Final Degree Thesis of Biomedical Engineering by CA of this report. The authors acknowledge the teaching team of the Unit of Biophysics and Bioengineering (School of Medicine and Health Sciences, University of Barcelona, Barcelona, Spain) for supporting this study.

SUPPLEMENTARY MATERIAL

The Supplementary Material for this article can be found online at: https://www.frontiersin.org/articles/10.3389/fphys.2021.719372/full#supplementary-material

REFERENCES

American Thoracic Society/European Respiratory Society (2002). ATS/ERS Statement on respiratory muscle testing. *Am. J. Respir. Crit. Care Med.* 166, 518–624. doi: 10.1164/rccm.166.4.518

Beyette, F. R. Jr., Gaydos, C. A., Kost, G. J., and Weigl, B. H. (2011). Point-of-care technologies for health care. *IEEE Trans. Biomed. Eng.* 58:732–735. doi: 10.1109/TBME.2011.2109251

Caruso, P., de Albuquerque, A. L. P., Santana, P. V., Cardenas, L. Z., Ferreira, J. G., Prina, E., et al. (2015). Diagnostic methods to assess

inspiratory and expiratory muscle strength. *J. Bras. Pneumol.* 41, 110–123. doi: 10.1590/S1806-37132015000004474

Clifford, K. L., and Zaman, M. H. (2016). Engineering, global health, and inclusive innovation: focus on partnership, system strengthening, and local impact for SDGs. *Glob. Health Action* 9:30175. doi: 10.3402/gha.v9.30175

De Maria, C., Mazzei, D., and Ahluwalia, A. (2014). "Open source biomedical engineering for sustainability in African healthcare: combining academic excellence with innovation," in *Proceedings of the ICDS 2014, The Eighth International Conference on Digital Society* (Barcelona), 48–53. Available online at: https://www.thinkmind.org/articles/icds_2014_2_40_10173.pdf (accessed August 10, 2021).

DePasse, J. W., Caldwell, A., Santorino, D., Bailey, E., Gudapakkam, S., Bangsberg, D., et al. (2016). Affordable medical technologies: bringing value-based design into global health. *BMJ Innov.* 2, 4–7. doi: 10.1136/bmjinnov-2015-000069

Eslambolchilar, P., and Thimbleby, H. (2016). Open-source hardware for medical devices. *BMJ Innov.* 2, 78–83. doi: 10.1136/bmjinnov-2015-000080

Farré, R., Montserrat, J. M., Solana, G., Gozal, D., and Navajas, D. (2019a). Easy-to-build and affordable continuous positive airway pressure CPAP device for adult patients in low-income countries. *Eur. Respir. J.* 53:1802290. doi: 10.1183/13993003.02290-2018

Farré, R., Trias, G., Solana, G., Ginovart, G., Gozal, D., and Navajas, D. (2019b). Novel approach for providing pediatric continuous positive airway pressure devices in low-income, underresourced regions. *Am. J. Respir. Crit. Care Med.* 199, 118–120. doi: 10.1164/rccm.201808-1452LE

Garmendia, O., Rodríguez-Lazaro, M. A., Otero, J., Phan, P., Stoyanova, A., Dinh-Xuan, A. T., et al. (2020). Low-cost, easy-to-build noninvasive pressure support ventilator for under-resourced regions: open source hardware description, performance and feasibility testing. *Eur. Respir. J.* 55:2000846. doi: 10.1183/13993003.00846-2020

Hamnegård, C. H., Wragg, S., Kyroussis, D., Aquilina, R., Moxham, J., and Green, M. (1994). Portable measurement of maximum mouth pressures. *Eur. Respir. J.* 7, 398–401. doi: 10.1183/09031936.94.07020398

Kelley, R. C., and Ferreira, L. F. (2017). Diaphragm abnormalities in heart failure and aging: mechanisms and integration of cardiovascular and respiratory pathophysiology. *Heart Fail. Rev.* 22, 191–207. doi: 10.1007/s10741-016-9549-4

Laghi, F., and Tobin, M. J. (2003). Disorders of the respiratory muscles. *Am. J. Respir. Crit. Care Med.* 168, 10–48. doi: 10.1164/rccm.2206020

Laveneziana, P., Albuquerque, A., Aliverti, A., Babb, T., Barreiro, E., Dres, M., et al. (2019). ERS statement on respiratory muscle testing at rest and during exercise. *Eur. Respir. J.* 53:1801214. doi: 10.1183/13993003.01214-2018

Mackintosh, M., Tibandebage, P., Karimi Njeru, M., Kungu, J. K., Israel, C., and Mujinja, P. G. M. (2018). Rethinking health sector procurement as developmental linkages in East Africa. *Soc. Sci. Med.* 200, 182–189. doi: 10.1016/j.socscimed.2018.01.008

Maruthy, K. N., and Vaz, M. (1999). The development and validation of a digital peak respiratory pressure monitor and its characteristics in healthy human subjects. *Indian J. Physiol. Pharmacol.* 43, 186–192.

Nambiar, V., Ravindra, S., and Kumar, B. N. (2018). Maximal inspiratory and expiratory pressures in men with chronic obstructive pulmonary disease: a cross-sectional study. *Indian J. Respir. Care* 7:88. doi: 10.4103/ijrc.ijrc_5_18

Osuna, A., Ulldemolins, A., Sanz-Fraile, H., Otero, J., Farré, N., Farré, R., et al. (2021). Experimental setting for applying mechanical stimuli to study the endothelial response of *ex vivo* vessels under realistic pathophysiological environments. *Life* 11:671. doi: 10.3390/life11070671

Pearce, J. M. (2012). Building research equipment with free, open-source hardware. *Science* 337, 1303–1304. doi: 10.1126/science.1228183

Pearce, J. M. (2017). Maximizing returns for public funding of medical research with open-source hardware. *Health Policy Technol.* 6, 381–382. doi: 10.1016/j.hlpt.2017.09.001

Ranger, B. J., and Mantzavinou, A. (2018). Design thinking in development engineering education: a case study on creating prosthetic and assistive technologies for the developing world. *Dev. Eng.* 3, 166–174. doi: 10.1016/j.deveng.2018.06.001

Smith, P. E., and Royall, R. A. (1992). A portable mouth pressure meter. *Anaesthesia* 47, 144–145. doi: 10.1111/j.1365-2044.1992.tb02014.x

Torres-Castro, R., Sepúlveda-Cáceres, N., Garrido-Baquedano, R., Barros-Poblete, M., Otto-Yáñez, M., Vasconcello, L., et al. (2019). Agreement between clinical and non-clinical digital manometer for assessing maximal respiratory pressures in healthy subjects. *PLoS ONE* 14:e0224357. doi: 10.1371/journal.pone.0224357

Conflict of Interest: The authors declare that the research was conducted in the absence of any commercial or financial relationships that could be construed as a potential conflict of interest.

Publisher's Note: All claims expressed in this article are solely those of the authors and do not necessarily represent those of their affiliated organizations, or those of the publisher, the editors and the reviewers. Any product that may be evaluated in this article, or claim that may be made by its manufacturer, is not guaranteed or endorsed by the publisher.

frontiers in Physiology

ORIGINAL RESEARCH
published: 13 September 2021
doi: 10.3389/fphys.2021.743153

Role of Fluid and Sodium Retention in Experimental Ventilator-Induced Lung Injury

Simone Gattarello[1], Iacopo Pasticci[1], Mattia Busana[1], Stefano Lazzari[1], Paola Palermo[1], Maria Michela Palumbo[1], Federica Romitti[1], Irene Steinberg[1], Francesca Collino[2], Francesco Vassalli[1], Thomas Langer[3,4], Onnen Moerer[1], Leif Saager[1], Peter Herrmann[1], Paolo Cadringher[1], Konrad Meissner[1], Michael Quintel[1,5] and Luciano Gattinoni[1]*

[1] Department of Anesthesiology, University Medical Centre Göttingen, Göttingen, Germany, [2] Department of Anesthesia, Intensive Care and Emergency, "Città della Salute e della Scienza" Hospital, Turin, Italy, [3] Department of Medicine and Surgery, University of Milano-Bicocca, Milan, Italy, [4] Department of Anesthesia and Intensive Care Medicine, Niguarda Ca' Granda, Milan, Italy, [5] Department of Anesthesiology, Intensive Care and Emergency Medicine Donau-Isar-Klinikum Deggendorf, Deggendorf, Germany

OPEN ACCESS

Edited by:
Walter Araujo Zin, Federal University of Rio de Janeiro, Brazil

Reviewed by:
Fernanda Ferreira Cruz, Federal University of Rio de Janeiro, Brazil
Carmen Silvia Valente Barbas, University of São Paulo, Brazil

***Correspondence:**
Simone Gattarello
gattarello@gmail.com

Specialty section:
This article was submitted to Respiratory Physiology, a section of the journal Frontiers in Physiology

Received: *17 July 2021*
Accepted: *20 August 2021*
Published: *13 September 2021*

Citation:
Gattarello S, Pasticci I, Busana M, Lazzari S, Palermo P, Palumbo MM, Romitti F, Steinberg I, Collino F, Vassalli F, Langer T, Moerer O, Saager L, Herrmann P, Cadringher P, Meissner K, Quintel M and Gattinoni L (2021) Role of Fluid and Sodium Retention in Experimental Ventilator-Induced Lung Injury. Front. Physiol. 12:743153. doi: 10.3389/fphys.2021.743153

Background: Ventilator-induced lung injury (VILI) via respiratory mechanics is deeply interwoven with hemodynamic, kidney and fluid/electrolyte changes. We aimed to assess the role of positive fluid balance in the framework of ventilation-induced lung injury.

Methods: *Post-hoc* analysis of seventy-eight pigs invasively ventilated for 48 h with mechanical power ranging from 18 to 137 J/min and divided into two groups: high vs. low pleural pressure (10.0 ± 2.8 vs. 4.4 ± 1.5 cmH_2O; $p < 0.01$). Respiratory mechanics, hemodynamics, fluid, sodium and osmotic balances, were assessed at 0, 6, 12, 24, 48 h. Sodium distribution between intracellular, extracellular and non-osmotic sodium storage compartments was estimated assuming osmotic equilibrium. Lung weight, wet-to-dry ratios of lung, kidney, liver, bowel and muscle were measured at the end of the experiment.

Results: High pleural pressure group had significant higher cardiac output (2.96 ± 0.92 vs. 3.41 ± 1.68 L/min; $p < 0.01$), use of norepinephrine/epinephrine (1.76 ± 3.31 vs. 5.79 ± 9.69 mcg/kg; $p < 0.01$) and total fluid infusions (3.06 ± 2.32 vs. 4.04 ± 3.04 L; $p < 0.01$). This hemodynamic status was associated with significantly increased sodium and fluid retention (at 48 h, respectively, 601.3 ± 334.7 vs. 1073.2 ± 525.9 mmol, $p < 0.01$; and 2.99 ± 2.54 vs. 6.66 ± 3.87 L, $p < 0.01$). Ten percent of the infused sodium was stored in an osmotically inactive compartment. Increasing fluid and sodium retention was positively associated with lung-weight ($R^2 = 0.43$, $p < 0.01$; $R^2 = 0.48$, $p < 0.01$) and with wet-to-dry ratio of the lungs ($R^2 = 0.14$, $p < 0.01$; $R^2 = 0.18$, $p < 0.01$) and kidneys ($R^2 = 0.11$, $p = 0.02$; $R^2 = 0.12$, $p = 0.01$).

Conclusion: Increased mechanical power and pleural pressures dictated an increase in hemodynamic support resulting in proportionally increased sodium and fluid retention and pulmonary edema.

Keywords: ventilation-induced lung injury, mechanical ventilation, fluid balance, sodium retention, non-osmotic sodium

INTRODUCTION

It is well known that positive pressure mechanical ventilation is associated with hemodynamic impairment and sodium and water retention (Drury et al., 1947). In the late 70 s, Hemmer and Suter suggested the use of vasoactive drugs rather than fluid infusions to achieve adequate perfusion while preventing fluid overload (Hemmer and Suter, 1979). In daily clinical practice, both fluids and cardiovascular drugs are commonly used to compensate for the detrimental hemodynamic effects of mechanical ventilation, despite the common notion that positive fluid balance is associated with worse outcomes (Mendes et al., 2020). However, it is not clear to what degree this is a simple association or a cause-effect relationship.

In a series of animal experiments aimed to elucidate some of the mechanisms of ventilator-induced lung injury (VILI), the animals often required large amounts of fluids and catecholamines to prevent hemodynamic collapse (Collino et al., 2019; Vassalli et al., 2020). This approach is similar to what it is routinely done in clinical practice: to maintain adequate hemodynamics the fluid infused into the patient can amount to several liters (Boyd et al., 2011). This is generally (and unfortunately) assumed to be an aesthetic rather than a harmful phenomenon, and at least not the primary cause of clinical worries (Vignon et al., 2020).

We hypothesized that an increased fluid balance may worsen the pulmonary function and VILI development, hence, the primary objective of the present study was to investigate whether the applied pleural pressure and positive fluid balance have a synergistic role in dictating the VILI severity, quantified by the increase of lung weight.

MATERIALS AND METHODS

In the present *post-hoc* analysis, data of seventy-eight pigs from two previous experimental studies investigating the relationship between mechanical power and VILI (Collino et al., 2019; Vassalli et al., 2020) were analyzed (see **Supplementary Material**). In the first study 36 pigs [weight (mean ± SD): 23.3 ± 2.3 kg] were ventilated for 48 h with tidal volume equal to the functional residual capacity, respiratory rate 30 bpm and different levels of PEEP: 0, 4, 7, 11, 14, and 18 cmH_2O. The applied mechanical power ranged between 18 to 120 J/min (Collino et al., 2019).

In the second study, 42 pigs (mean weight 24.2 ± 2.0 kg) were ventilated for 48 h and were randomized into six groups, 3 of which at low (15 J/min) and 3 at high mechanical power (30 J/min). In each group, the targeted mechanical power was reached with different combinations of PEEP, tidal volume and respiratory rate. In the whole cohort, the tidal volume ranged from 0.5 to 3.8 L, the respiratory rate from 5 to 44 bpm and the PEEP from 5 to 25 cmH_2O (Vassalli et al., 2020).

Management of Experimental Animals

In both experiments, anesthesia was induced and maintained with propofol, midazolam and sufentanil. After intubation, volume-control mechanical ventilation was initiated with tidal volume 6 mL/kg, PEEP 5 cmH_2O and a respiratory rate to maintain $PaCO_2$ between 35 and 45 mmHg.

The animals had the following devices: endotracheal tube (size 7/7.5 mm); urinary catheter (5 Fr); adult esophageal catheter (8 Fr) Smartcath with esophageal balloon (the correct positioning of the esophageal catheter was checked by an end-expiratory occlusion test); central venous catheter (5 Fr) in the jugular vein, ultrasound-guided; swan-Ganz catheter (5 Fr) through an introducer (7 Fr) in the jugular vein, ultrasound guided; arterial PiCCO catheter (5 Fr) in the femoral artery, ultrasound guided. The target temperature was maintained throughout the experiment between 38 and 39°C (normal central temperature of pigs), by using a thermic blanket. Glycaemia was measured throughout the experiment, if values lower than 60 mg/dL were observed, dextrose 40% was initiated and maintained at the lowest infusion rate, in order to ensure glycemic levels between 60 and 100 mg/dL.

At the end of the experiment the animal was euthanized, autopsy was performed and lung, kidney, liver, muscle and bowel samples were sent to the pathology department. Six lung samples were collected for each lung (basal-ventral, basal-dorsal, central-ventral, central dorsal, apical-ventral, apical-dorsal) and one sample for the other organs. Wet-to-dry ratio was calculated as follow: each sample (~2 g of weight) was weighted before and after being heated and dried in an oven at 50 degrees, during 24 h.

Both studies were approved by the local ethic committee (nr. 16/2223 and nr. 18/2795, Niedersächsisches Landesamt für Verbraucherschutz und Lebensmittelsicherheit LAVES, Oldenburg, Niedersachsen, Germany) (Collino et al., 2019; Vassalli et al., 2020).

Animal Experiments and Study Groups

For the purpose of this study, the animals were divided in two groups according to the median value of the calculated pleural pressure (Ppl_{mean}) (Gattinoni et al., 2003):

$$P_{pl_{mean}} = P_{aw_{mean}} \cdot \frac{E_{CW}}{E_{RS}}$$

where Paw_{mean} is the mean airway pressure, E_{CW} is the chest-wall elastance, and E_{RS} is the total elastance of the respiratory system. Pleural pressure was chosen as the study variable because it is the most established determinant of hemodynamic changes, in mechanical ventilation.

Measured Variables

Respiratory mechanics: plateau pressure, PEEP, tidal volume and esophageal pressure were recorded hourly, as well as their derived variables: total/chest-wall/lung elastances and total/lung mechanical power.

Hemodynamic variables: heart rate, pulmonary/systemic blood pressure, cardiac output, pulmonary/systemic vascular resistances were measured every 6 h.

Laboratory variables: sodium concentration (in plasma and urine) and osmolarity (in plasma) were measured at 0, 6, 12, 24, and 48 h.

Sodium retention (Na^+_{ret}; mmol) was computed at each timepoint as the infused sodium minus the sodium

excreted by urine (see **Supplementary Material** for detailed explanation and equation).

Fluid balance (V_{ret}) was computed as the amount of infused fluids minus the urinary output.

Fluid Management

Maintenance fluid consisted of 1–2 mL/h of Sterofundin infusion throughout the experiment. Additional fluids were administered in form of Sterofundin or Gelafundin ISO 4% fluid challenge (250 mL in 5–10 min) if: MAP < 60 mmHg; clinical signs of hypoperfusion (raised lactates, skin mottling, decreased urine output); hemodynamic monitoring dynamic indices (pulse pressure variation > 13% or systolic volume variation > 12%). Norepinephrine was initiate if the animal was not fluid responsive.

Calculation of Sodium Infusion

Milliliters of infused solutions times the sodium content of normal saline (0.154 mmol/mL), Sterofundin (0.145 mmol/mL) and Gelafundin ISO 4% (0.151 mmol/mL). All fluids were included in the analysis either if they were infused as fluid challenge, maintenance or for drug dilution.

Calculation of Retained Sodium and Fluids

Retained sodium: amount of infused fluid times the sodium concentration of the specific fluid (normal saline 154 mmol/L, sterofundin 145 mmol/L and gelafundin ISO 4% 151 mmol/L), minus the amount of urine in milliliters times the urinary sodium concentration:

$$Na^{+}_{ret} = [Na^{+}]_{inf} \times V_{inf} - [Na^{+}]_{u} \times V_{u}$$

where $[Na^{+}]_{inf}$ (mmol/L) is the sodium concentration of the infused fluids, V_{inf} (L) is the amount of fluid infused during an experiment interval, $[Na^{+}]_{u}$ (mmol/L) and V_{u} (L) are the urine sodium concentration and volume during the same interval. We only included the fraction of dissociated sodium, and excluded the sodium bound to drug molecules.

Fluid balance (V_{ret}) was computed as the amount of infused fluids minus the urinary output:

$$V_{ret} = V_{inf} - V_{u}$$

where V_{inf} (L) is the infused fluid and V_{u} (L) is the urinary output.

Two-Compartment Kinetic Model and Mass Balance Equations

To investigate the sodium distribution between intracellular/extracellular compartments and the non-osmotic sodium storage, the following assumptions were made: (1) extracellular and intracellular compartments equal 20 and 40% of the pig body weight (Svensson et al., 2020); (2) the osmotic concentration between the two compartments is equal and the equilibrium is maintained by means of water shifts; (3) the count of milliosmoles in the extracellular fluid at the end of any timepoint must be equal to the initial amount of milliosmoles plus the milliosmoles due to the retained sodium ($Na^{+}_{ret} \times 2$); (4) the milliosmoles exceeding this equilibrium were classified as missing sodium (Na^{+}_{miss}), i.e., sodium stored in a non-osmotic form.

Figure 1 depicts the two-chamber kinetic model we applied to assess the distribution of sodium and fluids across the body compartments. At baseline, the extracellular (ECV_{bas}) and intracellular (ICV_{bas}) volumes were assumed to be in osmotic equilibrium (Osm_{bas}), i.e., the osmolar concentration (Osm_{bas}) was equal in ECV_{bas} and ICV_{bas} (**Figure 1A**). As shown in **Figure 1B**, the net retained sodium and fluid (infused minus excreted) are confined within the extracellular volume, i.e., before the osmotic equilibrium (ECV_{beq}). In this condition, the osmotic and sodium concentrations are higher in the extracellular volume and therefore, to reach the osmotic equilibrium, water must shift from the intracellular to the extracellular compartment. Furthermore (**Figure 1C**), we assumed the osmotic concentration to be equal between compartments (ECV_{aeq} and ICV_{aeq}) and the osmotic equilibrium is achieved through the fluid shift from compartments.

The following equations were used to calculate osmolarity, extracellular and intracellular volumes, fluid shift and sodium concentration:

(1) We computed the osmolarity (Osm_{beq}) and the extracellular volume (ECV_{beq}) before the osmotic equilibrium as shown in **Figure 1B**, according to the following equations:

$$[Osm]_{beq} = ([Osm]_{bas} \times ECV_{bas} + 2Na^{+}_{ret})/(ECV_{bas} + V_{ret})$$

$$ECV_{beq} = ECV_{bas} + V_{ret}$$

Where $[Osm]_{bas}$ is osmolarity at baseline, ECV_{bas} is the baseline extracellular volume, Na^{+}_{ret} is the net retained sodium and V_{ret} is the fluid retained.

(2) We computed the osmolarity at equilibrium ($[Osm]_{aeq}$) and the fluid required to reach it (V_{shift}) with the following equations (**Figure 1C**):

$$[Osm]_{aeq} = ([Osm]_{beq} \times ECV_{beq} + [Osm]_{bas} \times ICV_{bas})$$

$$/(ECV_{bas} + ICV_{bas} + V_{ret})$$

$$V_{shift} = ([Osm]_{beq} \times ECV_{beq} - [Osm]_{aeq} \times ECV_{beq})/[Osm]_{aeq}$$

Where ICV_{bas} is the baseline intracellular volume.

(3) We computed the new values of extracellular (ECV_{aeq}) and intracellular (ICV_{aeq}) volumes after the osmotic equilibrium (**Figure 1C**):

$$ECV_{aeq} = ECV_{beq} + V_{shift}$$

$$ICV_{aeq} = ICV_{bas} - V_{shift}$$

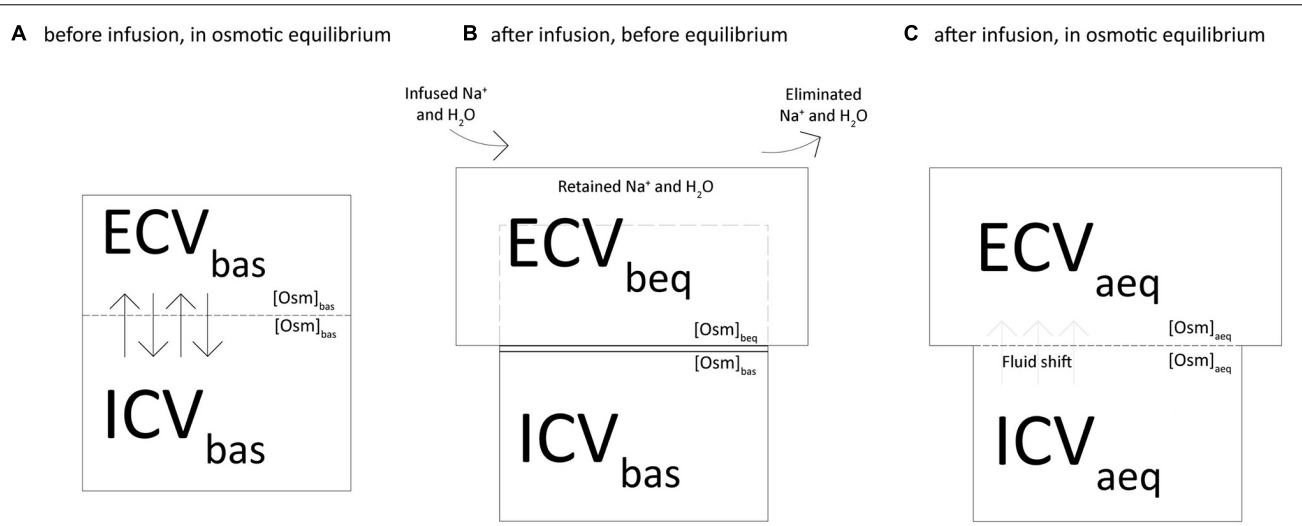

FIGURE 1 | Two-chamber kinetic model to assess the distribution of sodium and fluids across the body compartments.

(4) The following modified mass balance equations were used to calculate the expected sodium concentrations in plasma before ($[Na^+]_{beq}$) and after ($[Na^+]_{aeq}$) the osmotic equilibrium:

$$[Na^+]_{beq} = ([Na^+]_{bas} \times ECV_{bas} + Na^+_{ret})/(ECV_{bas} + V_{ret})$$

$$[Na^+]_{aeq} = ([Na^+]_{bas} \times ECV_{bas} + Na^+_{ret})/(ECV_{bas} + V_{ret} + V_{shift})$$

where $[Na^+]_{bas}$ is sodium plasma concentration at baseline.

(5) Finally, we used the following equation to assess the amount of sodium that justifies the difference between the measured and the calculated sodium concentration after osmotic equilibrium (Na^+_{miss}):

$$Na^+_{miss} = [Na^+]_{bas} \times ECV_{bas} + Na^+_{ret} - [Na^+]_{act} \times (ECV_{bas} + V_{ret} + V_{shift})$$

where $[Na^+]_{act}$ is the actually measured concentration of sodium at a specific experimental time.

Statistical Analysis

Data are reported as mean ± standard deviation. Baseline and end-experiment differences between groups were assessed by Student's *t*-test. The strength of the relationship between variables was tested with linear regression. We evaluated the effect of time and accounted for the repeated measures design by using a linear mixed effects model, where the fixed effect was the pleural pressure group and the random effect the animal ID. Two-tailed *p*-values < 0.05 were considered statistically significant. All analyses were performed with R for Statistical Computing 4.0.2.

RESULTS

In **Table 1** we reported the respiratory mechanics measured in both groups: all mechanical variables, except for respiratory rate and lung elastance, differed between the groups throughout the experiment. The difference in pleural pressure was maintained nearly unaltered throughout the experiment (see **Supplementary Figure 1**). The amount of fluids and electrolytes infused in the two groups is summarized in **Supplementary Table 1**.

Sodium Retention and Pleural Pressures

Sodium retention and fluid balance are presented in **Figure 2** as a function of the experimental time. As shown, sodium retention differed significantly between the groups and increased significantly increased over time. The mean ± SD end-experiment sodium retention was 601.3 ± 334.7 and 1,073.2 ± 525.9 mmol in the low and high pleural pressure groups, respectively ($p < 0.01$). Similarly, the fluid balance increased significantly over time, and was significantly larger in the high pleural pressure group (at 48 h: 2.99 ± 2.54 vs. 6.66 ± 3.87 L; $p < 0.01$). The fluid balance in both groups was similar to the difference in weight-gain measured at the end of the experiment: 2.8 ± 1.8 vs. 5.5 ± 3.0 Kg; ($p < 0.01$). The positive fluid balance derived by a combination of greater amount of infused fluids and a decrease in urinary output: at the end of the experiment 5.72 ± 2.40 vs. 8.76 ± 3.40 L ($p < 0.01$) and 2.72 ± 0.89 vs. 2.10 ± 0.93 L ($p = 0.01$), respectively (**Supplementary Figure 2**).

Sodium Retention and Hemodynamics

Table 1 shows the hemodynamic data from the two groups: heart rate, central venous pressure and pulmonary pressures were higher in the high pleural pressure group (all $p < 0.01$). Cardiac output was higher in the high pleural pressure group, and unexpectedly, it was significantly associated with greater sodium

TABLE 1 | Respiratory mechanics and hemodynamics in high and low pleural pressure groups.

Variables	Values at 0.5 h			Means (averaged over the four time-points: 6, 12, 24, 48 h)		
	Low P_{pl} group	High P_{pl} group	*p*-value	Low P_{pl} group	High P_{pl} group	*p*-value
Pleural pressure [cmH_2O]	4.6 (1.5)	9.4 (2.0)	< 0.01	4.4 (1.5)	10.0 (2.8)	< 0.01
Plateau pressure [cmH_2O]	25.4 (12.6)	35.4 (11.9)	< 0.01	24.5 (8.3)	35.5 (10.4)	< 0.01
PEEP [cmH_2O]	7.9 (6.6)	15.3 (6.5)	< 0.01	6.9 (5.1)	16.8 (6.6)	< 0.01
Respiratory rate [bpm]	26 (11)	26 (10)	0.78	27 (11)	26 (10)	0.30
Tidal volume [mL]	438 (235)	391 (149)	0.31	447 (227)	375 (133)	< 0.01
Total elastance [cmH_20/L]	42.7 (19.0)	54.9 (22.5)	0.01	42.3 (12.6)	52.1 (17.0)	< 0.01
Lung elastance [cmH_20/L]	28.0 (19.2)	32.6 (20.0)	0.31	27.7 (12.1)	30.6 (14.1)	0.06
Mechanical power [J/min]	45.5 (26.1)	67.8 (27.3)	< 0.01	42.9 (16.5)	70.8 (26.1)	< 0.01
Lung mechanical power [J/min]	31.7 (26.2)	39.7 (22.8)	0.15	28.3 (14.7)	41.3 (19.5)	< 0.01
Heart rate [bpm]	112 (29)	135 (24)	< 0.01	97 (22)	113 (27)	< 0.01
Systolic arterial pressure [mmHg]	100.1 (13.0)	103.0 (15.1)	0.38	104.7 (16.2)	103.3 (15.5)	0.43
Diastolic arterial pressure [mmHg]	60.1 (10.4)	64.2 (13.6)	0.14	57.0 (13.4)	55.6 (12.2)	0.37
Mean arterial pressure [mmHg]	75.7 (10.8)	80.2 (12.6)	0.10	73.5 (12.5)	73.0 (12.8)	0.73
Central venous pressure [mmHg]	8.9 (3.5)	12.0 (4.8)	< 0.01	8.5 (4.1)	13.2 (5.1)	< 0.01
Systolic pulmonary pressure [mmHg]	28.2 (8.3)	34.6 (8.6)	< 0.01	26.8 (7.1)	36.3 (10.0)	< 0.01
Diastolic pulmonary pressure [mmHg]	17.6 (6.9)	23.0 (6.7)	< 0.01	16.0 (5.3)	23.2 (7.1)	< 0.01
Mean pulmonary pressure [mmHg]	22.6 (7.3)	29.0 (7.0)	< 0.01	21.4 (6.2)	29.7 (8.2)	< 0.01
Wedge pressure [mmHg]	13.1 (5.8)	17.8 (7.3)	< 0.01	11.8 (5.5)	17.4 (5.8)	< 0.01
Cardiac output [L/min]	3.79 (1.03)	4.02 (1.24)	0.40	2.96 (0.92)	3.41 (1.68)	< 0.01
Systemic vascular resistances [(dyn × s)/L]	1, 588 (427)	1, 526 (671)	0.64	1, 924 (601)	1, 600 (672)	< 0.01
Pulmonary vascular resistances [(dyn × s) /L]	218 (122)	237 (112)	0.51	267 (126)	319 (170)	< 0.01
Infused fluids [L]	0.41 (0.27)	0.73 (0.44)	< 0.01	3.06 (2.32)	4.04 (3.04)	< 0.01
Infused dose of norepinephrine [mcg/kg]	0.01 (0.02)	0.07 (0.09)	< 0.01	1.76 (3.31)	5.79 (9.69)	< 0.01

Data expressed as: mean (SD). p-value assessed with Student's t-test. Number of animals at 0.5 h: 78. Number of animals at 6 h: 78; number of animals at 48 h: 65.

retention (**Figure 3A**). The systemic vascular resistances were higher in the low pleural pressure group and associated with less sodium retention, contrary to what was expected (**Figure 3B**). It must be noted that cardiac output and vascular resistances were a function of the infused fluids (**Supplementary Figure 3**) and the dose of catecholamines (**Supplementary Figure 4**).

Sodium Distribution

In **Figure 4A** shows the measured vs. the expected sodium concentration in the entire animal cohort, if all sodium and fluids had remained within the extracellular space (before the osmotic equilibrium), compared with the values obtained after the osmotic equilibrium with the intracellular space. As shown, the sodium concentration at 48 h calculated before and after osmotic equilibrium would be 162.5 ± 21.2 and 151.8 ± 5.2 mmol/L, respectively, instead of the measured 145.6 ± 3.7 mmol/L. Osmolarity before and after osmotic equilibrium would amount to 324.6 ± 31.4 and 306.5 ± 10.3 mOsm/L respectively, compared with the measured 304.1 ± 10.0 mOsm/L (**Figure 4B**). The calculated extracellular and intracellular volumes at 48 h were 10.04 ± 3.37 and 9.12 ± 0.84 L, after shifting 0.40 ± 0.33 L of water from the intracellular to the extracellular compartments (**Supplementary Figure 5**).

According to the calculated sodium concentrations before and after osmotic equilibrium, 74.9 ± 41.8 mmol of sodium out of 765.8 ± 479.2 mmol of the total retained sodium have to be removed from the extracellular volume to account for the measured sodium osmotic equilibrium.

Contribution of Sodium Retention to Lungs' Weight and Wet-to-Dry Ratio

At the end of the experiment, the weight of the lungs (463.2 ± 158.2 vs. 578.2 ± 162.6 g; $p < 0.01$) and the lung wet-to-dry ratio (6.38 ± 0.73 vs. 6.72 ± 0.58; $p = 0.04$) were significantly different between the low and high-pressure groups; **Supplementary Figure 6** shows the positive association between pleural pressure, and lung-weight and wet-to-dry ratio.

An increase of sodium and fluid retention was positively associated with a higher lung-weight ($R^2 = 0.48$, $p < 0.01$; $R^2 = 0.43$, $p < 0.01$) and higher wet-to-dry ratio of lung ($R^2 = 0.18$, $p < 0.01$; $R^2 = 0.14$, $p < 0.01$) and kidney ($R^2 = 0.12$, $p = 0.01$; $R^2 = 0.11$, $p = 0.02$). No association was found between sodium retention and the wet-to-dry ratio of liver, bowel and muscle (see **Supplementary Table 2**). As shown in **Figure 5**, at 48 h the increasing amount of retained sodium was significantly associated with an increase in lung-weight and wet-to dry-ratio.

DISCUSSION

The main findings of the present study are: (1) a higher pleural pressure leads to an increase in fluid and sodium retention; (2)

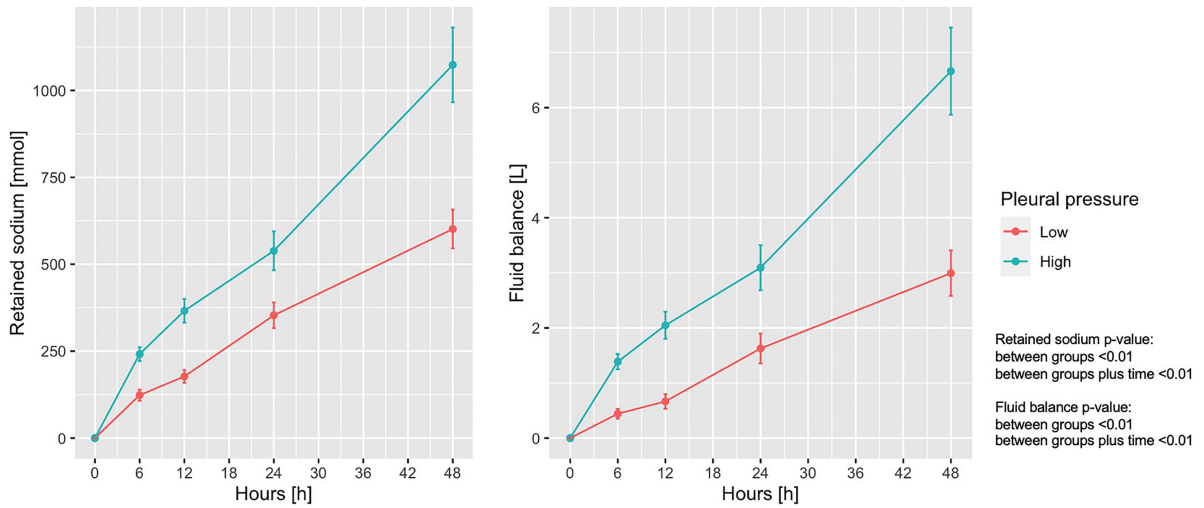

FIGURE 2 | Trend of retained sodium and fluid balance according to pleural pressure. Line-plot over the 48 h of the experiment. Statistic: linear mixed effects model. Retained sodium: data available in 78 animals at 0 h and in 60 at 48 h (36 in low-pressure group and 24 in the high-pressure group). Fluid balance: data available in 78 animals at 0 h and in 62 at 48 h (38 in low-pressure group and 24 in the high-pressure group).

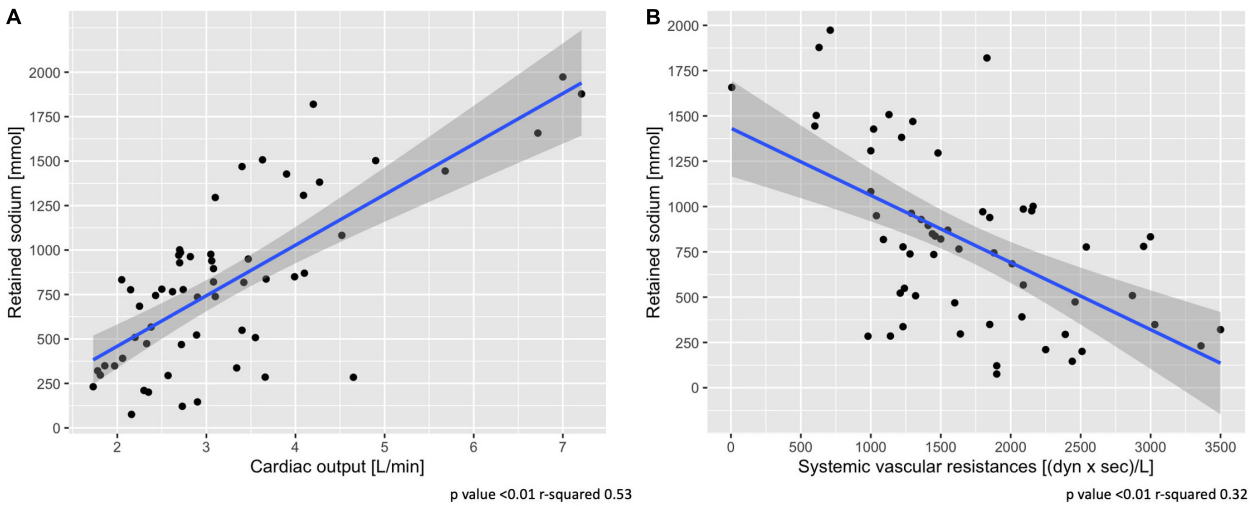

FIGURE 3 | Association between sodium retention and cardiac output **(A)** and systemic vascular resistances **(B)**. Scatter-plot of measures obtained at 48 h. Statistic: linear logistic regression. Data available in 58 animals for cardiac output and vascular resistances.

sodium and fluid retention were greater when cardiac output was higher and the systemic vascular resistance was lower; (3) about 10% of the retained sodium must be osmotically inactive to account for the measured sodium and osmotic equilibrium, and (4) pulmonary edema and the wet-to-dry ratio were positively associated with the amount of retained sodium and fluid.

The effects of mechanical ventilation on the sodium and fluid balance have been known since the first use of positive pressure ventilation (Cournand and Motley, 1948). Mechanical ventilation with positive pressure is an easy way to increase the intrathoracic pressure, whose immediate effect is a decrease in cardiac output proportional to the increase in intrathoracic pressure. We do not know exactly, among tidal volume, mean airway pressure, driving pressure or PEEP which is the main responsible for fluid retention. Previous experiments strongly suggest, however, that the PEEP level may play the most relevant role (Marshall et al., 1982).

The mechanisms of sodium and water retention as a consequence of decreased cardiac output and cardiac failure were described decades ago (Pinsky et al., 1983). Other mechanisms have been described to cause sodium and fluid retention, as the amount of infused sodium and the chloride dependent glomerulotubular feedback (Wilcox, 1983; Hansen et al., 1998). In any case, however, these mechanisms cannot operate alone in spontaneously breathing non-anesthetized

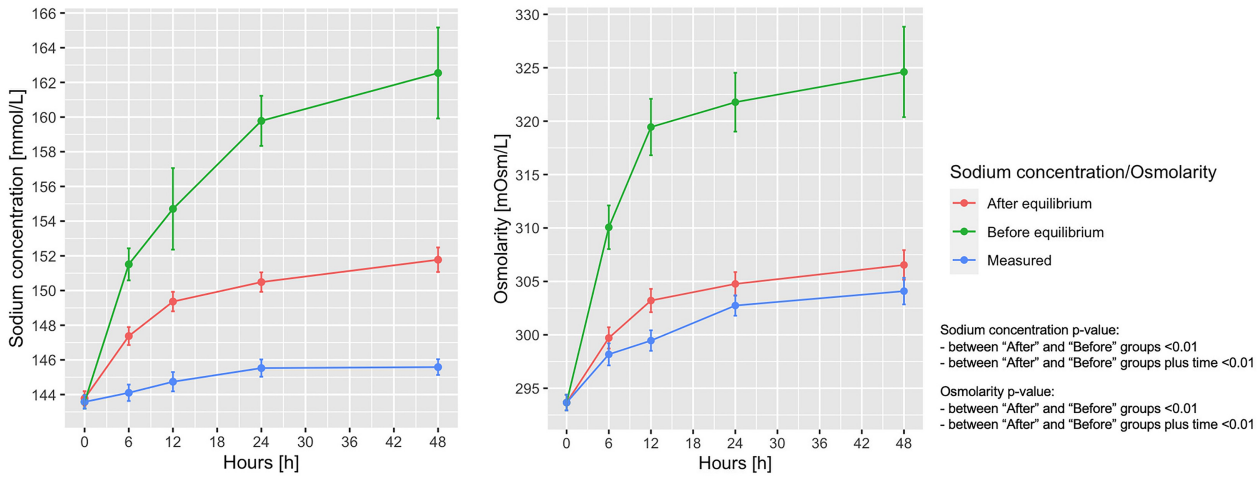

FIGURE 4 | Measured and calculated sodium concentration and osmolarity before and after osmotic equilibrium. Line-plot over the 48 h of the experiment. Statistic: linear mixed effects model comparing the "before" and "after" osmotic equilibrium values. Sodium concentration: data available in 78 animals at 0 h for the three items, and in 65 at 48 h for measured sodium, 65 for expected sodium before equilibrium, and 55 for expected sodium after equilibrium. Osmotic concentration: data available in 78 animals at 0 h in the three items, and in 65 for measured osmotic concentration, 55 for expected osmotic concentration before equilibrium, and 55 for expected osmotic concentration after equilibrium.

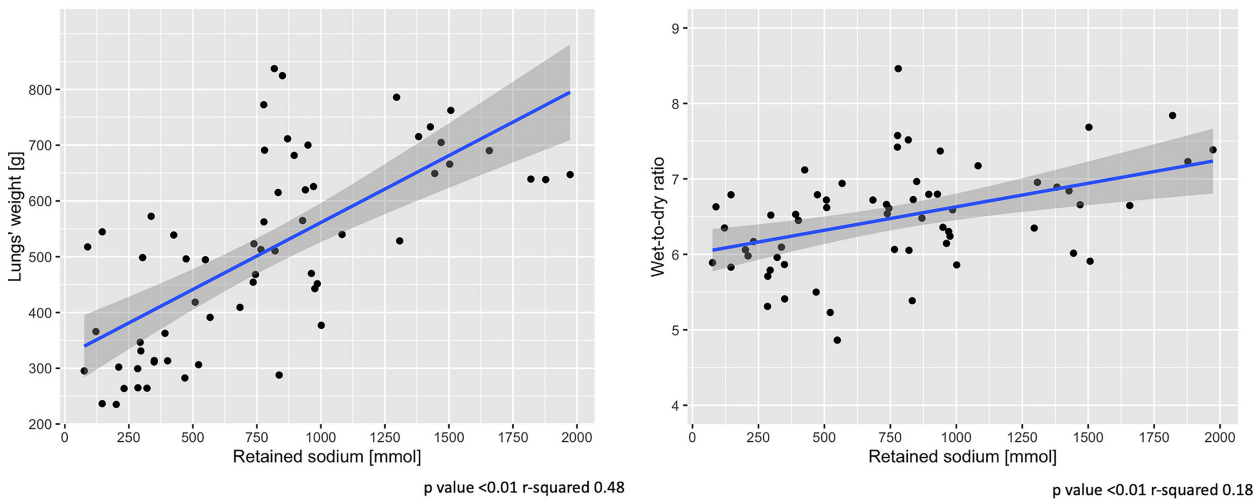

FIGURE 5 | End-of-experiment association between lung-weight and wet-to-dry ratio vs. retained sodium. Scatter-plot of measures obtained at 48 h. Statistic: linear logistic regression. Data available in 62 animals for lungs' weight and wet-to-dry ratio.

animals, which respond to the fluid load by a proportional increase of urinary output.

Our experiments were designed to study the effects of mechanical power on the lung parenchyma, collectively referred to as VILI. As the experiments were performed in healthy animals, the intensity of ventilation and the thoracic pressure required to produce lung damage were substantially elevated. Hemodynamics were severely compromised immediately after the increase in intrathoracic pressure, and, as a consequence, we observed a significant decrease in sodium excretion and urine volume contraction. This homeostatic response was maintained during the experiment as sodium retention and fluid balance increased linearly until the end of the experiment (**Figure 2**).

As discussed earlier, the decrease in cardiac output is the generally recognized mechanism that explains sodium retention by activating several hormonal pathways. Schrier (1988) proposed a unifying theory for volume regulation, where the arterial central volume is the regulating variable, through the baroreceptors, of the body fluid volume. Accordingly, an increase in intrathoracic pressure may lead to a decrease in cardiac output and in turn to a decrease in arterial intrathoracic volume. Surprisingly, however, we found that the cardiac output and sodium retention in our experiments were positively associated,

i.e., the higher the cardiac output, the larger the amount of retained sodium. This is exactly the opposite of what we may expect from Schrier's unifying theory, and in general, from what is observed in cardiac failure. We believe that the possible explanation of our observations may depend on two primary factors. First of all, in order to maintain the circulation according to the strict protocol, the study doctors were administering large volumes of fluids, primarily guided by the arterial pressure. And second, there was a large time lag between the circulatory support interventions, which were a continuous process, and when we obtained the hemodynamic and sodium balance data at the fixed 6-h intervals. Therefore, a possible explanation is that the animal reacted immediately to the abnormal increase in pleural pressure with a decrease in cardiac output, and possibly systolic arterial pressure, to which the immediate response was to infuse fluids and cardiovascular drugs according to the study protocol. This phenomenon is depicted in **Supplementary Figure 7**, where a constant systolic arterial pressure is maintained over a wide range of fluid or norepinephrine infusion rates. Despite the large infused volume, it is likely that only a fraction remained in the vascular compartment to adequately correct the central arterial volume. Thus, the decrease in the central arterial volume maintained the hormonal and kidney pathways that were activated to enhance sodium and water retention.

Although several studies have investigated the theory and practice of sodium distribution (Titze et al., 2014), the literature related to the distribution of the infused sodium is surprisingly scanty. Actually, the technology required to assess the destiny of the infused sodium require measurements of body compartments as well as the tracing the electrolytes of interest. In our experiment we did not measure body compartments nor did we trace the infused sodium. However, we attempted to determine whether a general understanding on sodium distribution could be obtained by utilizing the measured osmolarity and sodium concentrations. Over the past decades, several formulas have been proposed to estimate changes in plasma sodium after infusing sodium solutions (Fazekas et al., 2013). These are primarily based on the concept of exchangeable sodium and potassium and assume that all the sodium ultimately retained after urinary elimination is confined within the extracellular compartment. This concept, however, was challenged in recent years by a precise study of the sodium balance in long term human experiments. It was proposed that part of the sodium is retained in compartments where it has no osmotic action (Olde Engberink et al., 2017), e.g., in the glycosaminoglycan of bone, cartilage, and skin (Titze, 2009; Hofmeister et al., 2015; Olde Engberink et al., 2015).

In our experiment we were able to separately analyze the distribution of sodium and osmotically active solute particles between the extracellular and intracellular compartments. With this approach, at the end of the experiment, we observed the following: (a) an increase in the extracellular compartment of 111.4% (from 4.75 to 10.04 L) due to the retained volume after the infusions (92.4%) and to the volume shift from the intracellular fluid (7.6%; 0.40 L) (**Supplementary Figure 5**), (b) a 3.4% decrease in intracellular volume (9.50–9.18 L) (**Supplementary Figure 5**), and (c) 9.8% (74.0 mmol) of the retained sodium was not justified by the measured sodium and osmotic concentrations. This could be due to possible inaccuracies in our mass balance calculations or, alternatively, to accumulation of sodium in the non-osmotic storage compartments recently described (Olde Engberink et al., 2017). However, a similar percentage of "missing sodium" was computed by analyzing previous experiments performed in a different center by different personnel with a different experimental setup (Langer et al., 2012). Also in this case, the possible non-osmotic storage accounted for the 13.6% of the infused sodium (see **Supplementary Material** for the analysis).

The most striking results, however, are the clinical consequences of sodium and fluid retention in the framework of VILI. Actually, the present work was based on two large experiments aimed at investigating whether the level of mechanical power induced a proportional level of lung injury (Collino et al., 2019; Vassalli et al., 2020). Several data were acquired in both experiments: the lung-weight and wet-to-dry ratio showed a trend toward a greater increase in pigs with higher mechanical power, without achieving statistical significance in the single experiments. A significant association between lung-weight and mechanical power was reached only analyzing the data of the experiments together. Considering the data as a whole, it is likely that what we call "VILI" should be intended as a combination of structural changes of the lung, inflammatory reaction and pulmonary edema, in recognition of the hemodynamic effects on the lung structure and function. The latter, regardless the structural changes, may be exacerbated by the need for large fluid volumes to be infused in order to maintain the circulation during high pressure/volume ventilation.

CONCLUSION

In conclusion, increasing the intrathoracic pressure led to a significant increase in sodium and fluid retention, which may play a significant role in VILI induced by excessive mechanical power.

DATA AVAILABILITY STATEMENT

The raw data supporting the conclusions of this article will be made available by the authors, without undue reservation.

ETHICS STATEMENT

The animal study was reviewed and approved by the Niedersächsisches Landesamt für Verbraucherschutz und Lebensmittelsicherheit (LAVES). Oldenburg (Niedersachsen), Germany. Protocol nrs. 16/2223 and 18/2795.

AUTHOR CONTRIBUTIONS

SG and LG: conception and design. IP, MB, FR, FC, and FV: data acquisition. SG, MB, SL, PP, MP, FR, IS, PH, TL, and PC: analysis and interpretation. OM, LS, KM, MQ, and LG: drafting the manuscript for important intellectual content. All authors contributed to the article and approved the submitted version.

FUNDING

The support for this work was provided from departmental sources and from two unrestricted grants for research in respiratory medicine, apportioned by Sartorius AG (Otto-Brenner-Straße 20, 37079, Göttingen, Germany).

ACKNOWLEDGMENTS

We thank Drs. V. Reupke, A. Wiese, and H. Riedesel from the Zentrale Tierexperimentelle Einrichtung of the Medical University of Göttingen for their precious support in animal preparation. We thank Mr. Massimo Fileni (Italy) for the precious support he provided to the study group. We deeply thank Dr. Luigi Camporota for his valuable help and support in editing and reviewing the manuscript.

SUPPLEMENTARY MATERIAL

The Supplementary Material for this article can be found online at: https://www.frontiersin.org/articles/10.3389/fphys.2021.743153/full#supplementary-material

REFERENCES

Boyd, J. H., Forbes, J., Nakada, T. A., Walley, K. R., and Russell, J. A. (2011). Fluid resuscitation in septic shock: a positive fluid balance and elevated central venous pressure are associated with increased mortality. *Crit. Care Med.* 39, 259–265. doi: 10.1097/ccm.0b013e3181feeb15

Collino, F., Rapetti, F., Vasques, F., Maiolo, G., Tonetti, T., Romitti, F., et al. (2019). Positive end-expiratory pressure and mechanical power. *Anesthesiology* 130, 119–130.

Cournand, A., and Motley, H. L. (1948). Physiological studies of the effects of intermittent positive pressure breathing on cardiac output in man. *Am. J. Physiol.* 152, 162–174. doi: 10.1152/ajplegacy.1947.152.1.162

Drury, D. R., Henry, J. P., and Goodman, J. (1947). The effects of continuous pressure breathing on kidney function. *J. Clin. Invest.* 26, 945–951. doi: 10.1172/jci101889

Fazekas, A. S., Funk, G. C., Klobassa, D. S., Rüther, H., Ziegler, I., Zander, R., et al. (2013). Evaluation of 36 formulas for calculating plasma osmolality. *Intensive Care Med.* 39, 302–308. doi: 10.1007/s00134-012-2691-0

Gattinoni, L., Carlesso, E., Cadringher, P., Valenza, F., Vagginelli, F., and Chiumello, D. (2003). Physical and biological triggers of ventilator-induced lung injury and its prevention. *Eur. J. Respir. Suppl.* 47, 15s–25s.

Hansen, P. B., Jensen, B. L., and Skott, O. (1998). Chloride regulates afferent arteriolar contraction in response to depolarization. *Hypertension* 32, 1066–1070. doi: 10.1161/01.hyp.32.6.1066

Hemmer, M., and Suter, P. M. (1979). Treatment of cardiac and renal effects of PEEP with dopamine in patients with acute respiratory failure. *Anesthesiology* 50, 399–403. doi: 10.1097/00000542-197905000-00005

Hofmeister, L. H., Perisic, S., and Titze, J. (2015). Tissue sodium storage: evidence for kidney-like extrarenal countercurrent systems? *Pflugers Arch.* 467, 551–558. doi: 10.1007/s00424-014-1685-x

Langer, T., Carlesso, E., Protti, A., Monti, M., Comini, B., Zani, L., et al. (2012). In vivo conditioning of acid-base equilibrium by crystalloid solutions: an experimental study on pigs. *Intensive Care Med.* 38, 686–693. doi: 10.1007/s00134-011-2455-2

Marshall, B. E., Berry, A. J., Marshall, C., and Geer, R. T. (1982). Influence of ventilation on response to fluid load in dogs: body water and albumin distribution. *Anesthesiology* 57, 103–110. doi: 10.1097/00000542-198208000-00007

Mendes, R. D. S., Pelosi, P., Schultz, M. J., Rocco, P. R. M., and Silva, P. L. (2020). Fluids in ARDS: more pros than cons. *Intensive Care Med. Exp.* 8(Suppl. 1):32.

Olde Engberink, R. H. G., Rorije, N. M. G., Homan van der Heide, J. J., van den Born, B. J., and Vogt, L. (2015). Role of the vascular wall in sodium homeostasis and salt sensitivity. *J. Am. Soc. Nephrol.* 26, 777–783. doi: 10.1681/asn.2014050430

Olde Engberink, R. H. G., Rorije, N. M. G., van den Born, B. H., and Vogt, L. (2017). Quantification of nonosmotic sodium storage capacity following acute hypertonic saline infusion in healthy individuals. *Kidney Int.* 91, 738–745. doi: 10.1016/j.kint.2016.12.004

Pinsky, M. R., Summer, W. R., Wise, R. A., Permutt, S., and Bromberger-Barnea, B. (1983). Augmentation of cardiac function by elevation of intrathoracic pressure. *J. Appl. Physiol. Respir. Environ. Exerc. Physiol.* 54, 950–955. doi: 10.1152/jappl.1983.54.4.950

Schrier, R. W. (1988). Pathogenesis of sodium and water retention in high-output and low-output cardiac failure, nephrotic syndrome, cirrhosis, and pregnancy (1). *N. Eng. J. Med.* 319, 1065–1072. doi: 10.1056/nejm198810203191606

Svensson, R., Zdolsek, J., Malm, M., and Hahn, R. G. (2020). Electrolyte-based calculation of fluid shifts after infusing 0.9% saline in severe hyperglycemia. *Intensive Care Med. Exp.* 8:59.

Titze, J. (2009). Water-free sodium accumulation. *Semin. Dial.* 22, 253–255. doi: 10.1111/j.1525-139x.2009.00569.x

Titze, J., Dahlmann, A., Lerchl, K., Kopp, C., Rakova, N., Schröder, A., et al. (2014). Spooky sodium balance. *Kidney Int.* 85, 759–767. doi: 10.1038/ki.2013.367

Vassalli, F., Pasticci, I., Romitti, F., Duscio, E., Aßmann, D. J., Grünhagen, H., et al. (2020). Does iso-mechanical power lead to iso-lung damage? An experimental study in a porcine model. *Anesthesiology* 132, 1126–1137. doi: 10.1097/aln.0000000000003189

Vignon, P., Evrard, B., Asfar, P., Busana, M., Calfee, C. S., Coppola, S., et al. (2020). Fluid administration and monitoring in ARDS: which management? *Intensive Care Med.* 46, 2252–2264. doi: 10.1007/s00134-020-06310-0

Wilcox, C. S. (1983). Regulation of renal blood flow by plasma chloride. *J. Clin. Invest.* 71, 726–735. doi: 10.1172/jci110820

Conflict of Interest: LG reports a consultancy for General Electrics and SIDAM. He also receives lectures fees from Estor and Dimar. LS reports financial relationships with Medtronic, Ferrer Deutschland and Merck. Part of the salary support for the author MB was provided by an unrestricted research grant from Sartorius Inc. Göttingen, Germany.

The remaining authors declare that the research was conducted in the absence of any commercial or financial relationships that could be construed as a potential conflict of interest.

Publisher's Note: All claims expressed in this article are solely those of the authors and do not necessarily represent those of their affiliated organizations, or those of the publisher, the editors and the reviewers. Any product that may be evaluated in this article, or claim that may be made by its manufacturer, is not guaranteed or endorsed by the publisher.

frontiers in Physiology

ORIGINAL RESEARCH
published: 01 October 2021
doi: 10.3389/fphys.2021.724046

A Damaged-Informed Lung Ventilator Model for Ventilator Waveforms

Deepak K. Agrawal[1,2], Bradford J. Smith[1,3], Peter D. Sottile[4] and David J. Albers[1,2,5]**

[1] Department of Bioengineering, University of Colorado Denver|Anschutz Medical Campus, Aurora, CO, United States, [2] Section of Informatics and Data Science, Department of Pediatrics, School of Medicine, University of Colorado Anschutz Medical Campus, Aurora, CO, United States, [3] Section of Pulmonary and Sleep Medicine, Department of Pediatrics, University of Colorado Anschutz Medical Campus, Aurora, CO, United States, [4] Division of Pulmonary Sciences and Critical Care Medicine, Department of Medicine, University of Colorado School of Medicine, Aurora, CO, United States, [5] Department of Biomedical Informatics, Columbia University, New York, NY, United States

Motivated by a desire to understand pulmonary physiology, scientists have developed physiological lung models of varying complexity. However, pathophysiology and interactions between human lungs and ventilators, e.g., ventilator-induced lung injury (VILI), present challenges for modeling efforts. This is because the real-world pressure and volume signals may be too complex for simple models to capture, and while complex models tend not to be estimable with clinical data, limiting clinical utility. To address this gap, in this manuscript we developed a new damaged-informed lung ventilator (DILV) model. This approach relies on mathematizing ventilator pressure and volume waveforms, including lung physiology, mechanical ventilation, and their interaction. The model begins with nominal waveforms and adds limited, clinically relevant, hypothesis-driven features to the waveform corresponding to pulmonary pathophysiology, patient-ventilator interaction, and ventilator settings. The DILV model parameters uniquely and reliably recapitulate these features while having enough flexibility to reproduce commonly observed variability in clinical (human) and laboratory (mouse) waveform data. We evaluate the proof-in-principle capabilities of our modeling approach by estimating 399 breaths collected for differently damaged lungs for tightly controlled measurements in mice and uncontrolled human intensive care unit data in the absence and presence of ventilator dyssynchrony. The cumulative value of mean squares error for the DILV model is, on average, ≈12 times less than the single compartment lung model for all the waveforms considered. Moreover, changes in the estimated parameters correctly correlate with known measures of lung physiology, including lung compliance as a baseline evaluation. Our long-term goal is to use the DILV model for clinical monitoring and research studies by providing high fidelity estimates of lung state and sources of VILI with an end goal of improving management of VILI and acute respiratory distress syndrome.

Keywords: ventilator-induced lung injury, ventilator waveform, mathematical model, acute respiratory distress syndrome, statistical inference

OPEN ACCESS

Edited by:
Walter Araujo Zin, Federal University of Rio de Janeiro, Brazil

Reviewed by:
Norihiro Shinozuka, Chibaken Saiseikai Narashino Hospital, Japan
Carmen Silvia Valente Barbas, University of São Paulo, Brazil

****Correspondence:***
Deepak K. Agrawal
agwal.deepak@gmail.com
David J. Albers
David.Albers@cuanschutz.edu

Specialty section:
This article was submitted to Respiratory Physiology, a section of the journal Frontiers in Physiology

Received: *11 June 2021*
Accepted: *01 September 2021*
Published: *01 October 2021*

Citation:
Agrawal DK, Smith BJ, Sottile PD and Albers DJ (2021) A Damaged-Informed Lung Ventilator Model for Ventilator Waveforms. Front. Physiol. 12:724046. doi: 10.3389/fphys.2021.724046

INTRODUCTION

Mechanical ventilation is a life-saving therapy for patients who are unable to perform gas exchange by breathing on their own. When used incorrectly, mechanical ventilation has the potential to worsen lung injury through barotrauma, volutrauma, and atelectrauma that are collectively referred to as ventilator-induced lung injury (VILI). Furthermore, while the patient and ventilator always interact, when the patient and ventilator are dyssynchronous—known as ventilator dyssynchrony (VD)—the timing and delivery of a mechanical breath in response to a patient effort may lead VILI and poor outcomes (Sottile et al., 2018a). There are conditions or syndrome such as acute respiratory distress syndrome (ARDS) that carry a high mortality rate and may be exacerbated, or even caused, by VILI (Ware and Matthay, 2000; Phua et al., 2009; Force et al., 2012; Amato et al., 2015). Therefore, identifying lung-protective ventilation to reduce VILI is both important and challenging because the oxygenation needs are often in opposition to safe ventilation, leading to a complex interplay between the underlying pulmonary pathophysiology, ventilator mechanics, and patient-ventilator interactions (Chiumello et al., 2008; Gilstrap and MacIntyre, 2013; Blanch et al., 2015; Yoshida et al., 2017). The current standard of care dictates a formulaic application of low tidal volumes to reduce overdistension and positive end-expiratory pressure to maintain patency. This approach reduces VILI but does not prevent it in all cases and is not personalized (Network, 2000; Grasso et al., 2007; Khemani et al., 2018). While such protocols have provided measurable improvements in outcomes, the formulaic approach could potentially be improved through personalization of individual respiratory mechanics and VD (Bein et al., 2013).

Modern mechanical ventilators produce data in the form of time-dependent pressure, volume, and flow waveforms that contain a wealth of information about pulmonary physiology, patient-ventilator interactions, and ventilator settings. These data can be used to troubleshoot and optimize mechanical ventilation (Corona and Aumann, 2011; Mellema, 2013). However, ventilator waveforms are typically analyzed heuristically by visual inspection and, therefore, the outcome of such an analysis is limited by individual expertise and experience (Corona and Aumann, 2011; Mellema, 2013). A quantitative interpretation of these complex signals could increase diagnostic accuracy and repeatability while facilitating the application of personalized lung-protective ventilation. One simple example of waveform quantification that is currently used in clinical care is the driving pressure, which serves as a readout of both patient condition and ventilator settings (Amato et al., 2015). In the current study, we seek to develop a model that can systematically mathematize the pathophysiologic knowledge clinicians use to interpret lung conditions from ventilator waveform data as well as knowledge about the processes governed by the ventilator.

The analysis we present herein is a departure from traditional modeling methods that link measured pressures and flows through physiologically-based parameters, such as the well-recognized single-compartment model that lumps the spatially heterogeneous lung mechanical properties into single values of resistance and compliance (Chiew et al., 2011; Hamlington et al., 2016; Mori, 2016; Mellenthin et al., 2019). In the traditional models, the entirety of the pressure and volume dynamics emerge from the hypothesized physiological mechanics. Due to this straightforward formulation, the single-compartment model is computationally efficient but often not be able to reproduce all of the features in waveform data, such as patient-ventilator interaction. This is because the model lacks the complexity to allow such complex dynamics to emerge. Given the complexity of patient-ventilator interactions and pathophysiology present in real human ventilator data, it is unlikely that a two-parameter model that does not incorporate ventilator information will be capable of representing the information that a clinician may want about lung state and pathophysiology. On the other hand, more complicated formulations, including multi-compartment models, use many states and redundant parameters that cannot be uniquely estimated, causing identifiability problems where there is no unique solution, or more often no convergent solution for parameter values. As such, those models require expensive data to estimate that are not currently available for human subjects, and require substantial computational resources. Even then, complex multi-compartment models might not produce all the relevant features present in the pressure and volume waveform data (Rees et al., 2006; Bates, 2009; Reynolds et al., 2010; Molkov et al., 2014, 2017; Roth et al., 2017; Nguyen et al., 2014; Serov et al., 2016; Ellwein Fix et al., 2018). Because of these limitations, both types of models might have a limited use in clinical settings, as the model needs to be useful for a clinician and estimable in real time.

Our approach offers the potential to overcome these limitations and provides both identifiability and fidelity by using mathematical models with interpretable parameters to recapitulate pressure and volume signals. This high fidelity is due, in part, to the limited dependence between the pressure and volume models. The relationship between components of the pressure and volume waveforms are then used to define specific physiologic features, just as the quasi-static compliance is defined from the observed ratio of tidal volume and driving pressure.

Human ventilator waveform data represent several generating processes, lung physiology, ventilator mechanics, interventions, patient-ventilator interactions, and health care process model effects (Hripcsak and Albers, 2013b; Rossetti et al., 2021). In general, physiological models alone might be missing substantial contributing sources within the data. There are many potential approaches to manage this problem. One approach would be to include models for the lungs and the ventilator to capture the mechanics of the ventilator, the lungs, and their coupled interaction. Here, instead, we are incorporating both lung and health care process model (ventilator) effects into a single unified model with targeted features captured by lumped parameters. Our model is not a mechanistic model but it is not built arbitrarily either. It is built constructively starting with a lung waveform without pathophysiology or health care processes effects (e.g., the ventilator). We added in limited, e.g., compared to a neural network or other nonlinear regression model, flexibility to the model according to features that the team deemed connected to pathophysiology or health care process model effects. The model

parameters are not like Fourier components that are active during the entire breath, but rather are time-limited breath deformations that are hypothesized to relate to particular types of damage, damage inducing phenomena, and ventilator interactions and effects. It is in this way that the model is constructively anchored to physiology and health care process effects.

Therefore, in this manuscript, our objective is to build a model that takes as baseline "healthy" breaths, and then adds terms that correspond to deviations from healthy breaths whose hypothesized sources include VILI, VD, and pathophysiological features of ventilator waveforms. By estimating the model, we identify the presence and severity of deviations from normal in a way that has a physiologically-based hypothesis attached to it. In essence, this is a proof-in-principle model development manuscript with underlying constraints such that the model could potentially be of use with real clinical data. In future studies, we will tie these phenotypes to lung injury severity, VD, and the pathogenesis of VILI. We anticipate that this approach will eventually find applications in real-time clinical readouts of ventilation safety, long-term monitoring to detect changes in patient condition, and as a quantitative outcome measure for clinical trials.

In the current proof-in-principle study, our team identifies clinically important features in typical volume and pressure waveform data. We then define the models for volume and pressure waveforms as the sum of a set of terms through which we modularly capture physiologically relevant features. The pressure and volume models are coupled via the respiratory rate. This approach allows independent modeling of the waveform components so that clinical, physiologic, and ventilator-based knowledge can be used to constrain the model. We named this model the damage-informed lung-ventilator (DILV) as it contains information about both lung physiology and ventilator dynamics. To demonstrate the model's flexibility, the volume and pressure models are qualitatively validated in a simulation study where we show various relevant features that are commonly observed in health and disease. We then identify the parameters that may correspond to interpretable pathophysiology by using the DILV model to generate pressure-volume data and qualitatively assessing the effects of parameter changes. Finally, in a quantitative verification, we demonstrate that the model can accurately and uniquely represent laboratory and clinical ventilator data, which includes mouse model and human-intensive care unit (ICU) ventilator data in the absence and presence of VD (Sottile et al., 2018a,b). Through a comprehensive comparison between the DILV model and the single-compartment model, we demonstrate that our approach can accurately determine lung compliance as a baseline evaluation. Temporal changes in the model parameters are compared to other assessments of injury severity and qualitative features of the pressure and volume waveforms.

MATERIALS AND METHODS

Mechanical ventilation is characterized by three measured state variables which vary over time: volume, pressure and flow. These time-dependent signals have diverse features arising from pulmonary physiology, the ventilator, and health care process effects such as clinical interventions, and patient-ventilator interaction (Albers and Hripcsak, 2010; Hripcsak and Albers, 2013a,b). The flow is the time-derivative of volume and so the volume variable contains the same information about the underlying lung mechanics but in a different representation (Bates, 2009). In this study, we focused on two state variables, volume and pressure.

In the simplest ventilation modes, one variable is primarily controlled by the ventilator, e.g., pressure or volume, while the other variable, e.g., volume or pressure, is free to vary, referred to as pressure-controlled ventilation (PCV) or volume-controlled (VCV), respectively. In this case, only the "free" variable contains direct information about the respiratory mechanics of the patient (Tobin, 2001; Bates, 2009). Moreover, in some models there is a rigid coupling between the controlled and free states that often limits the model flexibility, precluding the model from reproducing some features that are present in the clinical data. For example, the single-compartment model performs a linear transformation between pressure and volume variables due to the fixed coupling defined as the sum of linear resistive and elastic contributions (Bates, 2009; Smith et al., 2015; Hamlington et al., 2016). We, therefore, do not explicitly couple the controlled (also known as an independent) and free (also known as a dependent) variables such that the volume and pressure models will be independent of one another. Modern clinical ventilators also have an expansive set of other modes, the most notable of which are the patient-triggered modes where the ventilator's action is triggered by patients such as inspiratory effort. These modes can be very lung-protective, but they can also lead to complex forms of VD that are difficult to model. Patient-triggered modes are the most commonly used modes for humans unless the human is given neuromuscular blockades (Sottile et al., 2018b).

Identifying Important Features in the Volume and Pressure Waveform

The volume waveform can have two characteristic features as shown schematically in **Figure 1A**. These features might reflect lung condition when volume is the free variable such as in PCV, otherwise these may be controlled via ventilator (Corona and Aumann, 2011; Mellema, 2013). The first feature is the inspiration, denoted as A in **Figure 1A**, which continues until the amount of gas delivered in that breath is reached (the tidal volume). The pressure and lung elastic recoil are at equilibrium. The second feature is expiration, denoted as B in **Figure 1A**. Depending on the ventilator settings and lung condition, the gradient of the rising and falling signals can vary across patients and in the same patient over time. Therefore, the model must be able to represent these features independently. Accordingly, the gradients of inspiration and expiration of volume are features that are variable and estimable in the volume model.

The characteristic shape of the pressure waveform can vary more dramatically than the volume waveform as shown in the hand drawn **Figure 1B**. When pressure is a free variable, such as in VCV, the pressure waveform has several important features

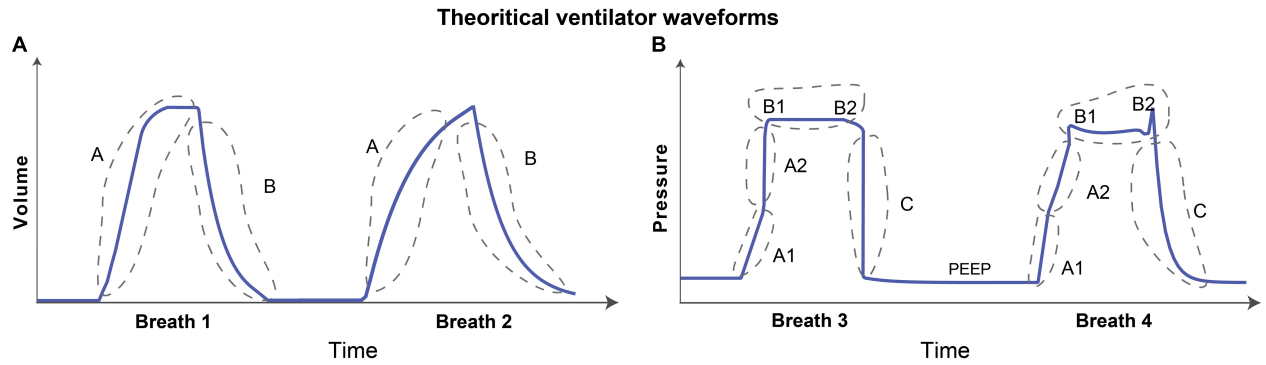

FIGURE 1 | Graphical representation of theoretical volume and pressure waveforms. **(A)** The volume signal generally has two distinct features. The rising and falling of the volume signal during inspiration and expiration, respectively, are denoted as features A and B. **(B)** The pressure signal can typically have multiple features in the waveform that contain useful information. The gradient of the rising signal in which pressure continues to increase during inspiration can have two distinct features, denoted as features A1 and A2. These two features define the gradient of the rising signal before and after the inflection point such that there may be abrupt increases (breath 1) or decreases (breath 2) in the signal gradient. The shape of the plateau pressure is captured using features B1 and B2 such that there may be a peak at the beginning (B1-breath 2) and/or at the end (B2-breath 2) of the plateau. Finally, the gradient of the falling signal is captured using feature C that represents the expiration process. The baseline pressure is known as positive end-expiratory pressure (PEEP), and often used in ARDS patients to maintain an open lung (Cavalcanti et al., 2017). Note that the breaths were drawn to highlight the features which might contain useful information about lung condition and ventilator-patient interaction when the respective variable is free. If the variable is controlled, e.g., volume during VCV, the waveform features represent ventilator settings.

that convey information about lung condition and ventilator-patient interaction. Based on observation of a large number of recorded breaths, we identified five important features in the pressure waveform. Features A1 and A2 in **Figure 1B** determine the gradient of the inspiration. The time-varying graph of inspiration can have two distinct modes where the gradient of the signal may increase (**Figure 1B**, breath 1) or decrease (**Figure 1B**, breath 2) during inspiration. These features are hypothesized to correspond to the volume-dependent decrease in lung compliance (breath 1) or an increase in compliance due to recruitment (breath 2) (Smith et al., 2015; Hamlington et al., 2016). Note that this interpretation is only valid if the flow rate is constant during inspiration (Grasso et al., 2004).

Features B1 and B2 (**Figure 1B**) are related to the shape of the waveform at the start and end of the plateau pressure, which is a period of constant pressure. There may be peaks at the beginning (B1) and/or at the end (B2) of the plateau pressure, which are hypothesized to correspond to inspiratory flow resistance and patient effort, respectively (Bates, 2009; Mellema, 2013). Feature C in **Figure 1B** corresponds to the gradient of expiration. We also model the constant baseline pressure, known as the positive end-expiratory pressure (PEEP), because it is a key independent variable in ARDS management (Guerin, 2011; Cavalcanti et al., 2017). Note that in hybrid ventilation modes, there may be scenarios where both pressure and volume variables are partially controlled and so, in those cases, both the waveforms can be confounded in additionally complex ways and would require more nuanced interpretation.

Constructing the Damage-Informed Lung Ventilator Model

Once we define the physiological and ventilation-related relevant features in the waveform data, we formulate the model for volume and pressure signals. During this process, we have chosen minimal number of parameters while ensuring that the model should have the ability to address the deep complexity present in the waveform data due to complex pathophysiology and patient-ventilator interactions. Additionally, the parameters have little overlap as they are not active at the same time within a given breath, and many of the parameters control only specific aspects of a given deformation such as a peak value. In this way, while we add parameters, they act locally along a breath and are tied to a deformation shape and timing that is hypothesized to be related to pathophysiology.

Construction of the Volume Model

Irrespective of the state variable, the models have periodic dynamics with a frequency defined by the respiratory rate (breaths/min) that should be the same in pressure and volume waveform models. In addition to this constraint, the volume model has two additional features, the rate of inspiration and expiration (A and B in **Figure 1A**, respectively). Volume model development begins by modeling the respiratory rate with a sinusoidal function (f_{s1}):

$$f_{s1} = \sin(2\pi\theta t - \phi_1) - b_1. \quad (1)$$

Here, the respiratory frequency (breaths/s) is set by θ and t represents time in seconds while parameter ϕ_1 allows to control the starting point in the respiratory cycle. To control the rate of inspiration or expiration while maintaining the periodicity, we create a periodic rectangular waveform function f_{b1} by combining the sinusoidal function with hyperbolic tangent function:

$$f_{b1} = \frac{1}{2}\left\{\tanh\left(a_1 f_{s1}\right) + 1\right\}. \quad (2)$$

To control the smoothness of the rectangular waveform, we added a smoothing parameter a_1. The other terms (1/2, +1)

are added to generate a rectangular waveform that has a zero-base value and unit amplitude. To control the duty cycle of the rectangular waveform that sets inspiratory:expiratory (I:E) ratio, we used parameter b_1 such that the zero value of b_1 corresponds to 1:1 I:E ratio. **Figure 1A** shows additional model features: the rate of inspiration (A) and expiration (B). To represent these rates independently, we define the volume (V) using the rectangular waveform as a base waveform:

$$V = A_v \left(f_{v1} + f_{v2}\right), \tag{3}$$

where f_{v1} term produces the inspiration part of the volume signal (feature A):

$$f_{v1}\,(i+1) = \left\{ \frac{1}{\beta_1} f_{b1}\,(i+1) + \left(1 - \frac{1}{\beta_1}\right) f_{v1}\,(i) \right\}; \quad i = 1:n,$$

$$f_{v1} = \left[f_{v1}\,(1)\; f_{v1}\,(2) \ldots f_{v1}\,(i) \ldots f_{v1}\,(n)\right] \frac{f_{b1}}{\max(f_{v1})}, \tag{4}$$

and f_{v2} term produces the expiration part of the volume signal (feature B):

$$f_{v2}\,(i+1) = \left\{ \frac{1}{\beta_2} f_{b1}\,(i+1) + \left(1 - \frac{1}{\beta_2}\right) f_{v2}\,(i) \right\}; \quad i = 1:n,$$

$$f_{v2} = \left[f_{v2}\,(1)\; f_{v2}\,(2) \ldots f_{v2}\,(i) \ldots f_{v2}\,(n)\right] \frac{f_{b1}}{\max(f_{v2})}. \tag{5}$$

Here, β_1 and β_2 control the gradient of the inspiration and expiration, respectively, while A_v controls the amplitude of the volume waveform. **Figure 2A** shows the volume waveform (top plot) and the constitutive terms added through with Eqs 1–5. Note that the expiration part of the breath (feature B) is generally spontaneous and could be model using a logarithmic function. We have opted for the current form of the model so that it can be converted into the ordinary differential equations-based model relatively easily in future studies where we plan to use Bayesian interference schemes (Gelman et al., 2013).

Construction of the Pressure Model

The pressure model has five explicit features that might be used to understand lung health and ventilator settings. These features are

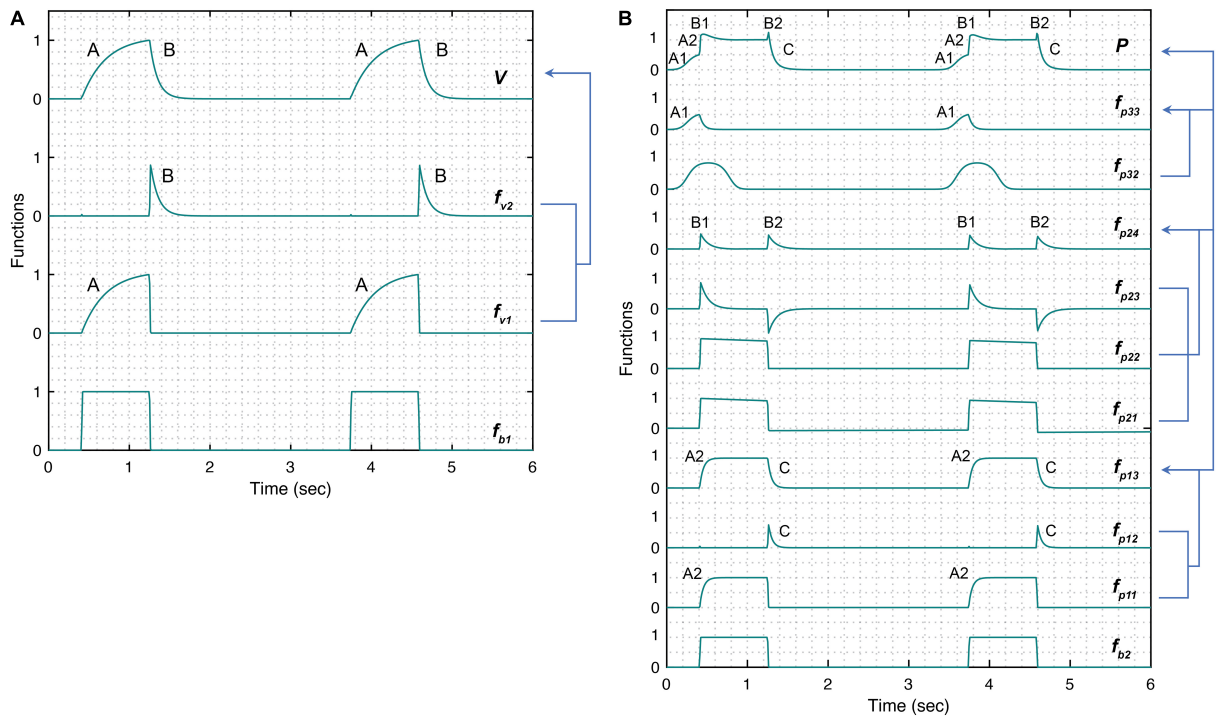

FIGURE 2 | Simulated response of various terms that make up the damage-informed volume (V) and pressure model (P). **(A)** A periodic rectangular waveform f_{b1} is used to create terms f_{v1} and f_{v2} through which the gradient of the rising (feature A) and falling (feature B) signals in the volume waveform are controlled, respectively. Equations 1–5 were used to simulate the response within each term with parameter values $\theta = 0.3$, $a_1 = 200$, $b_1 = 0.7$, $\phi_1 = 0$, $\beta_1 = 30$, $\beta_2 = 10$, and $A_v = 1$. **(B)** A periodic rectangular waveform (f_{b2}) serves as a basis of the pressure model. The overall shape of the pressure waveform, which defines the gradient of the inspiration and expiration signals, is formed using f_{p13} comprised of the rising signal of f_{p11} (A2) and falling signal of f_{p12} (C). The shape of the plateau pressure is defined by f_{p24}, where the output of f_{b2} is processed via f_{p21}, f_{p22}, and f_{p23} to produce peaks at the beginning (B1) and end (B2) of the plateau pressure. The shape of the rising signal at low volume (A1) is defined by f_{p33}, where a short pulse is produced via f_{p31} and reshaped via f_{p32}. Note that the amplitude terms A_{p1}, A_{p2}, and A_{p3} control the amplitude of f_{p13}, f_{p24}, and f_{p33}, respectively. Equations 6–18 were used to simulate the response of each term with parameter values $\theta = 0.3$, $a_2 = 200$, $b_2 = 0.7$, $\phi_2 = 0$, $a_3 = 10$, $b_3 = 0.9$, $\phi_3 = -0.6$, $\beta_3 = \beta_4 = 5$, $\beta_5 = 1.001$, $\beta_6 = 1.1111$, $A_{p1} = 1$, $A_{p2} = 0.5$, $A_{p3} = 0.5$, and $A_{p4} = 0$. Note that the model variability shown here is independent of the ventilator mode.

depicted in **Figure 1B**. Features A1 and A2 capture the gradient of the rising signal during inspiration at low (A1) and high (A2) volume and might be correlated with lung compliance. Features B1 and B2 capture the shape of the peaks at the beginning (B1) and end (B2) of the plateau pressure and might reflect changes in inspiratory flow resistance and patient effort, respectively. Finally, feature C captures the rate of change of the pressure during expiration. To build a model that can capture all these features and be able to estimate parameters reliably and uniquely, we used a modular approach to build the components of the pressure model where each component is controlled by set parameters that form those components.

The pressure model construction begins like the volume model, with a sinusoid. Because volume and pressure are coupled through their period (respiratory rate), we enforce this constraint by requiring that both models have the same respiratory frequency (θ) in their base periodic sinusoid:

$$f_{s2} = \sin(2\pi\theta t - \phi_2) - b_2. \tag{6}$$

Because the pressure may lag or lead the volume depending on the ventilator mode, we include a phase shift term, ϕ_2 in the sinusoid. To account for variations in the duty cycle of the rectangular waveform, we added the parameter b_2 that defines the I:E ratio. We then create a rectangular waveform f_{b2} as we did for the volume model using the hyperbolic tangent:

$$f_{b2} = \frac{1}{2}\left\{\tanh\left(a_2 f_{s2}\right) + 1\right\}. \tag{7}$$

The smoothness of the rectangular waveform is controlled via the parameter a_2. The five key features in pressure are represented with three additional terms: (i) f_{p13} defines the rates of pressure change during inspiration and expiration, (ii) f_{p24} determines the peaks at the beginning and end of the pressure plateau, and (iii) f_{p33} specifies the gradient of the initial rising signal during inspiration, leaving us with the full the pressure model (P):

$$P = f_{p13} + f_{p24} + f_{p33} + A_{p4}. \tag{8}$$

The constant parameter A_{p4} corresponds to the baseline pressure value (PEEP). The rates of pressure change during inspiration and expiration (see A2 and C in **Figure 1B**, respectively) are:

$$f_{p13} = A_{p1}\left(f_{p11} + f_{p12}\right), \tag{9}$$

where f_{p11} term produces the rising part of the pressure signal:

$$f_{p11}(i+1) = \left\{\frac{1}{\beta_3} f_{b2}(i+1) + \left(1 - \frac{1}{\beta_3}\right) f_{p11}(i)\right\}; \quad i = 1:n,$$

$$f_{p11} = \left[f_{p11}(1)\ f_{p11}(2) \ldots f_{p11}(i) \ldots f_{p11}(n)\right] \frac{f_{b2}}{\max(f_{p11})}, \tag{10}$$

and f_{p12} term produces the falling part of the pressure signal:

$$f_{p12}(i+1) = \left\{\frac{1}{\beta_4} f_{b2}(i+1) + \left(1 - \frac{1}{\beta_4}\right) f_{p12}(i)\right\}; \quad i = 1:n,$$

$$f_{p12} = \left[f_{p12}(1)\ f_{p12}(2) \ldots f_{p12}(i) \ldots f_{p12}(n)\right] \frac{f_{b2}}{\max(f_{p12})}. \tag{11}$$

Here, β_3 and β_4 control the gradient during inspiration and expiration, respectively. The next set of features, the peaks at the beginning and end of plateau pressure (B1 and B2 in **Figure 1B**), are represented by:

$$f_{p24} = A_{p2}\frac{f_{p23}}{\max(f_{p23})}, \tag{12}$$

where f_{p21} and f_{p22} terms create the initial shape of peaks at the plateau pressure:

$$f_{p21}(i+1) = \frac{1}{\beta_5}\left\{f_{p21}(i) + \left\{f_{b2}(i+1) - f_{b2}(i)\right\}\right\}; \quad i = 1:n,$$

$$f_{p21} = \left[f_{p21}(1)\ f_{p21}(2) \ldots f_{p21}(i) \ldots f_{p21}(n)\right], \tag{13}$$

$$f_{p22} = f_{p21} f_{b2}, \tag{14}$$

and f_{p23} term further reshapes both the peaks:

$$f_{p23}(i+1) = \frac{1}{\beta_6}\left\{f_{p23}(i) + \left\{f_{p22}(i+1) - f_{p22}(i)\right\}\right\}; \quad i = 1:n,$$

$$f_{p23} = abs\left(\left[f_{p23}(1)\ f_{p23}(2) \ldots f_{p23}(i) \ldots f_{p23}(n)\right]\right). \tag{15}$$

The parameters β_5 and β_6 control the shape of both the peaks, which are present at the plateau pressure. Finally, the gradient of the initial rate of inspiration (**Figure 1B**, A1) is modeled by:

$$f_{p33} = A_{p3}\frac{f_{p32}\left\{1 - \left(f_{p11} + f_{p12}\right)\right\}}{\max\left[f_{p32}\left\{1 - \left(f_{p11} + f_{p12}\right)\right\}\right]}, \tag{16}$$

where a short pulse is produced via f_{p31}:

$$f_{p31} = \sin(2\pi\theta t - \phi_3) - b_3, \tag{17}$$

and reshaped via f_{p32} term:

$$f_{p32} = \frac{1}{2}\left\{\tanh\left(a_3 f_{p31}\right) + 1\right\}. \tag{18}$$

The position, shape and gradient of the rising signal, produced by f_{p33} term are controlled using the parameters ϕ_3, b_3 and a_3, respectively. **Figure 2B** shows the pressure waveform and the constitutive terms added through Eqs 6–18. The pressure waveform (top plot) composed of the three terms f_{p13}, f_{p24}, and f_{p33} that capture the gradient of the inspiration (A2) and expiration signals (C), the shape of the plateau pressure (B1 and B2), and the shape of the rising signal at low volume (A1), respectively.

Mouse Mechanical Ventilation Experiments

Three 8 to 10-week-old female BALB/c mice (Jackson Laboratories, Bar Harbor, ME, United States) were studied under University of Colorado, Anschutz Medical Campus Institutional Animal Care and used Committee (IACUC)-approved protocol (#00230). The mice weighed 18.6, 19.1, and 19.9 g. Anesthesia was induced with an intraperitoneal (IP) injection of 100 mg/kg Ketamine and 16 mg/kg Xylazine, a tracheostomy was performed with a blunted 18 ga metal cannula, and ventilation was started on the flexiVent small animal ventilator (SCIREQ, Montreal, QC, Canada). Anesthesia was maintained with 50 mg/kg Ketamine or 50 mg/kg Ketamine with 8 mg/kg Xylazine at 30 min intervals along with 50 μL IP 5% dextrose lactated Ringer's solution. Heart rate was monitored via electrocardiogram.

Baseline ventilation, consisting of a tidal volume (Vt) = 6 ml/kg, PEEP = 3 cmH_2O, and respiratory rate (RR) = 250 breaths/min, was applied for a 10 min stabilization period with recruitment maneuvers at 3 min intervals. Pressure and volume were recorded with a custom flowmeter based on our previously published design (Jawde et al., 2018). Four types of ventilation were recorded for analysis: (1) VCV-PEEP0, consisting the baseline ventilation with PEEP = 0 cmH_2O, (2) VCV-PEEP12 that was the baseline ventilation with PEEP = 12 cmH_2O, (3) HighPressure-PEEP0 that consisted of a inspiratory pressure (Pplat) = 35 cmH_2O and PEEP = 0 cmH_2O with RR = 60 breaths/min, and (4) PCV-PEEP0 with Pplat = 10 and PEEP = 0 cmH_2O with RR = 70 breaths/min. After the initial measurements of the healthy lung, lung injury was induced with a 0.15 ml lavage with warm saline (Mellenthin et al., 2019). This fluid was pushed into the lung with an additional 0.3 ml air, and suction was applied to the tracheal cannula with an approximate return of 0.05 ml. The mouse was then ventilated for 10 mins with the HighPressure-PEEP0 settings. The sequence of four measurement ventilation patterns (above) was repeated, then the mouse received 0.8 mg/kg IP pancuronium bromide to suppress respiratory efforts, and the measurements were repeated again.

Human Data Collection

Between June 2014 and January 2017, 140 adult patients admitted to the University of Colorado Hospital medical intensive care unit (MICU) at risk for or with ARDS and requiring mechanical ventilation were enrolled within 12 h of intubation (Wheeler and Bernard, 2007). At risk patients were defined as intubated patients with hypoxemia and a mechanism of lung injury known to cause ARDS, who had not yet met chest X-ray or oxygenation criteria for ARDS. To facilitate the capture of continuous ventilator data, only patients ventilated with a Hamilton G5 ventilator were included. Patients requiring mechanical ventilation only for asthma, COPD, heart failure, or airway protection were excluded. Additionally, patients less than 18 years of age, pregnant, or imprisoned were excluded. The University of Colorado Hospital utilizes a ventilator protocol that incorporated the ARDS network low tidal volume protocol with the low PEEP titration table. The Colorado Multiple Institutional Review Board approved this study and waived the need for informed consent.

Baseline patient information including age, gender, height, and initial P/F ratio were collected. Human patient data shown in **Figures 6A–C** belong to a 62 years old female with an initial P/F 70, height 165 cm, and weight 127 kg. The data shown in **Figures 6D–F** belongs to a 47 years old male, initial P/F 230, height 177 cm, and weight 96.9 kg. Continuous ventilator data were collected using a laptop connected to the ventilator and using Hamilton Data Logger software (Hamilton, v5.0, 2011) to obtain pressure, flow, and volume measurements. Additionally, the DataLogger software allowed collection of ventilator mode and ventilator settings based on mode [i.e.: set tidal, respiratory rate, PEEP, and fraction inspired oxygen (FiO_2)]. Data were collected until extubation or for up to 7 days per patient.

Parameter Estimation Methodology

The damage-informed lung ventilator model is a complex model and we estimate its parameters for mouse and human clinical ventilator data. In clinical situations, the patient data are variable and often nonstationary because of interventions, patient-ventilator interactions, changes in health, etc., leading to complex parameter estimation issues. Moreover, the model we develop here is not likely to be structurally identifiable (Westwick and Kearney, 2003; Schoukens et al., 2016; Albers et al., 2019c). However, formally computing identifiability properties here is subtle because many parameters in the model functionally affect only part of the breath. This feature helps facilitate the convergence of parameter estimates and potentially leads to the uniqueness of those estimates, although because the DILV model is neither linear nor convex, there is no guarantee of unique global optima and no way of guaranteeing that the optimal solution we compute is a, or the, global optimum. Nevertheless, this feature—parameters being active at different times during a breath—also makes formal structural identifiability calculations complex to compute. These complexities force us to address four issues, (1) computational estimation methodology, (2) management of parameter identifiability issues and parameter selection methods, (3) uncertainty quantification, and (4) estimation evaluation methodology.

Computational Estimation Methodology

Our needs require an estimation methodology that allows us to estimate states and parameters of the model effectively and the respective uncertainties in the estimated parameters. While stochastic methods, e.g., Markov Chain Monte Carlo (MCMC) (Gelman et al., 2013), might guarantee to find global minima and quantifying uncertainty in the estimated parameters values, they are generally quite slow. On the other hand, deterministic methods, e.g., Nelder-Mead optimization (Nelder and Mead, 1965), are substantially faster and by choosing many initial conditions, we are still able to quantify the uncertainty of a solution. In particular, here we infer parameters with a standard class of deterministic, multivariate, constrained nonlinear optimization methods, interior-point methods (Bertsimas and Tsitsiklis, 1997; Nocedal, 2006), a choice that is not critical among constrained, nonlinear optimization algorithms. As such, we focus on a smoothing task that employs deterministic nonlinear optimization methods that work well with careful parameter selection and constraints and can be used to quantify uncertainty.

Management of Parameter Identifiability and Parameter Selection Methods

Irrespective of the estimation methodology, identifiability failure—non-uniqueness of non-convergence of solutions—can occur. In particular, the DILV model is likely not identifiable. To mitigate this problem, we use three different approaches to minimize impacts of identifiability failures while estimating parameters for a given waveform data. First, the model was constructed such that each parameter in the model contributes to the specific feature in the volume and pressure curves, allowing the parameter to be estimated relative to the specific, time-limited feature by definition. Second, we constrain the ranges of all parameters to lie within physically possible values. And third, we do not estimate every parameter in all circumstances but rather limit parameters estimated to those relevant for a given setting and fix many low-impact, low-sensitivity parameters (Law et al., 2015; Asch et al., 2016; Albers et al., 2019b).

In more detail, the DILV model includes two state variables, volume and pressure with one overlapping parameter, the frequency of the breath (θ). The volume model has six parameters (a_1, b_1, ϕ_1, β_1, β_2, and A_v). The pressure model has fourteen parameters (a_2, b_2, ϕ_2, a_3, b_3, ϕ_3, β_3, β_4, β_5, β_6, A_{p1}, A_{p2}, A_{p3}, and A_{p4}). Many of these parameters can effectively be uniquely estimated because they operate on a particular part of the waveform, e.g., parameters that control the gradient of the rising signal (β_1, β_3) and falling signal (β_2, β_4) and amplitudes of the waveforms (A_v, A_{p1}). Nevertheless, there are parameters that are not necessarily uniquely estimable, e.g., parameters that control feature A1 (a_3, b_3, ϕ_3, and A_{p3}) and features B1 and B2 (β_5, β_6, and A_{p2}).

Uncertainty Quantification

Because we use deterministic optimization methods whose final solution depends on the initialization, we quantify uncertainty by randomly sampling a set optimization initialization for the parameters we estimate from a uniform distribution within a bounded interval (upper and lower bounds) centered around initial values (Smith, 2013; Albers et al., 2019a). The boundaries of the intervals were chosen to exclude parameter variation that was unrealistic. The upper and lower boundaries of the intervals were chosen by computing parameters that provide a qualitative agreement between the model and the measured response. The optimal parameter estimate is then represented as a probability density in a similar way as is created using MCMC, allowing us to understand how informative, unique, and uncertain a given parameter solution set is. Additionally, we have uncertainty for individual breaths—we estimate every breath many times computing an uncertainty in by-breath parameter estimation—and uncertainty due to variation in many breaths over time. This allows us to both resolve and quantify single-breath features, and how those features vary over time, for different breaths, and even between individuals.

Estimation Evaluation Methodology

The output of this computational method is a *distribution* of optimal solutions. Through this distribution, we understand the robustness of the solution and the uncertainty of the solution. If the distribution of solutions has multiple modes with similar error then we can conclude that there are multiple plausible solutions. Similarly, if the distribution of solutions is narrow or wide with similar errors, we can conclude that the model either does or does not depend highly on a given parameter. And finally, it is the distribution of parameter solutions that *define the phenotype computed by the model* in the sense that the distribution of parameters explains the by-breath characterization of the patient. We verify a model's ability to represent data by computing the mean squared error between the model computed with parameter values taken as the medians of the optimally computed solution and the data. There is uncertainty in these MSE values too, and if one model has a lower MSE value than another with non-overlapping uncertainty in MSE, we conclude that the model with the lower median MSE more accurately represents the data.

RESULTS

In this section, we qualitative and quantitative validate the DILV model using numerical simulations and measured data, respectively.

Qualitative Model Validation, Parametric Descriptions, and Simulated Model Variability

The first step in model validation is the qualitative validation (Jolliffe and Stephenson, 2012) that involves demonstrating the model has enough flexibility to recapitulate the key features that are often seen in clinically collected volume and pressure waveform data. We then identify the parameters that correspond to hypothesized lung physiology by analyzing simulated pressure and volume waveforms.

Volume Model Flexibility

The volume model flexibility is demonstrated in **Figure 3** where we vary the rates of inspiration (feature A) and expiration (feature B) through the terms f_{v1} and f_{v2}, which are controlled by parameters β_1 and β_2 (**Figures 3A,B**), respectively. The full variability of terms f_{v1} and f_{v2} is shown in **Supplementary Figure 1**. Additionally, the amplitude of the volume waveform is controlled by A_v (**Figure 3C**), variations in respiratory rate are controlled by θ (**Figure 3D**). Finally, the I:E ratio, the starting point of the breath in the breathing cycle and the smoothness of the waveform are set by b_1, ϕ_1, and a_1 as shown in **Supplementary Figure 2**, respectively.

Pressure Model Flexibility

The pressure model flexibility is demonstrated in **Figure 4** where we vary the five features of the pressure waveform via respective parameters: variation in the rate of change of the pressure before (A1 in **Figure 1B**) and after (A2 in **Figure 1B**) the inflection point during inspiration; the shape of the peaks at the beginning (B1 in **Figure 1B**) and end (B2 in **Figure 1B**) of the plateau pressure; and variation in the rate of change of the pressure during expiration

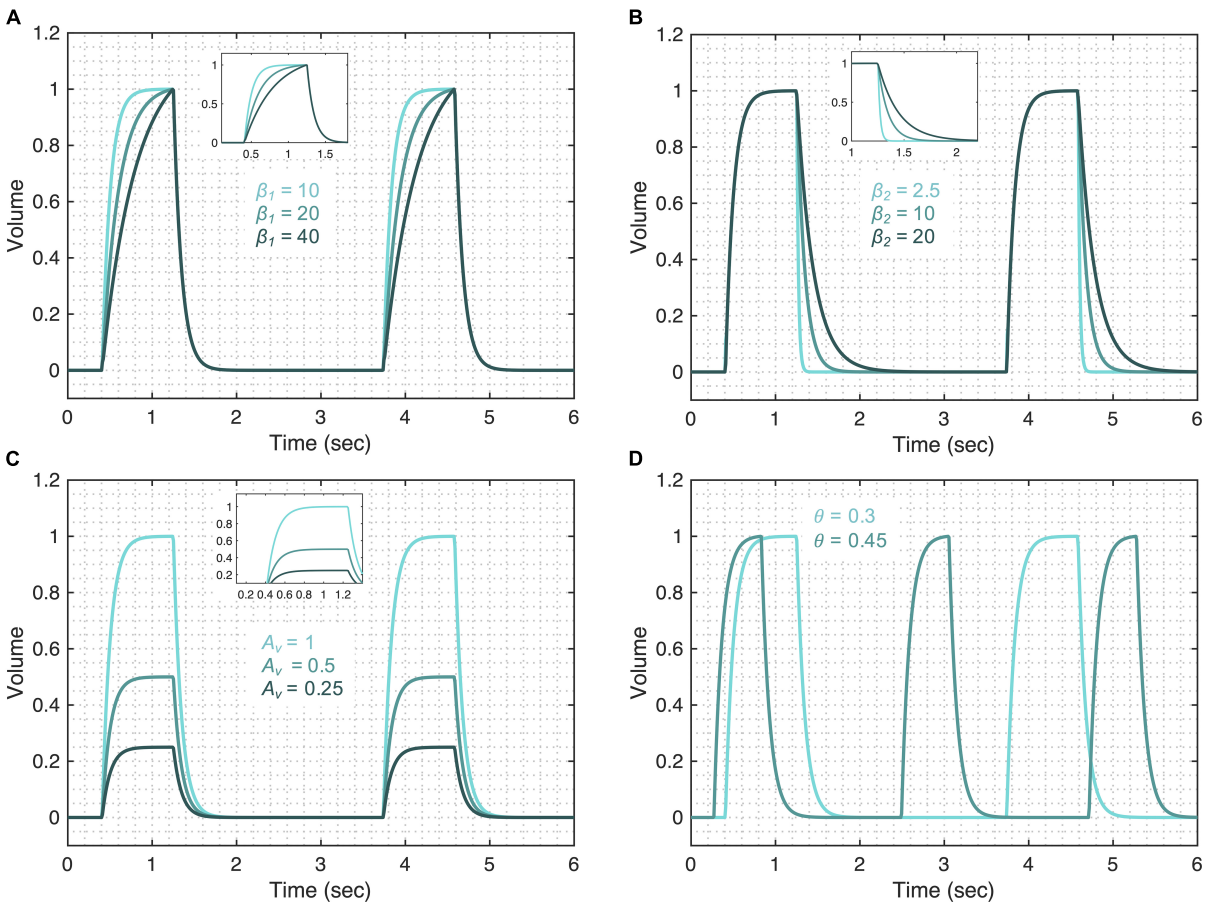

FIGURE 3 | Demonstrating the volume model flexibility by varying parameters that alter characteristic features of the volume waveform. The gradient of the rising and falling signals can be altered using the **(A)** β_1 and **(B)** β_2 parameters, respectively. Increased values of these parameters increase the transient time for the signal to reach the same volume level. **(C)** The amplitude of the waveform can be altered using the parameter A_v. **(D)** Changes in the respiratory frequency (θ) change the period of the breath. The output of the model (V) was calculated using Eqs 1–5 while considering $\theta = 0.3$, $a_1 = 200$, $b_1 = 0.7$, $\phi_1 = 0$, $\beta_1 = 30$, $\beta_2 = 10$, and $A_v = 1$. The respective variation in the functions that make the volume model is shown in **Supplementary Figure 1** for each case. Note that the model variability shown here is independent of the ventilator mode.

(C in **Figure 1B**). In brief, these features are controlled by the following parameters.

The initial gradient of the pressure during inspiration (A1) is controlled by the a_3 parameter such that higher values of a_3 result in a slower rising signal (**Figure 4A**). The full variation that these terms are capable of is shown in **Supplementary Figure 3**. The shape of the initial gradient signal (A1) before the inflection point can be altered using the b_3 parameter (**Supplementary Figure 4A**) and the amplitude of the initial gradient alteration is controlled by the A_{p3} parameter (**Supplementary Figure 4B**). By setting A_{p3} parameter to zero, feature A1 can be removed from the pressure waveforms. The rate of inspiratory pressure after the inflection point (A2) is specified by β_3 such that higher values of β_3 result in a slower rising signal (**Figure 4B**). The shapes of the peaks at the beginning (B1) and end (B2) of the plateau pressure are controlled by several parameters. The overall shape of the peaks is controlled by the β_5 (**Figure 4C**) and the sharpness of these peaks can be further altered by β_6 (**Supplementary Figure 4C**). The amplitude of the peaks is controlled by A_{p2} (**Supplementary Figure 4D**). By setting A_{p2} parameter to zero, features B1 and B2 can be turned off. Additional control of features B1 and B2 can be achieved in combination with parameter β_3 shown in **Supplementary Figures 4E,F**. The rate of pressure decrease during expiration (C) is specified by β_4 such that higher values of β_4 result in a slower falling signal (**Figure 4D**). Finally, the amplitude of the plateau pressure can be altered using the A_{p1} parameter (**Supplementary Figure 4G**). The I:E ratio is defined by the b_2 parameter in the same way that parameter b_1 controls the I:E ratio in the volume model (**Supplementary Figure 2A**). A summary of model parameters is provided in **Table 1**.

Qualitatively Relating the Model Parameters With the Lung Function Parameters

In order to be able to use the DILV model parameters to infer lung health, it is required that we set up the initial framework

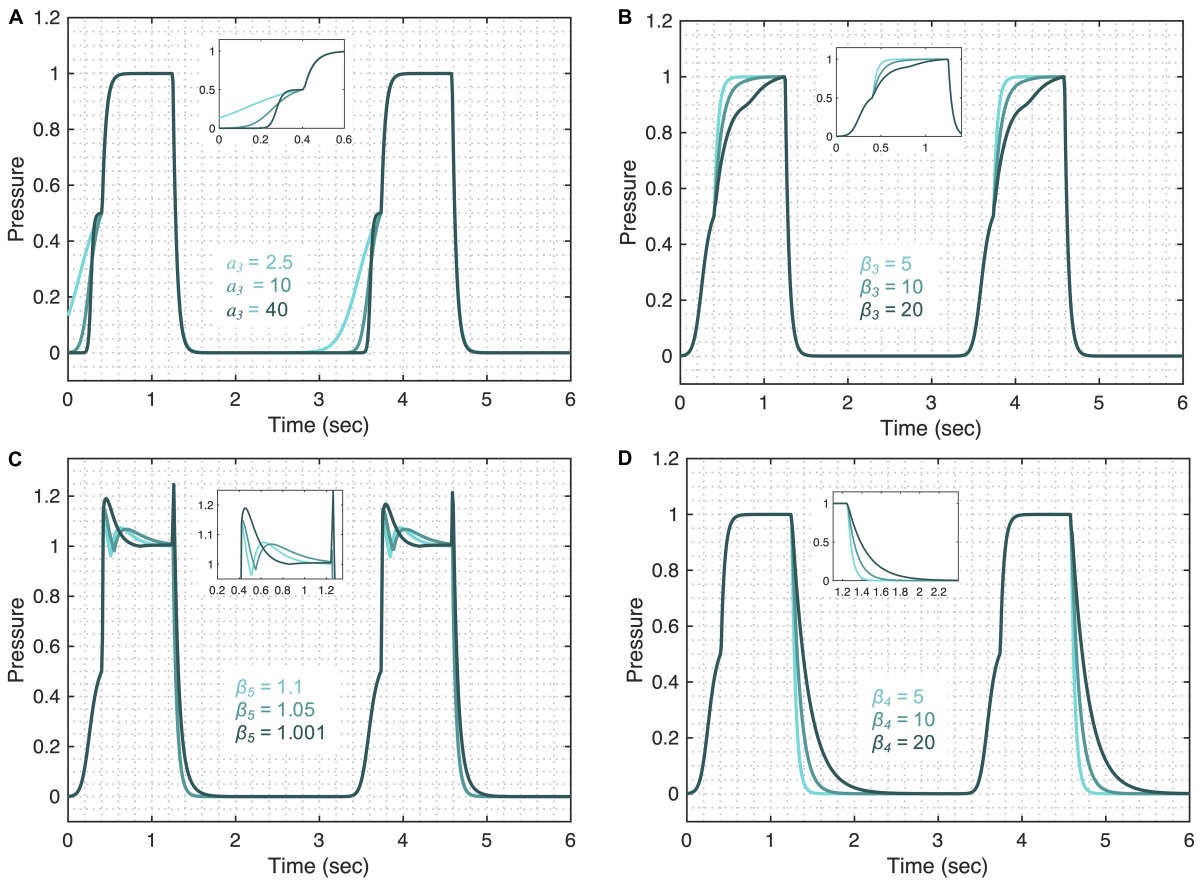

FIGURE 4 | Demonstrating the pressure model flexibility by altering relevant features in the pressure waveform. The initial gradient of the pressure signal during inspiration at low volume (feature A1) is controlled by **(A)** the a_3 parameter. **(B)** The gradient of the rising signal after the inflection point (feature A2), is controlled by the β_3 parameter. **(C)** The shapes of the peaks at the beginning (feature B1) and at the end (feature B2) of the plateau are regulated by the β_5 parameter when $A_{p4} = 0.5$. **(D)** The gradient of the falling signal (feature C) during expiration can be modified by the β_4 parameter. Equations 6–18 were used to simulate the response of the pressure model while considering $\theta = 0.3$, $a_2 = 200$, $b_2 = 0.7$, $\phi_2 = 0$, $a_3 = 10$, $b_3 = 0.9$, $\phi_3 = -0.6$, $\beta_3 = \beta_4 = 5$, $\beta_5 = 1.001$, $\beta_6 = 1.1111$, $A_{p1} = 1$, $A_{p2} = 0.5$, $A_{p3} = 0.5$, and $A_{p4} = 0$. The respective variations in the terms that make the pressure model are shown in the **Supplementary Figure 3** for each case. Note that the model variability shown here is independent of the ventilator mode.

to correlate the model parameter with the lung condition, given the model parameters are not physiological parameters but rather chosen to control specific features in the waveform data. On this account, the DILV model is anchored to physiology through variations or deviations from nominal breath waveforms that are hypothesized to relate to lung conditions observed in mechanical ventilation data collected in lab and clinical settings. Throughout the manuscript, we list the proposed physiological interpretations of the parameters – a short description of how the model parameters contribute to the model is provided in **Table 1** – but here we will go into interpretative depth regarding the qualitative correlation between model parameters and the fundamental characteristics of the lung such as compliance and resistance. In this qualitative interpretation, we consider only one variable (volume in PCV and pressure in VCV) while assuming the other waveform does not change breath-to-breath (pressure in PCV and volume in VCV).

We first show how the changes in the volume model parameters can be qualitatively related to changes in lung compliance and resistance when the volume variable is free. For that, we focus on three model parameters that might have direct physiological meaning: β_1, β_2, and A_v. The first parameter, β_1 might be inversely correlated with lung compliance as higher values of β_1 result in a lower inspiratory flow rate (**Figure 3A** and **Supplementary Figure 5A**). During PCV, the inspiratory flow rate will decrease with reduced compliance or increased resistance. A second parameter, β_2, controls the gradient of expiration and is captured as feature B in **Figure 1A**. Higher values of β_2 result in a longer expiration (cf. **Figure 3B** and **Supplementary Figure 5A**) and so β_2 is directly proportional to the expiratory time constant, which is the product of resistance and compliance. Finally, parameter A_v controls the amplitude of the volume waveform and for the same pressure waveform (in PCV) indicates a direct correlation with compliance (**Figure 3C** and **Supplementary Figure 5A**). In VCV, parameter A_v would present the tidal volume, which is set by the ventilator.

The pressure model has five parameters that may reflect aspects of lung compliance during VCV: a_3, b_3, β_3, A_{p1}, and

TABLE 1 | Interpreting damaged-informed lung ventilator model parameters.

Parameter	Model relevance	Physiological relevance (with increased values)
Volume model		
θ	Number of breaths/s. Higher values result in a higher number of breaths/s	–
a_1	Smoothness of the square waveform (f_{b1}). Higher values result in a sharper transition	–
b_1	I:E ratio. Higher values result in smaller inspiration cycle	–
Φ_1	Starting of the inspiration point. Higher value results in a more delayed response	–
$\boldsymbol{\beta_1}$	Gradient of the rising signal. Higher values result in a slower rising signal	Lower compliance and/or higher resistance
$\boldsymbol{\beta_2}$	Gradient of the falling signal. Higher values result in a slower falling signal	Higher expiration time constant
$\boldsymbol{A_v}$	Peak amplitude	Higher overall compliance
Pressure model		
b_2	I:E ratio. Higher values result in a smaller inspiration cycle	–
a_2	Smoothness of the square waveform. Higher values result in a sharper transition	–
Φ_2	Starting of the f_{b2} function. Higher value results in a more delayed response	–
$\boldsymbol{a_3, b_3}$	Gradient of the pressure signal at low volume. Higher values result in a slower rise	Higher low volume compliance
Φ_3	Starting of the inspiration point. Higher value results in a more delayed response	–
$\boldsymbol{\beta_3}$	Gradient of the rising signal after inflection point. Higher values result in a slower rising signal	Higher high-volume compliance
β_4	Gradient of the falling signal. Higher values result in a slower falling signal	–
β_5, β_6	Shape of plateau. Higher value means a sharper peak	Associated with ventilator desynchrony
$\boldsymbol{A_{p1}}$	Peak amplitude	Lower high-volume compliance
A_{p2}	Amplitude of the peaks at the plateau	
$\boldsymbol{A_{p3}}$	Higher values increase the amplitude of f_{p33} function	Moves upper inflection point up
A_{p4}	Pressure base line value	PEEP

The parameters that are correlated with known measures of lung physiology are in bold.

A_{p3}. The parameter a_3, which controls feature A1 (**Figure 4A**), may be directly correlated with low-volume compliance as higher values of a_3 result in slower pressure rise at low volume while maintaining the shape of the gradient (**Supplementary Figure 5B**). Additionally, parameter b_3 can also be used to control feature A1 (**Supplementary Figure 5B**) and is directly related to the low-volume compliance. A third parameter, β_3 controls the rate of pressure increase above the inspiratory inflection point (A2), and higher values of β_3 result in slower pressure increase (**Supplementary Figure 5B**), indicating β_3 might be correlated with high-volume compliance during VCV. A fourth parameter, A_{p1}, defines the plateau pressure with higher values of A_{p1} yielding higher plateau pressures (**Supplementary Figure 5B**), indicating an inverse correlation between A_{p1} and compliance during VCV. Finally, change in the upper inflection point (UIP) can be directly related to the A_{p3} parameter such that higher values of A_{p3} increase the UIP pressure as shown in **Supplementary Figure 5B**. During PCV, these (and other) parameters may be directly controlled via a ventilator.

It is important to note that these interpretations are qualitative and valid only when a change is observed in one of the variables (volume or pressure) while the other waveform (pressure or volume) is held fixed. In cases where both the volume and pressure waveforms change simultaneously, additional interpretation is needed to establish the relationships between pressure and volume parameters. For example, in the pressure signal, interpretation of feature A2 with respect to A1 will be valid only during the constant flow signal (Grasso et al., 2004). Similarly, when there is a change in the amplitude of volume and pressure simultaneously, we use the A_v/A_{p1} to assess compliance.

Damage-Informed Lung Ventilator Model Quantitative Verification for Experimental Mouse Model Ventilator Data

To demonstrate the effectiveness of the DILV model, we now quantitatively validate the model by estimating parameters for data sets corresponding to different phenotypes—e.g., injured versus healthy. We then show that differences in the estimated parameter values reflect different phenotypic states in a manner that is consistent with expected changes due to acute lung injury. Here we consider data from PCV and VCV, in healthy and lung-injured mice, and in the absence and presence of VD.

In Pressure Controlled Ventilation, the Model Outcomes Align With the Injury Status and Single Compartment Model

Figures 5A,B, panel 1 shows two different pressure-controlled breaths recorded in a healthy mouse (green) and after a lung injury induced by injurious lavage and mechanical ventilation (orange). The pressure-volume loops (**Figure 5C**) show a reduction in lung compliance and an increase in hysteresis that is characteristic of acute lung injury. The DILV model estimated states (dashed-dot lines) show the same trends. The estimated parameter values and the respective uncertainty for individual breaths are shown in **Table 2** with bold indicating physiological relevance.

In the volume model, the injured lung showed a lower inspiratory flow rate, quantified by an increase in β_1, and a faster expiration, quantified by a reduction in both β_2 and A_v than the healthy lung model estimates. Given that the inspiratory

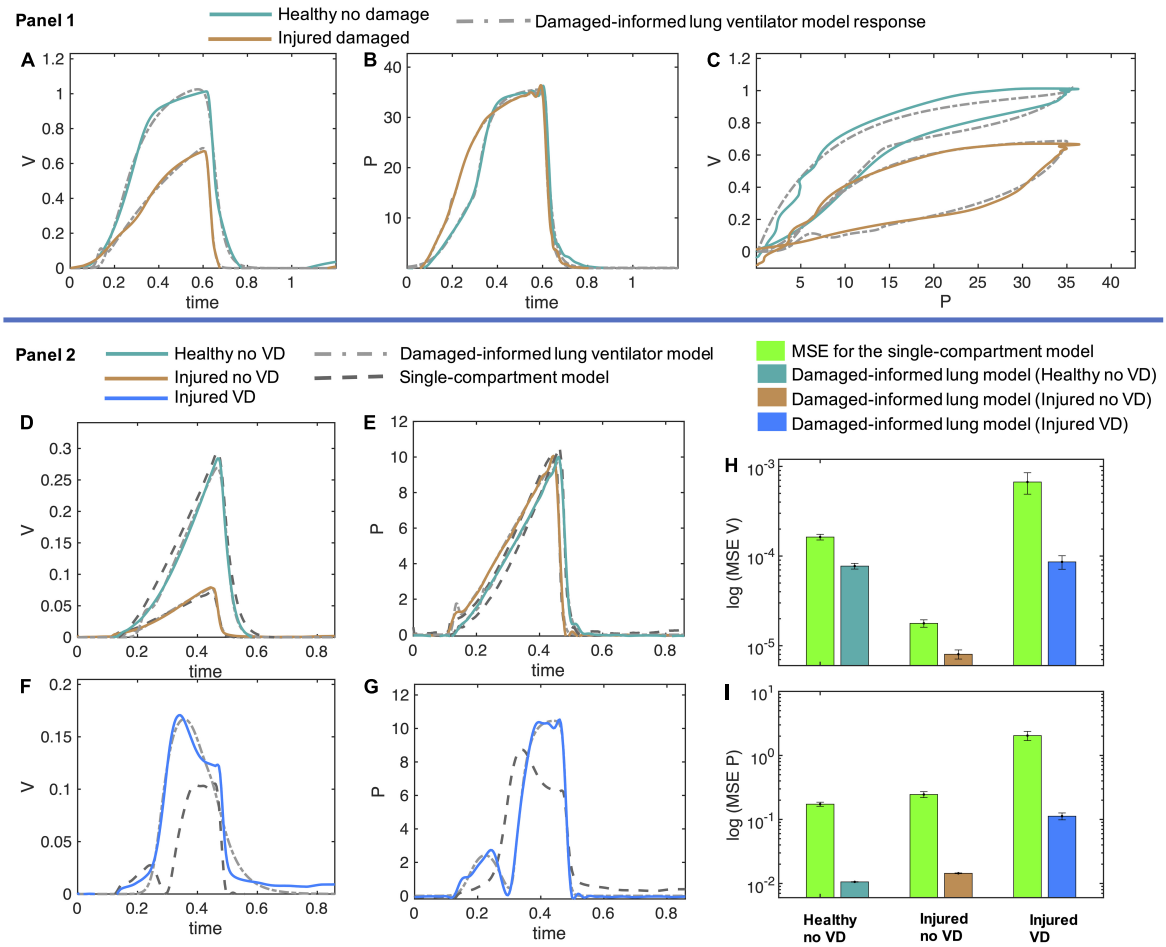

FIGURE 5 | Volume and pressure models' responses closely agree with the experimental data from the representative mice in healthy and injured condition. **(A–C)** In Panel 1, the measured breaths of first mouse are shown in healthy and injured conditions (solid lines) while the damaged-informed lung ventilator (DILV) model response is shown in dashed lines. Equations 1–18 were used to generate the best-fit model response using estimated mean parameter values shown in **Table 1**, respectively. **(D–G)** In Panel 2, three representative breaths of mouse two is shown here, which are corresponding to three different lung conditions (solid lines) while the damaged-informed lung ventilator model response is shown in the dashed-dot lines. For these breaths, histograms of the initial guesses and estimated parameters are shown in **Supplementary Figure 6A**. The response of the single-compartment model is shown in dashed-dashed lines. **(F–I)** The cumulative values of mean squares errors (MSE) of the two models are compared here. These values corresponded to sixty breaths for healthy no ventilator dyssynchrony (VD) and injured no VD cases while ten breaths for injured VD case. For each case and breath, the estimated parameter values and MSE are shown in the **Supplementary Figures 6B–D**. All the data shown here was collected in PCV (see "Materials and Methods").

pressures remain unchanged, this suggests a reduction in lung compliance, and the associated decrease in the expiratory time constant (See **Table 1**).

Physiologic interpretation of the pressure model is limited because of the use of PCV. In this case, the pressure signal is prescribed by the piston ventilator and the observed differences between the healthy and injured lungs are a result of the ventilator control system algorithms. Hence, the respective changes in the parameters' values, such as an increase in parameters a_3 and β_3 correspond to the changes in the ventilator dynamics and not in the respiratory mechanics. These results make an important point: it is essential to see the relative change in the parameters that control these features and to synthesize the model-based inference in a holistic fashion, instead of focusing on any one parameter or feature in isolation.

To analyze changes in lung mechanics in a manner that accounts for ventilator settings, we define the lung compliance $Cd = A_v/A_{p1}$ (**Table 2**), which is the ratio of volume and pressure model amplitudes. As expected, Cd decreases with injury. Furthermore, Cd shows a strong correlation with compliance (Cs) calculated with the single-compartment model (**Table 2**; Mellema, 2013).

Damaged-Informed Lung Ventilator Model Accurately Captures Mouse Model Data With Ventilator Dyssynchrony While the Single-Compartment Model Is Unable to Capture This Variability

In the previous section, we demonstrate that the DILV model can accurately estimate a single breath. We did not, however, validate that the model has enough flexibility to account

TABLE 2 | Estimated model parameters obtained from the optimization scheme for the results shown in **Figure 5** (Panel 1) and **Figure 6** (human patient 1) correspond to the mouse and human data, respectively.

	Figure 5 (Panel 1)		Figure 6 (Patient 1)	
Parameters	**Healthy**	**Injured**	**Beginning**	**Ending**
θ	0.66 ± 0.000	0.66 ± 0.000	0.34 ± 0.000	0.35 ± 0.000
a_1	9.67 ± 0.385	15.41 ± 0.397	7.51 ± 0.258	7.57 ± 0.282
b_1	0.59 ± 0.006	0.53 ± 0.006	0.66 ± 0.000	0.63 ± 0.000
Φ_1	0.09 ± 0.007	–0.01 ± 0.007	0.42 ± 0.003	0.51 ± 0.002
β_1	**112.97 ± 9.733**	**458.95 ± 8.179**	**10.96 ± 0.223**	**12.53 ± 0.240**
β_2	**28.35 ± 10.490**	**10.60 ± 10.590**	**12.42 ± 0.051**	**12.64 ± 0.039**
A_v	**1.03 ± 0.006**	**0.70 ± 0.003**	**402.61 ± 0.368**	**337.08 ± 0.531**
a_2	52.06 ± 1.440	32.11 ± 1.514	27.39 ± 0.118	17.73 ± 0.163
b_2	0.80 ± 0.002	0.66 ± 0.001	0.67 ± 0.000	0.66 ± 0.000
Φ_2	0.34 ± 0.002	0.09 ± 0.002	0.35 ± 0.002	0.32 ± 0.001
a_3	**2.55 ± 0.334**	**5.11 ± 0.205**	**7.71 ± 0.183**	**18.37 ± 0.146**
b_3	**1.00 ± 0.002**	**0.53 ± 0.003**	**0.91 ± 0.000**	**0.90 ± 0.000**
Φ_3	0.00 ± 0.002	0.00 ± 0.005	0.15 ± 0.001	0.14 ± 0.001
β_3	**50.00 ± 0.388**	**100.84 ± 0.262**	**7.25 ± 0.157**	**12.88 ± 0.147**
β_4	18.54 ± 0.239	11.93 ± 0.193	1.95 ± 0.121	2.52 ± 0.064
β_5	–	–	1.0014 ± 0.0001	1.0048 ± 0.0001
β_6	–	–	1.1262 ± 0.0012	1.0771 ± 0.0055
A_{p1}	**35.53 ± 0.018**	**35.02 ± 0.017**	**16.58 ± 0.018**	**11.64 ± 0.008**
A_{p2}	–	–	3.80 ± 0.011	2.48 ± 0.022
A_{p3}	**14.00 ± 0.081**	**9.60 ± 0.077**	**3.90 ± 0.022**	**4.10 ± 0.016**
A_{p4}	0.06 ± 0.035	0.00 ± 0.021	19.98 ± 0.011	17.91 ± 0.004
Cs	0.030	0.019	26.80	31.40
Cd	0.029	0.020	24.28	28.96

The error values were determined using the standard error of the mean for individual breaths. To quantify uncertainty in parameter estimates, each individual breath was estimated 1,000 times. The parameters that are correlated with a known measure of lung physiology are in bold. Here, Cs and Cd are lung compliance values extracted by fitting the single-compartment model to data (Cs) and from the damaged-informed lung ventilator model (Cd) = A_v/A_{p1}.

for large variations in the waveform data, or that the DILV model can estimate a large number of breaths reliably while maintaining unique and consistent solutions of parameters values for each breath. To show these characteristics, we estimate a large number of breaths for the second mouse in three different lung conditions: (1) healthy breaths without VD, (2) injured breaths without VD, and (3) injured breaths with VD (See "Materials and Methods"). In the 1st and 2nd cases, we selected sixty breaths in a sequence from the random location out of 424 and 128 breaths, respectively. In the 3rd case, we manually selected ten breaths out of 332 breaths that had VD from the data set containing breaths with and without VD. Here, we define VD as any substantial respiratory effort because the flexiVent small animal ventilators do not allow the subject to trigger a breath. A representative breath for each case is shown in **Figures 5D–G**, panel 2 along with the DILV model response at the optimum parameter values, which are listed in **Supplementary Table 1**. Histograms of the initial guesses and estimated parameters are shown in the **Supplementary Figure 6A**. We observed minor variability in most of the estimated parameters values for individual breaths, suggesting that those features are modularly controlled by the respective parameter. We do observe high variability in some parameters (a_1, β_1, a_3, and β_3) due to the low sensitivity of the model for those parameters (**Supplementary Figure 6A**).

To demonstrate what is gained by the DILV model we compare it to single-compartment model (Bates, 2009) estimated resistance and compliance to estimate the same breaths for each case (**Figure 5**, panel 2). The single-compartment model has substantially larger estimated mean squares errors (MSE) and these errors increase as the mouse lung condition worsens and in the presence of VD (**Figures 5H,I** and **Supplementary Figures 6B–D**). Consequently, in terms of lung compliance values, the two models' outcomes closely agree in the healthy lung case but then diverge somewhat for the injured lung and more substantially during VD (**Supplementary Figures 6E–G**). These discrepancies have their root in the limited ability of the single-compartment model to estimate VD (**Figures 5F,G**), errors that are quantified by the MSE between model estimates and data (**Supplementary Figures 6B–D**). Note that the calculated compliance values include the effects of muscle effort, which explain the differences in compliance with and without VD in the same injured mouse.

In Volume-Controlled Ventilation, the Pressure Model Outcomes Align With the Injury Status and the Single Compartment Model

Above we verified the DILV model using data sets collected during PCV, where the estimated volume model parameters reflected the lung dynamics since the volume was the free variable. We now consider data collected during VCV so that

the estimated pressure model parameters reflect changes in lung condition. Here, we consider variations in PEEP during low tidal volume ventilation (VCV). The pressure model indicates a reduction in compliance in the injured lung as quantified by lower values of parameters a_3, b_3, and β_3, and elevated estimates of in A_{p1} (**Table 1**, **Supplementary Figure 7**, and **Supplementary Table 1**). In contrast to the PCV results shown in **Figure 5**, differences in parameter estimates between healthy and injured lungs in the pressure model were much larger compared to those estimated differences in the volume model. This is expected since the tidal volumes were approximately equal during VCV, and the reduction in compliance is reflected in increased pressure. This effect can be inferred by analyzing the A_v/A_{p1} ratio showing a reduction in the injured cases at both the PEEP settings (**Supplementary Table 1**). We also note that the healthy lung becomes stiffer at PEEP = 12 cmH_2O due to strain stiffening. In contrast, the injured lung becomes more compliant at high PEEP, which our previous studies in this injury model attribute to recruitment (Mellenthin et al., 2019).

Damage-Informed Lung Ventilator Model Quantitative Verification for Intensive Care Unit Patient-Ventilator Data

The DILV model is intended to be used with both laboratory data and clinical ventilator data where standard models, such as the single-compartment model, cannot recapitulate all of the potentially relevant waveform features. To show the clinical applicability of the DILV model we consider waveform data of two ICU patients, the first—patient 1—includes waveform data without VD and the second—patient 2—has waveform data with VD. For each case, we estimate each individual breath 1,000 times to quantify uncertainty in parameter estimates for each of 263 breaths to quantify uncertainty in parameter estimates across many breaths. These data were recorded near extubation when ARDS had nearly resolved. For both patients, the ventilator was operating in patient-triggered mode, a ventilator mode that is not possible in our mouse ventilators but is commonly used in the ICU.

Intensive Care Unit Data-Driven Verification in the Absence of Ventilator Dyssynchrony (Patient 1)

For patient 1, we selected a sequence of 130 breaths without VD at a random location out of 1,829 breaths and performed parameters estimation breath by breath. The sequence of breaths starts at PEEP = 20 cmH_2O and switches to PEEP = 18 cmH_2O at breath number 68. **Figures 6A–C** shows two representative breaths along with the DILV model response at the optimum parameter values (**Table 2**). Histograms of the initial guesses and estimated parameters are shown in the **Supplementary Figure 8A** for the respective breaths. For all the model parameters, we observed unimodal estimated parameter distributions with low variance, suggesting that each parameter controls a specific feature of the waveform. We also estimated each breath using the single-compartment model and substantially higher MSE compared to the DILV model (**Figures 6G,H**). Note that in **Figures 6G–J**, an MSE ratio less than one indicates that the DILV model produced waveforms that were more similar to the measured data.

Pressure-volume (PV) loops for these cases (**Figure 6C**) suggest that lung compliance is increased by the prescribed change in PEEP. We found that the model-estimated parameters indicate an increase in compliance (the A_v/A_{p1} ratio) with a reduction in PEEP (**Table 2**). The increased compliance at lower PEEP agrees with the single-compartment model (Bates, 2009) response (**Supplementary Figures 8B,C**) and also the patient outcome (successful extubation). Moreover, a significant increase in parameters a_3 and β_3 suggested the same (**Table 2**). The prescribed reduction in PEEP was reflected in a reduction in A_{p4}.

Intensive Care Unit Data-Driven Verification in the Presence of Ventilator Dyssynchrony (Patient 2)

In the cases where VD is present a more thorough parameter interpretation is needed to quantify and understand the patient-ventilator interaction. To show this, from patient 2's data we randomly selected 133 breaths out of 3,201 breaths that showed mild to severe flow limited VD. Two representative breaths for this case are shown in **Figures 6D–F** along with the DILV model's estimate of these breaths at the optimum parameter values (**Supplementary Table 1**) and the single compartment model fit. Histograms of the initial guesses and estimated parameters for these breaths are shown in the **Supplementary Figure 9A**.

PV loops for these breaths (**Figure 6F**) suggest that lung compliance is increased prior to extubation compared to earlier in the ICU course. This qualitative observation is supported by the increased A_v/A_{p1} ratio (**Supplementary Table 1**) that is a measure of compliance. However, it is important to note that this compliance includes the additional effects of VD. To further demonstrate the importance of the DILV model, we compared the DILV model's estimate of the breaths with the single-compartment model (Bates, 2009) estimates for each breath. The single-compartment model estimates of the breaths have substantially higher MSE values for patient 2 compared to patient 1 (**Figures 6G–J**) due to the presence of VD. Accordingly, we expect large errors in the compliance values estimated with the single-compartment model (**Supplementary Figures 9B,C**). These results agree with the fact that the DILV model can estimate the volume and pressure waveform data more accurately, especially when the waveforms have high variability, as in the case of patient 2 with VD.

The mouse data verification showed that the DILV model is able to estimate most of the parameters for individual breaths. It is also important to quantify uncertainty across many breaths and in different patients. Analyzing the variability in the estimated parameters over several breaths might capture the lung condition's heterogeneous nature, including many potentially different and differently damaging breaths that show VD. In the ICU, there are no controlled experiments, and patients simultaneously experience many types and severities of VD, different interventions, heterogeneous injurious insults, etc. As such, we expect to see minor variability in parameter estimates when many breaths of a patient are approximately the same compared to large variability in the parameter estimates when breaths are heterogeneous. For example, we observed a low

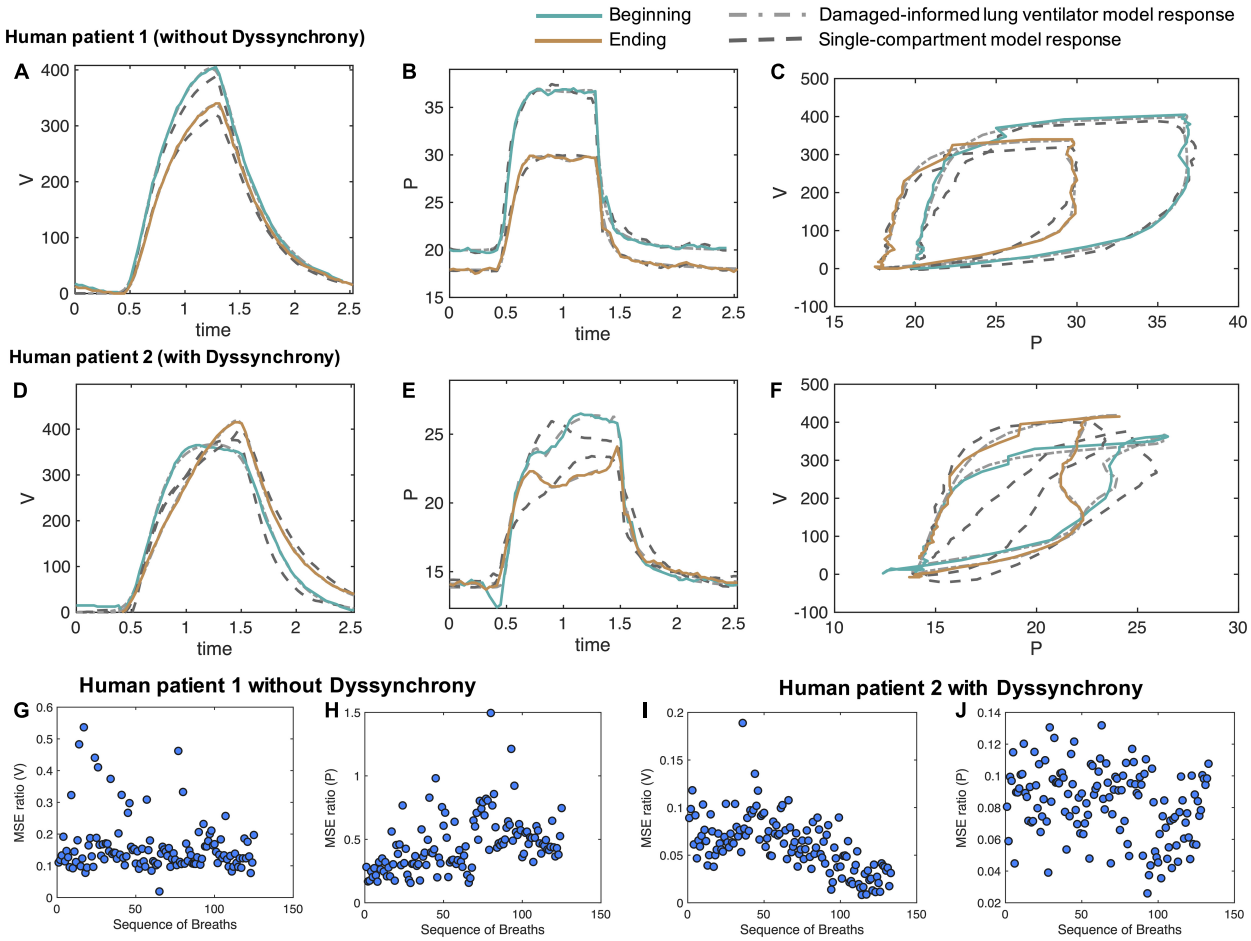

FIGURE 6 | Damaged-informed lung ventilator model can accurately follow breaths of the ICU patients with ARDS without and with dyssynchrony. Measured representative breaths of **(A–C)** patient 1 without dyssynchrony and **(D–F)** patient 2 with flow limited dyssynchrony are shown in solid lines, while the DILV model inferred response is shown in the dashed-dot lines. The response of the single-compartment model is shown in dashed-dashed lines. Histograms of the initial guesses and estimated parameters are shown in the **Supplementary Figure 8A**. For all the breaths in each case, the corresponding ratio of mean squares errors (MSE) between the DILV model and the single-compartment model is shown in panels **(G–J)**, respectively, while histograms are shown in **Supplementary Figures 9, 10**. The response of the DILV model was determined using Eqs 1–18 to generate the best-fit model response using estimated mean parameter values shown in **Table 1** and **Supplementary Table 1**. All the data shown here were collected in human-triggered mode (see "Materials and Methods").

variability in all the volume model parameters over several breaths with the exception of A_v for patient 1, indicating that the volume waveforms' characteristic shape remains the same at different time points except for variations in tidal volume. This contrasts with what we observed for patient 2 where VD drove heterogeneity and substantial deviations from more normal breaths (**Supplementary Figures 10, 11**). More importantly, parameters associated with patient-VD can be used to infer the presence of VD. In patient 2, we observed increases in the β_5, β_6, and A_{p2} parameters which align with the visual determination of VD in those breaths (**Supplementary Figures 10, 11**).

Taken together, these results suggest that the DILV model can reproduce a wide variety of waveform data and is capable of extracting hypothesis-driven, clinically-relevant information from the waveforms that might facilitate a systematic interpretation of the dynamics of the injured lung.

DISCUSSION

In this work, we developed a new damage-informed lung ventilator model that represents pressure and volume waveform data by reconstructing the waveforms from hypothesis-driven modular subcomponents. We then preformed a proof-in-principle verification that the model can potentially represent hypothesized damage in humans and mice. The model accurately estimated pressure and volume waveforms data and consistently distinguished healthy from injured lungs based on parameter estimation. Furthermore, we directly incorporate clinical and physiologic knowledge regarding important and observable features into the model that might be associated with the lung pathophysiology—the subcomponents of the model represent hypothesis-driven deviations from normal breaths. We also analytically define lung compliance in terms of model parameters and demonstrate changes in compliance values that agree with

experimentally induced lung injury. This is a proof of principle work where our objective was to develop a ventilator waveform data-based lung model and demonstrate that the model has the potential to be used both with the laboratory and clinical data and infer lung condition.

To demonstrate what is gained with this novel approach, we present a comprehensive comparison between the DILV model and the single-compartment model for a wide range of ventilator waveforms related to different lung conditions and patient-ventilator interactions. We include pressure- and volume-controlled ventilation in healthy and lung-injured mice and in humans in the absence and presence of VD. Through this comparison, we establish that the DILV model can reproduce the features present in the waveform data and report lung compliance values that agree with lung condition (**Figures 5**, **6** and **Supplementary Figures 6–11**). This is primarily possible because of our unique waveform-based approach that enabled the model to have enough flexibility. At the same time, the model is limited using prior knowledge so as not to have the capability to estimate every possible variation in PV waveforms, but rather is constrained to estimate the features of the ventilator data that are the most clinically impactful. This approach lives between a machine learning approach, where the model is flexible enough to estimate every feature and must then discern which features are important through regularization to prevent overfitting, and the fully mechanistic lung modeling approach where the observed physiology must emerge from the proposed lung mechanics. It is possible that taking this middle path will help advance all approaches.

The most direct application of the DILV modeling approach is to quantify the qualitative physiological interpretation of pressure and volume data. An experienced clinician or physiologist can infer the status of a patient, the safety of ongoing ventilation, the presence of VD, and other important details from visual inspection. However, we currently do not yet have methods to identify all of these characteristics in ventilator data quantitatively. The entire waveform may be utilized and this provides a rich repository of data that is challenging and time-consuming to use for diagnosis and treatment. In contrast, summarizing the waveform data in scalar values for resistance and compliance may cast aside important details such as identifying dyssynchrony. Our approach may offer a methodology for condensing the pressure-volume data to track changes in injury severity over time, and estimate injury phenotypes (**Supplementary Figures 10, 11**). A similar phenotype study on a large dataset could be used to categorize and understand lung injury, serve as outcome measures for interventions, and describe the impacts of dyssynchrony (Sottile et al., 2018a) and VILI (Chiumello et al., 2016; Aoyama et al., 2018).

Lung injury diagnosis and decision-making are based in part on the interpretation of the pressure, volume, and flow waveforms. However, different pathophysiologic mechanisms can lead to the same observed waveform features. For example, increased driving pressure could be a result of derecruitment (alveolar collapse) or alveolar flooding (Gattinoni et al., 1987; Smith et al., 2020). In other words, the human-based inference using limited waveform data can be ill-posed. The DILV modeling and parameter estimation approach could allow to estimate a large number of breaths efficiently with unique solutions (**Supplementary Figures 10, 11**). We could therefore use the DILV model to estimate over many similar but varied breaths, and might be able to better triangulate the most probable pathophysiologic drivers because the primary driver of damage will likely be present, and significant, despite inter-breath variations. At the same time, more extraneous details will not be consistently expressed in every breath.

Note that in the DILV model, an explicit coupling between pressure and volume signals is absent. We have intentionally taken this approach to preserve flexibility so that we can accurately recapitulate a wide variety of clinically and experimentally observed features in the pressure and volume signals, including the effects of VD (**Figures 5F,G**, **6D–F**). Such flexibility in the model outcome is not always possible with rigid coupling between pressure and volume data, as we have shown by comparing the DILV model response with the single-compartment model. This is not to say that pressure and volume are totally independent in the DILV model because we utilize the same respiratory rate for both. In addition, we show that the ratio of a volume and pressure model parameter (A_v and A_{p1}) describes lung compliance. In future studies, we will link additional specific components of the pressure and volume waveforms through physiologically relevant parameters such as the nonlinearity of lung elastance or inspiratory and expiratory flow resistance. Alternatively, a compartment-based model could be used to incorporate the physiologic coupling between pressure and volume data by utilizing the outputs from the DILV model presented here as inputs for compartment models. If the DILV model is used to preprocess the data before analysis using a compartment model, it is possible to formulate the problem entirely of ordinary differential equations, opening up a range of more efficient inference machinery (Bertsimas and Tsitsiklis, 1997; Nocedal, 2006; Albers et al., 2019b).

Finally, our work here has several notable limitations. *First*, this is a model development work, where we built a new lung model and showed that the model can accurately recapitulate waveforms and estimate accepted physiological parameters such as compliance as a baseline evaluation. This is sufficient for proof-in-principle that the model can capture physiologic differences. However, establishing that the model can accurately differentiate more specifically defined phenotypes will require validation on much larger laboratory and clinical populations. Moreover, to tie the model outputs to injury phenotypes, the pathogenesis of VILI, etc., we will have to establish the concordance between the model estimates of human and mouse-model data in similar settings and validate the phenotypes, etc., within the mouse lung. This work will be done in the following steps: hypothesize damage-related feature(s) within human ventilator, estimate model for humans and extract contextual clinical information (e.g., lung injury source), create mouse model data with a context similar to the human data, estimate the model for mice, validate concordance of model estimates between humans and mice, validate the damage severity and cause within the mice.

Second, the human data in this study were collected using a specific ventilator (Hamilton G5) operated in a pressure-controlled volume targeted mode. For the wider applicability of the model, additional data verification is required across different ventilators and ventilation modes. *Third*, in this work we did not explicitly relate our model parameters with the physiological or morphometric data. We rather pose hypotheses about the presence and physiological meaning of waveform features that deviate from normal instead of observing the deviant features emerging from lung physiology. For this interpretation, we relied on the expertise of a laboratory ventilation expert (BS) and a critical care physician (PS). However, it is likely that differing opinions will exist among experts. Collecting and synthesizing such information will require a different qualitative study. Moreover, there may be differing opinions regarding what should and should not be included in the model. This does not negate our novel methodology or the DILV model. In fact, the model was constructed with these issues in mind to be flexible, allowing for the testing of differing hypotheses mind. These issues suggest future work is necessary to understand better and verify clinically important features. Alternatively, we may instead seek to link model features to patient outcomes, thus establishing the important characteristics of the model by linking those parameters to outcomes. *Fourth*, in this manuscript, we have incorporated the human waveform data that has flow limited VD to demonstrated that the DILV has enough flexibility to recapitulate waveforms that have patient-VD. In order to identify and phenotype different types of VD, further model update and evaluation will be required, and this work in progress.

In summary, we developed a data-driven lung and ventilator model that can reproduce the commonly observed features in pressure and volume waveforms during mechanical ventilation. The performance of the model was verified with experimental and clinical data in healthy and injured lungs to demonstrate model efficacy in robustly estimating parameters. These parameters are hypothetically linked to both physiologic and ventilator-based mechanisms. Furthermore, the model outputs yield a pulmonary system compliance that is in good agreement with single compartment model estimates and, as expected, compliance decreases with acute lung injury. This methodology represents a departure from many lung modeling efforts, and suggests future directions of work that can provide another pathway for better understanding lung function during mechanical ventilation and can potentially form a bridge between experimental physiology and clinical practice.

DATA AVAILABILITY STATEMENT

The original contributions presented in the study are included in the article/**Supplementary Material**, further inquiries can be directed to the corresponding authors.

ETHICS STATEMENT

The studies involving human participants were reviewed and approved by Colorado Multiple Institutional Review Board. The Ethics Committee waived the requirement of written informed consent for participation. The animal study was reviewed and approved by University of Colorado, Anschutz Medical Campus Institutional Animal Care Committee (IACUC)-approved protocol (#00230).

AUTHOR CONTRIBUTIONS

DKA, BS, and DJA conception and design of the research, analyzed the data, and evaluated the model. DJA and DKA developed the mathematical model. DKA, BS, and PS designed and conducted the experiments. DKA prepared the figures and wrote the original draft of the manuscript. DKA, BS, PS, and DJA interpreted the results, edited and revised the manuscript, and approved the final version of the manuscript.

FUNDING

This work was supported by National Institutes of Health R01 LM012734 "Mechanistic machine learning," R01 LM006910 "Discovering and applying knowledge in clinical databases," R01 HL151630 "Predicting and Preventing Ventilator-Induced Lung Injury" along with R00 HL128944 and K24 HL069223.

SUPPLEMENTARY MATERIAL

The Supplementary Material for this article can be found online at: https://www.frontiersin.org/articles/10.3389/fphys.2021.724046/full#supplementary-material

REFERENCES

Albers, D., Levine, M., Sirlanci, M., and Stuart, A. (2019a). A simple modeling framework for prediction in the human glucose-insulin system. *arXiv* [preprint]. arXiv:1910.14193,

Albers, D. J., Blancquart, P.-A., Levine, M. E., Seylabi, E. E., and Stuart, A. (2019b). Ensemble Kalman methods with constraints. *Inverse Problems* 35:095007. doi: 10.1088/1361-6420/ab1c09

Albers, D. J., and Hripcsak, G. (2010). A statistical dynamics approach to the study of human health data: resolving population scale diurnal variation in laboratory data. *Phys. Lett. A.* 374, 1159–1164. doi: 10.1016/j.physleta.2009.12.067

Albers, D. J., Levine, M. E., Mamykina, L., and Hripcsak, G. (2019c). The Parameter Houlihan: a solution to high-throughput identifiability indeterminacy for brutally ill-posed problems. *Mathematical. biosciences* 316:108242. doi: 10.1016/j.mbs.2019.108242

Amato, M. B., Meade, M. O., Slutsky, A. S., Brochard, L., Costa, E. L., Schoenfeld, D. A., et al. (2015). Driving pressure and survival in the acute respiratory distress syndrome. *N. Engl. J. Med.* 372, 747–755.

Aoyama, H., Pettenuzzo, T., Aoyama, K., Pinto, R., Englesakis, M., and Fan, E. (2018). Association of driving pressure with mortality among ventilated patients with acute respiratory distress syndrome: a systematic review and meta-analysis. *Crit. Care Med.* 46, 300–306. doi: 10.1097/ccm.0000000000002838

Asch, M., Bocquet, M., and Nodet, M. (2016). *Data Assimilation: Methods, Algorithms, and Applications*. Philadelphia, PA: SIAM.

Bates, J. H. (2009). *Lung Mechanics: An Inverse Modeling Approach*. Cambridge: Cambridge University Press.

Bein, T., Weber-Carstens, S., Goldmann, A., Müller, T., Staudinger, T., Brederlau, J., et al. (2013). Lower tidal volume strategy (≈ 3 ml/kg) combined with extracorporeal CO 2 removal versus 'conventional'protective ventilation (6 ml/kg) in severe ARDS. *Intens. Care Med.* 39, 847–856.

Bertsimas, D., and Tsitsiklis, J. N. (1997). *Linear Optimization*. Belmont, MA: Athena Scientific.

Blanch, L., Villagra, A., Sales, B., Montanya, J., Lucangelo, U., Luján, M., et al. (2015). Asynchronies during mechanical ventilation are associated with mortality. *Intens. Care Med.* 41, 633–641. doi: 10.1007/s00134-015-3692-6

Cavalcanti, A. B., Suzumura, ÉA., Laranjeira, L. N., de Moraes Paisani, D., Damiani, L. P., Guimarães, H. P., et al. (2017). Effect of lung recruitment and titrated positive end-expiratory pressure (PEEP) vs low PEEP on mortality in patients with acute respiratory distress syndrome: a randomized clinical trial. *JAMA* 318, 1335–1345.

Chiew, Y. S., Chase, J. G., Shaw, G. M., Sundaresan, A., and Desaive, T. (2011). Model-based PEEP optimisation in mechanical ventilation. *Biomed. Eng. Online* 10:111.

Chiumello, D., Carlesso, E., Brioni, M., and Cressoni, M. (2016). Airway driving pressure and lung stress in ARDS patients. *Crit. Care* 20:276. doi: 10.1186/s13054-016-1446-7

Chiumello, D., Carlesso, E., Cadringher, P., Caironi, P., Valenza, F., Polli, F., et al. (2008). Lung stress and strain during mechanical ventilation for acute respiratory distress syndrome. *Am. J. Respiratory Crit. Care Med.* 178, 346–355.

Corona, T. M., and Aumann, M. (2011). Ventilator waveform interpretation in mechanically ventilated small animals. *J. Veter. Emerg. Crit. Care* 21, 496–514. doi: 10.1111/j.1476-4431.2011.00673.x

Ellwein Fix, L., Khoury, J., Moores, R. R. Jr., Linkous, L., Brandes, M., and Rozycki, H. J. (2018). Theoretical open-loop model of respiratory mechanics in the extremely preterm infant. *PLoS One* 13:e0198425. doi: 10.1371/journal.pone.0198425

Force, A. D. T., Ranieri, V., Rubenfeld, G., Thompson, B., Ferguson, N., and Caldwell, E. (2012). Acute respiratory distress syndrome. *JAMA* 307, 2526–2533.

Gattinoni, L., Pesenti, A., Avalli, L., Rossi, F., and Bombino, M. (1987). Pressure-volume curve of total respiratory system in acute respiratory failure: computed tomographic scan study. *Am. Rev. Respirat. Dis.* 136, 730–736. doi: 10.1164/ajrccm/136.3.730

Gelman, A., Carlin, J. B., Stern, H. S., Dunson, D. B., Vehtari, A., and Rubin, D. B. (2013). *Bayesian Data Analysis*. Boca Raton: CRC press.

Gilstrap, D., and MacIntyre, N. (2013). Patient–ventilator interactions. implications for clinical management. *Am. J. Respirat. Crit. Care Med.* 188, 1058–1068. doi: 10.1164/rccm.201212-2214ci

Grasso, S., Stripoli, T., De Michele, M., Bruno, F., Moschetta, M., Angelelli, G., et al. (2007). ARDSnet ventilatory protocol and alveolar hyperinflation: role of positive end-expiratory pressure. *Am. J. Respirat. Crit. Care Med.* 176, 761–767. doi: 10.1164/rccm.200702-193oc

Grasso, S., Terragni, P., Mascia, L., Fanelli, V., Quintel, M., Herrmann, P., et al. (2004). Airway pressure-time curve profile (stress index) detects tidal recruitment/hyperinflation in experimental acute lung injury. *Crit. Care Med.* 32, 1018–1027. doi: 10.1097/01.ccm.0000120059.94009.ad

Guerin, C. (2011). The preventive role of higher PEEP in treating severely hypoxemic ARDS. *Minerva Anestesiol* 77, 835–845.

Hamlington, K. L., Smith, B. J., Allen, G. B., and Bates, J. H. (2016). Predicting ventilator-induced lung injury using a lung injury cost function. *J. Appl. Physiol.* 121, 106–114.

Hripcsak, G., and Albers, D. J. (2013a). Correlating electronic health record concepts with healthcare process events. *J. Am. Med. Inform. Assoc.* 20, 311–318. doi: 10.1136/amiajnl-2013-001922

Hripcsak, G., and Albers, D. J. (2013b). Next-generation phenotyping of electronic health records. *J. Am. Med. Inform. Assoc.* 20, 117–121. doi: 10.1136/amiajnl-2012-001145

Jawde, S. B., Smith, B. J., Sonnenberg, A., Bates, J. H. T., and Suki, B. (2018). Design and nonlinear modeling of a sensitive sensor for the measurement of flow in mice. *Physiol. Meas.* 39:075002. doi: 10.1088/1361-6579/aacb1b

Jolliffe, I. T., and Stephenson, D. B. (2012). *Forecast Verification: A Practitioner's Guide in Atmospheric Science*. Hoboken, NJ: John Wiley & Sons.

Khemani, R. G., Parvathaneni, K., Yehya, N., Bhalla, A. K., Thomas, N. J., and Newth, C. J. (2018). Positive end-expiratory pressure lower than the ARDS network protocol is associated with higher pediatric acute respiratory distress syndrome mortality. *Am. J. Respirat. Crit. Care Med.* 198, 77–89. doi: 10.1164/rccm.201707-1404oc

Law, K., Stuart, A., and Zygalakis, K. (2015). *Data Assimilation*. Cham: Springer.

Mellema, M. S. (2013). Ventilator waveforms. *Top. Companion Animal Med.* 28, 112–123.

Mellenthin, M. M., Seong, S. A., Roy, G. S., Bartolák-Suki, E., Hamlington, K. L., Bates, J. H., et al. (2019). Using injury cost functions from a predictive single-compartment model to assess the severity of mechanical ventilator-induced lung injuries. *J. Appl. Physiol.* 127, 58–70. doi: 10.1152/japplphysiol.00770.2018

Molkov, Y. I., Rubin, J. E., Rybak, I. A., and Smith, J. C. (2017). Computational models of the neural control of breathing. *Wiley Int. Rev. Syst. Biol. Med.* 9:e1371.

Molkov, Y. I., Shevtsova, N. A., Park, C., Ben-Tal, A., Smith, J. C., Rubin, J. E., et al. (2014). A closed-loop model of the respiratory system: focus on hypercapnia and active expiration. *PLoS One* 9:e109894. doi: 10.1371/journal.pone.0109894

Mori, K. (2016). From macro-scale to micro-scale computational anatomy: a perspective on the next 20 years. *Med. Image Anal.* 33, 159–164. doi: 10.1016/j.media.2016.06.034

Nelder, J. A., and Mead, R. (1965). A simplex method for function minimization. *Comput. J.* 7, 308–313. doi: 10.1093/comjnl/7.4.308

Network, A. R. D. S. (2000). Ventilation with lower tidal volumes as compared with traditional tidal volumes for acute lung injury and the acute respiratory distress syndrome. *N. Engl. J. Med.* 342, 1301–1308. doi: 10.1056/nejm200005043421801

Nguyen, B., Bernstein, D. B., and Bates, J. H. (2014). Controlling mechanical ventilation in acute respiratory distress syndrome with fuzzy logic. *J. Crit. Care* 29, 551–556. doi: 10.1016/j.jcrc.2014.03.009

Nocedal, J. W. S. (2006). *Numerical Optimization*. New York: Springer.

Phua, J., Badia, J. R., Adhikari, N. K., Friedrich, J. O., Fowler, R. A., Singh, J. M., et al. (2009). Has mortality from acute respiratory distress syndrome decreased over time? A systematic review. *Am. J. Respirat. Crit. Care Med.* 179, 220–227. doi: 10.1164/rccm.200805-722oc

Rees, S. E., Allerød, C., Murley, D., Zhao, Y., Smith, B. W., Kjærgaard, S., et al. (2006). Using physiological models and decision theory for selecting appropriate ventilator settings. *J. Clin. Monit. Comput.* 20:421. doi: 10.1007/s10877-006-9049-5

Reynolds, A., Ermentrout, G. B., and Clermont, G. (2010). A mathematical model of pulmonary gas exchange under inflammatory stress. *J. Theor. Biol.* 264, 161–173. doi: 10.1016/j.jtbi.2010.01.011

Rossetti, S. C., Knaplund, C., Albers, D., Dykes, P. C., Kang, M. J., Korach, T. Z., et al. (2021). Healthcare process modeling to phenotype clinician behaviors for exploiting the signal gain of clinical expertise (HPM-ExpertSignals): development and evaluation of a conceptual framework. *J. Am. Med. Inform. Assoc.* 28, 1242–1251. doi: 10.1093/jamia/ocab006

Roth, C. J., Ismail, M., Yoshihara, L., and Wall, W. A. (2017). A comprehensive computational human lung model incorporating inter-acinar dependencies: application to spontaneous breathing and mechanical ventilation. *Int. J. Numer. Methods Biomed. Eng.* 33:e02787. doi: 10.1002/cnm.2787

Schoukens, J., Vaes, M., and Pintelon, R. (2016). Linear system identification in a nonlinear setting: Nonparametric analysis of the nonlinear distortions and their impact on the best linear approximation. *IEEE Control. Syst. Magazine* 36, 38–69. doi: 10.1109/mcs.2016.2535918

Serov, A. S., Salafia, C., Grebenkov, D. S., and Filoche, M. (2016). The role of morphology in mathematical models of placental gas exchange. *J. Appl. Physiol.* 120, 17–28. doi: 10.1152/japplphysiol.00543.2015

Smith, B. J., Lundblad, L. K., Kollisch-Singule, M., Satalin, J., Nieman, G., Habashi, N., et al. (2015). Predicting the response of the injured lung to the mechanical breath profile. *J. Appl. Physiol.* 118, 932–940. doi: 10.1152/japplphysiol.00902.2014

Smith, B. J., Roy, G. S., Cleveland, A., Mattson, C., Okamura, K., Charlebois, C. M., et al. (2020). Three alveolar phenotypes govern lung function in murine ventilator-induced lung injury. *Front. Physiol.* 11:660.

Smith, R. C. (2013). *Uncertainty Quantification: Theory, Implementation, and Applications*. London: SIAM.

Sottile, P. D., Albers, D., Higgins, C., Mckeehan, J., and Moss, M. M. (2018a). The association between ventilator dyssynchrony, delivered tidal volume, and sedation using a novel automated ventilator dyssynchrony detection algorithm. *Crit. Care Med.* 46:e151. doi: 10.1097/ccm.0000000000002849

Sottile, P. D., Albers, D., and Moss, M. M. (2018b). Neuromuscular blockade is associated with the attenuation of biomarkers of epithelial and endothelial injury in patients with moderate-to-severe acute respiratory distress syndrome. *Crit. Care* 22:63. doi: 10.1186/s13054-018-1974-4

Tobin, M. J. (2001). Advances in mechanical ventilation. *N. Eng. J. Med.* 344, 1986–1996.

Ware, L. B., and Matthay, M. A. (2000). The acute respiratory distress syndrome. *N. Eng. J. Med.* 342, 1334–1349.

Westwick, D. T., and Kearney, R. E. (2003). *Identification of Nonlinear Physiological Systems*. Hoboken, NJ: John Wiley & Sons.

Wheeler, A. P., and Bernard, G. R. (2007). Acute lung injury and the acute respiratory distress syndrome: a clinical review. *Lancet* 369, 1553–1564. doi: 10.1016/S0140-6736(07)60604-7

Yoshida, T., Fujino, Y., Amato, M. B., and Kavanagh, B. P. (2017). Fifty years of research in ARDS. spontaneous breathing during mechanical ventilation. risks, mechanisms, and management. *Am. J. Respirat. Crit. Care Med.* 195, 985–992. doi: 10.1164/rccm.201604-0748cp

Conflict of Interest: The authors declare that the research was conducted in the absence of any commercial or financial relationships that could be construed as a potential conflict of interest.

Publisher's Note: All claims expressed in this article are solely those of the authors and do not necessarily represent those of their affiliated organizations, or those of the publisher, the editors and the reviewers. Any product that may be evaluated in this article, or claim that may be made by its manufacturer, is not guaranteed or endorsed by the publisher.

frontiers in Physiology

MINI REVIEW
published: 21 October 2021
doi: 10.3389/fphys.2021.757857

Non-invasive Measurement of Pulmonary Gas Exchange Efficiency: The Oxygen Deficit

G. Kim Prisk and John B. West*

Department of Medicine, University of California, San Diego, La Jolla, CA, United States

The efficiency of pulmonary gas exchange has long been assessed using the alveolar-arterial difference in PO_2, the A-aDO_2, a construct developed by Richard Riley ~70 years ago. However, this measurement is invasive (requiring an arterial blood sample), time consuming, expensive, uncomfortable for the patients, and as such not ideal for serial measurements. Recent advances in the technology now provide for portable and rapidly responding measurement of the PO_2 and PCO_2 in expired gas, which combined with the well-established measurement of arterial oxygen saturation *via* pulse oximetry (SpO_2) make practical a non-invasive surrogate measurement of the A-aDO_2, the oxygen deficit. The oxygen deficit is the difference between the end-tidal PO_2 and the calculated arterial PO_2 derived from the SpO_2 and taking into account the PCO_2, also measured from end-tidal gas. The oxygen deficit shares the underlying basis of the measurement of gas exchange efficiency that the A-aDO_2 uses, and thus the two measurements are well-correlated ($r^2 \sim 0.72$). Studies have shown that the new approach is sensitive and can detect the age-related decline in gas exchange efficiency associated with healthy aging. In patients with lung disease the oxygen deficit is greatly elevated compared to normal subjects. The portable and non-invasive nature of the approach suggests potential uses in first responders, in military applications, and in underserved areas. Further, the completely non-invasive and rapid nature of the measurement makes it ideally suited to serial measurements of acutely ill patients including those with COVID-19, allowing patients to be closely monitored if required.

Keywords: alveolar-arterial PO_2 difference, A-aDO_2, pulse oximetry, hypoxemia, Bohr effect

OPEN ACCESS

Edited by:
Walter Araujo Zin, Federal University of Rio de Janeiro, Brazil

Reviewed by:
Stephen Rees, Aalborg University, Denmark
David Hill, University of North Texas, United States

****Correspondence:***
G. Kim Prisk
kprisk@health.ucsd.edu

Specialty section:
This article was submitted to Respiratory Physiology, a section of the journal Frontiers in Physiology

Received: *12 August 2021*
Accepted: *24 September 2021*
Published: *21 October 2021*

Citation:
Prisk GK and West JB (2021) Non-invasive Measurement of Pulmonary Gas Exchange Efficiency: The Oxygen Deficit. Front. Physiol. 12:757857. doi: 10.3389/fphys.2021.757857

INTRODUCTION

For the lung to exchange gas (O_2 from the inspired air into the blood, and CO_2 from the blood to the expired gas), alveolar gas and pulmonary capillary blood must be brought into close apposition across the thin alveolar-capillary membrane. Any degree of spatial mismatch between ventilation and perfusion [ventilation-perfusion (VA/Q) inequality] will lower the efficiency of the exchange of any gas, resulting in a difference between the partial pressure of a gas in the arterial blood leaving the lung, and gas in the exhaled breath (Rahn and Fenn, 1955; West, 1969).

For O_2 and CO_2, the dissociation curves that describe the content of the gas in blood as a function of partial pressure, are markedly different. The sigmoidal shaped O_2 dissociation curve rapidly flattens at higher values of PO_2. Thus, the presence of any regions of the lung with a low VA/Q ratio will result in the addition of poorly oxygenated blood to the arterial circulation, but a compensatory increase in overall ventilation (from chemoreceptive responses) cannot add more oxygen to blood exiting regions of high VA/Q. In contrast, the quasi-linear CO_2 dissociation curve means that low and high VA/Q regions can compensate for each other. Thus, it is common to see patients with pulmonary disease with arterial hypoxemia, while having a normal arterial PCO_2 (West and Luks, 2016).

A small increase in VA/Q inequality occurs with healthy aging (Cardus et al., 1997), and increased VA/Q inequality is a hallmark of virtually all pulmonary diseases (Hopkins and Wagner, 2017). Therefore, the measurement of the alveolar-arterial PO_2 difference ($A\text{-}aDO_2$) has long been a mainstay in assessing the disruption to pulmonary gas exchange caused by disease (Filley et al., 1954).

HISTORICAL CONTEXT OF MEASURING THE ALVEOLAR-ARTERIAL DIFFERENCE IN PO_2

While conceptually simple, measuring the $A\text{-}aDO_2$ is technically challenging. Richard Riley first showed that the PO_2 in arterial blood could be measured by equilibrating a small bubble of air with the blood and measuring the PO_2 in the gas (Riley et al., 1957). However, at the time, the technical difficulties of reliably sampling alveolar gas were overwhelming. To bypass this problem, Riley developed the construct of the "ideal alveolar PO_2." This was the alveolar PO_2 in the lung that *would have been present* if there was no ventilation-perfusion inequality, the PCO_2 in the alveolar gas was the same as that in arterial blood, and the respiratory exchange ratio was the same as that in the actual lung.

The ideal alveolar PO_2 can be obtained from an arterial blood sample using the alveolar gas equation (Rahn and Fenn, 1955):

$$\text{ideal } PAO_2 = PIO_2 - PaCO_2 / R - \left[PaCO_2 * FIO_2 * (1-R) / R\right]$$

where A refers to alveolar, a to arterial, I to inspired, and R is the respiratory exchange ratio, the CO_2 production divided by the O_2 consumption (generally assumed to be 0.8 at rest). The final term in this equation is often ignored as it typically has a magnitude of only a few mmHg. A more detailed description of Riley's innovative approach can be found in West et al. (2020). This approach provides a number representing the alveolar PO_2, and it does so without actually measuring alveolar gas.

THE ALTERNATIVE APPROACH OF THE OXYGEN DEFICIT

Compact, rapidly responding gas analysis devices are now readily available, allowing direct measurement of expired PO_2 and PCO_2. The Riley construct utilizes the ideal alveolar PO_2 to obviate the need to make a "technically difficult" measurement to calculate the $A\text{-}aDO_2$. The oxygen deficit (OD) comes from a direct measurement of expired gas partial pressures and uses a non-invasive means to determine what would otherwise be an invasive measurement, the arterial PO_2.

The approach is to continuously measure expired O_2 and CO_2 while the patient breathes quietly on a mouthpiece while wearing a noseclip. The final concentrations measured just before the abrupt transition to inspired gas are taken as the end-tidal values of PO_2 and PCO_2. An example of the expired gas record is shown in **Figure 1**. The end-tidal values for partial pressure are a good reflection of the values within the alveolus (discussed in detail in reference West et al., 2020) and are highly reproducible. Previous work has shown that the breath-to-breath within-subject standard deviation of normal subjects breathing air is ~1.4 mmHg for PO_2 and ~0.7 mmHg for PCO_2 (West et al., 2020), with somewhat lower numbers when breathing a hypoxic gas. A trend plot of the last 30 values of these (covering 1–2 min) provides a direct indication of whether the patient is in steady-state, an important consideration since highly variable breathing would result in considerable variation in end-tidal partial pressures for both O_2 and CO_2.

Having directly measured the alveolar partial pressure for O_2 (and CO_2), the $A\text{-}aDO_2$ could be measured directly by taking an arterial blood sample to measure arterial PO_2. However, to make the process both rapid and non-invasive, arterial PO_2 is estimated from the arterial oxygen saturation (SaO_2) as measured by pulse oximetry (SpO_2) as determined simultaneously using a fingertip pulse oximeter. This is then used to determine the corresponding arterial PO_2 from the Hill equation:

$$PO_2{}^n = P_{50}{}^n * SaO_2 / (1 - SaO_2)$$

where P_{50} is the PO_2 at a saturation of 50%, and the SaO_2 is expressed as the fractional saturation; range [0, 1]. PO_2 is determined by taking the logarithm of the equation and solving algebraically.

The term n (commonly referred to as the "Hill-n") is that required to match the sigmoidal shape of the O_2-Hb dissociation curve, and a value of 2.7 is commonly used (Severinghaus, 2002; Prisk and West, 2019). While a Hill-n of 2.7 provides an excellent fit to the experimentally determined values of saturation and PO_2 over the entire range of saturation (Severinghaus, 1966; Prisk and West, 2019), in practice, only blood oxygen saturations in the range of 75–100% are likely to be encountered in patients. Over this limited range, an improved fit to the experimental data is achieved with a Hill-n = 2.88 (Liu et al., 2020).

The P_{50} of blood is normally ~27 mmHg, however this varies with alterations in PCO_2, body temperature, base excess, and levels of 2,3-diphosphoglycerate (2,3-dpg; West and Luks, 2016). Because the end-tidal gas partial pressure reflects the alveolar PCO_2, the leftward or rightward shift of the O_2-Hb dissociation curve from a PCO_2 different to the normal value of 40 mmHg (the Bohr effect) can be accounted for. Using the Kelman routines (Kelman, 1966, 1968) an empiric relationship for P_{50}

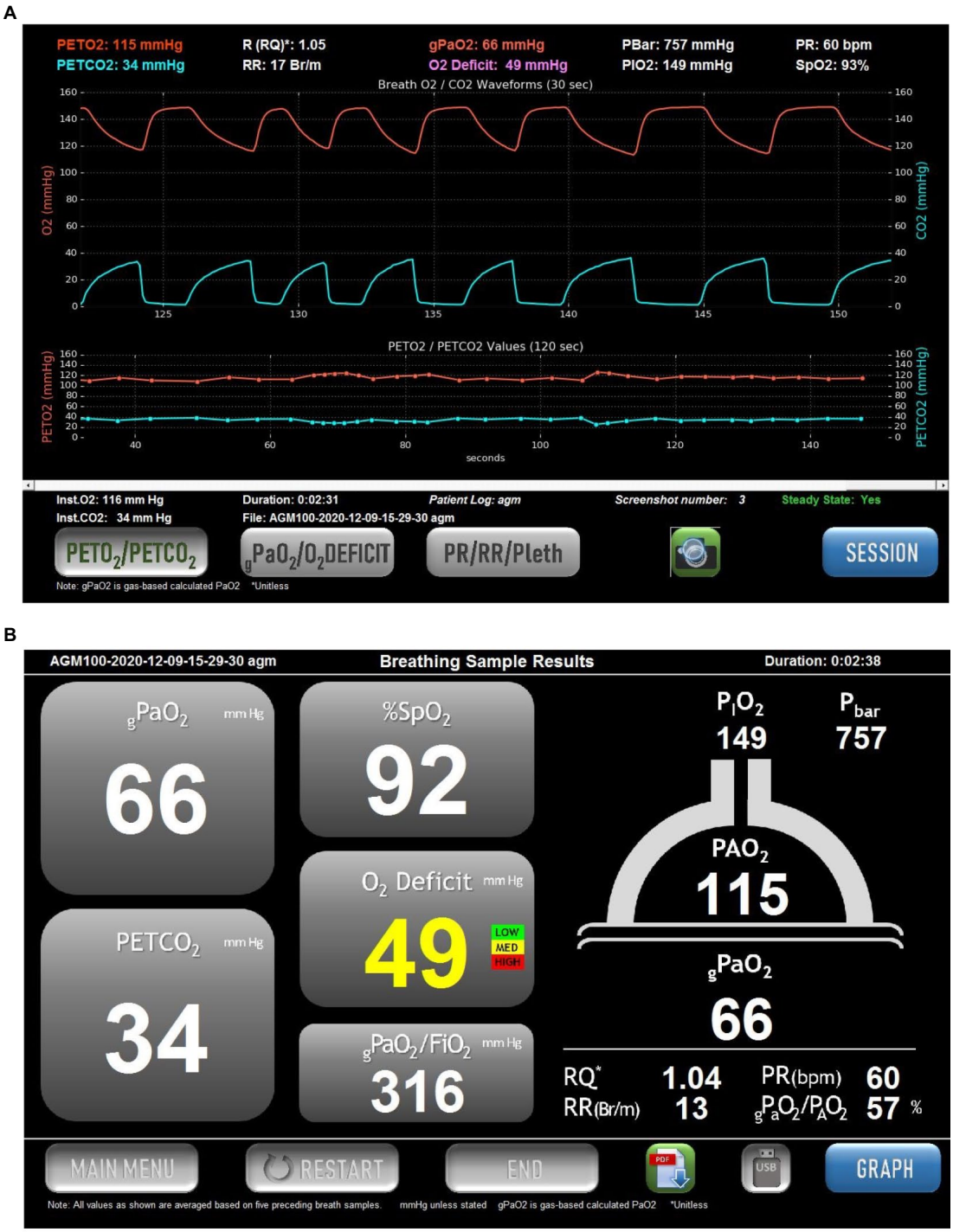

FIGURE 1 | Example of the screens displayed in the commercial version of the Alveolar Gas Meter (AGM100™, MediPines Corp, Costa Mesa, CA). Data are taken from a spontaneously breathing patient suffering from COVID-19. **(A)** Continuous records of PO_2 (red) and PCO_2 (blue) over a 30-s period of quiet breathing (upper traces). Note that in this patient there is a steep alveolar plateau for O_2 and CO_2, indicative of marked heterogeneity in the lung. Below these are plots of end-tidal PO_2 (red) and PCO_2 (blue) over the preceding 150 s. The lower traces allow an assessment of whether the patient is in a steady state. This is also indicated by the Steady State indicator in the lower right of the screen. At the top of the screen are numerical values for the end-tidal partial presses of O_2 and CO_2, the respiratory quotient (RQ), respiratory rate (RR), barometric pressure (PBar), inspired PO_2 (PIO_2), pulse rate (PR) and arterial oxygen saturation *via* pulse oximetry (SpO_2). In the center at the top is the calculated arterial PO_2 (termed $gPaO_2$, red text), and the O_2 Deficit (the difference between end-tidal PO_2 and calculated arterial PO_2). **(B)** A screen summarizing the data from **(A)** without the graphical displays. The cartoon of the lung on the right shows the measured end-tidal PO_2 (115 mmHg in this example), and the calculated arterial PO_2 ($gPaO_2$, 66 mmHg in this example), which together result in the oxygen deficit in traffic-light color-coded text (49 mmHg in this example). The operator may toggle between this screen and that in **(A)** as desired.

assuming otherwise normal conditions for temperature, base excess and 2,3-dpg is determined (Prisk and West, 2019). This is used to correct for changes in alveolar PCO_2, assuming this is equal to arterial PCO_2, an equivalence that has been long established (Comroe and Dripps, 1944). Alterations in base excess, 2,3-dpg, or body temperature are not accounted for, because a blood sample is not obtained.

The difference between the calculated arterial PO_2 and the measured end-tidal (alveolar) PO_2 is termed the OD. This can be thought of as a surrogate measurement of the A-aDO_2. In the latter case the arterial value is measured, and the alveolar value estimated as described by Riley (above), while in the case of the OD, the alveolar value is measured, and the arterial value estimated. This should not be confused with the "oxygen deficit" that provides a measure of the anaerobic contribution during exercise (Krogh and Lindhard, 1920; Medbo et al., 1988).

LIMITATIONS OF THE MEASUREMENT OF THE OXYGEN DEFICIT

In the normal lung there is variation in the regional alveolar PO_2, and this is often exaggerated in lung disease. The expired gas is a mixture of gas from all regions of the lung, just as the arterial blood is a mixture of blood from all regions of the lung. Further as gas exchange continues throughout expiration, PO_2 continues to fall. However, provided the end-tidal values are measured at functional residual capacity (FRC), the naturally occurring volume for end expiration at rest, the effect of ongoing gas exchange is minimal. Thus, the end tidal PO_2 is a direct and useful measurement of the alveolar PO_2 (West et al., 2020).

The obvious challenge of determining the OD is the estimation of the arterial PO_2 from the SpO_2 given the shape of the O_2-Hb dissociation curve which is very flat at higher values of PO_2. At high values, even small errors in SpO_2 translate into large differences in the calculated PaO_2. However, this problem becomes smaller at lower values of SpO_2 as the O_2-Hb dissociation curve becomes steeper. A study addressing the likely errors in calculated PaO_2 showed that for SpO_2 values of 94% and below, the error in the calculated PaO_2 was less than 5 mmHg (Prisk and West, 2019). Above a SpO_2 of 94% the calculation of PaO_2 was, as expected, unreliable. However, if SpO_2 is greater than 94% while breathing air at sea level, then no major gas exchange impairment exists, and so there is no need to measure OD.

Because the approach considers the alveolar PCO_2 as well as the PO_2, the left or right shift in the O_2-Hb dissociation curve from changes in alveolar PCO_2 (the Bohr effect) can be directly accounted for. This effect is the principal cause of shifts in the O_2-Hb dissociation curve, and so the ability to correct for this is critical. Failure to do so would result in errors in the OD of >5 mmHg for SpO_2 values of 94% (see figure 4 of Prisk and West, 2019 for details). Shifts in the O_2-Hb dissociation curve from other causes (base excess, temperature, 2–3 dpg) are not taken into account with the non-invasive approach. These however, are much smaller, and produce only minor errors in the calculated OD (Prisk and West, 2019). A Monte Carlo simulation of the typical simultaneously present errors in the measurements of SpO_2 and alveolar PCO_2 showed that the calculated OD had a slight negative bias (<5 mmHg) and typical variability of ~5 mmHg at an SpO_2 of 94%, with both of these values decreasing as SpO_2 fell, showing the viability of the approach (Prisk and West, 2019).

OXYGEN DEFICIT IN NORMAL SUBJECTS

Initial studies in normal subjects were performed with the subjects breathing a hypoxic gas mixture ($FIO_2 = 0.125$) to ensure that the SpO_2 fell into the range in which OD could be reliably measured ($SpO_2 < 95\%$). A study of 20 young subjects (19–31 years) and 11 older subjects (47–88 years) showed a very small OD in the young cohort (~2 mmHg), which was increased in the older (~8 mmHg; West et al., 2018b). The increase in OD with increasing age is consistent with the well-known increase in the A-aDO_2 with healthy aging (Raine and Bishop, 1963).

A more extensive subsequent study explored the effects of varying the inspired oxygen between the previously used hypoxic gas ($FIO_2 = 0.125$) up to and including breathing air (FIO_2 values of 0.15, 0.175, and 0.21; Liu et al., 2020). This study again showed a higher OD in the older cohort compared to the young, with the difference persisting at all values of inspired oxygen, including air. Importantly, there was no statistical difference in the measured values of OD between and FIO_2 of 0.125 and 0.175, although OD rose in both cohorts when the subjects were breathing air. The result is consistent with an expected reduction in the A-aDO_2 as inspired PO_2 is lowered due to minimization of the effect of VA/Q inequality as the saturation falls and gas exchange occurs on the steeper and more linear portion of the O_2-Hb dissociation curve. The intra-subject variability in the measured OD was large at high values of SpO_2, and fell rapidly as SpO_2 was reduced below 94%, consistent with the simulation studies performed (Prisk and West, 2019). The study showed that the OD was sensitive to the mild gas exchange impairment associated with healthy aging, even while breathing air, but that individual errors at high values of SpO_2 meant that the measurement was not likely to be useful in individual subjects at SpO_2 values above 94%.

A recent study has also demonstrated the validity of the non-invasive approach to measure a gas exchange deficit. A direct comparison between OD and arterial blood gas (ABG) was performed in 25 normal subjects during hypoxic exercise, showing a correlation between OD and A-aDO_2 with an $r^2 = 0.71$, and with a small bias between the two, with OD being on average 5.2 ± 5.0 mmHg higher than A-aDO_2 (Howe et al., 2020). The non-invasive nature of the measurement serves to enable measurements in conditions in where it would be challenging to perform ABGs, and in particular, serial ABGs. Recent examples are measurements performed in trained breath-hold divers before and after dives at an open-water dive site (Patrician et al., 2021a,b).

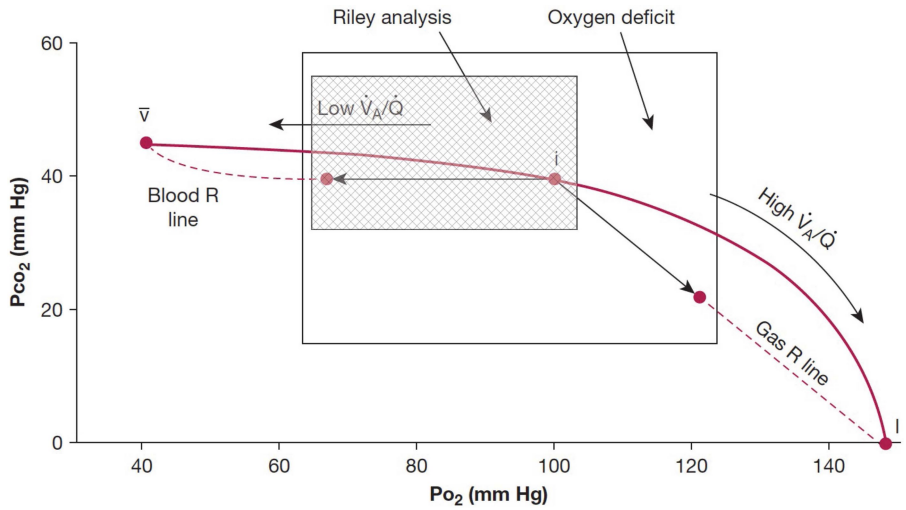

FIGURE 2 | Classic O_2-CO_2 diagram with the ventilation-perfusion line joining the points for mixed venous blood and inspired gas. The traditional Riley analysis is based on the composition of arterial blood and ideal alveolar gas, and it is strongly biased by lung units with low ventilation-perfusion ratios that lie to the left of the ideal point (hatched area). By contrast, the new test also includes contributions from lung units with high ventilation-perfusion ratios that are located to the right of the ideal point. Modified from West et al. (2018a).

The studies showed a substantial but transient decrement in gas exchange efficiency as measured by increased OD, in some cases to nearly 70 mmHg. This was likely due to the development of pulmonary edema from the hydrostatically induced lung compression (lung-squeeze).

OXYGEN DEFICIT IN PATIENTS WITH LUNG DISEASE

A small initial study in a cohort of ambulant patients from a general pulmonary outpatient clinic with a variety of pulmonary diseases showed that the OD was greatly elevated in this group compared to normal, with an average OD of ~49 mmHg (West et al., 2018a). When the OD was directly compared to the A-aDO_2 measured by the collection of an ABG in 23 patients with an SpO_2 of 95% or less, there was a high correlation ($r^2 = 0.72$; West et al., 2018c). There were similar strength correlations between the calculated PaO_2 and that measured from the ABG, and between end-tidal PCO_2 and that from the ABG. The calculated PaO_2 was on average ~4 mmHg higher than that measured from the ABG. This study showed that the non-invasive approach provided a convenient, low cost, and accurate alternative to the use of an ABG to measure the magnitude of the gas exchange disruption in patients with pulmonary disease.

A recent case report highlighted the use of the non-invasive approach in determining the underlying cause of a gas exchange defects in a patient in whom ABGs could not readily be obtained (Amaza et al., 2021). This report served to highlight the potential of the non-invasive approach, and further showed that the approach was useful as a teaching tool.

In the context of the ongoing SARS-CoV-2 pandemic, a small preliminary study investigated the usefulness of the non-invasive approach to measuring the impairment of pulmonary gas exchange in patients with suspected COVID-19 considered to be at risk of deterioration before obvious respiratory failure had ensued (McGuire et al., 2021). Patients were either breathing air, or on supplemental low-dose oxygen, which was temporarily discontinued for ~10 min before measurements were taken. Of 13 patients studied, five were discharged home and the other eight were admitted based on physician decision using standard procedures. The OD was significantly greater in the patients who were admitted than in those who were discharged (OD 55 ± 20 vs. 32 ± 14 respectively, $p = 0.041$), suggesting that the measurement was a potentially useful means of assessing severity. Similarly, the oxygen deficit was significantly higher in the patients requiring supplemental O_2 than in those who did not (65 ± 9 vs. 30 ± 1 respectively, $p < 0.001$) again suggesting that the non-invasive measurement of gas exchange impairment provided useful clinical insight in a rapid non-invasive manner.

DISCUSSION

The studies performed to date show that a non-invasive approach can be used to quantitatively assess the gas exchange deficit in patients with pulmonary disease. The approach taken is in many respects comparable to the traditional measurement of the A-aDO_2 first developed by Riley, and there is considerable physiological overlap in the measurements. This is shown in **Figure 2** which shows the classic O_2-CO_2 diagram and highlights the aspects of the VA/Q inequality that the two methods encompass.

The traditional method of Riley focuses on the consequences of the presence of regions of low VA/Q that serve to add end-capillary blood with a low PO_2 to the arterial blood

(so-called venous admixture), the result being arterial hypoxemia and an increased A-aDO_2. The measurement of oxygen deficit encompasses the effects of low VA/Q and high VA/Q, although the effect of high VA/Q regions on arterial PO_2 is small because of the shape of the O_2-Hb dissociation curve. The large overlap in the areas of influence of the two methods (**Figure 2**) means that the two measurements would be expected to be highly correlated, albeit not the same, and this was demonstrated with a strong correlation between measures of A-aDO_2 and OD (West et al., 2018c; Howe et al., 2020).

It is reasonable to question what additional information is gained by measuring the OD as opposed to simply measuring SpO_2. While both VA/Q mismatch and shunt will serve to decrease arterial PO_2 (and thus SpO_2) and increase OD, so too will hypoventilation. Because the alveolar PCO_2 is also measured, hypoventilation can readily be detected which may provide an important clinical distinction of the cause of hypoxemia in some patients. Further, the OD takes into account the effect of changes in PCO_2 on the O_2-Hb dissociation curve. Thus, the oxygen deficit directly addresses the efficiency of gas exchange, in the same way that the A-aDO_2 does.

The important clinical measurement of the A-aDO_2 has been performed using an invasive approach for ~70 years. However, its use has become less common in recent years, likely due to the cost, time required for the measurement, and the uncomfortable and invasive nature of the procedure. In contrast, the OD is a rapid, non-invasive measurement that can be readily performed on patients ranging from ambulatory to those on mechanical ventilation. The measurement takes only a few minutes, requiring only that the patient breathe quietly on a mouthpiece while wearing a noseclip for ~2 min, while wearing a fingertip pulse oximeter. The equipment is portable, making it suitable for use not only in the hospital, but in the field, and in underserved areas.

AUTHOR CONTRIBUTIONS

GP wrote, edited, and approved the article. JW edited and approved the article. All authors contributed to the article and approved the submitted version.

FUNDING

Support for some was provided by MediPines Corporation which provided AGM100™ units for use in some of the studies referenced. Support was provided by MediPines Corporation to cover publication costs.

REFERENCES

Amaza, I., Kalra, H., Eberlein, M., Jethava, Y., McDonell, J., Wolfe, B., et al. (2021). Case studies in physiology: untangling the cause of hypoxemia in a patient with obesity with acute leukemia. *J. Appl. Physiol.* 131, 788–793. doi: 10.1152/japplphysiol.00867.2020

Cardus, J., Burgos, F., Diaz, O., Roca, J., Barbera, J. A., Marrades, R. M., et al. (1997). Increase in pulmonary ventilation-perfusion inequality with age in healthy individuals. *Am. J. Respir. Crit. Care Med.* 156, 648–653. doi: 10.1164/ajrccm.156.2.9606016

Comroe, J. H., and Dripps, R. D. (1944). The oxygen tension of arterial blood and alveolar air in normal human subjects. *Am. J. Phys.* 142, 700–707.

Filley, G. F., Gregoire, F., and Wright, G. W. (1954). Alveolar and arterial oxygen tensions and the significance of the alveolar-arterial oxygen tension difference in normal men. *J. Clin. Invest.* 33, 517–529. doi: 10.1172/JCI102922

Hopkins, S. R., and Wagner, P. D. (2017). *The Multiple Inert Gas Elimination Technique*. New York, NY: Springer.

Howe, C. A., MacLeod, D. B., Wainman, L., Oliver, S. J., and Ainslie, P. N. (2020). Validation of a noninvasive assessment of pulmonary gas exchange during exercise in hypoxia. *Chest* 158, 1644–1650. doi: 10.1016/j.chest.2020.04.017

Kelman, G. R. (1966). Calculation of certain indices of cardio-pulmonary function, using a digital computer. *Respir. Physiol.* 1, 335–343. doi: 10.1016/0034-5687(66)90050-8

Kelman, G. R. (1968). Computer program for the production of O_2-CO_2 diagrams. *Respir. Physiol.* 4, 260–269. doi: 10.1016/0034-5687(68)90057-1

Krogh, A., and Lindhard, J. (1920). The changes in respiration at the transition from work to rest. *J. Physiol.* 53, 431–439. doi: 10.1113/jphysiol.1920.sp001889

Liu, M. A., Stark, P. C., Prisk, G. K., and West, J. B. (2020). Oxygen deficit is a sensitive measure of mild gas exchange impairment at inspired O_2 between 12.5% and 21%. *Am. J. Physiol. Lung Cell. Mol. Physiol.* 319, L91–L94. doi: 10.1152/ajplung.00003.2020

McGuire, W. C., Crouch, D. R., Pearce, A., West, J. B., Prisk, G. K., Elliott, A. R., et al. (2021). "The use of the alveolar gas meter for assessment of gas exchange abnormalities in COVID–19." in *International Conference of the American Thoracic Society*; May 14–19, 2021.

Medbo, J. I., Mohn, A. C., Tabata, I., Bahr, R., Vaage, O., and Sejersted, O. M. (1988). Anaerobic capacity determined by maximal accumulated O_2 deficit. *J. Appl. Physiol.* 64, 50–60. doi: 10.1152/jappl.1988.64.1.50

Patrician, A., Gasho, C., Spajic, B., Caldwell, H. G., Bakovic-Kramaric, D., Barak, O., et al. (2021a). Case studies in physiology: breath-hold diving beyond 100 meters-cardiopulmonary responses in world-champion divers. *J. Appl. Physiol.* 130, 1345–1350. doi: 10.1152/japplphysiol.00877.2020

Patrician, A., Spajic, B., Gasho, C., Caldwell, H. G., Dawkins, T., Stembridge, M., et al. (2021b). Temporal changes in pulmonary gas exchange efficiency when breath-hold diving below residual volume. *Exp. Physiol.* 106, 1120–1133. doi: 10.1113/EP089176

Prisk, G. K., and West, J. B. (2019). Deriving the arterial PO_2 and oxygen deficit from expired gas and pulse oximetry. *J. Appl. Physiol.* 127, 1067–1074. doi: 10.1152/japplphysiol.01100.2018

Rahn, H., and Fenn, W. O. (1955). *A Graphical Analysis of the Respiratory Gas Exchange. The O2-CO2 Diagram*. Washington, DC: American Physiological Society.

Raine, J. M., and Bishop, J. M. (1963). A-a difference in O_2 tension and physiological dead space in normal man. *J. Appl. Physiol.* 18, 284–288. doi: 10.1152/jappl.1963.18.2.284

Riley, R. L., Campbell, E. J., and Shepard, R. H. (1957). A bubble method for estimation of PCO_2 and PO_2 in whole blood. *J. Appl. Physiol.* 11, 245–249. doi: 10.1152/jappl.1957.11.2.245

Severinghaus, J. W. (1966). Blood gas calculator. *J. Appl. Physiol.* 21, 1108–1116. doi: 10.1152/jappl.1966.21.3.1108

Severinghaus, J. W. (2002). The invention and development of blood gas analysis apparatus. *Anesthesiology* 97, 253–256. doi: 10.1097/00000542-200207000-00031

West, J. B. (1969). Ventilation-perfusion inequality and overall gas exchange in computer models of the lung. *Respir. Physiol.* 7, 88–110. doi: 10.1016/0034-5687(69)90071-1

West, J. B., Crouch, D. R., Fine, J. M., Makadia, D., Wang, D. L., and Prisk, G. K. (2018a). A new, noninvasive method of measuring impaired pulmonary gas exchange in lung disease: an outpatient study. *Chest* 154, 363–369. doi: 10.1016/j.chest.2018.02.001

West, J. B., Liu, M. A., Stark, P. C., and Prisk, G. K. (2020). Measuring the efficiency of pulmonary gas exchange using expired gas instead of arterial

blood: comparing the "ideal" PO_2 of Riley with end-tidal PO_2. *Am. J. Phys. Lung Cell. Mol. Phys.* 319, L289–L293. doi: 10.1152/ajplung.00150.2020

West, J. B., and Luks, A. M. (2016). *Respiratory Physiology: The Essentials*. Philadelphia: Wolters Kluwer.

West, J. B., Wang, D. L., and Prisk, G. K. (2018b). Measurements of pulmonary gas exchange efficiency using expired gas and oximetry: results in normal subjects. *Am. J. Physiol. Lung Cell. Mol. Physiol.* 314, L686–L689. doi: 10.1152/ajplung.00499.2017

West, J. B., Wang, D. L., Prisk, G. K., Fine, J. M., Bellinghausen, A., Light, M. P., et al. (2018c). Noninvasive measurement of pulmonary gas exchange: comparison with data from arterial blood gases. *Am. J. Phys. Lung Cell. Mol. Phys.* 316, L114–L118. doi: 10.1152/ajplung.00371.2018

Conflict of Interest: The University of California, San Diego, has exclusively licensed technology to MediPines Corporation, Orange County, CA, to develop a device (the AGM100™) used in some studies referenced in this work. JW declares a financial interest with MediPines Corporation.

The remaining author declares that the research was conducted in the absence of any commercial or financial relationships that could be construed as a potential conflict of interest.

Publisher's Note: All claims expressed in this article are solely those of the authors and do not necessarily represent those of their affiliated organizations, or those of the publisher, the editors and the reviewers. Any product that may be evaluated in this article, or claim that may be made by its manufacturer, is not guaranteed or endorsed by the publisher.

frontiers in Physiology

METHODS
published: 04 November 2021
doi: 10.3389/fphys.2021.737493

Inspiratory Muscle Training for Obstructive Sleep Apnea: Protocol Development and Feasibility of Home Practice by Sedentary Adults

*Beatrix Krause-Sorio[1], Eunjoo An[1], Andrea P. Aguila[1], Fernando Martinez[1], Ravi S. Aysola[2] and Paul M. Macey[1]**

[1] UCLA School of Nursing, University of California, Los Angeles, Los Angeles, CA, United States, [2] Division of Pulmonary and Critical Care, David Geffen School of Medicine, University of California, Los Angeles, Los Angeles, CA, United States

Background: Inspiratory muscle training (IMT) may improve respiratory and cardiovascular functions in obstructive sleep apnea (OSA) and is a potential alternative or adjunct treatment to continuous positive airway pressure (CPAP). IMT protocols were originally designed for athletes, however, we found some OSA patients could not perform the exercise, so we aimed for a more OSA-friendly protocol. Our feasibility criteria included (1) participants successfully managing the technique at home; (2) participants completing daily practice sessions and recording data logs; and (3) capturing performance plateaus to determine an optimal length of the intervention.

Methods: Five sedentary OSA patients participated in this feasibility study (three men, mean age = 61.6 years, SD = 10.2). Using a digital POWERbreathe K4 or K5 device, participants performed 30 daily inhalations against a resistance set at a percentage of maximum, recalculated weekly. Participants were willing to perform one but not two daily practice sessions. Intervention parameters from common IMT protocols were adapted according to ability and subjective feedback. Some were unable to perform the typically used 75% of maximum inspiratory resistance so we lowered the target to 65%. The technique required some practice; therefore, we introduced a practice week with a 50% target. After an initial 8 weeks, the intervention was open-ended and training continued until all participants demonstrated at least one plateau of inspiratory strength (2 weeks without strength gain). Weekly email and phone reminders ensured that participants completed all daily sessions and logged data in their online surveys. Weekly measures of inspiratory resistance, strength, volume, and flow were recorded.

Results: Participants successfully completed the practice and subsequent 65% IMT resistance targets daily for 13 weeks. Inspiratory strength gains showed plateaus in all subjects by the end of 10 weeks of training, suggesting 12 weeks plus practice would be sufficient to achieve and capture maximum gains. Participants reported no adverse effects.

OPEN ACCESS

Edited by:
Walter Araujo Zin, Federal University of Rio de Janeiro, Brazil

Reviewed by:
Pei-Ying Sarah Chan, Chang Gung University, Taiwan
Lance Bollinger, University of Kentucky, United States

****Correspondence:***
Paul M. Macey
pmacey@ucla.edu

Specialty section:
This article was submitted to Respiratory Physiology, a section of the journal Frontiers in Physiology

Received: *07 July 2021*
Accepted: *12 October 2021*
Published: *04 November 2021*

Citation:
Krause-Sorio B, An E, Aguila AP, Martinez F, Aysola RS and Macey PM (2021) Inspiratory Muscle Training for Obstructive Sleep Apnea: Protocol Development and Feasibility of Home Practice by Sedentary Adults. Front. Physiol. 12:737493. doi: 10.3389/fphys.2021.737493

Conclusion: We developed and tested a 13-week IMT protocol in a small group of sedentary, untreated OSA patients. Relative to other IMT protocols, we successfully implemented reduced performance requirements, a practice week, and an extended timeframe. This feasibility study provides the basis for a protocol for clinical trials on IMT in OSA.

Keywords: sleep apnea, breathing, sleep, training, intervention, inspiratory muscle training, respiration, strength

INTRODUCTION

Over 10% of the population suffers from obstructive sleep apnea (OSA), a disorder characterized by repeated pauses in breathing during sleep due to collapsing of the upper airway (Peppard et al., 2013; Marshall et al., 2014). The condition is a major risk factor for cardiovascular disease including hypertension and cardiovascular disease (Monahan et al., 2009; Peppard et al., 2013; Javaheri et al., 2017; Whelton et al., 2018). Nightly use of continuous positive airway pressure (CPAP), the standard treatment for OSA, resolves the breathing disruptions and improves some of the symptoms, but shows mixed results for reducing blood pressure (BP) (Barbé et al., 2012; McEvoy et al., 2016; Whelton et al., 2018). Furthermore, CPAP adherence is often low, as patients experience it as intrusive and difficult to wear throughout the night. In some patients, weight loss and physical exercise improve daytime symptoms and breathing during sleep, but as with other chronic conditions, more often than not, stable long-term health behavior change in OSA is not achieved (Aiello et al., 2016; Vranish and Bailey, 2016; Souza et al., 2018; Carneiro-Barrera et al., 2019). Consequently, there remains a need for complementary or alternative interventions for treating OSA and its comorbidities.

One potentially beneficial intervention for people with OSA is inspiratory muscle training (IMT). IMT is the practice of strengthening respiratory muscles involved in inhalations (Larson et al., 1988). Simplistically, OSA arises from a failure of breathing, therefore training breathing may improve symptoms. More specifically, since OSA involves the collapse of the upper airways with inspiration during sleep, IMT may reduce the number and/or severity of apneas by improving upper airway muscle tone (How et al., 2007). In addition, IMT may also improve cardiovascular symptoms, since studies in normotensive adults and patients with OSA found significant reductions in BP with IMT, and improved functional capacity in people with heart failure (Ferreira et al., 2013; Vranish and Bailey, 2015, 2016; Posser et al., 2016; DeLucia et al., 2018; Fernandez-Rubio et al., 2020; Ramos-Barrera et al., 2020). The mechanism of IMT effects on cardiovascular function is unknown, but may be due to either associations between respiratory and cardiovascular activity, or due to potential positive IMT-related effects on stress (Grossman et al., 2001; HajGhanbari et al., 2013; de Abreu et al., 2017; Fernandez-Rubio et al., 2020). Regardless of the mechanism, the evidence suggests that IMT has the potential to improve both breathing and cardiovascular symptoms in OSA.

Inspiratory muscle training can be performed systematically using devices that provide quantifiable resistance targets and instant performance feedback. These targets are usually set as a percentage of the maximum inspiratory pressure that an individual can generate, as measured by a sensor in the device. The technique is akin to weight training where a set of repetitions is performed using a fixed weight. As the respiratory muscles gain strength, the IMT device allows the target resistance to be increased, so the training adapts to the person's current strength. A common target resistance in IMT studies is 75% of the maximum capacity, in a set of 30 repetitions performed twice daily for 6 weeks (HajGhanbari et al., 2013). However, such parameters are not achievable by all non-athletes or people with other chronic conditions who may have limited fitness or mobility. Therefore, modifications are needed for such populations. For example, in IMT studies with older adults, parameters vary from 4 to 8 weeks of training duration, 30–80% target resistance, and between 5 and 7 weekly sessions (Seixas et al., 2020). Although one research group developed and successfully tested a protocol for people with OSA for 6 weeks, 75% of maximum target resistance performed twice daily (Vranish and Bailey, 2016; Ramos-Barrera et al., 2020), several of our participants required repeated practice sessions across several days to learn the technique, and were still unable to inhale against the 75% target resistance. Hence, they were unable to complete the exercise. Other participants were reluctant to practice two times a day. We speculate that compared to earlier studies, our participants were sedentary with reduced capacity to perform the resistance training, and that they had less time and motivation to practice twice daily, since they were not retired. To develop a protocol that was suited to our sedentary patient population, we aimed to modify the previously tested parameters, such that participants could successfully perform the practice and adhere to the training schedule. Our objective was to develop a clinical trial IMT protocol for untreated, sedentary OSA patients. Our approach was to work with a small group of sedentary OSA patients to test and adapt previously tested IMT parameters based on subjective feedback and quantitative measures. We also aimed to derive an empirical basis for a clinical trial duration. Therefore, the trial began with an 8-week minimum duration and continued until performance plateaued or until participants reported unwillingness to continue.

Our feasibility criteria for the protocol included:

(1) All participants had to be able to successfully perform the practice using the same settings (e.g., starting resistance);
(2) Participants had to complete daily practice sessions;
(3) Participants had to complete the protocol until the end; and

(4) Participants had to show sustained increases and eventually plateaus in inspiratory strength.

METHODS

Participants

We recruited participants at the University of California, Los Angeles (UCLA) campus and the local community *via* digital and printed fliers. Inclusion criteria were a diagnosis of mild, moderate, or severe OSA based on a two-night home sleep study using a polysomnography device scored according to the 2012 American Academy of Sleep Medicine criteria (Ayappa et al., 2008; Berry et al., 2012); aged 21–75; and no current or previous sustained use of OSA treatment. Exclusion criteria included a history of stroke, heart failure, or other major cardiovascular disease, a history of diagnosed mental health conditions other than unipolar depression or anxiety disorder, respiratory illness other than OSA (including contraindications for IMT such as pulmonary hypertension), cystic fibrosis, presence of mass brain lesions, renal failure (requiring dialysis) and drug abuse. While IMT is considered a low risk practice, the resulting large negative pressure swings within the chest (intra-thoracic decompression) hold a potential risk of sub-atmospheric pressures in the chest, throat, inner ear, and sinuses (McConnell et al., 2005). Therefore, exclusion criteria due to IMT contraindications also included a history of spontaneous pneumothorax, traumatic pneumothorax that was not fully healed at the time of recruitment, burst eardrum or other conditions of the eardrum, including recent eardrum surgery, unstable asthma, and abnormally low perception of dyspnea.

The procedures were approved by the UCLA Institutional Review Board. Participants provided written informed consent signed digitally for initial remote activities and in written form at the first in-person visit. There was no public involvement as this was an early-stage study.

Screening

Participants initiated contact by phone, email, or text, whereupon a researcher contacted them by phone. The telephone screening involved assessing potential participants' medical history, including the assessment of the previously listed inclusion and exclusion criteria. Potential participants then completed an online survey assessing further details about medical history, demographics, sleeping times, subjective sleep quality, and daytime sleepiness. Participants who met the study criteria were subsequently referred for a home sleep study.

Home Sleep Study

Home sleep studies were executed by a third party, SleepMed (SleepMed Inc., Peabody, MA, United States), in conjunction with the UCLA Sleep Disorders Center. Within 48 h of enrollment into the study, participants received a phone call by a SleepMed representative to schedule an appointment for delivery. Upon receiving the portable SleepMed polysomnography device [ARES^{TM} Home Sleep Test system (Ayappa et al., 2008)] in the mail, participants wore the device strapped to their foreheads for two consecutive nights with a nightly minimum of 4 h. The device recorded heart rate, breathing, oxygen saturation, snoring from auditory recordings, and electroencephalogram (EEG) during their sleep. The return packaging and paid postage was included in the original shipment. After completion of the second night, participants returned the device to SleepMed by mail, where the data was uploaded and scored by a sleep technologist in a draft report. This report was made available to the research group and interpreted by the sleep physician of our research group. The apnea hypopnea index (AHI) is the sum of apneas and hypopneas during sleep per hour and was derived from the SleepMed data. Mild sleep apnea is reflected by 5–15 events per hour, moderate by 15–30 and severe by over 30 events per hour. The Respiratory Disturbance Index (RDI) was computed from the number of apneas per hour, the number of hypopneas per hour, and the number of respiratory effort-related arousals (RERAs) per hour during sleep. Mild OSA is indicated by an RDI score from 5 to 15, moderate 15 to 30, and severe over 30. An OSA diagnosis was provided within 2 weeks of the data upload. Participants subsequently received their sleep report *via* a secure and password protected system from the research group. If a diagnosis of OSA was made, participants were eligible for the study.

Inspiratory Muscle Training

Inspiratory muscle training is performed by inhaling against a resistance a given number of times. For the purposes of controlling the intervention parameters and verifying the number of repetitions, we used a device that would provide a consistent, fixed resistance. POWERbreathe (POWERbreathe International Ltd., Southam, United Kingdom) provides such palm-sized, handheld devices for IMT. Previous studies have used the K3 model (Vranish and Bailey, 2016), but upon testing this model, we were unable to manually adjust the resistance settings, therefore we selected models K4 and K5 instead. Both are digital devices and include software that logs and tracks performance over time. Both models provide immediate feedback to the user. These devices adapt the resistance to match the decline in strength of each individual breath to allow for greater flow and maximum volume. The target resistance was set as a percentage of the maximum inspiratory strength based on the average of three trials. A nose clip was used to prevent nasal breathing. The participant was instructed to stand up with their backs straight so they could maximally fill their lungs and expand their rib cages. The mouthpiece was inserted between the lips upon switching on of the device. Basic instructions were as follows: "*Thirty breaths reaching the target threshold should be completed in the following way: inhalations should be fast, deep and noisy, with the shoulders remaining relaxed. The diaphragm should be expanding, and the lungs should be filled as much as possible. You should feel the deep breaths stretching the rib cage and shoulder muscles. Exhalations should be much slower and quieter than inhalations. In order to prevent lightheadedness, the breath should be held after each exhalation until you feel you need to breathe in again. The IMT device displays a count-down from 30 to 0, and only records inhalations that exceed the target resistance.*" If the participant was unable to reach the target resistance, another

TABLE 1 | Protocol modifications after testing five OSA participants.

Component	Standard	Modified	Rationale
Training period	None	1 week at 50% resistance	Training period allowed people to learn the technique correctly. Fifty percent target provides resistance without being overly challenging.
Training materials	None	Online videos and paper handout demonstrating techniques and troubleshooting	Participants were able to address difficulties, especially in the first 2–3 weeks of training, as they were becoming familiar with the technique. These materials improved people's correct use of the device.
Target resistance	75%	65%	We aimed for consistency across participants. The standard 75% resistance were not attainable by all participants. However, 65% was achievable by all participants. We concluded that sedentary OSA participants may not be able to reach the standard target resistance that is used by people who exercise.
Daily practice sessions	Twice a day (more recent studies once a day)	Once a day	In order to maintain 100% adherence and consistency across participants for the entire training period, we reduced the number of training sessions a day to one. Some participants expressed concerns about practicing twice a day, while none expressed concerns about one session a day.
Duration	6 weeks	13 weeks (1 week 50% and 12 weeks 65%)	We determined the duration based on a plateau of strength increases and participant acceptability.

trial was added to complete the 30 breaths. Each set required 5–10 min to complete.

Intervention

Prior to starting the training, a research team member worked with the participants to test and adapt the IMT parameters. Experiences with initial attempts to train participants on the use of the device demonstrated that the maximum starting target resistance settings for each individual participant varied, even though each was calibrated to the maximum strength of the individual. While some participants found it easy to start at 75% resistance or more, some struggled to complete even a few breaths at this level. After discussions and feedback from the participants, we made two adaptations: (1) Participants initially practiced at a lower target resistance with the goal of learning the technique without the performance pressure. Typically, this required them to start with an inhale followed by a full exhale in preparation of the intended forceful inhalation. This allowed them to take a longer than usual sustained inhalation; (2) We set the ongoing target at 65% of the maximum, a level that was achievable for all participants. We found 65% to be the highest resistance that all five participants were able to perform.

We found that some participants had difficulties interacting with the device and required more demonstrations and guidance. Therefore, in addition to the instructions above, we provided in-person training and created a video demonstrating the correct technique that participants could watch at home. Participants were also provided with a paper copy of instructions on usage of the device and proper technique. The resulting protocol and modifications are shown in **Table 1**. The daily session duration was reported to be initially 10 min, and after a week of practice reduced to typically 5 min.

Data Acquisition

Data entry of the IMT device data was completed by participants at home *via* an online survey software with encrypted connectivity using their unique study identifier. The variables included inspiratory resistance in percent of the maximum, strength index (cmH_2O), volume in liters (L) and flow in liters per second (L/s). Measures of interest included performance data from the IMT device (target resistance, volume, and strength index). Data acquired with the polysomnography device during sleep included SaO_2, which was also used for OSA diagnosis. These sleep study data and reports were available online *via* the SleepMed portal, but only de-identified data were recorded locally by the research team. This included AHI and RDI scores. Other measures of interest acquired from the sleep study and subjective ratings provided during the online survey included self-rated sleep quality ranging from 0 to 10 (poor to good), and excessive daytime sleepiness (ESS) score.

Analysis

We computed descriptive statistics in Microsoft Excel, including means, medians, standard deviations (SD), and range (minimum to maximum). We used SPSS version 27 to test within-group changes in sleep data, SaO_2 and IMT device data using the non-parametric Wilcoxon signed-rank test. Non-parametric correlations were tested using Kendall's tau. In addition, we visualized individual data points for each participant, as well as the group mean and standard deviation. The visualizations aided the detection of the performance increases and plateaus, based on which we adapted the duration of the intervention. We defined a plateau as the absence of an increase in inspiratory strength for three consecutive weeks.

Protocol Duration

We aimed to derive an empirical basis for trial duration, so the trial duration began open-ended, with participants consenting to participate for up to 8 weeks at a time. We aimed to continue the intervention until we could no longer observe substantial strength increases as measured with the IMT device, or until participants reported unwillingness to continue. Our criterion

was to end the protocol after all participants demonstrated a 3-week period with no further increase in strength. This duration differed between participants; therefore, the weakest participants would serve as the criterion.

Based on difficulties of some participants to operate the device and successfully perform the inspirations at the same time, the target resistance was set to 50% for a practice week. This allowed the participants to familiarize themselves with the device use at home without struggling to also complete 30 breaths at a higher resistance. At the beginning of the second week of training, the target resistance was then increased to 65%. At the beginning of each following week, a new maximum strength was determined, and the 65% target re-calculated accordingly. The target could only be increased, not decreased. If a lower maximum strength was measured, the target was kept at the previous level. Therefore, it was important that participants were able to build strength from the beginning without struggling with too high of a resistance. Once a week, the project director reached out to participants by phone to discuss exercise progress and answer questions, record subjective experiences and support protocol adherence.

RESULTS

Five sedentary adults with OSA completed the protocol (three men; two women; mean age = 62.2 years, SD = 10.5; mean body-mass index = 33.9, SD = 4.3). All participants reported to be willing and motivated to complete one daily session for the initial 8 weeks. Since our criterion of all participants reaching

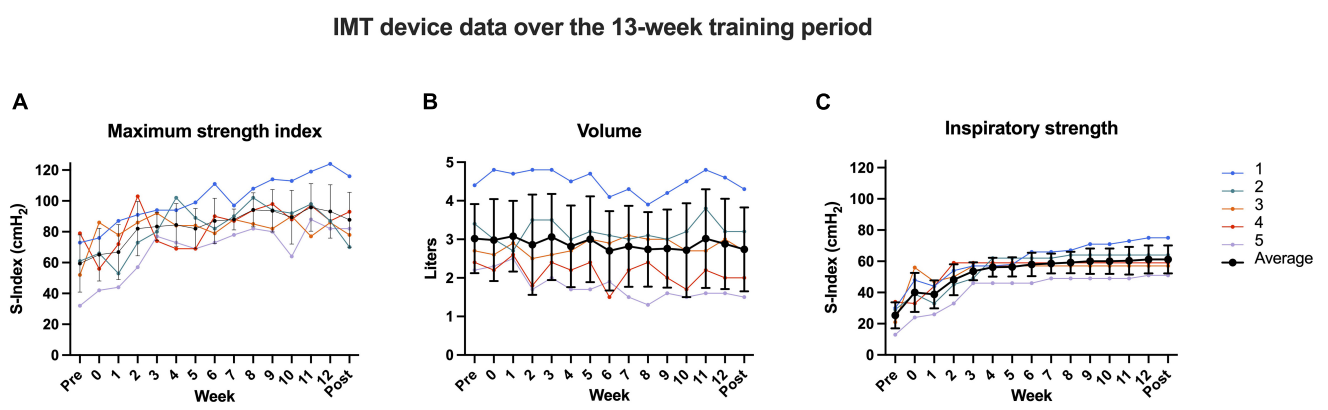

FIGURE 1 | Inspiratory muscle training (IMT) device data over the course of the intervention. Each colored line depicts a different participant, while the thick black line reflects the group average with its standard deviation. Panels: maximum inspiratory strength index **(A)**, respiratory volume in liters **(B)**, and average inspiratory strength **(C)** of five untreated OSA patients from baseline across 13 weeks of IMT. While participant 1 had a higher baseline on all measures and continued to increase both resistance and strength until the end of the trial, the average of the group reached a ceiling effect in strength index after approximately 8 weeks (with slight fluctuations) and after ca. 4 weeks in resistance.

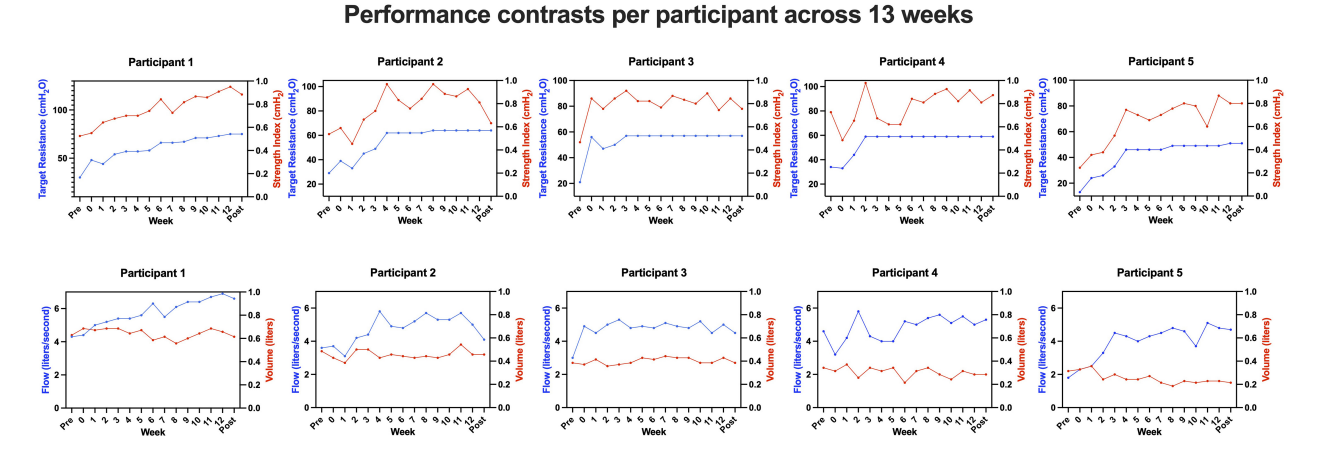

FIGURE 2 | Inspiratory muscle training (IMT) device data for each participant per week. Note the fluctuations in strength index (top panel, right *y*-axis, red) despite the flattening of the curve of the target resistance (top panel, left *y*-axis, blue) for participants 2–5. Only for participant 1, there was a steady increase in both measures over the entire course of the intervention. The pattern of the flow curve (bottom panel, blue) corresponds to the pattern of the strength index (top panel, red). For better visualization of the different scales, both are depicted in separate graphs. The volume curve (bottom panel, red) shows less fluctuations and no overall gain across the training period.

TABLE 2 | Descriptive statistics and within-group change of IMT device data from baseline to follow-up.

	Baseline (week 0)		13-week follow-up		Within-group change
	Mean (SD)	**Range**	**Mean (SD)**	**Range**	**Wilcoxon signed rank test**
Target resistance (cmH_2O)	40.0 (12.5)	24–56	61.2 (9.0)	51–75	$S = 15$, $p = 0.04$*
Strength index (cmH_2O)	65.2 (17.2)	42–86	87.8 (17.8)	70–116	$S = 13$, $p = 0.14$
Flow (L/s)	3.7 (1.02)	2.3–4.9	5.0 (1.0)	4.1–6.6	$S = 13.5$, $p = 0.1$
Volume (L)	3.0 (1.1)	2.2–4.8	2.7 (1.1)	1.5–4.3	$S = 3.5$, $p = 0.28$
	Baseline (pre-practice)		**13-week follow-up**		
AHI	19.4 (14.2)	9–44	16.8 (8.7)	8–30	$S = 5.5$, $p = 0.59$
RDI	31.4 (15.8)	15–54	28.8 (9.8)	18–40	$S = 4.0$, $p = 0.72$
ESS	9.6 (8.3)	2–22	7.4 (6.5)	1–14	$S < 0.0001$, $p = 1.0$
SaO_2 nadir (%)	84.9 (2.6)	82.3–87.8	84.4 (5.6)	76.3–90.4	$S = 6.5$, $p = 0.79$
SaO_2 baseline (%)	94.9 (1.2)	93.3–96.2	94.8 (1.3)	93.3–96.0	$S = 2.5$, $p = 0.79$

*Mean, SD, and range are shown for each time point. *$p < 0.05$.*

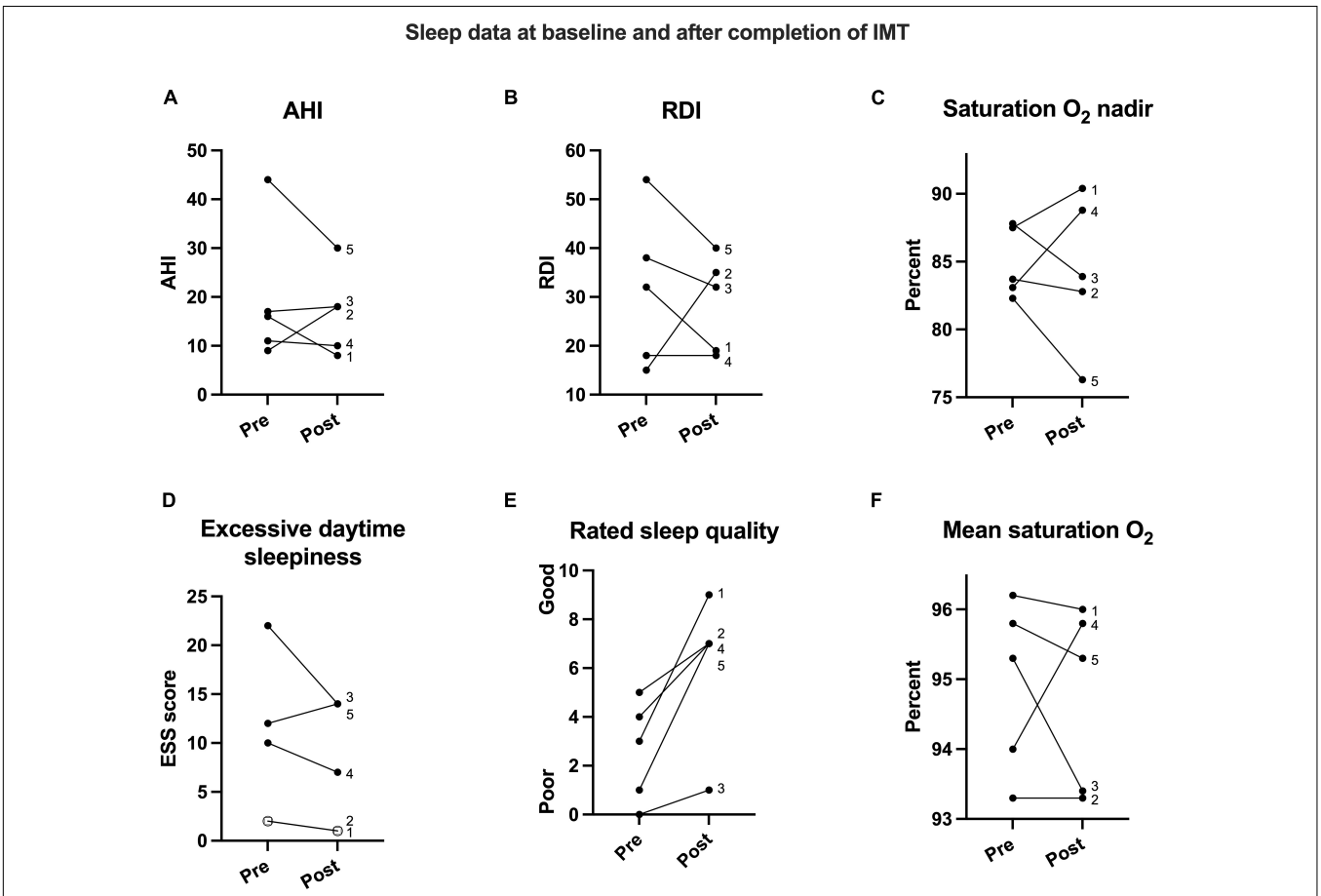

FIGURE 3 | Sleep data for all five participants labeled 1 through 5. While apnea hypopnea index (AHI; **A**), respiratory disturbance index (RDI; **B**), oxygen saturation at nadir (SaO_2; **C**), and the all-night oxygen saturation average (SaO_2; **F**) showed individual variation, subjective rating for daytime sleepiness (**D**; participants 1 and 2 overlap here) decreased and therefore improved, and rated sleep quality **(E)** improved in all five participants from baseline to post-IMT intervention.

a plateau had not been met after 8 weeks, all participants were enrolled in a second open-ended period. After 13 weeks, all participants had achieved a plateau. Therefore, we finalized the intervention after 13 weeks. Week 0 reflects the practice week in which participants practiced at 50% maximum resistance, which was a low effort for all five participants. Week one subsequently involved the first week of enhanced effort. Participants then continued IMT until the end of week 13 (see **Figure 1**). Resistance

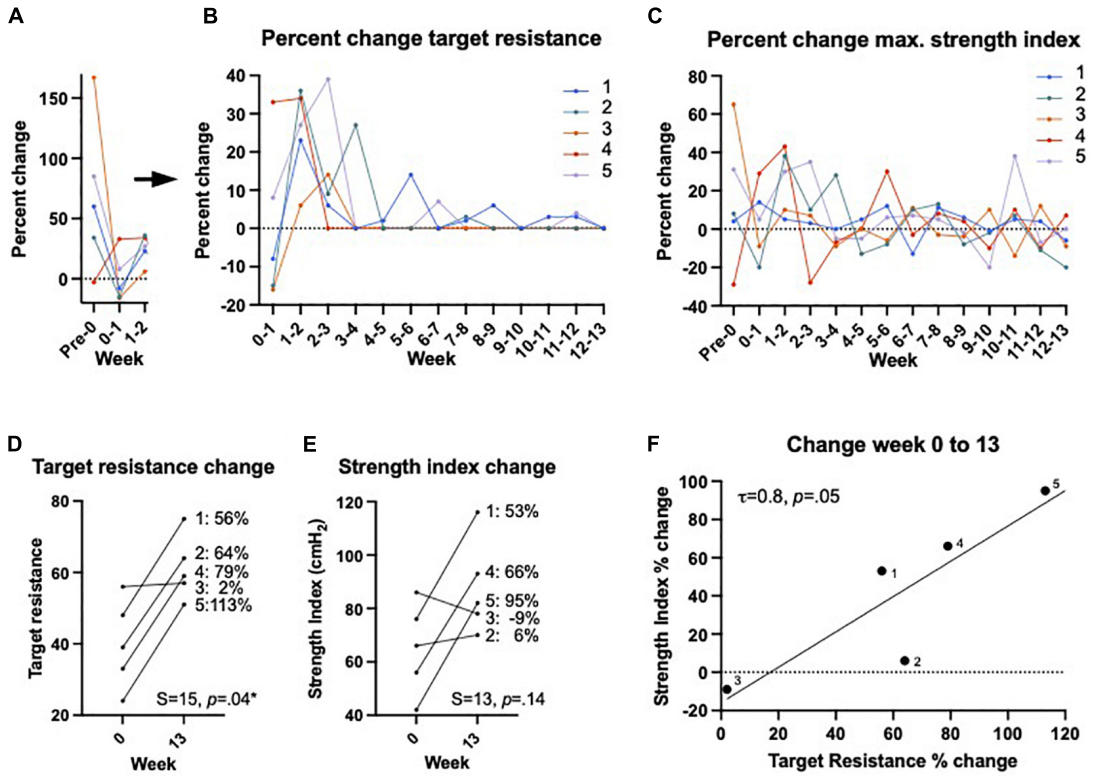

FIGURE 4 | Inspiratory muscle training (IMT) effects on device performance in percentage change. Panels **(A,B)** show the percent change in target resistance measured in cmH_2O from 1 week to the next. For better visualization and due to the large drop from the first attempt until the end of the practice week (week 0), panel **(A)** shows the data points at a different *y*-axis scale separately from panel **(B)** the following weeks. After 8–9 weeks, there was little to no change in target resistance, i.e., participants were unable to increase their inspiratory strength further at that point. Note that this was not the case for participant 1, whose performance was superior to the other 4. **(C)** The percent change of maximum strength index from 1 week to the next showed greater overall variability but except individual peaks, the general trend evened on the lower end after 4–5 weeks. **(D)** The overall percentage of change in target resistance (measured in cmH_2O) and **(E)** maximum strength index from week 0 to week 13. **(F)** There was a significant association between target resistance and strength index change in percent from week 0 to week 13 as one would expect.

across the group still increased through weeks 6–8 and appeared to plateau at week 10. Even though resistance stagnated before week 10 for some participants, we still observed significant individual variability in strength until the end of the 13 weeks. **Figure 2** depicts each participant's time course of target resistance relative to strength index (top panel) and volume relative to flow (bottom panel). Technical difficulties were reported and resolved in communication with the team members whenever necessary, but participants reported no side effects or discomfort throughout or after completion of the intervention.

All baseline and follow-up data are listed in **Table 2**: there were no significant within-subject changes from baseline to 13-week follow-up for AHI, RDI, ESS, SaO_2 at nadir, and baseline SaO_2 (*p*s > 0.59; **Figure 3**). There was a significant increase in target resistance (cmH_2O) from week 0 to week 13 ($S = 15$, $p = 0.04$), but not in strength index ($p = 0.27$; see 13-week individual data **Figures 4A–C** and pre-to-post differences **Figures 4D,E**). The association between this 12-week increase in percent change target resistance and strength index was marginal ($\tau = 0.8$, $p = 0.05$; **Figure 4F**). The IMT device data demonstrated that participants gained an average of 15–20% in inspiratory muscle strength over the course of 4 weeks (see **Figure 1C**).

DISCUSSION

We developed a protocol for IMT for sedentary adults with untreated OSA. We found that a 1-week practice period at 50% of maximum inspiratory resistance followed by 12 weeks at 65% with single daily practice sessions for a total of 13 weeks was achievable, manageable, and resulted in an average of 15–20% inspiratory muscle strength improvement. This was a significant increase, despite the small sample size. Target resistance and strength index data varied greatly between weeks in some patients. While the target resistance was fixed and only attempts counted that exceeded the target, any observed variation stemmed from patients taking stronger than necessary

inspirations. We further established that initial IMT training should be supplemented with online and other digital resources and the opportunity to ask the research team members questions directly, especially during the first 2 weeks of training. We found increases in subjective daytime sleepiness, sleep quality, AHI, and RDI. While these effects were not significant, they provide an effect size for power calculations.

Our initial intention of participants performing two IMT sessions a day was not well received by our sample. Participants raised concerns about their ability to complete two sessions a day. The single daily session, however, did not elicit concerns and we observed 100% adherence across the 13 weeks, which was one of our major goals. During these 13 weeks, each participant completed a total of 91 IMT sessions involving 30 breaths each. This high adherence was potentially influenced by the initial rapport between participants and research team members, as well as the weekly phone contact. No participant reported logistical or motivation difficulties in performing the daily IMT practice, therefore we suggest that adherence may be increased in a clinical trial after participants are successfully introduced to IMT.

With regards to inspiratory muscle strength, our results suggest that ceiling or plateau effects in strength index occur after 6 weeks of training in some participants, consistent with previous published IMT studies. However, even in our small sample, there was variability in baseline performance capacity. One of our participants (Peppard et al., 2013) demonstrated a higher baseline capacity and continued to increase until 13 weeks. It is therefore possible that there is greater individual variability in both baseline performance, practice effects, and end results, including ceiling effects. The results from our sleep measurements demonstrate sharp improvements for participant 1 and less pronounced changes for the other four participants. However, only participant 1 had a greater than mild OSA severity. The subjective sleep quality rating showed improvements for all participants with a minimum of a 2-point improvement on a scale from 0 to 10.

While most existing IMT studies consist of 6 weeks of training and symptom-tracking (HajGhanbari et al., 2013), our 12-plus-1 week intervention was able to better detect potential ceiling effects in the data tracked daily or weekly. For instance, our results show the largest increases in average target resistance across the group from the practice period until the end of week 2. The slope then flattened but continued to increase in minor increments until the end of the intervention period. If we had only focused on the first 6 weeks, it would be unclear whether and with what increments the target resistance continued to increase or whether it remained at a plateau. Additionally, the extended intervention period allowed us to track and evaluate individual performance over time. Participant number 3 reached a target resistance of 57% after week 3 and was unable to increase the resistance for the rest of the intervention, while participant number 1 continued to increase the percentage in small steps to the end with 75% being the highest final resistance of the group. In terms of subjective experience, all participants reported positive changes, so one question that can be addressed in a clinical trial using a low-resistance control group, is whether any symptom improvements will be related to the mere daily practice (i.e., a placebo effect), or whether it was specific to the inspiratory strength gains. Participants reported appreciating the 1-week practice period at a moderate target resistance (50%). While this practice week may have induced a practice effect, the strength gains were likely due to the familiarity with the technique rather than muscle gain. We conclude that our adapted IMT protocol is suitable for testing whether IMT might be a beneficial alternative or complementary treatment to CPAP in sedentary people with untreated OSA. Using these modifications, we intend to perform a trial in which we randomize untreated OSA patients to active vs. low-resistance intervention arms, and investigate the effects of IMT on respiratory performance, sleep, and cardiovascular symptoms.

DATA AVAILABILITY STATEMENT

The raw data supporting the conclusions of this article will be made available by the authors, without undue reservation.

ETHICS STATEMENT

The studies involving human participants were reviewed and approved by the University of California, Los Angeles Institutional Review Board (UCLA IRB #17-000918). The patients/participants provided their written informed consent to participate in this study.

AUTHOR CONTRIBUTIONS

PM conceived the idea for the pilot and trial and was the principal investigator. RA helped with the initial design, served as the medical professional and diagnosed participants. BK-S visualized and summarized the data and wrote the manuscript. AA and FM coordinated the study and gathered the data. EA contributed to the writing of the manuscript. RA served as the medical professional and diagnosed participants. All authors reviewed the manuscript.

FUNDING

This work was supported by the UCLA School of Nursing at the University of California, Los Angeles.

REFERENCES

Aiello, K. D., Caughey, W. G., Nelluri, B., Sharma, A., Mookadam, F., and Mookadam, M. (2016). Effect of exercise training on sleep apnea: a systematic review and meta-analysis. *Respir. Med.* 116, 85–92.

Ayappa, I., Norman, R. G., Seelall, V., and Rapoport, D. M. (2008). Validation of a self-applied unattended monitor for sleep disordered breathing. *J. Clin. Sleep Med.* 4, 26–37. doi: 10.5664/jcsm.27075

Barbé, F., Durán-Cantolla, J., Sánchez-de-la-Torre, M., Martínez-Alonso, M., Carmona, C., Barceló, A., et al. (2012). Effect of continuous positive airway

pressure on the incidence of hypertension and cardiovascular events in nonsleepy patients with obstructive sleep apnea: a randomized controlled trial. *JAMA* 307, 2161–2168.

Berry, R. B., Budhiraja, R., Gottlieb, D. J., Gozal, D., Iber, C., Kapur, V. K., et al. (2012). Rules for scoring respiratory events in sleep: update of the 2007 AASM manual for the scoring of sleep and associated events. Deliberations of the sleep apnea definitions task force of the american academy of sleep medicine. *J. Clin. Sleep. Med.* 8, 597–619. doi: 10.5664/jcsm.2172

Carneiro-Barrera, A., Díaz-Román, A., Guillén-Riquelme, A., and Buela-Casal, G. (2019). Weight loss and lifestyle interventions for obstructive sleep apnoea in adults: systematic review and meta-analysis. *Obes. Rev.* 20, 750–762.

de Abreu, R. M., Rehder-Santos, P., Minatel, V., Dos Santos, G. L., and Catai, A. M. (2017). Effects of inspiratory muscle training on cardiovascular autonomic control: a systematic review. *Auton. Neurosci.* 208, 29–35. doi: 10.1016/j.autneu.2017.09.002

DeLucia, C. M., De Asis, R. M., and Bailey, E. F. (2018). Daily inspiratory muscle training lowers blood pressure and vascular resistance in healthy men and women. *Exp. Physiol.* 103, 201–211. doi: 10.1113/ep086641

Fernandez-Rubio, H., Becerro-de-Bengoa-Vallejo, R., Rodriguez-Sanz, D., Calvo-Lobo, C., Vicente-Campos, D., and Chicharro, J. L. (2020). Inspiratory muscle training in patients with heart failure. *J. Clin. Med.* 9:1710. doi: 10.3390/jcm9061710

Ferreira, J. B., Plentz, R. D., Stein, C., Casali, K. R., Arena, R., and Lago, P. D. (2013). Inspiratory muscle training reduces blood pressure and sympathetic activity in hypertensive patients: a randomized controlled trial. *Int. J. Cardiol.* 166, 61–67. doi: 10.1016/j.ijcard.2011.09.069

Grossman, E., Grossman, A., Schein, M. H., Zimlichman, R., and Gavish, B. (2001). Breathing-control lowers blood pressure. *J. Hum. Hypertens.* 15, 263–269. doi: 10.1038/sj.jhh.1001147

HajGhanbari, B., Yamabayashi, C., Buna, T. R., Coelho, J. D., Freedman, K. D., Morton, T. A., et al. (2013). Effects of respiratory muscle training on performance in athletes: a systematic review with meta-analyses. *J. Strength Cond. Res.* 27, 1643–1663. doi: 10.1519/JSC.0b013e318269f73f

How, S. C., McConnell, A. K., Taylor, B. J., and Romer, L. M. (2007). Acute and chronic responses of the upper airway to inspiratory loading in healthy awake humans: an MRI study. *Respir. Physiol. Neurobiol.* 157, 270–280. doi: 10.1016/j.resp.2007.01.008

Javaheri, S., Barbe, F., Campos-Rodriguez, F., Dempsey, J. A., Khayat, R., Javaheri, S., et al. (2017). Sleep apnea: types, mechanisms, and clinical cardiovascular consequences. *J. Am. Coll. Cardiol.* 69, 841–858.

Larson, J. L., Kim, M. J., Sharp, J. T., and Larson, D. A. (1988). Inspiratory muscle training with a pressure threshold breathing device in patients with chronic obstructive pulmonary disease. *Am. Rev. Respir. Dis.* 138, 689–696.

Marshall, N. S., Wong, K. K., Cullen, S. R., Knuiman, M. W., and Grunstein, R. R. (2014). Sleep apnea and 20-year follow-up for all-cause mortality, stroke, and cancer incidence and mortality in the busselton health study cohort. *J. Clin. Sleep Med.* 10, 355–362. doi: 10.5664/jcsm.3600

McConnell, A. K., Romer, L. M., and Weiner, P. (2005). Inspiratory muscle training in obstructive lung disease. *Breathe* 2, 38–49. doi: 10.1183/18106838.0201.38

McEvoy, R. D., Antic, N. A., Heeley, E., Luo, Y., Ou, Q., Zhang, X., et al. (2016). CPAP for prevention of cardiovascular events in obstructive sleep apnea. *N. Engl. J. Med.* 375, 919–931.

Monahan, K., Storfer-Isser, A., Mehra, R., Shahar, E., Mittleman, M., Rottman, J., et al. (2009). Triggering of nocturnal arrhythmias by sleep-disordered breathing events. *J Am. Coll. Cardiol.* 54, 1797–1804.

Peppard, P. E., Young, T., Barnet, J. H., Palta, M., Hagen, E. W., and Hla, K. M. (2013). Increased prevalence of sleep-disordered breathing in adults. *Am. J. Epidemiol.* 177, 1006–1014.

Posser, S. R., Callegaro, C. C., Beltrami-Moreira, M., and Moreira, L. B. (2016). Effect of inspiratory muscle training with load compared with sham training on blood pressure in individuals with hypertension: study protocol of a double-blind randomized clinical trial. *Trials* 17:382. doi: 10.1186/s13063-016-1514-y

Ramos-Barrera, G. E., DeLucia, C. M., and Bailey, E. F. (2020). Inspiratory muscle strength training lowers blood pressure and sympathetic activity in older adults with OSA: a randomized controlled pilot trial. *J. Appl. Physiol. (1985)* 129, 449–458. doi: 10.1152/japplphysiol.00024.2020

Seixas, M. B., Almeida, L. B., Trevizan, P. F., Martinez, D. G., Laterza, M. C., Vanderlei, L. C. M., et al. (2020). Effects of inspiratory muscle training in older adults. *Respir. Care* 65, 535–544. doi: 10.4187/respcare.06945

Souza, A. K. F., de Andrade, A. D., de Medeiros, A. I. C., de Aguiar, M. I. R., de Souza Rocha, T. D., Pedrosa, R. P., et al. (2018). Effectiveness of inspiratory muscle training on sleep and functional capacity to exercise in obstructive sleep apnea: a randomized controlled trial. *Sleep Breath.* 22, 631–639.

Vranish, J. R., and Bailey, E. F. (2015). Daily respiratory training with large intrathoracic pressures, but not large lung volumes, lowers blood pressure in normotensive adults. *Respir. Physiol. Neurobiol.* 216, 63–69. doi: 10.1016/j.resp.2015.06.002

Vranish, J. R., and Bailey, E. F. (2016). Inspiratory muscle training improves sleep and mitigates cardiovascular dysfunction in obstructive sleep apnea. *Sleep* 39, 1179–1185. doi: 10.5665/sleep.5826

Whelton, P. K., Carey, R. M., Aronow, W. S., Casey, D. E., Collins, K. J., Himmelfarb, C. D., et al. (2018). 2017 ACC/AHA/AAPA/ABC/ACPM/AGS/APhA/ASH/ASPC/NMA/PCNA guideline for the prevention, detection, evaluation, and management of high blood pressure in adults: a report of the American college of cardiology/American heart association task force on clinical practice guidelines. *J. Am. Coll. Cardiol.* 71, e127–e248.

Conflict of Interest: The authors declare that the research was conducted in the absence of any commercial or financial relationships that could be construed as a potential conflict of interest.

Publisher's Note: All claims expressed in this article are solely those of the authors and do not necessarily represent those of their affiliated organizations, or those of the publisher, the editors and the reviewers. Any product that may be evaluated in this article, or claim that may be made by its manufacturer, is not guaranteed or endorsed by the publisher.

frontiers in Physiology

METHODS
published: 30 November 2021
doi: 10.3389/fphys.2021.748261

Isolation of Mitochondria From Fresh Mice Lung Tissue

*Dayene de Assis Fernandes Caldeira[1†], Dahienne Ferreira de Oliveira[2†], João Paulo Cavalcanti-de-Albuquerque[1], Jose Hamilton Matheus Nascimento[1], Walter Araujo Zin[1] and Leonardo Maciel[1,3]**

[1] Carlos Chagas Filho Institute of Biophysics, Federal University of Rio de Janeiro, Rio de Janeiro, Brazil, [2] Institute of Medical Biochemistry, Federal University of Rio de Janeiro, Rio de Janeiro, Brazil, [3] Professor Geraldo Cidade Campus, Federal University of Rio de Janeiro, Duque de Caxias, Brazil

Direct analysis of isolated mitochondria enables a better understanding of lung dysfunction. Despite well-defined mitochondrial isolation protocols applicable to other tissues, such as the brain, kidney, heart, and liver, a robust and reproductive protocol has not yet been advanced for the lung. We describe a protocol for the isolation of mitochondria from lung tissue aiming for functional analyses of mitochondrial O_2 consumption, transmembrane potential, reactive oxygen species (ROS) formation, ATP production, and swelling. We compared our protocol to that used for heart mitochondrial function that is well-established in the literature, and achieved similar results.

Keywords: lung mitochondria isolation, O_2-consumption, ROS, ATP, mitochondrial assessment

OPEN ACCESS

Edited by:
Tzong-Shyuan Lee,
National Taiwan University, Taiwan

Reviewed by:
Chun-Chun Hsu,
Taipei Medical University, Taiwan
Anna Blumental-Perry,
University at Buffalo, United States
Carlos Palmeira,
University of Coimbra, Portugal

***Correspondence:**
Leonardo Maciel
leonardomaciel2306@gmail.com

† These authors have contributed equally to this work and share first authorship

Specialty section:
This article was submitted to Respiratory Physiology, a section of the journal Frontiers in Physiology

Received: *27 July 2021*
Accepted: *29 October 2021*
Published: *30 November 2021*

Citation:
Caldeira DAF, Oliveira DF, Cavalcanti-de-Albuquerque JP, Nascimento JHM, Zin WA and Maciel L (2021) Isolation of Mitochondria From Fresh Mice Lung Tissue. Front. Physiol. 12:748261. doi: 10.3389/fphys.2021.748261

INTRODUCTION

The assessment of mitochondrial function in organs and tissues is essential for a better understanding of their biochemistry, physiology, and pathophysiology (Weissig, 2005; Picard et al., 2011; Meyer et al., 2017; Murphy and Hartley, 2018). The evaluation of mitochondrial function is usually accomplished in isolated mitochondria (Picard et al., 2011; Gedik et al., 2017; Maciel et al., 2020, 2021; Caldeira et al., 2021) permeabilized fibers (Perry et al., 2013) or cells (Perry et al., 2013). These techniques are very well-defined in several types of tissue, e.g., heart (Gedik et al., 2017), kidney (Schulz et al., 2015), liver (Goudarzi et al., 2018), adipose tissue (Matta et al., 2021), and brain (Marques Neto et al., 2020), presenting peculiarities and different indications depending on the tissue and the purpose of the investigation. However, assessment of lung mitochondrial function presents difficulties associated with obtaining isolated, intact, coupled, and functional mitochondria. The methodological difficulty of obtaining viable lung mitochondria derives mainly from an elevated fatty acid content, low amount of mitochondria in the cell, fibrous and air-filled tissue, and the required amount of tissue (Spear and Lumeng, 1978; Kuznetsov et al., 2008; Lanza and Sreekumaran Nair, 2009). Recently, we have shown that the isolation of pulmonary mitochondria with preserved structure and function is possible by means of adaptations of existing techniques and standardization of a specific method of isolation by differentiated centrifugation (Caldeira et al., 2021). However, the differences related to mitochondrial isolation procedures for obtaining these well-preserved pulmonary mitochondria have not been addressed in detail, and the characteristics of reagents and equipment have not been fully described (Caldeira et al., 2021). Therefore, the main objective of this article is to provide a practical step-by-step user protocol upgraded to isolate pulmonary mitochondria. Our isolation protocol is founded on the differentiated centrifugation method of mice lung homogenate. However, unlike the classical procedures currently in use, we will use some innovative steps because of the intrinsic characteristics of the tissue to obtain better and more functional isolated mitochondria. In addition, we describe in detail the mitochondrial function pertaining to several respiratory complexes.

MATERIALS AND EQUIPMENT

Materials and Reagents

1. Teflon beaker (BRAND® beaker, PTFE, low form, catalog number: Z322660; Merck, Darmstadt, Germany).
2. 50 ml Falcon tubes (FALCON® Brand, 50 ml polypropylene conical tube 30 mm × 115 mm style, catalog number: 352070; Coring Science Mexico, Col del, Mexico).
3. 14 ml round-bottom tubes (Thermo Scientific™, Nunc™ 14 ml round-bottom tube, catalog number: 150268; Thermo Fisher Scientific™, Waltham, MA, United States).
4. 1.5 and 2 ml microfuge tubes (Eppendorf Safe-Lock Tubes, 1.5 and 2 ml Eppendorf Quality™, catalog numbers: 0030120086 and 0030120094, respectively; Eppendorf, Hamburgo, Germany).
5. Syringe filter (Corning® syringe filters, nylon membrane, diameter 25 mm, pore size 0.2 μm, catalog number: CLS431224; Merck, Darmstadt, Germany).
6. Adjustable volumetric pipettes: 10 and 100 μl; and 5 ml (PIPETMAN L P10L, 1–10 μl; PIPETMAN L P100L, 10–100 μl; PIPETMAN L P1000L, 100–1,000 μl; PIPETMAN L P5000L, 500–5,000 μl, metal ejector, catalog numbers: FA10002M, FA10004M, FA10006M, and FA10007, respectively; Gilson, Middleton, WI, United States).
7. Dispenser pipette (BRAND® pipette withdraw volume 3.5 ml, catalog number: 747755; Merck, Darmstadt, Germany).
8. Hamilton syringe: 10 and 25 μl (Hamilton® TLC syringes. catalog number: Z264385 and Z264393, respectively; Merck, Darmstadt, Germany).
9. Potter-Elvehjem PTFE pestle and glass tube (catalog number: P7859; Sigma-Aldrich, San Luis, MO, United States).
10. Silica glass cuvettes (Starna Scientific Ltd., Ilford, United Kingdom).
11. 96-well white plate, polystyrene, High Bind, white flat-bottom wells, non-sterile, white (catalog number: CLS3922; Sigma-Aldrich, San Luis, MO, United States, Corning®).
12. 96-well black plate, polystyrene, flat bottom, black polystyrene, matrix active group High Bind, non-sterile (catalog number: CLS3925; Sigma-Aldrich, San Luis, MO, United States, Corning®).
13. 4-Morpholinepropanesulfonic (MOPS) acid (catalog number: M1254; CAS number: 1132-61-2; Sigma-Aldrich, San Luis, MO, United States); stored at room temperature (RT).
14. Adenosine 5′-diphosphate monopotassium salt dihydrate (ADP, catalog number: A5285, CAS number: 72696-48-1: Sigma-Aldrich, San Luis, MO, United States); stored at −20°C.
15. Adenosine 5′-triphosphate (ATP) assay mix (catalog number: FLAAM; Sigma-Aldrich, San Luis, MO, United States) stored at −20°C.
16. Amplex™ Red Reagent (catalog number: A12222; Thermo Fisher Scientific, Waltham, MA, United States) stored at −20°C.
17. Cyclosporin A (CsA, catalog number: 30024, CAS number: 59865-13-3; Sigma-Aldrich, San Luis, MO, United States) stored at −20°C.
18. Ethylene-bis(oxyethylene dinitrilo)tetraacetic acid (EGTA, catalog number: E0396, CAS number: 67-42-5; Sigma-Aldrich, San Luis, MO, United States) stored at RT.
19. Glutamic acid potassium (glutamate, catalog number: G1501, CAS number: 6382-01-0; Sigma-Aldrich, San Luis, MO, United States) stored at RT.
20. Bovine serum albumin (BSA, catalog number: A6003, CAS number: 9048-46-8; Sigma-Aldrich, San Luis, MO, United States) stored at 4°C. Critical: BSA is used to remove (bind) free fatty acids; therefore, use BSA-free fatty acids.
21. Calcium chloride dihydrate ($CaCl_2$, catalog number: C3306, CAS number: 10035-04-8; Sigma-Aldrich, San Luis, MO, United States) stored at RT.
22. Carbonyl cyanide 4-(trifluoromethoxy)phenylhydrazone (FCCP, catalog number: C2920, CAS number: 370-86-5; Sigma-Aldrich, San Luis, MO, United States) stored at 4°C.
23. L-Ascorbic acid (ascorbate, catalog number: A5960, CAS number: 50-81-7; Sigma-Aldrich, San Luis, MO, United States) stored at 4°C.
24. Magnesium chloride hexahydrate ($MgCl_2$, catalog number: M2393, CAS number: 7791-18-6; Sigma-Aldrich, San Luis, MO, United States) stored at 4°C.
25. L-(-)-Malic acid (malate, catalog number: M1000; CAS number: 97-67-6; Sigma-Aldrich, San Luis, MO, United States) stored at RT.
26. N-(2-Hydroxyethyl)piperazin-N′-(2-ethanesulfonic acid)] (HEPES, catalog number: H7006; CAS number: 75277-39-3; Sigma-Aldrich, San Luis, MO, United States) stored at RT.
27. N,N,N,N-Tetramethyl-p-phenylenediamine dihydrochloride (TMPD, catalog number: T739; Sigma-Aldrich, San Luis, MO, United States) stored at RT.
28. Potassium chloride (KCl, catalog number: P5405, CAS number: 7447-40-7; Sigma-Aldrich, San Luis, MO, United States) stored at RT.
29. Potassium dihydrogen phosphate (KH_2PO_4, catalog number: P5655, CAS number: 7778-77-0; Sigma-Aldrich, San Luis, MO, United States) stored at RT.
30. Sodium phosphate dibasic (Na_2HPO_4, catalog number: S3264, CAS number: 7558-79-4; Sigma-Aldrich, San Luis, MO, United States) stored at RT.
31. Succinic acid (succinate, catalog number: S3674, CAS number: 110-15-6; Sigma-Aldrich, San Luis, MO, United States) stored at RT.
32. Sucrose (catalog number: S7903, CAS number: 57-50-1; Sigma-Aldrich, San Luis, MO, United States) stored at RT.
33. Trizma base (Tris, catalog number: T6066, CAS number: 77-86-1; Sigma-Aldrich, San Luis, MO, United States) stored at RT.
34. Tetramethylrhodamine methyl ester perchlorate (TMRM, catalog number: T5428, CAS number: 115532-50-8; Sigma-Aldrich, San Luis, MO, United States) stored at −20°C.

Recipes

1. Isolation buffer in mmol/l: sucrose 250; HEPES 10; EGTA 1, pH 7.4. Dissolve 85.58 g of sucrose, 2.6 g of HEPES, and 0.38 g of EGTA in 800 ml of ultrapure water. Adjust pH to 7.4 using 2 mol/l Tris, and bring the solution to 1 L and store at 4°C.
2. BSA isolation buffer: Dissolve 400 mg of BSA fat-free in 50 ml isolation buffer.
3. Electrolyte solution in mmol/l: Na_2HPO_4 374; KH_2PO_4 191; KCl 139.5; NaN_3 15.38. Dissolve 2.655 g of Na_2HPO_4, 1.3 g of KH_2PO_4, and 0.52 g of KCl in 50 ml ultrapure water. Add 0.05 g of NaN_3 and a few crystals of AgCl to provide a saturated solution. Filtrate the solution and store at 4°C. Caution: NaN_3 is highly toxic.
4. Incubation buffer for respiration pyruvate/malate (IBRP/M) in mmol/l: 125 KCl; 10 MOPS; 5 $MgCl_2$; 5 KH_2PO_4;0.02 EGTA; 5 pyruvate/malate, pH 7.4. Add 6.25 ml of 1 mol/l KCl, 1 ml of 500 mmol/l MOPS, 0.1 ml of 1 mol/l $MgCl_2$, 0.25 ml of 1 mol/l KH_2PO_4, 0.1 ml of 100 mmol/l EGTA, and 1 ml of 250/250 mol/l pyruvate/malate. Adjust pH to 7.4 using 500 mmol/l Tris, and bring the solution to 50 ml using ultrapure water and filtrate it. Store at 4°C.
5. Incubation buffer for respiration succinate (IBRS) in mmol/l: 125 KCl; 10 MOPS; 5 $MgCl_2$; 5 KH_2PO_4;0.02 EGTA; 5 succinate, pH 7.4. Add 6.25 ml of 1 mol/l KCl, 1 ml of 500 mmol/l MOPS, 0.1 ml of 1 mol/l $MgCl_2$, 0.25 ml of 1 mol/l KH_2PO_4, 0.1 ml of 100 mmol/l EGTA, and 1 ml of 250 mmol/l succinate. Adjust pH to 7.4 using 0.5 mol/l Tris, and bring the solution to 50 ml using ultrapure water, and filtrate it and store at 4°C.
6. 100 mmol/l ADP: Dissolve 427 mg of ADP in 10 ml of ultrapure water. Prepare 100 µl aliquots and store at −20°C.
7. 500 mmol/l ascorbate: Dissolve 880.65 mg of ascorbic acid in 10 ml of ultrapure water. Prepare 100 µl aliquots and store at −20°C.
8. 10 mmol/l calcium chloride: Dissolve 55.49 mg of $CaCl_2$ in 50 ml of ultrapure water and store at −20°C.
9. 10 mmol/l cyclosporin A: Dissolve 12 mg of cyclosporin A in 1 ml of absolute ethanol and store at −20°C.
10. 0.1 mol/l EGTA stock solution: Dissolve 1.9 g of EGTA in 30 ml of ultrapure water. Adjust pH to 7.4 using 0.5 mol/l Tris and dilute to 50 ml. Store at 4°C.
11. 10 mmol/l FCCP stock solution: Dissolve 2.5 mg of FCCP in 1 ml of absolute ethanol. Store at −20°C. Dilute the stock solution to 5 µM by adding 5 µl of 10 mmol/l FCCP in 10 ml of absolute ethanol. Prepare 20 µl aliquots and store at −20°C.
12. 0.25 mol/l Pyruvate/0.25 mol/l malate stock solution: Dissolve 1.38 g of pyruvate and 1.68 g of malate in 30 ml of ultrapure water and adjust pH to 7.4 with 2 mol/l Tris. Dilute to 50 ml and store at 4°C.
13. 1 mol/l KCl stock solution: Dissolve 18.64 g of KCl in 250 ml of ultrapure water and store at 4°C.
14. 1 mol/l KH_2PO_4 stock solution: Dissolve 6.8 g of KH_2PO_4 in 30 ml of ultrapure water. Adjust pH to 7.4 using 0.5 mol/l Tris and dilute to 50 ml. Store at 4°C.
15. 1 mol/l $MgCl_2$ stock solution: Dissolve 4.7 g of $MgCl_2$ in 50 ml of ultrapure water and store at 4°C.
16. 0.5 mol/l MOPS stock solution: Dissolve 10.46 g of MOPS in 30 ml of ultrapure water. Adjust pH to 7.4 using 0.5 mol/l Tris and dilute to 100 ml. Store at 4°C.
17. 1 mmol/l rotenone stock solution: Dissolve 3.9 mg of rotenone in 10 ml of absolute ethanol. Dilute the stock solution to 500 µmol/l by adding 5 ml of 1 mM rotenone in 5 ml of absolute ethanol. Prepare 200-µl aliquots and store at −20°C (critical step). Rotenone is light-sensitive. The stock solution should be protected from direct light.
18. 0.25 mol/l succinate stock solution: Dissolve 2.02 g of succinate in 30 ml of ultrapure water and adjust pH to 7.4 with 2 mol/l Tris. Dilute to 50 ml and store at 4°C.
19. 150 mmol/l TMPD: Dissolve 49.3 mg of TMPD in 2 ml DMSO. Prepare 10-µl aliquots and store at −20°C.
20. 2 mol/l Tris: Dissolve 121.14 g of Tris in 500 ml of ultrapure water. Dilute to 0.5 mol/l by adding 250 ml 2 mol/l Tris in 750 ml ultrapure water and store at RT.
21. 5 mmol/l TMRM stock solution: Dissolve 5 mg of TMRM in 2 ml of DMSO. Store at −20°C.

Equipment

1. Surgery scissors (ABC *instrumentos cirúrgicos*, surgery scissors straight 12 cm, code: 321. Catalog number: 10304850053).
2. Refrigerated highest-speed centrifuge (Mikro 200R; Hettich, Tuttlingen, Germany).
3. Tissue homogenizer (T 25 Digital ULTRA-TURRAX®, catalog number: 3725000; Merck, Darmstadt, Germany).
4. Clark-type oxygen electrode and respirometer MT200A (oxygen meter, 782, MT200A; Strathkelvin, Motherwell, Scotland).
5. Spectrofluorimeter SpectraMax® M3 (SpectraMax® M3; Molecular Devices, San Jose, CA, Untied States).
6. Centrifuges and rotors: Precool centrifuges and rotors to 4°C.
7. Oxygraph chamber: Adjust the temperature of the water bath to 37°C. Calibrate the Clarke-type oxygen electrode. Procedures may vary from instrument to instrument. Follow the manual for the oxygen electrode and chamber you are using (Strathkelvin 782 2-channel Oxygen System version 1.0; Strathkelvin, Motherwell, Scotland).
8. Spectrophotometer: Adjust the temperature of the cuvette block to 37°C.

Software

1. Strathkelvin 782 2-channel Oxygen System version 1.0 (Oxygenmeter, 782; Strathkelvin, Motherwell, Scotland).
2. SoftMax® Pro Software (Molecular Devices, San Jose, CA, United States).
3. GraphPad Prism 8.4.3 (San Diego, CA, United States).

METHODS

Animals

CD-1 mice (25–30 g BW) were used. The animal study was reviewed and approved by our institutional ethics committee on the use of animals (Health Sciences Center, Federal University of Rio de Janeiro (protocol 015/17) and followed the guidelines of the Brazilian National Council for Animal Experimentation Control, Ministry of Science, Technology, and Innovation (CONCEA/MCTI), and the Guide for the Care and Use of Laboratory Animals published by the United States National Institutes of Health (8th edition, 2011).

Isolation of Mitochondria

The experimental protocol must be available after lung mitochondrial isolation, because mitochondria are viable for about 4 h only (critical step).

Collection of Tissue Samples (Timing Is 2–5 Min Per Animal)

The mice were euthanized and underwent a bilateral thoracotomy. The lungs were carefully removed *en bloc* and immediately placed in a tube containing an ice isolation buffer at 4°C (see section "Recipes") to remove excess blood.

Isolation of Mitochondria (Timing Is Approximately 40–90 Min)

The following steps are critical for the isolation of mitochondria (critical step). Mistakes during mitochondria isolation are irreversible and can spoil the running experiment. All processes must be performed on ice. Centrifugation steps at 4°C and buffers should be precooled during processing. It is important to work fast to avoid delays in tissue preparation (**Figure 1**).

a. Remove the adipose tissue and all large vessels using scissors.
b. Mince the tissue into 1–2 g fragments and transfer each one into a Teflon beaker with 10 ml BSA isolation buffer on ice.
c. Remove all remaining fat. The tissue must be thoroughly minced, since the size of the sample directly affects the subsequent homogenization step and eventually the yield of mitochondria (critical step). Ensure the removal of all fats that also affect the yield of mitochondria.
d. Split the minced tissue from one Teflon beaker into two 14-ml round-bottom tubes. The tube should not contain more than 2 ml tissue volume. Whenever necessary, use more 14-ml round-bottom tubes.
e. Wash the minced tissue samples: fill the 14-ml round-bottom tubes with 10 ml BSA isolation buffer, let the tissue sink, remove the buffer, and repeat tissue washing until the buffer is clear (the minced tissue would then contain no blood). Usually, four or five washings are enough to obtain a clean BSA isolation buffer. Hence, fill the 14-ml round-bottom tubes up to 6 ml with isolation buffer. The optimal tissue/buffer ratio is 1:3 or less. After mincing the tissue, part of it precipitates and some pieces float because of the air in the air spaces (critical step). Be careful in removing the blood during washing to avoid tissue loss.
f. Homogenize the samples with the tissue homogenizer (Ultra-Turrax) using two 10-s treatments at a shaft rotation rate of 6,500 × g each. Perform the homogenization on ice with slight movements of the centrifuge tube. Wait for 10 s between the homogenization steps to avoid heating of the homogenizer and the samples, and to avoid foaming (critical step).
g. Collect the samples and transfer them to a tissue glass Potter-Elvehjem homogenizer. Homogenize the samples, and stroke the suspension about 30–40 times. This procedure can compromise mitochondrial integrity if not done carefully (critical step). It Is recommended to precool the glassware in an ice bath 5–10 min before starting the procedure. Attention: The use of proteases, e.g., nargase, during mitochondrial isolation, commonly performed in other tissues such as the heart, ruins the whole process.
h. Centrifuge the homogenate at 700 × g for 10 min at 4°C.
i. Collect the supernatant in 2-ml microfuge tubes and discard the pellets. Centrifuge the supernatant at 12,300 × g for 10 min at 4°C.
j. Discard the supernatant and resuspend the pellet in 0.5 ml of ice-cold isolation buffer by gentle pipetting, and collect the mitochondrial suspensions in 2-ml microfuge tubes. Avoid the formation of foam during the resuspension process (critical step).
k. Centrifuge the supernatant in ice-cold isolation buffer at 10,300 × g for 10 min at 4°C.
l. Pool all the mitochondrial suspensions in one 2-ml microfuge tube and repeat the previous step.
m. Resuspend the resulting pellet in 100–200 μl isolation buffer and store it on ice. Resuspend the pellets carefully by gentle pipetting to obtain a uniform suspension without any visible clump (critical step).
n. Measure mitochondrial concentration using the Lowry or BSA method.

Pause Point

At this point, the mitochondria are ready to be used in experiments to explore their function. Use the preparation within 4 h for better functional responses. Store the mitochondrial suspension on ice.

Note: The isolated mitochondria by this protocol can be used in different oximeter equipment, and can be analyzed with different software and methodologies.

Mitochondrial Oxygen Consumption (Timing: Approximately 10–20 Min Per Measurement)

In each experiment, use 200 μg of protein per ml for good acquisition data. The oxygen consumption gives information about the electron transport chain and the oxidative phosphorylation of the mitochondria. By the addition of substrates and inhibitors, or by uncoupling oxidative phosphorylation, it is possible to modulate the rate of oxygen

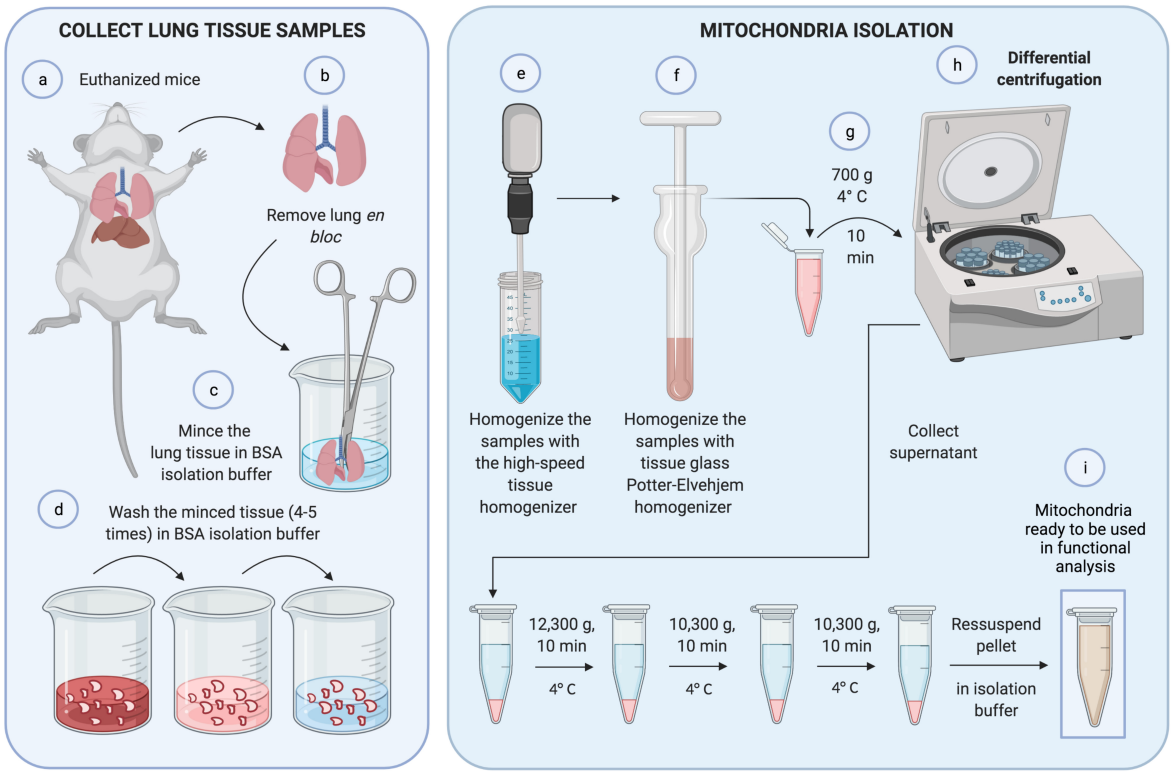

FIGURE 1 | Mitochondrial isolation. First, **(a,b)** lungs were removed *in bloc* from euthanized mice. **(c)** Lung tissue was minced with scissors and **(d)** washed with BSA isolation buffer four to five times to eliminate blood. **(e)** The sample was homogenized with a high-speed tissue homogenizer and, again, with tissue glass Potter-Elvehjem homogenizer carefully, to achieve cell disruption without compromising mitochondrial integrity **(f)**. **(g)** The homogenate was centrifuged at 700 g for 10 min at 4°C. **(h)** The pellet was discarded, and the supernatant was collected and submitted to differential centrifugation. Finally, **(i)** the resultant pellet containing mitochondria was ready to be used in functional analyses.

consumption and gain further insight into the activity of each complex of the electron transport chain.

At this point, mitochondrial complexes I (states 1, 2, and 3), II (state 3), and IV respiration with subsequent uncoupling of oxidative phosphorylation were measured in a two-chamber respirometer. With two different chambers, it is possible to measure two different experimental groups at the same time, observing results in mitochondrial function in parallel (critical step). Moreover, the respiration of complex I and complex II can be available in parallel using two different chambers.

a. Add 0.5 ml of IBRP/M buffer to the chambers. One can opt to add IBRP/M without pyruvate/malate (or 5 mmol/l glutamate/5 mmol/l malate, bypassing the critical step of pyruvate decarboxylation, which is highly dependent on NAD^+) to measure the state 1 respiration of complex I and to add IBRS plus 2 μmol/l rotenone to the other chamber to measure complex II respiration. Make sure that the magnetic stirrer moves constantly. Rotenone is sticky and inhibits complex I respiration (critical step). Therefore, we suggest washing each chamber that received rotenone with a cardiac or liver tissue homogenate to assist the removal of rotenone. Additionally, we recommend washing the chamber three times with 70° alcohol, followed by three washes with EDTA 100 mmol/l. Finally, wash 10 times with MilliQ water.
b. Equilibrate the temperature and oxygen tension of the buffer and close the chamber. Usually, 3–4 min are sufficient until the oxygen concentration in the chamber remains stable.
c. Start the recording of the oxygen concentration in the chamber. Steady-state recording without drifts is mandatory (critical step). Wait for 1–5 min to obtain a stable baseline. A maximal drift of ±10 nmol O_2/min is considered acceptable once endogenous substrates could be present in the preparation starting State 2 respiration before the addition of the exogenous substrate. Add 200 μg of mitochondrial protein using a Hamilton syringe and record for 3 min. If one chooses to add IBRP/M without pyruvate/malate, the state 1 of complex I is measured. One should add pyruvate/malate 5 μmol/l, and the oxygen concentration in the chamber will decrease because of oxygen consumption by the mitochondria, which can be referred to as state 2 complex 1 respiration. and record for 3 min (**Figure 2**).
d. Add 4 μl of 100 mmol/l ADP to obtain a final concentration of 400 μmol/l using a Hamilton syringe and record oxygen concentration for 3 min (**Figure 2**).

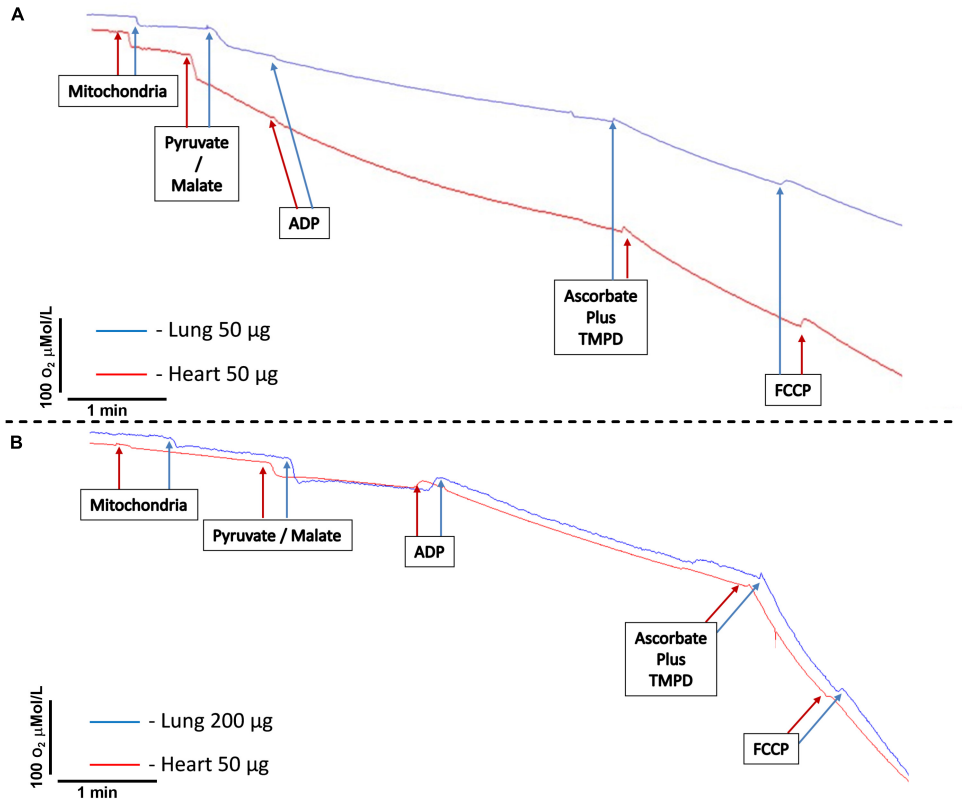

FIGURE 2 | Representative tracings of mitochondria oxygen consumption. **(A)** Comparison between isolated mitochondria loading from heart (50 µg) and lung (50 µg) tissues. **(B)** Comparison between isolated mitochondria loading from heart (50 µg) and lung (200 µg) tissues. Mitochondria represents the moment of the addition of isolated mitochondria. Pyruvate/malate represents the time of addition of pyruvate 5 µmol/L/malate 5 µmol/L. ADP signals the time to add ADP 400 µmol/L. Ascorbate 3 mmol/L plus N,N,N,N-tetramethyl-p-phenylenediamine dihydrochloride (TMPD) 300 µmol/L indicates the addition of ascorbate and TMPD. FCCP indicates the addition of carbonyl cyanide 4-(trifluoromethoxy)phenylhydrazone 30 nmol/L.

e. The decrease in oxygen concentration speeds up, caused by stimulating mitochondrial respiration with ADP (state 3). ADP-stimulated respiration should be faster than baseline respiration, reflecting good coupling of mitochondria (critical step). The respiration could slow down and return to a rate comparable to that of the baseline respiratory state, as result of the conversion of all added ADP and phosphate into ATP.
f. Add simultaneously 2 µl of 150 mmol/l TMPD and 6 µl of 500 mmol/l ascorbate to obtain final concentrations of 300 and 3 mmol/l, respectively. Record oxygen concentration for 1 min. The oxygen concentration will decrease faster than with ADP stimulation. TMPD is an electron donor to complex VI, which is readily reduced by ascorbate and oxidized by cytochrome C (**Figure 2**).
g. Add 6 µl of 5 µmol/l FCCP to obtain a final concentration of 30 nmol/l. Record oxygen concentration for 1 min. The oxygen concentration will decrease further. FCCP is an uncoupling agent, which turns the mitochondrial membrane permeable to protons and, therefore, eliminates the chemiosmotic gradient. As a result, ATP synthesis is disrupted (**Figure 2**).
h. Stop recording.
i. Calculate mitochondrial oxygen consumption using the software Analysis (Strathkelvin 782 2-channel Oxygen System version 1.0; Strathkelvin, North Lanarkshire, Scotland) or similar. Calculate baseline oxygen consumption 75 s after the addition of mitochondria. Calculate state 2 complex I oxygen consumption 75 s after the addition of pyruvate/malate. Determine ADP-stimulated respiration 30 s after the addition of ADP. Determine complex VI respiration 30 s after the addition of ascorbate/TMPD. Calculate maximal uncoupled respiration rate 30 s after the addition of FCCP.

Measurement of Adenosine 5′-Triphosphate Production (Timing: Approximately 20 Min)

In the respiration chamber, repeat all the steps up to adding 4 µl of 100 mmol/l ADP to obtain a final concentration of 400 µmol/l. Then, record the ADP-stimulated respiration

for 3 min. Thereafter, the incubation buffer containing mitochondria should be transferred to an Eppendorf tube and immediately supplemented with ATP assay mix (ATP Bioluminescence Assay Kit; Sigma-Aldrich, St. Louis, MO, United States) diluted to 1:5 (incubation buffer containing mitochondria: ATP assay mix). Mitochondrial ATP production was determined immediately after each respiration measurement and compared with ATP standards using a 96-well white plate in a spectrofluorometer (SpectraMax® M3; Molecular Devices, San Jose, CA, United States) at 560-nm emission.

Measurement of Mitochondrial ROS (Timing: Approximately 30 Min)

The Amplex Red Hydrogen Peroxide Assay (catalog number: A12222; Thermo Fisher Scientific, Waltham, MA, United States) was used to determine mitochondrial ROS concentration. Amplex Red reacts in 1:1 stoichiometry with peroxide in the presence of horseradish peroxidase (HRP) and produces highly fluorescent 95% resorufin. The incubation buffer containing mitochondria should be transferred to an Eppendorf tube and immediately supplemented with 50 μmol/l Amplex UltraRed Reagent (Thermo Fisher Scientific, Waltham, MA, United States) and 2 U/ml Pierce™ horseradish peroxidase (HRP, catalog number: 31491; Thermo Fisher Scientific, Waltham, MA, United States). The supernatant was collected after 20 min of incubation in the dark. Mitochondrial ROS concentration was determined and compared with H_2O_2 standards using a 96-well black plate and a spectrofluorometer (SpectraMax® M3; Molecular Devices, San Jose, CA, United States) at 540-nm emission and 580-nm extinction (Maciel et al., 2020).

Measurement of Mitochondrial Swelling

The integrity of the mitochondrial membrane was assessed by osmotically induced volume changes of the mitochondria and spectrophotometric determination of the apparent absorption of the suspension at 540 nm. A mitochondrial suspension (200 mg/ml) was added to the respiration medium in the absence of respiratory substrates, at 37°C, and under constant stirring. Mitochondrial swelling was stimulated with 1 μl of calcium chloride at 20 μmol/l to reach 100 nmol/l in 200 μl of mitochondrial suspension. Swelling was expressed as percentage of the absorption of the solution containing mitochondria in the presence of cyclosporin A 10 μmol/l (mitochondrial swelling = 0%) in relation to that absorbed after the addition of FCCP 1 μmol/l (mitochondrial swelling = 100%).

Measurement of Mitochondrial Transmembrane Potential ($\Delta\Psi m$)

For $\Delta\Psi m$ determination, the probe tetramethylrhodamine methyl ester (TMRM, 400 nmol/l) was added to the respiration solution containing 200 mg/ml of mitochondria and incubated for 1 h at 4°C before the experiment. $\Delta\Psi m$ was estimated by the fluorescence emitted by TMRM under 580-nm excitation. $\Delta\Psi m$ was expressed as the percentage of fluorescence emitted by TMRM-labeled mitochondria in the presence of cyclosporin A (mitochondrial despolarization = 0%), relative to that emitted after the addition of FCCP to fully depolarize the mitochondria (mitochondrial despolarization = 100%).

Electron Leakage and ATP/ROS Production Ratio

Electron leakage is the loss of the electron from the electron transport chain to form superoxide (O_2-). However, other reactive oxygen species, such as hydroperoxyl radical (HO_2) and hydrogen peroxide (H_2O_2), might occur spontaneously (e.g., pH-dependent) or under the action of antioxidant enzymes (e.g., superoxide dismutase). The site of initial leakage is often considered to be a semiquinone radical (QH) or reduced flavin (FMN and FAD) (A–B). To calculate the fraction of electrons that leaked out of the respiratory chain, the rate of H_2O_2 formation (see section E) is divided by the rate of mitochondrial O_2 consumption (see section C). H_2O_2 production and oxygen consumption rates must be expressed using the same units and correspond to the same respiratory state (C–E). The ATP/ROS reason should be measured to determine the formation of ROS linked to O_2 consumption. Thus, we were able to determine the electron leakage inherent to ROS production (Santiago et al., 2008; Murphy, 2009; Jastroch et al., 2010; Daussin et al., 2012).

Statistical Analysis

Three experimental groups were tested. The first one corresponded to isolated mitochondria from hearts with a protein load of 50 μg in each experiment. The second group consisted of isolated mitochondria from lungs with a protein load of 50 μg in each experiment. The third group contained mitochondria isolated from lungs with a protein load of 200 μg in each experiment. For graphic and statistical analysis, the software GraphPad Prism 8.4.3 (San Diego, CA, United States) was used. The significance of observed differences in mitochondrial oxygen consumption and functions was evaluated by the parametric one-Way ANOVA test followed by Tukey's multiple comparisons test. In all cases, $p < 0.05$ was considered to be significant. Experimental values are reported as mean ± standard deviation.

RESULTS

The differences between the present protocol and previous protocols are shown in **Table 1**.

Mitochondrial Respiration

Figure 3A depicts that the mitochondrial oxygen consumption by complex I under state 1 was smaller in lung mitochondria-50 μg (1.43 ± 0.39 nmol O_2/min/mg protein) than in heart mitochondria (2.68 ± 0.46 nmol O_2/min/mg protein, $p = 0.006$) and in lung mitochondria-200 μg (2.52 ± 0.45 nmol O_2/min/mg protein, $p = 0.01$), which did not differ between them ($p = 0.7$).

As shown in **Figure 3B**, the mitochondrial oxygen consumption by Complex I under state 2 is smaller in lung mitochondria-50 μg (10.79 ± 3.3 nmol O_2/min/mg protein) than in heart mitochondria (33.51 ± 4.7 nmol O_2/min/mg protein, $p = 0.001$) and in lung mitochondria-200 μg (33.78 ± 7 nmol

TABLE 1 | Differences between the present protocol and previous protocols.

Present protocol	**Spear and Lumeng, 1978**	Zhang et al. (2018)	**Gedik et al., 2017**	**Maciel et al., 2020**
BSA fat-free **0.8%**	BSA fat-free **0.5%**	BSA fat-free **2%** and computational model	BSA fat-free **0.5%**	BSA fat-free **0.1%**
Remove blood content from the tissue **without** losing large amounts of sample.	Remove blood content from the tissue losing large amounts of sample	Remove blood content from the tissue losing large amounts of sample and computational model	Remove blood content from the tissue losing large amounts of sample	Remove blood content from the tissue losing large amounts of sample
Mitochondria concentration **200 μ g/ml**	**No information**	Mitochondria concentration **1 mg/ml** computational model	Mitochondria concentration **50 μ g/ml**	Mitochondria concentration **50 μ g/ml**
No use of proteases	**No information**	Protease inhibitor cocktail Set III	Use of proteases (nargase)	Use of proteases (nargase)
Lung tissue	Lung tissue	Lung mitocôndria, and computational model	Heart tissue	Heart tissue
Enough material to grant the completion of several experiments	**No** Enough material to grant the completion of several experiments	**No** Enough material to grant the completion of several experiments, computational model	Enough material to grant the completion of several experiments	Enough material to grant the completion of several experiments
Mice	Rat, rabbits, and mice	Rat and computational model	Rat	Rat

The bold terms highlight the difference between the protocols.

O_2/min/mg protein, $p = 0.006$), which did not differ between them ($p = 0.99$).

The mitochondrial oxygen consumption by complex I under state 3 was smaller in lung mitochondria-50 μg (26.75 ± 8.2 nmol O_2/min/mg protein) than in heart mitochondria (73.83 ± 8.38 nmol O_2/min/mg protein, $p = 0.01$) and in lung mitochondria-200 μg (61.67 ± 9.1 nmol O_2/min/mg protein, $p = 0.0006$), which did not differ, $p = 0.99$, as presented in **Figure 3C**.

The mitochondrial oxygen consumption by complex II under state 3 was smaller in lung mitochondria-50 μg (35.54 ± 11 nmol O_2/min/mg protein) than in heart mitochondria-50 μg (100.5 ± 12.4 nmol O_2/min/mg protein, respectively, $p = 0.003$), and in lung mitochondria-200 μg (69.32 ± 11.3 nmol O_2/min/mg protein, $p = 0.0053$). However, the increase in oxygen consumption by lung mitochondria-200 μg did not reach the level of the heart mitochondria-50 μg ($p = 0.009$), as shown in **Figure 3D**.

Figure 3E shows that the mitochondrial oxygen consumption by complex IV was smaller in lung mitochondria-50 μg (273.3 ± 59 nmol O_2/min/mg protein) than in heart mitochondria-50 μg (419.5 ± 43 nmol O_2/min/mg protein, $p = 0.003$) and lung mitochondria-200 μg (392.1 ± 72.4 nmol O_2/min/mg protein, $p = 0.047$), which did not differ between them ($p = 0.19$). The mitochondrial oxygen consumption by maximal oxygen uptake of uncoupled mitochondria was similar in heart mitochondria-50 μg and lung mitochondria-50 μg (402.5 ± 57.5 and 369.51 ± 72.8 nmol O_2/min/mg protein, respectively, $p = 0.7$). Lung mitochondria-200 μg showed similar respiration to heart mitochondria-50 μg (393.45 ± 86.12 nmol O_2/min/mg protein, $p = 0.17$ vs. heart mitochondria-50 μg) and $p = 0.5$ vs. lung mitochondria-50 μg) (**Figure 3E**).

Mitochondrial ROS Production

Mitochondrial ROS production by lung mitochondria-50 μg (21.87 ± 9.6 nmol/loaded protein) was lower than that by heart mitochondria-50 μg (66.08 ± 12.5 nmol/loaded protein, $p = 0.003$) and lung mitochondria-200 μg (63.64 ± 12.3 nmol/loaded μg protein, $p = 0.0015$), which was similar ($p = 0.87$), as displayed in **Figure 4A**.

Mitochondrial Adenosine 5′-Triphosphate Production

Figure 4B shows that mitochondrial the ATP production by lung mitochondria-50 μg (22.92 ± 9.12 μmol ATP/loaded protein) was lower than that by heart mitochondria-50 μg (91.62 ± 5.9 μmol ATP/loaded protein, $p = 0.0001$) and lung mitochondria-200 μg (83.51 ± 9.49 μmol ATP/loaded protein, $p = 0.006$), which was similar ($p = 0.075$).

Mitochondrial Swelling

The mitochondrial swelling of lung mitochondria-50 μg (68.5 ± 19.7% maximum), heart mitochondria-50 μg (63.9 ± 13.8% maximum), and lung mitochondria-200 μg (81.84 ± 15.35% maximum) did not differ among them ($p = 0.3$), as depicted in **Figure 4C**.

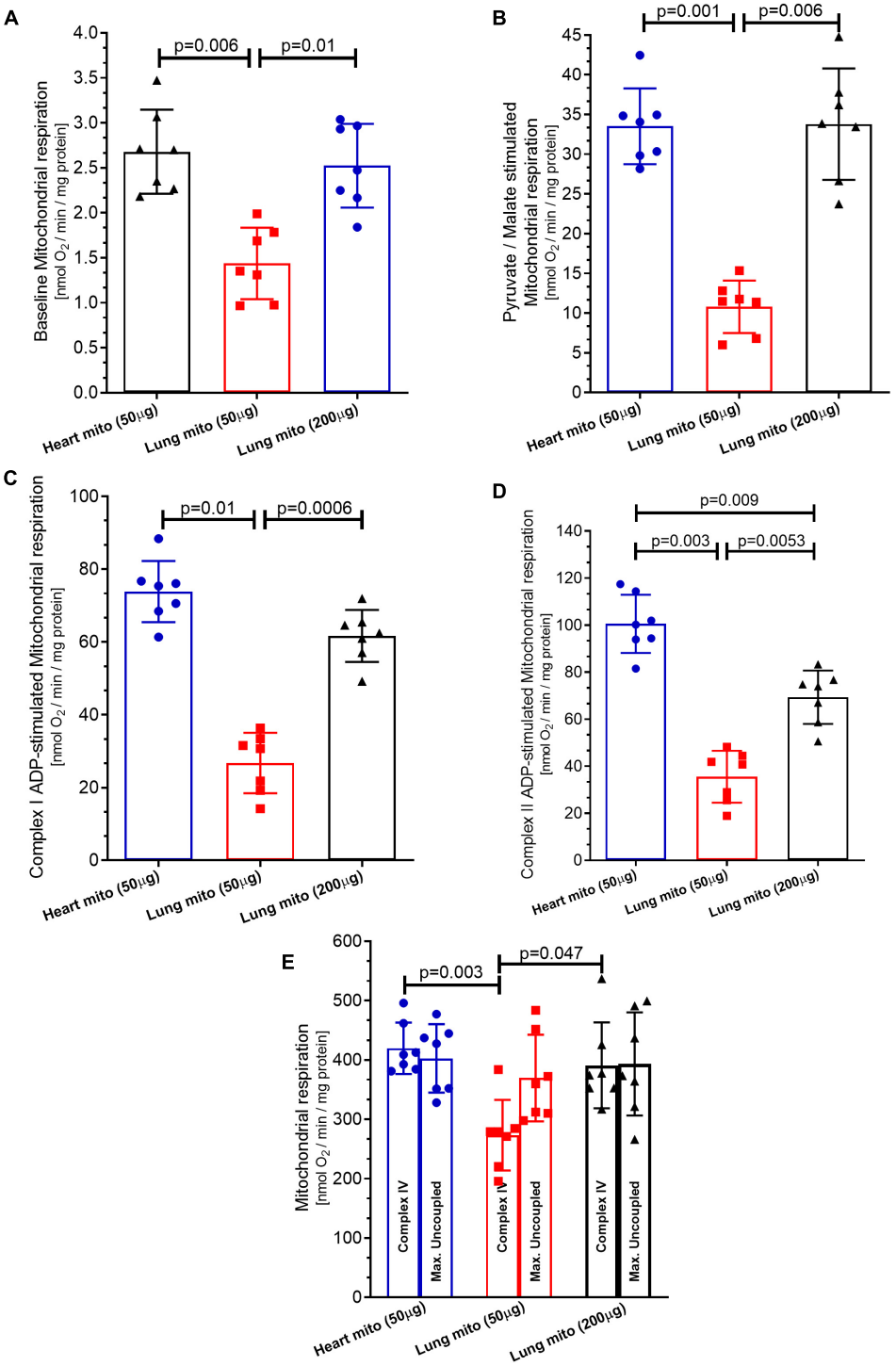

FIGURE 3 | Mitochondrial respiration. **(A)** Baseline respiration (state 1 complex 1), **(B)** pyruvate/malate stimulation (state 2 complex 1) respiration, **(C)** adenosine diphosphate (ADP) stimulation (state 3 complex 1) respiration. **(D)** Complex II respiration was stimulated with succinate and using the complex I inhibitor Rotenone. **(E)** Complex IV respiration stimulated with N,N,N,N-tetramethyl-p-phenylenediamine dihydrochloride (TMPD) and ascorbate and maximal uncoupled oxygen uptake induced by carbonyl cyanide 4-(trifluoromethoxy)phenylhydrazone (FCCP) of isolated mitochondria from mice heart and lung. Heart mito (50 µg) represents the group of isolated mitochondria from hearts. Lung mito (50 µg) indicates the group of isolated mitochondria from lungs with loading of 50 µg. Lung mito (200 µg) signals the group of isolated mitochondria from lungs with loading of 200 µg. Each symbol represents one animal. The values are reported as mean ± standard deviation. Horizontal square brackets indicate significantly different differences and the corresponding *p*-value.

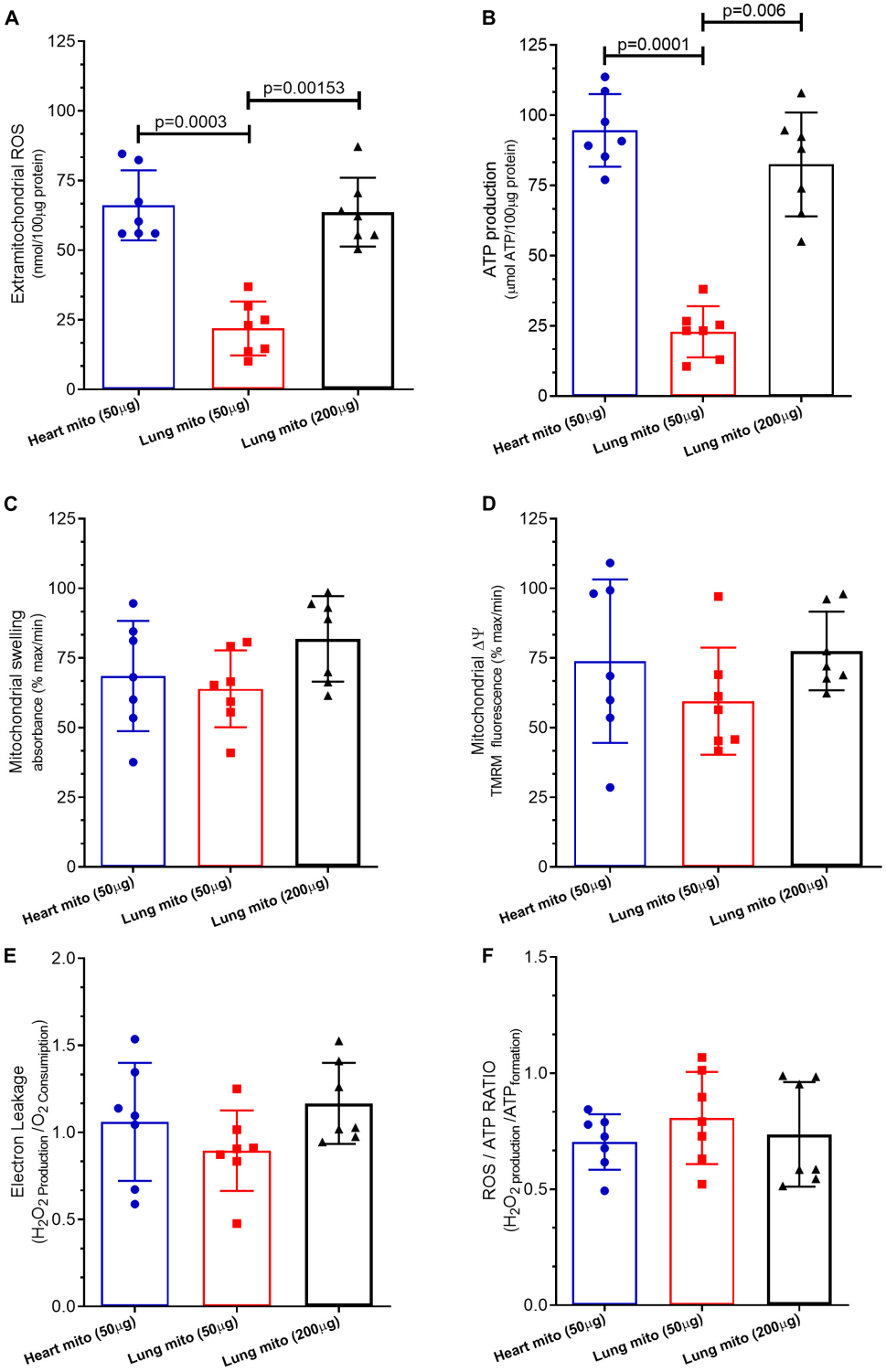

FIGURE 4 | Mitochondrial products and characteristics. **(A)** Reactive oxygen species (ROS) production, **(B)** adenosine triphosphate (ATP) production, **(C)** mitochondrial swelling, **(D)** mitochondrial transmembrane potential (m$\Delta\psi$), **(E)** electron leakage, and **(F)** ROS/ATP ratio of isolated mitochondria from mice heart and lung. Heart mito (50 µg) represents the group of isolated mitochondria from hearts. Lung mito (50 µg) indicates the group of isolated mitochondria from lungs with loading of 50 µg. Lung mito (200 µg) signals the group of isolated mitochondria from lungs with loading of 200 µg. Each symbol represents one animal. Data are expressed as mean ± standard deviation. Horizontal square brackets indicate significantly different differences and the corresponding *p*-value.

Mitochondrial $\Delta\psi$

The mitochondrial $\Delta\psi$m of lung mitochondria-50 μg (73.84 ± 29.3% maximum), heart mitochondria-50 μg (59.46 ± 19.2% maximum), and lung mitochondria-200 μg (77.51 ± 14.1% maximum) did not differ among them ($p = 0.52$) (**Figure 4D**).

Mitochondrial Proton Leakage

Figure 4E shows that the mitochondrial proton leakage by lung mitochondria-50 μg (1.04 ± 0.39 H_2O_2 production/O_2 consumption), heart mitochondria-50 μg (0.84 ± 0.31 H_2O_2 production/O_2 consumption), and lung mitochondria-200 μg (0.97 ± 0.22 H_2O_2 production/O_2 consumption) was similar ($p = 0.48$).

Mitochondrial ATP/ROS Ratio

The mitochondrial ATP/ROS ratio of lung mitochondria-50 μg (1.26 ± 0.19 H_2O_2 production/ATP formation), heart mitochondria-50 μg (1.07 ± 0.42 H_2O_2 production/ATP formation), and lung mitochondria-200 μg (1.39 ± 0.35 H_2O_2 production/ATP formation) did not differ ($p = 0.54$), as depicted in **Figure 4F**.

DISCUSSION

We used herein a new protocol with specific and detailed steps aiming to improve mitochondrial isolation from lung tissue. It was abridgedly published (Caldeira et al., 2021) but not tested against a well-documented and broadly used one (Gedik et al., 2017). This new protocol improves the acquisition of a robust and preserved sample of isolated mitochondria, allowing a range of analyses with the same sample, increasing mitochondria viability and experimental reproducibility. Here, we describe step-by-step the instructions for lung mitochondria isolation and warn for critical steps (steps of the procedure in which the researcher must be extremely careful, or attentive, with the procedure for the perfect execution of the isolation). Before our improved method, there was no consensus concerning protocols for mitochondrial isolation from the lung tissue (Zhang et al., 2018). The isolation of mitochondria from lung tissue is extremely difficult, because of the elevated fatty acid content and low load of mitochondria in pulmonary cells (Spear and Lumeng, 1978). Therefore, the isolation buffer most contain a high amount of fat-free BSA to be bound to free fatty acids. Noteworthy is that the amount of fat-free BSA used to isolate mitochondria from cardiomyocytes (Maciel et al., 2020) is half of that used to isolate mitochondria from the lung.

The integrity of the membrane in the lung-isolated mitochondria is of paramount importance (Zhang et al., 2018). Consequently, we detailed each step of our protocol very carefully. Because of lung intrinsic characteristic as an air-filled organ, there are difficulties in stages that aim to mince the tissue and remove the residual blood (Spear and Lumeng, 1978). The removal of blood (including hemoglobin) from tissue is mandatory to avoid oxygen sequestration during O_2-consumption assay. This singular lung characteristic undermines the isolation of mitochondria, resulting in low success rate and small amount of mitochondria available for putatively several functional tests (Spear and Lumeng, 1978). These issues pertaining to an air-filled highly perfused organ were overcome by our improved method. Thus, we showed that it is possible to appropriately mince the lung and remove its blood content without losing large amounts of sample.

We compared mitochondrial functional characteristics using three experimental groups. The first one (control group) comprised mitochondria isolated from the heart carrying 50 μg of protein per experiment. Heart mitochondria are isolated by means of a well-established broadly used protocol (Schulz et al., 2015; Gedik et al., 2017; Maciel et al., 2020, 2021). The second experimental group contained isolated lung mitochondria carrying 50 μg of protein per experiment, the same loading as isolated heart mitochondria. The third experimental group consisted of isolated lung mitochondria at a concentration of 200 μg of protein per experiment. Mitochondrial respiration was measured with a Clark-type electrode at 37°C during magnetic stirring and consistently demonstrated that the concentration of lung-isolated mitochondria can affect the results. An identical concentration of lung- and cardiomyocyte-isolated mitochondria (50 μg) yielded smaller oxygen consumption by lung mitochondria at baseline respiration (**Figures 2A**, **3A**), following pyruvate/malate (**Figures 2A,B**), ADP (**Figures 2A**, **3C**), and TMPD/ascorbate (**Figures 2A**, **3D**) titration. Taken together, these data strongly indicate that the loading of the lung mitochondria is not adequate using the 50 μg protein concentration. Protein dosage is an indirect measure of the concentration of mitochondria; therefore, a loading control that assesses functionality is necessary (Maciel et al., 2020). For such a purpose, the activation of mitochondrial complex IV is commonly employed as a loading control (Schulz et al., 2015; Gedik et al., 2017; Maciel et al., 2020, 2021), and we observed that the oxygen consumption in complex IV was less in isolated lung mitochondria loaded with 50 μg of protein than in the group of isolated heart mitochondria. Interestingly, heart isolated mitochondria presented similar values to those from lung isolated mitochondria loaded with 200 μg of protein (**Figures 2B**, **3**). These data could suggest that lung tissue yields fewer mitochondria, and that greater loading is required to generate data comparable to those from heart tissue mitochondria. However, we cannot exclude the possibility that cardiac mitochondrion may have higher metabolism than lung mitochondria (Zhang et al., 2018; Spear and Lumeng; 1978). On the other hand, our FCCP-induced uncoupled respiration did not differ between all groups, suggesting that the mitochondria groups appear to have similar viability and behavior (Schulz et al., 2015; Gedik et al., 2017; Maciel et al., 2020, 2021). Indeed, 200 μg of protein per experiment is an acceptable amount, and our samples of isolated mitochondria had enough material to grant the completion of several experiments. Other techniques to analyze mitochondrial function, such as ATP production (**Figure 4A**) and ROS formation (**Figure 4B**), display the same trend. On the other hand, mitochondrial swelling (**Figure 4C**), mitochondrial transmembrane potential (**Figure 4D**), electron leakage (**Figure 4E**), and ROS/ATP ratio (**Figure 4F**) did not show a significant difference among the three groups, perhaps

because mitochondrial swelling is analyzed by light scattering in the assay (Chapa-Dubocq et al., 2018). Mitochondrial transmembrane potential is analyzed by the stimulation of a fluorophore (Creed and McKenzie, 2019); and electron leakage and ROS/ATP ratio are calculated from existing data that were not challenged by experimental maneuvers (Santiago et al., 2008; Murphy, 2009; Jastroch et al., 2010; Daussin et al., 2012).

Limitations

The lung is an extremely complex organ with regard to the heterogeneity of cells. Our method does not contemplate analyzing all 40 subtypes of cells found in the lung. However, this heterogeneity is an intrinsic part of the lung, and all methods of mitochondria isolation, for most diverse tissues, contemplate entire organ isolation, because different cells form a syncytium for the organ to work, e.g., the heart (Gedik et al., 2017), kidney (Schulz et al., 2015), liver (Goudarzi et al., 2018), adipose tissue (Matta et al., 2021), and brain (Marques Neto et al., 2020).

CONCLUSION

Based on the method briefly described by Caldeira et al. (2021), we developed an optimized and successful technique for the isolation of mitochondria from lung tissue. We extensively described the technical difficulties concerning tissue quantity, tissue characteristics, tissue adjunct components, time of isolation, and the use of proteinases. Additionally, we described the experimental determination of several mitochondrial functional characteristics, providing information that might improve the reproducibility and analysis of lung tissue mitochondria. Ultimately, the method yielded a robust, maintained, and viable sample of pulmonary mitochondria.

DATA AVAILABILITY STATEMENT

The raw data supporting the conclusions of this article will be made available by the authors, without undue reservation.

ETHICS STATEMENT

The animal study was reviewed and approved by the UFRJ–local Institutional Animal Care and Use Committee (015/17). Written informed consent was obtained from the owners for the participation of their animals in this study.

AUTHOR CONTRIBUTIONS

LM, WZ, and JN: conception and design, data acquisition, analysis and interpretation of data, drafting or revising the article, and contribution with reagents. DC, DO, and JC-d-A: data acquisition, and analysis and interpretation of data. LM was the principal investigator. All the authors discussed the results, commented on the manuscript, and approved the final version of the manuscript.

FUNDING

This study was supported by the Brazilian Council for Scientific and Technological Development (CNPq, grants 302702/2017-2) and the Carlos Chagas Filho Rio de Janeiro State Research Supporting Foundation (FAPERJ, grants E-26/202.785/2017 and E26/010.002585/2019). The funding sources had no involvement in study design; collection, analysis, and interpretation of data; writing of the report; and decision to submit the article for publication.

REFERENCES

Caldeira, D., Mesquita, F. M., Pinheiro, F. G., Oliveira, D. F., Oliveira, L., Nascimento, J., et al. (2021). Acute exposure to C60 fullerene damages pulmonary mitochondrial function and mechanics. *Nanotoxicology* 15, 352–365. doi: 10.1080/17435390.2020.1863498

Chapa-Dubocq, X., Makarov, V., and Javadov, S. (2018). Simple kinetic model of mitochondrial swelling in cardiac cells. *J. Cell. Physiol.* 233, 5310–5321. doi: 10.1002/jcp.26335

Creed, S., and McKenzie, M. (2019). Measurement of mitochondrial membrane potential with the fluorescent dye tetramethylrhodamine methyl ester (TMRM). *Methods Mol. Biol.* 1928, 69–76. doi: 10.1007/978-1-4939-9027-6_5

Daussin, F. N., Rasseneur, L., Bouitbir, J., Charles, A. L., Dufour, S. P., Geny, B., et al. (2012). Different timing of changes in mitochondrial functions following endurance training. *Med. Sci. Sports Exerc.* 44, 217–224. doi: 10.1249/mss.0b013e31822b0bd4

Gedik, N., Maciel, L., Schulte, C., Skyschally, A., Heusch, G., and Kleinbongard, P. (2017). Cardiomyocyte mitochondria as targets of humoral factors released by remote ischemic preconditioning. *Arch. Med. Sci.* 13, 448–458. doi: 10.5114/aoms.2016.61789

Goudarzi, M., Kalantari, H., and Rezaei, M. (2018). Glyoxal toxicity in isolated rat liver mitochondria. *Hum. Exp. Toxicol.* 37, 532–539. doi: 10.1177/0960327117715900

Jastroch, M., Divakaruni, A. S., Mookerjee, S., Treberg, J. R., and Brand, M. D. (2010). Mitochondrial proton and electron leaks. *Essays Biochem.* 47, 53–67. doi: 10.1042/bse0470053

Kuznetsov, A. V., Veksler, V., Gellerich, F. N., Saks, V., Margreiter, R., and Kunz, W. S. (2008). Analysis of mitochondrial function in situ in permeabilized muscle fibers, tissues and cells. *Nat. Protoc.* 3, 965–976. doi: 10.1038/nprot.2008.61

Lanza, I. R., and Sreekumaran Nair, K. (2009). Functional assessment of isolated mitochondria in vitro. *Methods Enzymol.* 457, 349–372. doi: 10.1016/s0076-6879(09)05020-4

Maciel, L., de Oliveira, D. F., Mesquita, F., Souza, H., Oliveira, L., Christie, M., et al. (2021). New cardiomyokine reduces myocardial ischemia/reperfusion injury by PI3K-AKT pathway via a putative KDEL-receptor binding. *J. Am. Heart Assoc.* 10:e019685. doi: 10.1161/JAHA.120.019685

Maciel, L., de Oliveira, D. F., Monnerat, G., Campos de Carvalho, A. C., and Nascimento, J. (2020). Exogenous 10 kDa-heat shock protein preserves mitochondrial function after hypoxia/reoxygenation. *Front. Pharmacol.* 11:545. doi: 10.3389/fphar.2020.00545

Marques Neto, S. R., Castiglione, R. C., da Silva, T., Paes, L., Pontes, A., Oliveira, D. F., et al. (2020). Effects of high intensity interval training on neuro-cardiovascular dynamic changes and mitochondrial dysfunction induced by high-fat diet in rats. *PLoS One* 15:e0240060. doi: 10.1371/journal.pone.0240060

Matta, L., Fonseca, T. S., Faria, C. C., Lima-Junior, N. C., De Oliveira, D. F., Maciel, L., et al. (2021). The effect of acute aerobic exercise on redox homeostasis and mitochondrial function of rat white adipose tissue. *Oxid. Med. Cell. Longev.* 2021:4593496. doi: 10.1155/2021/4593496

Meyer, J. N., Leuthner, T. C., and Luz, A. L. (2017). Mitochondrial fusion, fission, and mitochondrial toxicity. *Toxicology* 391, 42–53. doi: 10.1016/j.tox.2017.07.019

Murphy, M. P. (2009). How mitochondria produce reactive oxygen species. *Biochem. J.* 417, 1–13. doi: 10.1042/bj20081386

Murphy, M. P., and Hartley, R. C. (2018). Mitochondria as a therapeutic target for common pathologies. *Nat. Rev. Drug Discov.* 17, 865–886.

Perry, C. G., Kane, D. A., Lanza, I. R., and Neufer, P. D. (2013). Methods for assessing mitochondrial function in diabetes. *Diabetes Metab. Res. Rev.* 62, 1041–1053. doi: 10.2337/db12-1219

Picard, M., Taivassalo, T., Gouspillou, G., and Hepple, R. T. (2011). Mitochondria: isolation, structure and function. *J. Physiol.* 589, 4413–4421. doi: 10.1113/jphysiol.2011.212712

Santiago, A. P., Chaves, E. A., Oliveira, M. F., and Galina, A. (2008). Reactive oxygen species generation is modulated by mitochondrial kinases: correlation with mitochondrial antioxidant peroxidases in rat tissues. *Biochimie* 90, 1566–1577. doi: 10.1016/j.biochi.2008.06.013

Schulz, S., Lichtmannegger, J., Schmitt, S., Leitzinger, C., Eberhagen, C., Einer, C., et al. (2015). A protocol for the parallel isolation of intact mitochondria from rat liver, kidney, heart, and brain. *Methods Mol. Biol.* 1295, 75–86. doi: 10.1007/978-1-4939-2550-6_7

Spear, R. K., and Lumeng, L. (1978). A method for isolating lung mitochondria from rabbits, rats, and mice with improved respiratory characteristics. *Anal. Biochem.* 90, 211–219. doi: 10.1016/0003-2697(78)90025-8

Weissig, V. (2005). Targeted drug delivery to mammalian mitochondria in living cells. *Expert Opin. Drug Deliv.* 2, 89–102. doi: 10.1517/17425247.2.1.89

Zhang, X., Dash, R. K., Jacobs, E. R., Camara, A. K. S., Clough, A. V., and Audi, S. H. (2018). Integrated computational model of the bioenergetics of isolated lung mitochondria. *PLoS One* 13:e0197921. doi: 10.1371/journal.pone.0197921

Conflict of Interest: The authors declare that the research was conducted in the absence of any commercial or financial relationships that could be construed as a potential conflict of interest.

Publisher's Note: All claims expressed in this article are solely those of the authors and do not necessarily represent those of their affiliated organizations, or those of the publisher, the editors and the reviewers. Any product that may be evaluated in this article, or claim that may be made by its manufacturer, is not guaranteed or endorsed by the publisher.

frontiers in Physiology

ORIGINAL RESEARCH
published: 08 December 2021
doi: 10.3389/fphys.2021.755468

Three-Dimensional Whole-Organ Characterization of the Regional Alveolar Morphology in Normal Murine Lungs

*Mauricio A. Sarabia-Vallejos[1], Pedro Ayala-Jeria[2] and Daniel E. Hurtado[3,4,5]**

[1] Faculty of Engineering and Technology, Universidad San Sebastián, Santiago, Chile, [2] Department of Respiratory Diseases, School of Medicine, Center of Medical Research, Pontificia Universidad Católica de Chile, Santiago, Chile, [3] Department of Structural and Geotechnical Engineering, School of Engineering, Pontificia Universidad Católica de Chile, Santiago, Chile, [4] Schools of Engineering, Medicine and Biological Sciences, Institute for Biological and Medical Engineering, Pontificia Universidad Católica de Chile, Santiago, Chile, [5] Millennium Nucleus for Cardiovascular Magnetic Resonance, Santiago, Chile

Alveolar architecture plays a fundamental role in the processes of ventilation and perfusion in the lung. Alterations in the alveolar surface area and alveolar cavity volume constitute the pathophysiological basis of chronic respiratory diseases such as pulmonary emphysema. Previous studies based on micro-computed tomography (micro-CT) of lung samples have allowed the geometrical study of acinar units. However, our current knowledge is based on the study of a few tissue samples in random locations of the lung that do not give an account of the spatial distributions of the alveolar architecture in the whole lung. In this work, we combine micro-CT imaging and computational geometry algorithms to study the regional distribution of key morphological parameters throughout the whole lung. To this end, 3D whole-lung images of Sprague–Dawley rats are acquired using high-resolution micro-CT imaging and analyzed to estimate porosity, alveolar surface density, and surface-to-volume ratio. We assess the effect of current gold-standard dehydration methods in the preparation of lung samples and propose a fixation protocol that includes the application of a methanol-PBS solution before dehydration. Our results show that regional porosity, alveolar surface density, and surface-to-volume ratio have a uniform distribution in normal lungs, which do not seem to be affected by gravitational effects. We further show that sample fixation based on ethanol baths for dehydration introduces shrinking and affects the acinar architecture in the subpleural regions. In contrast, preparations based on the proposed dehydration protocol effectively preserve the alveolar morphology.

Keywords: alveolar morphology, pulmonary porosity, alveolar surface density, surface-to-volume ratio, tissue dehydration methods

OPEN ACCESS

Edited by:
Mona Eskandari, University of California, Riverside, United States

Reviewed by:
Norihiro Shinozuka, Chibaken Saiseikai Narashino Hospital, Japan
Steven Mink, University of Manitoba, Canada

****Correspondence:***
Daniel E. Hurtado
dhurtado@ing.puc.cl

Specialty section:
This article was submitted to Respiratory Physiology, a section of the journal Frontiers in Physiology

Received: *08 August 2021*
Accepted: *15 November 2021*
Published: *08 December 2021*

Citation:
Sarabia-Vallejos MA, Ayala-Jeria P and Hurtado DE (2021) Three-Dimensional Whole-Organ Characterization of the Regional Alveolar Morphology in Normal Murine Lungs. Front. Physiol. 12:755468. doi: 10.3389/fphys.2021.755468

INTRODUCTION

Ventilation and perfusion are vital processes to facilitate gas exchange at the alveolar level, which is the primary function of the respiratory system. Pulmonary ventilation is defined as the process where air enters and leaves the alveolar units, which supplies with O_2 to the alveolus and removes the expired CO_2. Perfusion refers to the blood flow in the capillaries that surround the alveolar

surface, which is fundamental for gas transport. The relationship between both processes is one of the cornerstones of respiratory physiology, as it not only allows us to understand the mechanisms underlying respiration but also explains the genesis and evolution of diseases such as hypoxemia and pulmonary emphysema, among others (Bajc and Jonson, 2011; Jögi et al., 2011).

Ventilation and perfusion have long been associated with the alveolar architecture, constituting another clear example of the celebrated structure-function paradigm in physiology. To maximize gas exchange between alveoli and capillaries, the mammalian lung takes on a highly porous structure that maximizes the perfused alveolar surface and, at the same time, maximizes the alveolar airspace volume (Hsia et al., 2016). Alterations in the balance between the alveolar surface and the alveolar airspace constitute the pathophysiological basis of chronic respiratory diseases such as pulmonary emphysema. In emphysematous lungs, the rupture of alveolar walls results in a marked decrease in the alveolar surface available for perfusion and gas exchange and in the loss of alveolar tissue recoil, ultimately deteriorating the respiratory function (Suga et al., 2010). This highlights the importance of characterizing the morphology of the alveolar tissue in the lung and elucidates how it influences lung function and pulmonary performance (Weibel, 2017).

From a morphological point of view, alveolar ventilation is associated with porosity, defined as the ratio between the volume of the alveolar cavity (airspace volume) divided by the nominal (reference) volume of lung tissue. Similarly, perfusion can be associated with alveolar surface density, defined as the ratio between the alveolar surface area over the nominal volume of lung tissue (Hsia et al., 2016). It is important to note that both definitions are independent of each other, as the alveolar cavity volume and surface are not necessarily related. Given its close relationship with the gas exchange process, the study of the spatial distribution of morphological parameters such as porosity and alveolar surface density provides a quantitative evaluation that can be related to ventilation and perfusion with regional resolution (Soldati et al., 2014; Clark et al., 2019).

To date, the characterization of alveolar morphology has been difficult due to its micrometric size and intricate architecture. Advances in micro-computed tomography (micro-CT) techniques have allowed the study of the shape and structure of pulmonary acini with high resolution and less destructively than traditional histological methods (Langheinrich et al., 2004; Vasilescu et al., 2012b). Besides, micro-CT has enabled the three-dimensional visualization of the acinar structure with high accuracy, which motivated a volumetric characterization of alveoli (Litzlbauer et al., 2006). Current morphometric studies of the lung tissue have analyzed the acinar morphology in terms of alveolar volume, alveolar diameter, surface-to-volume ratio, and porosity, among other parameters (Parameswaran et al., 2009; Vasilescu et al., 2012a; Concha et al., 2018; Sarabia-Vallejos et al., 2019). In particular, porosity and alveolar surface density emerge as insightful parameters in the study of diseases such as pulmonary emphysema (Yuan et al., 2010), as they quantify the evolution of abnormally large airspaces produced by alveolar enlargement. In effect, septum rupture in emphysema results in higher porosity and lower density of the surface area than those found in normal lungs, which directly affects the ventilation–perfusion ratio, making it challenging to exchange gases with the bloodstream (Parameswaran et al., 2009).

While morphometric studies reported in the literature have provided vital information about the structural parameters of the lung parenchyma, current knowledge is based on a small number of micrometric samples that are randomly located in the lung. Such localized information does not provide information on the spatial distribution of alveolar structural properties throughout the organ (Hsia et al., 2010). Based on this limitation, the scientific question that guides our work is: How is the regional distribution of morphological parameters in the whole lung? To answer this question, in this work, we combine micro-CT image acquisition, advanced image processing techniques, and computational geometry methods to unveil the three-dimensional spatial distribution of porosity, alveolar surface density, and surface-to-volume ratio in normal rat lungs. We also assess the effect of current gold-standard dehydration methods in the preparation of lung samples and their impact on related morphological parameters and propose a novel fixation protocol that considers the application of a methanol-PBS solution before hydration.

MATERIALS AND METHODS

The bioethics committee of the Pontificia Universidad Católica de Chile approved the following protocol. Nine adult Sprague–Dawley rats (∼300 g, sex-matched) were randomly assigned to three experimental groups according to the fixation method (see below, each group with $N = 3$). Subjects were kept under controlled humidity, light, and temperature conditions before the lung *in situ* fixation step. Food and water were provided *ad libitum* during this period.

Lung Sample Preparation

The preparation of lung samples consisted of three subsequent steps: *in situ* fixation of the lung, *ex vivo* fixation of the lung, and dehydration of the lung sample. For the *in situ* fixation stage of the lung, we followed the protocol described by Hausmann (2007). Subjects were anesthetized with an intraperitoneal injection of ketamine and xylazine (30 mg^{-1} kg^{-1}, Drag Pharma Invetec S.A., Santiago, Chile, and 5 mg^{-1} kg^{-1}, Alfasan, Woerden, Holland, respectively). A cannula with a three-way in-line valve was introduced through the trachea of each subject in the supine position and was subsequently sealed using a cuff to instill into the lungs a formalin phosphate-buffered saline (F-PBS) solution at 4%. During the installation process, the pressure across the respiratory system was maintained at 20 cm H_2O for 30 min using a syringe with a pressure transducer (AG Cuffil, Hospitech Respiration Ltd., Kfar Saba, Israel). Then, the three-way valve was closed to maintain pressure in the lungs, and the animal was refrigerated at 4°C for 8 h.

For the *ex vivo* lung fixation step, subjects were removed from the refrigerator, after which a median sternotomy was performed to remove the lungs out of the rib cage. During the whole surgery,

care was exercised to avoid puncturing the organ, preventing leakage of the fixative solution. The left lung was dissected with the left bronchus clamped and then immersed into an F-PBS bath for 24 h. Only the left lung was further considered for analysis due to the sample size restrictions imposed by the micro-CT platform.

For the dehydration step, three different drying methods were assessed, which define the three experimental groups in this study. The drying methods were:

- Standard alcohol fixation (SAF): This method is the gold standard in histology and pathology (Hausmann, 2007; Braber et al., 2010). The sample was immersed for periods of 2 h in subsequent baths with increasing ethanol graduations (70, 80, and 90% ethanol in PBS), and finally in a 100% ethanol bath for 12 h. After this, the lung was removed from the last bath and left on a semi-covered plastic container to let it dry under ambient conditions for 3 h, to eliminate the remaining ethanol by evaporation.
- Modified alcohol fixation (MAF): Our research group designed this method as an alternative to the SAF method. First, the sample was immersed for 2 h in a 70% methanol-PBS solution, which is the main difference between SAF and MAF. Subsequently, the same steps described in the SAF fixation method were performed. It is important to remark that the action of methanol is different than ethanol. While ethanol only removes water from the tissue, methanol increases cellular permeability, thus allowing an enhanced alcohol diffusion during the posterior dehydration step.
- Standard alcohol fixation and HMDS (SAF-HMDS): This fixation method is recommended by the micro-CT manufacturer (Bruker-MicroCT, 2016). The sample was treated following the protocol in the SAF method. As a final and additional step, the sample was immersed in a hexamethyldisilazane solution (HMDS) for 2 h, after which the sample was allowed to dry under ambient conditions on a semi-covered plastic container for 3 h.

To characterize the volumetric change associated with the drying methods, the displaced volume of fluid was measured for each subject at the end of the dehydration stage and at the beginning of the *ex vivo* fixation stage. From these volumes, the lung volume ratio was calculated for each subject. Volume ratio values below 100% imply that the fixation and dehydration process resulted in sample shrinking.

Micro-Computed Tomography Scanning Protocol and 3D Image Reconstruction

All lung samples obtained were scanned using a commercial micro-CT (SkyScan 1272, Bruker Inc., Kontich, Belgium). During imaging, the samples were placed on the sample plate with the axial axis of the lung vertically aligned. The voltage and current of the X-ray source were set at 10 kV and 250 μA, respectively. Pulmonary tomographic images were obtained using two voxel resolutions: isotropic 15 μm (low resolution) and isotropic 4 μm (high resolution). The first low-resolution acquisition was used as a scout scan to confirm that the sample fixation step did not introduce errors such as regions with marked alveolar collapse. The second high-resolution acquisition was used to generate images with an accurate definition of the alveolar architecture. Images were reconstructed using NRecon software (Bruker Inc., Kontich, Belgium) where misalignment compensation, ring artifact reduction, hardening, and Kuwahara filters were used to improve the signal-to-noise ratio. The acquired images were processed using median and Wiener filters to reduce the inherent noise, as well as a mix of top-hat and bottom-hat filters and histogram equalization to improve contrast, which delivered 3D grayscale images of the lung. For the morphological quantification of the images, grayscale images were segmented using a threshold filter on the Hounsfield unit scale based on the Otsu method (Xu et al., 2011) to obtain 3D binary images of the alveolar microstructure (see **Figure 1**). The intensity value in a voxel of the binary image was set equal to 1 if the voxel corresponded to tissue, or to 0 if the voxel corresponded to air.

Three-dimensional cubic domains of representative volume elements (RVE) with a border size of ∼500 μm were selected from the enhanced images of the lung. During the selection procedure, acinar regions were targeted, and zones with large portions of bronchi or blood vessels were avoided. For each experimental group, 9 RVEs were selected per subject (3 in each region of the lung; basal, mid, and apical), resulting in a population of 27 RVEs per group. RVE images were then segmented to obtain binary masks, which were the basis for the morphological analysis.

Morphological Analysis, and Construction of 3D Porosity and Alveolar Surface Density Maps

The following morphological parameters were calculated for each RVE analyzed in this study: surface-to-volume ratio, mean alveolar diameter, alveolar wall thickness, porosity, and alveolar surface density. Parameter quantification was carried out using an in-house code written in Matlab (MathWorks, Version R2017a, Natick, MA, United States). The determination of the alveolar diameter was performed using the Sphere-fit method (Lesouple et al., 2021), which fits spheres within a point cloud using a least-squares algorithm. From the spheres obtained, an active contour algorithm was used to determine the surface and volume of the alveolar cavity (Strzelecki et al., 2013; Aganj et al., 2018). The ratio between these values allowed us to determine the surface-to-volume ratio for each alveolar cavity. The thickness of the alveolar wall was obtained by subtracting the alveolar radius of two contiguous spheres and the separation between the centers of these spheres. For each RVE, the global porosity was computed as the ratio between the volume of the alveolar cavities and the total RVE volume (reference volume).

Three-dimensional porosity maps were computed following the workflow sketched in **Figure 1**. Using binary images as a starting point, we constructed a moving 3D mask centered around each voxel of the lung image. The value of voxels inside the mask was set equal to 1, while voxels outside the mask were set equal to 0. For each lung image voxel, the associated mask was convoluted with the binary image to obtain the mask tissue volume, measured as the total number of non-zero voxels

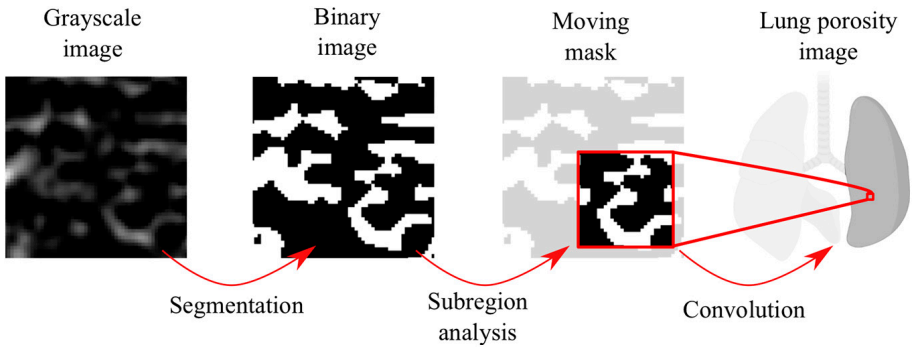

FIGURE 1 | Workflow for the construction of alveolar porosity maps.

inside the mask. The mask airspace volume was computed as the difference between the total mask volume and the mask tissue volume. Finally, the porosity associated to one voxel in the lung image was determined as the ratio of mask airspace volume over the mask total volume. The final voxel porosity took values between 0 and 1, where 0 corresponded to a region only composed by airspace and 1 corresponded to a region only occupied by tissue with no gas. To assess the dependence on the choice of the mask size, we considered the results for five different mask sizes (140, 105, 70, 35, and 17.5 μm) when computing the porosity maps for the same segmented image. The resulting porosity maps were used to construct frequency histograms, which were then represented using kernel density estimation techniques to enable a direct comparison between all mask size cases.

Three-dimensional maps of alveolar surface-density maps were computed based on the workflow sketched in **Figure 2**. Using binary images as the starting point, the boundaries between alveolar tissue and airspace were detected using the Canny method for edge detection (Canny, 1986). To improve the boundary accuracy, the Marching Cubes algorithm (Zhao et al., 2018) was applied to obtain a smooth representation of the tissue-airspace boundary. To compute the surface area of the tissue-airspace boundary, we employed a level-set segmentation method (Vasilescu et al., 2012a; Magee et al., 2013) implemented in Matlab (Li et al., 2011). Finally, for each voxel in the lung image, the tissue-airspace surface area inside the moving mask around the voxel was obtained by convoluting the mask image with the smoothed boundary image, from which the surface density was obtained as the total surface area inside the mask divided by the volume of the mask. To assess the dependence of alveolar surface-density maps on the choice of the mask size, a sensitivity analysis similar to the one described for the case of porosity was carried out using the same mask size range.

Surface-to-volume ratio maps were constructed using the information from alveolar surface-density and porosity maps. For this purpose, let A_{alv}, $V_{airspace}$, and V_{ref} be the alveolar surface area, the alveolar airspace volume, and the reference volume of the cubic sample to be analyzed (RVE or moving mask), respectively. The surface-to-volume ratio (ρ) is then defined as the ratio of the alveolar surface area over the airspace enclosed by this surface, i.e.,

$$\rho = \frac{A_{alv}}{V_{airspace}}. \tag{1}$$

Considering a reference cubic region whose volume is V_{ref}, the alveolar surface area inside the reference volume can be estimated from the alveolar surface density (η) as

$$A_{alv} = \eta \cdot V_{ref}, \tag{2}$$

and the alveolar airspace volume for the same reference volume can be obtained from the porosity value (ϕ) as

$$V_{airspace} = \phi \cdot V_{ref}. \tag{3}$$

Substituting Eqs 2, 3 into the definition of surface-to-volume ratio described in (1), we obtain the relation

$$\rho = \frac{\eta}{\phi}. \tag{4}$$

Using Eq. 4, surface-to-volume ratio maps can be constructed from the porosity and the alveolar surface-density maps in a voxel-wise way. Eq. 4 can also be used to estimate the surface-to-volume ratio in the RVEs considered in the analysis.

To assess the regional distribution of alveolar porosity, alveolar surface density, and surface-to-volume ratio, regions of interest (ROI) were defined along the ventral-dorsal direction of each subject, following a method similar to that used in the regional characterization of lung deformation (Cruces et al., 2019; Hurtado et al., 2020). The regions of interest are connected sets of voxels selected from advancing planes in the selected direction, to achieve 10 contiguous regions with the same volume. The regional value of porosity and alveolar surface density is obtained as the average of the values contained in each ROI.

Statistical Analysis

To detect significant differences in the morphological parameters between the study groups, nine RVE samples were selected per subject from randomly chosen sectors of the lung, which generates a total of 27 RVE samples per group. The comparison between groups was performed using the Mann–Whitney

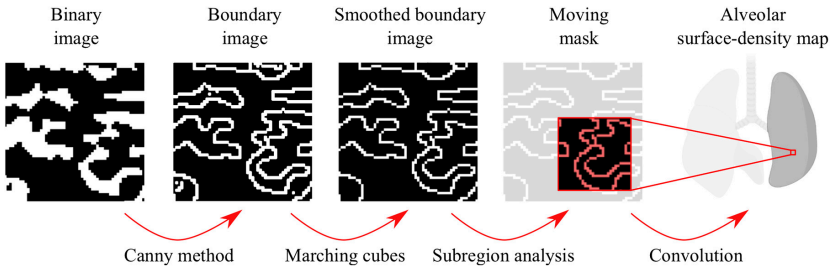

FIGURE 2 | Workflow for the construction of alveolar surface-density maps.

TABLE 1 | Alveolar morphological parameters for the representative volume elements (RVE) samples.

Group	Surface-to-volume ratio (mm^{-1})	Mean alveolar diameter (μm)	Alveolar wall thickness (μm)	Porosity	Alveolar surface density (μm^{-1})	Lung volume ratio (%)
SAF (n = 27)	89.5 ± 10.9*†	29.48 ± 3.96*†	6.92 ± 0.86	0.51 ± 0.05*†	44.31 ± 1.91	56 ± 12*†
MAF (n = 27)	67.7 ± 8.8*	40.51 ± 4.82*#	7.09 ± 1.08	0.65 ± 0.05*	42.05 ± 0.72	87 ± 3*
SAF-HMDS (n = 27)	61.6 ± 5.5†	54.68 ± 5.18#†	7.02 ± 0.45	0.65 ± 0.03†	40.83 ± 1.53	92 ± 2†

*Statistical significance between SAF and MAF methods (p-value ≤ 0.05).
#Statistical significance between MAF and SAF-HMDS methods (p-value ≤ 0.05).
†Statistical significance between SAF and SAF-HMDS methods (p-value ≤ 0.05).

two-sided U test, considering a p-value of 0.05 corrected by the Bonferroni method to allow the comparison between multiple groups.

For the inter-group comparison of regional values of porosity and alveolar surface density, three sections were selected per anatomical region (apical, mid, or basal) in each subject, which gives a total of nine samples for each ROI per group. The comparison between the same ROI in different groups was carried out using the Mann-Whitney two-sided U test, considering a p-value of 0.05 corrected by the Bonferroni method to allow the comparison of multiple groups. The error bars in figures show the standard deviation. The variability of porosity and alveolar surface density between different anatomical sections in a single lung was assessed using the analysis of variance (ANOVA) test for each of the subjects in the experimental groups studied (SAF, MAF, and SAF-HMDS), after confirming normality of the samples considered using the D'Agostino and Pearson test.

RESULTS

Values for the surface-to-volume ratio, mean alveolar diameter, alveolar wall thickness, porosity, alveolar surface density, and lung volume ratio are reported in **Table 1**. The SAF group was significantly different than the MAF and SAF-HMDS groups for the surface-to-volume ratio, mean alveolar diameter, porosity, and lung volume ratio. Further, the mean alveolar diameter of the SAF-HMDS group resulted in significant differences when compared to the SAF and MAF groups. No significant differences were detected between the three groups for the case of the alveolar wall thickness and the alveolar surface density.

Figure 3 shows the results from 3D micro-CT imaging processing and the spatial morphological analysis for the whole lung of a representative subject in the SAF-HMDS group. Micro-CT images of the whole lung displayed major airway and vasculature structures at the macroscopic level, as well as delivered detailed information of bronchioli, respiratory ducts, and acinar structures (see **Figure 3A**). The spatial distribution of porosity and alveolar surface density were visually found to be homogeneous throughout the entire domain of the lung (see **Figures 3B,C**, respectively).

The regional distribution of alveolar porosity for the apical, mid, and basal zones of the lung is shown in **Figures 4A–C**, respectively. For the three areas analyzed, we found that the

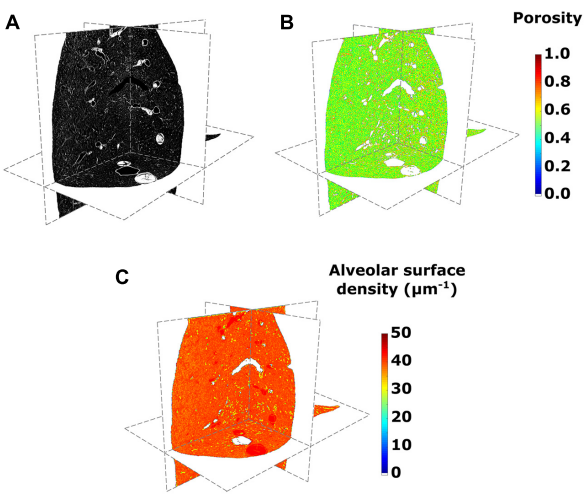

FIGURE 3 | (A) Micro-computed tomography (CT) images of a lung in its axial, sagittal, and coronal views, **(B)** porosity, and **(C)** alveolar surface density maps for the SAF-HMDS group in the different anatomical planes.

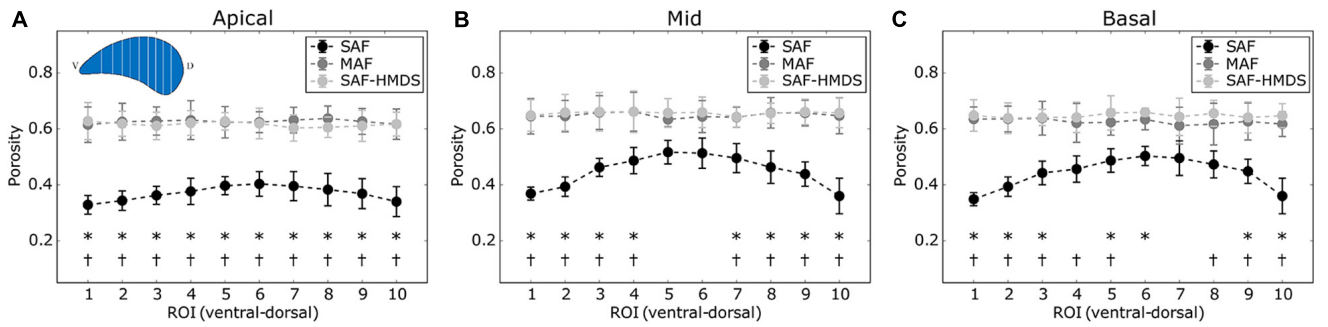

FIGURE 4 | Regional distribution of porosity in the ventral-dorsal direction for three regions of the lung: **(A)** apical zone, **(B)** mid zone, and **(C)** basal zone. Significant differences (p-value ≤ 0.05) between the SAF and MAF, SAF and SAF-HMDS, MAF, and SAF-HMDS groups are indicated by *, †, respectively. Each group ROI considered $n = 9$ samples.

regional porosity values of the SAF group are significantly different (typically lower) than the values of the MAF and SAF-HMDS groups, with some exceptions in the mid and basal zones. No significant differences were found between the MAF and SAF-HMDS groups. Regarding the spatial distribution of porosity, uniform values were observed along the ventral-dorsal direction in all the areas analyzed in the MAF and SAF-HMDS groups. In contrast, a concave distribution is observed in the SAF group, with a tendency to reduce porosity toward the most ventral and dorsal areas.

The regional distribution of the alveolar surface density for the apical, mid, and basal areas of the lung is shown in **Figures 5A–C**, respectively. For the mid and basal cases, significant differences were observed between the SAF and SAF-HMDS groups for almost all ROIs. Furthermore, significant differences between the MAF and SAF-HMDS groups are observed for half of the ROIs in the same areas. In the three groups, a uniform distribution of values is observed along the ventral–dorsal direction, for the apical, mid, and basal zones.

The regional distribution of the surface-to-volume ratio for the apical, mid, and basal lung zones is shown in **Figures 6A–C**, respectively. With the particular exception of two ROIs, virtually all the regional values of the SAF group were found to be significantly different (higher) than the values of the MAF and SAF-HMDS groups. No significant differences were found between the MAF and SAF-HMDS. Furthermore, a uniform distribution of values is observed along the ventral–dorsal direction in all the areas analyzed for MAF and SAF-HMDS groups. In contrast, a convex distribution is observed in the SAF group, with a tendency to increase the surface-to-volume ratio values toward the most ventral and dorsal areas of the lung.

When comparing the alveolar porosity in different sections of a single lung, no significant differences were found between the apical, mid, and basal sections for lungs in the MAF group (see **Figure 7** for a graphical account of the results in Subject 1 and **Supplementary Table 1** for the ANOVA results). In contrast, significant differences in alveolar porosity between anatomical sections were found in all of the lungs in the SAF group. For the case of alveolar surface density, no significant differences between sections were detected in lungs of the MAF and SAF-HDMS groups (see **Figure 8** for Subject 1 and **Supplementary Table 2** for the ANOVA results).

The effects of mask size on the generation of porosity and alveolar surface density maps are reported in **Supplementary Figures 1, 2**. For both, porosity, and alveolar surface density, we observe that mask sizes above 70 μm result in unimodal histograms with similar characteristics (see **Supplementary Figures 1F, 2F**). In contrast, mask sizes smaller than 70 μm result in density functions that are not consistent with larger size masks, and that show oscillations in the range of smaller values. **Figure 9** shows magnifications of a pleural sector for three representative subjects from each group, where pleural thickening is observed for the case representing the SAF group. In contrast, a thinner pleural thickness is observed in the MAF and SAF-HDMS group representatives.

DISCUSSION

In this work, we have studied the alveolar architecture of rat lungs using micro-CT and advanced computational geometry techniques. To the best of our knowledge, this work constitutes one of the first attempts to characterize the three-dimensional morphological parameters such as surface-to-volume ratio, porosity, and alveolar surface density in the whole lung of Sprague–Dawley subjects. One of the major findings is that regional porosity, alveolar surface density, and surface-to-volume ratio have a uniform distribution in normal lungs, which do not seem to be affected by gravitational effects.

Structural studies based on micro-CT imaging have focused on C57BL/6 murine lungs, both under normal and diseased conditions (Parameswaran et al., 2009; Vasilescu et al., 2012a), where the fixation procedure of the lung samples was similar to that performed in the SAF group. In 10-week-old normal mice, the mean alveolar diameter reported is 59 ± 2 μm (Parameswaran et al., 2009), which is comparable to the mean alveolar diameter found in the SAF-HMDS group in our work, and in the order of magnitude of the other two groups. Previous studies have shown that the alveolar volume and diameter in mice are smaller than in rats (Faffe et al., 2002). It is worth

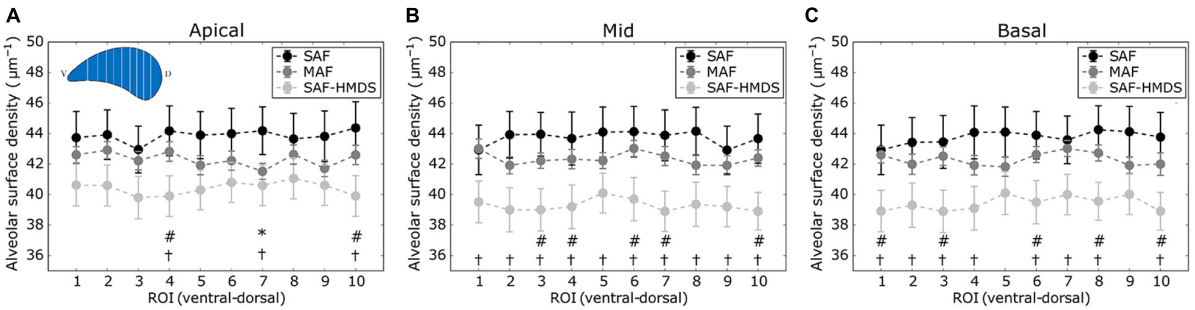

FIGURE 5 | Regional distribution of alveolar surface density in the ventral-dorsal direction for three regions of the lung: **(A)** apical zone, **(B)** mid zone, and **(C)** basal zone. Significant differences (p-value ≤ 0.05) between the SAF and MAF, SAF and SAF-HMDS, and MAF and SAF-HMDS groups are indicated by *, †, and #, respectively. Each ROI datapoint represents the mean ± standard deviation of $n = 9$ samples.

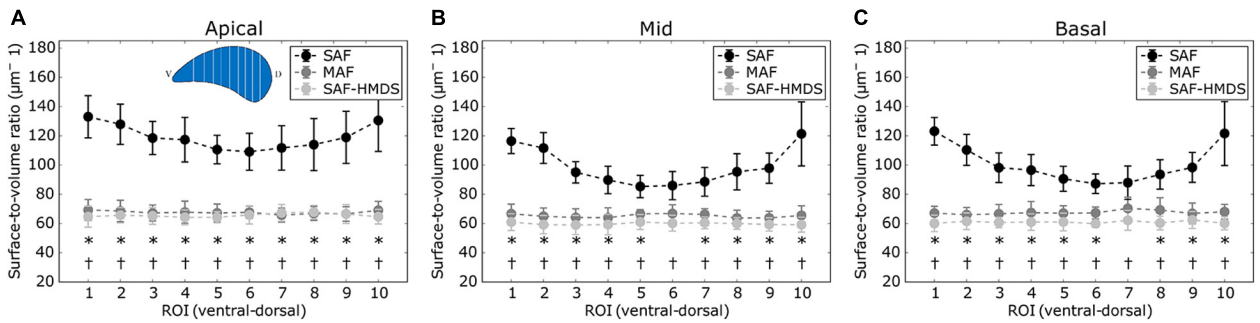

FIGURE 6 | Regional distribution of surface-to-volume ratio in the ventral-dorsal direction for three regions of the lung: **(A)** apical zone, **(B)** mid zone, and **(C)** basal zone. Significant differences (p-value ≤ 0.05) between the SAF and MAF, SAF and SAF-HMDS, and MAF and SAF-HMDS groups are indicated by *, †, respectively. Each ROI datapoint represents the mean ± standard deviation of $n = 9$ samples.

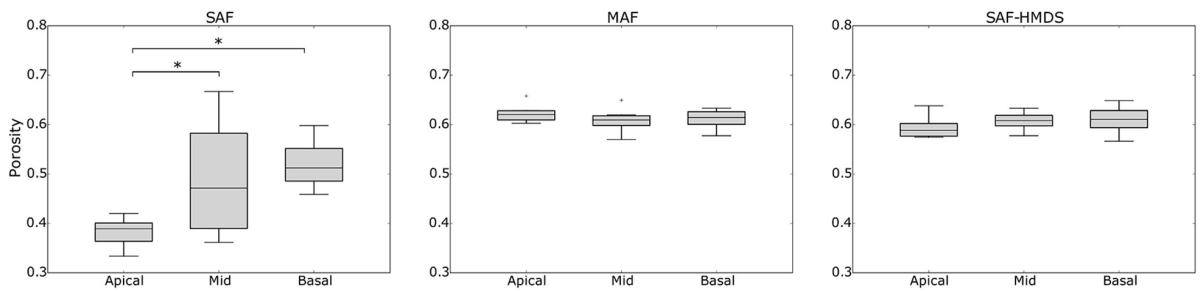

FIGURE 7 | Single-lung (Subject 1) analysis of variability of alveolar porosity in different anatomical sections in Subject 1. Nomenclature: *$p \leq 0.05$.

remarking that studies in mice use a higher tracheal pressure (30 cm H_2O) during *in situ* fixation than the pressure considered in this work (20 cm H_2O). More substantial tracheal pressures result in a larger alveolar expansion in mice, which may explain the similarity with the alveolar diameter values found in this work. The morphological analysis performed by Vasilescu et al. (2012a) in the same species delivered surface-to-volume ratio values of 52 ± 3.7 and 47.7 ± 6 mm^{-1} in young (12-week-old) and adult (91-week-old) subjects, respectively. These values are smaller than the ones found in this study for all groups (**Table 1**) but coincide in the order of magnitude. Similarly, Xiao et al. (2016) studied the acini of A/J mouse *in situ* using synchrotron-based micro-CT. They found surface-to-volume ratio values of 79.8 ± 8.9 mm^{-1}, which are very close to those reported in this work in **Table 1**. We note that if the alveolus cavity is idealized as a sphere, then the surface-to-volume ratio is inversely proportional to the alveolar diameter. This, in turn, would imply that larger values of surface-to-volume ratio are to be expected in mice than in rats, which is not the case. Again, we attribute these differences to the high tracheal pressure applied in mice experiments (30 cm H_2O), which results in larger alveoli dimensions. We note that in our work, the choice of applying an applied tracheal pressure of 20 cm H_2O was made to target physiological values of tidal volume, as a tracheal pressure of

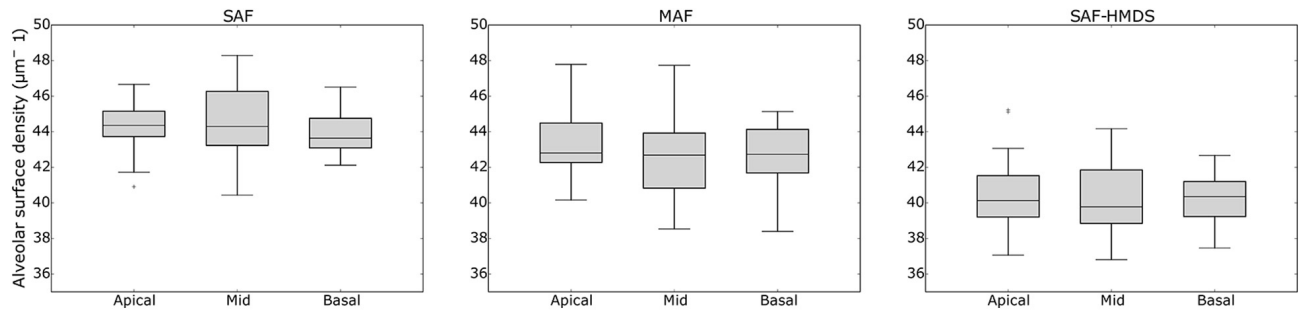

FIGURE 8 | Single-lung analysis of variability of alveolar surface density in different anatomical sections in Subject 1. Nomenclature: $^{*}p \leq 0.05$.

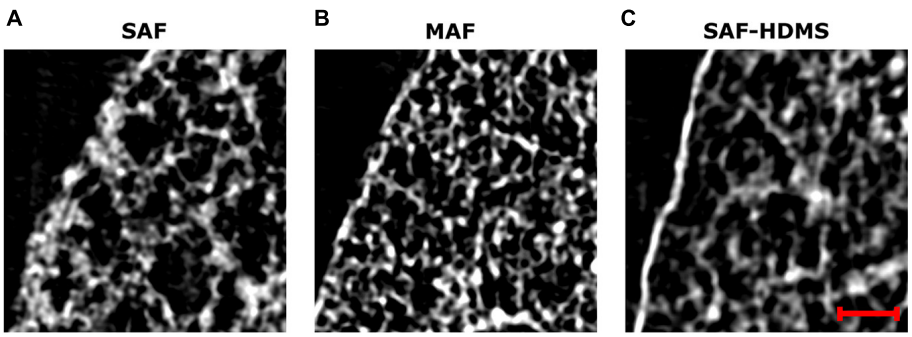

FIGURE 9 | Magnifications of grayscale micro-CT images for subpleural regions of three representative subjects: **(A)** SAF group, **(B)** MAF group, and **(C)** SAF-HMDS group. The red scale bar corresponds to 100 μm.

30 cm H_2O typically corresponds to total lung capacity in murine subjects (Namati et al., 2006). The group of Litzlbauer et al. (2006) measures the alveolar surface density from micro-CT images using stereological methods for morphological quantification. In their study, left porcine lungs were fixed by using ventilation of formaldehyde vapors at 35 cm H_2O. The alveolar surface density was measured as the alveolar surface area divided by the volume of interest, giving values close to the obtained in this study (between 30.5 and 35.5 mm^{-1}).

Three-dimensional maps displaying the distribution of porosity in the lung were successfully constructed for all subjects (see **Figure 3B** for a representative case). The resulting maps showed a convergent distribution for mask sizes greater than 70 μm (see **Supplementary Figure 1**). Porosity in the pulmonary parenchyma was found to be regionally uniform everywhere in the lung and locally similar in the MAF and SAF-HMDS groups (see **Table 1** and **Figure 4**). These results suggest that the spatial distribution of regional porosity is homogeneous and is not subject to gravitational effects. This conclusion is supported by previous studies, like the one reported by Hoffman et al. (Mullan et al., 1997; Namati et al., 2006). They estimated the air content on primate lungs in different anatomical regions, observing that air content is uniformly distributed in the lung and does not depend on the location of measurement. Another study that supports this conclusion is the work of Hogg et al., where 16 parenchyma samples were randomly dissected from different regions of frozen human lungs and analyzed using micro-CT (McDonough et al., 2015). The alveolar density, defined as the number of alveoli in a reference volume, was found to be uniform regardless of their original location in the lung.

In our study, a marked reduction in alveolar porosity was observed toward the subpleural regions in the SAF group (most dorsal and ventral zones, see **Figure 4**). Further, in every single lung of the SAF group, the porosity was found to be significantly different depending on the lung region (see **Figure 7** and **Supplementary Table 1**). A careful examination of micro-CT images in those regions for a representative subject of the SAF-group revealed thickened alveolar septums, which is suggestive of alveolar collapse (micro-atelectasis) (see **Figure 9A**). In contrast, alveolar structures close to the pleura in representative subjects of the MAF and SAF-HMDS groups do not display alterations when compared to proximal acinar structures (see **Figures 9B,C**, respectively). These observations, along with the strong volume reductions observed in the SAF group (**Table 1**, lung volume ratio), suggest that the decrease in regional porosity in the SAF group is likely to be an artifact of the method rather than a physiological condition.

Similarly to the case of porosity, three-dimensional maps of alveolar surface density were obtained for all lung samples (see **Figure 3C** for a representative case). The resulting maps showed a convergent distribution for mask sizes greater than 70 μm (see **Supplementary Figure 2**). All three groups suggest that the distribution of alveolar surface density is homogeneous throughout the lung (see **Figures 5**, **8**). Groups typically do

differ in their assessment of ROI values. For example, significant differences between the SAF and SAF-HMDS groups were found in 21 out of 30 ROIs considered. More conclusive results were found in the study of the regional surface-to-volume ratio, where uniform distributions with similar values were found in the MAF and SAF-HMDS groups. These results suggest that the surface-to-volume ratio is homogeneous throughout the lung and does not exhibit a gravitational dependence. In contrast, the SAF group resulted in heterogenous distribution that largely deviated from the values found in the MAF and SAF-HMDS groups. We note that, since the surface-to-volume ratio is inversely proportional to the porosity, we conclude that the seemingly increasing values toward the most ventral and dorsal regions can be regarded as artifacts in the alveolar architecture induced the SAF method, based on the conclusions reached in the study of regional porosity.

Throughout this work, three methods for dehydration have been considered in the fixation of lung samples. The gold-standard and most popular method in studies involving the histological analysis and micro-CT imaging of murine lungs has been the SAF method, which employs ethanol solutions for the dehydration step (Puchtler et al., 1970; Hausmann, 2007; Braber et al., 2010). However, in our work, we have shown that the SAF method results in considerable lung shrinking (**Table 1**) that markedly affects the alveolar architecture in subpleural regions (**Figure 9A**). An alternative method is the SAF-HMDS, which is predominantly used to prepare samples for electron microscopy, with some applications in micro-CT sample preparations. One advantage of the SAF-HMDS method is that it allows a rapid drying that has been shown to preserve the alveolar morphology without significant alterations (Bray et al., 1993; Lee and Chow, 2012). However, the SAF-HMDS method has important operational disadvantages and risks to the user, as inhalation or skin exposure to HMDS is known to be hazardous to health (Chou and Chang, 2007). Another disadvantage is the management of HMDS residuals, as degradation results in products that can be harmful to the environment and that require special disposal procedures (Alleni et al., 1997). Here, we propose and assess the use of the MAF method as an alternative in the dehydration of lung samples. The MAF dehydration method has been commonly employed in molecular biology to quantify the presence of biomarkers and to detect specific genetic alterations in organs/tissues (Noguchi et al., 1997; Anami et al., 2000). However, to the best of our knowledge, its application in the preparation of samples for micro-CT analysis is novel and has not been reported in the literature. Our results show that the application of a methanol-PBS solution before subsequent baths of ethanol solutions in lung samples preserves their volume (**Table 1**) and alveolar architecture everywhere in the lung, as most of the morphological parameters analyzed in this work do not display substantial differences between the MAF and SAF-HMDS groups. We believe that the success of the MAF method is related to the ability of the methanol bath to increase cellular permeability, which then allows for enhanced diffusion properties during the ethanol bath dehydration step (Puchtler et al., 1970). We further note that methanol and PBS are safer in health terms than HMDS [lethal dose (LD_{50}) and lethal concentration (LC_{50}) values are considerably smaller for HMDS than methanol], and their disposal can be done without special requirements (the biodegradability of methanol is 99% while for HMDS is just 15.3%) (Sullivan and Cummins, 2005; Jang et al., 2019). Thus, we conclude that the proposed MAF dehydration method represents a convenient, sustainable, and safe procedure that does not alter the alveolar morphology in treated lung samples.

Several aspects of this work can be improved in future contributions. We have shown in our study that all fixation methods lead to different levels of tissue shrinking, which directly affects the alveolar architecture and the associated morphological parameters. Recently, *in vivo* micro-CT imaging of murine lungs has been reported (Lovric et al., 2017), where the acinar structure was reconstructed with high precision in living subjects. Future efforts on the morphological characterization of the lung may benefit from these *in vivo* imaging techniques, which may confirm or correct the values reported in this work. Another limitation of our study was the use of a single airway pressure level. Due to the elastic nature of the alveolar wall, the morphological values described in this work are expected to change in the event of different levels of airway pressure. Besides, our results have been obtained using only three subjects per group. While this small sample has allowed us to detect significant differences between groups, larger populations of Sprague–Dawley rats and other species should be considered in future works to confirm and extend our conclusions. Finally, in this work, we have advocated for the characterization of alveolar porosity, which is a microstructural parameter that is not commonly reported in respiratory physiology. We note, however, that porosity plays a crucial role in describing the mechanical response of porous biomaterials (Currey, 1988). A recent theoretical study shows that porosity, along with the alveolar wall elasticity, is the most relevant microstructural parameter in the mechanical response of the lung parenchyma (Concha et al., 2018; Concha and Hurtado, 2020). Further, the study shows that an increase in porosity, which can be directly associated with alveolar airspace enlargement, may signify a loss of parenchymal elastance, a mechanical relationship that has long been observed in lungs with pulmonary emphysema (Nagai et al., 1991). Therefore, a deep understanding of the porosity distribution in the whole lung plays a vital role in the creation of microstructurally-informed constitutive models (Eskandari et al., 2019; Álvarez-Barrientos et al., 2021) that can predict the overall properties of the lung, as well as in informing organ-level computational models of the respiratory system (Eskandari et al., 2015).

DATA AVAILABILITY STATEMENT

The raw data supporting the conclusion of this article will be made available by the authors, without undue reservation.

ETHICS STATEMENT

The animal study was reviewed and approved by the Bioethics Committee of the Pontificia Universidad Católica de Chile.

AUTHOR CONTRIBUTIONS

MS-V and PA-J carried out the experiments. MS-V and DH designed the computational methods, interpreted the results, and wrote the manuscript. MS-V wrote computer codes and performed image analysis and statistical analysis. MS-V, PA-J, and DH designed the experiments, reviewed the final manuscript, contributed to the article, and approved the submitted version.

FUNDING

This work was funded by the National Agency for Research and Development (ANID) of Chile through grant FONDECYT Regular # 1180832 and from ANID, Chile – Millennium Science Initiative Program – NCN17 129. MS-V would like to acknowledge the financial support given by CONICYT through the Doctoral Scholarship Grant. The authors also acknowledge the support of ANID through FONDEQUIP project EQM130028, which enabled micro-CT image acquisitions.

SUPPLEMENTARY MATERIAL

The Supplementary Material for this article can be found online at: https://www.frontiersin.org/articles/10.3389/fphys.2021.755468/full#supplementary-material

REFERENCES

Aganj, I., Harisinghani, M. G., Weissleder, R., and Fischl, B. (2018). Unsupervised medical image segmentation based on the local center of mass. *Sci. Rep.* 8:13012. doi: 10.1038/s41598-018-31333-5

Alleni, R. B., Kochs, P., and Chandra, G. (1997). "Industrial organosilicon materials, their environmental entry and predicted fate," in *Organosilicon Materials. The Handbook of Environmental Chemistry*, ed. G. Chandra (Berlin: Springer), 1–25. doi: 10.1007/978-3-540-68331-5_1

Álvarez-Barrientos, F., Hurtado, D. E., and Genet, M. (2021). International journal of engineering science pressure-driven micro-poro-mechanics: a variational framework for modeling the response of porous materials. *Int. J. Eng. Sci.* 169:103586. doi: 10.1016/j.ijengsci.2021.103586

Anami, Y., Takeuchi, T., Mase, K., Yasuda, J., Hirohashi, S., Perucho, M., et al. (2000). Amplotyping of microdissected, methanol-fixed lung carcinoma by arbitrarily primed polymerase chain reaction. *Int. J. Cancer* 89, 19–25.

Bajc, M., and Jonson, B. (2011). Ventilation/perfusion SPECT for diagnosis of pulmonary embolism and other diseases. *Int. J. Mol. Imaging* 2011, 1–7. doi: 10.1155/2011/682949

Braber, S., Verheijden, K. A. T., Henricks, P. A. J., Kraneveld, A. D., and Folkerts, G. (2010). A comparison of fixation methods on lung morphology in a murine model of emphysema. *Am. J. Physiol. Cell. Mol. Physiol.* 299, L843–L851. doi: 10.1152/ajplung.00192.2010

Bray, D. F., Bagu, J., and Koegler, P. (1993). Comparison of hexamethyldisilazane (HMDS), Peldri II, and critical-point drying methods for scanning electron microscopy of biological specimens. *Microsc. Res. Tech.* 26, 489–495. doi: 10.1002/jemt.1070260603

Bruker-MicroCT (2016). *Chemical Drying of Specimens to Enhance Contrast. Bruker-Skyscan Method Notes*. Belgium: Bruker-MicroCT, 1–8.

Canny, J. (1986). A computational approach to edge detection. *IEEE Trans. Pattern Anal. Mach. Intell.* 8, 679–698. doi: 10.1109/TPAMI.1986.4767851

Chou, M.-S., and Chang, K.-L. (2007). UV/ozone degradation of gaseous hexamethyldisilazane (HMDS). *Chemosphere* 69, 697–704. doi: 10.1016/j.chemosphere.2007.05.040

Clark, A. R., Burrowes, K. S., and Tawhai, M. H. (2019). Ventilation/perfusion matching: of myths, mice, and men. *Physiology* 34, 419–429. doi: 10.1152/physiol.00016.2019

Concha, F., and Hurtado, D. E. (2020). Upscaling the poroelastic behavior of the lung parenchyma: a finite-deformation micromechanical model. *J. Mech. Phys. Solids* 145:104147. doi: 10.1016/j.jmps.2020.104147

Concha, F., Sarabia-Vallejos, M., and Hurtado, D. E. (2018). Micromechanical model of lung parenchyma hyperelasticity. *J. Mech. Phys. Solids* 112, 126–144. doi: 10.1016/j.jmps.2017.11.021

Cruces, P., Erranz, B., Lillo, F., Sarabia-Vallejos, M. A., Iturrieta, P., Morales, F., et al. (2019). Mapping regional strain in anesthetised healthy subjects during spontaneous ventilation. *BMJ Open Respir. Res.* 6:e000423. doi: 10.1136/bmjresp-2019-000423

Currey, J. D. (1988). The effect of porosity and mineral content on the Young's modulus of elasticity of compact bone. *J. Biomech.* 21, 131–139. doi: 10.1016/0021-9290(88)90006-1

Eskandari, M., Kuschner, W. G., and Kuhl, E. (2015). Patient-specific airway wall remodeling in chronic lung disease. *Ann. Biomed. Eng.* 43, 2538–2551. doi: 10.1007/s10439-015-1306-7

Eskandari, M., Nordgren, T. M., and O'Connell, G. D. (2019). Mechanics of pulmonary airways: linking structure to function through constitutive modeling, biochemistry, and histology. *Acta Biomater.* 97, 513–523. doi: 10.1016/j.actbio.2019.07.020

Faffe, D. S., Rocco, P. R. M., Negri, E. M., and Zin, W. A. (2002). Comparison of rat and mouse pulmonary tissue mechanical properties and histology. *J. Appl. Physiol.* 92, 230–234. doi: 10.1152/japplphysiol.01214.2000

Hausmann, R. (2007). "Methods of lung fixation," in *Forensic Pathology Reviews*, ed. M. Tsokos (Totowa, NJ: Humana Press), 437–451. doi: 10.1007/978-1-59259-921-9_15

Hsia, C. C. W., Hyde, D. M., Ochs, M., and Weibel, E. R. (2010). An official research policy statement of the American Thoracic Society/European Respiratory Society: standards for quantitative assessment of lung structure. *Am. J. Respir. Crit. Care Med.* 181, 394–418. doi: 10.1164/rccm.200809-1522ST

Hsia, C. C. W., Hyde, D. M., and Weibel, E. R. (2016). Lung structure and the intrinsic challenges of gas exchange. *Compr. Physiol.* 6, 827–895. doi: 10.1002/cphy.c150028

Hurtado, D. E., Erranz, B., Lillo, F., Sarabia-Vallejos, M., Iturrieta, P., Morales, F., et al. (2020). Progression of regional lung strain and heterogeneity in lung injury: assessing the evolution under spontaneous breathing and mechanical ventilation. *Ann. Intensive Care* 10:107. doi: 10.1186/s13613-020-00725-0

Jang, M., Yoon, C., Park, J., and Kwon, O. (2019). Evaluation of hazardous chemicals with material safety data sheet and by-products of a photoresist used in the semiconductor-manufacturing industry. *Saf. Health Work* 10, 114–121. doi: 10.1016/j.shaw.2018.08.001

Jögi, J., Ekberg, M., Jonson, B., Bozovic, G., and Bajc, M. (2011). Ventilation/perfusion SPECT in chronic obstructive pulmonary disease: an evaluation by reference to symptoms, spirometric lung function and emphysema, as assessed with HRCT. *Eur. J. Nucl. Med. Mol. Imaging* 38, 1344–1352. doi: 10.1007/s00259-011-1757-5

Langheinrich, A. C., Leithäuser, B., Greschus, S., Von, G., Breithecker, A., Matthias, F. R., et al. (2004). Acute rat lung injury: feasibility of assessment with micro-CT. *Radiology* 233, 165–171. doi: 10.1148/radiol.2331031340

Lee, J. T. Y., and Chow, K. L. (2012). SEM sample preparation for cells on 3D scaffolds by freeze-drying and HMDS. *Scanning* 34, 12–25. doi: 10.1002/sca.20271

Lesouple, J., Pilastre, B., Altmann, Y., and Tourneret, J.-Y. (2021). Hypersphere fitting from noisy data using an EM algorithm. *IEEE Signal Process. Lett.* 28, 314–318. doi: 10.1109/LSP.2021.3051851

Li, B. N., Chui, C. K., Chang, S., and Ong, S. H. (2011). Integrating spatial fuzzy clustering with level set methods for automated medical image segmentation. *Comput. Biol. Med.* 41, 1–10. doi: 10.1016/j.compbiomed.2010.10.007

Litzlbauer, H. D., Neuhaeuser, C., Moell, A., Greschus, S., Breithecker, A., Franke, F. E., et al. (2006). Three-dimensional imaging and morphometric analysis of

alveolar tissue from microfocal X-ray-computed tomography. *Am. J. Physiol. Lung Cell. Mol. Physiol.* 291, L535–L545. doi: 10.1152/ajplung.00088.2005

Lovric, G., Mokso, R., Arcadu, F., Vogiatzis Oikonomidis, I., Schittny, J. C., Roth-Kleiner, M., et al. (2017). Tomographic *in vivo* microscopy for the study of lung physiology at the alveolar level. *Sci. Rep.* 7:12545. doi: 10.1038/s41598-017-12886-3

Magee, D., Bulpitt, A., and Berry, E. (2013). "Combining 3D deformable models and level set methods for the segmentation of abdominal aortic aneurysms," in *Proceedings of the British Machine Vision Conference*. (Manchester), 35.1–35.9. doi: 10.5244/c.15.35

McDonough, J. E., Knudsen, L., Wright, A. C., Mark Elliott, W., Ochs, M., and Hogg, J. C. (2015). Regional differences in alveolar density in the human lung are related to lung height. *J. Appl. Physiol.* 118, 1429–1434. doi: 10.1152/japplphysiol.01017.2014

Mullan, B. F., Galvin, J. R., Zabner, J., and Hoffman, E. A. (1997). Evaluation of *in vivo* total and regional air content and distribution in primate lungs with high-resolution CT. *Acad. Radiol.* 4, 674–679. doi: 10.1016/S1076-6332(97)80138-9

Nagai, A., Yamawaki, I., Takizawa, T., and Thurlbeck, W. M. (1991). Alveolar attachments in emphysema of human lungs. *Am. Rev. Respir. Dis.* 144, 888–891. doi: 10.1164/ajrccm/144.4.888

Namati, E., Chon, D., Thiesse, J., Hoffman, E. A., De Ryk, J., Ross, A., et al. (2006). *In vivo* micro-CT lung imaging via a computer-controlled intermittent iso-pressure breath hold (IIBH) technique. *Phys. Med. Biol.* 51, 6061–6075. doi: 10.1088/0031-9155/51/23/008

Noguchi, M., Furuya, S., Takeuchi, T., and Hirohashi, S. (1997). Modified formalin and methanol fixation methods for molecular biological and morphological analyses. *Pathol. Int.* 47, 685–691. doi: 10.1111/j.1440-1827.1997.tb04442.x

Parameswaran, H., Bartolák-Suki, E., Hamakawa, H., Majumdar, A., Allen, P. G., and Suki, B. (2009). Three-dimensional measurement of alveolar airspace volumes in normal and emphysematous lungs using micro-CT. *J. Appl. Physiol.* 107, 583–592. doi: 10.1152/japplphysiol.91227.2008

Puchtler, H., Waldrop, F. S., Meloan, S. N., Terry, M. S., and Conner, H. M. (1970). Methacarn (methanol-Carnoy) fixation. *Histochemie* 21, 97–116. doi: 10.1007/BF00306176

Sarabia-Vallejos, M. A., Zuñiga, M., and Hurtado, D. E. (2019). The role of three-dimensionality and alveolar pressure in the distribution and amplification of alveolar stresses. *Sci. Rep.* 9:8783. doi: 10.1038/s41598-019-45343-4

Soldati, G., Smargiassi, A., Inchingolo, R., Sher, S., Nenna, R., Valente, S., et al. (2014). Lung ultrasonography may provide an indirect estimation of lung porosity and airspace geometry. *Respiration* 88, 458–468. doi: 10.1159/000368086

Strzelecki, M., Szczypinski, P., Materka, A., and Klepaczko, A. (2013). A software tool for automatic classification and segmentation of 2D/3D medical images. *Nucl. Instrum. Methods Phys. Res. A* 702, 137–140. doi: 10.1016/j.nima.2012.09.006

Suga, K., Kawakami, Y., Koike, H., Iwanaga, H., Tokuda, O., Okada, M., et al. (2010). Lung ventilation-perfusion imbalance in pulmonary emphysema: assessment with automated V/Q quotient SPECT. *Ann. Nucl. Med.* 24, 269–277. doi: 10.1007/s12149-010-0369-7

Sullivan, B., and Cummins, K. (2005). OSHA compliance issues. *J. Occup. Environ. Hyg.* 2, D54–D56. doi: 10.1080/15459620590959849

Vasilescu, D. M., Gao, Z., Saha, P. K., Yin, L., Wang, G., Haefeli-Bleuer, B., et al. (2012a). Assessment of morphometry of pulmonary acini in mouse lungs by nondestructive imaging using multiscale microcomputed tomography. *Proc. Natl. Acad. Sci. U.S.A.* 109, 17105–17110. doi: 10.1073/pnas.1215112109

Vasilescu, D. M., Knudsen, L., Ochs, M., Weibel, E. R., and Hoffman, E. A. (2012b). Optimized murine lung preparation for detailed structural evaluation via micro-computed tomography. *J. Appl. Physiol.* 112, 159–166. doi: 10.1152/japplphysiol.00550.2011

Weibel, E. R. (2017). Lung morphometry: the link between structure and function. *Cell Tissue Res.* 367, 413–426. doi: 10.1007/s00441-016-2541-4

Xiao, L., Sera, T., Koshiyama, K., and Wada, S. (2016). Morphological characterization of acinar cluster in mouse lung using a multiscale-based segmentation algorithm on synchrotron micro-CT images. *Anat. Rec.* 299, 1424–1434. doi: 10.1002/ar.23452

Xu, X., Xu, S., Jin, L., and Song, E. (2011). Characteristic analysis of Otsu threshold and its applications. *Pattern Recognit. Lett.* 32, 956–961. doi: 10.1016/j.patrec.2011.01.021

Yuan, R., Nagao, T., Paré, P. D., Hogg, J. C., Sin, D. D., Elliott, M. W., et al. (2010). Quantification of lung surface area using computed tomography. *Respir. Res.* 11, 1–9. doi: 10.1186/1465-9921-11-153

Zhao, L., Shi, X., and Xia, H. (2018). The research of the digital core construction based on marching cubes. *IOP Conf. Ser. Mater. Sci. Eng.* 394. doi: 10.1088/1757-899X/394/4/042065

Conflict of Interest: The authors declare that the research was conducted in the absence of any commercial or financial relationships that could be construed as a potential conflict of interest.

Publisher's Note: All claims expressed in this article are solely those of the authors and do not necessarily represent those of their affiliated organizations, or those of the publisher, the editors and the reviewers. Any product that may be evaluated in this article, or claim that may be made by its manufacturer, is not guaranteed or endorsed by the publisher.

frontiers in Physiology

REVIEW
published: 17 January 2022
doi: 10.3389/fphys.2021.815601

Airway Closure and Expiratory Flow Limitation in Acute Respiratory Distress Syndrome

Claude Guérin[1,2,3]*, *Martin Cour*[1,2] *and Laurent Argaud*[1,2]

[1] *Médecine Intensive - Réanimation Hôpital Edouard Herriot Lyon, Lyon, France,* [2] *Faculté de Médecine Lyon-Est, Université de Lyon, Lyon, France,* [3] *Institut Mondor de Recherches Biomédicales, INSERM-UPEC UMR 955 Team 13 - CNRS ERL 7000, Créteil, France*

Acute respiratory distress syndrome (ARDS) is mostly characterized by the loss of aerated lung volume associated with an increase in lung tissue and intense and complex lung inflammation. ARDS has long been associated with the histological pattern of diffuse alveolar damage (DAD). However, DAD is not the unique pathological figure in ARDS and it can also be observed in settings other than ARDS. In the coronavirus disease 2019 (COVID-19) related ARDS, the impairment of lung microvasculature has been pointed out. The airways, and of notice the small peripheral airways, may contribute to the loss of aeration observed in ARDS. High-resolution lung imaging techniques found that in specific experimental conditions small airway closure was a reality. Furthermore, low-volume ventilator-induced lung injury, also called as atelectrauma, should involve the airways. Atelectrauma is one of the basic tenet subtending the use of positive end-expiratory pressure (PEEP) set at the ventilator in ARDS. Recent data revisited the role of airways in humans with ARDS and provided findings consistent with the expiratory flow limitation and airway closure in a substantial number of patients with ARDS. We discussed the pattern of airway opening pressure disclosed in the inspiratory volume-pressure curves in COVID-19 and in non-COVID-19 related ARDS. In addition, we discussed the functional interplay between airway opening pressure and expiratory flow limitation displayed in the flow-volume curves. We discussed the individualization of the PEEP setting based on these findings.

Keywords: acute respiratory distress syndrome, airway closure, COVID-19, respiratory mechanics, expiratory flow limitation, positive end-expiratory pressure

OPEN ACCESS

Edited by:
Walter Araujo Zin, Federal University of Rio de Janeiro, Brazil

Reviewed by:
Alysson Roncally Silva Carvalho, University of Porto, Portugal
Ahmet Baydur, University of Southern California, United States

***Correspondence:**
Claude Guérin
claude.guerin@chu-lyon.fr

Specialty section:
This article was submitted to Respiratory Physiology, a section of the journal Frontiers in Physiology

Received: *15 November 2021*
Accepted: *09 December 2021*
Published: *17 January 2022*

Citation:
Guérin C, Cour M and Argaud L (2022) Airway Closure and Expiratory Flow Limitation in Acute Respiratory Distress Syndrome. Front. Physiol. 12:815601. doi: 10.3389/fphys.2021.815601

INTRODUCTION

Acute respiratory distress syndrome (ARDS), a non-cardiogenic pulmonary edema with lung inflammation, loss of aeration, higher intra-pulmonary shunt, lower compliance of respiratory system, and hypoxemia, is primarily driven by pneumonia, aspiration, and extra-pulmonary sepsis (Bellani et al., 2016; Thompson et al., 2017). Before the COVID-19 pandemic, it accounted for 10% of intensive care unit (ICU) admissions and supported a 28-day median mortality rate of about 35%, and >40% in the severe ARDS category (Bellani et al., 2016). With the COVID-19 pneumonia, the number of ARDS cases exploded worldwide and the mortality remained in the same range as that of non-COVID-19 (Grasselli et al., 2020; Matthay et al., 2020).

The role of airways in the pathophysiology of ARDS has largely remained unknown even though airway collapsibility in this setting was suspected many years ago (Bindslev et al., 1980; Hedenstierna and McCarthy, 1980). As discussed below, the histological involvement of airways was marginally described in ARDS. However, recent data suggest that airways may play a role in the pathophysiology of both COVID-19 and non-COVID-19 ARDS.

In this narrative review, we aimed to decipher the data subtending the implication of airways in the pathogenesis of ARDS and discuss some therapeutic approaches.

LUNG PATHOLOGY OF ARDS

Post-mortem examination of 7 patients in the 12 originally described as ARDS by Ashbaugh et al. reported that the lungs were heavier than normal and disclosed capillary congestion, areas of alveolar atelectasis, interstitial and alveolar hemorrhage, and hyalines membranes (Ashbaugh et al., 1967). The pulmonary vasculature and the trachea-bronchial tree were free of obstruction (Ashbaugh et al., 1967). Then, Katzenstein et al. (1976) popularized the term of diffuse alveolar damage (DAD) that has long been tightly associated with ARDS and thought of as its pathognomonic pathological feature. DAD includes lung epithelial and endothelial injury, lung edema, hyalines membranes, and then proliferation of alveolar, interstitial, and bronchial cells (Katzenstein et al., 1976). Three distinct phases have been described during the ARDS course: the exudative phase with lung edema formation, the fibro-proliferative stage, and the fibrotic stage (Thompson et al., 2017). The transition from phase 2 to phase 3 is not predictable, and the phase 3 may evolve toward either a complete recovery or a persistence of post-aggressive fibrosis that may itself recover. Interestingly, Thille et al. were able to describe these three phases from autopsy lung examination in patients who died with ARDS in the ICU (Thille et al., 2013). Over time, it turned out, however, that DAD was not the main histopathological feature of ARDS. Libby et al. in a meta-analysis of studies reporting on the open lung biopsy in patients with ARDS found a 9% rate of DAD in the 1,205 pooled patients (Libby et al., 2014). The most frequent diagnoses of the ARDS cause after lung histology assessment were interstitial lung disease (25%) and infection (24%) (Libby et al., 2014). In a subsequent study, which included 83 patients from two ICUs with non-resolving ARDS, the rate of DAD diagnosed on lung biopsies was 58% (Guerin et al., 2015a). Three factors may contribute to a lower rate of DAD than expected: (1) part of the DAD may have been related to ventilator-induced lung injury and has decreased over time with the wider use of lung-protective ventilation and lower tidal volume (Acute Respiratory Distress Syndrome Network, 2000), (2) patients with an underlying lung disease may present with the clinical ARDS figure (Guerin et al., 2015b; Aublanc et al., 2017), and (3) DAD is more frequently observed in non-resolving or fatal ARDS than in the other cases.

In patients with COVID-19, lung histopathology is close to that pertaining to classic ARDS. A meta-analysis on 27 studies providing the results of surgical lung biopsy or post-mortem lung autopsy in 195 patients who died from COVID-19, found DAD in 80% of the studies and heterogeneous histopathology (Pannone et al., 2021). The severity of lung histopathology may explain out-of-hospital cardiac arrest (Fanton et al., 2021). Copin et al. described the pattern of organizing pneumonia in 6 patients, associated with fibrin deposition in the bronchioles (Copin et al., 2020), and Fox et al. emphasized on lung microangiopathy in African-American subjects (Fox et al., 2020).

AIRWAY CLOSURE IN NORMAL HUMAN PHYSIOLOGY

In normal humans, the lung deflates from total lung capacity (TLC) down to 10% TLC due to its own elastic recoil. At zero trans-pulmonary pressure (P_L), the airways may be kept open under the action of their internal structure and of the traction of the surrounding lung parenchyma that stems from the lung elastic recoil. The cartilaginous walls of the central airways make them more likely to stay open while the patency of non-cartilaginous peripheral airways depends on the radial traction of the surrounding lung. At low lung volume, the elastic recoil is less and so the radial traction is also less and hence the peripheral airways are more likely to collapse. The pattern of deflation in a static volume-pressure (VP) curve of a normal subject in the sitting position is different in the absence or presence of airway closure (**Figure 1**). Though the lung does not fully empty over the vital capacity range in absence of airway closure (Agostoni and Mead, 1964; Agostoni and Hyatt, 1986), the presence of airway closure, which happens below functional residual capacity (FRC), deviates the static lung VP curve to the left (Sutherland et al., 1968) (**Figure 1**). With the use of the VP curve method, different values of critical P_L at which airways start closing have been found across animal species and experimental preparations. When airways start closing at 4 cm H_2O P_L in excised lungs dogs (Glaister et al., 1973), they were found still open at negative P_L in *in situ* closed-chest lungs rabbits (Cavagna et al., 1967). In closed-chest pigs, cats, dogs, and rabbits, the airways remain open at P_L of −8.3 (Bayle et al., 2006), −12.4 (Cavagna et al., 1967), −11.9 (Cavagna et al., 1967), and −12.7 (Cavagna et al., 1967) cmH_2O, respectively. The closing volume is the lung volume at which airways start closing and the closing capacity is the sum of closing volume and residual volume. Both can be measured by the single breath N_2 washout after 100% oxygen inhalation as a distinct phase IV (McCarthy et al., 1972). The closing capacity increases with age and FRC is lower in obese than in non-obese subjects (**Figure 2**). Therefore, airway closure is more likely to occur at a younger age and in obese than in non-obese patients (**Figure 2**).

When the airways of mammalians are closed, the lungs still contain some air behind the closure in the amount of roughly 0.5 ml/100 g lung tissue (Greaves et al., 1986), meaning that alveoli closed after the airways became closed. In a very elegant *in vivo* experiment by Cavagna et al. in animals (Cavagna et al., 1967), deflation lung VP curves were drawn during: (1) absorption of pure oxygen after tracheal clamping and (2) withdrawal of air-filled lungs from the trachea. The comparison of VP curves in

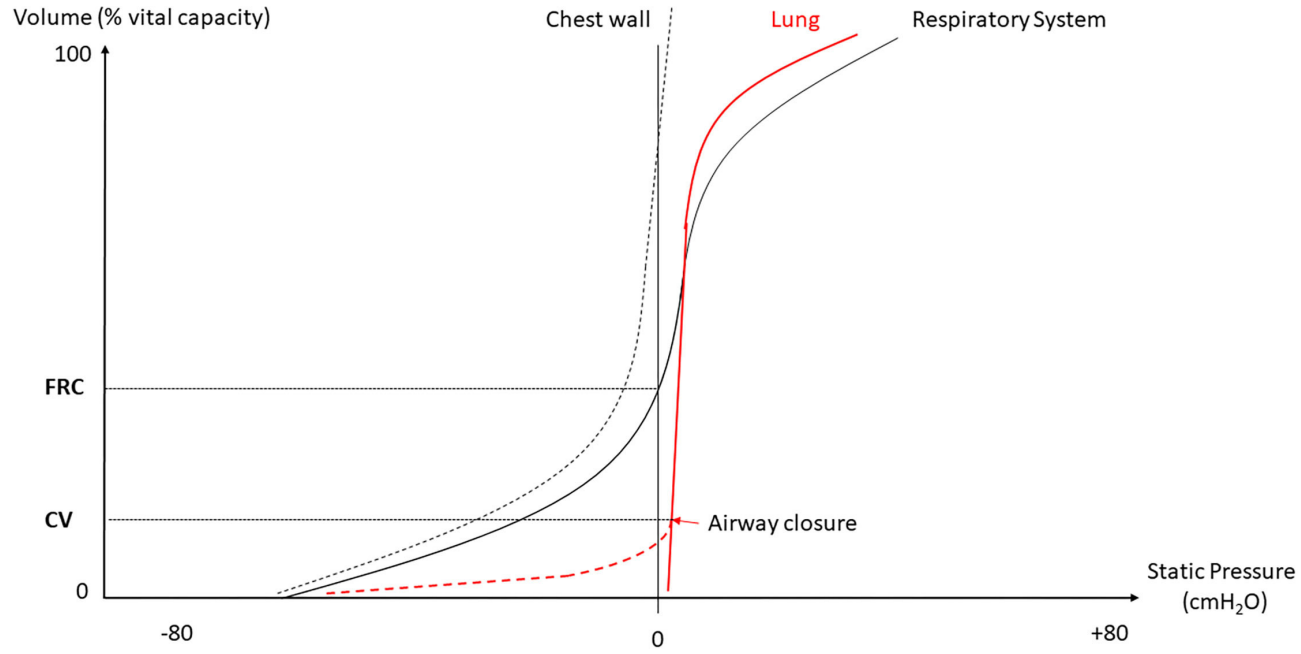

FIGURE 1 | Deflation static volume-pressure (VP) curve of the lung, chest wall and whole respiratory system. FRC, functional residual capacity; CV, closing volume.

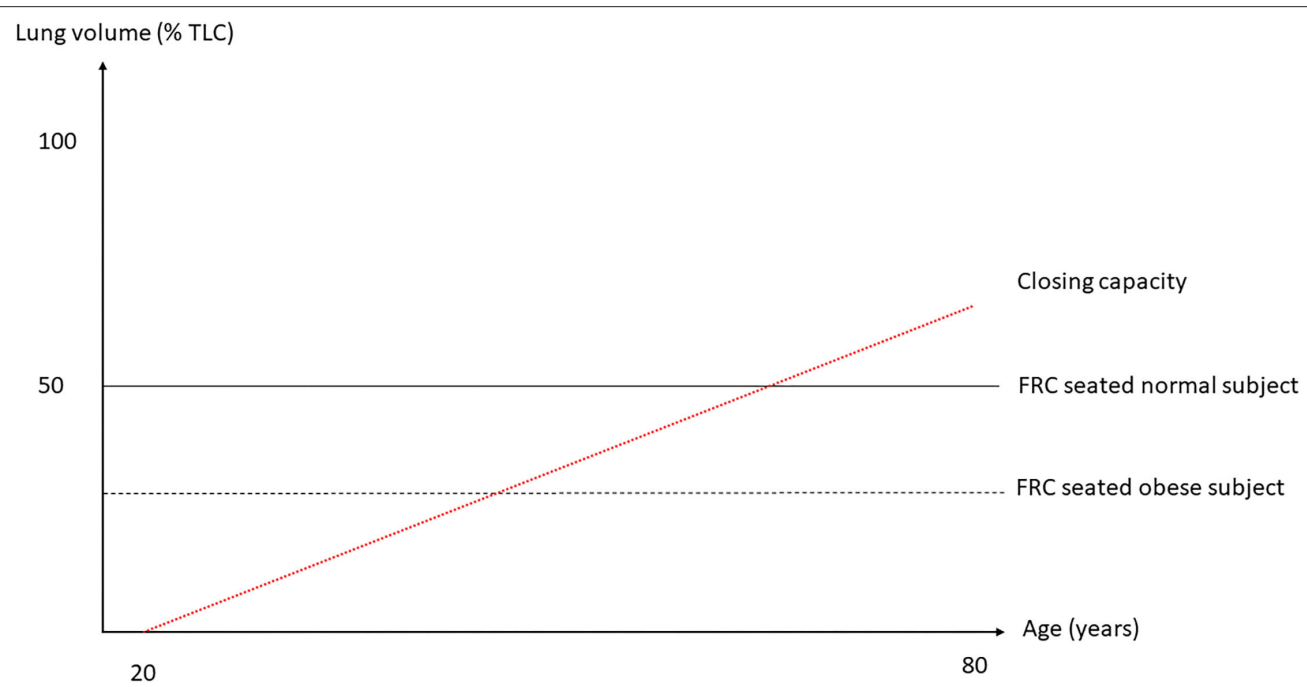

FIGURE 2 | Lung volumes as a function of total lung capacity (TLC) against age. The two horizontal broken lines are FRC seated in normal and obese subject and the red broken line the trend of closing capacity with age. As closing capacity increases with age, an obese subject, in whom FRC is lower, would be likely to exhibit airway closure at a younger age than a non-obese subject. Not shown here is the fact that FRC goes down with increasing body mass index.

both experimental conditions showed that terminal lung units remained in continuity with the trachea till a negative P_L in order of -2 cm H_2O happens, meaning that both airways and alveoli have an elastic resistance to collapse. The mechanisms of that resistance to collapse may result from the erectile effect of vascular distension at low lung volume that tethered the peripheral airways (Goldberg et al., 1975). The sequence of closure, airways then alveoli, allows gas exchange to continue

behind the closure. Once the alveoli are closed, atelectasis occurs and reopening atelectatic lung requires greater P_L than that required for reopening closed airways.

When closing capacity becomes near to FRC (**Figure 2**), the likelihood of tidal expiratory flow limitation (EFL) increases with the ease of airways to get closed. In normal subjects, any increase in expiratory driving pressure (alveolar pressure minus atmospheric pressure) is followed by an increase in expiratory flow for a given lung volume. EFL occurs whenever the expiratory flow does not increase after an increase in expiratory driving pressure. This feature is the expression of airway collapse that occurs when the intraluminal pressure of the airways is lower than the external pressure, which is the pleural pressure. Tidal EFL heralds airway closure. Its measurement can be done by the atmospheric method that consists in changing abruptly the airway-to-atmospheric pressure gradient over one breath.

In normal subjects under mechanical ventilation and general anesthesia, airway closure was measured at 4.5 cm H_2O P_L in some studies (Hedenstierna and McCarthy, 1980) and atelectasis was disclosed by using CT scan (Gunnarsson et al., 1989). Both airway closure and atelectasis contributed to gas exchange abnormalities that occurred early after anesthesia induction in normal subjects (Rothen et al., 1998).

AIRWAY CLOSURE IN ARDS

Causes

In patients with ARDS many factors can contribute to airway closure:

1. Intraluminal factors:
   a. The surfactant impairment in qualitative or quantitative terms will reduce the surface tension at the air-liquid interface in the terminal bronchioles and favor closure (Albert, 2012; Coudroy et al., 2019).
   b. Some fluid may accumulate in the lumen of the airways and in the alveoli, forming a foam that may completely or partly obstruct the small airways lumen (Wilson et al., 2001).
   c. Absorption atelectasis in the terminal lung units of lung regions with low ventilation-to-perfusion ratio can result from higher levels of F_IO_2 (Aboab et al., 2006).
2. Parietal factors:
   a. Some bronchoconstriction may arise from the mediators that are released during the acute inflammatory process (D'Angelo et al., 2008).
3. External factors:
   a. The loss of elastic recoil that results from elastic fibers destruction will reduce the tethering effect of the radial traction of the surrounding lung parenchyma.
   b. The airways may be compressed by the higher mass of the lung according to the sponge model of ARDS (Gattinoni et al., 2013).

Consequences

In turn, the reduction of airways lumen will increase the airway flow resistance. Indeed, an increased airway flow resistance has been described in ARDS (Wright and Bernard, 1989; Eissa et al., 1991). However, this finding was related to the reduction in aerated lung volume (Pelosi and Rocco, 2007). Functionally speaking, ARDS is a restrictive lung disease with a reduction in lung volumes. The FRC is lower than the expected normal values and the reduction in FRC goes up with the increased ARDS severity (Cressoni et al., 2015). The baby lung important concept originated from this finding (Gattinoni and Pesenti, 2005).

Another consequence of airway closure is that it would favor the repeated opening and closure of the terminal respiratory units from breath to breath that would further injure the lung. This low volume barotrauma is another mechanism of ventilator-induced lung injury (Muscedere et al., 1994). When it occurs in those lung regions near to those consolidated and not re-openable, considerable forces are applied that produce major lung stress (Mead et al., 1970).

What is totally unknown in ARDS is the role of collateral ventilation that should theoretically prevent some alveolar collapse by feeding with air through the Köhn pores step by step the neighborhood airways tree (Woolcock and Macklem, 1971; Hogg et al., 1972).

Expiratory Flow Limitation and Airway Closure

As mentioned above, tidal EFL and airway closure are distinct phenomena and their temporal occurrence is not fully understood. However, both have been described in patients with ARDS. In a very elegant study using the atmospheric method (Valta et al., 1994), tidal EFL was found in 8 out of 10 patients with ARDS under zero end-expiratory pressure (Koutsoukou et al., 2000). In a subsequent study, the same authors found that tidal EFL was present in 7 patients out of 13 on zero end-expiratory pressure and was no longer present at positive end-expiratory pressure (PEEP) 5 cm H_2O in 2 patients and 3 others at PEEP 10 cm H_2O (Armaganidis et al., 2000). It is not surprising that some patients became not flow limited on PEEP if the latter is above the critical pressure at which those airways would collapse. These early pioneering studies were done when the principles of lung-protective mechanical ventilation were not widely applied. Furthermore, a PEEP of at least 5 cm H_2O is now mandatory to define ARDS according to the Berlin definition (Ranieri et al., 2012); this minimal PEEP has to be set at the ventilator unless the upper safety limit of plateau pressure is surpassed (a condition, which occurs in late ARDS with a fibrotic lung or a very low baby lung). In the current era of lung-protective ventilation, Yonis et al. found that tidal EFL measured with the atmospheric method was present in 13 out of 65 patients with ARDS under a PEEP of 5 cm H_2O in semi-recumbent position (**Figure 3**). Patients with tidal EFL had higher body mass index, higher total PEEP, and higher ICU mortality than patients without tidal EFL for similar ventilator settings (Yonis et al., 2018). In a subsequent study on 25 patients with ARDS enrolled in two centers, tidal EFL measured with the atmospheric method was observed in 8 of

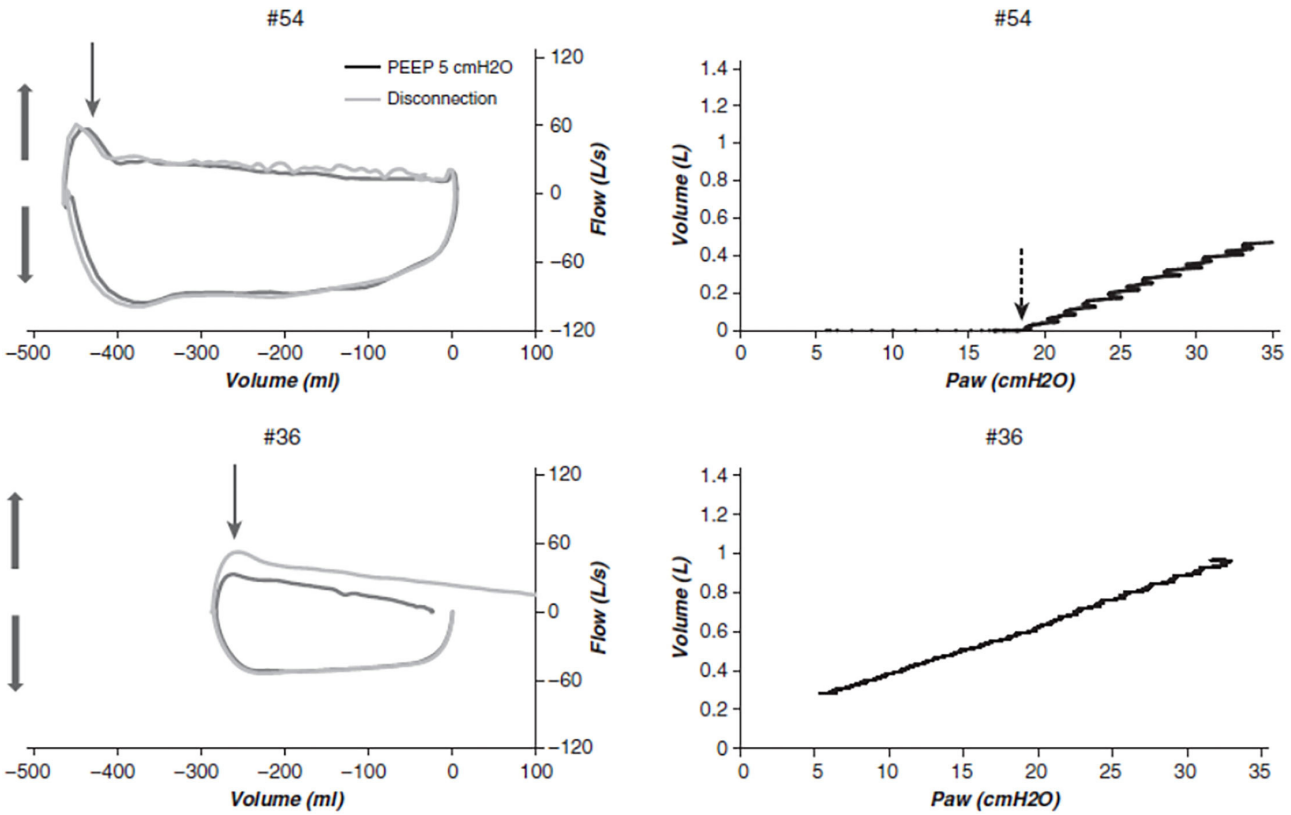

FIGURE 3 | Confrontation of flow-volume and VP relationships in two patients with acute respiratory distress syndrome (ARDS). Flow–volume and pressure–volume (PV) curves from two representative patients (#54 and #36) in the present study. **Left**: flow–volume loops during baseline mechanical ventilation and after disconnecting (thin arrows) to the atmosphere. **Upper**: A patient with expiratory flow limitation (EFL) over the whole expiratory volume, meaning that the whole breath happens in the closing volume. **Lower**: A patient without EFL. Thick vertical arrows indicate expiration (upward) and inspiration (downward) directions. The expiratory time constant was measured during disconnection as the time required to exhale 63% of the insufflated volume. **Right**: Corresponding low-flow PV curves. Upper: An early increase in pressure does not result in an increase in volume up to a point (vertical dashed arrow), at which the volume suddenly increases. This pattern is consistent with airway reopening in this patient with EFL. The airway opening pressure was determined by visual inspection, and the compliance of the PV curve from PEEP with the Paw was computed. **Lower**: A sustained increase in volume from the onset of pressurization indicates the absence of a critical airway opening pressure in this patient without EFL. Paw, airway pressure; PEEP, positive end-expiratory pressure. Reprinted with permission of the American Thoracic Society. Copyright © 2021 American Thoracic Society. All rights reserved. Cite: Yonis, Mortaza, Baboi, Mercat, Guérin/2018/Expiratory Flow Assessment in patients with ARDS. A reappraisal/AJRCCM/198/Pages 131-134. The American Journal of Respiratory and Critical Care Medicine is an official journal of the American Thoracic Society.

them (Guerin et al., 2020). Patients with tidal EFL had higher lung elastance than those without EFL (Guerin et al., 2020). It should be noted that in experimental porcine models of ARDS (saline lavage with surfactant depletion and oleic acid injection), tidal EFL was not disclosed on zero end-expiratory pressure, casting some doubts about the relevance of experimental models in their extrapolation to human ARDS (Guérin et al., 2008).

Some fresh air has recently blown up onto the inspiratory VP curves. Chen et al. showed in patients with ARDS during the low inflation of the respiratory system that in some of them, the lung volume did not change until a certain airway pressure was reached and above which the volume suddenly increased linearly with further pressure (Chen et al., 2018). A pattern like this (**Figure 3**) suggests a critical opening pressure, which was henceforth called airway opening pressure (AOP). To make this finding more robust, the authors measured the compliance of the ventilator circuit and found that the slope of the VP relationship from the onset of inflation to AOP was equal to that of the compliance of the circuit. Accordingly, from onset of inflation to AOP air circulation happens within the ventilator circuit only. It turned out that AOP was found in almost 30% of either classic ARDS or COVID-19-related ARDS (**Table 1**). The prevalence of AOP was even greater in obese, which is not surprising as obesity increased the elastic load superimposed to the chest wall (Coudroy et al., 2020). The static elastic chest wall compliance is normal in obese, i.e., the chest wall is not stiffer, it is overloaded (Behazin et al., 2010).

Simultaneous assessment of EFL and AOP in patients with ARDS at PEEP 5 in semi-recumbent position found that both are not synonymous (Guerin et al., 2020). EFL was observed in 8 patients, 7 of them exhibiting AOP, and AOP was present in 13 patients, meaning that 6 patients had AOP without EFL. Patients with AOP had higher lung dynamic elastance and higher mechanical power than patients without AOP and the

TABLE 1 | Values of airway opening pressure in non-COVID-19 or COVID-19-related acute respiratory distress syndrome.

References	Cause of ARDS	Percentage of patients with AOP (N/total)	Median or mean AOP (cmH_2O)
Chen et al. (2018)	Non-COVID-19	27 (8/30)	13
Yonis et al. (2018)	Non-COVID-19	32 (21/65)	NA
Maggiore et al. (2001)	Non-COVID-19	33 (15/45)	5–20
Guerin et al. (2020)	Non-COVID-19	52 (13/25)	9
Haudebourg et al. (2020)	Non-COVID-19	10 (3/30)	5
Grieco et al. (2020)	Non-COVID-19	30 (10/30)	NA
Haudebourg et al. (2020)	COVID-19	40 (12/30)	8
Stevic et al. (2021)	COVID-19	33 (8/24)	NA
Cour et al. (2021)	COVID-19	22 (4/18)	NA
Beloncle et al. (2020)	COVID-19	24 (6/25)	8
Grieco et al. (2020)	COVID-19	7 (2/30)	NA
Pan et al. (2020)	COVID-19	0 (0/12)	NA
Brault et al. (2020)	COVID-19	44 (12/27)	8

ARDS, acute respiratory distress syndrome; AOP, airway opening pressure; NA, not available.

same was true between patients with EFL and without EFL. The additional lung tissue resistance measured with the airway occlusion technique at the end of inspiration was higher in patients with EFL than without EFL but did not differ between patients with and without AOP, and the interrupter resistance, i.e., the resistance in the conducting airways did not differ between patients with EFL and without EFL. This may suggest that EFL occurs in the most distal parts of the small airways. AOP was also present in patients with COVID-19 related ARDS as mentioned above but EFL was not explored in them.

X-ray techniques in the Synchrotron facilities can dynamically image the lung *in vivo* in three dimensions at a resolution of 20 μm. Thanks to this technique, some light was shed on airway closure. In rabbits, small airways closure occurred more frequently when the lungs had been injured than in the animals whose lungs were normal. Furthermore, airway closure can occur at more than one site in a given small airway during mechanical ventilation (Broche et al., 2019). Moreover, small airway closure was observed either during inspiration or during expiration in different lung areas (Fardin, 2019). One limitation of this technique is that the animals received mechanical ventilation in the erect position rather than the supine or prone position.

THERAPEUTIC ASPECTS

One pharmacological approach and one ventilator setting will be discussed in this section as examples of therapeutic implications of the previous considerations.

Bronchodilator Agents

Beta-2 adrenergic receptors agonists relax the smooth muscle fiber within the airway wall of the cartilaginous airways in case of bronchoconstriction and hence increase their lumen and reduce airway resistance. If airway closure and/or EFL mostly result from bronchoconstriction, its relief should make the airways larger. Wright et al. found that aerosolized metaproterenol as compared with placebo significantly reduced air-flow resistance and increased dynamic lung compliance in 8 patients with ARDS intubated and mechanically ventilated (Wright and Bernard, 1989). Pesenti et al. found that intravenous salbutamol reduced air-flow resistance but did not change additional tissue resistance in patients with ARDS (Pesenti et al., 1993). Koutsoukou et al. found that nebulized salbutamol did not change the amount of EFL in patients with ARDS (Koutsoukou et al., 2000), a finding that is in accordance with the previous results of Guérin et al. (lung tissue resistance higher in EFL patients) (Guerin et al., 2020) and Pesenti et al. (no effect of salbutamol on lung tissue resistance) (Pesenti et al., 1993). Beta-2 adrenergic receptors agonists have not only bronchodilatating properties in broncho-constricted airways but also contribute to lung edema clearance. This results from the upregulation of the apical Na/K ATPase in type II alveolar cells. From this basis, Perkins et al. found that intravenous salbutamol significantly reduced the extravascular lung water as compared with a placebo group (Perkins et al., 2006) and improved epithelial repair (Perkins et al., 2008) in patients with ARDS. However, random controlled trials (RCTs) did not confirm these physiological benefits. One trial was stopped early for the safety concern of higher mortality in the salbutamol group (Gao Smith et al., 2012). In another trial, aerosolized albuterol did not change the patient outcome as compared with placebo (Matthay et al., 2011). Therefore, the use of beta-2 adrenergic receptors agonists is not recommended in patients with ARDS.

Setting PEEP

Positive end-expiratory pressure is an expiratory ventilator setting that allows to maintain the lung recruitment generated during the preceding inspiration or resulting from a voluntary recruitment maneuver. During the tidal breathing setting, PEEP should therefore be selected with the goal to minimize the tidal recruitment/derecruitment, i.e., atelectrauma. However, atelectrauma is linked to recruitability of the lung. In ARDS patients with a high potential of recruitment, the risk of

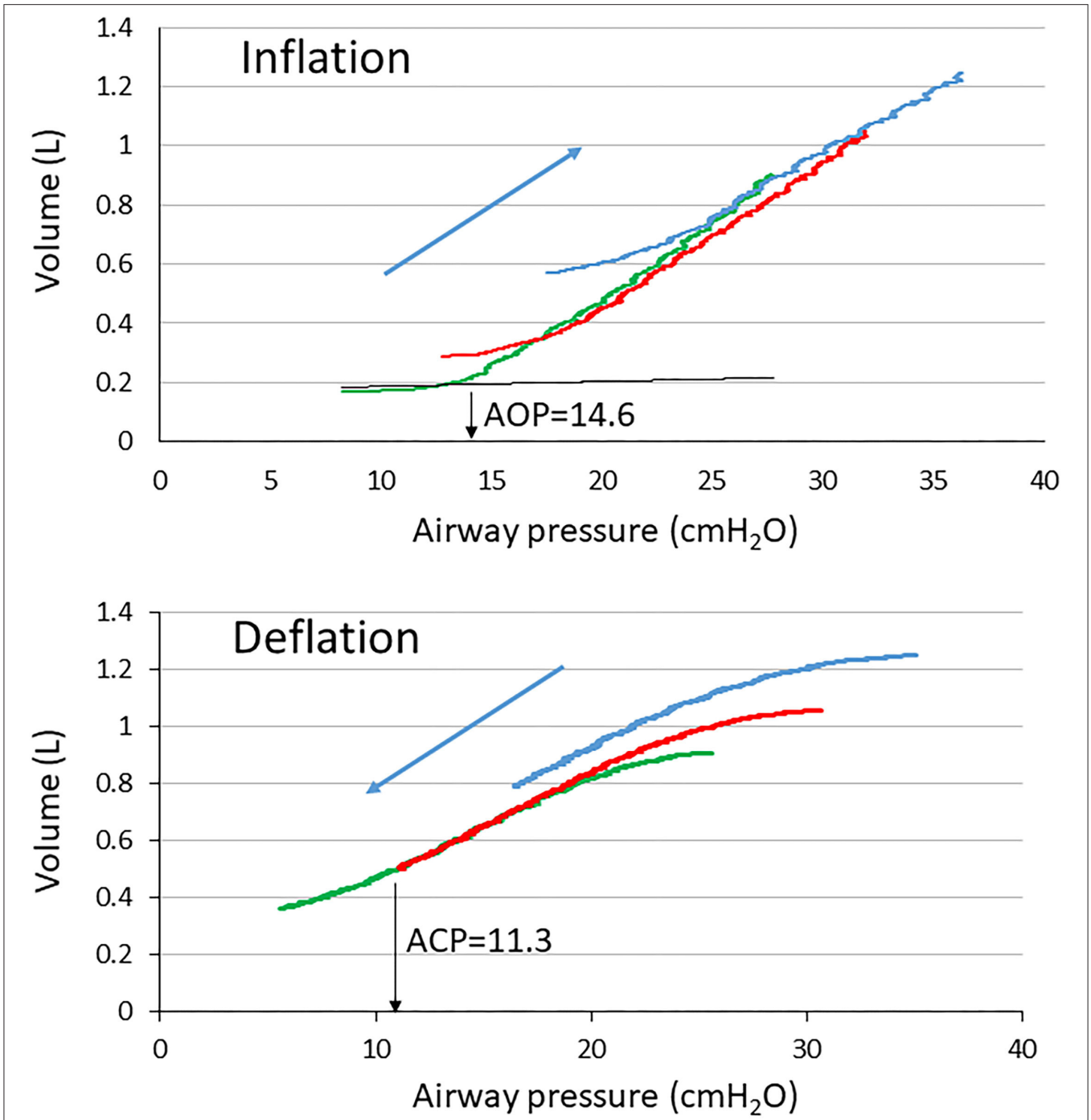

FIGURE 4 | Volume-Pressure curves of the respiratory system at PEEP of 5 (green), 10 (red), and 15 (blue) cmH_2O in a patient with ARDS with EFL. The black broken curve is the curve of the ventilator tubing used to define airway opening pressure (down black arrow AOP) at PEEP 5. ACP, airway closing pressure (down black arrow ACP).

atelectrauma is higher than in those with a lower recruitability at low PEEP (Caironi et al., 2009). Setting PEEP based on the presence of airway closure indicators is therefore attractive. As discussed above, the presence of AOP may reflect airway closure and hence be used to set PEEP. At this point, some considerations should be taken into account. Hickling provided a comprehensive mathematical model of the series of events that occurred during incremental PEEP starting from a totally degassed lung up to 50 cm H_2O plateau pressure followed by decremental PEEP from this fully recruited lung to zero volume

(Hickling, 2001). In this model, open-lung PEEP was defined as the PEEP that maintained aerated 97.5% of the alveoli in the most dependent parts of the lungs. The open-lung PEEP was made dependent on both the superimposed pressure due to gravity (0 cm H_2O in the non-dependent and 14.5 cm H_2O in the dependent lung) and the critical closing pressure set in the 0–4 cm H_2O range. The critical opening pressure was the P_L above which alveoli suddenly increased volume. Given a 18.5 cm H_2O set open-lung PEEP and a 0–20 cm H_2O range of critical opening pressure, the PEEP level needed to maximize the compliance was 19 cm H_2O during incremental limb and 16 cm H_2O during decremental PEEP, and 20 and 16 cm H_2O, respectively, for a 2 cm H_2O critical closing pressure (Hickling, 2001). Therefore, based on the computation of compliance, the open-lung PEEP is lower during deflation than inflation. It has been shown that the lung recruitment continued well above the "knee" (Gattinoni et al., 1987) or lower inflection point on the inflation VP curve (Crotti et al., 2001; Pelosi et al., 2001) and was a continuous process during insufflation, so that the point at which on VP curve the compliance started to decline would rather identify the end of recruitment (Jonson et al., 1999). However, it is likely that setting PEEP below this "knee" would be harmful to the lung as it should not prevent atelectrauma (Downie et al., 2004). Indeed, the "knee" correlates with the lower critical opening pressure (Hickling, 1998). One could argue that setting PEEP above AOP, being an opening pressure, makes sense if it is also a closing pressure, i.e., a pressure at which airways start closing. Due to the lung hysteresis, the closing pressure is different (e.g., lower) from the opening pressure. However, the identification of such a critical closing pressure was not so clear in ARDS and the "knee" was not an indication of airway closure when using VP curves at different PEEP in patients with ARDS (Maggiore et al., 2001). When performing slow deflation from zero end-expiratory pressure at constant flow up to a complete closure in an experimental model of ARDS, we found that airways remained open over a substantial range of airway pressure (Bayle et al., 2006), which is in line with the fact that EFL was not disclosed in this kind of experimental setting. However, since AOP happens and assuming it reflects airway reopening, airway closure should have occurred during the preceding expiration. In the study on 25 patients with ARDS already mentioned, deflation VP curves at constant low flow were performed (Guerin et al., 2020). In the patient shown in **Figure 4**, who had EFL at PEEP 5 cm H_2O, the AOP was 14.6 cm H_2O and increased with increasing PEEP, indicating that the closure was not overwhelmed up to PEEP 15, and indeed EFL was still present at that PEEP. On the deflation VP curve, the closing pressure at PEEP 5 disclosed from an unbiased analysis was lower than AOP (**Figure 4**).

In conclusion, airway closure happens in patients with ARDS, but the location within the airway tree and the mechanisms which originate in, need further investigation. Combining AOP and EFL assessment may help better define the pattern of airway closure and help better PEEP selection. Assuming that EFL informs about small airway collapse, for a given AOP, PEEP would be more likely to reopen the airways and maintain lung volume in the presence than in the absence of EFL.

AUTHOR CONTRIBUTIONS

CG drafted the first version of the manuscript. MC made substantial revisions. LA made substantial revisions. All authors contributed to manuscript revision, read, and approved the submitted version.

REFERENCES

Aboab, J., Jonson, B., Kouatchet, A., Taille, S., Niklason, L., and Brochard, L. (2006). Effect of inspired oxygen fraction on alveolar derecruitment in acute respiratory distress syndrome. *Intensive Care Med.* 32, 1979–1986. doi: 10.1007/s00134-006-0382-4

Acute Respiratory Distress Syndrome Network (2000). Ventilation with lower tidal volumes as compared with traditional tidal volumes for acute lung injury and the acute respiratory distress syndrome. *The Acute Respiratory Distress Syndrome Network. N. Engl. J. Med.* 342, 1301–1308. doi: 10.1056/NEJM200005043421801

Agostoni, E., and Hyatt, R. (1986). "Static behavior of the respiratory system," in *Handbook of Physiology. The Respiratory System*, eds M. P. Fishman, A. P., Mead, J. Geiger, and S. R. Williams (Bethesda: Wilkins), 113–130. doi: 10.1002/cphy.cp030309

Agostoni, E., and Mead, J. (1964). "Statics of the respiratory system," in *Handbook of Physiology*, eds Society AP (Washington, DC:, American Physiological Society), 387–409.

Albert, R. K. (2012). The role of ventilation-induced surfactant dysfunction and atelectasis in causing acute respiratory distress syndrome. *Am. J. Respir. Crit. Care Med.* 185, 702–708. doi: 10.1164/rccm.201109-1667PP

Armaganidis A., Stavrakaki-Kallergi, K., Koutsoukou, A., Lymberis, A., Milic-Emili, J., and Roussos, C. (2000). Intrinsic positive end-expiratory pressure in mechanically ventilated patients with and without tidal expiratory flow limitation. *Crit. Care Med.* 28, 3837–3842. doi: 10.1097/00003246-200012000-00015

Ashbaugh, D. G., Bigelow, D. B., Petty, T. L., and Levine, B. E. (1967). Acute respiratory distress in adults. *Lancet* 2, 319–323. doi: 10.1016/S0140-6736(67)90168-7

Aublanc, M., Perinel, S., and Guerin, C. (2017). Acute respiratory distress syndrome mimics: the role of lung biopsy. *Curr. Opin. Crit. Care* 23, 24–29. doi: 10.1097/MCC.0000000000000373

Bayle, F., Guérin, C., Debord, S., Badet, M., Lemasson, S., Poupelin, J.-C., et al. (2006). Assessment of airway closure from deflation lung volume-pressure curve: sigmoidal equation revisited. *Intensive Care Med.* 32, 894–898. doi: 10.1007/s00134-006-0160-3

Behazin, N., Jones, S. B., Cohen, R. I., and Loring, S. H. (2010). Respiratory restriction and elevated pleural and esophageal pressures in morbid obesity. *J. Appl. Physiol.* 108, 212–218. doi: 10.1152/japplphysiol.913 56.2008

Bellani, G., Laffey, J. G., Pham, T., Fan, E., Brochard, L., Esteban, A., et al. (2016). Epidemiology patterns of care, and mortality for patients with acute respiratory distress syndrome in intensive care units in 50 countries. *JAMA* 315, 788–800. doi: 10.1001/jama.2016.0291

Beloncle, F. M., Pavlovsky, B., Desprez, C., Fage, N., Olivier, P. Y., Asfar, P., (2020). Recruitability and effect of PEEP in SARS-Cov-2-associated acute respiratory distress syndrome. *Ann. Intensive Care* 10, 55. doi: 10.1186/s13613-020-00675-7

Bindslev, L., Hedenstierna, G., Santesson, J., Norlander, O., and Gram, I. (1980). Airway closure during anaesthesia, and its prevention by positive end expiratory pressure. *Acta Anaesthesiol. Scand.* 24, 199–205. doi: 10.1111/j.1399-6576.1980.tb01534.x

Brault, C., Zerbib, Y., Kontar, L., Fouquet, U., Carpentier, M., Metzelard, M., (2020). COVID-19- versus non-COVID-19-related acute respiratory distress syndrome: differences and similarities. *Am. J. Respir. Crit. Care Med.* 202, 1301–1304.

Broche, L., Pisa, P., Porra, L., Degrugilliers, L., Bravin, A., Pellegrini, M., et al. (2019). Individual airway closure characterized *in vivo* by phase-contrast CT imaging in injured rabbit lung. *Crit. Care Med.* 47, e774–e781. doi: 10.1097/CCM.0000000000003838

Caironi, P., Cressoni, M., Chiumello, D., Ranieri, M., Quintel, M., Russo, S. G., et al. (2009). Lung opening and closing during ventilation of acute respiratory distress syndrome. *Am. J. Respir. Crit. Care Med.* 181, 578–586. doi: 10.1164/rccm.200905-0787OC

Cavagna, G. A., Stemmler, E. J., and DuBois, A. B. (1967). Alveolar resistance to atelectasis. *J. Appl. Physiol.* 22, 441–452. doi: 10.1152/jappl.1967.22.3.441

Chen, L., Del Sorbo, L., Grieco, L. G., Shklar, B., Junhasavasdikul, D., Telias, I., et al. (2018). Airway closure in acute respiratory distress syndrome: an underestimated and misinterpreted phenomenon. *Am. J. Respir. Crit. Care Med.* 197, 132–135. doi: 10.1164/rccm.201702-0388LE

Copin, M. C., Parmentier, E., Duburcq, T., Poissy, J., Mathieu, D., Lille, C.-I., et al. (2020). Time to consider histologic pattern of lung injury to treat critically ill patients with COVID-19 infection. *Intensive Care Med.* 46, 1124–1126. doi: 10.1007/s00134-020-06057-8

Coudroy, R., Lu, C., Chen, L., Demoule, A., and Brochard, L. (2019). Mechanism of airway closure in acute respiratory distress syndrome: a possible role of surfactant depletion. *Intensive Care Med.* 45, 290–291. doi: 10.1007/s00134-018-5501-5

Coudroy, R., Vimpere, D., Aissaoui, N., Younan, R., Bailleul, C., Couteau-Chardon, A., et al. (2020). Prevalence of complete airway closure according to body mass index in acute respiratory distress syndrome. *Anesthesiology* 133, 867–878. doi: 10.1097/ALN.0000000000003444

Cour, M., Bussy, D., Stevic, N., Argaud, L., and Guerin, C. (2021). Differential effects of prone position in COVID-19-related ARDS in low and high recruiters. *Intensive Care Med.* 47, 1044–1046.

Cressoni, M., Cadringher, P., Chiurazzi, C., Amini, M., Gallazzi, E., Marino, A., et al. (2015). Lung inhomogeneity in patients with acute respiratory distress syndrome. *Am. J. Respir. Crit. Care Med.* 189, 149–158. doi: 10.1164/rccm.201308-1567OC

Crotti, S., Mascheroni, D., Caironi, P., Pelosi, P., Ronzoni, G., Mondino, M., et al. (2001). Recruitment and derecruitment during acute respiratory failure: a clinical study. *Am. J. Respir. Crit. Care Med.* 164, 131–140. doi: 10.1164/ajrccm.164.1.2007011

D'Angelo, E., Koutsoukou, A., Della Valle, P., Gentile, G., and Pecchiari, M. (2008). Cytokine release, small airway injury, and parenchymal damage during mechanical ventilation in normal open-chest rats. *J. Appl. Physiol.* 104, 41–49. doi: 10.1152/japplphysiol.00805.2007

Downie, J. M., Nam, A. J., and Simon, B. A. (2004). Pressure-volume curve does not predict steady-state lung volume in canine lavage lung injury. *Am. J. Respir. Crit. Care Med.* 169, 957–962. doi: 10.1164/rccm.200305-614OC

Eissa, N. T., Ranieri, V. M., Corbeil, C., Chasse, M., Braidy, J., and Milic-Emili, J. (1991). Effects of positive end-expiratory pressure, lung volume, and inspiratory flow on interrupter resistance in patients with adult respiratory distress syndrome. *Am. Rev. Respir. Dis.* 144, 538–543. doi: 10.1164/ajrccm/144.3_Pt_1.538

Fanton, L., Nahmani, I., Epain, M., Advenier, A. S., Cour, M., Meyronet, D., et al. (2021). Forensic autopsy-confirmed COVID-19-induced out-of-hospital cardiac arrest. *Ann. Transl. Med.* 2021 9, 1715. doi: 10.21037/atm-21-3918

Fardin, L. (2019). *In-vivo Dynamic 3D Phase-Contrast Microscopy: A Novel Tool to Investigate the Mechanisms of Ventilator-Induced Lung Injury, European Synchrotron Radiation Facility*, Grenoble. Grenoble.

Fox, S. E., Akmatbekov, A., Harbert, J. L., Li, G., Quincy Brown, J., and Vander Heide, R. S. (2020). Pulmonary and cardiac pathology in African American patients with COVID-19: an autopsy series from New Orleans. *Lancet Respir. Med.* 8, 681–686. doi: 10.1016/S2213-2600(20)30243-5

Gao Smith, F., Perkins, G. D., Gates, S., Young, D., McAuley, D. F., Tunnicliffe, W., et al. (2012). Effect of intravenous beta-2 agonist treatment on clinical outcomes in acute respiratory distress syndrome (BALTI-2): a multicentre, randomised controlled trial. *Lancet* 379, 229–235. doi: 10.1016/S0140-6736(11)61623-1

Gattinoni, L., Mascheroni, D., Basilico, E., Foti, G., Pesenti, A., and Avalli, L. (1987). Volume/pressure curve of total respiratory system in paralysed patients: artefacts and correction factors. *Intensive Care Med.* 13, 19–25. doi: 10.1007/BF00263552

Gattinoni, L., and Pesenti, A. (2005). The concept of "baby lung". *Intensive Care Med.* 31, 776–784. doi: 10.1007/s00134-005-2627-z

Gattinoni, L., Pesenti, A., and Carlesso, E. (2013). Body position changes redistribute lung computed-tomographic density in patients with acute respiratory failure: impact and clinical fallout through the following 20 years. *Intensive Care Med.* 39, 1909–1915. doi: 10.1007/s00134-013-3066-x

Glaister, D. H., Schroter, R. C., Sudlow, M. F., and Milic-Emili, J. (1973). Bulk elastic properties of excised lungs and the effect of a transpulmonary pressure gradient. *Respir. Physiol.* 17, 347–364. doi: 10.1016/0034-5687(73)90009-1

Goldberg, H. S., Mitzner, W., Adams, K., Menkes, H., Lichtenstein, S., and Permutt, S. (1975). Effect of intrathoracic pressure on pressure-volume characteristics of the lung in man. *J. Appl. Physiol.* 38, 411–417. doi: 10.1152/jappl.1975.38.3.411

Grasselli, G., Tonetti, T., Protti, A., Langer, T., Girardis, M., Bellani, G., et al. (2020). Pathophysiology of COVID-19-associated acute respiratory distress syndrome: a multicentre prospective observational study. *Lancet Respir. Med.* 8, 1201–1208. doi: 10.1016/S2213-2600(20)30370-2

Greaves, I. A., Hildebrandt, J., and Hoppin, J. F. G. (1986). "Micromechanics of the lung," in *Handbook of Physiology*, ed Society AP (Baltimore: Williams and Wilkins), 217–232. doi: 10.1002/cphy.cp030314

Grieco, D.L., Bongiovanni, F., Chen, L., Menga, L. S., Cutuli, S. L., and Pintaudi, G., (2020). Respiratory physiology of COVID-19-induced respiratory failure compared to ARDS of other etiologies. *Crit. Care.* 24, 529. doi: 10.1186/s13054-020-03253-2

Guerin, C., Bayle, F., Leray, V., Debord, S., Stoian, A., Yonis, H., et al. (2015a). Open lung biopsy in nonresolving ARDS frequently identifies diffuse alveolar damage regardless of the severity stage and may have implications for patient management. *Intensive Care Med.* 41, 222–230. doi: 10.1007/s00134-014-3583-2

Guerin, C., Terzi, N., Galerneau, L. M., Mezidi, M., Yonis, H., Baboi, L., Kreitmann, L., et al. (2020). Lung and chest wall mechanics in patients with acute respiratory distress syndrome, expiratory flow limitation, and airway closure. *J. Appl. Physiol.* 128, 1594–1603. doi: 10.1152/japplphysiol.00059.2020

Guerin, C., Thompson, T., and Brower, R. (2015b). The ten diseases that look like ARDS. *Intensive Care Med.* 41, 1099–1102. doi: 10.1007/s00134-014-3608-x

Guérin, Levrat, A., Pontier, S., and Annat, G. (2008). A study of experimental acute lung injury in pigs on zero end-expiratory pressure. *Vet. Anaesth. Analg.* 35, 122–131. doi: 10.1111/j.1467-2995.2007.00363.x

Gunnarsson, L., Strandberg, A., Brismar, B., Tokics, L., Lundquist, H., and Hedenstierna, G. (1989). Atelectasis and gas exchange impairment during enflurane/nitrous oxide anaesthesia. *Acta Anaesthesiol. Scand.* 33, 629–637. doi: 10.1111/j.1399-6576.1989.tb02981.x

Haudebourg, A. F., Perier, F., Tuffet, S., de Prost, N., Razazi, K., Dessap A. M., et al. (2020) Respiratory Mechanics of COVID-19- versus Non-COVID-19-associated acute respiratory distress syndrome. *Am. J. Respir. Crit. Care Med.* 202, 287–290.

Hedenstierna, G., and McCarthy, G. S. (1980). Airway closure and closing pressure during mechanical ventilation. *Acta Anaesthesiol. Scand.* 24, 299–304. doi: 10.1111/j.1399-6576.1980.tb01552.x

Hickling, K. G. (1998). The pressure-volume curve is greatly modified by recruitment. a mathematical model of ARDS lungs. *Am. J. Respir. Crit. Care Med.* 158, 194–202. doi: 10.1164/ajrccm.158.1.9708049

Hickling, K. G. (2001). Best compliance during a decremental, but not incremental, positive end-expiratory pressure trial is related to open-lung positive end-expiratory pressure: a mathematical model of acute respiratory distress syndrome lungs. *Am. J. Respir. Crit. Care Med.* 163, 69–78. doi: 10.1164/ajrccm.163.1.9905084

Hogg, W., Brunton, J., Kryger, M., Brown, R., and Macklem, P. (1972). Gas diffusion across collateral channels. *J. Appl. Physiol.* 33, 568–575. doi: 10.1152/jappl.1972.33.5.568

Jonson, B., Richard, J. C., Straus, C., Mancebo, J., Lemaire, F., and Brochard, L. (1999). Pressure-volume curves and compliance in acute lung injury: evidence

of recruitment above the lower inflection point. *Am. J. Respir. Crit. Care Med.* 159, 1172–1178. doi: 10.1164/ajrccm.159.4.9801088

Katzenstein, A. L., Bloor, C. M., and Leibow, A. A. (1976). Diffuse alveolar damage–the role of oxygen, shock, related factors. a review. *Am. J. Pathol.* 85, 209–228.

Koutsoukou, A., Armaganidis, A., Stavrakaki-Kallergi, C., Vassilakopoulos, T., Lymberis, A., Roussos, C., et al. (2000). Expiratory flow limitation and intrinsic positive end-expiratory pressure at zero positive end-expiratory pressure in patients with adult respiratory distress syndrome. *Am. J. Respir. Crit. Care Med.* 161, 1590–1596. doi: 10.1164/ajrccm.161.5.9904109

Libby, L. J., Gelbman, B. D., Altorki, N. K., Christos, P. J., and Libby, D. M. (2014). Surgical lung biopsy in adult respiratory distress syndrome: a meta-analysis. *Ann. Thorac. Surg.* 98, 1254–1260. doi: 10.1016/j.athoracsur.2014.05.029

Maggiore, S. M., Jonson, B., Richard, J. C., Jaber, S., Lemaire, F., and Brochard, L. (2001). Alveolar derecruitment at decremental positive end-expiratory pressure levels in acute lung injury: comparison with the lower inflection point, oxygenation, and compliance. *Am. J. Respir. Crit. Care Med*. 164, 795–801. doi: 10.1164/ajrccm.164.5.2006071

Matthay, M. A., Aldrich, J. M., and Gotts, J. E. (2020). Treatment for severe acute respiratory distress syndrome from COVID-19. *Lancet Respir. Med.* 8, 433–434. doi: 10.1016/S2213-2600(20)30127-2

Matthay, M. A., Brower, R. G., Carson, S., Douglas, I. S., Eisner, M., Hite, D., et al. (2011). Randomized, placebo-controlled clinical trial of an aerosolized beta(2)-agonist for treatment of acute lung injury. *Am. J. Respir. Crit. Care Med.* 184, 561–568. doi: 10.1164/rccm.201012-2090OC

McCarthy, D. S., Spencer, R., Greene, R., and Milic-Emili, J. (1972). Measurement of "closing volume" as a simple and sensitive test for early detection of small airway disease. *Am. J. Med.* 52, 747–753. doi: 10.1016/0002-9343(72)90080-0

Mead, J., Takishima, T., and Leith, D. (1970). Stress distribution in lungs: a model of pulmonary elasticity. *J. Appl. Physiol.* 28, 596–608. doi: 10.1152/jappl.1970.28.5.596

Muscedere, J. G., Mullen, J. B., Gan, K., and Slutsky, A. S. (1994). Tidal ventilation at low airway pressures can augment lung injury. *Am. J. Respir. Crit. Care Med.* 149, 1327–1334. doi: 10.1164/ajrccm.149.5.8173774

Pan, C., Chen, L., Lu, C., Zhang, W., Xia, J. A., and Sklar, M. C., (2020). Lung Recruitability in COVID-19-associated Acute Respiratory Distress Syndrome: A Single-Center Observational Study. *Am. J. Respir. Crit. Care Med.* 201, 1294–1297.

Pannone, G., Caponio, V. C. A., De Stefano, I. S., Ramunno, M. A., Meccariello, M., Agostinone, A., et al. (2021). Lung histopathological findings in COVID-19 disease - a systematic review. *Infect. Agents Cancer* 16:34. doi: 10.1186/s13027-021-00369-0

Pelosi, P., Goldner, M., McKibben, A., Adams, A., Eccher, G., Caironi, P., et al. (2001). Recruitment and derecruitment during acute respiratory failure: an experimental study. *Am. J. Respir. Crit. Care Med.* 164, 122–130. doi: 10.1164/ajrccm.164.1.2007010

Pelosi, P., and Rocco, P. R. (2007). Airway closure: the silent killer of peripheral airways. *Crit Care* 11:114. doi: 10.1186/cc5692

Perkins, G. D., Gao, F., and Thickett, D. R. (2008). *In vivo* and *in vitro* effects of salbutamol on alveolar epithelial repair in acute lung injury. *Thorax* 63, 215–220. doi: 10.1136/thx.2007.080382

Perkins, G. D., McAuley, D. F., Thickett, D. R., and Gao, F. (2006). The beta-agonist lung injury trial (BALTI): a randomized placebo-controlled clinical trial. *Am. J. Respir. Crit. Care Med.* 173 281–287. doi: 10.1164/rccm.200508-1302OC

Pesenti, A., Pelosi, P., Rossi, N., Aprigliano, M., Brazzi, L., and Fumagalli, R. (1993). Respiratory mechanics and bronchodilator responsiveness in patients with the adult respiratory distress syndrome. *Crit. Care Med.* 21, 78–83. doi: 10.1097/00003246-199301000-00016

Ranieri, V. M., Rubenfeld, G. D., Thompson, B. T., Fergsuon, N. D., Cladwell, E., Fan, E., et al. (2012). Acute Respiratory distress syndrome. the berlin definition. *JAMA* 307, E1–E8. doi: 10.1001/jama.2012.5669

Rothen, H. U., Sporre, B., Engberg, G., Wegenius, G., and Hedenstierna, G. (1998). Airway closure, atelectasis and gas exchange during general anaesthesia. *Br. J. Anaesth.* 81, 681–686. doi: 10.1093/bja/81.5.681

Stevic, N., Chatelain, E., Dargent, A., Argaud, L., Cour, M., and Guerin, C. (2021). Lung recruitability evaluated by recruitment-to-inflation ratio and lung ultrasound in COVID-19 acute respiratory distress syndrome. *Am. J. Respir. Crit. Care Med.* 203, 1025–1027.

Sutherland, P. W., Katsura, T., and Milic-Emili, J. (1968). Previous volume history of the lung and regional distribution of gas. *J. Appl. Physiol.* 25, 566–574. doi: 10.1152/jappl.1968.25.5.566

Thille, A. W., Esteban, A., Fernandez-Segoviano, P., Rodriguez, J. M., Aramburu, J. A., Penuelas, O., et al. (2013). Comparison of the Berlin definition for acute respiratory distress syndrome with autopsy. *Am. J. Respir. Crit. Care Med.* 187, 761–767. doi: 10.1164/rccm.201211-1981OC

Thompson, B. T., Chambers, R. C., and Liu, K. D. (2017). Acute respiratory distress syndrome. *N. Engl. J. Med.* 377, 1904–1905. doi: 10.1056/NEJMra1608077

Valta, P., Corbeil, C., Lavoie, A., Campodonico, R., Koulouris, N., Chasse, M., et al. (1994). Detection of expiratory flow limitation during mechanical ventilation. *Am. J. Respir. Crit. Care Med.* 150, 1311–1317. doi: 10.1164/ajrccm.150.5.7952558

Wilson, T. A., Anafi, R. C., and Hubmayr, R. D. (2001). Mechanics of edematous lungs. *J. Appl. Physiol.* 90, 2088–2093. doi: 10.1152/jappl.2001.90.6.2088

Woolcock, A. J., and Macklem, P. T. (1971). Mechanical factors influencing collateral ventilation in human, dog, pig lungs. *J. Appl. Physiol.* 30, 99–115. doi: 10.1152/jappl.1971.30.1.99

Wright, P. E., and Bernard, G. R. (1989). The role of airflow resistance in patients with the adult respiratory distress syndrome. *Am. Rev. Respir. Dis.* 139, 1169–1174. doi: 10.1164/ajrccm/139.5.1169

Yonis, H., Mortaza, S., Baboi, L., Mercat, A., and Guerin, C. (2018). Expiratory flow limitation assessment in patients with acute respiratory distress syndrome. a reappraisal. *Am. J. Respir. Crit. Care Med.* 198, 131–134. doi: 10.1164/rccm.201711-2326LE

Conflict of Interest: The authors declare that the research was conducted in the absence of any commercial or financial relationships that could be construed as a potential conflict of interest.

frontiers in Physiology

METHODS
published: 17 February 2022
doi: 10.3389/fphys.2022.808588

A Physical Analog to Assess Surgical Face Mask Air Flow Resistance During Tidal Ventilation

*Bruno Demoulin[1], Claude Duvivier[1], François Marchal[1] and Silvia Demoulin-Alexikova[2,3]**

[1]EA 3450 DevAH, Université de Lorraine, Vandœuvre-lès-Nancy, France, [2]Service des Explorations Fonctionnelles Respiratoires, CHU Lille, Lille, France, [3]CNRS, Inserm, CHU Lille, Institut Pasteur de Lille, U1019-UMR9017-CIIL-Centre d'Infection et d'Immunité de Lille, University of Lille, Lille, France

A large variety of disposable face masks have been produced since the onset of the COVID-19 pandemic. Decreased resistance to inspiration improves adherence to the use of the mask; the so called breathability is usually estimated by the measurement of air flow across a section of the tissue under a given pressure difference. We hypothesized that the mask pressure—flow relationship studied in conditions that mimic tidal breathing could allow a more comprehensive characterization of airflow resistance, a major determinant of mask comfort. A physical analog was made of a plaster cast dummy head connected through a pneumotachograph to a series of bellows inflated/deflated by a respirator. Pressure was measured at the mock airway opening over which the mask was carefully secured. The precision of the measurement equipment was quantified using two estimates of measurement error: repeatability coefficient (RC) and within-mask coefficient of variation (CV_{wm}). The airflow resistance of 10 surgical masks was tested on 4 different days. Resistance means did not differ significantly among four repeated measures (0.34 hPa.s.L^{-1}; 0.37 hPa.s.L^{-1}; 0.37 hPa.s.L^{-1}; and 0.37 hPa.s.L^{-1}; $p = 0.08$), the estimated RC was 0.08 hPa.s.L^{-1} [95%CI: 0.06–0.10 hPa.s.L^{-1}], and CV_{wm} was 8.7% [95%CI: 1.5–12.2%]. Multiple comparisons suggest the presence of a learning effect by which the operator reduced the error over the course of repetitive resistance measurements. Measurement precision improved considerably when the first set of measures was not taken into account [RC ~ 0.05 hPa.s.L^{-1} (95%CI: 0.03–0.06 hPa.s.L^{-1}); CV_{wm}~4.5% (95%CI: 1.9–6.1%)]. The testing of the face mask resistance (R) appears simple and highly repeatable in conditions that resemble tidal breathing, once operator training was assured. The procedure adds further to the current standard assessment of breathability and allows estimating the maximal added respiratory load, about 10–20% of the respiratory resistance reported in heathy adult subjects.

Keywords: face masks, surgical masks, breathability, COVID-19, SARS-CoV-2, pressure-flow relationship, tidal breathing, airway resistance

OPEN ACCESS

Edited by:
Lorenzo Ball, University of Genoa, Italy

Reviewed by:
Sam Bayat, Université Grenoble Alpes, France
Haipeng Liu, Coventry University, United Kingdom

****Correspondence:***
Silvia Demoulin-Alexikova
silvia.alexikova@chu-lille.fr

Specialty section:
This article was submitted to Respiratory Physiology, a section of the journal Frontiers in Physiology

Received: *03 November 2021*
Accepted: *24 January 2022*
Published: *17 February 2022*

Citation:
Demoulin B, Duvivier C, Marchal F and Demoulin-Alexikova S (2022) A Physical Analog to Assess Surgical Face Mask Air Flow Resistance During Tidal Ventilation. Front. Physiol. 13:808588. doi: 10.3389/fphys.2022.808588

INTRODUCTION

The SARS-CoV-2 pandemic has led to the generalized use of face covering materials to minimize respiratory transmission of the disease. Saliva droplet projection was identified as the major route for respiratory transmission for which surgical masks appear to provide equally efficient protection compared to face piece respirators, although with furthering the knowledge in COVID mechanisms, aerosols may also represent a possible route especially at the bedside of COVID patients, where ambient air may contain high concentration of viral particles (Sommerstein et al., 2020). In mask design, one attempts to determine an optimal compromise between efficient particulate filtration and ease of wear, referred to as breathability (Aydin et al., 2020; Ju et al., 2021), which is related to the added respiratory load. Breathability of surgical face masks usually is estimated *in vitro* from the pressure drop across a given section of the filtering tissue under conditions of unidirectional, constant air flux (Forouzandeh et al., 2021), on which recommendations are based. The end point in conceiving any protection material is optimal compromise between filtering efficiency and breathability.

During tidal breathing, the added resistance may vary with flow amplitude or direction; however, we are aware of little characterization of such properties. It would also be helpful to be able to quantify the magnitude of the added maximal load as a fraction of the subject's respiratory resistance. The fact that, in the long term, mask comfort significantly contributes to a subject's adherence to its use justifies more detailed studies of mask mechanics under conditions that resemble tidal breathing.

Such evaluation requires a set up under which the mask can be subjected to rhythmic flow changes that mimic tidal breathing, while pressure and flow are being measured. This allows the determination of mask resistance to breathing. Once validated under controlled conditions with the reference surgical face mask, we surmised that this set up could be used to test any type of face protection. This is of special interest in view of the initial non-reusable masks shortage during the first months of the SARS-CoV-2 pandemic (Lepelletier et al., 2020; Maher et al., 2020; Forouzandeh et al., 2021) that prompted the production of a variety of face protection. A recent paper proposed a computerized system to study mask breathability on a dummy head in dynamic conditions. The dynamic pressure difference across the mask was used to compare different types of materials (Yao et al., 2019). The current study is intended to go a step further, i.e., to express the mask resistance by relating pressure to flow so as to have the potential to describe its time course, flow dependence, and magnitude relative to the subject's own respiratory resistance.

The aim of this study was to determine the characteristics of surgical mask resistance using a physical analog under conditions that resemble physiological breathing and to quantify its precision under the same operating conditions over a short interval of time (repeatability). More specifically, it was intended to validate a model set up closer to real life than the current reference procedure measuring a pressure drop generated across a fabric surface at constant, unidirectional flow. This approach would also allow to estimate the maximal load to breathing offered by the mask as a fraction of the total respiratory resistance. During the tests, the mask covered the airway opening of a dummy head; standard measuring conditions, minimal leakage, and optimal reproducibility were insured by tightly fitting the mask to the cast. The resistance of a mask tissue section was also tested in order to assess breathability in conditions similar to the standard procedure (Forouzandeh et al., 2021).

MATERIALS AND METHODS

Physical Analog

The device is illustrated in **Figure 1**. The mask support system consists of a plaster cast dummy head. Nostrils and mouth were connected from behind to a time cycled, pressure limited respirator (O'nyx Plus Pierre Medical SA, France) that delivers airflow to a set of identical bellows mechanically coupled through rails and springs. Both bellows exhibit the same excursion, hence identical volume change. Valve devices triggered by the respirator determine bi-directional flow, mimicking inspiration and expiration. The respirator is set to deliver a peak pressure of 40 hPa at a frequency of 25 cycle.min^{-1} and a peak flow of 1.5 L.s^{-1} (3 L.s^{-1} peak to peak). Experiments were performed under ambient conditions of pressure (950 hPa), temperature (22°C), and relative humidity (40%).

Pressure was measured at four different points behind the mask using a Honeywell 176 PC 14HD1 transducer previously calibrated using a slanted manometer. Flow was measured in the circuit close to the plaster head (**Figure 1**) using a Fleisch # 2 pneumotachograph (Metabo Lausanne Suisse; Fleisch, 1956). The device is linear within 5 L.s^{-1} peak to peak. The flowmeter was attached to an identical pressure transducer and calibrated by the integral method (Varene et al., 1974). The frequency response of both transducers is matched within 1% of amplitude and 2° of phase up to 30 Hz (Duvivier et al., 1991). Pressure (P) and flow (V') signals were sampled at a frequency of 40 Hz and passed through a digital band pass filters (0.1–5 Hz) and fed to a lab-chart recorder (Power Lab 16/30 AD Instruments United States). The signals were continuously displayed on a screen during the acquisition period and stored on disk for later analysis.

Protocol

A set of 10 surgical face masks (Foshan Xinbao Technology Co. Ltd., China, Zhejiang Longde Pharmaeutical Co. Ltd., China) was tested on the dummy head on 4 separate days by the same operator. The order of measurements was randomly determined prior to the study and kept throughout. The mask was applied to cover nose and mouth, the flexible metallic edge pinched over the nose bridge, and elastic bands adjusted around each ear lobe and retracted together at the back. The mask contours were then carefully secured on the plaster using adhesive tape (3M Micropore Professional Care 3M Deutschland GmbH). The mask tissue surface area available to airflow was 180 cm^2. Trials were first performed to examine mask contours for gross air leaks. Thereafter, the P – V′ acquisition was tracked for at least 1 min.

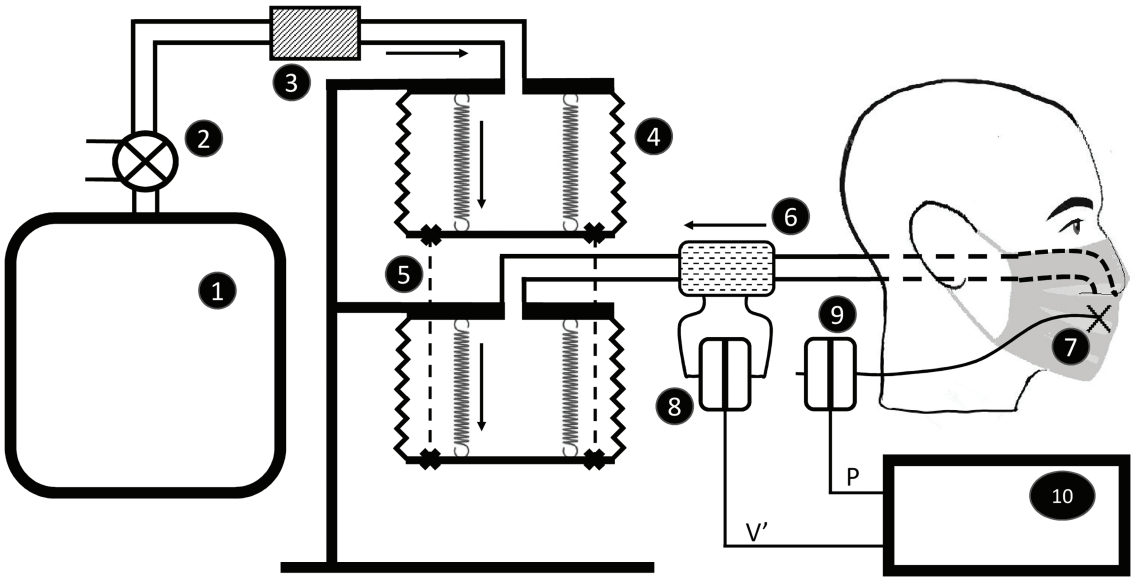

FIGURE 1 | Sketch of the apparatus to measure resistance of the face mask secured on the dummy head. The respirator (1) is connected through a valve (2) and a resistor (3) to bellows (4) attached through rails and springs (5). The second bellow is connected through a pneumotachograph (6) to the mock airways. Pressure is measured at four different points behind the mask (7). Flow (8) and pressure (9) signals are fed to a chart lab recorder (10). Dark arrows indicate the direction of flow during inspiration.

Data Analysis

Resistance Computation

Each acquisition period included more than 2,400 sets of P and V′. The mask resistance (R) was computed from each set as the ratio of P to V′. Those V′ values ranging from −0.2 to +0.2 $L.s^{-1}$ were filtered out, since R computations using V′ close to 0 generated artefacts (e.g., **Figure 2**).

Among different models used to describe airway/respiratory resistance, a convenient and valuable expression relates R to V′ by linear regression (Peslin et al., 1992). This empirical approach allows to take into account both linear (K1) and non-linear (K2) components of R such that:

$$R = K1 + K2 \times |V'|$$

K1 may also be known as the resistance extrapolated at zero flow and K2 includes its flow dependent component, if any. The latter may frequently be neglected under low ventilation regimen but may be worth taking into account when ventilation is increased such as during exercise or cough. The analysis was performed on the whole data set as well as separately on inspiration and expiration using a Borland C++ program specifically developed to correlate resistance to flow.

Statistics

Statistical analysis was performed using Prism (GraphPad Software, LLC). For a given trial, the mean values of R, K1, and K2 were obtained. All intermediate calculations were carried out to full precision and rounded to three decimal places at the reporting stage. In order to estimate precision of mask resistance measurement performed by equipment, several estimates of measurement error have been assessed. Repeatability coefficient (RC) was used to express the precision in dimensional and within-mask coefficient of variation (CV_{wm}) in non-dimensional terms.

Repeatability coefficient was calculated from the within-mask variance estimated using repeated measures ANOVA. It is the maximum difference that is likely to occur between repeated measurements which is defined by

$$1.96 \times \sqrt{2} \times s_w$$

Where s_w is the within-mask SD, a square root of within-mask variance (Bland and Altman, 1996; Bartlett and Frost, 2008).

In order to check whether the measurement errors for each mask do not depend on the magnitude of the measurement, we performed Kendall correlation between SD for each mask (SD_m) and each mask mean ($Mean_m$). Assumption of sphericity was checked using Mauchly's test. In the case of violation of sphericity assumption, the degrees of freedom and *p*-value were adjusted using Greenhouse–Geisser epsilon correction. The normality of residuals was tested using the Kolmogorov–Smirnov test. In the case of violation of normality assumption, RC was calculated from within subject variance estimated from repeated measures of ANOVA, but CIs for RC were calculated using bootstrapping technique (Bartlett and Frost, 2008).

CV_{wm} was calculated using the root mean square method (Hyslop and White, 2009) as

$$CV_{wm}(\%) = 100 \times \sqrt{\left[\frac{1}{n}\sum CV_m^2\right]}$$

Where CV_m^2 is the squared coefficient of variation of each mask's repeated measurements and n is the number of repeated measurements.

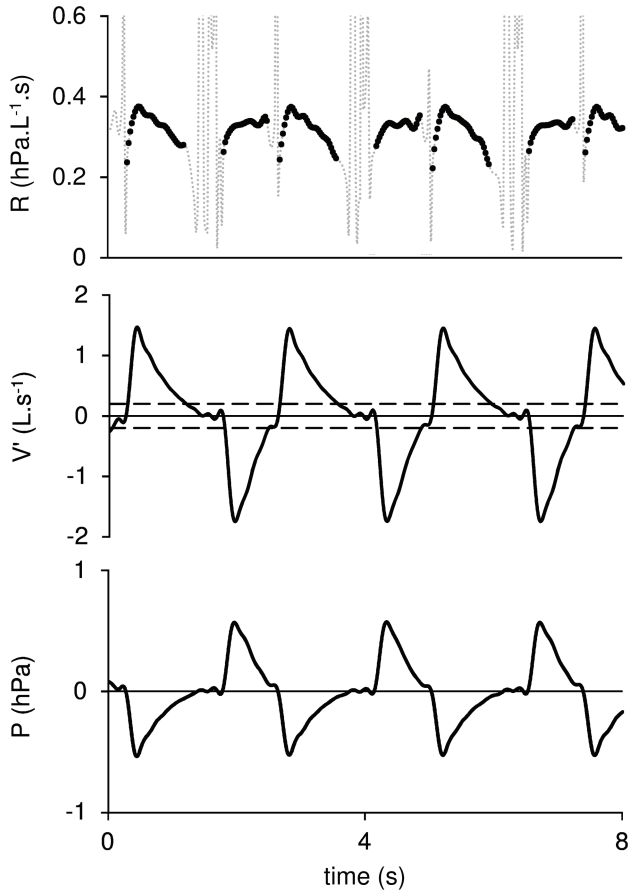

FIGURE 2 | Mask resistance (R), Flow (V′), and pressure (P) are plotted against time. The dotted lines on R tracing correspond to data rejected from the computation. Horizontal broken lines on V′ indicate the −0.2 L.s^{-1} to +0.2 L.s^{-1} interval beyond which R values are rejected. Positive V′ values indicate inspiration.

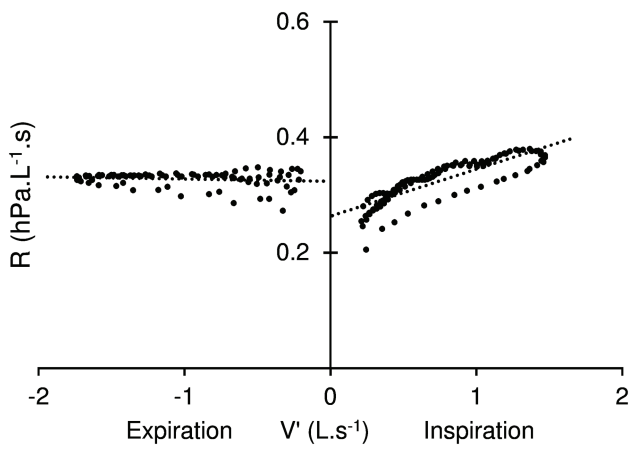

FIGURE 3 | Resistance (R) – Flow (V′) diagram. Positive flow dependence, more apparent in inspiration (positives values of V′) than expiration is indicated by dotted line. K1 (the resistance extrapolated at zero flow) is represented by the intersection with V′ axis. Also note some looping in the relationship during both inspiration and expiration.

The effect of V′ direction was estimated by comparing respectively R, K1, and K2 between inspiration and expiration using Student paired *t*-test.

Additional Experiment: Tissue Airflow Resistance and Breathability

At the end of repeated measurements of mask resistance, breathability was also assessed under conditions similar to the standard procedure. A section of each mask was tightly fitted to a circular—26 cm^2—support, so that the measurement could be performed on the fabric under leak proof conditions. The support was connected to the respirator circuit in place of the dummy head and the acquisition performed as previously described. A statistical comparison was performed between this measurement and the 4th series of whole masks, after correcting for the estimated surface area available to flow (180 cm^2).

RESULTS

P, V′, and R are plotted against time in **Figure 2**. The dotted lines in the R tracing indicate values discarded from the computation, i.e., corresponding to the V′ interval from −0.2 L.s^{-1} to +0.2 L.s^{-1}. R is plotted against V′ in **Figure 3**. Positive flow dependence is also indicated, mainly in inspiration. In addition, some looping between R and V′ is apparent in both inspiration and expiration.

The mask resistance data are summarized in **Table 1**. There were no evidence of relationship between measurement error and the magnitude of the measurement of each mask (Kendall's $\tau = -0.25$; $p = 0.082$). Overall residuals were normally distributed and Greenhouse–Geisser epsilon correction was applied as sphericity assumption was violated.

Repeated measures ANOVA did not show a significant difference among the four sets of measures ($F = 3.1$; $p = 0.085$). The estimated within-mask variance and s_w were 0.0008 hPa.s.L^{-1} and 0.028 hPa.s.L^{-1}, respectively. The value of RC was 0.078 hPa.s.L^{-1} [95%CI: 0.058–0.098 hPa.s.L^{-1}] and that of CV_{wm} was 8.734% [95%CI: 1.535–12.255%].

Multiple comparisons were performed in order to analyze all paired differences between resistance means. As can be seen from **Table 2**, the absolute mean differences between 1st set and any subsequent set are at least 3.5-fold greater compared to paired differences among sets 2 to 4.

When calculating the precision estimates from set 2–4, the estimated within-mask variance and s_w were 0.0003 hPa.s.L^{-1} and 0.017 hPa.s.L^{-1}. The value of RC was 0.047 hPa.s.L^{-1} [95%CI: 0.032–0.062 hPa.s.L^{-1}] and that of CV_{wm} was 4.525% [95%CI: 1.906–6.108%].

The use of a mask tissue section showed significantly higher resistance compared to the 4th set of repeated measures ($t = 2.7$; $p = 0.024$).

When computing mask resistance separately during the two phases of the V′ cycle for sets 2–4, both R and K1 were found slightly but systematically lower in inspiration compared to expiration that resulted in a significant difference (R: $t = -9.8$;

TABLE 1 | Repeated measurements of mean resistance (hPa.s.L^{-1}) for 10 masks (Set 1–4) and their tissue airflow resistance (Tissue).

Mask #	Tissue	Set 1	Set 2	Set 3	Set 4	$Mean_m$	SD_m	CV_m
1	0.475	0.431	0.427	0.420	0.402	0.396	0.013	0.033
2	0.426	0.281	0.390	0.430	0.387	0.387	0.064	0.164
3	0.422	0.408	0.409	0.390	0.404	0.384	0.008	0.022
4	0.432	0.304	0.413	0.388	0.357	0.379	0.047	0.124
5	0.372	0.395	0.400	0.393	0.386	0.386	0.006	0.0153
6	0.382	0.351	0.387	0.342	0.402	0.387	0.0314	0.081
7	0.376	0.404	0.395	0.387	0.394	0.338	0.007	0.021
8	0.368	0.214	0.296	0.298	0.313	0.295	0.045	0.152
9	0.351	0.297	0.325	0.312	0.302	0.311	0.013	0.041
10	0.396	0.308	0.311	0.312	0.324	0.338	0.007	0.021
$Mean_s$	0.400	0.338	0.375	0.367	0.367	0.360	0.024	0.067
SD_s	0.038	0.070	0.047	0.047	0.040	N/A	N/A	N/A

Each row corresponds to the repeated measures of one mask. $Mean_s$ (SD_s) = mean (SD) of each set; $Mean_{wm}$ (SD_{wm}, CV_{wm}) = mean (SD, CV) of each mask, calculated from set 1–4, calculated from set 1. All intermediate calculations were carried out to full precision and rounded to three decimal places at the reporting stage.

TABLE 2 | Pairwise comparisons matrix for resistance measurements.

Paired comparisons	Mean 1	Mean 2	Mean difference	95% CI of mean difference
Set 1 vs. Set 2	0.339	0.375	−0.036	−0.08225 to 0.01055
Set 1 vs. Set 3	0.339	0.367	−0.028	−0.08446 to 0.02852
Set 1 vs. Set 4	0.339	0.367	−0.028	−0.07444 to 0.01925
Set 2 vs. Set 3	0.375	0.367	0.008	−0.01351 to 0.02926
Set 2 vs. Set 4	0.375	0.367	0.008	−0.01398 to 0.03048
Set 3 vs. Set 4	0.367	0.367	0.0004	−0.02804 to 0.02879

$p = 0.00001$, K1: $t = -14.9$; $p = 0.0001$) of these variables between the two phases of the respiratory cycle (**Table 3**). Concerning K2, this variable was significantly higher in inspiration compared to expiration ($t = 21.4$; $p = 0.0000001$).

DISCUSSION

Surgical mask air flow resistance has been measured on a dummy head under conditions that simulate quiet tidal breathing in an adult subject. Estimated precision of mask resistance measurement appear satisfactory, at least once adequate sealing procedure was assured. In fact, the first series R was lower than any of the further sets that all recovered the same 0.37 hPa.L^{-1}.s value.

The model described here resembles the Sheffield dummy head that has been developed for the validation of filtering face pieces and respirators in the context of airway protection of workers in dusty environments (Mogridge et al., 2016). To the best of our knowledge, the standard testing for tissue face mask breathability measures the pressure drop across a given tissue surface area, while a constant air flow is passed through (Konda et al., 2020; Zangmeister et al., 2020; Cortes et al., 2021; Forouzandeh et al., 2021). According to guidelines currently available in this country (AFNOR SPEC S76-001:2020), breathability should correspond to a flow at least 96 L.s^{-1} through a tissue area of 1 m^2 under a differential pressure of 1 hPa; that is, a resistance of 104 hPa.s.L^{-1}.cm^{-2}. From the current average measurements (**Table 1**), the resistance would be 65.2 hPa.s.L^{-1}.cm^{-2} for the mask tested *in situ* and 72.0 hPa.s.L^{-1}.cm^{-2} for the isolated tissue. Corresponding breathability would be 153.35 L.m^2.s^{-1} and 138.9 L.m^2.s^{-1}, respectively. Both estimates are largely above the recommended threshold (96 L.m^2.s^{-1}), but the whole mask value is significantly larger. This could be explained by small air leaks still occurring with measurement on the dummy head, despite the great care taken to insure optimal adhesion. Another possible explanation would be related to some imprecision in determining the exact mask surface area available to airflow on the model. Alternatively, a different dynamic behavior between tissue alone and whole mask during the measurement could help explain the finding, as developed below.

The average 0.37 hPa.s.L^{-1} mask resistance measured here during simulated tidal breathing would represent an increased airway resistance of 20.6 and 16.8%, respectively in healthy adult males and females, based upon recent plethysmographic measurements (Koch et al., 2013). A recent plethysmographic study in a similar population of healthy adults found an almost doubling of the airway resistance measured through a surgical mask (Lassing et al., 2020). For the sake of measuring conditions, however, the airway opening was connected to the breathing apparatus through a rigid face mask, likely excluding a significant surgical mask area available to airflow, hence magnifying the total airway resistance. Nevertheless, that the surgical mask resistance may impede breathing is also supported by measurements of FEV1 (Fikenzer et al., 2020). We are unaware of further direct assessment of airway resistance when breathing through a surgical face mask, but *in vivo* measurements using rhinomanometry and rhinospirometry in healthy subjects breathing through N95 respirators demonstrated a doubling of the nasal resistance (Lee and Wang, 2011). The data are in keeping with an airway pressure of 2–5 hPa reported at a

TABLE 3 | The mask resistance (R), the mask resistance extrapolated at zero flow (K1) and flow dependent component of resistance (K2) during inspiration and expiration, expressed as mean calculated from set 1–4.

Mask #	R		K1		K2	
	Inspiration	Expiration	Inspiration	Expiration	Inspiration	Expiration
1	0.419	0.422	0.345	0.396	0.104	−0.026
2	0.370	0.375	0.289	0.351	0.109	−0.025
3	0.401	0.405	0.322	0.381	0.105	−0.024
4	0.363	0.369	0.287	0.355	0.094	−0.014
5	0.392	0.395	0.329	0.372	0.088	−0.023
6	0.369	0.373	0.303	0.355	0.090	−0.019
7	0.394	0.397	0.326	0.374	0.084	−0.023
8	0.279	0.282	0.221	0.264	0.082	0.018
9	0.306	0.312	0.242	0.312	0.085	−0.0003
10	0.312	0.316	0.251	0.308	0.083	−0.008
Mean	0.360	0.365*	0.291	0.347*	0.092	−0.018*
SD	0.046	0.046	0.042	0.040	0.010	0.008

*All intermediate calculations were carried out to full precision and rounded to three decimal places at the reporting stage. *R, K1, and K2 inspiration vs. expiration $p<0.0001$.*

peak flow of $1.4\,L.s^{-1}$ in subjects breathing through respirators masks (Louhevaara, 1984).

Performing repeated measurements of mask resistance using the current analog highlights several important points. Assuming no difference in resistance between 10 surgical masks from the same manufacturer, the estimates of repeatability should reflect precision of the measurements, provided they are repeated under the same conditions (Bland and Altman, 1999; Hyslop and White, 2009). The maximum difference that is likely to occur between four repeated mask resistance measurements (RC) was estimated to be $0.08\,hPa.s.L^{-1}$ [95%CI: 0.06–$0.1\,hPa.s.L^{-1}$] and the CV_{wm} was estimated to be 9% [95%CI: 1.5–12.2%] pointing to the fact that the precision of the measurement process was satisfactory. However, analysis of all paired comparisons between resistance measures revealed that: (a) absolute differences between 1st set of measures are considerably higher (at least 3.5-fold) compared to any subsequent set and (b) all mean differences between 1st and any subsequent set were negative (**Table 2**). This suggests the existence of a learning effect by which the operator reduced the error over the course of repetitive resistance measurements. Indeed, measurement precision improved considerably when the first set of measures was not taken into account in the calculation of repeatability [$RC \sim 0.047\,hPa.s.L^{-1}$ (95%CI: 0.03–$0.06\,hPa.s.L^{-1}$); $CV_{wm} \sim 4.5\%$ (95%CI: 1.9–6.1%)]. Altogether, these results suggest that a great part of measurement error was operator-related, i.e., caused by imperfections in the sealing procedure. Owing to the fact that the mean resistance of the first series was lower than any further set (**Table 1**) and the mean difference between 1st and any subsequent was negative (**Table 2**), it is suggested that imperfections in the sealing procedure resulted from air leaks occurring during measurement. These observations highlight the requirement for a mask fixation training.

With the current analog, a careful examination of the pressure flow relationship can be done under conditions that resemble tidal breathing. The difference between inspiration and expiration was significant for the resistance, even more so for K1, the resistance extrapolated at zero flow (**Table 3**). In addition, some degree of looping of the resistance flowdiagram—such as shown in **Figure 3**—was usually apparent. These observations, together with the significant K2 difference between inspiration and expiration may appear somewhat counterintuitive, should flow be the sole determinant to the time variation of resistance. In fact, some change in mask shape and surface area was usually detectable—although to a variable extent—throughout the simulated breath. Most noticeable was the sudden bulging at onset of expiration, with the reverse motion in inspiration being somewhat limited by contact with the plaster cast. In fact, when the mask excursion was minimized by manually holding its edges, both looping and difference between inspiration and expiration were minimized (**Figure 4**). We therefore believe the observed mask surface area change and rate of change, as well as elastic/rheological properties and possibly minimal residual leakage should account for the difference between inspiration and expiration, as well as for the resistance—flow looping. Altogether, the observed flow dependence of the mask resistance was probably of trivial relevance under conditions of quiet breathing, and the usefulness of K2 may be questioned in such circumstances. On the other hand, it was thought that it may be of help in more fully describing the mask mechanical properties and contribution to increasing work of breathing during exercise, where ventilation is significantly increased. Furthermore, it may be worth applying to a more detailed analysis of $V' - R$ relationship during cough which is known to develop several folds increase in expiratory flow and thus promotes long distance aerosol dispersion through turbulent airflow (Sommerstein et al., 2020).

It is a common observation that, once settled on his face, a subject may become oblivious to the presence of the mask; awareness of it resumes when more ventilation is required, for instance, by walking up the stairs. In a recent review of the literature assessing face mask or respirator during exercise however (Hopkins et al., 2021), little effect of either type of equipment was reported on work of breathing or on arterial

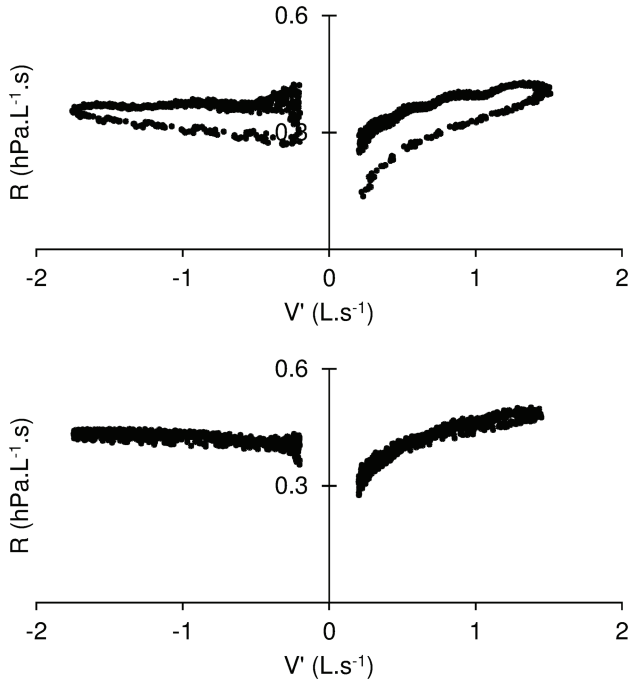

FIGURE 4 | Resistance (R) – Flow (V′) diagram during standard measuring conditions (top) and while the mask motion is prevented by manually holding its edges. The manoeuver is associated with disappearance of the looping of R vs. V′.

oxygen saturation in healthy individuals. Dyspnoea did not appear to be increased when external resistances were added to the breathing equipment in subjects exercising in laboratory-controlled conditions. On the other hand, wearing a face mask may increase both respiratory load and dead space. Rebreathing may lead to minute increase in alveolar PCO_2, a strong determinant of the sensation of air hunger (Banzett et al., 1990). Generally, various physiological mechanisms may be triggered by wearing a face mask, altering breathing and breathing sensation. For instance, the increase in face skin temperature was found to be associated with breathing discomfort in healthy subjects performing treadmill exercise, while wearing FFP respirators (Kim et al., 2016). The possibility may not be excluded that face skin temperature may also increase as a result of a surgical mask and impact on breathing or breathing related sensations. That a neural pathway exists from facial thermoreceptors to respiratory motoneurons is demonstrated by the long known trigeminal diving reflex (Widdicombe, 2006). It is interesting that refinement in mask design may include assessment devices for breathing conditions (Liu et al., 2019).

This study indicates that surgical mask airflow resistance may be reproducibly measured under conditions of tidal breathing, when the mask has been carefully sealed on the dummy head. We are aware that the mask mechanics remains to be evaluated under real-life conditions; i.e., while simply attached to the back of the head and ears. In this regard, the current estimates of surgical mask maximal mechanical load may be quite helpful to test different ways of attaching the face protections. A further limitation of the current model relates to the range of flow limited to tidal breathing. This however may be improved to generate ventilation regimens that encompass those occurring at exercise or during such respiratory manoeuvres as coughing or sighing, i.e., large air flow conditions favoring aerosol particle dispersion (Sommerstein et al., 2020). We also surmise that the current model could be implemented to study the change in resistance when the mask is exposed to hot and humidified air flow over a prolonged period, so as to more precisely estimate the mechanical deterioration with time. Studies may also be developed to compare different types of face protection. The more recent knowledge that aerosol dispersion of viral particles may be a significant contributor to COVID-19 transmission further deserves detailed assessments of less filterable and more resistive material such face piece respirators.

Altogether, the face mask tolerance *in vivo* is likely to depend not only on its own mechanical properties but also on other effects, such as the added dead space, let alone the respiratory condition of the subject. Improving breathability of face mask is critical to insure compliance with the protection and therefore to prevent dissemination of air borne viral infections.

DATA AVAILABILITY STATEMENT

The original contributions presented in the study are included in the article/supplementary material, further inquiries can be directed to the corresponding author.

AUTHOR CONTRIBUTIONS

BD, FM, CD, and SD-A have prepared the project of this study. BD constructed physical analog and managed with CD preparatory phase of the study, assured technical assistance during resistance measures, and performed data collection. SD-A performed statistical analysis. FM, SD-A, and BD prepared the draft of manuscript. All authors contributed to the article and approved the submitted version.

FUNDING

This work was supported by Ministry of Higher Education and Research of France (Ministère de l'Enseignement supérieur et de la Recherche) under contract EA 3450 DevAH.

ACKNOWLEDGMENTS

The authors gratefully acknowledge the contribution of B. Dautzenberg for helpful discussion and N. Coleman for editing the manuscript.

REFERENCES

Aydin, O., Emon, B., Cheng, S., Hong, L., Chamorro, L. P., and Saif, M. T. A. (2020). Performance of fabrics for home-made masks against the spread of COVID-19 through droplets: a quantitative mechanistic study. *Extreme Mech. Lett.* 40:100924. doi: 10.1016/j.eml.2020.100924

Banzett, R. B., Lansing, R. W., Brown, R., Topulos, G. P., Yager, D., Steele, S. M., et al. (1990). 'Air hunger' from increased PCO_2 persists after complete neuromuscular block in humans. *Respir. Physiol.* 81, 1–17. doi: 10.1016/0034-5687(90)90065-7

Bartlett, J. W., and Frost, C. (2008). Reliability, repeatability and reproducibility: analysis of measurement errors in continuous variables. *Ultrasound Obstet. Gynecol.* 31, 466–475. doi: 10.1002/uog.5256

Bland, J. M., and Altman, D. G. (1996). Measurement error. *BMJ* 313:744. doi: 10.1136/bmj.313.7059.744

Bland, J. M., and Altman, D. G. (1999). Measuring agreement in method comparison studies. *Stat. Methods Med. Res.* 8, 135–160. doi: 10.1177/096228029900800204

Cortes, M. F., Espinoza, E. P. S., Noguera, S. L. V., Silva, A. A., de Medeiros, M., Villas Boas, L. S., et al. (2021). Decontamination and re-use of surgical masks and respirators during the COVID-19 pandemic. *Int. J. Infect. Dis.* 104, 320–328. doi: 10.1016/j.ijid.2020.12.056

Duvivier, C., Rotger, M., Felicio da Silva, L., Peslin, R., and Navajas, D. (1991). Static and dynamic performances of variable reluctance and piezoresitive pressure transducers for forced oscillation measurement. *Eur. Respir. Rev.* 3, 146–150.

Fikenzer, S., Uhe, T., Lavall, D., Rudolph, U., Falz, R., Busse, M., et al. (2020). Effects of surgical and FFP2/N95 face masks on cardiopulmonary exercise capacity. *Clin. Res. Cardiol.* 109, 1522–1530. doi: 10.1007/s00392-020-01704-y

Fleisch, A. (1956). The pneumotachograph. *Helv. Physiol. Pharmacol. Acta* 14, 363–368.

Forouzandeh, P., O'Dowd, K., and Pillai, S. C. (2021). Face masks and respirators in the fight against the COVID-19 pandemic: an overview of the standards and testing methods. *Saf. Sci.* 133:104995. doi: 10.1016/j.ssci.2020.104995

Hopkins, S. R., Dominelli, P. B., Davis, C. K., Guenette, J. A., Luks, A. M., Molgat-Seon, Y., et al. (2021). Face masks and the cardiorespiratory response to physical activity in health and disease. *Ann. Am. Thorac. Soc.* 18, 399–407. doi: 10.1513/AnnalsATS.202008-990CME

Hyslop, N. P., and White, W. H. (2009). Estimating precision using duplicate measurements. *J. Air Waste Manage. Assoc.* 59, 1032–1039. doi: 10.3155/1047-3289.59.9.1032

Ju, J. T. J., Boisvert, L. N., and Zuo, Y. Y. (2021). Face masks against COVID-19: standards, efficacy, testing and decontamination methods. *Adv. Colloid Interf. Sci.* 292:102435. doi: 10.1016/j.cis.2021.102435

Kim, J. H., Wu, T., Powell, J. B., and Roberge, R. J. (2016). Physiologic and fit factor profiles of N95 and P100 filtering facepiece respirators for use in hot, humid environments. *Am. J. Infect. Control* 44, 194–198. doi: 10.1016/j.ajic.2015.08.027

Koch, B., Friedrich, N., Volzke, H., Jorres, R. A., Felix, S. B., Ewert, R., et al. (2013). Static lung volumes and airway resistance reference values in healthy adults. *Respirology* 18, 170–178. doi: 10.1111/j.1440-1843.2012.02268.x

Konda, A., Prakash, A., Moss, G. A., Schmoldt, M., Grant, G. D., and Guha, S. (2020). Aerosol filtration efficiency of common fabrics used in respiratory cloth masks. *ACS Nano* 14, 6339–6347. doi: 10.1021/acsnano.0c03252

Lassing, J., Falz, R., Pokel, C., Fikenzer, S., Laufs, U., Schulze, A., et al. (2020). Effects of surgical face masks on cardiopulmonary parameters during steady state exercise. *Sci. Rep.* 10:22363. doi: 10.1038/s41598-020-78643-1

Lee, H. P., and Wang, Y. (2011). Objective assessment of increase in breathing resistance of N95 respirators on human subjects. *Ann. Occup. Hyg.* 55, 917–921. doi: 10.1093/annhyg/mer065

Lepelletier, D., Grandbastien, B., Romano-Bertrand, S., Aho, S., Chidiac, C., Gehanno, J. F., et al. (2020). What face mask for what use in the context of COVID-19 pandemic? The French guidelines. *J. Hosp. Infect.* 105, 414–418. doi: 10.1016/j.jhin.2020.04.036

Liu, H., Allen, J., Zheng, D., and Chen, F. (2019). Recent development of respiratory rate measurement technologies. *Physiol. Meas.* 40:07TR01. doi: 10.1088/1361-6579/ab299e

Louhevaara, V. A. (1984). Physiological effects associated with the use of respiratory protective devices. A review. *Scand. J. Work Environ. Health* 10, 275–281. doi: 10.5271/sjweh.2327

Maher, B., Chavez, R., Tomaz, G. C. Q., Nguyen, T., and Hassan, Y. (2020). A fluid mechanics explanation of the effectiveness of common materials for respiratory masks. *Int. J. Infect. Dis.* 99, 505–513. doi: 10.1016/j.ijid.2020.07.066

Mogridge, R., Stacey, P., and Forder, J. (2016). A new miniature respirable sampler for in-mask sampling: part 2-tests performed inside the mask. *Ann. Occup. Hyg.* 60, 1084–1091. doi: 10.1093/annhyg/mew051

Peslin, R., Ying, Y., Gallina, C., and Duvivier, C. (1992). Within-breath variations of forced oscillation resistance in healthy subjects. *Eur. Respir. J.* 5, 86–92.

Sommerstein, R., Fux, C. A., Vuichard-Gysin, D., Abbas, M., Marschall, J., Balmelli, C., et al. (2020). Risk of SARS-CoV-2 transmission by aerosols, the rational use of masks, and protection of healthcare workers from COVID-19. *Antimicrob. Resist. Infect. Control* 9:100. doi: 10.1186/s13756-020-00763-0

Varene, P., Vieillefond, H., Saumon, G., and Lafosse, J. E. (1974). Calibration of pneumotachographs by an "integral method" (author's transl). *Bull. Physiopathol. Respir.* 10, 349–360.

Widdicombe, J. (2006). Reflexes from the lungs and airways: historical perspective. *J. Appl. Physiol.* 101, 628–634. doi: 10.1152/japplphysiol.00155.2006

Yao, B. G., Wang, Y. X., Ye, X. Y., Zhang, F., and Peng, Y. L. (2019). Impact of structural features on dynamic breathing resistance of healthcare face mask. *Sci. Total Environ.* 689, 743–753. doi: 10.1016/j.scitotenv.2019.06.463

Zangmeister, C. D., Radney, J. G., Vicenzi, E. P., and Weaver, J. L. (2020). Filtration efficiencies of nanoscale aerosol by cloth mask materials used to slow the spread of SARS-CoV-2. *ACS Nano* 14, 9188–9200. doi: 10.1021/acsnano.0c05025

Conflict of Interest: The authors declare that the research was conducted in the absence of any commercial or financial relationships that could be construed as a potential conflict of interest.

Publisher's Note: All claims expressed in this article are solely those of the authors and do not necessarily represent those of their affiliated organizations, or those of the publisher, the editors and the reviewers. Any product that may be evaluated in this article, or claim that may be made by its manufacturer, is not guaranteed or endorsed by the publisher.

frontiers in Physiology

METHODS
published: 08 March 2022
doi: 10.3389/fphys.2022.853317

Human Multi-Compartment *Airways-on-Chip* Platform for Emulating Respiratory Airborne Transmission: From Nose to Pulmonary Acini

Eliram Nof[1†‡], Hikaia Zidan[1‡], Arbel Artzy-Schnirman[1†], Odelia Mouhadeb[1,2], Margarita Beckerman[1], Saurabh Bhardwaj[1], Shani Elias-Kirma[1†], Didi Gur[2], Adi Beth-Din[2], Shulamit Levenberg[1], Netanel Korin[1], Arie Ordentlich[2] and Josué Sznitman[1]*

[1] Department of Biomedical Engineering, Technion—Israel Institute of Technology, Haifa, Israel, [2] Israel Institute for Biological Research, Ness Ziona, Israel

OPEN ACCESS

Edited by:
Deepak A. Deshpande,
Thomas Jefferson University,
United States

Reviewed by:
Jesus Perez-Gil,
Complutense University of Madrid,
Spain
Manfred Frick,
University of Ulm, Germany

***Correspondence:**
Josué Sznitman
sznitman@bm.technion.ac.il

†Present addresses:
Eliram Nof,
Memorial Sloan Kettering Cancer Center, New York, NY, United States

Arbel Artzy-Schnirman,
Applied Medical Technology Research Center, Rambam Health Care Campus, Haifa, Israel

Shani Elias-Kirma,
Department of Chemical Engineering and Biotechnology, University of Cambridge, Cambridge, United Kingdom

‡These authors have contributed equally to this work

Specialty section:
This article was submitted to Respiratory Physiology, a section of the journal Frontiers in Physiology

Received: 12 January 2022
Accepted: 15 February 2022
Published: 08 March 2022

The past decade has witnessed tremendous endeavors to deliver novel preclinical *in vitro* lung models for pulmonary research endpoints, including foremost with the advent of *organ-* and *lung-on-chips*. With growing interest in aerosol transmission and infection of respiratory viruses within a host, most notably the SARS-CoV-2 virus amidst the global COVID-19 pandemic, the importance of crosstalk between the different lung regions (i.e., extra-thoracic, conductive and respiratory), with distinct cellular makeups and physiology, are acknowledged to play an important role in the progression of the disease from the initial onset of infection. In the present Methods article, we designed and fabricated to the best of our knowledge the first multi-compartment human *airway-on-chip* platform to serve as a preclinical *in vitro* benchmark underlining regional lung crosstalk for viral infection pathways. Combining microfabrication and 3D printing techniques, our platform mimics key elements of the respiratory system spanning (i) nasal passages that serve as the alleged origin of infections, (ii) the mid-bronchial airway region and (iii) the deep acinar region, distinct with alveolated airways. Crosstalk between the three components was exemplified in various assays. First, viral-load (including SARS-CoV-2) injected into the apical partition of the nasal compartment was detected in distal bronchial and acinar components upon applying physiological airflow across the connected compartment models. Secondly, nebulized viral-like dsRNA, poly I:C aerosols were administered to the nasal apical compartment, transmitted to downstream compartments via respiratory airflows and leading to an elevation in inflammatory cytokine levels secreted by distinct epithelial cells in each respective compartment. Overall, our assays establish an *in vitro* methodology that supports the hypothesis for viral-laden airflow mediated transmission through the respiratory system cellular landscape. With a keen eye for broader end user applications, we share detailed

methodologies for fabricating, assembling, calibrating, and using our multi-compartment platform, including open-source fabrication files. Our platform serves as an early proof-of-concept that can be readily designed and adapted to specific preclinical pulmonary research endpoints.

Keywords: lungs, *organ-on-chip*, *in vitro*, preclinical models, inhalation, respiratory disease, microfluidics, SARS-CoV-2

INTRODUCTION

The past decade has seen tremendous endeavors to deliver novel preclinical *in vitro* lung models for pulmonary research endpoints (Sakagami, 2006, 2020; Hittinger et al., 2015; Ehrmann et al., 2020; Selo et al., 2021). The motivation for such human-relevant *in vitro* respiratory models is multifold but has been significantly thrusted by efforts to circumvent critical hurdles prevalent in *in vivo* animal experiments. Notably, animal models differ by important underlying discrepancies with humans, spanning amongst other anatomical and physiological differences between species (Hogg and Timens, 2009) to broad divergences in immunological (Mestas and Hughes, 2004) and genetic (Seok et al., 2013) responses to inflammatory diseases. Not only do these dissimilarities translate to contrasting delivery protocols when considering *in vivo* animal experiments (Wylie et al., 2018), but the translational impact of *in vivo* findings remains frequently questioned in characterizing human diseases (van der Worp et al., 2010). Most significantly, the gap between humans and animals constitutes an inevitable barrier to new therapeutic development (Barnes et al., 2015a; Prakash et al., 2017) and is underscored with as high as 80% failure on drug efficacy in human trials leveraging molecules previously screened in rodent lungs (Miller and Spence, 2017). This reality is of important concern as respiratory diseases represent a growing worldwide healthcare burden associated with high morbidity and mortality (Barnes et al., 2015b; Wisnivesky and De-Torres, 2019); meanwhile, respiratory therapies have seen much fewer drugs approved in past decades than other areas of medicine (Barnes et al., 2015a) (e.g., cardiovascular, neurology).

In light of ongoing *in vivo* limitations, *in vitro* cell-based assays have served as useful preclinical "gold standards" in respiratory research. This has included transwell inserts, where human-relevant cell cultures are grown on porous membranes that recapitulate the luminal airway barrier characteristics and, crucially, the air-liquid interface (ALI) (Forbes and Ehrhardt, 2005; Nahar et al., 2013; de Souza Carvalho et al., 2014; Nichols et al., 2014; Faber and McCullough, 2018; Lacroix et al., 2018). Yet, the most exciting progress has arguably arisen from the field of microfluidic *lung*- and *organ-on-chips*. Unlike traditional *in vitro* setups, *airway-on-chips* enable the exchange and collection of media (e.g., analytics of inflammation) with the integration of continuous perfusion from either the basal (i.e., fluid) and/or apical (i.e., air) side of a porous membrane (Tenenbaum-Katan et al., 2018). In recent years, microfluidic platforms that recapitulate more intimately physiological and biological functions have opened new opportunities for human disease modeling, drug discovery and screening, as well as other translational applications (Bhatia and Ingber, 2014; Benam et al., 2015; Esch et al., 2015; Liu et al., 2017; Zhang et al., 2018; Haddrick and Simpson, 2019; Mittal et al., 2019; Shrestha et al., 2020; Artzy-Schnirman et al., 2021; Ma et al., 2021). In turn, various commercial *lung-on-chip* models (Ainslie et al., 2019) are now widely available to the scientific and biopharmaceutical community. In parallel recent microfluidic open-source designs of perfused ALI models (Carius et al., 2021) have been made accessible toward broader and simpler end-user applicability (Artzy-Schnirman et al., 2019a). Altogether, the growing prevalence of these human-relevant *organ-on-chips* has opened new debates on whether preclinical *in vitro* research has reached maturity in so far as to bypass *in vivo* animal validation studies (Ingber, 2020).

Despite the aforementioned advances, *lung-on-chips* are still overwhelmingly limited to models of single channels or individual alveolar-like cavities that often forfeit anatomical traits of the respiratory organ and corresponding respiratory airflow physiology characteristics (Tenenbaum-Katan et al., 2018; Artzy-Schnirman et al., 2021). Most recently, *in vitro* cytotoxicity and inflammatory assays have highlighted more realistic microfabricated tree-like anatomies of either bronchial (Elias-Kirma et al., 2020) or alveolar (Artzy-Schnirman et al., 2019b) airway networks. Nevertheless, by and large virtually all existing microfluidic *in vitro* lung models still focus on isolated airway assays that discard the anatomical continuity between the distinct regions of the lungs, i.e., spanning the extra-thoracic (i.e., nose-throat), conductive (i.e., bronchial) and respiratory (i.e., alveolar) airways, and ensuing crosstalk that can arise *in vivo* between one another. This latter aspect becomes critical when addressing for example the fate of inhaled aerosols and the so-called "journey" of airborne particles along the respiratory tract (Artzy-Schnirman et al., 2020); an area that has drawn considerable interest from numerical *in silico* modeling efforts (Koullapis et al., 2019), most notably with computational fluid-particle dynamic (CFPD) simulations of respiratory airflows and aerosol transport, but is otherwise notoriously challenging to mimic *in vitro* (Artzy-Schnirman et al., 2019a).

The call for novel *in vitro* solutions has been further strengthened amid the ongoing coronavirus disease 2019 (COVID-19) pandemic in deciphering the determinants governing the aerosol transmission of respiratory viruses (Leung, 2021; Wang et al., 2021). It is now established that infection with the severe acute respiratory syndrome-related

coronavirus 2 (SARS-CoV-2) virus typically initiates in the upper respiratory tract (e.g., nasal-oral cavities), highlighting the nasal susceptibility to SARS-CoV-2 due to higher presence of angiotensin-converting enzyme 2 (ACE2) expression in the nasal epithelium with decreasing expression throughout the lower respiratory tract (Hou et al., 2020). Yet, severe symptoms of the disease are acknowledged to arise from infection and associated inflammation of alveolar epithelial cells in the distal lungs (Borczuk et al., 2020; Tay et al., 2020). While infection could originally initiate in the deep lungs via inhalation of fine virus-laden aerosols that may directly deposit on the alveolar surfaces (Wang et al., 2021), it has been hypothesized that deep lung viral infection likely ensues from subsequent aspirations following early infection in the naso-oropharyngeal region (Hou et al., 2020). In the absence of definitive evidence, advanced human-relevant *in vitro* pulmonary models that recapitulate key aspects of the different lung regions could offer attractive opportunities to shed new light on the mechanistic determinants at the origin of the initial onset of respiratory infections in the distal lungs.

Motivated by these broad questions, we introduce in the present Methods article, to the best of our knowledge, the first multi-compartment airway-on-chip model recapitulating key anatomical and physiological components of the respiratory regions. Our versatile platform (see **Figure 1A**) encompasses three distinct chips mimicking, respectively, (i) nasal passages, (ii) mid-bronchial airways, and (iii) distal alveolated airways reminiscent of the pulmonary acinus. First, we detail the engineering methods to microfabricate each distinct fluidic compartment (i.e., nasal, bronchial and acinar) that may be sequentially inter-connected to recreate crosstalk via representative inhalation airflows. We next describe detailed protocols to recreate human-relevant epithelial airways at the ALI, pertinent to the cellular makeup of each respective lung region. As a proof-of-concept of the multi-compartment's usability, we explore *in vitro* determinants of aerosol transmission of respiratory viruses in several exemplary assays. To this end, we isolate the nasal chip from the other compartments and expose its epithelium with an instilled viral suspension. Following infection of the nasal compartment as the alleged site of initial COVID-19 infection in the lungs, bronchial and alveolar compartments are then connected in series to the nasal chip and subjected to inhalation airflows spanning the nose to acini. We subsequently observe infection in both distal epithelial compartments mediated via airflows. Finally, we showcase the initial onset of an inflammatory response across the respective airway barriers in each compartment upon inhalation of nebulized viral-like dsRNA laden aerosols. Together, these preliminary *in vitro* assays support the hypothesis of subsequent aspiration as a potent mechanism for viral transmission across the broader respiratory landscape. Overall, the Methods presented herein underline the applicability of the multi-compartment microfluidic platform toward a broad array of preclinical *in vitro* respiratory research endpoints, where airflow crosstalk and airborne transmission mechanisms are presumed central.

MATERIALS AND METHODS

Device Design

The respiratory tract is an intrinsically complex and multi-scale organ that exhibits a vast network of anatomical structures with a distinct cellular makeup spread over length scales spanning several orders of magnitude (Tenenbaum-Katan et al., 2018; Artzy-Schnirman et al., 2021). By definition, all *in vitro* models are limited in mimicking some but not all characteristics of the *in vivo* environment; a realism that has been recently discussed in some depth (Artzy-Schnirman et al., 2021). As with all *in vitro* pulmonary assays, our designs do not claim to recreate the entire airway pathlength from extra-thoracic regions (i.e., head) to the pulmonary acini. Rather, our specific endpoints lie in capturing some key anatomical and cellular features of the lungs' relevant airway regions; a strategy in line with delivering human-advanced preclinical *in vitro* solutions to elucidate critical aspects relevant to the airborne journey and aerosol transmission phenomenon across the lungs (Artzy-Schnirman et al., 2019a). To this end, we select the nasal passages, bronchial airways and acinar regions as three compartments representative of the extra-thoracic, conductive and respiratory regions, respectively (see **Figure 1A**). Here, specifically, the apical partition of each chip compartment is designed to recapitulate relevant geometrical features of each lung region, and most critically where anatomical structures are known to influence airflow mechanics (Sznitman, 2021). Below we detail design considerations relevant to each compartment.

Nasal Compartment Design

The nose plays a vital role as the first exposure site between the respiratory system and the external environment during normal breathing (**Figure 2A**). The nasal passages' complex, sinuous geometry consisting of multiple pathways (i.e., turbinates) and side chambers (i.e., sinuses) are optimized for the principal tasks of filtering, heating, and humidifying inhaled air destined for downstream transport to the lungs. Concurrently, during such filtering process, the nasal passages can act as a prime infection and replication site for viral airborne pathogens that are trapped and deposit. Here, we developed the *in vitro* nasal compartment chip based on the previously established Carlton-Civic Standardized Nasal Model; an open-source standardized human nose geometry (Liu et al., 2009). Over the years, the model has been established as a geometric standard for both *in vitro* and *in silico* investigations to overcome the challenge of limited comparability between patient-specific nasal anatomies (Brüning et al., 2020). We select a small enough yet relevant section of the Carlton-Civic model (**Figure 2B**) that can fit on a glass slide but also captures key elements of the nasal anatomy, and specifically the turbinate structures that give rise to unique airflow patterns, including recirculation zones and winding streamlines (Schreck et al., 1993), as illustrated schematically in **Figure 2A**. Our *in vitro* efforts are driven to integrate the most dominant anatomical structures and airflow features, thus directly influencing the initial site of viral infection and subsequent proliferation pathways via the nasal compartment. In turn, the airflow rate fed into the resulting polydimethylsiloxane (PDMS)-made nasal compartment (**Figure 2C**) is selected following physiologically

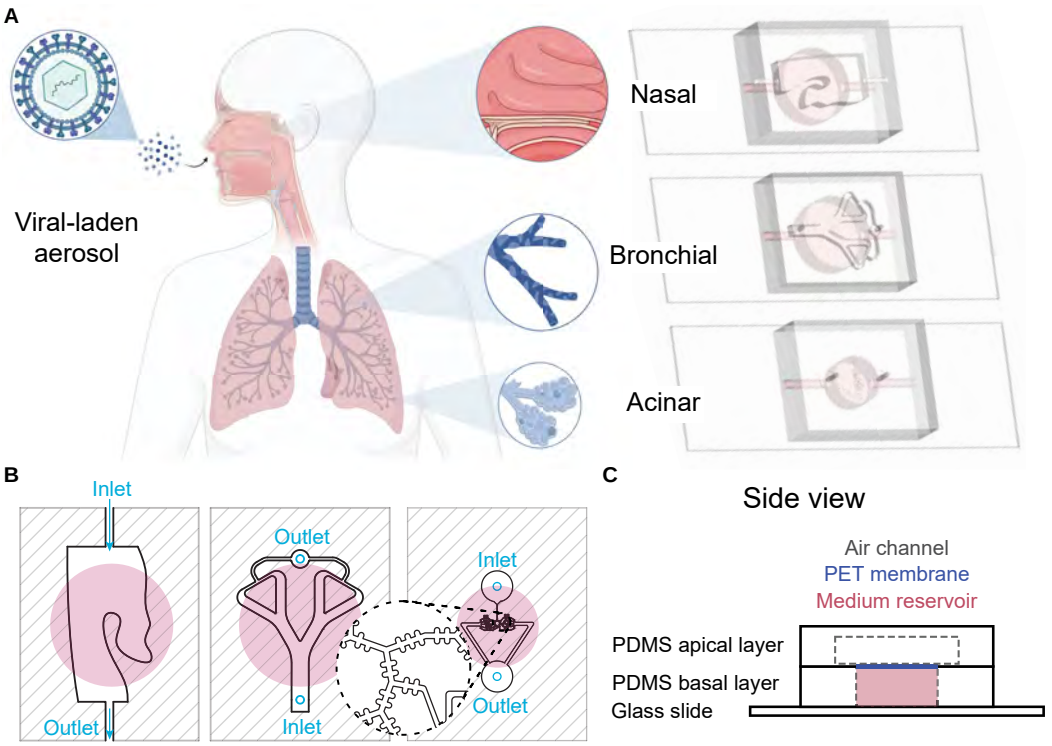

FIGURE 1 | Multi-compartment *lung-on-chip* platform. **(A)** The *in vitro* multi-compartment platform recapitulates three key elements of the flow physiology and cellular makeup across the respiratory tract: (i) nasal passages, (ii) bronchial airways, and (iii) acinar airways, respectively. The platform's "plug and play" modularity may be leveraged toward various benchmark *in vitro* assays for human host-pathogen interaction studies, including investigations of viral airborne transmission. **(B)** Schematic of the three individual chips (top view). From left to right: nasal, bronchial, and acinar airways, respectively. Inlets and outlets of apical chambers are designated with light blue, and reservoir chambers marked with pink circles (reservoir inlets and outlets are not shown in the figure). **(C)** Example of the side view for the nasal chip, composed of (1) an apical PDMS layer that captures relevant nasal passages (see top view in **B**); (2) a polyester-based (PET) porous membrane between apical and basal layers, where epithelial cells are grown; (3) a basal PDMS layer containing a fluidic reservoir to supply media and essential nutrients needed for cell culture.

relevant references for a typical adult breathing at rest (see details on flow characteristics below and **Figure 3**).

Bronchial Compartment Design

The bronchial *airway-on-chip* compartment is based on a recent design from our own group and previously introduced for *in vitro* cytotoxicity assays following realistic *in situ*-like inhalation exposure to immunogenic airborne particulate matter (Elias-Kirma et al., 2020). Briefly, the bronchial geometry consists of a planar, symmetric airway tree spanning three bifurcating generations with a total of four distal branches (**Figure 3B**). The underlying generic airway tree geometry is based on well-established anatomical models of Weibel (1965) and Horsfield et al. (1971). Representative of small bronchial airway branches of the conducting region of the lungs, the model's primary airway diameter is 2.5 mm, along with an idealized constant planar bifurcating angle of 60° across all generations. For further details on the airway tree geometry (see Elias-Kirma et al., 2020).

Acinar Compartment Design

The acinar airway compartment is based on a recent microfluidic *airway-on-chip* developed in our group (Tenenbaum-Katan et al., 2018) and used to explore inflammatory endpoints following the inhalation of lipopolysaccharide (LPS)-laden nebulized aerosols to simulate bacterial infection *in vitro* (Artzy-Schnirman et al., 2019b). The general acinar tree design features a multi-generation asymmetrically bifurcating network with alveolated airways that span several generations. Briefly, the device holds one inlet airway splitting into six branching generations of 170 μm width and 100 μm height channels, with spherical-like cavities mimicking alveoli of 155 μm diameter; the dimensions of the acinar airway chip are selected to match realistic anatomical dimensions pertinent to the distal respiratory regions of the lungs (Artzy-Schnirman et al., 2019b; Sznitman, 2021). Note that the microfluidic chip provides equal airflow to each terminal end of the model by adjusting the length of a channel connecting the unified outlet of the device and the last generation of the acinar tree (**Figure 3C**); this design guarantees equal airflow at each terminal end of the acinar model (for further details, see Artzy-Schnirman et al., 2019b).

Device Fabrication

The nasal and bronchial airway compartments were made using 3D-printed molds filled with polydimethylsiloxane (PDMS) that were subsequently broken apart and removed once the PDMS

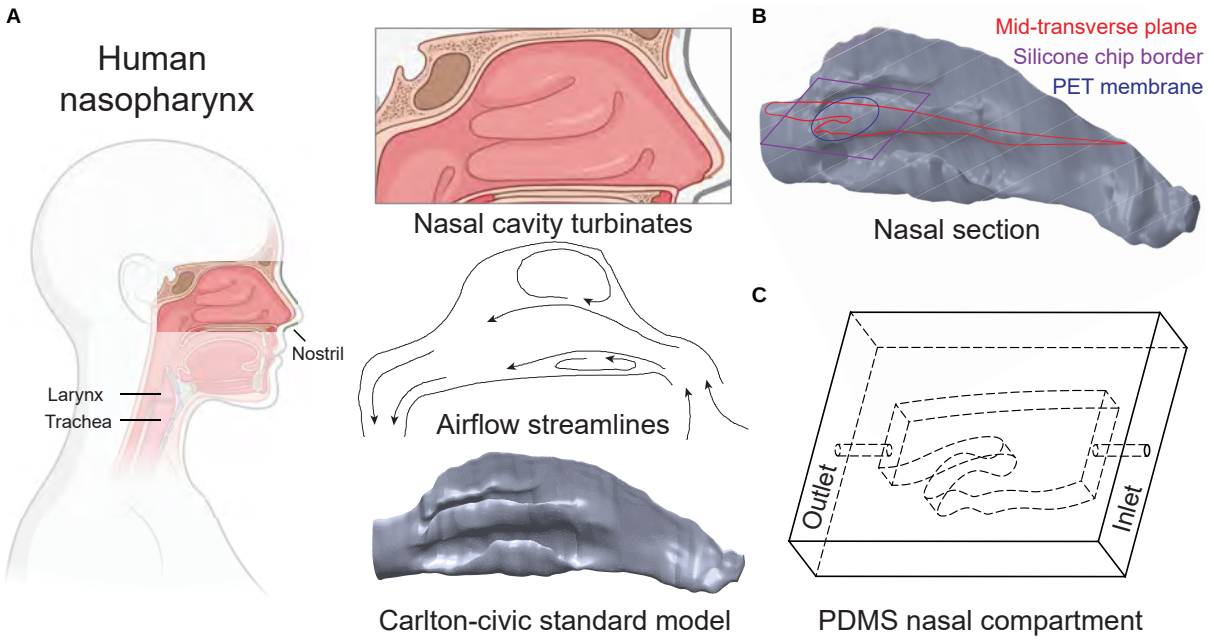

FIGURE 2 | Design of the nasal compartment chip. **(A)** The nasal cavity features a complex network of turbinate airway passages. The Carlton-Civic Standard Nasal model serves as the basis for our nasal chip design. Nasal flows are dominated by the turbinate structures giving rise to recirculating zones, as illustrated schematically by airflow streamlines in the nasal passages. **(B)** We recapitulate elements of nasal flow characteristics in a PDMS compartment based on the generic nasal model. A cross-section of the selected geometry is defined parallel to the bulk flow direction (i.e., beginning upwards through the nostril but then curves toward the elongated axis of the trachea) and bound to a maximal size fitting a standard glass microscopy slide (i.e., 40 mm). **(C)** Schematic drawing depicts the resulting nasal chip compartment, with inner cavities marked by dashed lines and labeled "inlet" and "outlet," respectively, where holes are punched into the PDMS material to connect tubing (see text for details).

was entirely cured. Molds were first created using computer-aided design (CAD) (Solidworks 2020, Dassault Systems) before exporting in raw, unstructured triangulated surface format (STL); a format suitable for 3D printing and provided as open-source files in **Supplementary Material**. STL mold files were prepared (Preform, Formlabs) and subsequently 3D printed in-house via stereo-lithography (Form 2, Formlabs) and made available in the SM. Manufacturer post-print processing instructions were followed, i.e., rinsing in isopropyl alcohol (IPA) and removal of supports, except no post-curing was performed to avoid further hardening the mold material. Liquid PDMS (Dow Corning, Sylgard184) was mixed with a curing agent per the manufacturer's instructions (1:10 mass ratio) and poured into the molds. Curing was done in ambient (i.e., room temperature) conditions overnight. Subsequently, the 3D-printed mold material was removed leaving a transparent PDMS phantom compartment. Note that the airway inlet and outlet in the nasal compartment are already part of the mold, whereas in the bronchial chip compartment the inlet and outlet are created using a biopsy punch of 1 mm size (Miltex, 3331; see **Figure 1B**).

Concurrently, the acinar airway tree compartment was fabricated using standard soft-lithography techniques combined with a modified method for master production using dry reactive ion etching (DRIE) of silicon on an insulator wafer to manufacture the small ($<$ 100 μm) features characteristic of the acinar model, as previously described (Artzy-Schnirman et al., 2019b). Briefly, the resulting models were used as a master template for PDMS casting. PDMS mixed with the curing agent was poured on the template, and baked for 1 h at ∼65°C (or overnight at RT). Cured PDMS was subsequently peeled from the mold and punched using a biopsy punch of 1 mm size to create inlet and outlets (**Figure 1B**).

To assemble completely each individual compartment, a 10 μm thick polyethylene terephthalate (PET) membrane with 0.4 μm pore size (Corning, CLS3450) was bonded to the PDMS channel compartment (i.e., apical compartment) using a "stamping" technique such that channels were irreversibly sealed. Thereafter, the structure was placed using the stamping method on a PDMS well to be filled with culture media (i.e., basal compartment). Finally, a microscope glass slide (Paul Marienfeld, 1000412) was cleaned with ethanol and bonded to the device's bottom side (reservoir), as shown in **Figure 1C**. The structure was cured at 65°C for 1 h to complete bonding. We note that only the model's apical side was sealed to the PET membrane (without the PDMS-glass reservoir) when used for permeability assays (see details below).

Flow Setup and Characterization

To establish the multi-compartment model's relevance for recapitulating physiological airflows in the apical compartments of the three selected regions of the lungs, we conducted airflow simulations using computational fluid dynamics (CFD), as shown in **Figures 3D–F**. This approach gives prior qualitative and quantitative insight into the airflow characteristics anticipated

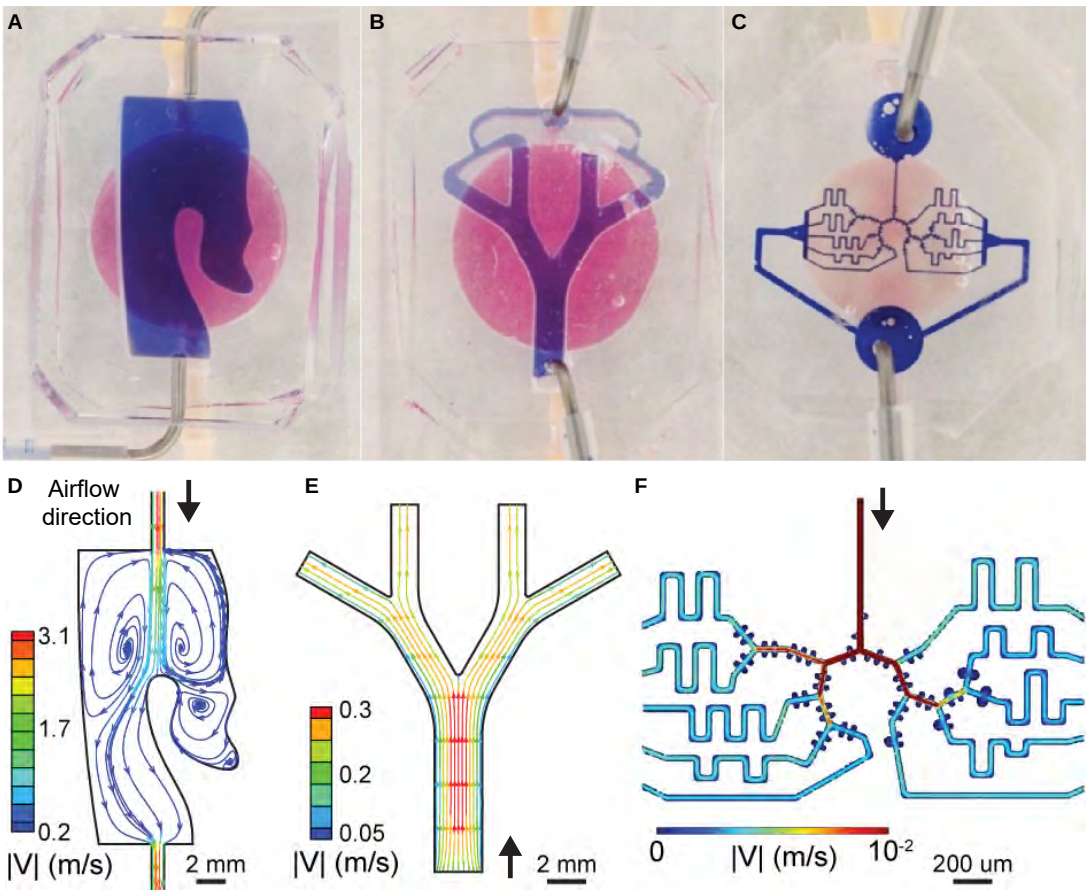

FIGURE 3 | Characteristic flow features in the multi-compartment airway-on-chip platform. **(A–C)** View of the inter-connected chip compartments, where the reservoir, i.e., basal chamber, filled with pink media, and the geometry channel, i.e., apical chamber, filled with blue media are shown for imaging contrast only. **(D–F)** Steady-state flow patterns are resolved in each of the three compartments using CFD simulations and visualized by plotting streamlines colored according to velocity magnitude (see text for detail). Each compartment is subject to physiologically relevant flows (see **Table 1**), highlighting order of magnitude changes in the velocity scales between each lung compartment, reminiscent of physiological pulmonary fluid dynamics. **(D)** Flow in the nasal compartment is characterized by recirculation zones attributed to the turbinate pocket structure. **(E)** Poiseuille-like flows develop at the inlet of the bronchial model, subsequently splitting and weakened as is typical of flow in a symmetrically bifurcating bronchial airway geometry. **(F)** Flow velocity contours in the acinar model, characterized by generation-level attenuation in velocity and small, recirculating flows in the alveolar-like cavities (reproduced with permission from Tenenbaum-Katan et al., 2018).

across the individual airway compartments. Briefly, each of the apical airway geometries was meshed with tetrahedral cells using a commercial meshing software (ANSYS, ICEM v18) from the CAD geometry files used in the device fabrication pipeline. Next, a commercial flow simulation software (ANSYS, Fluent v19.2) was used to solve the governing physical equations (i.e., mass continuity and momentum conservation) resolving the airflow fields inside the airway volumes. Here, we simulated steady-state airflow conditions (i.e., equivalent to a steady inhalation) by imposing predefined flow rates (see **Table 1**) at each compartment inlet and corresponding pressure conditions at the outlets. These simplified conditions were chosen to mimic average respiratory flow rates that may be anticipated within these compartments based on either their respective volume (e.g., the nasal chip's volume relative to the entire nasal cavity) or anatomical location along the respiratory tract (i.e., lung generation number for the bronchial and acinar chips). While more complex airflows can be introduced to more closely mimic *in vivo* inhalation (e.g., see previous work modeling cyclic ventilation at varying frequencies and flowrates; Nof et al., 2020), we chose here a simplified approach analogous to the perfusion setup employed in our exposure assays that features a nebulizer providing a constant flow output (see details below).

We note here that our *in silico* results are limited to simulations of the inhalation airflows anticipated in each of the compartments and do not encompass Lagrangian particle tracking or ensuing aerosol deposition characteristics. We have previously explored, both in simulations and experiments, characteristics of aerosol deposition of airborne particles in similar bronchial (Elias-Kirma et al., 2020) and alveolar (Fishler et al., 2015) airway models that address the mechanistic determinants of aerosol deposition in *airway-on-chips*. While particle shape, size and density are known to significantly affect deposition patterns within the respiratory

tract (Shachar-Berman et al., 2019, Shachar-berman et al., 2020; Koullapis et al., 2021), an extensive study of particle dynamics within our multi-compartment model lies beyond the scope of this work.

To visualize airflow patterns and deliver intuition for possible pathways of particulate matter within the respiratory flow, interpolated streamlines are plotted in **Figures 3D–F** and colored according to the magnitude of the velocity field. Briefly, in the nasal chamber a recirculation zone is apparent and located in a pocket formed by the turbinate structure (**Figure 3D**), thereby extending airborne travel time due to reduced flow velocities and longer travel paths inside the cavity before exiting via the outlet port. These flow characteristics recapitulate some of the complexity of nasal flows that may play a role in viral transmission pathways, considering the nose is often regarded as a hospitable replication site. However, we remark that under natural breathing conditions *in vivo*, air does not directly transit through tubes connecting the nose and other regions of the human airways. In contrast, this represents an engineering necessity and limitation featured within our platform that introduce flow artifacts requiring careful further considerations. In the nasal compartment, we see a short jet flow exiting the tube-shaped inlet port resulting in a pair of vortical structures; a well-known fluid dynamics' characteristic of elongated tube flow emptying into larger ambient spaces. While *in vivo,* the nasal turbinate structures similarly divert flow via impaction, which may lead to vortical or rotational flows, their relative location and sizes likely differ significantly from those introduced here in our platform, which artificially introduces a tube a short distance from a turbinate-like shape within a small section of the nasal cavity.

In the bronchial compartment (**Figure 3E**), airflow enters through the top of the PDMS compartment before branching twice through two generations of daughter branches and converges again to exit through an outlet passage. Flow characteristics in this airway structure are typical of symmetrically bifurcating airway geometries (see above section on the compartment design), with velocities reduced in more distal airway generations as the flow is split into smaller (in cross-section) but collectively larger (in volume) passages; a direct outcome of mass conservation across a bifurcating tree structure. Note that for small micron-sized aerosols subject to gravitational sedimentation as the leading deposition mechanism, deposition outcomes (not simulated here) have been recently shown to follow a monotonically decreasing trend as velocity decreases with each increasing airway generation number (Elias-Kirma et al., 2020). Flow velocity contours in the acinar compartment (**Figure 3F**) are similarly characterized by a gradual decrease in velocity magnitudes with each increasing acinar generation. Concurrently, small, recirculating flows in the alveolar-like cavities are present along the alveolated airway channels. Further details on the flow characteristics, including aerosol deposition, in microfluidic acinar airways are available elsewhere using the same geometry (Sznitman, 2021).

Due to high pressure buildup in the small tubing and syringe tip ports (< 1 mm) used in our platform, we could not directly provide high (> 1 ml/s) flow rates into the nasal compartment's inlet and instead chose a flow rate based on the downstream bronchial compartment that would work well with ordinary laboratory equipment such as a small syringe pump or peristaltic pump (i.e., larger flowrates may for example require ventilators). Thus, we selected a flow rate of 6.5 ml/min (see **Table 1**) corresponding to a Reynolds number of $\sim$10 which is typical for the mid-bronchial regions (e.g., 12th generation of the airway tract). We note that the entire Carlton-civic standard nasal model is $\sim$13.2 ml in volume, while our nasal chip comprises 0.5 ml and represents only 3.5% of the nasal chip volume. Assuming a linear relationship between volume and flow rate (i.e., nasal airflow during rest is laminar and incompressible (Zwicker et al., 2018)), an input flowrate of 6.5 ml/min (i.e., 0.1 ml/s) to the nasal chip would translate to approximately 3 ml/s in a full adult. Unilateral (i.e., from one nostril) nasal airflow rates in adults are reported to vary approximately between a resting rate of 80–200 ml/s and upwards of 1,000 ml/s during physical exertion, with peak Reynolds numbers ranging from several hundreds to thousands (Li et al., 2017). Significant inter-individual nasal anatomical variation results also in diverse air flow rates and due to the cyclic rhythm of breathing (i.e., oscillations between inhalation and exhalation), actual flowrates fluctuate between 0 (at the reversal point between breathing phases) and the maximum reported typical rates. Therefore, while the nasal flows used in our experiments are typically lower than those expected in the nasal passages, they lie nevertheless within the physiological range of resting activity.

Next, flowrates in the bronchial and acinar chips are selected based on typical average physiological flowrates under quiet breathing conditions in an adult human (see **Table 1** for selected values at the inlet of each compartment). Airway generation numbers in the bronchial (12–14) and acinar (20–23) chips are given as approximative (Weibel, 1965). Equivalent Reynolds numbers are calculated using the average flowrates, diameter of inlet ports (1 mm), and the rheological properties of ambient air (kinematic viscosity of 1.5 10^{-5} m^2/s). A 6.5 ml/min (0.1 ml/s) air flowrate through a 1 mm inlet translates to a Reynolds number $\sim$10, which is appropriate for the 12th generation bronchial airway generation. Note that while the nasal and bronchial apical compartments are connected directly (i.e., flow rate is conserved), air flow continuing from the bronchial to the acinar apical compartment is split by a flow diverter, which releases pressure to the ambient environment thereby reducing the flowrate into the acinar chip (see details below). Following the Y-joint

TABLE 1 | Characteristic properties and flow parameters of the multi-compartment *airway-on-chip* platform.

Compartment	Units	Nasal	Bronchial	Acinar
Inner volume	V [mm^3]	506.07	138.26	3.24
Total inner surface area	S [mm^2]	168.69	75.97	32.4
Height	L [mm]	3	1.82	0.1
Flow rate	Q [ml/min]	6.5	6.5	0.2
Inlet diameter	D [mm]	1	1	1
Inlet Reynolds number	Re_{inlet}	10	10	0.3
Lung generation	G	-	12–14	20–23

diverter, flow measurements reflect a reduced input flowrate of approximately 0.2 ml/min (i.e., 0.003 ml/s) corresponding to an inlet Reynolds number of ∼0.3 at the first generation of the acinar tree and well in line with characteristic acinar flows (Sznitman, 2013, 2021). This implies that only 3% of the flow continues past the Y-joint to the acinar compartment, due to the pressure gradient between the open end (ambient, low pressure) and high pressure from an increasingly smaller passage in the acinar chip.

Perfusion System

Each of the three airway compartments was connected via silicone tubing (Cole-Parmer, EW- 95702-00), allowing independent perfusion of maintenance media (i.e., culture medium and air) or experimental inputs such as viral-laden aerosols (apical side only; see results below) applied to the nasal compartment and subsequently transmitted to bronchial and acinar models (see **Figure 4**). During experiments, a Y-joint tube-to-tube connector (Nordson Medical, Y210-1) was used to "bleed off" or reduce the flowrate fed to the acinar model, based on the physiologically relevant range (see **Table 1**) mimicking airflows at such airway depths and in line with previous microfluidic efforts (Sznitman, 2021).

For the convenience of cell culture maintenance and to restrict the spread of potential infections, each compartment is initially handled separately (see **Figure 4B**) before conducting any experimental protocol (see below). Briefly, the apical compartment (filled with blue dye for contrast visualization in **Figure 4**) is accessible via two Luer ports connected via silicone tubing to holes in the PDMS material, made with a 1 mm biopsy punch and strengthened with either straight (nasal compartment only) or 90 deg. bent 18-gauge syringe tips (Techcon, TE720050B90) for robustness and protection from tearing PDMS material. Note that the metal syringe tips are stripped from their original plastic hubs and sterilized before integrating with the model.

Closing all Luer ports to either apical or basal compartments (see **Figure 4C**), is accomplished via insertion of male Luer plugs (not shown) or clamps. While plugs (Nordson medical, LP4-1) are robust and stable, simply bending the tubes and applying a clamp (Nordson Medical, FSLLR-1), proved quicker and more amenable to the maintenance of sterility necessary for cell culture. Similarly, the basal compartment (filled with pinkish dye in **Figure 4**) is accessed via two Luer ports connected via silicone tubing to holes in the PDMS material and strengthened with nylon, straight barbed tube-to-tube connectors (Nordson Medical, N210-1); these latter connectors are of larger inner diameter than the apical side's syringe tips thus allowing for easier perfusion of culture medium (see **Figure 4C**).

Cell Culture

To capture key aspects of the cellular makeup relevant to our principal lung regions, we use well-established airway epithelial cell lines (Selo et al., 2021). Our strategy thus provides a human-relevant pulmonary benchmark that can be adapted for and compared with future studies using primary cells and patient-derived samples. We recall that cell lines afford increased control over experimental parameters with reduced genetic variation and facilitated culture requirements (Kaur and Dufour, 2012) to culture, maintain and transduce, and thus may, be used to mimic some of their tissue origin behavior and characteristics (Masters, 2000). With that said, cell lines still hold limitations that should be taken into consideration. Notably, they have been shown to have genetic and phenotypic alterations form their origin tissue (Alge et al., 2006; Pan et al., 2009), compared to primary cells that are isolated directly from the tissue of interest, and thus capture more closely cellular heterogeneity.

As representative of our model compartments, we chose to work with three cell lines originating from matching tissues: (i) RPMI-2650 is an epithelial cell line derived from the human nasal septum, (ii) Calu-3 are isolated from human lung adenocarcinoma and resemble the bronchial epithelium (Kreft et al., 2015a), and finally (iii) the alveolar epithelial hAELVi cell line originated from alveolar type I cells (Kuehn et al., 2016).

To first evaluate cell line characteristics, we made use of established epithelium integrity characterization methods, in addition to staining techniques using 4′,6-diamidino-2-phenylindole (DAPI) as nuclear stain, phalloidin as actin filaments stain, along with tight junction anti-Zonula occludens-1 (ZO-1) antibody followed by fluorescent secondary antibodies. Initially, we conducted a standard evaluation in 24 transwells for both liquid-liquid interface (LLI) and ALI conditions (see **Supplementary Figures 1–3**) using cell inserts. Next, we repeated such evaluations directly in our PDMS-made *airway-on-chip* models (**Figure 5**). Comparing staining results in both (ALI) inserts chip models reveals strong qualitatively similar cell behavior across, suggesting compatible growth conditions in the models.

MATERIALS AND INTEGRITY ASSAYS

Cells

RPMI2650 (ATCC, CCL-30) and Calu3 (ATCC, HTB-55) were cultured in ATCC-formulated Eagle's Minimum Essential Medium (Biological Industries, 01-040-1A) supplemented with fetal bovine serum (FBS) (Biological Industries, 04-127-1A) to a final concentration of 10%, 1% L-glutamine (Biological Industries, 03-020-1B) and 1% antimycotic antibiotics (Sigma-Aldrich, A5955). The medium was changed every other day. When cells reached 90% confluency, they were trypsinized, using Trypsin EDTA Solution B (0.25%), EDTA (0.05%) (Biological Industries, 03-052-1B), and used for maintenance or experiments, as described below. hAELVi cells (InSCREENeX, INS-CI-1015) were cultured in a small airway epithelial cell growth medium (SAGM) BulletKit (Lonza CC-3118) supplemented with 1% FBS and 1% penicillin/streptomycin (P/S) (Life Technologies, 15140-122). Prior to seeding, flasks were coated with coating buffer; (1% (v/v) fibronectin (Corning, 33016015) and 1% (v/v) collagen (Sigma, C4243) for 2 h in 37°C or overnight in 4 °C. The medium was changed every 2–3 days. When cells reached 90% confluency, they were trypsinized using Trypsin-EDTA (0.05%) (Gibco, 25300054) and used for

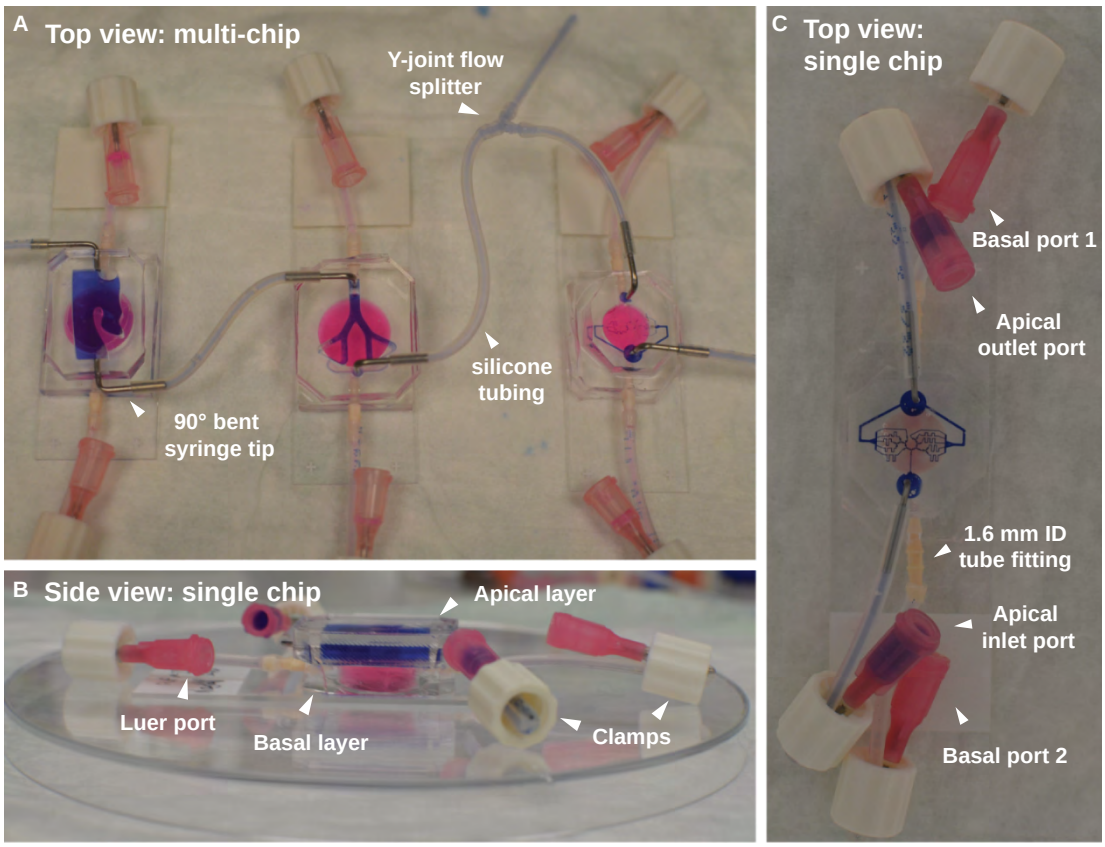

FIGURE 4 | Airflow (apical) and fluidic perfusion (basal) setup for the complete multi-compartment airway-on-chip platform, including silicone tubing and connector fittings. **(A)** Top view of the three airway compartments, with apical partitions connected in series by tubes. A Y-joint tube fitting allows partial bleeding of the airflow between the bronchial and acinar compartments, necessary for reducing the flowrate to the acinar region to lie within a physiologically relevant range (see **Table 1**). The basal partitions in each chip (filled with pink dye) are fitted with straight nylon tube-to-tube connectors. **(B)** Side view of a single chip (nasal model shown here) highlighting the apical layer (filled with purple dye) atop the basal layer (filled with pinkish dye). Other than when perfusion between the consecutive models is performed, ports remain closed using clamps fitted over a bent section of the tubing near the Luer port end piece. **(C)** Top view of a single representative chip (i.e., acinar compartment shown here) demonstrating the port and tubing configuration used outside of perfusion experiments (e.g., during incubation, microscopy, etc.).

maintenance or experiments, as described below. Cells were incubated in humidified incubators at 5% CO_2, 37°C at all times.

For SARS-CoV-2 virus incubation (see assays below), the Vero E6 (ATCC, Vero C1008, CRL-1586) cell line was used. Briefly, cells were grown in Dulbecco's modified Eagle's medium (Biological Industries, 01-055-1A) containing 10% Fetal bovine serum (Biological Industries, 04-127-1A), MEM non-essential amino acids (Biological Industries, 01-340-1B), 1% L-glutamine (Biological Industries, 03-020-1B), 1% penicillin/streptomycin (Biological Industries, 03-031-5C).

Viruses

SARS-CoV-2 viruses (GISAID accession EPI_ISL_406862) were kindly provided by Bundeswehr Institute of Microbiology, Munich, Germany. Virus stocks were propagated (4 passages) and tittered on Vero E6 cells before it was used. Handling and working with SARS-CoV-2 virus were conducted in a BSL3 facility in accordance with the biosafety guidelines of the Israel Institute for Biological Research (IIBR).

Recombinant lentiviral particles were generated using a Lenti-X Packaging Single Shots (VSV-G) System (Takara Bio USA, #631275). This system produces replication-incompetent VSV-G pseudotyped lentiviruses. The lentiviruses were generated according to the manufacturer's instructions. Briefly, the expression vector for the fluorescent protein tdTomato (Takara Bio USA, #632564) was transfected, in a Lenti-X Packaging Single Shot, into the Lenti-X 293T packaging cells (Takara Bio USA, #632180). After 48 h, the lentiviral supernatant produced by the transfected packaging cells was collected and filtered through a 45 μm filter (Merck, Millipore SLHP033RS) to remove cellular debris, and then used to transduce the devices.

Insert Cell Culture

RPMI 2650 (5×10^5 cells) and Calu-3 cells (1×10^5 cells) were seeded on uncoated transwells polyester membranes (Corning 3470; growth area 0.33 cm^2; pore size 0.4 μm), while hAELVi cells (1×10^5 cells) were seeded on precoated transwells (as described previously). All cells were seeded under liquid-liquid interface (LLI) conditions. 200 μL of culture medium was perfused on the

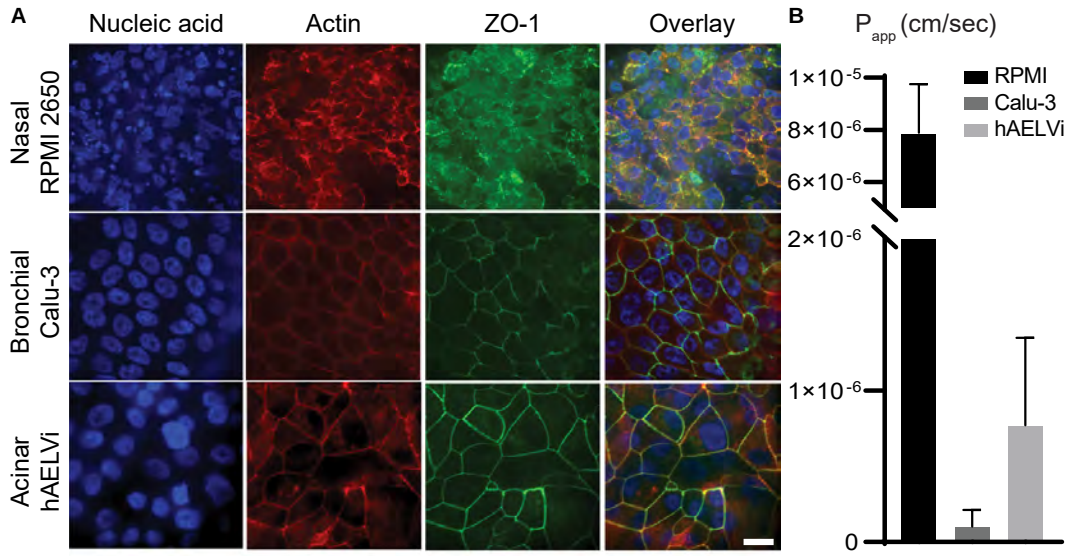

FIGURE 5 | Characterization of human-relevant cell lines mimicking relevant airway epithelial cells of the respective lung compartments. **(A)** Immunofluorescence micrographic views for three cell lines: RPMI 2650 seeded in nasal models, Calu-3 seeded in bronchial models, and hAELVi seeded in acinar models, respectively, and immunolabeled with: 4′,6-diamidino-2-phenylindole (DAPI) for nucleic acid staining (blue), phalloidin for actin filaments staining (red), anti-Zonula occludens-1 (ZO-1) (green), with an overlay view. The scale bar is 20 μm for all images. **(B)** Transport assay of fluorescein sodium salt (FluNa), a functional permeability test for cellularized models, conducted ∼3 weeks post-seeding. RPMI 2650 shows high apparent permeability (Papp) value of 8×10^{-6} cm s^{-1} indicating poor barrier properties, while Calu-3 and hAELVi yield low Papp values of 1×10^{-7} and 7×10^{-7} cm s^{-1}, respectively, indicating effective airway barriers.

apical side and 500 μL through the basolateral side. The medium was changed every second day. For ALI conditions, the medium from the apical compartment was aspirated 2 days post-seeding, and the cells were further fed from the basolateral compartment with 500 μL of the medium.

Microfluidic Cell Culture

The devices were sterilized following three rounds of exposure to ultraviolet light (254 nm), 15 min each. Afterward, the apical side of acinar devices was incubated with coating buffer for 2 h in 37°C, 5% CO_2, and 95% humidity, washed with PBS, and seeded without drying the membrane. RPMI 2650 (1×10^6 cells ml^{-1}), Calu-3 (1×10^6 cells ml^{-1}), and 10 μL of hAELVi cells suspension were seeded on the apical side of the membrane of the nasal, bronchial, and acinar airway chips, respectively. All basolateral compartments were filled with suitable growth medium. After 48 h of seeding, the apical compartment was washed with fresh media to wash out non-attached cells. Following 48 h in LLI conditions, the medium from the apical compartment was aspirated, allowing the cells to grow at ALI conditions. Next, the cells were supplied medium once a week from the basolateral compartment by withdrawing the liquid from the basolateral side and injecting fresh medium.

Transport Studies

Inserts and devices were seeded with cell cultures as described above. The cells were allowed to grow for about 3 weeks (in ALI when confluency is reached). Transport experiments were then performed as previously described (Elbert et al., 1999). Briefly, the cells were washed twice with prewarmed Krebs–Ringer Buffer (KRB: NaCl 142.03×10^{-3} m, KCl 2.95×10^{-3} m, $K_2HPO_4{}^*3H_2O$ 1.49×10^{-3} m, HEPES 10.07×10^{-3} m, d-glucose 4.00×10^{-3} m, $MgCl_2{}^*6H_2O$ 1.18×10^{-3} m, $CaCl_2{}^*2H_2O$ 4.22×10^{-3} m; pH 7.4), and incubated in KRB for 45 min. Next, the medium was aspirated. Fluorescein sodium salt (FluNa) (Sigma-Aldrich, F6377) was added to the apical compartment (first diluted in KRB buffer for a final concentration of 0.01 μg ml^{-1}), and KRB was added to the basolateral compartment. The devices were next placed in the incubator, and 30 μL samples were taken every 30 min from the basolateral compartment only and transferred into a 384-well plate to measure FluNa concentrations. Sampled volumes were refilled with 30 μL KRB. The samples in the 384-well plates were measured with a Synergy H1 microplate reader (Agilent BioTek, #1902191C) using wavelengths of 488 nm (excitation) and 530 nm (emission).

Transepithelial Electrical Resistance Measurement

Transepithelial Electrical Resistance (TEER) was measured as previously described (Kuehn et al., 2016). Briefly, 24 h post cells seeding on transwells, and every other day, per the routine care, media was aspirated, the apical side was refilled with 200 μL prewarmed medium, and the basolateral compartments were filled up to a final volume of 500 μL. Following 1 h of incubation, TEER was measured in all samples using a dedicated epithelial volt-ohm meter (Millicell ERS-2) equipped with chopstick electrodes (Millicell, MERSSTX01). In transwells grown under ALI conditions, media of apical compartment

was aspirated immediately following the measurements. The electrical resistance was calculated by subtracting the value of blank inserts containing medium from all samples and multiplication with the cultivation area of the inserts (i.e., 0.33 cm^2).

BIOCHEMICAL ASSAYS

Measurement of Viral RNA

A total of 200 mL of samples from each compartment were added to LBF lysis buffer (supplied with the kit) and viral RNA was extracted using RNAdvance Viral Kit (Beckman Coulter) and further processed on the Biomek i7 Automated Workstation (Beckman Coulter), according to the manufacturer's protocol. Each sample was eluted in 50 μL of RNase-free water. Realtime RT-PCR assays, targeting the SARS-CoV-2 E gene, were performed using the SensiFAST Probe Lo-ROX One-Step kit (Bioline). The final concentration of primers was 600 nM and the probe concentration was 300 nM. Primers and probe for the E gene assay were taken from the Berlin protocol published in the World Health Organization (WHO) recommendation for the detection of SARS-CoV-2. Thermal cycling was performed at 480°C for 20 min for reverse transcription, followed by 95°C for 2 min, and then 45 cycles of 94°C for 15 s, 60°C for 35 s. Cycle Threshold (Ct) values were converted to calculated plaque-forming unit (PFUs) with the aid of a calibration curve tested in parallel.

Plaque Forming Unit Assay

Vero E6 cells were seeded in 12-well plates (5×10^5 cells/well) and grown overnight. Dilutions of SARS-CoV-2 were prepared in MEM containing 2% FCS with NEAA, glutamine, and P/S, and used to infect Vero E6 monolayers (500 μL/well). Plates were incubated for 1 h at 37°C to allow viral adsorption. Then, 1 ml/well of overlay [MEM containing 2% FBS and 0.4% Tragacanth (Merck)] was added to each well and plates were incubated at 37°C, 5% CO_2 for 48 h. The media was then aspirated, and the cells were fixed and stained with 500 μL/well of crystal violet solution (Biological Industries). The number of plaques in each well was determined.

Cytokine Secretion Assay

Cell culture supernatants were assayed using ELISA for Interleukin-6 (IL-6) (Thermo Fisher Scientific, #88-7066-88) following the manufacturer's instructions. Briefly, the basal media of exposed inserts and models were collected, centrifuged to discard precipitated cell fractions, and diluted if necessary. Samples were added to pre-coated plates-conjugated to capture antibodies and blocked to exclude non-specific interactions. A detection antibody was added to generate sandwich reaction. Avidin-HRP was added, followed by TMB solution to generate detection reaction, which was stopped using sulfuric acid (2N H_2SO_4) upon saturation of calibration wells.

Immunofluorescence Microscopy

Directly after cell fixation using 4% PFA, cells were treated with 0.05% Triton X-100 (Sigma–Aldrich, T8787) for 3 min at room temperature (RT) to increase membrane permeability. Afterward, cells were blocked for non-specific binding using 2% BSA (MP Biomedicals, 02160069-CF) for 1 h at RT. For F-actin staining, cells were incubated with Alexa Fluor 568 Phalloidin (Thermo Fisher Scientific, A12380) diluted with PBS (ratio of 1:200) for 40 min at RT. For DAPI nucleic acid staining, cells were incubated with DAPI solution (ThermoFisher Scientific, D1306), diluted with PBS (ratio of 1:500) for 5 min at RT. For tight junction protein-1 (ZO1) staining, cells were incubated with the primary antibody rabbit anti-ZO1 (Thermo Fisher Scientific, 617300) diluted with BSA (ratio of 1:200) overnight at 4°C, followed by incubation with secondary antibody Alexa Fluor 488 anti-rabbit (Jackson ImmunoResearch, 111-545-144) diluted with BSA (ratio of 1:500) for 1 h at RT. After each step, cells were washed three times with PBS. Finally, fluorescent immunostaining confocal microscopy imaging was performed (Nikon Eclipse Ti with spinning disk).

RESULTS

Epithelium Integrity Characterization

We conducted two well-established integrity assays (Sakagami, 2020; Artzy-Schnirman et al., 2021) in 24 transwells to evaluate epithelial barrier functionality. First, we measured trans-epithelial electrical resistance (TEER) for a span of 3–4 weeks during cell culture. This was followed by tracking fluorescein sodium salt transport through the apical to basal chamber, and subsequently extracting the apparent permeability coefficient (Papp) across the airway epithelium. RPMI 2650 results revealed a culture of multi-layer clusters, with ambiguous ZO-1 formation (**Supplementary Figure 1**), low TEER and high Papp values (**Supplementary Figures 4A,D**), in accordance with other *in vitro* characterization assays (De Fraissinette et al., 1995; Psimadas et al., 2012). Conversely, Calu-3 and hAELVi cells exhibited a uniform polarized monolayer, with clear tight junction staining (**Supplementary Figures 2**, **3**), corresponding to high TEER (**Supplementary Figures 4B,C**) and very low Papp values (**Supplementary Figure 4D**), underlining a functional barrier and in line with previous works (Kreft et al., 2015a; Kuehn et al., 2016). Furthermore, for all cell lines, we note that cultures grown at the ALI showed comparatively higher TEER and Papp values, in addition to visually clearer and smoother staining resulting from a more polarized epithelial cell organization, in contract with more noisy and blurry results for cultures maintained in LLI; a well-known feature of epithelial airway cells grown under more physiologically faithful conditions (Sakagami, 2020; Artzy-Schnirman et al., 2021).

Similarly, we examined cell behavior in our microfluidic models, grown at ALI conditions for a period of 3 weeks. We stained for DAPI, phalloidin, and ZO-1, in addition to FluNa transport assays. The devices used for barrier functionality evaluation consisted of the model's apical compartment sealed to the PET membrane, placed in 24 mm well (of a 6 well

plate) in lieu of the basal compartment and medium reservoir, rather than PDMS-glass reservoir. As previously described (**Figure 1**), the upper side of the apical compartment is sealed with PDMS (except for the openings in place at the inlet and outlet holes); this setup is inconvenient for conducting routine TEER measurements. However, in the present modified form, the basal reservoir is readily accessible for media sampling necessary for transport assays. Hence, we examined the models' barrier functionality with the permeability assay only, shown to correlate with TEER behavior in transwell inserts. Similar to our previous observations, RPMI 2650 in nasal models formed cell clusters, blurry images, incomplete ZO1 staining and high Papp values. This comes in contrast to confluent monolayer formation, unified tight junctions, as well as low Papp values reported in both bronchial Calu-3 models and acinar hAELVi models (Artzy-Schnirman et al., 2019b; **Figure 5B**). We also compared barrier characterization for chip models in LLI and observed similar patterns to those seen in transwells (**Supplementary Figure 4E**).

Development of the Multi Compartment Platform

The methods described herein establish our multi-compartment *airway-on-chip* platform with endpoints aimed at recapitulating three representative elements of the respiratory system underlining both physiological (i.e., airflow patterns) and biological (i.e., cellular) relevance. In what follows, we now exemplify the usability of the platform for some selected, but not exhaustive, *in vitro* endpoints linked to viral airborne transmission of respiratory infections. In the first proof-of-concept embodiment, we measured the transmission of the SARS-CoV-2 through the platform, demonstrating the physical capabilities of the platform for recapitulating *in vitro* an attenuated viral transmission pathway through the respiratory tract following infection in the nasal airways. The second assay employed transduced non-replicating Lenti-X-Lentivirus to isolate and measure the extent of airflow-mediated viral deposition stemming from an initial infection site in the nasal compartment. Finally, in the third proof-of-concept, we measured the compartment-specific inflammatory cellular response to inhaled viral transmission in the airways using a non-replicating viral simulant (i.e., Poly I:C) and biochemical analysis of cytokine secretion.

We underscore that in all three proof-of-concept assays, we attempted to follow a realistic pulmonary infection pathway, initiating in the nasal compartment as the acknowledged initial exposure site. Subsequently, viral (or viral-like) laden aerosols were sequentially transmitted to the bronchial and acinar compartments subject to air flow-mediated mechanisms (**Figure 6**).

Syndrome-Related Coronavirus 2 Deposition in the Multi-Compartment *Airways-on-Chip* Platform

For this proof-of-concept assay, we used a human respiratory virus (SARS-CoV-2) where airflow transmission was conducted using a peristaltic pump (MRC, PP-X-575). The apical compartment of the nasal device was first injected with SARS-CoV-2 (1.2×10^6 PFU). Afterward, the apical compartments of all devices were sequentially connected. The Peristaltic Pump was connected to the apical compartment of the nasal device, and airflow (6.5 ml/min) was applied for 10 min, a relatively short exposure period chosen for safety precaution reasons. Right afterward, apical compartments were washed with MEM containing 2% FCS with NEAA, glutamine, and P/S, and samples were analyzed for viral RNA and PFU.

Both viral RNA and PFU results (**Figure 7**) support the plausible transmission of viral-laden aerosols from the nasal to bronchial compartments, and subsequently to the acinar unit. We note a stark reduction in viral load that decreases monotonically across the compartmental pathways, where most of the initial load reaches the first exposure site in the nasal passages. The most drastic reduction in viral presence seen in the acinar compartment likely results from aerosol deposition and flow diversion arising at the Y-joint (**Figure 6**). While the described *in vitro* assay supports and demonstrates the multi-compartmental platform's utility for delivering viable and functional SARS-CoV-2 airborne particles to the different compartments from a methodological and experimental standpoint, we note that further investigations would be nevertheless required to deliver a broader cellular characterization to test the susceptibility of the cells to the specific virus and the *in vitro* pathology of SARS-CoV-2, or any other virus.

Transduced Lenti-X-Lentivirus for Non-replicating Inhaled Viral Transmission Simulation

In this next proof-of-concept assay, we used a transduced non-replicating Lenti-X-Lentivirus to simulate initial viral exposure and transport, isolating the pathways of invading particles in our platform from the effects of replicative viral transmission. We then measured deposition in the three compartments under both physiological airflow and control (i.e., zero flow) conditions, revealing the determining role of airflow-mediated viral deposition in our platform (see **Figure 8**).

The exposure assay is conducted as follows: 150 μL of lentiviral supernatant was injected into the nasal compartment and set for 15 min (see **Figure 6**). Meanwhile, bronchial and acinar models were connected, and the whole *airways-on-chip* platform was assembled. Airflow (6.5 ml/min) was applied using a peristaltic pump (Ismatec, ISM597D) to the assembled devices, flowing from the nasal model to the bronchial model and lastly through the acinar model for 72 h in a humidified incubator. The experiment was terminated only 2 h post flow arrest to allow the deposition under gravitational sedimentation of any remaining airborne viral aerosols. In parallel, as a control the nasal model was similarly exposed to the transduced virus and connected in series with other compartments (**Figure 6**), but no airflow was applied. The devices were imaged using a tile scan with the Axio Observer 7 microscope (Zeiss). Images were processed using ZEN Blue v2.3 (Zeiss).

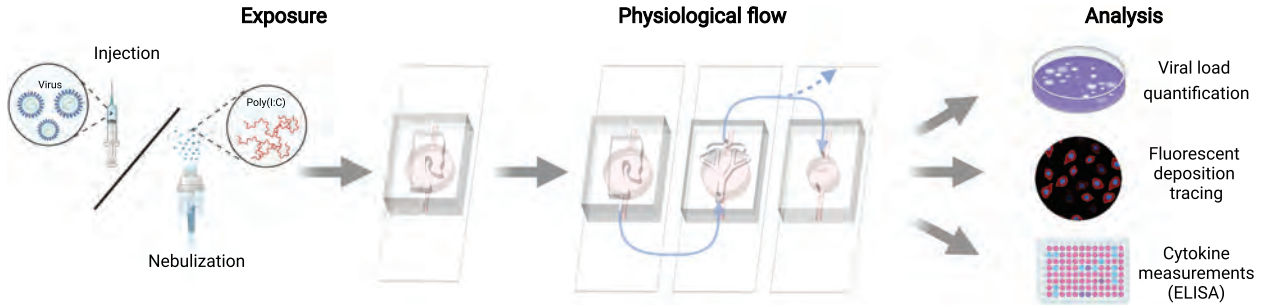

FIGURE 6 | Schematic of the experimental proof-of-concept protocols for inhalation assays. Exposure is limited first to the nasal compartment, either via direct instillation of the virus or nebulized Poly I:C viral simulant. Following exposure, all three apical compartments are connected in series to airflow supplied via a peristaltic pump. Note that airflow to the acinar compartment is reduced to a physiologically relevant range in the deep lungs (see **Table 1**). Each compartment is analyzed separately for viral quantity, deposition sites, and cellular cytokine secretion to the basal media.

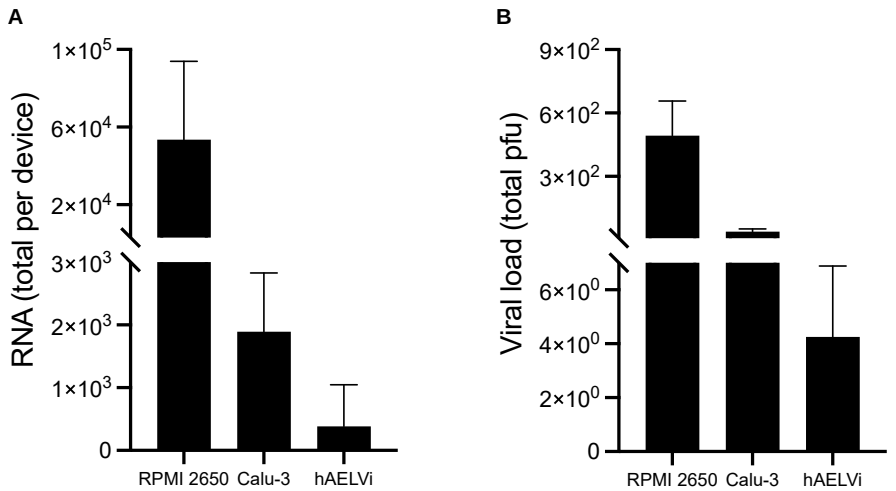

FIGURE 7 | Functional viral transmission of SARS-CoV-2 in the multi-compartment *airways-on-chip*. Compartmental viral load was quantified via **(A)** real-time PCR and **(B)** Plaque-forming units (PFU). In both assays, viral traces were detected in all three compartments, indicating the crosstalk in the chips. A monotonically decreasing viral presence is measured across the model, with considerable reduction observed between nasal and bronchial compartments owing to high deposition in the nasal compartment and tube connections. Further reduction in viral presence is measured in the acinar compartment, likely resulting from aerosol deposition in conjunction with flow diversion resulting from the Y-joint. Data are the average of three experiments presented as mean and the standard deviation (SD).

Our imaging results show that epithelial cells expressing fluorescent protein tdTomato were detected in all three distinctive compartments (**Figure 8**), supporting the airflow-mediated hypothesis toward transmission of primary viral load to all regions. Concurrently, no fluorescence was detected in either bronchial or acinar models when no airflow was applied, further underscoring the central role of airflow-mediated transmission.

Poly I:C for Non-replicating Viral Transmission Simulation

In a final proof-of-concept assay, we used Poly I:C, a synthetic double-stranded ribonucleic acid (dsRNA) molecule, to examine the initial cellular inflammatory response upon exposure to virus components as a pathogen-associated molecular pattern (PAMP). Poly I:C molecules are recognized by toll-like receptor-3 (TLR-3) expressed on the surface of epithelial cells, and elicit intracellular signaling pathways, subsequently secreting inflammatory cytokines such as interleukin-6 (IL-6) (Alexopoulou et al., 2001; Akira et al., 2006).

Using a standard compressor nebulizer (Bi-rich medical, BR-CN116), we supplied aerosolized poly I:C to the nasal compartment. The nebulizer cup (see the enlarged region in **Figure 9A**) was filled with diluted (100 $\mu g\ ml^{-1}$ in PBS) Poly I:C solution and connected via silicone tubing and a 19-gauge syringe tip to the nasal compartment's inlet port. Following 4 min of aerosol exposure, the nebulizer was turned off, and the platform was left to stabilize for 15 min, during which the bronchial and acinar compartments were connected in series (as shown in **Figure 6**). Once the multi-compartment platform was fully assembled, physiological airflow was perfused through the model for 72 h using a peristaltic pump (Ismatec, ISM597D). Thereafter, we placed the models in a −80°C freezer to induce freeze-burst of cells and discharge intracellular content. Subsequently, we collected the basal media and quantified the inflammatory cytokine interleukin 6 (IL-6) via Enzyme-Linked Immunosorbent

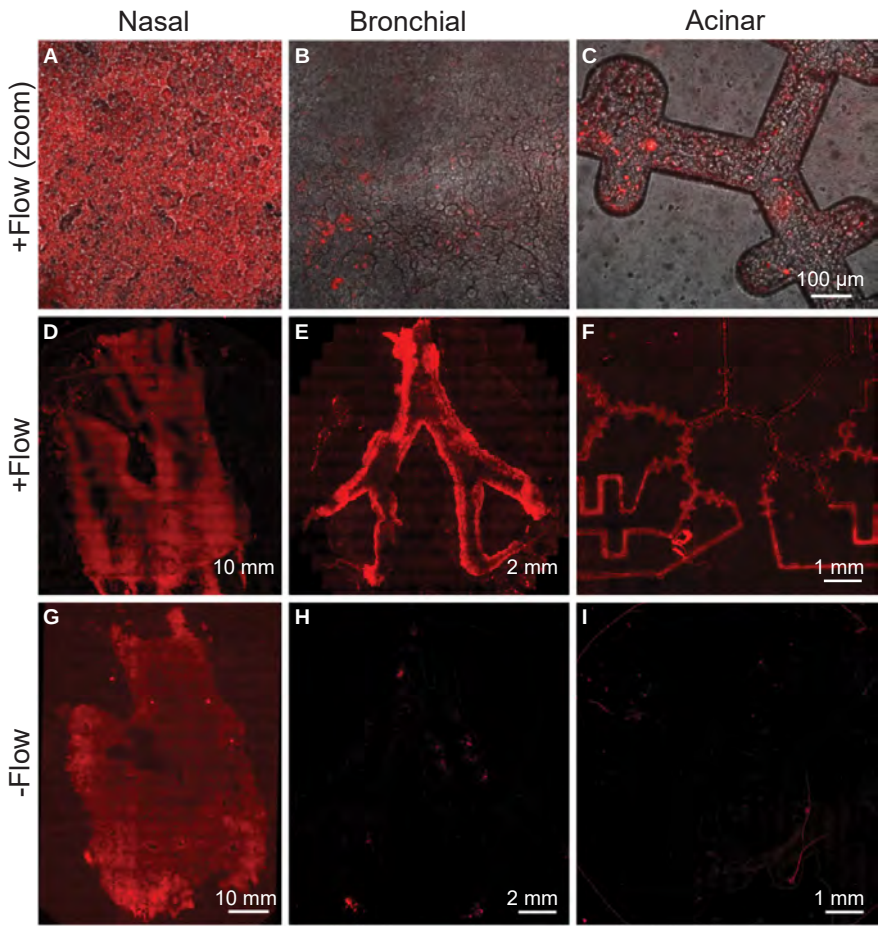

FIGURE 8 | Viral deposition tracing using Lenti-X-Lentivirus, a transduced non-replicating virus. Epithelial cells in each of three compartments are infected with virus expressing red fluorescent protein following exposure to physiological flow conditions. **(A–C)** Top row images (all the same scale) show cell-level magnification, while the bottom rows **(D–I)** show stitched microscopy images to view each compartment entirely. **(D–F)** Infection supports the airflow crosstalk in the chip's multi-compartments, as the transfer of virus is witnessed in each compartment downstream from the nasal passages. The bottom row **(G–I)** shows the control experiment, in the absence of any airflow applied, and showing thus the lack of airflow-mediated airborne transport. The figure represents one of three experiments yielding similar results.

Assay (ELISA). Quantitative analysis (**Figure 9B**) showed poly I:C induced elevation in IL-6 levels in all cell lines.

Calibration experiments (**Supplementary Figure 5**) show significant increases in cytokine secretion following direct poly I:C exposure across all cell lines, indicating the biological compatibility of the platform and selected cell populations for measuring inflammatory response to poly I:C. Exposure to aerosols generated via nebulization from equivalent concentrations of poly I:C follow similar patterns of elevated cytokine secretions. However, repeated experiments in RPMI2650 and hAELVi cells generated larger statistical variance indicating a noisier signal. The greater variability of aerosolized poly I:C molecules coming into contact with the cultured epithelial cell populations emphasizes the importance of flow-mediated exposure phenomena for the transmission pathway and the delicate caution needed for interpreting aerosol-based *in vitro* assays.

DISCUSSION AND OUTLOOK

With the Methods presented herein, our multi-compartment *airways-on-chip* is a versatile *in vitro* platform that can be further modulated and adapted for the needs of a wide variety of preclinical research endpoints, including for example questions pertaining to respiratory viral transmission in the human lungs. Specifically, we have provided all the necessary source files, including 3D printing formats needed to fabricate our platform (see **Supplementary Data**) and perform subsequent calibrations. Our three experimental proof-of-concept embodiments, spanning SARS-CoV-2, a transduced Lentivirus, and dsRNA Poly I:C were selected to showcase several biological and cellular capabilities of our platform as an attractive proof of concept. These include recapitulating physiological and biological characteristics of distinct respiratory tract key regions, alongside the capability to assess viral laden and cellular response in the different respiratory compartments and the

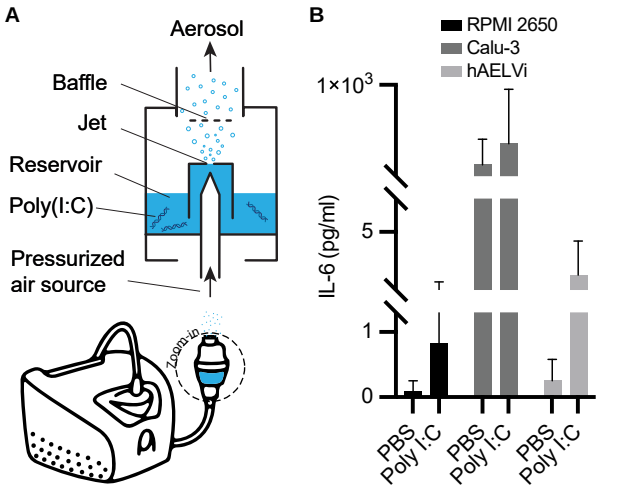

FIGURE 9 | Non-replicating viral transmission simulation using poly I:C and subsequent IL-6 secretions across the three compartments. **(A)** Schematic of the nebulization setup used to supply aerosolized poly I:C to the multi-compartment model. Following exposure, cells are freeze-burst and their media collected for **(B)** differentiated quantification of inflammatory cytokines in each compartment. Interleukin 6 (IL-6) was measured via enzyme-linked immunosorbent assay (ELISA). In all models, an elevation of IL-6 levels can be seen upon exposure to poly I:C compared to PBS exposure as a control. Bars represent the average and error bars of the standard deviation (*SD*) ($N = 3$ for PBS, $N = 5$ for poly I:C).

opportunity to mimic *in vitro* aspects of airborne crosstalk and transmission in the lungs.

Much of our initial motivation has been rooted in a platform for investigating transmission pathways, cell infection, and inflammation initiation by airborne viruses such as SARS-Cov-2. The compartmentalized, regional representations in each of the three compartments can be leveraged and adapted further for various *in vitro* assays to quantify regional differences in viral exposure under the influences of varying exposure conditions, aerosol dispersion characteristics and related airflow patterns and importantly, distinct epithelial cell populations.

As a first step, we examined the platform's compatibility for harboring and transporting SARS-CoV-2, of heightened interest amidst the ongoing global pandemic. Downstream transmission of viral particles to distal compartments from an initially isolated nasal compartment supports the model's crosstalk for airflow-mediated viral transmission, alongside a gradual reduction of viral load. However, the use of SARS-CoV-2 in experiments introduces tremendous safety risks and logistical burden (e.g., PPE, bio-safety rooms) that are intrinsically cumbersome when developing a new *in vitro* platform intended for more general virological studies. Furthermore, we hoped to demonstrate our platform's utility in laboratory settings that may lack the special safety conditions necessary for handling such dangerous and infections viruses. Consequently, in subsequent experiments, we employed other, less harmful and non-replicating viral proxies such as transduced lentivirus and the viral simulant poly I:C, demonstrating our platform's broader utility and opening the way for experimental protocols such as aerosolization, that would be limited by safety considerations when handling for example SARS-CoV-2.

We exposed our model to transduced Lenti-X-Lentivirus to estimate the initial dispersion and deposition of viral-laden aerosols, identifying infected cells via fluorescence microscopy. Fluorescent cells were imaged in all compartments, further confirming the crosstalk between the compartments and the existence of a viable transmission pathway. This experiment tracked the viability of the cell monolayer covering the whole model surface throughout and following the exposure event, necessary for subsequent biochemical analyses of cellular response. We note here that our assay demonstrates transmission, deposition, and initial viral or viral-like exposure, while a study of infection as well as the full biologic mode of action lies beyond the scope of this methods paper.

Due to the safety limitations mentioned above, SARS-CoV-2 and lentivirus were injected via a syringe to the nasal compartment in both experiments, in contrast to *in situ* viruses introduced into the respiratory system as aerosols, affecting the transmission mechanism and deposition outcomes (Artzy-Schnirman et al., 2019a). Acknowledging the importance of aerosol effects, and in order to mimic transmission pathways more realistically (Artzy-Schnirman et al., 2019a,b; Wang et al., 2021), we used a nebulizer to create an aerosolized exposure of poly I:C, a synthetic double-stranded ribonucleic acid (dsRNA) molecule that can be handled in a biosafety room 2 in a safety hood. Beyond its safer suitability for nebulization, poly I:C can still be recognized by toll-like receptor-3 (TLR-3) in epithelial cells, thus eliciting inflammatory response and secretion of inflammatory cytokines. Quantifying such cytokines in each compartment may enable to assess the local cellular stress, dependent on each compartment's particular physiology, airflow pattern, and cellular composure.

Whereas our platform was designed to have a relatively small height to improve optical clarity for microscopy, higher three-dimensionality may be incorporated where imaging is less of a priority or in tandem with more advanced three-dimensional imaging technology. Additionally, more complex flow patterns may be used for perfusing air in the apical compartments to more realistically mimic human breathing, such as using a programmable linear actuator or mechanical ventilator as done in previous works (Nof et al., 2020, 2021).

In parallel, we note that human cell lines differ from cells *in vivo*, both genotypically and phenotypically (Pan et al., 2009) and thus exhibit different functionality. Amongst other, such differences are embodied in the absence of cilia structure and mucus production in both the nasal RPMI2650 (Christiane Schmidt et al., 1998; Kreft et al., 2015b) and bronchial Calu-3 (Foster et al., 2000; Mathias et al., 2002; Fiegel et al., 2003) cell lines, thereby leading to underestimating mucociliary clearance on the distribution of the viral and viral-like particles in the three compartments. In parallel, hAELVi cells are alveolar type I like epithelial cells, and thus cannot produce surfactant (Ferguson and Schlesinger, 2000); a unique composite of lipids and proteins that play a crucial role in initial immunity (Ferguson and Schlesinger, 2000; Glasser and Mallampalli, 2011), that may

further affect the ability of infectious particles to attain the cells. Alternatively, primary patient-derived cells can be used when patient variation response is of interest or to improve the biological relevance of the cellular response assays at the cost of throughput. Here, our choice for selecting cell lines lies in their reliability, robustness, and non-patient-specific variability in serving as a benchmark for end users (Hittinger et al., 2015; Sakagami, 2020; Selo et al., 2021), in particular during preclinical *in vitro* stages. Note nevertheless that cellular assays can be adapted to include additional co-cultures, including but not limited to immune cells in the apical compartment (Ainslie et al., 2019; Artzy-Schnirman et al., 2019b) (e.g., macrophages) (Ainslie et al., 2019), but also reconstructing an air-blood barrier (ABB) with endothelial cells cultures on the basal side of the membrane (Barnes et al., 2015a; Artzy-Schnirman et al., 2021).

Lastly, we raise the point that our *in vitro* platform exhibits distinct cellularized airway compartments, connected via silicon tubing exclusively during experimental procedures (see section "Materials and Methods" above). The isolation of the individual compartments during the preparation phase allows for experimental easiness in maintenance as well as during cellular differentiation, and finally during independent compartmental viral load measurements. Furthermore, our platform's modular "plug and play" design leverages easier adoption and adaptability for other preclinical research needs, specifically with the end user in mind (Ainslie et al., 2019; Artzy-Schnirman et al., 2019a). With such functionalities enabled during experimentation, we note, however, here that these advantages come at the cost of introducing various artifacts relative to the natural *in vivo* lung environment, including foremost a discontinuity in the epithelial lining that is anticipated to affect viral propagation characteristics along a continuous airway tract (Leung, 2021; Wang et al., 2021). Notably, this includes innate clearing and defense mechanisms (Nicod, 2005) via mucociliary clearance in the conducting regions of the lungs, as well displacements of the surfactant-rich liquid lining layer in the deep respiratory regions. With these limitations in mind, our *in vitro* efforts offer to the best of our knowledge the first *airway-on-chip* attempt to deliver a more comprehensive recapitulation of the broader lung regions via key lung compartments that breaks away from current state-of-the-art individual isolated *lung-on-chip* models (Benam et al., 2015; Artzy-Schnirman et al., 2021).

Altogether, our efforts deliver an open-source *in vitro* multi-compartment platform available to end users across the academic and biopharmaceutical communities that can be utilized and adapted further as a powerful tool in preclinical research for investigating amongst other respiratory infections, host-pathogen interactions as well as potential drug screens and discovery endpoints.

DATA AVAILABILITY STATEMENT

The original contributions presented in the study are included in the article/**Supplementary Material**, further inquiries can be directed to the corresponding author.

AUTHOR CONTRIBUTIONS

EN, HZ, and AA-S: methodology. EN and SB: software. EN and AA-S: validation. EN, HZ, AA-S, OM, MB, DG, and AB-D: investigation. SE-K: resources. EN and HZ: writing–original draft. EN, HZ, AA-S, and JS: writing—review and editing. AA-S, SL, NK, AO, and JS: supervision. AA-S, AO, and JS: funding acquisition and conceptualization. All authors contributed to the article and approved the submitted version.

FUNDING

This work was supported by the European Research Council (ERC) under the European Union's Horizon 2020 Research and Innovation Program (Grant Agreement No. 677772), the Israel Science Foundation (Grant No. 1840/21) and the Ministry of Science and Technology (MOST, Israel) (Grant No. 3-17350).

ACKNOWLEDGMENTS

We would like to thank the support of the Multidisciplinary Infrastructure Center at the Russel Berrie Nanotechnology Institute (Technion). Some of the figures in this article were created using artwork from Biorender.com with license.

SUPPLEMENTARY MATERIAL

The Supplementary Material for this article can be found online at: https://www.frontiersin.org/articles/10.3389/fphys.2022.853317/full#supplementary-material

REFERENCES

Ainslie, G. R., Davis, M., Ewart, L., Lieberman, L. A., Rowlands, D. J., Thorley, A. J., et al. (2019). Microphysiological lung models to evaluate the safety of new pharmaceutical modalities: a biopharmaceutical perspective. *Lab Chip* 19, 3152–3161. doi: 10.1039/c9lc00492k

Akira, S., Uematsu, S., and Takeuchi, O. (2006). Pathogen recognition and innate immunity. *Cell* 124, 783–801. doi: 10.1016/j.cell.2006.02.015

Alexopoulou, L., Holt, A., Medzhitov, R., and Flavell, R. A. (2001). Recognition of double-stranded RNA and activation of NF-kappaB by Toll-like receptor 3. *Nature* 413, 732–738. doi: 10.1038/35099560

Alge, C. S., Hauck, S. M., Priglinger, S. G., Kampik, A., and Ueffing, M. (2006). Differential protein profiling of primary versus immortalized human RPE cells identifies expression patterns associated with cytoskeletal remodeling and cell survival. *J. Proteome Res.* 5, 862–878. doi: 10.1021/pr050420t

Artzy-Schnirman, A., Arber Raviv, S., Doppelt Flikshtain, O., Shklover, J., Korin, N., Gross, A., et al. (2021). Advanced human-relevant in vitro pulmonary platforms for respiratory therapeutics. *Adv. Drug Deliv. Rev.* 176:113901. doi: 10.1016/j.addr.2021.113901

Artzy-Schnirman, A., Hobi, N., Schneider-Daum, N., Guenat, O. T., Lehr, C., and Sznitman, J. (2019a). Advanced in vitro lung-on-chip platforms for inhalation assays: from prospect to pipeline. *Eur. J. Pharm. Biopharm.* 144, 11–17. doi: 10.1016/j.ejpb.2019.09.006

Artzy-Schnirman, A., Lehr, C. M., and Sznitman, J. (2020). Advancing human in vitro pulmonary disease models in preclinical research: opportunities for lung-on-chips. *Expert Opin. Drug Deliv.* 17, 621–625. doi: 10.1080/17425247.2020.1738380

Artzy-Schnirman, A., Zidan, H., Elias-Kirma, S., Ben-Porat, L., Tenenbaum-Katan, J., Carius, P., et al. (2019b). Capturing the onset of bacterial pulmonary infection in acini-on-chips. *Adv. Biosyst.* 3:1900026. doi: 10.1002/adbi.201900026

Barnes, P. J., Bonini, S., Seeger, W., Belvisi, M. G., Ward, B., and Holmes, A. (2015a). Barriers to new drug development in respiratory disease. *Eur. Respir. J.* 45, 1197–1207. doi: 10.1183/09031936.00007915

Barnes, P. J., Burney, P. G., Silverman, E. K., Celli, B. R., Vestbo, J., Wedzicha, J. A., et al. (2015b). Chronic obstructive pulmonary disease. *Nat. Rev. Dis. Prim.* 1:15076.

Benam, K. H., Dauth, S., Hassell, B., Herland, A., Jain, A., Jang, K. J., et al. (2015). Engineered in vitro disease models. *Annu. Rev. Pathol. Mech. Dis.* 10, 195–262.

Bhatia, S. N., and Ingber, D. E. (2014). Microfluidic organs-on-chips. *Nat. Biotechnol.* 32, 760–772.

Borczuk, A. C., Salvatore, S. P., Seshan, S. V., Patel, S. S., Bussel, J. B., Mostyka, M., et al. (2020). COVID-19 pulmonary pathology: a multi-institutional autopsy cohort from Italy and New York City. *Mod. Pathol.* 33, 2156–2168. doi: 10.1038/s41379-020-00661-1

Brüning, J., Hildebrandt, T., Heppt, W. J., Schmidt, N., Lamecker, H., Szengel, A., et al. (2020). Characterization of the airflow within an average geometry of the healthy human nasal cavity. *Sci. Rep.* 10:3755. doi: 10.1038/s41598-020-60755-3

Carius, P., Dubois, A., Ajdarirad, M., and Artzy-schnirman, A. (2021). PerfuPul — a versatile perfusable platform to assess permeability and barrier function of air exposed pulmonary epithelia. *Front. Bioeng. Biotechnol.* 9:743236. doi: 10.3389/fbioe.2021.743236

Christiane Schmidt, M., Peter, H., Lang, S. R., Ditzinger, G., and Merkle, H. P. (1998). In vitro cell models to study nasal mucosal permeability and metabolism. *Adv. Drug Deliv. Rev.* 29, 51–79. doi: 10.1016/s0169-409x(97)00061-6

De Fraissinette, A., Brun, R., Felix, H., Vonderscher, J., and Rummelt, A. (1995). Evaluation of the human cell line RPMI 2650 as an in vitro nasal model. *Rhinology* 33, 194–198.

de Souza Carvalho, C., Daum, N., and Lehr, C.-M. (2014). Carrier interactions with the biological barriers of the lung: advanced in vitro models and challenges for pulmonary drug delivery. *Adv. Drug Deliv. Rev.* 75, 129–140. doi: 10.1016/j.addr.2014.05.014

Ehrmann, S., Schmid, O., Darquenne, C., Rothen-Rutishauser, B., Sznitman, J., Yang, L., et al. (2020). Innovative preclinical models for pulmonary drug delivery research. *Expert Opin. Drug Deliv.* 17, 463–478. doi: 10.1080/17425247.2020.1730807

Elbert, K. J., Schäfer, U. F., Schäfers, H. J., Kim, K. J., Lee, V. H., and Lehr, C. M. (1999). Monolayers of human alveolar epithelial cells in primary culture for pulmonary absorption and transport studies. *Pharm. Res.* 16, 601–608. doi: 10.1023/a:1018887501927

Elias-Kirma, S., Artzy-Schnirman, A., Das, P., Heller-Algazi, M., Korin, N., and Sznitman, J. (2020). In situ-Like aerosol inhalation exposure for cytotoxicity assessment using airway-on-chips platforms. *Front. Bioeng. Biotechnol.* 8:91. doi: 10.3389/fbioe.2020.00091

Esch, E. W., Bahinski, A., and Huh, D. (2015). Organs-on-chips at the frontiers of drug discovery. *Nat. Rev. Drug Discov.* 14, 248–260. doi: 10.1038/nrd4539

Faber, S. C., and McCullough, S. D. (2018). Through the looking glass: *In Vitro* models for inhalation toxicology and interindividual variability in the airway. *Appl. In Vitro Toxicol.* 4, 115–128. doi: 10.1089/aivt.2018.0002

Ferguson, J. S., and Schlesinger, L. S. (2000). Pulmonary surfactant in innate immunity and the pathogenesis of tuberculosis. *Tuber. Lung Dis.* 80, 173–184. doi: 10.1054/tuld.2000.0242

Fiegel, J., Ehrhardt, C., Schaefer, U. F., Lehr, C. M., and Hanes, J. (2003). Large porous particle impingement on lung epithelial cell monolayers – Toward improved particle characterization in the lung. *Pharm. Res.* 20, 788–796. doi: 10.1023/a:1023441804464

Fishler, R., Hofemeier, P., Etzion, Y., Dubowski, Y., and Sznitman, J. (2015). Particle dynamics and deposition in true-scale pulmonary acinar models. *Sci. Rep.* 5:14071. doi: 10.1038/srep14071

Forbes, B., and Ehrhardt, C. (2005). Human respiratory epithelial cell culture for drug delivery applications. *Eur. J. Pharm. Biopharm.* 60, 193–205. doi: 10.1016/j.ejpb.2005.02.010

Foster, K. A., Avery, M. L., Yazdanian, M., and Audus, K. L. (2000). Characterization of the Calu-3 cell line as a tool to screen pulmonary drug delivery. *Int. J. Pharm.* 208, 1–11. doi: 10.1016/s0378-5173(00)00452-x

Glasser, J. R., and Mallampalli, R. K. (2011). Surfactant and its role in the pathobiology of pulmonary infection. *Microbes Infect.* 14, 17–25. doi: 10.1016/j.micinf.2011.08.019

Haddrick, M., and Simpson, P. B. (2019). Organ-on-a-chip technology: turning its potential for clinical benefit into reality. *Drug Discov. Today* 24, 1217–1223. doi: 10.1016/j.drudis.2019.03.011

Hittinger, M., Juntke, J., Kletting, S., Schneider-Daum, N., de Souza Carvalho, C., and Lehr, C. M. (2015). Preclinical safety and efficacy models for pulmonary drug delivery of antimicrobials with focus on in vitro models. *Adv. Drug Deliv. Rev.* 85, 44–56. doi: 10.1016/j.addr.2014.10.011

Hogg, J. C., and Timens, W. (2009). The pathology of chronic obstructive pulmonary disease. *Annu. Rev. Pathol. Mech. Dis.* 4, 435–459.

Horsfield, K., Dart, G., Olson, D. E., Filley, G. F., and Cumming, G. (1971). Models of the human bronchial tree. *J. Appl. Physiol.* 31, 207–217.

Hou, Y. J., Okuda, K., Edwards, C. E., Martinez, D. R., Asakura, T., Dinnon, K. H. III, et al. (2020). SARS-CoV-2 reverse genetics reveals a variable infection gradient in the respiratory tract. *Cell* 182, 429–446.e14. doi: 10.1016/j.cell.2020.05.042

Ingber, D. E. (2020). Is it time for reviewer 3 to request human organ chip experiments instead of animal validation studies? *Adv. Sci.* 7:2002030. doi: 10.1002/advs.202002030

Kaur, G., and Dufour, J. M. (2012). *Do Not Distribute*. Austin, TX: Landes Bioscience, 1–5.

Koullapis, P., Ollson, B., Kassinos, S. C., and Sznitman, J. (2019). Multiscale in silico lung modeling strategies for aerosol inhalation therapy and drug delivery. *Curr. Opin. Biomed. Eng.* 11, 130–136. doi: 10.1016/j.cobme.2019.11.003

Koullapis, P., Stylianou, F., Lin, C.-L., Kassinos, S., and Sznitman, J. (2021). "In silico methods to model dose deposition," in *Inhaled Medicines. Optimizing Development through Integration of In Silico, In Vitro and In Vivo Approaches*, eds S. Kassinos, P. Bäckman, J. Conway, and A. J. Hickey (Cambridge, MA: Academic Press), 167–195. doi: 10.1016/B978-0-12-814974-4.00012-2

Kreft, M. E., Jerman, U. D., Lasič, E., Hevir-Kene, N., Rižner, T. L., Peternel, L., et al. (2015a). The characterization of the human cell line Calu-3 under different culture conditions and its use as an optimized in vitro model to investigate bronchial epithelial function. *Eur. J. Pharm. Sci.* 69, 1–9. doi: 10.1016/j.ejps.2014.12.017

Kreft, M. E., Jerman, U. D., Lasič, E., Lanišnik Rižner, T., Hevir-Kene, N., Peternel, L., et al. (2015b). The characterization of the human nasal epithelial cell line RPMI 2650 under different culture conditions and their optimization for an appropriate in vitro nasal model. *Pharm. Res.* 32, 665–679. doi: 10.1007/s11095-014-1494-0

Kuehn, A., Kletting, S., de Souza Carvalho-Wodarz, C., Repnik, U., Griffiths, G., Fischer, U., et al. (2016). Human alveolar epithelial cells expressing tight junctions to model the air-blood barrier. *ALTEX* 33, 251–260. doi: 10.14573/altex.1511131

Lacroix, G., Koch, W., Ritter, D., Gutleb, A. C., Larsen, S. T., Loret, T., et al. (2018). Air – liquid interface *In Vitro* models for respiratory toxicology research: consensus workshop and recommendations. *Appl. In Vitro Toxicol.* 4, 91–106. doi: 10.1089/aivt.2017.0034

Leung, N. H. L. (2021). Transmissibility and transmission of respiratory viruses. *Nat. Rev. Microbiol.* 19, 528–545. doi: 10.1038/s41579-021-00535-6

Li, C., Jiang, J., Dong, H., and Zhao, K. (2017). Computational modeling and validation of human nasal airflow under various breathing conditions. *J. Biomech.* 64, 59–68. doi: 10.1016/j.jbiomech.2017.08.031

Liu, D., Zhang, H., Fontana, F., Hirvonen, J. T., and Santos, H. A. (2017). Current developments and applications of microfluidic technology toward clinical translation of nanomedicines. *Adv. Drug Deliv. Rev.* 128, 54–83. doi: 10.1016/j.addr.2017.08.003

Liu, Y., Johnson, M. R., Matida, E. A., Kherani, S., and Marsan, J. (2009). Creation of a standardized geometry of the human nasal cavity. *J. Appl. Physiol.* 106, 784–795. doi: 10.1152/japplphysiol.90376.2008

Ma, C., Peng, Y., Li, H., and Chen, W. (2021). Organ-on-a-Chip: a new paradigm for drug development. *Trends Pharmacol. Sci.* 42, 119–133. doi: 10.1016/j.tips.2020.11.009

Masters, J. R. W. (2000). Human cancer cell lines: fact and fantasy. *Nat. Rev. Mol. Cell Biol.* 1, 233–236. doi: 10.1038/35043102

Mathias, N. R., Timoszyk, J., Stetsko, P. I., Megill, J. R., Smith, R. L., and Wall, D. A. (2002). Permeability characteristics of Calu-3 human bronchial epithelial cells: in vitro-in vitro correlation to predict lung absorption in rats. *J. Drug Target.* 10, 31–40. doi: 10.1080/10611860290007504

Mestas, J., and Hughes, C. C. W. (2004). Of mice and not men: differences between mouse and human immunology. *J. Immunol.* 172, 2731–2738. doi: 10.4049/jimmunol.172.5.2731

Miller, A. J., and Spence, J. R. (2017). *In Vitro* models to study human lung development, disease and homeostasis. *Physiology (Bethesda)* 32, 246–260. doi: 10.1152/physiol.00041.2016

Mittal, R., Woo, F. W., Castro, C. S., Cohen, M. A., Karanxha, J., Mittal, J., et al. (2019). Organ-on-chip models: implications in drug discovery and clinical applications. *J. Cell. Physiol.* 234, 8352–8380. doi: 10.1002/jcp.27729

Nahar, K., Gupta, N., Gauvin, R., Absar, S., Patel, B., Gupta, V., et al. (2013). In vitro, in vivo and ex vivo models for studying particle deposition and drug absorption of inhaled pharmaceuticals. *Eur. J. Pharm. Sci.* 49, 805–818. doi: 10.1016/j.ejps.2013.06.004

Nichols, J. E., Niles, J. A., Vega, S. P., Argueta, L. B., Eastaway, A., and Cortiella, J. (2014). Modeling the lung: design and development of tissue engineered macro- and micro-physiologic lung models for research use. *Exp. Biol. Med. (Maywood)* 239, 1135–1169. doi: 10.1177/1535370214536679

Nicod, L. P. (2005). Lung defences: an overview. *Eur. Respir. Rev.* 14, 45–50.

Nof, E., Artzy-Schnirman, A., Bhardwaj, S., Sabatan, H., Waisman, D., Hochwald, O., et al. (2021). Ventilation-induced epithelial injury drives biological onset of lung trauma in vitro and is mitigated with prophylactic anti-inflammatory therapeutics. *Bioeng. Transl. Med.* e10271. doi: 10.1002/BTM2.10271

Nof, E., Heller-Algazi, M., Coletti, F., Waisman, D., and Sznitman, J. (2020). Ventilation-induced jet suggests biotrauma in reconstructed airways of the intubated neonate. *J. R. Soc. Interface* 17:20190516.

Pan, C., Kumar, C., Bohl, S., Klingmueller, U., and Mann, M. (2009). Comparative proteomic phenotyping of cell lines and primary cells to assess preservation of cell type-specific functions. *Mol. Cell. Proteomics* 8, 443–450.

Prakash, Y. S., Halayko, A. J., Gosens, R., Panettieri, R. A. Jr., Camoretti-Mercado, B., and Penn, R. B. (2017). An official American thoracic society research statement: current challenges facing research and therapeutic advances in airway remodeling. *Am. J. Respir. Crit. Care Med.* 195, e4–e19.

Psimadas, D., Georgoulias, P., Valotassiou, V., and Loudos, G. (2012). Molecular nanomedicine towards cancer. *J. Pharm. Sci.* 101, 2271–2280.

Sakagami, M. (2006). In vivo, in vitro and ex vivo models to assess pulmonary absorption and disposition of inhaled therapeutics for systemic delivery. *Adv. Drug Deliv. Rev.* 58, 1030–1060.

Sakagami, M. (2020). In vitro, ex vivo and in vivo methods of lung absorption for inhaled drugs. *Adv. Drug Deliv. Rev.* 161–162, 63–74.

Schreck, S., Sullivan, K. J., Ho, C. M., and Chang, H. K. (1993). Correlations between flow resistance and geometry in a model of the human nose. *J. Appl. Physiol. (1985)* 75, 1767–1775.

Selo, M. A., Sake, J. A., Kim, K. J., and Ehrhardt, C. (2021). In vitro and ex vivo models in inhalation biopharmaceutical research — advances, challenges and future perspectives. *Adv. Drug Deliv. Rev.* 177:113862.

Seok, J., Warren, H. S., Cuenca, A. G., Mindrinos, M. N., Baker, H. V., Xu, W., et al. (2013). Genomic responses in mouse models poorly mimic human inflammatory diseases. *Proc. Natl. Acad. Sci. U.S.A.* 110, 3507–3512.

Shachar-berman, L., Bhardwaj, S., Ostrovski, Y., Das, P., Koullapis, P., Kassinos, S., et al. (2020). In Silico optimization of fiber-shaped aerosols in inhalation therapy for augmented targeting and deposition across the respiratory tract. *Pharmaceutics* 12:230.

Shachar-Berman, L., Ostrovski, Y., Koshiyama, K., Wada, S., Kassinos, S. C., and Sznitman, J. (2019). Targeting inhaled fibers to the pulmonary acinus: opportunities for augmented delivery from in Silico simulations. *Eur. J. Pharm. Sci.* 137:105003.

Shrestha, J., Razavi Bazaz, S., Aboulkheyr Es, H., Yaghobian Azari, D., Thierry, B., Ebrahimi Warkiani, M., et al. (2020). Lung-on-a-chip : the future of respiratory disease models and pharmacological studies. *Crit. Rev. Biotechnol.* 40, 213–230.

Sznitman, J. (2013). Respiratory microflows in the pulmonary acinus. *J. Biomech.* 46, 284–298.

Sznitman, J. (2021). Revisiting airflow and aerosol transport phenomena in the deep lungs with microfluidics. *Chem. Rev.* 15. doi: 10.1021acs.chemrev.1c00621

Tay, M. Z., Poh, C. M., Rénia, L., MacAry, P. A., and Ng, L. F. P. (2020). The trinity of COVID-19: immunity, inflammation and intervention. *Nat. Rev. Immunol.* 20, 363–374.

Tenenbaum-Katan, J., Artzy-Schnirman, A., Fishler, R., Korin, N., and Sznitman, J. (2018). Biomimetics of the pulmonary environment *in vitro*: a microfluidics perspective. *Biomicrofluidics* 12:042209.

van der Worp, H. B., Howells, D. W., Sena, E. S., Porritt, M. J., Rewell, S., O'Collins, V., et al. (2010). Can animal models of disease reliably inform human studies? *PLoS Med.* 7:e1000245. doi: 10.1371/journal.pmed.1000245

Wang, C. C., Prather, K. A., Sznitman, J., Jimenez, J. L., Lakdawala, S. S., Tufekci, Z., et al. (2021). Airborne transmission of respiratory viruses. *Science* 373:eabd9149.

Weibel, E. R. (1965). Morphometry of the human lung. *Anesthesiology* 26:367.

Wisnivesky, J., and De-Torres, J. P. (2019). The global burden of pulmonary diseases: most prevalent problems and opportunities for improvement. *Ann. Glob. Health* 85, 1–2.

Wylie, J. L., House, A., Mauser, P. J., Sellers, S., Terebetski, J., Wang, Z., et al. (2018). Inhaled formulation and device selection: bridging the gap between preclinical species and first-in-human studies. *Ther. Deliv.* 9, 387–404.

Zhang, B., Korolj, A., Lai, B. F. L., and Radisic, M. (2018). Advances in organ-on-a-chip engineering. *Nat. Rev. Mater.* 3, 257–278.

Zwicker, D., Ostilla-Mónico, R., Lieberman, D. E., and Brenner, M. P. (2018). Physical and geometric constraints shape the labyrinth-like nasal cavity. *Proc. Natl. Acad. Sci. U.S.A.* 115, 2936–2941.

Conflict of Interest: The authors declare that the research was conducted in the absence of any commercial or financial relationships that could be construed as a potential conflict of interest.

Citation: Nof E, Zidan H, Artzy-Schnirman A, Mouhadeb O, Beckerman M, Bhardwaj S, Elias-Kirma S, Gur D, Beth-Din A, Levenberg S, Korin N, Ordentlich A and Sznitman J (2022) Human Multi-Compartment Airways-on-Chip Platform for Emulating Respiratory Airborne Transmission: From Nose to Pulmonary Acini. Front. Physiol. 13:853317. doi: 10.3389/fphys.2022.853317

frontiers in Physiology

MINI REVIEW
published: 08 March 2022
doi: 10.3389/fphys.2022.825433

Imaging Regional Lung Structure and Function in Small Animals Using Synchrotron Radiation Phase-Contrast and K-Edge Subtraction Computed Tomography

Sam Bayat[1,2], Luca Fardin[3]*, José Luis Cercos-Pita[4], Gaetano Perchiazzi[4] and Alberto Bravin[5]*

[1] Univ. Grenoble Alpes, Inserm UA07 STROBE Laboratory, University of Grenoble Alpes, Grenoble, France, [2] Department of Pulmonology and Clinical Physiology, Grenoble University Hospital, Grenoble, France, [3] European Synchrotron Radiation Facility, Grenoble, France, [4] Hedenstierna Laboratory, Department of Surgical Sciences, Uppsala University, Uppsala, Sweden, [5] Department of Physics, University of Milano-Bicocca,, Milan, Italy

OPEN ACCESS

Edited by:
Walter Araujo Zin, Federal University of Rio de Janeiro, Brazil

Reviewed by:
Stefan Sawall, German Cancer Research Center (DKFZ), Germany
Hari Arora, Imperial College London, United Kingdom

***Correspondence:**
Sam Bayat
sbayat@chu-grenoble.fr
Luca Fardin
luca.fardin@esrf.fr

Specialty section:
This article was submitted to Respiratory Physiology, a section of the journal Frontiers in Physiology

Received: *30 November 2021*
Accepted: *14 February 2022*
Published: *08 March 2022*

Citation:
Bayat S, Fardin L, Cercos-Pita JL, Perchiazzi G and Bravin A (2022) Imaging Regional Lung Structure and Function in Small Animals Using Synchrotron Radiation Phase-Contrast and K-Edge Subtraction Computed Tomography. Front. Physiol. 13:825433. doi: 10.3389/fphys.2022.825433

Synchrotron radiation offers unique properties of coherence, utilized in phase-contrast imaging, and high flux as well as a wide energy spectrum which allow the selection of very narrow energy bands of radiation, used in K-edge subtraction imaging (KES) imaging. These properties extend X-ray computed tomography (CT) capabilities to quantitatively assess lung morphology, and to map regional lung ventilation, perfusion, inflammation, aerosol particle distribution and biomechanical properties, with microscopic spatial resolution. Four-dimensional imaging, allows the investigation of the dynamics of regional lung functional parameters simultaneously with structural deformation of the lung as a function of time. These techniques have proven to be very useful for revealing the regional differences in both lung structure and function which is crucial for better understanding of disease mechanisms as well as for evaluating treatment in small animal models of lung diseases. Here, synchrotron radiation imaging methods are described and examples of their application to the study of disease mechanisms in preclinical animal models are presented.

Keywords: pulmonary function, synchrotrons, computed tomography, respiration artificial, regional blood flow

INTRODUCTION

An ideal technique for imaging regional lung function should provide both high spatial and temporal resolution, allow for quantitative measurements of functional parameters and provide the ability to image the underlying lung morphology. Structural and functional imaging data along with computational modeling have significantly contributed to our understanding that lung function as a whole cannot be predicted by the sum of the behavior of individual components, but results rather from the interaction of components at multiple scales ranging from biomolecular and cellular to different lung regions, which leads to

complex dynamic phenomena such as self-organization and emergence (Suki and Bates, 2011). Human, animal and cell culture studies have demonstrated that mechanical strain on the lung tissue and alveoli, plays a crucial role in processes such as lung growth and repair, surfactant release and inflammation (Roan and Waters, 2011). However, capturing lung structure and function simultaneously at small length scales remains a very technically challenging goal *in vivo*, and despite advances in both imaging technology and understanding of lung mechanics over the past decades, still little is known about lung micromechanics and how lung alveoli and acini deform during breathing (Roan and Waters, 2011; Smaldone and Mitzner, 2012).

Conventional X-ray imaging with laboratory or clinical sources, is based on absorption contrast. A multitude of interesting methods and algorithms have been developed for conventional micro-CT of the lung, with prospective and retrospective gating, motion compensation, and radiation dose reduction *via* sophisticated reconstruction algorithms. These have been extensively reviewed previously (Ashton et al., 2015; Clark and Badea, 2021). However, conventional CT is limited by the low radiation flux available in standard X-ray imaging systems, which reduces the spatial and temporal resolution, particularly in *in vivo* imaging.

Synchrotron radiation on the other hand, offers unique properties of high flux, wide energy spectrum and coherence, meaning that the photons are to a large degree spatially and temporally in phase. The high flux as well as a wide energy spectrum allow the selection of very narrow energy bands of radiation, utilized in K-edge subtraction imaging (KES) imaging. The coherence of the radiation is utilized instead in phase-contrast imaging. Here, the distortion of the X-ray wave front in the lung leads to strong edge enhancement within the images due to interference of the transmitted and refracted radiation. In weakly attenuating tissues such as the lung, refraction can be orders of magnitude greater than absorption, particularly at higher energies. The propagation-based imaging technique (PBI) has proven to be especially suited for lung imaging due to sharp edge enhancement caused by the air-to-tissue interfaces in the lung microstructures (4, 5).

Four-dimensional (4D) CT imaging, in which high-resolution mapping of lung functional parameters is recorded simultaneously with structural deformation of tissue morphology as a function of time, provides the basis for comprehensive modeling of the dynamics of lung function, at spatial resolutions allowing the visualization of alveoli. Recently, impressive results toward this goal have been achieved using synchrotron radiation sources (Cercos-Pita et al., DOI: 10.21203/rs.3.rs-970496/v1, *under review*).

The physical instrumentation and optical methods of these imaging techniques has been reviewed in detail recently (Bayat et al., 2020). In this mini-review, methodological aspects of KES-CT and propagation-based 4D-CT lung microscopy are summarized.

ANIMAL PREPARATION

In vivo imaging with synchrotron radiation requires dedicated instrumentation and remote control. The synchrotron beam is a stationary horizontal fan so that the animal is subjected to rotation up to 180–360°/s as well as vertical displacement for 2D-projection imaging. While it is possible to acquire images during free breathing, obtaining high resolution maps of regional ventilation using this imaging method usually requires the respiration to be controlled by mechanical ventilation while the physiological parameters are continuously monitored and recorded. Other global measurements of cardiovascular (e.g., ECG, invasive blood pressure) and respiratory function such as respiratory mechanics (Bayat et al., 2009) or inert gas multiple breath washout (Bayat et al., 2013) can be performed in parallel to image acquisition using the experimental setup (**Figure 1**). Mechanical ventilation can be ensured using *ad hoc* systems allowing synchronization with the image acquisition or commercial and even clinical mechanical ventilators (Porra et al., 2016), as long as these devices can be remotely controlled for example to pause respiration in inspiration or expiration for imaging. Imaging the lung in static conditions in apnea typically requires pauses of 1–3 s in lower-resolution KES imaging and 10–60 s in higher resolution phase-contrast imaging. Longer apnea durations in small animals require preoxygenation followed by apneic oxygenation by high-flow O_2 at the airway opening, in order to avoid O_2 desaturation during imaging (Frumin et al., 1959).

Anesthesia is usually induced by intramuscular injection of a mixture of ketamine and xylazine (rabbit, rat, mouse), or IV injection of thiopental sodium *via* a catheter (22 G) introduced into the marginal ear vein under local anesthesia (5% topical lidocaine) in rabbits. Anesthesia is then maintained by IV infusion (rabbit, rat) or IP injection (mouse) of a ketamine and xylazine mixture. Anesthesia can also be maintained by inhaled volatile anesthetics. Controlled mechanical ventilation can be delivered through tracheal intubation or most often tracheostomy with a polyethylene tracheal tube. For some imaging protocols, after ensuring adequate depth of anesthesia, muscle relaxation is induced by continuous IV infusion of atracurium (rabbit) or IP pancuronium bromide (rat, mouse). Depth of anesthesia is monitored by regularly assessing the state of the pupils (rabbit) and heart rate. Because the radiation beam is horizontal, the animal is typically placed in a custom-made plastic holder for imaging in upright position (Porra et al., 2004). However, local tomography can also be performed in supine position in small animals (unpublished data).

Physiological parameters, such as the ECG, respiratory pressure and flow, arterial pressure, oxygen saturation, among other parameters, can be monitored using an analog/digital interface. This allows not only to monitor and record such parameters in order to assess the physiological condition and welfare of the animal, but also to collect scientifically important data such as respiratory mechanics and hemodynamic parameters. Parameters such as the ECG and respiratory pressures also allow to trigger image acquisition in a prospectively

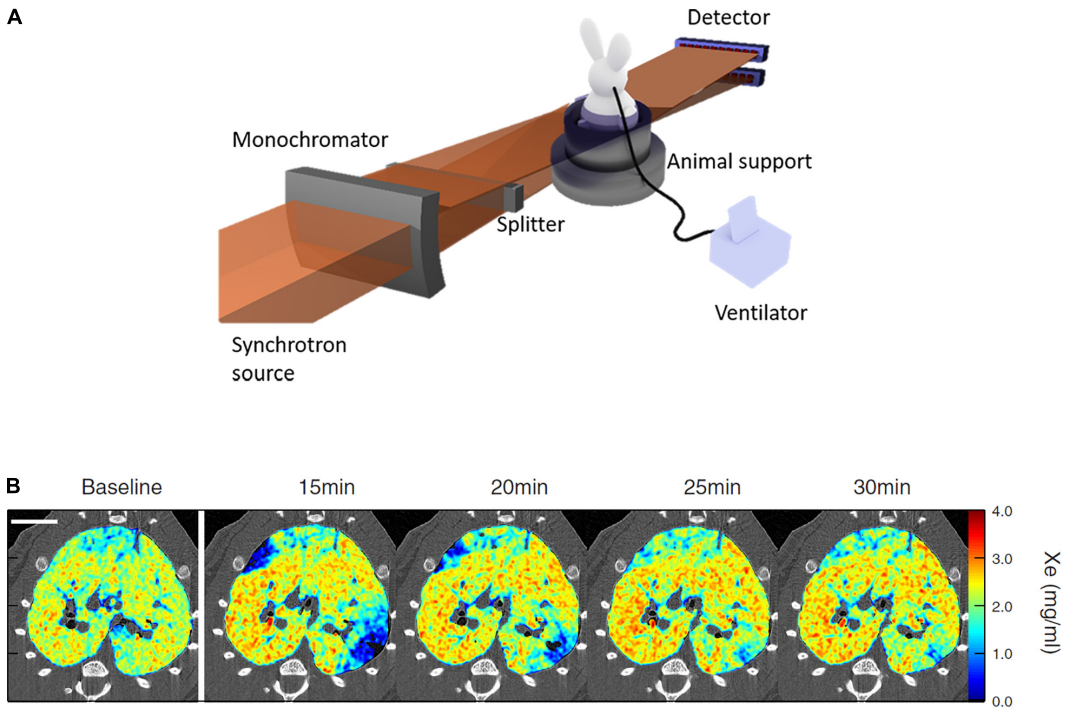

FIGURE 1 | (A) Schematic of synchrotron radiation K-edge subtraction imaging (KES) setup; **(B)** sample composite images showing the Xe concentration distribution repeatedly imaged by KES with 47 μm voxel size, in ovalbumin-sensitized Brown-Norway Rats challenged with inhaled ovalbumin. Scale bar represents 10 mm. Note the transient emergence of regional lung ventilation defects after ovalbumin challenge. Reproduced with permission from Layachi et al. (2013), Bayat et al. (2021).

synchronized fashion with cardiac and respiratory function (Fardin et al., 2021). Also, the inhaled fraction of O_2 can be set and inert or tracer gas administration switched remotely by the image acquisition software or manually (Bayat et al., 2021) in order to image regional lung ventilation.

K-EDGE SUBTRACTION COMPUTED TOMOGRAPHY FUNCTIONAL LUNG IMAGING

The K-edge subtraction computed tomography (KES-CT) technique allows simultaneous imaging of the lung tissue morphology, and the concentration (mass per unit of volume) of inhaled Xenon gas within the airspaces. The instrumental setup for this imaging modality has been reviewed in detail previously (Bayat et al., 2020). This imaging technique uses two monochromatic X-ray beams at slightly different energies bracketing the K-edge of inhaled Xe (34.56 keV) for ventilation imaging, or injected iodine (33.17 keV) for blood volume and perfusion imaging. Visualization and quantitative measurement of contrast concentration in the lung is based on the property that the attenuation coefficient of a contrast element increases severalfold when the energy of the incident X-ray beam exceeds the K-edge of that element. X-rays from a synchrotron radiation source are required because, as opposed to standard X-ray sources, they allow the selection of monochromatic beams from the full X-ray spectrum while conserving enough intensity for imaging with sufficient temporal resolution. KES-CT imaging is performed in parallel-beam geometry. Two CT images are simultaneously acquired during the Xe inhalation maneuver, using a solid state (Bayat et al., 2021) or a charge-coupled device (CCD) detector (Layachi et al., 2013; **Figure 1A**). The size of the field of view is determined by that of the radiation beam and the detector resolution. For example, in a recent study (Bayat et al., 2021) the horizontal beams were 98 mm wide and 0.6 mm in height, and focused on a rabbit. In that study, each CT image consisted in 720 projections over 360° per 1.5 s. CT images were reconstructed using a filtered back projection algorithm with resulting voxel dimensions of 350 μm × 350 μm × 700 μm. At this voxel size, the distribution of xenon gas within lung acini could be assessed in rabbits, in order to investigate down to which length scale ventilation remains inhomogeneous in normal lungs. Using fractal analysis, it was demonstrated that ventilation becomes internally uniform within regions about the size of rabbit lung acini (∼5 mm^3) (Bayat et al., 2021).

At a higher voxel resolution of 47 μm^2, the acquisition time is longer (∼10 s) (**Figure 1B**). Using the dual-energy KES synchrotron imaging method, X-ray attenuation by tissue density and Xe concentration is computed separately, using a custom material decomposition algorithm as described previously (Bayat et al., 2001). At this resolution, Layachi et al. (2013) found higher eosinophil, monocyte and total cell densities within vs. outside

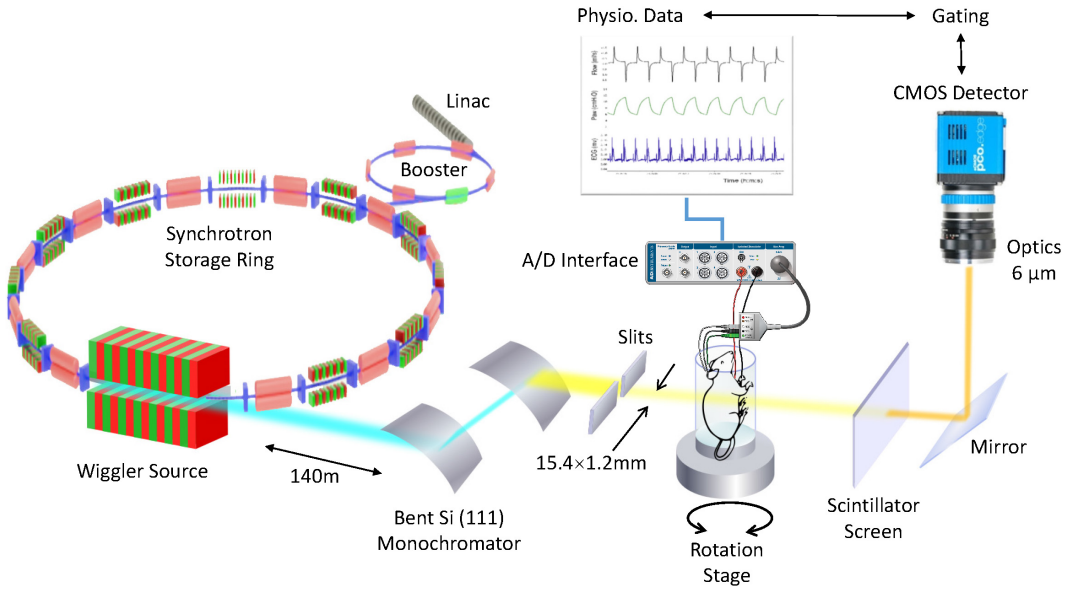

FIGURE 2 | 4D microscopy of rat lung using a synchrotron X-ray source. High-intensity coherent X-rays generated from electrons orbiting in a storage ring, are rendered monochromatic using bent silicon crystal optics, and detected by a PCO Edge 5.5 camera coupled to a Cerium-doped Lutetium Aluminum Garnet (LuAG:Ce) scintillator and optics yielding an isotropic pixel size of 6 μm^3. The *in vivo* anesthetized rat is mechanically ventilated while the electrocardiogram and respiration are monitored and recorded. Reproduced from (Cercos-Pita et al., doi: 10.21203/rs.3.rs-970496/v1, *under review*).

lung regions where ventilation defects emerged following allergen inhalation in ovalbumin-sensitized Brown-Norway rats.

K-edge subtraction computed tomography image acquisition can be performed dynamically during a single (Bayat et al., 2021) or in-between multiple inspirations or expirations (Bayat et al., 2013). The resulting images can be used to compute a map of regional ventilation based on the regional time-constant of Xenon washin or washout. In the case of Xenon washin, as the alveoli are gradually filled by the gas (Porra et al., 2004):

$$C_t = C_{as}\left[1 - e^{-(t-t_0)\tau}\right]$$

where C_t is the gas concentration as function of time, C_{as} the asymptotic concentration and τ the time constant. As ventilation within a lung region increases, the time constant of regional Xe washin or washout becomes shorter. Specific ventilation ($s\dot{V}$), or ventilation per unit of regional gas volume, is defined by:

$$s\dot{V} = \frac{1}{\tau}$$

A similar approach can be used to compute maps of regional blood volume and perfusion (Suhonen et al., 2008).

The spatial resolution and contrast sensitivity of KES imaging is mainly determined by the characteristics of the detection system. For example, in studies performed using a solid-state cooled germanium detector, a pixel size of 0.33^2 mm^2 and a sensitivity better than 0.1 mg/ml could be obtained. Smaller pixel sizes of 47 μm^2 have previously been achieved in *in vivo* KES-CT imaging using a charge coupled device (CCD) detector (Layachi et al., 2013). This makes KES a unique method because of the high spatial resolution and absolute scale of the contrast element distributions.

PHASE-CONTRAST FUNCTIONAL LUNG IMAGING

The lung poorly attenuates X-rays. However, the numerous air-tissue interfaces within the lung airways and alveoli result in refraction and phase changes of the incident X-rays. Phase-contrast X-ray imaging (PCI), uses the phase information in addition to attenuation to enhance contrast within poorly-attenuating structures (Bravin et al., 2013). This technique takes advantage of the high degree of spatial coherence provided by synchrotron X-ray sources. In addition to improving contrast, this imaging approach has the advantage of reducing the radiation dose in comparison to conventional X-ray attenuation imaging (Lewis et al., 2005). The numerous air-tissue interfaces crossed by the incident beam within the lung produce phase gradient patterns which resemble random noise or "speckles," unlike the surrounding soft tissues (Kitchen et al., 2004).

Propagation-Based Imaging (PBI), is the simplest and most widely used method because no X-ray optical devices are needed (**Figure 2**). In this configuration a small X-ray source provides a high spatial coherence, an essential condition to visualize the phase effects. Another essential condition is a sufficient distance between the object and the detector, which is chosen as a function of the X-ray energy and the detector pixel size. There are several methods for phase retrieval from the observed intensity distribution, which also includes the effects of absorption (Nesterets et al., 2015).

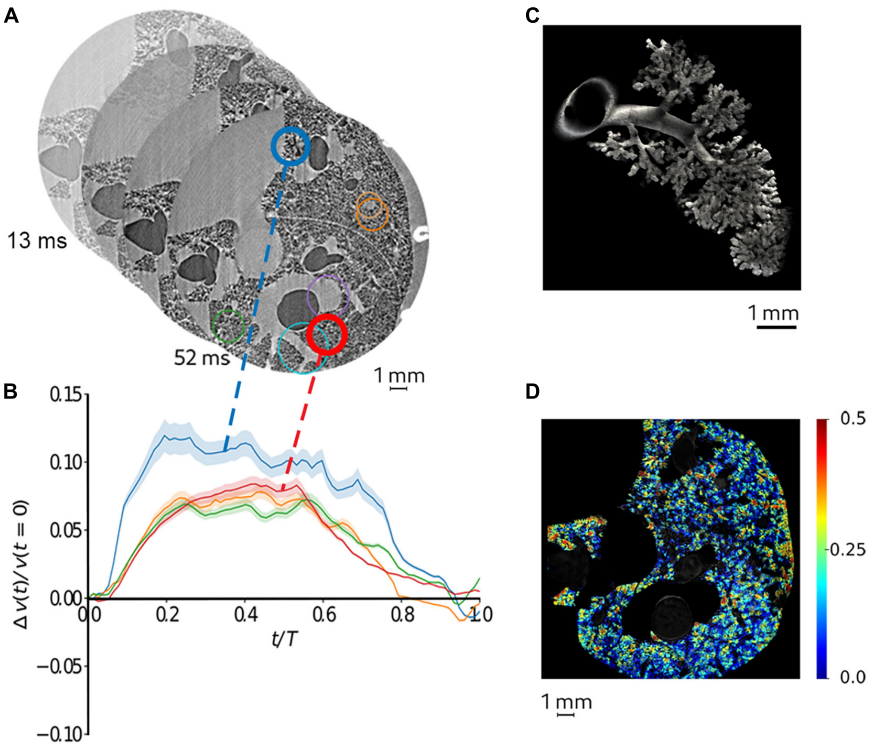

FIGURE 3 | Quantitative mapping of lung tissue biomechanics in a live rat. **(A)** sample sequential X-ray phase-contrast CT images at successive time points, reconstructed by retrospectively sorting of 250,000 individual 2 ms image projections with respect to the phase of heart contraction and breathing, yielding 78 time points during the breath; **(B)** regional strain as a function of time computed within airspaces in the regions of interest of same color as in panel **(A)**. The shaded area represents within-ROI standard deviation; **(C)** a segmented airway with subtending conducting airways and terminal acinar structures at end-expiration in a live rat; **(D)** sample regional strain map of airspaces *in vivo* in the same animal. Color bars indicate strain ($\delta V/V_{t0}$, where t_0 is the start of the breath). Reproduced from (Cercos-Pita et al., doi: 10.21203/rs.3.rs-970496/v1, *under review*).

Examples of the application of this imaging technique to study regional lung deformation and function are discussed in a recent review (Bayat et al., 2021). *In vivo* phase-contrast synchrotron radiation tomography allows the measurement of regional lung aeration with high contrast sensitivity, short acquisition times compatible with *in vivo* imaging, and the ability to acquire 3D data at sub acinar spatial resolution. However, the spatial resolution of static imaging approaches is limited by blurring due to cardiac and vascular motion, which hinders the study of aeration and deformation within individual alveoli.

This issue is addressed by 4DCT imaging. This approach involves gating the acquisition of individual image projections with the cardiac and respiratory motions. Moreover, the exposure time of each image projection needs to be reduced as the microscopic features of interest become smaller, which makes 4DCT microscopy technically challenging (Bayat et al., 2018). The high photon flux and coherence of synchrotron radiation are necessary for this technique, as well as accurate physiologic signal acquisition and control software allowing precise triggering of all components of the image acquisition process. Resolving alveolar structure in the lung is particularly challenging due to inhomogeneous speed and magnitude of the physiological tissue motion. Acquiring abundant tomographic data can help resolve this issue.

Under static lung inflation conditions, Lovric et al. (2017) studied lung inflation patterns during diastole at the alveolar scale *in vivo*, with a voxel size of 2.9^3 μm^3, in anesthetized 9-day old rats. They acquired 450 individual projections at 3 ms exposure time, for a total acquisition time of 2 min (Lovric et al., 2017). Their data demonstrate the feasibility of eliminating motion artifacts due to cardiac activity and resolving alveolar structure *in vivo*. Using a prospective cardiac gating technique, the authors were able to image mouse lungs at 1.1 μm voxel size during static breath hold conditions (Lovric et al., 2017). However, imaging the lung in static conditions is less physiological and does not allow capturing the full scope of local lung mechanics. This is because the lung tissue is viscoelastic, meaning that its apparent elastic properties depend on the rate of volume change (Suki and Bates, 2011). Dynamic imaging techniques are therefore needed to map lung biomechanics, ideally at spatial resolutions allowing to resolve the pulmonary alveoli.

Recently, Cercos et al. investigated lung tissue deformation induced by cardiac contractions and respiration in anesthetized adult rats, showing the magnitude and regional inhomogeneity in this deformation in intact *in vivo* lungs (Cercos-Pita et al., DOI: 10.21203/rs.3.rs-970496/v1, *under review*). By synchronizing image acquisition with both respiration and cardiac activity, 250,000 projections with 2 ms integration

time were retrospectively acquired over 180° in 8.8 min. Both the respiratory and cardiac-induced motion could be resolved using this technique in mechanically ventilated live rats, at 6 μm^3, and 78 time points during a breath (**Figure 3**). This study shows that 4D tomographic microscopy is a valuable technique not only for assessing local lung structure but also for quantitatively mapping local biomechanics at microscopic length scales. The main limitations of the technique are the length of data acquisition ranging up to several minutes, and the risk of excessive radiation dose which can alter the underlying tissue structures. Also, dynamic imaging limits the spatial resolution due to motion blurring induced by breathing in addition to cardiovascular motion. More sensitive detection devices and specifically designed imaging end stations can help mitigate these limitations in the future.

FUTURE PERSPECTIVES AND CHALLENGES

Real-time imaging of lung function is highly challenging, particularly *in vivo* due to motion blurring and the non-linear deformation of the lung tissue with breathing and cardiovascular motion. There is a trade-off between spatial and temporal resolutions, and both are difficult to achieve simultaneously. *In vivo* synchrotron radiation micro-CT also faces limitations due to radiation dose, and a limited field of view. However, in KES-CT, limitations due to radiation exposure can be overcome by reducing the number of projections and using iterative reconstruction algorithms while maintaining sufficient contrast resolution for quantitative mapping of ventilation (Strengell et al., 2014), while PCI has the advantage of reducing the radiation dose in comparison to conventional X-ray attenuation imaging (Lewis et al., 2005; Zhao et al., 2012). The radiation beam produced by a synchrotron source is stationary, which imposes translation and rotation of the sample through the beam for image acquisition. Another challenge posed by fast acquisition 3D imaging is handling the large volume of data, which can rapidly represent several terabytes. Large data volumes cannot be visualized in real time with conventional approaches. A change in the data representation paradigm, from the classical Cartesian grid to a hierarchical data structure is therefore mandatory to allow a real-time visualization on different planes as well as morphological analysis in a reasonable time. This in turn, requires adapting image processing algorithms. Synchrotrons are large research infrastructures that are not widely available. However, several facilities worldwide are accessible to the scientific community through a competitive peer-reviewed process based on scientific merit (Quitmann and Rayment, 2020).

A limitation of KES-CT is a contrast sensitivity that is far smaller than fluorescence or radionuclide imaging. However, an exciting development is the ability to track high atomic number nanoparticles loaded within cells (Schültke et al., 2014; Hubert et al., 2021), or functionalized in order to reveal a specific molecular target. This would allow taking functional imaging utilizing synchrotron radiation a step further toward molecular imaging. Possibilities to achieve these challenging goals exist at current synchrotron facilities with recent progress in detection, acquisition and data processing capabilities.

AUTHOR CONTRIBUTIONS

SB wrote the first draft of the manuscript. LF, JC-P, GP, and AB wrote sections of the manuscript. All authors contributed to manuscript revision, read, and approved the submitted version.

FUNDING

This work was supported by the Swedish Research Council (grant 2018-02438), the Swedish Heart-Lung Foundation (grant 20170531), the European Synchrotron Radiation Facility, by the French Institute of Health and Medical Research (INSERM UA07), and by the French National Research Agency (ANR-15-IDEX-02).

REFERENCES

Ashton, J.R., West, J.L., and Badea, C.T. (2015). In vivo small animal micro-CT using nanoparticle contrast agents. *Front. Pharmacol.* 6:256. doi: 10.3389/fphar.2015.00256

Bayat, S., Broche, L., Degrugilliers, L., Porra, L., Paiva, M., and Verbanck, S. (2021). Fractal analysis reveals functional unit of ventilation in the lung. *J. Physiol.* 599, 5121–5132. doi: 10.1113/JP282093

Bayat, S., Duc, G.L., Porra, L., Berruyer, G., Nemoz, C., Monfraix, S., Fiedler, S., Thomlinson, W., Suortti, P., Standertskjöld-Nordenstam, C.G., and Sovijärvi, A.R.A. (2001). Quantitative functional lung imaging with synchrotron radiation using inhaled xenon as contrast agent. *Phys. Med. Biol.* 46, 3287–3299. doi: 10.1088/0031-9155/46/12/315

Bayat, S., Dullin, C., Kitchen, M.J., and Lovric, G. (2018). "Synchrotron X-Ray-Based Functional and Anatomical Lung Imaging Techniques," in *Advanced High-Resolution Tomography in Regenerative Medicine* (Ed)A. Cedola (Berlin: Springer), 151–167.

Bayat, S., Porra, L., Albu, G., Suhonen, H., Strengell, S., Suortti, P., Sovijarvi, A., Petak, F., and Habre, W. (2013). Effect of positive end-expiratory pressure on regional ventilation distribution during mechanical ventilation after surfactant depletion. *Anesthesiology* 119, 89–100. doi: 10.1097/ALN.0b013e318291c165

Bayat, S., Porra, L., Suortti, P., and Thomlinson, W. (2020). Functional lung imaging with synchrotron radiation: Methods and preclinical applications. *Phys. Med.* 79, 22–35. doi: 10.1016/j.ejmp.2020.10.001

Bayat, S., Strengell, S., Porra, L., Janosi, T.Z., Petak, F., Suhonen, H., Suortti, P., Hantos, Z., Sovijarvi, A.R., and Habre, W. (2009). Methacholine and ovalbumin challenges assessed by forced oscillations and synchrotron lung imaging. *Am. J. Respir. Crit. Care. Med.* 180, 296–303. doi: 10.1164/rccm.200808-1211OC

Bravin, A., Coan, P., and Suortti, P. (2013). X-ray phase-contrast imaging: from pre-clinical applications towards clinics. *Phys. Med. Biol.* 58, R1–35. doi: 10.1088/0031-9155/58/1/R1

Clark, D.P., and Badea, C.T. (2021). Advances in micro-CT imaging of small animals. *Phys.Med.* 88, 175–192. doi: 10.1016/j.ejmp.2021.07.005

Fardin, L., Broche, L., Lovric, G., Mittone, A., Stephanov, O., Larsson, A., Bravin, A., and Bayat, S. (2021). Imaging atelectrauma in Ventilator-Induced Lung Injury using 4D X-ray microscopy. *Sci. Rep.* 11, 4236. doi: 10.1038/s41598-020-77300-x

Frumin, M.J., Epstein, R.M., and Cohen, G. (1959). Apneic oxygenation in man. *Anesthesiology* 20, 789–798.

Hubert, V., Hristovska, I., Karpati, S., Benkeder, S., Dey, A., Dumot, C., Amaz, C., Chounlamountri, N., Watrin, C., Comte, J.C., Chauveau, F., Brun, E., Marche, P., Lerouge, F., Parola, S., Berthezene, Y., Vorup-Jensen, T., Pascual, O., and Wiart, M. (2021). Multimodal Imaging with NanoGd Reveals Spatiotemporal Features of Neuroinflammation after Experimental Stroke. *Adv. Sci.* 8, e2101433. doi: 10.1002/advs.202101433

Kitchen, M.J., Paganin, D., Lewis, R.A., Yagi, N., Uesugi, K., and Mudie, S.T. (2004). On the origin of speckle in X-ray phase contrast images of lung tissue. *Phys. Med. Biol.* 49, 4335–4348. doi: 10.1088/0031-9155/49/18/010

Layachi, S., Porra, L., Albu, G., Trouillet, N., Suhonen, H., Petak, F., Sevestre, H., Suortti, P., Sovijarvi, A., Habre, W., and Bayat, S. (2013). Role of cellular effectors in the emergence of ventilation defects during allergic bronchoconstriction. *J. Appl. Physiol.* 115, 1057–1064. doi: 10.1152/japplphysiol.00844.2012

Lewis, R.A., Yagi, N., Kitchen, M.J., Morgan, M.J., Paganin, D., Siu, K.K.W., Pavlov, K., Williams, I., Uesugi, K., Wallace, M.J., Hall, C.J., Whitley, J., and Hooper, S.B. (2005). Dynamic imaging of the lungs using X-ray phase contrast. *Phys. Med. Biol.* 50, 5031–5040. doi: 10.1088/0031-9155/50/21/006

Lovric, G., Mokso, R., Arcadu, F., Oikonomidis, I.V., Schittny, J.C., Roth-Kleiner, M., and Stampanoni, M. (2017). Tomographic in vivo microscopy for the study of lung physiology at the alveolar level. *Sci. Rep.* 7:12545. doi: 10.1038/s41598-017-12886-3

Nesterets, Y.I., Gureyev, T.E., Mayo, S.C., Stevenson, A.W., Thompson, D., Brown, J.M.C., Kitchen, M.J., Pavlov, K.M., Lockie, D., Brun, F., and Tromba, G. (2015). A feasibility study of X-ray phase-contrast mammographic tomography at the Imaging and Medical beamline of the Australian Synchrotron. *J. Synchrotron Radiat.* 22, 1509–1523. doi: 10.1107/S160057751501766X

Porra, L., Bayat, S., Malaspinas, I., Albu, G., Doras, C., Broche, L., Strengell, S., Petak, F., and Habre, W. (2016). Pressure-regulated volume control vs. volume control ventilation in healthy and injured rabbit lung: An experimental study. *Eur. J. Anaesthesiol.* 33, 767–775. doi: 10.1097/EJA.0000000000000485

Porra, L., Monfraix, S., Berruyer, G., Le Duc, G., Nemoz, C., Thomlinson, W., Suortti, P., Sovijarvi, A.R., and Bayat, S. (2004). Effect of tidal volume on distribution of ventilation assessed by synchrotron radiation CT in rabbit. *J. Appl. Physiol.* 96, 1899–1908. doi: 10.1152/japplphysiol.00866.2003

Quitmann, C., and Rayment, T. (2020). Synchrotron radiation. *CERN Yellow Rep.* 1, 5–5.

Roan, E., and Waters, C.M. (2011). What do we know about mechanical strain in lung alveoli? *Am. J. Physiol. Lung. Cell. Mol. Physiol.* 301, L625–L635. doi: 10.1152/ajplung.00105.2011

Schültke, E., Menk, R., Pinzer, B., Astolfo, A., Stampanoni, M., Arfelli, F., Harsan, L.-A., and Nikkhah, G. (2014). Single-cell resolution in high-resolution synchrotron X-ray CT imaging with gold nanoparticles. *J. Synchrotron Radiat.* 21, 242–250. doi: 10.1107/S1600577513029007

Smaldone, G.C., and Mitzner, W. (2012). Viewpoint: unresolved mysteries. *J. Appl. Physiol.* 113, 1945–1947.

Strengell, S., Keyrilainen, J., Suortti, P., Bayat, S., Sovijarvi, A.R., and Porra, L. (2014). Radiation dose and image quality in K-edge subtraction computed tomography of lung in vivo. *J. Synchrotron Radiat.* 21, 1305–1313. doi: 10.1107/S160057751401697X

Suhonen, H., Porra, L., Bayat, S., Sovijarvi, A.R., and Suortti, P. (2008). Simultaneous in vivo synchrotron radiation computed tomography of regional ventilation and blood volume in rabbit lung using combined K-edge and temporal subtraction. *Phys. Med. Biol.* 53, 775–791. doi: 10.1088/0031-9155/53/3/016

Suki, B., and Bates, J.H. (2011). Lung tissue mechanics as an emergent phenomenon. *J. Appl. Physiol.* 110, 1111–1118. doi: 10.1152/japplphysiol.01244.2010

Zhao, Y., Brun, E., Coan, P., Huang, Z., Sztrokay, A., Diemoz, P.C., Liebhardt, S., Mittone, A., Gasilov, S., Miao, J., and Bravin, A. (2012). High-resolution, low-dose phase contrast X-ray tomography for 3D diagnosis of human breast cancers. *Proc. Natl. Acad. Sci. U.S.A.* 109, 18290–18294. doi: 10.1073/pnas.1204460109

Conflict of Interest: The authors declare that the research was conducted in the absence of any commercial or financial relationships that could be construed as a potential conflict of interest.

Publisher's Note: All claims expressed in this article are solely those of the authors and do not necessarily represent those of their affiliated organizations, or those of the publisher, the editors and the reviewers. Any product that may be evaluated in this article, or claim that may be made by its manufacturer, is not guaranteed or endorsed by the publisher.

frontiers in Physiology

HYPOTHESIS AND THEORY
published: 28 March 2022
doi: 10.3389/fphys.2022.811129

Role of the Air-Blood Barrier Phenotype in Lung Oxygen Uptake and Control of Extravascular Water

Giuseppe Miserocchi, Egidio Beretta, Ilaria Rivolta and Manuela Bartesaghi*

Dipartimento di Medicina e Chirurgia, Università di Milano-Bicocca, Monza, Italy

The air blood barrier phenotype can be reasonably described by the ratio of lung capillary blood volume to the diffusion capacity of the alveolar membrane (*Vc/Dm*), which can be determined at rest in normoxia. The distribution of the *Vc/Dm* ratio in the population is normal; *Vc/Dm* shifts from ∼1, reflecting a higher number of alveoli of smaller radius, providing a high alveolar surface and a limited extension of the capillary network, to just opposite features on increasing *Vc/Dm* up to ∼6. We studied the kinetics of alveolar-capillary equilibration on exposure to edemagenic conditions (work at ∼60% maximum aerobic power) in hypoxia (HA) (P_IO_2 90 mmHg), based on an estimate of time constant of equilibration (τ) and blood capillary transit time (*Tt*). A shunt-like effect was described for subjects having a high *Vc/Dm* ratio, reflecting a longer τ (>0.5 s) and a shorter *Tt* (<0.8 s) due to pulmonary vasoconstriction and a larger increase in cardiac output (>3-fold). The tendency to develop lung edema in edemagenic conditions (work in HA) was found to be directly proportional to the value of *Vc/Dm* as suggested by an estimate of the mechanical properties of the respiratory system with the forced frequency oscillation technique.

Keywords: alveolar-capillary equilibration, hypoxia, exercise, alveolar diffusion, alveolar perfusion, shunt effect

OPEN ACCESS

Edited by:
Walter Araujo Zin, Federal University of Rio de Janeiro, Brazil

Reviewed by:
Paulo Hilario Nascimento Saldiva, University of São Paulo, Brazil
Lars Knudsen, Hannover Medical School, Germany

****Correspondence:***
Giuseppe Miserocchi
giuseppe.miserocchi@unimib.it

Specialty section:
This article was submitted to Respiratory Physiology and Pathophysiology, a section of the journal Frontiers in Physiology

Received: *08 November 2021*
Accepted: *24 February 2022*
Published: *28 March 2022*

Citation:
Miserocchi G, Beretta E, Rivolta I and Bartesaghi M (2022) Role of the Air-Blood Barrier Phenotype in Lung Oxygen Uptake and Control of Extravascular Water. Front. Physiol. 13:811129. doi: 10.3389/fphys.2022.811129

INTRODUCTION

It is a common experience that, in edemagenic conditions, inter-individual differences in the control of lung fluid balance are observed; the characteristic example is the proneness to develop lung edema on exposure to high altitude (Busch et al., 2001; Dehnert et al., 2006; Richalet et al., 2012, 2021; Eichstaedt et al., 2020a,b).

Finding the reason for these differences relating to the lung fluid balance has remained elusive for a long time. A line of research from our laboratory analyzed this problem and developed a project along the following lines of research:

(1) To determine the inter-individual differences in the morpho-functional features of the air-blood barrier in terms of membrane diffusion capacity (*Dm*) and extension of the capillary network from the estimate of capillary blood volume (*Vc*).
(2) To estimate the phenotype-dependent adaptive functional response of the air-blood barrier on exposure to edemagenic factors.
(3) To estimate the impact of points 1 and 2 on oxygen alveolar-capillary equilibration.

The results supported the hypothesis that the tendency to develop lung edema can be explained, considering a functional link between inborn features, perturbation in the capillary-to-interstitial fluid exchange, and the corresponding impact on the efficiency of gas exchange.

We shall, therefore, start this review by summarizing key principles of control of extravascular lung water as they represent the basis to understand the individual phenotype-dependent functional response to the edemagenic condition.

THE CONTROL OF EXTRAVASCULAR WATER IN THE AIR-BLOOD BARRIER

The time course of the events leading to the development of lung edema has been described in a recent review (Beretta et al., 2021). We summarized here only the basic concepts useful to delineate the inter-individual differences in response to edemagenic conditions.

The very high surface area of the air-blood barrier (∼2,000 cm^2/g) and its extreme thinness (∼0.1 μm in its thin portion) serve the gas diffusion function. The thinness of the air-blood barrier reflects a strict control of extravascular water volume that is kept at minimum, thanks to the extremely low water permeability across the endothelial and the epithelial barriers that strongly limit water fluxes. The water content of the lung is well defined by the wet weight to the dry weight ratio (W/D) that, in physiological conditions, is ∼5. Trans-capillary and trans-epithelial water exchanges (J_v) are governed by the Starling law (Eq. 1), where P and Π are the hydraulic and the colloidosmotic pressures across any two compartments, $Kf \quad \left(filtration\ coefficient\right) = Lp \cdot A$, being Lp the water conductance, A the surface area available for flow, $[(P_1 - P_2) - \sigma\,(\Pi_1 - \Pi_2)]$ is the Starling pressure gradient generating flows, σ being the protein reflection coefficient that defines the selectivity of the barriers to plasma proteins:

$$J_v = Kf \cdot [(P_1 - P_2) - \sigma\,(\Pi_1 - \Pi_2)] \quad (1)$$

A valid representative model of structure-function of the air-blood barrier rests on the comparison between oxygen diffusion that is in the range of 15×10^{-2} ml/(min cm^2) in resting conditions, with capillary microvascular filtration that would be at least 10,000 less (Miserocchi, 2009); in other words, the air-blood barrier is very permeable to gases but minimally permeable to water. Edemagenic conditions include the increase in pulmonary blood flow, causing an increase in Kf due to the increase in both water conductance (Lp), the surface area of fluid exchange (A), as well as protein permeability (decrease in σ). The lung is normally well equipped to respond to increased microvascular filtration due to a specific morpho-functional feature, namely, the very low compliance of the interstitial structure, ∼0.5 ml $mmHg^{-1}$·100 g of wet $weight^{-1}$ (Miserocchi et al., 1993). The latter reflects the macromolecular organization of the proteoglycan component (Negrini et al., 1996; Miserocchi et al., 1999). In case of increased filtration in the interstitial space, water is captured by hyaluronan to form a gel, whose increase in steric hindrance causes a remarkable increase in interstitial pressure from ∼ −10 cm H_2O (physiological condition) up to ∼ +5 cm H_2O (Miserocchi et al., 1993). Gel formation, as long as the filtration coefficient and the protein reflection coefficient remain within physiological values, provides a "*safety factor*" against edema formation as the increase in interstitial pressure buffers further filtration and may actually favor fluid reabsorption. To offset an increase in microvascular filtration rate, lymphatics can provide a passive negative-feedback control loop (Miserocchi, 2009). Lymph flow increases in proportion with the rate of increase in lung weight, which reflects the microvascular filtration (Roselli et al., 1984; Mitzner and Sylvester, 1986).

With the "*safety factor*" on, the water accumulation in the interstitial compartment is maintained within 10% of the control value; thus, the W/D ratio is kept at ∼ 5.5 (Miserocchi et al., 2001; Negrini et al., 2001). Inflammatory states (e.g., severe hypoxia, hyperoxia, surgery, excessive parenchymal stress/strain, and bacterial/viral infection) may cause severe damage to the native architecture of the proteoglycan family (Negrini et al., 1996; Miserocchi et al., 1999; Passi et al., 1999); the ensuing result is an uncontrolled increase of water and protein permeability. The critical phase of developing edema pivots on reaching a W/D of ∼ 6.5 (Beretta et al., 2021); modeling of this phase reveals an abrupt onset of edema with a short time constant (∼4–6 min) (Parker and Townsley, 2004; Mazzuca et al., 2016). Neither CT scan nor ultrasound can correlate with W/D ratios, corresponding to the early stages of perturbation in lung fluid balance before the condition becomes life-threatening.

INTER-INDIVIDUAL DIFFERENCES IN DIFFUSION LUNG CAPACITANCE AND MICROVASCULAR PERFUSION OF THE AIR-BLOOD BARRIER

Wide inter-individual differences have been reported for alveolar oxygen uptake, even after normalizing diffusive parameters to individual total lung volume (Hughes and Pride, 2001). A breakthrough to interpret these differences came from the measurement of DO_2, Dm, and Vc (oxygen diffusion capacitance, membrane diffusive capacitance, and capillary blood volume, respectively, Roughton and Forster, 1957) at different lung volumes from functional residual volume up to total lung volume. The lung volume dependence of these parameters allows delineation of the individual morpho-functional features of the air-blood barrier and to relate the differences in oxygen uptake and transport to match oxygen requirement, reflecting the individual phenotype (Miserocchi et al., 2008).

Figure 1A shows that the increase in Dm on increasing lung volume remarkably differs among subjects. The highest Dm values at total lung capacity (TLC) were found in subjects displaying the highest increase in Dm on increasing lung volume. These differences have been interpreted, considering that Dm is proportional to $\frac{S_A}{d}$, S_A being the overall surface of the air-blood barrier and d its thickness. The decrease in d of the air–blood barrier on increasing lung volume was calculated as $1/S_A$, considering the air-blood barrier as a lamina of constant volume (for details of the computational model, refer to Miserocchi et al., 2008). The simple geometrical reasoning is that lung diffusion is proportional to the alveolar surface; for a given lung volume, a greater increase in the lung surface on increasing

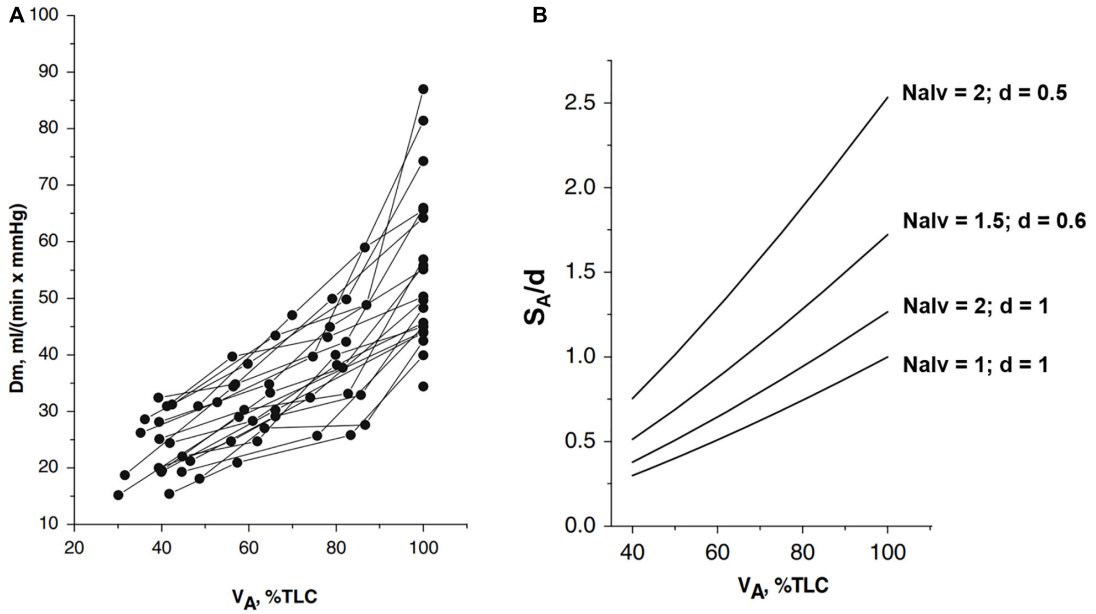

FIGURE 1 | (A) Individual plots of *Dm* (a membrane diffusing capacity) vs. lung volume (V_A) from *FRC* (about 40% *TLC*) up to 100% *TLC*. **(B)** Numerical simulation to show the lung volume dependence of surface to the thickness ratio of the air-blood barrier (S_A/d). The various relationships were obtained by changing *Nalv* (number of alveoli) that affects S_A/d, as indicated; for the reference condition, S_A, *Nalv*, and *d* are set to unity (from Miserocchi et al., 2008).

lung volume is expected the higher the number of alveoli. A numerical simulation (**Figure 1B**) allows estimation of the dependence of $\frac{S_A}{d}$ on lung volume by considering different phenotypes having different numbers of alveoli *Nalv* and/or different values of *d*, as specified in the figure. One can appreciate that a ∼3-fold difference (say from 0.25 to 0.75) in SA/d at Functional Residual Capacity (FRC) may justify a similar difference found in *Dm* on increasing lung volume up to *TLC* (Panel A). Accordingly, an inter-individual difference in alveolar number and thickness of the air-blood barrier can justify a corresponding difference in *Dm*. Regardless of an individual number of alveoli, we may recall that (Miserocchi et al., 2008), up to a volume of ∼70% TLC, most of the increase in $\frac{S_A}{d}$ is due to the increase in S_A; above this volume, the increase in $\frac{S_A}{d}$ mostly reflects the decrease in *d* (the unfolding/folding zone, Beretta et al., 2021).

Figure 2 shows that *Vc* (normalized to lung volume V_A) decreases on increasing lung volume (as *% TLC*) due to the parenchymal stretching, squeezing the pulmonary capillaries and, thus, reducing their patency (Glazier et al., 1969; Mazzone et al., 1978; Brower et al., 1990; Koyama and Hildebrandt, 1991). Large inter-individual differences of *Vc* were also found; higher values at *FRC* suggest a greater extension of the alveolar-capillary network. Furthermore, the higher the *Vc* value at *FRC*, the greater its decease in increasing lung volume.

We rely on the *Vc/Dm* ratio to identify the differences in the phenotype of the air-blood barrier to derive indications on the geometry of the alveoli and the extension of the capillary network. Note that, at *FRC*, this ratio would be mostly affected by the value of *Vc*, while, at 100% *TLC*, the ratio would be most affected by the increase in *Dm*. Since lung diffusion and subcomponents are routinely measured at 100% *TLC*, we present in **Figure 3** the distribution of *Vc/Dm*, referring to 100% *TLC* at sea level (SL) at rest that appears to be normal (Shapiro-Wilk test, Orgin pro-2020; at the 0.05% level, the data were significantly drawn from a normally distributed population). The coefficient of variation for repeated intra-subject measurements did not exceed 12%,

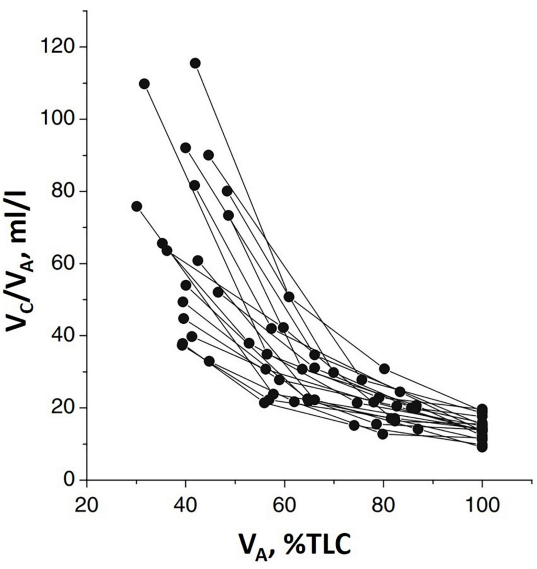

FIGURE 2 | Individual plots of the ratio of pulmonary capillary blood volume (*Vc*) vs. lung volume (V_A) as % of total lung capacity V_A (% *TLC*) (from Miserocchi et al., 2008).

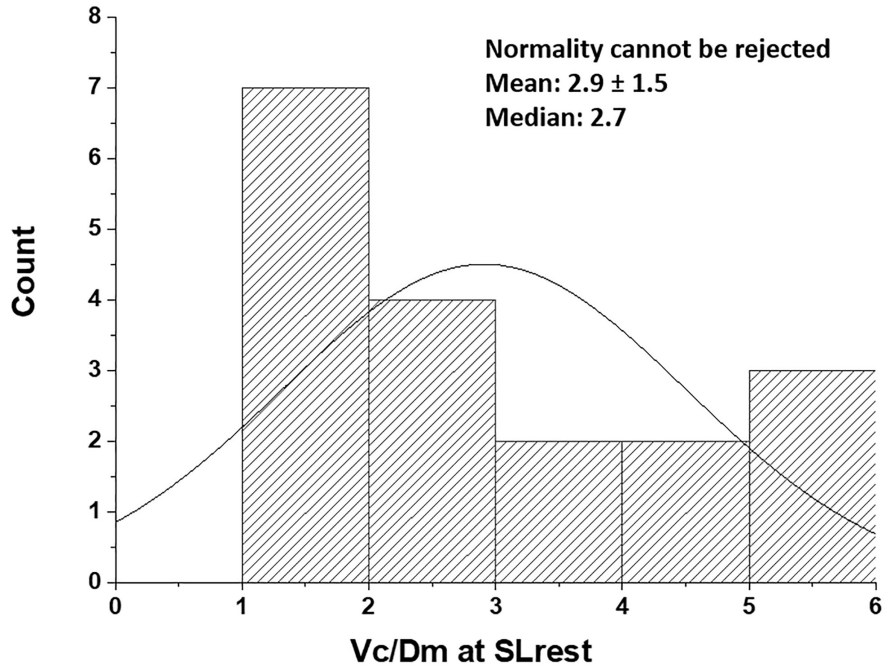

FIGURE 3 | Distribution of *Vc/Dm* in the population studied at the sea level rest at 100% *TLC* [data from Bartesaghi et al. (2014)]. Values are expressed as ml/(ml ·min^{-1} ·mmHg^{-1}).

while, on pooled data, the coefficient of variation approached 50%, confirming the inter-individual differences.

Thus, subjects with low *Vc/Dm* on the left tail have a less developed capillary network and a relatively high number of small alveoli, providing a high surface of the air-blood barrier, while subjects with high *Vc/Dm* on the right tail have a more extended capillary network and a lower number of larger alveoli.

INTER-INDIVIDUAL DIFFERENCES IN VASOMOTION IN EDEMAGENIC CONDITIONS

Given the differences in the air-blood barrier phenotype based on the *Vc/Dm* ratio, a reasonable question was to estimate how edemagenic conditions would affect pulmonary vasomotion in the capillary bed. The experimental model has shown that precapillary vasoconstriction involves vessels with a diameter of about 80 μm (Negrini et al., 2001). The question appeared justified, considering that subjects with a high *Vc/Dm* ratio would be more exposed to edemagenic conditions, being endowed with a more extended alveolar capillary network and, thus, a greater overall capillary surface (*A*). Subjects were studied at rest and in various conditions, implying exposure to edemagenic factors, namely, work at an SL, hypobaric HA at rest, and during work [∼ 60% maximum aerobic power at two heights (3,269 m, P_IO_2 107 mmHg and at 3,840 m, $P_IO_2$90 mmHg)]. Work represents an edemagenic factor as it implies increased lung blood flow (McKenzie et al., 2005; Hodges et al., 2007), and HA is a well-known potent factor causing an increase in microvascular permeability to water and solutes (Hansen et al., 1994; Dehler et al., 2006).

On exposure to edemagenic factors, remarkable de-recruitment of pulmonary capillaries was found in the subjects with high *Vc/Dm* while minor-derecruitment or some recruitment was documented in the subjects with low *Vc/Dm* (Bartesaghi et al., 2014; Beretta et al., 2017). The mechanical properties of the respiratory system were also determined on hypoxia exposure with the forced frequency oscillation technique; results showed that, relative to the SL at rest, the respiratory reactance decreased to a greater extent in the subjects with high *Vc/Dm;* furthermore, in the same subjects, a 4-fold increase in the frequency dependence of respiratory resistance was found (Bartesaghi et al., 2014). Both results may be considered as indexes of greater perturbation of lung fluid balance (Dellacà et al., 2008).

The effect of pulmonary precapillary vasomotion should be considered specifically in relation to the change in water permeability (*Lp*). In case *Lp* remains unmodified, capillary recruitment favors gas diffusion by increasing the capillary gas exchange surface area (*A*) and the pool of hemoglobin to bind oxygen. On the other hand, if *Lp* is increased, capillary recruitment would lead to a remarkable increase in *Kf* due to the multiplicative effect of $Lp \cdot A$ (Mazzuca et al., 2016). As stressed in the recent paper (Beretta et al., 2021), massive filtration may occur down a large increase in *Kf* but a small Starling driving pressure gradient.

The advantage of capillary recruitment seems to prevail in the subjects with low *Vc/Dm* while, in the high *Vc/Dm* subjects, the disadvantage may justify the capillary de-recruitment.

A computational model of a morphologically based alveolar-capillary unit showed that, besides precapillary vasoconstriction, a further mechanism contributes to capillary de-recruitment. This resides in the compressive effect of positive interstitial pressure acting on the capillary surface during edema formation (Mazzuca et al., 2016). This phenomenon may also well occur in humans as the administration of a vasodilator agent cannot restore blood flow in edematous lung regions (Scherrer et al., 1996). In the presence of capillary derecruitment, blood flow is directed toward nonedematous regions and corner vessels (Koyama et al., 1989; Rivolta et al., 2011; Mazzuca et al., 2019). Interestingly, in unperfused capillaries, fluid reabsorption from the interstitial compartment may occur due to a decrease in capillary hydraulic pressure, thus, favoring recovery from edema (Kurbel et al., 2001).

In vivo imaging data from an experimental model were also used to derive semi-quantitative estimates of the role of vasomotion in the control of blood flow and microvascular filtration (Mazzuca et al., 2019). Based on the model developed by Mazzuca et al. (2016), the results indicated that in alveolar units with larger alveoli and a greater extension of the septal network, microvascular filtration flow was greater on exposure to HA, as indicated by the increase in thickness of the interstitial space, and in these units, blood flow limitation increased over time. This can be appreciated in **Figure 4**, showing a 2D image-based model of the decrease in capillary blood flow as a change in color from yellow to blue (Mazzuca et al., 2019) in regions becoming edematous on exposure to hypoxia (12% of O_2 balanced nitrogen). The model also showed that flow limitation in the alveolar-capillary network caused greater perfusion of alveolar corner vessels.

From the experimental model to humans, the point can be made that the subjects having a high *Vc/Dm* ratio appear to be endowed with larger alveoli compared to the subjects with a low *Vc/Dm* ratio and, thus, for this reason, more exposed to the risk of edema. Precapillary vasoconstriction has been reported as the reflex response to stimulation of interstitial vagal "*J*" (juxta-capillary) receptors whose afferent discharge was found to increase in exposure to edemagenic factors (Paintal, 1969).

It appears, therefore, tempting to hypothesize that precapillary vasoconstriction in the high *Vc/Dm* subjects represents a functional response aimed at limiting microvascular filtration to prevent/attenuate edema formation in edemagenic conditions. Inborn differences in microvascular permeability may also be invoked to justify differences in a tendency to develop edema.

Notably, the subjects more prone to develop lung edema in HA have a greater increase in pulmonary arterial pressure. In this respect, the clinical overlap of high-altitude pulmonary edema and pulmonary arterial hypertension has been recently discussed in terms of genetic background (Sharma et al., 2014; Eichstaedt et al., 2020a,b). Interestingly, the opposite behavior concerning lung vasomotion in hypoxia was also described for the systemic circulation. Indeed, in high-altitude pulmonary edema-susceptible (HAPE-S) mountaineers, a decrease in forearm blood flow was found on HA exposure, unlike in non HAPE-S subjects. This finding was attributed to impaired vascular endothelial function due to decreased bioavailability of NO (Berger et al., 2005). A decrease in exhaled NO was also found in HAPE-S subjects on exposure to normobaric hypoxia (Busch et al., 2001), as well as in patients with HAPE (Duplain et al., 2000). On a causative basis, it remains to be established whether the low bioavailability of NO depends on impairment of the biochemical pathway or, conversely, represents the functional response to counteract edema formation.

INTER-INDIVIDUAL DIFFERENCES IN THE KINETICS OF ALVEOLAR-CAPILLARY EQUILIBRATION

The venous admixture, which includes the mismatch of ventilation to blood perfusion, $\dot{V}_A/\dot{Q}$ (Domino et al., 1993), and shunt (Stickland et al., 2004; Lovering et al., 2006, 2008) are well-known causes leading to incomplete alveolar-capillary oxygen equilibration. We present here the relevance of a shunt-like effect, depending on the transit time in the pulmonary capillaries that reflect the increase in a cardiac output and the individual control of lung vasomotion in edemagenic conditions. A valid model defining the alveolar-capillary equilibration across the air-blood barrier (Piiper and Scheid, 1981) has been presented based on a mass balance equation. Defining $d\dot{M}$, the oxygen mass transport across the air-blood barrier; $\dot{Q}$, the cardiac output; and dC, the increase in blood oxygen concentration along the length of the pulmonary capillary (x), the following equation holds:

$$d\dot{M}(x) = \dot{Q} \cdot dC(x) \tag{2}$$

The mathematical development of Equation 2 allows description of an exponential increase of $dC(x)$ to reach an equilibrium at the exit of the pulmonary capillary (Leq) given by:

$$Leq = e^{-\frac{DO_2}{\beta \dot{Q}}}, \tag{3}$$

where DO_2 is the O_2 diffusive capacity and β is the Hb-binding capacity for O_2.

A development of this model allows the definition of the equilibration process as a function of time (t) as blood flows along the capillary, thus:

$$d\dot{M}(t) = \dot{Q} \cdot dC(t) \tag{4}$$

Based on Equation 4, the equilibrium at the exit from the capillary may be written as (Beretta et al., 2019):

$$L_{eq} = e^{-\frac{Tt}{\tau}}, \tag{5}$$

Being Tt the blood transit time in the pulmonary capillary estimated as the ratio of the lung capillary volume (Vc) to a cardiac output ($\dot{Q}$):

$$Tt = \frac{Vc}{\dot{Q}} \tag{6}$$

and the time constant of the equilibration process is defined as:

$$\tau = \frac{\beta Vc}{DO_2} \tag{7}$$

At the exit from the pulmonary capillary, the value of *Leq* is the same from Equations 3 and 5. The *Leq* can vary from 0 (the case of perfect equilibration) to 1 (the case of 100% shunt).

Equation 5 allows the definition of the time course of the equilibration process in response to increased oxygen demand based on the blood transit time in the pulmonary capillary, resulting from the interaction between the increase in cardiac output and the available lung capillary network.

Continuous lines in **Figure 5** show the time course of alveolar-capillary equilibration for the two subjects at rest in normoxia *Vc/Dm* of 4.28 (Panel A) and 1.08 (Panel B), respectively. For the sake of graphical representation, we put on the ordinate 1-*Leq*, meaning that the case of perfect equilibration implies *Leq* = 1. In normoxia at rest, equilibration kinetics were remarkably slower in the subjects with a high *Vc/Dm* due to a correspondingly longer time constant (Eq. 7); in both subjects, *Tt* was long enough to allow complete equilibration. During work in severe HA (3,840 m, $P_IO_2$90 mmHg, dashed lines) in both subjects, the time constant was increased, slowing down the kinetics of equilibration. However, the remarkable shortening of *Tt* (Panel A), reflecting precapillary vasoconstriction, limited the equilibration at 0.6, while, in Panel B, equilibration was only slightly decreased due to a longer *Tt*. Thus, during work performed in hypoxia, facing an average $P_AO_2 \sim 55$ mmHg (Beretta et al., 2017), some individuals can still reach a satisfactory alveolar-capillary equilibration, while, in other subjects, this process may be strongly limited by precapillary vasoconstriction (Mazzuca et al., 2016; see also **Figure 4**).

Figure 6A shows the pooled data of *Leq* vs. *Tt* in various conditions, as indicated by the legend. It appears that *Leq* remains at zero (complete alveolar-capillary equilibration for O_2) as long as *Tt* is greater than ∼1.5 s, while it increases exponentially for Tt <1.5 s. Of course, we refer to an average value of *Tt* along the pulmonary vascular tree, although a regional dispersion of this index has been reported (Capen et al., 1990; Clough et al., 1998).

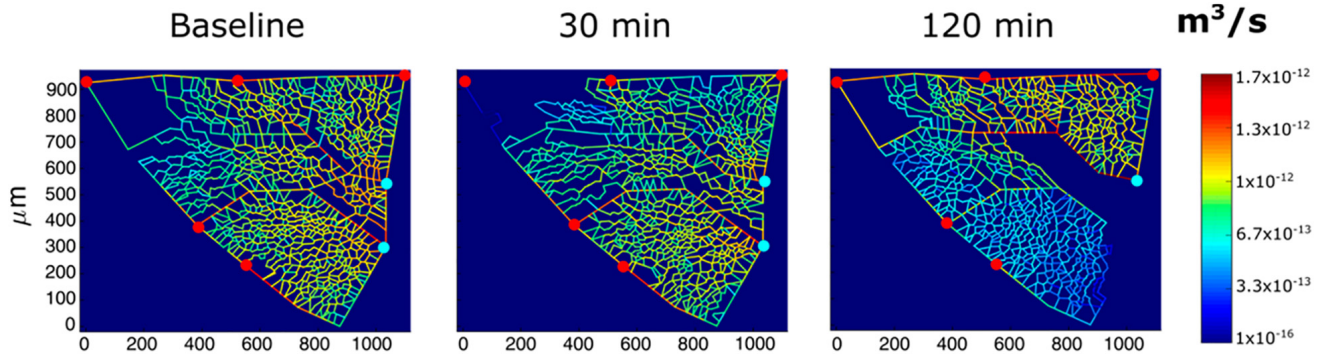

FIGURE 4 | Results from modeling of alveolar perfusion in edemagenic condition (12% O_2 exposure). Red and light blue dots identify, respectively, arteriolar accesses and venular exits. The color panels show capillary blood flow rates at different time points (baseline, 30; and 120 min) with color-coded log-scale intensity. In regions where edema develops, capillary blood flow is progressively reduced, approaching zero (from Mazzuca et al., 2019).

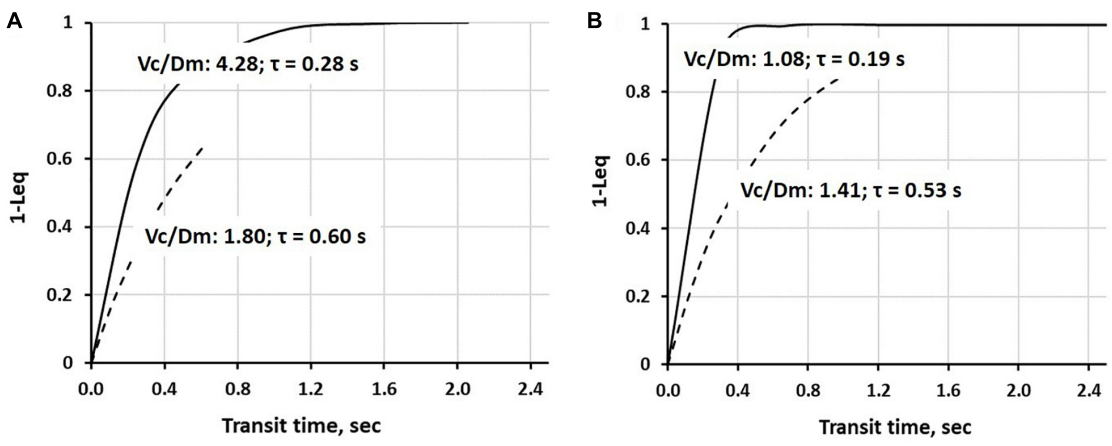

FIGURE 5 | Time course of 1-*Leq* (an index of alveolar-capillary equilibration) in normoxia at rest (a continuous line) and on exposure to severe hypoxia (3,840 m, $P_IO_2$90 mmHg, a dashed line) in two representative subjects having a high **(A)** or a low **(B)** *Vc/Dm* ratio at the sea level (SL) in resting condition (data from Beretta et al., 2019).

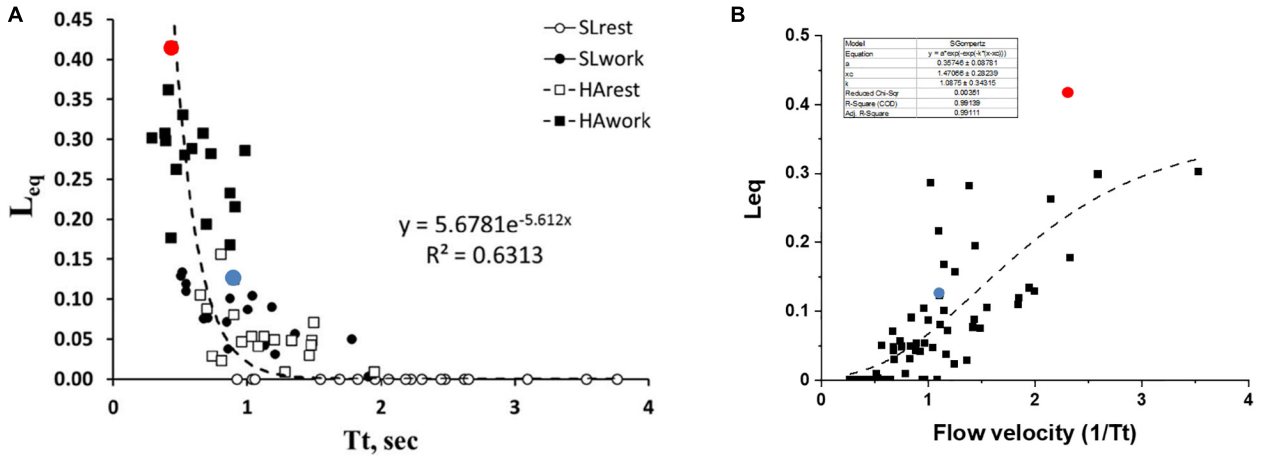

FIGURE 6 | (A) Correlation between transit time (*Tt*) and *Leq* in various conditions as indicated in the inset. **(B)** A plot of *Leq* vs. *1/Tt* (an index of blood velocity). Red and blue dots refer to the two subjects shown in **Figures 5A,B**, respectively (data from Beretta et al., 2019).

One may further consider that blood flow velocity in the alveolar capillaries can be expressed as: $Vel \propto 1/Tt$; **Figure 6B** shows the values of *Leq* plotted vs. *1/Tt*.

The shear rate at the endothelial capillary wall is a recognized cause of the increase in microvascular and protein permeability and is expected to increase with increasing blood flow velocity (Sill et al., 1995; Lakshminarayanan et al., 2000; Kang et al., 2014). Looking at the dispersion of the data in **Figure 6B**, one shall comment that the balance between an anti-edemagenic response (precapillary vasoconstriction) and its inevitable edemagenic consequence (the increase in the shear rate) might vary among individuals. One can hypothesize that, for a given value of *1/Tt*, the prevalence of the shear-dependent increase in permeability may justify a greater value of *Leq* due to some degree of interstitial fluid accumulation. This may be the case for the subjects with high *Vc/Dm* (a red dot, **Figure 6B**) as opposed to the subjects with low *Vc/Dm* (a blue dot, **Figure 6B**).

It should be considered that *Tt* reflects both a local phenomenon relating to vasomotion as well as the increase in cardiac output (Eq. 6). The latter varied remarkably among subjects. The impact of the increase in the cardiac output on *Leq* can be appreciated in **Figure 7**, showing the relationships between the cardiac output vs. *Leq* in the same conditions reported in **Figure 6A**. The remarkable shift to the right of the relationship referring to work in normoxia at an SL to work in HA reflects the effect of precapillary vasoconstriction for a given cardiac output. During work in hypoxia at a similar percentage of oxygen consumption (relative to maximum), the cardiac output

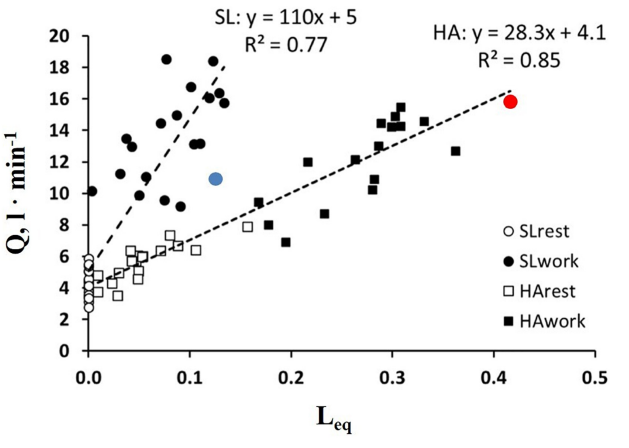

FIGURE 7 | Correlation between *Leq* and a cardiac output ($\dot{Q}$) in the condition indicated. Red and blue dots refer to the two subjects shown in **Figures 5A,B**, respectively (from Beretta et al., 2019).

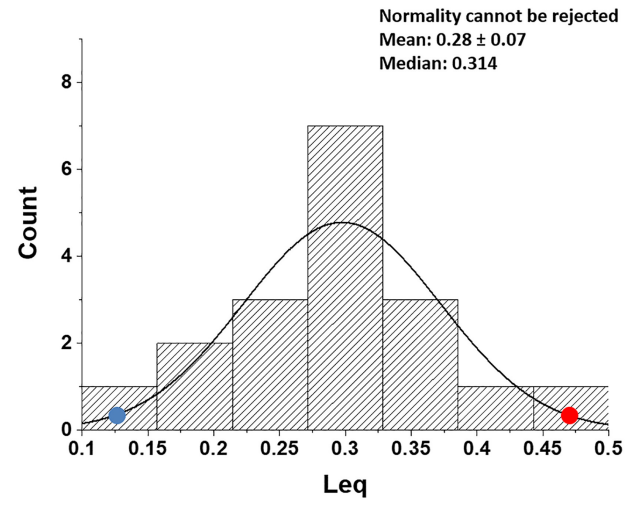

FIGURE 8 | Distribution of *Leq* values in all subjects at the end of exercise in severe hypoxia (HA) (3,840 m, P_IO_2 90 mmHg). Red and blue dots refer to the two subjects shown in **Figures 5A,B**, respectively (data from Beretta et al., 2019).

(normalized to body weight) was ∼50% greater in the subjects with high *Vc/Dm* (a red dot) compared to the subjects with low *Vc/Dm* (a blue dot).

Figure 8 shows that, in healthy people, in the most edemagenic conditions (work in severe HA, $P_AO_2 \sim 55$ mmHg), the distribution of *Leq* is normal. The positions of the two subjects referring to **Figure 5** within the distribution (red and blue dots) reflect the inter-individual variability.

SUMMARY

The conceptual contribution of the research studies referred to in this review may be summarized as follows:

1. The air-blood barrier phenotype can be described by the distribution of the *Vc/Dm* ratio. *Vc/Dm* shifts from ∼1, reflecting a higher number of alveoli of smaller radius, providing a high alveolar surface and a limited extension of the capillary network, to opposite features for *Vc/Dm* increasing up to ∼ 4.
2. Differences in air-blood barrier phenotype impact the efficiency in gas exchange and control of extravascular lung water when facing an increase in oxygen demand in edemagenic conditions. A lower *Vc/Dm* appears to be more efficient to guarantee gas exchange, as predicted by a theoretical morpho-functional model (Sapoval et al., 2002). There are indications that a lower/*Dm* is more protective against the risk of lung edema; conversely, a high *Vc/Dm* implies a greater tendency to develop lung edema.
3. A shunt-like effect can be described based on capillary blood kinetics that reflects the individual lung vasomotor control and the increase in cardiac output. This effect is minimal for low *Vc/Dm*, while it may remarkably increase in the subjects with high *Vc/Dm* due to increasing lung capillary blood velocity, reflecting precapillary vasoconstriction and a greater increase in cardiac output.
4. The data confirm that the lung response to an edemagenic condition is functionally aimed at protecting the air blood barrier to avoid a perturbation of fluid balance.

CONCLUSION

As far as we know, the present studies are the first ones of this nature, and we think they may provide a valuable contribution in terms of "*human integrative and translational physiology across a range of applied contexts, including exercise and environmental.*" Studies were performed in healthy subjects; accordingly, there is a potential interest to consider people reaching high altitudes on trekking expeditions being exposed to the risk of HAPE. Potential clinical relevance may also be considered as cardio-pulmonary disorders as well as conditions of decrease in vascular bed (lung resection and thrombosis) are at risk of developing lung edema. Defining the *Vc/Dm* ratio through ambulatory pneumological evaluation may turn useful to define the patient's tendency to develop edema before an acute severe disease occurs.

From an operational point of view, the subject's functional evaluation requires:

- The estimate of *Vc/Dm* at 100% *TLC*, relying on the *DLNO*/*DLCO* technique, at the SL at rest, and on exercise.
- The estimate of *Tt* that requires the measurement of cardiac output (by echocardiography with a semi-recumbent set-up at rest and on exercise).
- A valid potentiation of the trial requires the same determinations on exposure to normobaric HA.

DATA AVAILABILITY STATEMENT

The original contributions presented in the study are included in the article/supplementary material, further inquiries can be directed to the corresponding author.

AUTHOR CONTRIBUTIONS

GM conceived the research project and wrote the manuscript. EB, IR, and MB contributed to the discussion and analysis. All authors contributed to the article and approved the submitted version.

REFERENCES

Bartesaghi, M., Beretta, E., Pollastri, L., Scotti, V., Mandolesi, G., Lanfranconi, F., et al. (2014). Inter-individual differences in control of alveolar capillary blood volume in exercise and hypoxia. *Respir. Physiol. Neurobiol.* 190, 96–104. doi: 10.1016/j.resp.2013.08.021

Beretta, E., Grasso, G. S., Forcaia, G., Sancini, G., and Miserocchi, G. (2019). Differences in alveolo-capillary equilibration in healthy subjects on facing O_2 demand. *Sci. Rep.* 9:16693. doi: 10.1038/s41598-019-52679-4

Beretta, E., Lanfranconi, F., Grasso, G. S., Bartesaghi, M., Alemayehu, H. K., Pratali, L., et al. (2017). Air blood barrier phenotype correlates with alveolo-capillary O2 equilibration in hypobaric hypoxia. *Respir. Physiol. Neurobiol.* 246, 53–58. doi: 10.1016/j.resp.2017.08.006

Beretta, E., Romanò, F., Sancini, G., Grotberg, J. B., Nieman, G. F., and Miserocchi, G. (2021). Pulmonary interstitial matrix and lung fluid balance from normal to the acutely injured lung. *Front. Physiol.* 12:781874. doi: 10.3389/fphys.2021.781874

Berger, M. M., Hesse, C., Dehnert, C., Siedler, H., Kleinbongard, P., Bardenheuer, H. J., et al. (2005). Hypoxia impairs systemic endothelial function in individuals prone to high-altitude pulmonary edema. *Am. J. Respir. Crit. Care Med.* 172, 763–767. doi: 10.1164/rccm.200504-654OC

Brower, R. G., Sylvester, J. T., and Permutt, S. (1990). Flow-volume characteristics in the pulmonary circulation. *J. Appl. Physiol.* 69, 1746–1753. doi: 10.1152/jappl.1990.69.5.1746

Busch, T., Bärtsch, P., Pappert, D., Grünig, E., Hildebrandt, W., Elser, H., et al. (2001). Hypoxia decreases exhaled nitric oxide in mountaineers susceptible to high-altitude pulmonary edema. *Am. J. Respir. Crit. Care Med.* 163, 368–373. doi: 10.1164/ajrccm.163.2.2001134

Capen, R. L., Hanson, W. L., Latham, L. P., Dawson, C. A., and Wagner, W. W. Jr. (1990). Distribution of pulmonary capillary transit times in recruited networks. *J. Appl. Physiol.* 69, 473–478. doi: 10.1152/jappl.1990.69.2.473

Clough, A. V., Haworth, S. T., Hanger, C. C., Wang, J., Roerig, D. L., Linehan, J. H., et al. (1998). Transit time dispersion in the pulmonary

arterial tree. *J. Appl. Physiol.* 85, 565–574. doi: 10.1152/jappl.1998.85.2.565

Dehler, M., Zessin, E., Bärtsch, P., and Mairbäurl, H. (2006). Hypoxia causes permeability oedema in the constant-pressure perfused rat lung. *Eur. Respir. J.* 27, 600–606. doi: 10.1183/09031936.06.00061505

Dehnert, C., Risse, F., Ley, S., Kuder, T. A., Buhmann, R., Puderbach, M., et al. (2006). Magnetic resonance imaging of uneven pulmonary perfusion in hypoxia in humans. *Am. J. Respir. Crit. Care Med.* 174, 1132–1138. doi: 10.1164/rccm.200606-780OC

Dellacà, R. L., Zannin, E., Sancini, G., Rivolta, I., Leone, B. E., Pedotti, A., et al. (2008). Changes in the mechanical properties of the respiratory system during the development of interstitial lung edema. *Respir. Res.* 9:51. doi: 10.1186/1465-9921-9-51

Domino, K. B., Eisenstein, B. L., Tran, T., and Hlastala, M. P. (1993). Increased pulmonary perfusion worsens ventilation-perfusion matching. *Anesthesiology* 79, 817–826. doi: 10.1097/00000542-199310000-00025

Duplain, H., Sartori, C., Lepori, M., Egli, M., Allemann, Y., Nicod, P., et al. (2000). Exhaled nitric oxide in high-altitude pulmonary edema: role in the regulation of pulmonary vascular tone and evidence for a role against inflammation. *Am. J. Respir. Crit. Care Med.* 162, 221–224. doi: 10.1164/ajrccm.162.1.9908039

Eichstaedt, C. A., Benjamin, N., and Grünig, E. (2020a). Genetics of pulmonary hypertension and high-altitude pulmonary edema. *J. Appl. Physiol.* 128, 1432–1438. doi: 10.1152/japplphysiol.00113.2020

Eichstaedt, C. A., Mairbäurl, H., Song, J., Benjamin, N., Fischer, C., Dehnert, C., et al. (2020b). Genetic predisposition to high-altitude pulmonary edema. *High Alt. Med. Biol.* 21, 28–36. doi: 10.1089/ham.2019.0083

Glazier, J. B., Hughes, J. M., Maloney, J. E., and West, J. B. (1969). Measurements of capillary dimensions and blood volume in rapidly frozen lungs. *J. Appl. Physiol.* 26, 65–76. doi: 10.1152/jappl.1969.26.1.65

Hansen, J. M., Olsen, N. V., Feldt-Rasmussen, B., Kanstrup, I. L., Déchaux, M., Dubray, C., et al. (1994). Albuminuria and overall capillary permeability of albumin in acute altitude hypoxia. *J. Appl. Physiol.* 76, 1922–1927. doi: 10.1152/jappl.1994.76.5.1922

Hodges, A. N., Sheel, A. W., Mayo, J. R., and McKenzie, D. C. (2007). Human lung density is not altered following normoxic and hypoxic moderate-intensity exercise: implications for transient edema. *J. Appl. Physiol.* 103, 111–118. doi: 10.1152/japplphysiol.01087.2006

Hughes, J. M., and Pride, N. B. (2001). In defence of the carbon monoxide transfer coefficient Kco (TL/VA). *Eur. Respir. J.* 17, 168–174. doi: 10.1183/09031936.01.17201680

Kang, H., Cancel, L. M., and Tarbell, J. M. (2014). Effect of shear stress on water and LDL transport through cultured endothelial cell monolayers. *Atherosclerosis* 233, 682–690. doi: 10.1016/j.atherosclerosis.2014.01.056

Koyama, S., and Hildebrandt, J. (1991). Air interface and elastic recoil affect vascular resistance in three zones of rabbit lungs. *J. Appl. Physiol.* 70, 2422–2431. doi: 10.1152/jappl.1991.70.6.2422

Koyama, S., Lamm, W. J., Hildebrandt, J., and Albert, R. K. (1989). Flow characteristics of open vessels in zone 1 rabbit lungs. *J. Appl. Physiol.* 66, 1817–1823. doi: 10.1152/jappl.1989.66.4.1817

Kurbel, S., Kurbel, B., Belovari, T., Marić, S., Steiner, R., and Bozić, D. (2001). Model of interstitial pressure as a result of cyclical changes in the capillary wall fluid transport. *Med. Hypotheses.* 57, 161–166. doi: 10.1054/mehy.2001.1288

Lakshminarayanan, S., Gardner, T. W., and Tarbell, J. M. (2000). Effect of shear stress on the hydraulic conductivity of cultured bovine retinal microvascular endothelial cell monolayers. *Curr. Eye Res.* 21, 944–951. doi: 10.1076/ceyr.21.6.944.6985

Lovering, A. T., Romer, L. M., Haverkamp, H. C., Pegelow, D. F., Hokanson, J. S., and Eldridge, M. W. (2008). Intrapulmonary shunting and pulmonary gas exchange during normoxic and hypoxic exercise in healthy humans. *J. Appl. Physiol.* 104, 1418–1425. doi: 10.1152/japplphysiol.00208.2007

Lovering, A. T., Stickland, M. K., and Eldridge, M. W. (2006). Intrapulmonary shunt during normoxic and hypoxic exercise in healthy humans. *Adv. Exp. Med. Biol.* 588, 31–45. doi: 10.1007/978-0-387-34817-9_4

Mazzone, R. W., Durand, C. M., and West, J. B. (1978). Electron microscopy of lung rapidly frozen under controlled physiological conditions. *J. Appl. Physiol. Respir. Environ. Exerc. Physiol.* 45, 325–333. doi: 10.1152/jappl.1978.45.2.325

Mazzuca, E., Aliverti, A., and Miserocchi, G. (2016). Computational micro-scale model of control of extravascular water and capillary perfusion in the air blood barrier. *J. Theor. Biol.* 400, 42–51. doi: 10.1016/j.jtbi.2016.03.036

Mazzuca, E., Aliverti, A., and Miserocchi, G. (2019). Understanding vasomotion of lung microcirculation by *In Vivo* imaging. *Imaging* 5:22. doi: 10.3390/jimaging5020022

McKenzie, D. C., O'Hare, T. J., and Mayo, J. (2005). The effect of sustained heavy exercise on the development of pulmonary edema in trained male cyclists. *Respir. Physiol. Neurobiol.* 145, 209–218. doi: 10.1016/j.resp.2004.06.010

Miserocchi, G. (2009). Mechanisms controlling the volume of pleural fluid and extravascular lung water. *Eur. Respir. Rev.* 18, 244–252. doi: 10.1183/09059180.00002709

Miserocchi, G., Messinesi, G., Tana, F., Passoni, E., Adamo, S., Romano, R., et al. (2008). Mechanisms behind inter-individual differences in lung diffusing capacity. *Eur. J. Appl. Physiol.* 102, 561–568. doi: 10.1007/s00421-007-0625-2

Miserocchi, G., Negrini, D., Del Fabbro, M., and Venturoli, D. (1993). Pulmonary interstitial pressure in intact *in situ* lung: transition to interstitial edema. *J. Appl. Physiol.* 74, 1171–1177. doi: 10.1152/jappl.1993.74.3.1171

Miserocchi, G., Passi, A., Albertini, R., Negrini, D., and De Luca, G. (1999). Interstitial pressure and proteoglycan degradation in hydraulic- and elastase-induced lung edema. *Chest* 116(1 Suppl.):31S. doi: 10.1378/chest.116.suppl_1.31s

Miserocchi, G., Passi, A., Negrini, D., Del Fabbro, M., and De Luca, G. (2001). Pulmonary interstitial pressure and tissue matrix structure in acute hypoxia. *Am. J. Physiol. Lung Cell Mol. Physiol.* 280, L881–L887. doi: 10.1152/ajplung.2001.280.5.L881

Mitzner, W., and Sylvester, J. T. (1986). Lymph flow and lung weight in isolated sheep lungs. *J. Appl. Physiol.* 61, 1830–1835. doi: 10.1152/jappl.1986.61.5.1830

Negrini, D., Candiani, A., Boschetti, F., Crisafulli, B., Del Fabbro, M., Bettinelli, D., et al. (2001). Pulmonary microvascular and perivascular interstitial geometry during development of mild hydraulic edema. *Am. J. Physiol. Lung Cell. Mol. Physiol.* 281, L1464–L1471. doi: 10.1152/ajplung.2001.281.6.L1464

Negrini, D., Passi, A., de Luca, G., and Miserocchi, G. (1996). Pulmonary interstitial pressure and proteoglycans during development of pulmonary edema. *Am. J. Physiol.* 270(6 Pt 2), H2000–H2007. doi: 10.1152/ajpheart.1996.270.6.H2000

Paintal, A. S. (1969). Mechanism of stimulation of type J pulmonary receptors. *J. Physiol.* 203, 511–532. doi: 10.1113/jphysiol.1969.sp008877

Parker, J. C., and Townsley, M. I. (2004). Evaluation of lung injury in rats and mice. *Am. J. Physiol. Lung Cell Mol. Physiol.* 286, L231–L246. doi: 10.1152/ajplung.00049.2003

Passi, A., Negrini, D., Albertini, R., Miserocchi, G., and De Luca, G. (1999). The sensitivity of versican from rabbit lung to gelatinase A (MMP-2) and B (MMP-9) and its involvement in the development of hydraulic lung edema. *FEBS Lett.* 456, 93–96. doi: 10.1016/s0014-5793(99)00929-1

Piiper, J., and Scheid, P. (1981). Model for capillary-alveolar equilibration with special reference to O2 uptake in hypoxia. *Respir. Physiol.* 46, 193–208. doi: 10.1016/0034-5687(81)90121-3

Richalet, J. P., Larmignat, P., Poitrine, E., Letournel, M., and Canouï-Poitrine, F. (2012). Physiological risk factors for severe high-altitude illness: a prospective cohort study. *Am. J. Respir. Crit. Care Med.* 185, 192–198. doi: 10.1164/rccm.201108-1396OC

Richalet, J. P., Pillard, F., Le Moal, D., Rivière, D., Oriol, P., Poussel, M., et al. (2021). Validation of a score for the detection of subjects with high risk for severe high-altitude illness. *Med. Sci. Sports Exerc.* 53, 1294–1302. doi: 10.1249/MSS.0000000000002586

Rivolta, I., Lucchini, V., Rocchetti, M., Kolar, F., Palazzo, F., Zaza, A., et al. (2011). Interstitial pressure and lung oedema in chronic hypoxia. *Eur. Respir. J.* 37, 943–949. doi: 10.1183/09031936.00066710

Roselli, R. J., Parker, R. E., and Harris, T. R. (1984). A model of unsteady-state transvascular fluid and protein transport in the lung. *J. Appl. Physiol. Respir. Environ Exerc. Physiol.* 56, 1389–1402. doi: 10.1152/jappl.1984.56.5.1389

Roughton, F., and Forster, R. E. (1957). Relative importance of diffusion and chemical reaction rates in determining rate of exchange of gases in the human lung with special reference to true diffusing capacity of pulmonary membrane

and volume of blood in the lung capillaries. *J. Appl. Physiol.* 11, 290–302. doi: 10.1152/jappl.1957.11.2.290

Sapoval, B., Filoche, M., and Weibel, E. R. (2002). Smaller is better–but not too small: a physical scale for the design of the mammalian pulmonary acinus. *Proc. Natl. Acad. Sci. U.S.A.* 99, 10411–10416. doi: 10.1073/pnas.122352499

Scherrer, U., Vollenweider, L., Delabays, A., Savcic, M., Eichenberger, U., Kleger, G. R., et al. (1996). Inhaled nitric oxide for high-altitude pulmonary edema. *N. Engl. J. Med.* 334, 624–629. doi: 10.1056/NEJM199603073341003

Sharma, M., Singh, S. B., and Sarkar, S. (2014). Genome wide expression analysis suggests perturbation of vascular homeostasis during high altitude pulmonary edema. *PLoS One* 9:e85902. doi: 10.1371/journal.pone.0085902

Sill, H. W., Chang, Y. S., Artman, J. R., Frangos, J. A., Hollis, T. M., and Tarbell, J. M. (1995). Shear stress increases hydraulic conductivity of cultured endothelial monolayers. *Am. J. Physiol.* 268(2 Pt 2), H535–H543. doi: 10.1152/ajpheart.1995.268.2.H535

Stickland, M. K., Welsh, R. C., Haykowsky, M. J., Petersen, S. R., Anderson, W. D., Taylor, D. A., et al. (2004). Intra-pulmonary shunt and pulmonary gas exchange during exercise in humans. *J. Physiol.* 561(Pt 1), 321–329. doi: 10.1113/jphysiol.2004.069302

Conflict of Interest: The authors declare that the research was conducted in the absence of any commercial or financial relationships that could be construed as a potential conflict of interest.

Publisher's Note: All claims expressed in this article are solely those of the authors and do not necessarily represent those of their affiliated organizations, or those of the publisher, the editors and the reviewers. Any product that may be evaluated in this article, or claim that may be made by its manufacturer, is not guaranteed or endorsed by the publisher.

frontiers | Frontiers in Physiology

ORIGINAL RESEARCH
published: 20 April 2022
doi: 10.3389/fphys.2022.814320

Surfactant Treatment Shows Higher Correlation Between Ventilator and EIT Tidal Volumes in an RDS Animal Model

Yoon Zi Kim[1], Hee Yoon Choi[1], Yong Sung Choi[1], Chae Young Kim[1], Young Joo Lee[2] and Sung Hoon Chung[1]*

[1]Department of Pediatrics, College of Medicine Kyung Hee University, Seoul, South Korea, [2]Department of Obstetrics and Gynecology, College of Medicine Kyung Hee University, Seoul, South Korea

Neonatal respiratory distress syndrome (RDS) is a condition of pulmonary surfactant insufficiency in the premature newborn. As such, artificial pulmonary surfactant administration is a key treatment. Despite continued improvement in the clinical outcomes of RDS, there are currently no established bedside tools to monitor whether pulmonary surfactant is effectively instilled throughout the lungs. Electrical impedance tomography (EIT) is an emerging technique in which physiological functions are monitored on the basis of temporal changes in conductivity of different tissues in the body. In this preliminary study, we aimed to assess how EIT tidal volumes correlate with ventilator tidal volumes in an RDS animal model, namely untreated, surfactant-treated, and normal control rabbit pups. Tidal volumes were measured simultaneously on an EIT system and a mechanical ventilator and compared at different peak inspiratory pressures. The linear correlation between tidal volumes measured by EIT and by ventilator had an R^2 of 0.71, 0.76 and 0.86 in the untreated, surfactant-treated, and normal control groups, respectively. Bland–Altman analysis showed a good correlation between the measurements obtained with these two modalities. The intraclass correlation coefficients (ICC) between ventilator tidal volume and EIT tidal volume were 0.83, 0.87, and 0.93 (all $p < 0.001$) in the untreated, surfactant-treated, and normal control groups, respectively, indicating that the higher ICC value, the better inflated status of the lung. In conclusion, we demonstrated that EIT tidal volume correlated with ventilator tidal volume. ICC was higher in the surfactant treated group.

Keywords: electronic impedance tomography, respiratory distress syndrome, premature infant, neonatal intensive care unit (NICU), mechanical ventilator, alveoli collapse, homogeneity

OPEN ACCESS

Edited by:
Andrew John Halayko, University of Manitoba, Canada

Reviewed by:
Sam Bayat, Université Grenoble Alpes, France
Christopher G. Wilson, Loma Linda University, United States

****Correspondence:***
Yong Sung Choi
feelhope@khu.ac.kr

Specialty section:
This article was submitted to Respiratory Physiology and Pathophysiology, a section of the journal Frontiers in Physiology

Received: *13 November 2021*
Accepted: *17 March 2022*
Published: *20 April 2022*

Citation:
Kim YZ, Choi HY, Choi YS, Kim CY, Lee YJ and Chung SH (2022) Surfactant Treatment Shows Higher Correlation Between Ventilator and EIT Tidal Volumes in an RDS Animal Model. Front. Physiol. 13:814320. doi: 10.3389/fphys.2022.814320

INTRODUCTION

Neonatal respiratory distress syndrome (RDS) is a condition of pulmonary surfactant insufficiency in the premature newborn; without treatment, morbidity and mortality increase during the first 2 days of life. Administration of artificial pulmonary surfactant reduces surface tension of the alveoli and improves functional residual capacity by expanding the collapsed alveoli (Knudsen and Ochs, 2018).

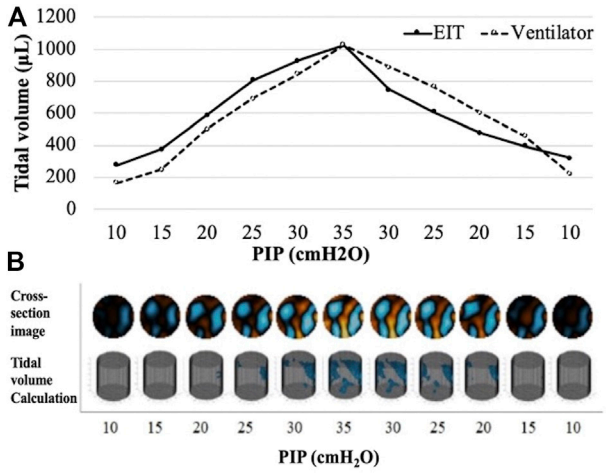

FIGURE 1 | An example of tidal volume measurement and EIT images in a subject from preterm treated group **(A)** Pressure-volume curves of ventilator tidal volume and EIT tidal volume. **(B)** The reconstructed chest cross-section EIT according to PIP change. PIP, peak inspiratory pressure.

Despite continued improvement of the clinical outcomes in RDS, there is a scarcity of bedside tools that can be used to monitor the state of the instilled surfactant throughout the lungs, excepting chest x-ray and blood gas analysis. Electrical impedance tomography (EIT) is an emerging technique in which ventilation is monitored on the basis of temporal changes in conductivity of different tissues in the body. With small currents, conducting electrodes attached to the skin can analyze body composition during ventilation without radiation exposure (Metherall et al., 1996; Adler and Boyle, 2017; Kallio et al., 2019). However, its application to neonatal RDS is not yet established.

We analyzed the calculated tidal volumes using the EIT technique. The aim of this study was to determine how pulmonary surfactant administration affects tidal volume parameters measured by mechanical ventilator and EIT in a preterm rabbit model of RDS.

MATERIALS AND METHODS

Animals

According to the ARRIVE guidelines, we obtained approval from the Institutional Animal Review Board of Kyung Hee University Hospital (KHMC-IACUC-2017-026). Zoletil® (15 mg/kg) was used to induce sedative anesthesia of the mother rabbit (intravascular injection, marginal ear vein) and each pup (intramuscular injection, unilateral thigh muscle) before procedures. We harvested preterm rabbit pups on day 27 (D27) of gestation and term pups on day 31 (D31) *via* caesarean section of pregnant New Zealand white

TABLE 1 | Measured tidal volumes according to stepwise inflation and deflation.

Ventilator[a]		**Untreated preterm (*n* = 9)**		**Treated preterm (*n* = 6)**		**Term (*n* = 3)**	
		Median	**Range**	**Median**	**Range**	**Median**	**Range**
Inflation peak inspiratory pressure (cmH_2O)	10	186	(32–709)	161	107–397	194	110–266
	15	316	(110–997)	288.5	(232–553)	342	(188–396)
	20	419	(160–1,252)	419	(338–681)	477	(266–552)
	25	496	(214–1,467)	523	(444–788)	631	(370–812)
	30	599	(370–1754)	655	(545–913)	865	(600–1,097)
	35	781	(604–1929)	776	(705–1,026)	1,261	(916–1,435)
Deflation peak inspiratory pressure (cmH_2O)	30	607	(499–1726)	628	(547–890)	1,076	(788–1,253)
	25	471	(318–1,519)	539	(444–766)	896	(682–1,071)
	20	393	(214–1,334)	408	(340–626)	717	(552–864)
	15	289	(134–1,157)	292.5	(237–496)	506	(396–604)
	10	210	(31–944)	189	(154–368)	291	(214–344)
EIT[b]		**Untreated preterm**		**Treated preterm**		**Term**	
		Median	**Range**	**Median**	**Range**	**Median**	**Range**
Inflation peak inspiratory pressure (cmH_2O)	10	81.8	(10.5–735.7)	222.2	(154.4–293.0)	277.2	(208.3–316.2)
	15	65.2[c]	(17.9–541.0)	316.2[c]	(257.3–386.8)	397.3	(247.6–562.0)
	20	299.8	(29.8–833.1)	443.4	(317.9–587.5)	564.0	(308.7–825.7)
	25	391.9	(51.1–1,114.0)	536.45	(470.4–804.4)	819.9	(375.5–1,028.0)
	30	515.9	(190.3–1,632.5)	650.12	(591.2–925.9)	1,102.9	(654.9–1,109.9)
	35	781.0	(632.0–1,632.5)	776.0	(705.0–1,026.0)	1,261.0	(825.6–1,444.0)
Deflation peak inspiratory pressure (cmH_2O)	30	637.1	(542.0–1,594.7)	709.8	(540.4–914.1)	848.8	(721.0–1,257.9)
	25	468.9	(325.5–1929.0)	579.9	(439.3–729.9)	723.3	(625.8–1,079.6)
	20	354.9	(56.4–1926.1)	454.5	(319.6–517.9)	519.6	(485.2–870.3)
	15	212.3[c]	(17.9–1754.6)	375.0[c]	(226.2–454.5)	541.5	(371.8–618.3)
	10	88.89	(4.9–1812.7)	253.7	(149.6–332.1)	282.9	(223.1–350.8)

[a]*Tidal volumes were recorded as shown by the small animal ventilator panel, according to peak inspiratory pressure changes.*

[b]*Tidal volumes were calculated through the EIT, signals analysis.*

[c]*Means statistical significance between untreated preterm group and surfactant treated preterm group (*p *= 0.018, 0.026, Mann-Whitney U test).*

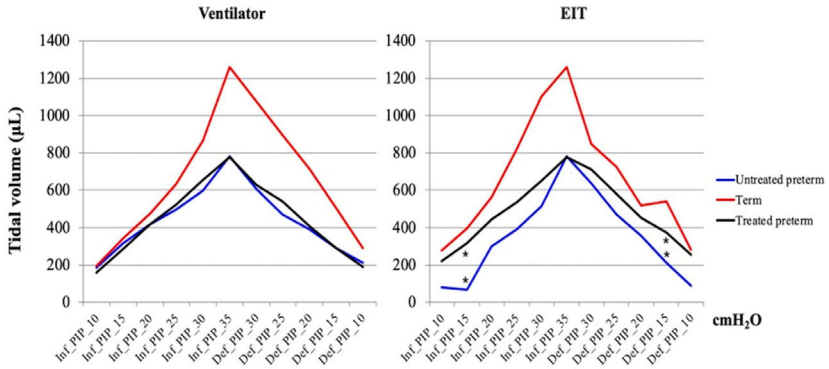

FIGURE 2 | Pressure-volume curves. The graphs were based on the median values of the untreated preterm group (n = 9), surfactant treated group (n = 6), and term group (n = 3). Maximum and minimum values are shown in **Table 1**. * means statistical significance between the untreated preterm group and surfactant treated preterm group (p = 0.018, 0.026, Mann-Whitney U test). PIP, peak inspiratory pressure; Inf, inflation; Def, deflation.

rabbits. The study groups were as follows: 1) Untreated (preterm pups), 2) surfactant-treated (preterm pups), and 3) normal controls (term pups). Soon after delivery, we performed a tracheostomy procedure on the pups using a 24G intravenous catheter and applied a small animal ventilator (VentElite, Harvard Apparatus, Holliston, MA, United States) set to the pressure-controlled mandatory ventilation mode (**Supplementary Figure S1**). The treated group were given 100 mg/kg of Curosuf ® (Chiesi Farmaceutici, Parma, Italy) by the intratracheal route, immediately after application of the ventilator.

Electrical Impedance Measurement

We used the KHU Mark2.5 EIT system, a non-commercial prototype designed by the Impedance Imaging Research Center of Kyung Hee University. Since the rabbit pups were small and had an average weight of 43.06 ± 14.75 g and a chest circumference of 7.64 ± 0.61 mm, we prepared a specialized bed that had an electrode interface (**Supplementary Figure S1**). The pups were placed in the interface with sixteen spring-loaded pin electrodes that surrounded the chest, just below the level of the forelimbs. The zigzag electrode attachment and a measurement protocol robust against noise and electrode attachment position error were selected because of the small chest circumference of the preterm pups (Graham and Adler, 2007). To collect time series of EIT images at 50 frames/s, 16 electrode leads were connected in two layers at the perimeter of the thorax of each rabbit pup.

The EIT measurement was undertaken during the following ventilator maneuver: An initial respiratory rate set at 120 breaths/min and positive end-expiratory pressure

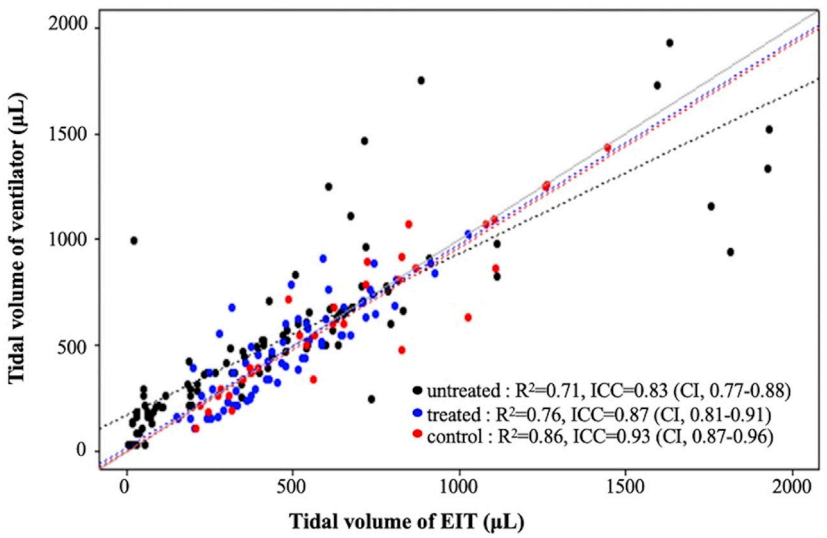

FIGURE 3 | Linear regression analysis and intraclass correlation coefficient (ICC) of tidal volumes determined by the ventilator and EIT V_T in each group.

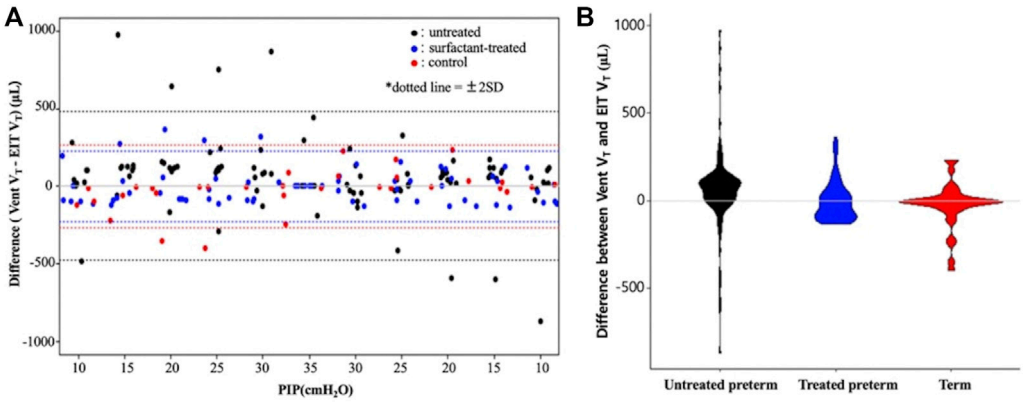

FIGURE 4 | A Bland–Altman plot **(A)** and violin plot **(B)** showing differences between the ventilator and EIT with the 95% limits of agreement. PIP, peak inspiratory pressure; Vent V_T, ventilator tidal volume; EIT V_T, EIT tidal volume.

of 5 cm H_2O (Basoalto, et al., 2021; Ferrini, et al., 2021; Joelsson et al., 2021). Over 120 s, PIP was increased from 10 to 35 cm H_2O in 5 cm H_2O increments (stepwise inflation) and thereafter returned in 5 cm H_2O steps back to the baseline (stepwise deflation). EIT images were reconstructed from the difference in voltage data measured between adjacent electrode pairs using the 3D GREIT algorithm (**Figures 1A,B**) (Adler and Lionheart, 2006). At each PIP level, the tidal volumes (V_T) measured by the ventilator were recorded, and the EIT signals were transformed into aeration area and calculated tidal volumes. The calculation was done by subtracting the individual pixel values of relative impedance changes in EIT during each PIP step. Finally, the local impedance change was plotted in the selected regions of interest.

Statistical Analysis

The volume of air in the lungs and the tidal volume, was the major determinant of thoracic impedance change. Within each group, we calculated the differences in tidal volume (Diff V_T) measured by the ventilator and EIT during PIP changes as follows:

$$\text{Diff } V_T \ (\mu L) = \text{Vent } V_T - \text{EIT } V_T$$

The relationship between ventilator tidal volume (Vent V_T) and EIT tidal volume (EIT V_T) was assessed by Spearman's correlation and linear regression. Agreement between Diff V_T in the same PIP was analyzed by Wilcoxon signed rank test with paired test and equivalence test. In addition, the agreement was confirmed through the Bland–Altman plot. The intraclass correlation coefficient (ICC) was calculated for each group, and the ICCs were compared between different groups using Kruskal-Wallis test. Mann-Whitney U test was used in between-group comparisons. Statistical significance was set at $p < 0.05$ and SAS version 9.4 (SAS Institute Inc., Cary, NC, United States) as well as the R4.0.4 program was used for analyses.

RESULTS

Twenty three newborn pups were harvested from 6 mother rabbits. Five pups were excluded as a result of early death (n = 2) or measurement failure due to pneumothorax, which was recognizable by sight (n = 3). Among 18 pups, 3 were term, 9 were untreated preterm and 6 were surfactant treated preterm pups. We obtained 198 tidal volume sets in total (99 in treated, 66 in untreated and 33 in term group). One tidal volume set was made from 120 s of the specific PIP level.

Assessment of Changes in Tidal Volume and Electrical Impedance Tomography

We obtained pressure-volume curves according to inflation and deflation pressures. **Table 1** and **Figure 2** show the median values in the curves of Vent V_T and EIT V_T. There was a significant difference between the untreated and surfactant-treated preterm pups in both inflation and deflation curves at PIP of 15 cm H_2O (p = 0.018, 0.026).

Correlation Analysis of Tidal Volume Measured by the Ventilator and Electrical Impedance Tomography

An increase in PIP increased the tidal volume and lung impedance. A highly positive correlation between ventilator tidal volume and EIT tidal volume was found in all 18 pups; linear regression equations for each group are shown in **Figure 3**. The determination coefficients (R^2) of all groups were greater than 0.7, showing good correlation between ventilator and EIT. Moreover, the ICC between Vent V_T and EIT V_T was 0.85 ($p < 0.001$) in all groups, indicating very good agreement. The ICC values of each group were 0.83 ($p < 0.001$), 0.87 ($p < 0.001$), and 0.93 ($p < 0.001$) in the untreated, surfactant-treated, and normal control groups, respectively. ICCs of inflation PIP 10, 20, 25 cm H_2O ($p <$

0.001) and deflation PIP 20, 15 and 10 cm H_2O ($p < 0.001$) were significantly different between untreated and surfactant treated groups. The Diff V_T values at different PIP were analyzed by the Bland–Altman plot and the violin plot chart (**Figure 4**). The mean Diff V_T was 72.50 μL (range, 14.61 to 109.88 μL) in the untreated preterm group, −21.76 μL (−31.87 to 24.51 μL) in the surfactant-treated preterm group, and −7.88 μL (−71.46 to 21.96 μL) in the normal control group.

DISCUSSION

In our study, New Zealand white rabbit pups were used as a model of both premature lung physiology as well as RDS pathology. Rabbit pups harvested on D27 correspond to preterm births with RDS and those harvested on D31 correspond to normal term births (Kikkawa et al., 1968; Choi et al., 2017). Human infant RDS is a disease of prematurity. Its incidence is 92% at 24–25 weeks' gestation, 88% at 26–27 weeks, 76% at 28–29 weeks, and 57% at 30–31 weeks of gestation (Sweet et al., 2013). As pulmonary surfactant is not ready to function in RDS infants, the mainstay of treatment is artificial surfactant instillation through the trachea. It recruits alveolar volume and hence increases lung residual functional capacity by reducing surface tension in the alveoli and equilibrating the uneven pressures of different parts of the lungs, present in RDS.

The purpose of this study was to determine whether EIT can generate some sort of practical benefit in the bedside treatment of artificial surfactant in the rabbit pup model of RDS. Overall, our findings show good correlations and agreement analysis between the measurements of tidal volumes that were obtained from the two modalities, small animal ventilator and EIT. The most interesting finding was of higher ICC values in the surfactant treated group (0.87) compared to the untreated group (0.83), not to mention the highest ICC values in the term group (0.93, **Figure 3**) and its narrow distribution in the treated group (**Figure 4**). Although our study design precludes before and after intervention comparisons, it is feasible to assume that surfactant instillation could increase the ICC from a lower pretreatment state, in mechanically ventilated pups. We attempted for pre- and post-intervention comparisons, however, the preterm pups could not survive long enough for the measurements. As such, we simplified our model into 3 groups instead of performing longitudinal analyses.

In terms of the ICC differences, a possible explanation could be that unlike untreated pups, unevenly inflated or collapsed alveoli were minimized in the surfactant treated preterm pup lungs, as opposed to the untreated pups, eventually empowering the agreement analysis. Accordingly, the higher ICC values and R^2 may indicate more recruited alveoli.

EIT technology is already an emerging option in various ICU environments such as adult type acute respiratory distress syndrome, pneumothorax, atelectasis, and pleural effusion (Bodenstein et al., 2009; Burkhardt et al.,. 2013; Davies et al., 2019; Jang et al., 2019; Tomicic and Cornejo, 2019). In neonatal settings, there are several publications regarding infants with RDS (Frerichs et al., 2001; Chatziioannidis et al., 2011; Miedema et al., 2011; Chatziioannidis et al., 2013). Unlike these studies, however, we analyzed tidal volumes from two different modalities and observed higher ICC in the surfactant treated group. We suggest that EIT technology may be a promising option as a real-time bedside monitoring tool in mechanically ventilated RDS infants, but further study is needed.

The most challenging problem of the rabbit pup model in our study, especially the preterm model, is that they are very small (42.1 ± 14 g in this study). They cannot be cannulated, blood gas analyses are not available, and imaging studies are limited. However, the premature lung physiology that encompasses RDS pathology is a great strength that allows for testing of artificial surfactant efficacy (Almlén et al., 2010; Otsubo and Takei, 2002).

This study has several limitations. First, our study lacks assessment of pre and post effects of surfactant administration. The pups were small and premature, and they could not survive long enough to endure another set of procedures. Second, this was a preliminary study using animal subjects, conducted with a small sample size. In addition, we regarded all measured tidal volumes to be a result of intact ventilation without any leakage. Finally, we compared only the tidal volume sets without the regional ventilation data of EIT.

CONCLUSION

In conclusion, in this preliminary animal study, we observed good correlation of tidal volumes between Vent V_T and EIT V_T. Furthermore, there were better ICC and Diff V_T in surfactant treated RDS group than in the untreated group. EIT can detect an improvement in lung ventilation in surfactant treated and term pups, compared to untreated rabbit pups.

DATA AVAILABILITY STATEMENT

The original contributions presented in the study are included in the article/**Supplementary Material**, further inquiries can be directed to the corresponding author.

ETHICS STATEMENT

The animal study was reviewed and approved by the Institutional animal review board of Kyung Hee University Hospital (KHMC-IACUC-2017-026).

AUTHOR CONTRIBUTIONS

YC and SC have contributed to the conception and design of the study, acquisition of data, analysis and interpretation of

data. YC and YK analysis of data and contributed to the interpretation of the results. The first draft of the manuscript was written by YK and YC commented on previous versions of the manuscript. CK, YL and HC revised it critically for important intellectual content and the final approval of the version to being submitted. YC will act as guarantor for this paper.

ACKNOWLEDGMENTS

We would like to thank Impedance Imaging Research Center, Kyung Hee University and Medical Science Research Institute, Kyung Hee University Medical Center for their dedication and support for the experiment.

SUPPLEMENTARY MATERIAL

The Supplementary Material for this article can be found online at: https://www.frontiersin.org/articles/10.3389/fphys.2022.814320/full#supplementary-material

Supplementary Figure S1 | Experimental setting of EIT and a small animal ventilator with a rabbit pup.

Supplementary Figure S2 | The specialized bed designed by the Kyung Hee University Impedance Imaging Research Center (IIRC).

REFERENCES

Adler, A., and Boyle, A. (2017). Electrical Impedance Tomography: Tissue Properties to Image Measures. *IEEE Trans. Biomed. Eng.* 64 (11), 2494–2504. doi:10.1109/TBME.2017.2728323

Adler, A., and Lionheart, W. R. B. (2006). Uses and Abuses of EIDORS: an Extensible Software Base for EIT. *Physiol. Meas.* 27 (5), S25–S42. Epub 2006 Apr 18. doi:10.1088/0967-3334/27/5/S03

Almlén, A., Walther, F. J., Waring, A. J., Robertson, B., Johansson, J., and Curstedt, T. (2010). Synthetic Surfactant Based on Analogues of SP-B and SP-C Is superior to Single-Peptide Surfactants in Ventilated Premature Rabbits. *Neonatology* 98 (1), 91–99. doi:10.1159/000276980

Basoalto, R., Damiani, L. F., Bachmann, M. C., Fonseca, M., Barros, M., Soto, D., et al. (2021). Acute Lung Injury Secondary to Hydrochloric Acid Instillation Induces Small Airway Hyperresponsiveness. *Am. J. Transl Res.* 13 (11), 12734–12741. eCollection 2021.

Bodenstein, M., David, M., and Markstaller, K. (2009). Principles of Electrical Impedance Tomography and its Clinical Application. *Crit. Care Med.* 37 (2), 713–724. doi:10.1097/CCM.0b013e3181958d2f

Burkhardt, W., Kurth, F., Pitterle, M., Blassnig, N., Wemhöner, A., and Rüdiger, M. (2013). Continuous Noninvasive Monitoring of Lung Recruitment during High-Frequency Oscillatory Ventilation by Electrical Impedance Measurement: an Animal Study. *Neonatology* 103 (3), 218–223. doi:10.1159/000345612

Chatziioannidis, I., Samaras, T., Mitsiakos, G., Karagianni, P., and Nikolaidis, N. (2013). Assessment of Lung Ventilation in Infants with Respiratory Distress Syndrome Using Electrical Impedance Tomography. *Hippokratia* 17 (2), 115–119.

Chatziioannidis, I., Samaras, T., and Nikolaidis, N. (2011). Electrical Impedance Tomography: a New Study Method for Neonatal Respiratory Distress Syndrome? *Hippokratia* 15 (3), 211–215.

Choi, Y.-S., Chung, S.-H., and Bae, C.-W. (2017). A Combination of Short and Simple Surfactant Protein B and C Analogues as a New Synthetic Surfactant: *In Vitro* and Animal Experiments. *Yonsei Med. J.* 58 (4), 823–828. doi:10.3349/ymj.2017.58.4.823

Davies, P., Yasin, S., Gates, S., Bird, D., and Silvestre, C. (2019). Clinical Scenarios of the Application of Electrical Impedance Tomography in Paediatric Intensive Care. *Sci. Rep.* 9 (1), 5362. doi:10.1038/s41598-019-41774-1

Ferrini, E., Leo, L., Corsi, L., Catozzi, C., Salomone, F., Ragionieri, L., et al. (2021). A New Anesthesia Protocol Enabling Longitudinal Lung-Function Measurements in Neonatal Rabbits by Micro-CT. *Am. J. Physiology-Lung Cell Mol. Physiol.* 321 (6), L1206–L1214. Epub 2021 Nov 17. doi:10.1152/ajplung.00328.2021

Frerichs, I., Schiffmann, H., Hahn, G., and Hellige, G. (2001). Non-invasive Radiation-free Monitoring of Regional Lung Ventilation in Critically Ill Infants. *Intensive Care Med.* 27 (8), 1385–1394. doi:10.1007/s001340101021

Graham, B. M., and Adler, A. (2007). Electrode Placement Configurations for 3D EIT. *Physiol. Meas.* 28 (7), S29–S44. doi:10.1088/0967-3334/28/7/S03

Jang, G. Y., Ayoub, G., Kim, Y. E., Oh, T. I., Chung, C. R., Suh, G. Y., et al. (2019). Integrated EIT System for Functional Lung Ventilation Imaging. *Biomed. Eng. Online* 18 (1), 83. doi:10.1186/s12938-019-0701-y

Joelsson, J. P., Ingthorsson, S., Kricker, J., Gudjonsson, T., and Karason, S. (2021). Ventilator-induced Lung-Injury in Mouse Models: Is There a Trap? *Lab. Anim. Res.* 37 (1), 30. doi:10.1186/s42826-021-00108-x

Kallio, M., van der Zwaag, A.-S., Waldmann, A. D., Rahtu, M., Miedema, M., Papadouri, T., et al. (2019). Initial Observations on the Effect of Repeated Surfactant Dose on Lung Volume and Ventilation in Neonatal Respiratory Distress Syndrome. *Neonatology* 116 (4), 385–389. doi:10.1159/000502612

Kikkawa, Y., Motoyama, E. K., and Gluck, L. (1968). Study of the Lungs of Fetal and Newborn Rabbits. Morphologic, Biochemical, and Surface Physical Development. *Am. J. Pathol.* 52 (1), 177–210.

Knudsen, L., and Ochs, M. (2018). The Micromechanics of Lung Alveoli: Structure and Function of Surfactant and Tissue Components. *Histochem. Cell Biol* 150 (6), 661–676. doi:10.1007/s00418-018-1747-9

Metherall, P., Barber, D. C., Smallwood, R. H., and Brown, B. H. (1996). Three-dimensional Electrical Impedance Tomography. *Nature* 380 (6574), 509–512. doi:10.1038/380509a0

Miedema, M., de Jongh, F. H., Frerichs, I., van Veenendaal, M. B., and van Kaam, A. H. (2011). Changes in Lung Volume and Ventilation during Surfactant Treatment in Ventilated Preterm Infants. *Am. J. Respir. Crit. Care Med.* 184 (1), 100–105. doi:10.1164/rccm.201103-0375OC

Otsubo, E., and Takei, T. (2002). Effects of the Human Pulmonary Surfactant Protein-C (SP-C), SP-Cl16(6-28) on Surface Activities of Surfactants with Various Phospholipids. *Biol. Pharm. Bull.* 25 (10), 1303–1306. doi:10.1248/bpb.25.1303

Sweet, D. G., Carnielli, V., Greisen, G., Hallman, M., Ozek, E., Plavka, R., et al. (2013). European Consensus Guidelines on the Management of Neonatal Respiratory Distress Syndrome in Preterm Infants - 2013 Update. *Neonatology* 103 (4), 353–368. doi:10.1159/000349928

Tomicic, V., and Cornejo, R. (2019). Lung Monitoring with Electrical Impedance Tomography: Technical Considerations and Clinical Applications. *J. Thorac. Dis.* 11 (7), 3122–3135. doi:10.21037/jtd.2019.06.27

Conflict of Interest: The authors declare that the research was conducted in the absence of any commercial or financial relationships that could be construed as a potential conflict of interest.

Publisher's Note: All claims expressed in this article are solely those of the authors and do not necessarily represent those of their affiliated organizations, or those of the publisher, the editors and the reviewers. Any product that may be evaluated in this article, or claim that may be made by its manufacturer, is not guaranteed or endorsed by the publisher.

frontiers | Frontiers in Physiology

MINI REVIEW
published: 02 May 2022
doi: 10.3389/fphys.2022.829534

Thoracic Computed Tomography to Assess ARDS and COVID-19 Lungs

Carmen Silvia Valente Barbas *

Associate Professor of Pneumology, University of São Paulo Medical School, Medical Staff Adult ICU Albert Einstein Hospital, São Paulo, Brazil

This review was designed to discuss the role of thoracic-computed tomography (CT) in the evaluation and treatment of patients with ARDS and COVID-19 lung disease. Non-aerated lungs characterize the ARDS lungs, compared to normal lungs in the lowermost lung regions, compressive atelectasis. Heterogenous ARDS lungs have a tomographic vertical gradient characterized by progressively more aerated lung tissues from the gravity-dependent to gravity-independent lungs levels. The application of positive pressure ventilation to these heterogeneous ARDS lungs provides some areas of high shear stress, others of tidal hyperdistension or tidal recruitment that increases the chances of appearance and perpetuation of ventilator-induced lung injury. Other than helping to the correct diagnosis of ARDS, thoracic-computed tomography can help to the adjustments of PEEP, ideal tidal volume, and a better choice of patient position during invasive mechanical ventilation. Thoracic tomography can also help detect possible intra-thoracic complications and in the follow-up of the ARDS patients' evolution during their hospital stay. In COVID-19 patients, thoracic-computed tomography was the most sensitive imaging technique for diagnosing pulmonary involvement. The most common finding is diffuse pulmonary infiltrates, ranging from ground-glass opacities to parenchymal consolidations, especially in the lower portions of the lungs' periphery. Tomographic lung volume loss was associated with an increased risk for oxygenation support and patient intubation and the use of invasive mechanical ventilation. Pulmonary dual-energy angio-tomography in COVID-19 patients showed a significant number of pulmonary ischemic areas even in the absence of visible pulmonary arterial thrombosis, which may reflect micro-thrombosis associated with COVID-19 pneumonia. A greater thoracic tomography severity score in ARDS was independently related to poor outcomes.

Keywords: ARDS, COVID-19, thoracic-computed tomography, pulmonary dual-energy angio-tomography, mechanical ventilation, patient position, PEEP, recruitment

OPEN ACCESS

Edited by:
Lorenzo Ball,
University of Genoa, Italy

Reviewed by:
Franco Laghi,
Loyola University Chicago, United States
Biniam Kidane,
University of Manitoba, Canada

***Correspondence:**
Carmen Silvia Valente Barbas
carmen.barbas@gmail.com

Specialty section:
This article was submitted to Respiratory Physiology and Pathophysiology, a section of the journal Frontiers in Physiology

Received: *05 December 2021*
Accepted: *28 March 2022*
Published: *02 May 2022*

Citation:
Barbas CSV (2022) Thoracic Computed Tomography to Assess ARDS and COVID-19 Lungs. Front. Physiol. 13:829534. doi: 10.3389/fphys.2022.829534

INTRODUCTION

Since 2012, the diagnosis of acute respiratory distress syndrome (ARDS) is made by the finding of a recent (less than 1 week) bilateral lung infiltrates in the chest radiography of a patient with PaO2/FIO2 less than 300 and a risk factor for ARDS according to Berlin definition (Ranieri et al., 2012). This new re-classification of ARDS (Ranieri et al., 2012) recognized that bilateral opacities consistent with pulmonary edema on the chest radiograph as defining criteria for ARDS could also be demonstrated on thoracic-computed tomography. The images of thoracic-computed tomography in patients with ARDS helped to confirm the diagnosis of ARDS (Bombino et al., 1991; Barbas et al., 2003; Caser et al., 2014; Barbas et al., 2014; Pesenti et al., 2016) (**Figure 1**), detecting parenchymal and interstitial alterations as well as the

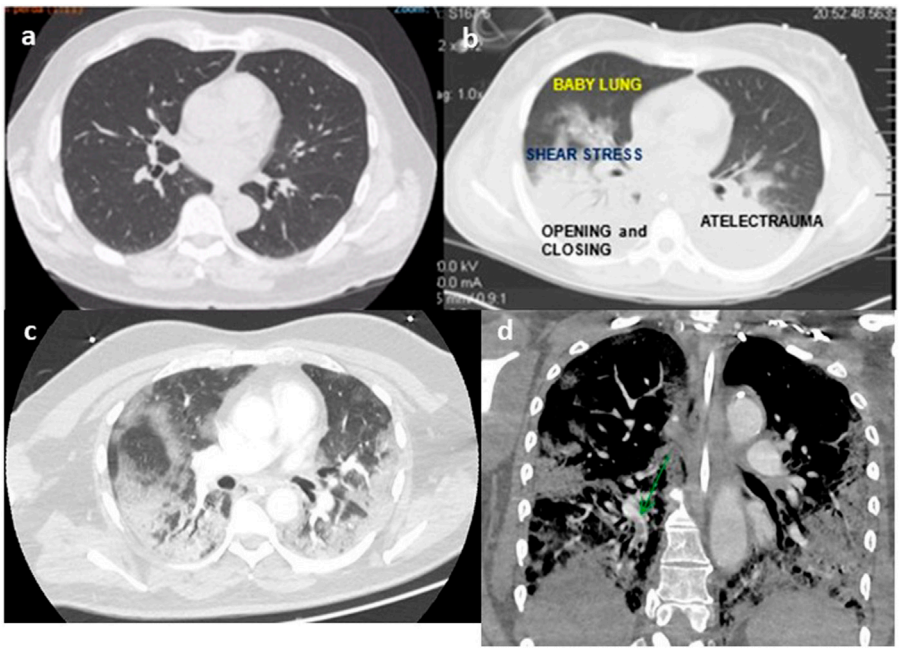

FIGURE 1 | Thoracic tomography of a normal person **(A)**, person with ARDS **(B)**, person with COVID-19 **(C)**, and angio-tomography with pulmonary embolism **(D)** (authors own material from reference 14,17 and 45).

quantification of the amount and regional lung distribution of the non-aerated, poorly-aerated, aerated, and hyperinflated lung tissue (Pesenti et al., 2016). Moreover, thoracic-computed tomography can help to differentiate ARDS from cardiogenic pulmonary edema, alveolar hemorrhage, and acute interstitial pneumonia (Barbas et al., 2003).

In 2003, Pelosi et al. (2003) reviewed pulmonary (caused by pneumonia, aspiration) and extra-pulmonary (caused by sepsis, pancreatitis) ARDS, they reported that a prevalent alveolar consolidation characterized the radiological presentation of pulmonary ARDS while the extra-pulmonary ARDS was characterized by ground-glass opacities. They also reported that in pulmonary ARDS the lung compliance was decreased, while in extra-pulmonary ARDS the chest wall and intra-abdominal chest compliance were decreased. They also showed that the effects of positive end-expiratory pressure (PEEP), recruitment maneuvers, and prone position were greater in extra-pulmonary ARDS (Pelosi et al., 1994).

So, this mini-review aims to discuss crucial articles that helped to better understand the role of thoracic-computed tomography to improve the diagnosis of the syndrome ARDS and COVID-19 lungs, to better understand its pathophysiology and the distribution of pulmonary edema according to the gravity force in different positions of the patients in the ICU bed and the ARDS lungs heterogeneity that could induce and perpetuate ventilator lung injury during inadequate positive pressure ventilation. This mini-review also discusses the role of thoracic tomography in detecting complications, prognosticating ARDS, and the part of dual-energy angio-tomography in COVID-19 patients.

QUANTITATIVE THORACIC-COMPUTED TOMOGRAPHY ANALYSIS IN ARDS

A pathophysiological hallmark of ARDS is the increased permeability of the alveolo-capillary membrane, leading to interstitial and alveolar flooding with edema rich in proteins and consequent collapse of the bottom areas of the lungs (Pesenti et al., 2016), shunt, and hypoxemia. In studying thoracic tomography of ARDS patients, the Gattinoni' s group showed a greater vertical gradient of regional lung inflation in ARDS patients than normal patients (Cressoni et al., 2014). ARDS lungs compared to normal lungs are characterized by non-aerated lungs in the lowermost lung regions, compressive atelectasis, and progressively more aerated lung tissues from the lower to upper lung levels characterizing the ARDS heterogenous lungs (Cressoni et al., 2014), with areas of possible high shear stress and possible ventilator-induced lung injury during positive pressure ventilation.

The Gattinoni's group reported the effects of PEEP on regional distribution of tidal volume and recruitment, while increasing PEEP from 0 to 20 cm H20, they observed that tidal volume distribution decreased significantly in the upper lungs regions, did not change in the middle levels, and increased significantly in the lower lungs regions. Studying ARDS patient's lung recruitability and CT scan-derived PEEP, they observed that to overcome ARDS lungs compressive forces and to lift up the thoracic cage, a similar amount of PEEP was required in higher and lower recruiters (16.8 ± 4 vs. 16.6 ± 5.6 cm H20, $p = 1$) (Gattinoni et al., 1995). The Gattinoni's group also reported the analysis of 68 patients who underwent whole-lung CT during breathing–holding sessions at airway pressures of 5, 15, and 45 cm H20, showing that the lung

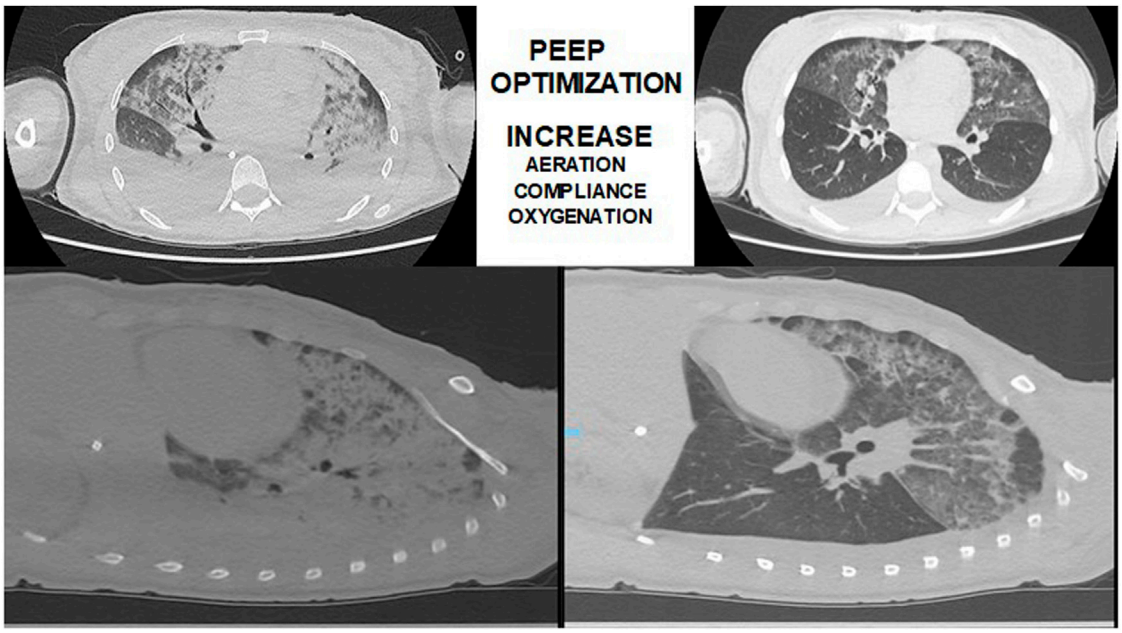

FIGURE 2 | Thoracic-computed tomography guided recruitment and PEEP titration in a patient with ARDS (authors own material from reference 14).

recruitability is heterogeneous and associated with the response to PEEP (Gattinoni et al., 2006).

Studies from Borges et al. (2006) and de Matos et al. (2012) reported that most of the collapsed lung tissue observed in early ARDS could be reversed using an image-monitored recruitment maneuver. After the lungs were opened up, a decremental PEEP titration maneuver guided by thoracic tomography was made to guarantee the lungs open, with less than 5% of collapsed lungs tissue. De Matos reported a case series of 51 ARDS patients, in which PEEP titration was guided by CT scan suggesting that it could be a good option to adjust PEEP and positive pressure ventilation in difficult and complex cases of ARDS (de Matos et al., 2012) (**Figure 2**). The ART, prospective, controlled, and clinical trial in ARDS patients (Cavalcanti et al., 2017) reported that unmonitored recruitment maneuvers with PEEP titration to the best compliance (titrated by respiratory mechanics and not guided by thoracic tomography) resulted in increased mortality compared to the control group. Therefore, it is not recommended carrying out lung recruitment maneuvers in invasively ventilated ARDS patients without respiratory image monitoring in ARDS patients.

By studying thoracic tomography of ARDS patients in the prone position (Langer et al., 1988; Gattinoni et al., 2013a; Gattinoni et al., 2013b), it has been shown that in the prone position, computed thoracic tomography scan densities redistribute from the dorsal to ventral regions of the lungs as the dorsal region tends to reexpand preventing the ventral zone to hyperinflate. Recently, Guérin et al. (2013) studied early ARDS patients with PaO2/FIO2 less than 150, with PEEP > than 5 cm H20 comparing mechanical ventilation in the prone position (periods of 16 h) vs. the supine position showed a significant improvement in survival rates in the patients submitted to the prone position.

The quantitative thoracic-computed tomography in ARDS patients improved the knowledge of pathophysiology of ARDS, showing a vertical gradient from the most gravity-dependent parts of the lung to the independent parts of the lungs, and the studies of different tidal volumes, PEEPs, recruitment maneuvers, and the influence of the prone position helped to guide clinical studies testing different approaches of invasive mechanical ventilation in the evolution and prognosis of ARDS patients (Amato et al., 1998; Barbas et al., 2012; Barbas and Nemer, 2018; Barbas et al., 2019; Pelosi et al., 2021).

THORACIC-COMPUTED TOMOGRAPHY TO DETECT COMPLICATIONS OF ARDS AND POSSIBLE COMPLICATIONS RELATED TO RADIATION EXPOSURE

Simon et al. (2016), analyzing 204 thoracic-computed tomography of ARDS patients that full filled the Berlin definition criteria reported that the most common alterations of the lungs parenchyma were consolidations (94.1% of cases) and ground-glass opacities (85.3%). They also observed pleural effusions, mediastinal lymphadenopathy, signs of right ventricular strain and pulmonary hypertension, pericardial effusion, emphysema of the chest wall, pneumothorax, emphysema of the mediastinum, and pulmonary embolism, resulting in the change of ARDS patients' management about 26.5% of cases. Chest CT allows the localization of invasive chest devices. Patients with more than 80% of involvement of the lung parenchyma had a significant increase in mortality ($p < 0.004$. Intrahospital transport was associated with critical incidents in 8.3% of cases (Simon et al., 2016).

Regarding the risks of radiation exposure, Chiumello et al. (2014) showed that a 70% reduction in the effective dose of radiation can be

achieved in patients with ARDS during the acquisition of low-dose chest CT images, maintaining lung quantitative and anatomical results. The use of low-dose chest CT could reduce the risks associated with radiation exposure, and therefore potentially allow a more frequent application of CT to characterize the lungs and optimize mechanical ventilation in patients with ARDS.

THORACIC-COMPUTED TOMOGRAPHY ANALYSIS IN COVID-19 PATIENTS

Thoracic-computed tomography is the most sensitive imaging technique for the diagnosis of COVID-19 lung involvement (Chung et al., 2020; Shi et al., 2020), showing diffuse infiltrates, especially in lungs periphery, ranging from ground-glass opacities to parenchymal consolidations. Multiple radiological patterns were observed at different times throughout the course of the disease. Lanza et al. (2020) analyzed 222 patients with RT-PCR positive for SARS-COV 2 virus who received a thoracic-computed tomography at admission because of dyspnea or desaturation. Compromised lung volume was the most accurate outcome predictor (logistic regression, $p < 0.001$). Tomographic lung volume loss in the range of 6–23% increased the risk for oxygenation support and ranges above 23% increased the risk for patient intubation. Compromised lung volume % showed a negative correlation with PaO2/FiO2 ratio ($p < 0.001$) and was a risk factor for inhospital mortality ($p < 0.001$).

The Fleischner Society published a consensus statement on the use of chest radiography and computed tomography during the COVID-19 pandemic to guide physicians in the use of chest imaging in the management of COVID-19 (Kwee and Kwee, 2020; Rubin et al., 2020). The statement noted that uncertainty still exists whether thoracic tomography should be used as a stand-alone screening tool, or as an adjunct tool to RT-PCR tests, to exclude occult infection before immunosuppression or surgery in regions with high prevalence of COVID-19 (Kwee and Kwee, 2020; Rubin et al., 2020).

The statement indicated thoracic tomography for patients with moderate to severe respiratory symptoms to demonstrate features of SARS-COV 2 infection or alternative diagnosis (Rubin et al., 2020). The statement also suggested guidance in reporting thoracic tomography findings are potentially attributable to COVID-19 pneumonia (Rubin et al., 2020) 1. typical appearance, 2. indeterminate appearance, 3. atypical appearance, and 4. negative for pneumonia. For a proper COVID-19 pneumonia diagnosis it is decisive to associate thoracic tomography findings with RT-PCR results, clinical manifestations, and epidemiological data (Kwee and Kwee, 2020).

A total of 1,431 symptomatic and at a high risk for COVID-19 patients, reported in a meta-analysis, revealed a thoracic CT-pooled sensitivity of 94.6% (95% CI: 91.9% and 96.4%) and a pooled specificity of 46.0% (95% CI: 31.9% and 60.7%) in the detection of COVID-19 (Adams et al., 2020). Another meta-analysis showed that 10.6% of symptomatic patients with positive RT-PCR for SARS-COV-2 infection had normal thoracic tomography (Raptis et al., 2020).

Patients with COVID-19 and respiratory failure have an increased rate of 11.8% of pulmonary embolism. COVID-19 patients diagnosed with thrombo-embolic complications have a more than 5-fold increase in mortality (Berger et al., 2020; Zhang et al., 2020). In COVID-19 patients with hypoxemia and relatively poor lung parenchymal alterations in thoracic tomography, high D-dimer, low (Sakr et al., 2020) plasmatic fibrinogen, signs of pulmonary hypertension, or signs of venous thrombosis (lower legs or intravenous devices) should be investigated with angio-thoracic tomography or dual-energy CT scan to the possible diagnosis of pulmonary embolism (McFadyen et al., 2020; Yu et al., 2020; Zhou et al., 2020).

DUAL-ENERGY CT SCAN IN COVID-19

Dual-energy tomography, also known as spectral CT or dual source CT, is a computed tomography technique that uses two separate x-ray photon energy spectra, allowing the interrogation of materials that have different attenuation properties at different energies, being used to reconstruct numerous images type, including iodine maps of lungs perfusion. A dual-energy CT scan has been recently studied to investigate ventilation–perfusion relationships in COVID-19 patients. Ball et al. (2021) analyzed pulmonary gas and blood distribution using a technique for quantitative analysis of dual-energy computed tomography in 35 COVID-patients needing non-invasive or invasive mechanical ventilation. Lung aeration loss (percentage of normally aerated lung tissue) and the extent of gas/blood volume mismatch (percentage of non-aerated, perfused lung tissue—shunt; aerated, non-perfused dead space; and non-aerated/non-perfused regions) were evaluated. Compared to patients requiring non-invasive ventilation, patients requiring invasive ventilation had both a lower percentage of normally aerated lung tissue [median (interquartile range) 33% (24–49%) vs. 63% (44–68%), $p < 0.001$]; and a larger extent of gas/blood volume mismatch [43% (30–49%) vs. 25% (14–28%), $p = 0.001$], due to higher shunt [23% (15–32%) vs. 5% (2–16%), $p = 0.001$] and non-aerated/non-perfused regions [5% (3–10%) vs. 1% (0–2%), $p = 0.001$]. The PaO2/FiO2 ratio correlated positively with normally aerated tissue ($\rho = 0.730$, $p < 0.001$). In patients with severe COVID-19 pneumonia, the need for invasive mechanical ventilation and the degree of hypoxemia were associated with loss of lungs aeration and the extent of gas/blood volume mismatch.

Aydin et al. (2021) studied 40 patients with positive RT-PCR to SARS-COV-2 with dual-energy thoracic tomography. All the patients had perfusion deficits at dual-CT images. Their mean perfusion deficit severity score was 8.45 ± 4.66 (min.-max, 1–19). In 24 of the 40 patients (60%), perfusion deficits and parenchymal lesions matched completely. In 15 of the 40 patients (37.5%), there was a partial match. The perfusion deficit severity score had a significantly positive correlation with D-dimer, reactive-C-protein levels, and thoracic tomography severity score (a score that is used in ARDS patients to assess severity and prognostication of patients) (Abbasi et al., 2020). The authors observed that perfusion deficits are seen not only in opacification areas but also in parenchyma of normal appearance.

Grillet et al. (2020) studied 85 patients with COVID-19 with dual-energy angio-tomography with iodine contrast and

pulmonary iodine map. They observed that twenty-nine patients (34%) were diagnosed with pulmonary artery thrombosis, mainly segmental (83%). Semi-quantitative analysis revealed parenchymal ischemia in 68% of the 85 patients with no significant difference between the patients with or without pulmonary artery thrombosis (23 vs. 35, $p = 0.144$). Volume of ischemia was greater in patients with pulmonary artery thrombosis [29 (IQR, 8–100) vs. 8 (IQR, 0–45) cm^3, $p = 0.041$]. Pulmonary perfusion evaluated by iodine maps shows extreme heterogeneity in COVID-19 patients and lower iodine levels in normal parenchyma. Pulmonary dual-energy angio-tomography revealed a significant number of pulmonary ischemic areas even in the absence of visible pulmonary arterial thrombosis, which may reflect micro-thrombosis associated with COVID-19 pneumonia.

Dual-energy angio-tomography studies in COVID-19 patients helped to understand the macro- and microvasculature involvement of the lungs in this disease. This vascular micro-thrombosis leads to severe alterations in the ventilation/perfusion ratio of the lungs and to high percentages of patients with hypoxemia and challenging to ventilate lungs (Abbasi et al., 2020; Grillet et al., 2020; Aydin et al., 2021; Ball et al., 2021).

ALTERNATIVE DIAGNOSIS TO COVID-19 AND COMPLICATIONS REVEALED BY THORACIC-COMPUTED TOMOGRAPHY

The finding of peripheral, bilateral, ground-glass opacities, predominantly in the lower lobes of the lungs is the typical finding of COVID-19 pneumonia, but can be the presentation features of other types of viral pneumonia, especially influenza (Yin et al., 2020). In the cases of typical findings of COVID pneumonia in the thoracic CT, but a negative RT-PCR for SARS-COV 2, a second RT-PCR for SARS-COV-2 must be made, and if negative, a molecular panel for respiratory virus must be asked for a correct diagnosis. Other alternative diagnosis includes: acute interstitial pneumonias, drug-induced lung diseases, alveolar hemorrhage, and ANCA-associated vasculitis.

In the cases of confirmed COVID-19 pneumonia, thoracic CT and angio-tomography is very helpful in diagnosing complications such as pulmonary embolism, acute respiratory distress syndrome, superimposed pneumonia, barotrauma (pneumomediastinum, pneumothorax, subcutaneous emphysema, pleural effusion, and pericardial effusions), organizing pneumonia, COVID-19 progression lung disease, secondary fungal infections, signs of pulmonary fibrosis, and mechanical ventilation-induced lung injury (barotrauma, lung cavitation, and cysts) (Kwee and Kwee, 2020).

COVID-19-associated pulmonary aspergillosis is reported in around 3. 3% of COVID-19 patients, with severe ARDS-receiving corticosteroids or tocilizumab (Machado et al., 2021). Diagnosis is established after a median of 15 days of invasive mechanical ventilation with bronchoalveolar lavage positive galactomannan or aspergillus positive culture. Thoracic tomography findings are compatible with pulmonary aspergilloma or invasive pulmonary aspergillosis (Machado et al., 2021).

SEVERITY CT SCORE AND PROGNOSTICATION OF COVID-19 PATIENTS

Abbasi et al. (Yin et al., 2020) retrospectively studied 262 hospitalized COVID-19 patients with a severity score that divided the lungs into three zones: upper, middle, and lower zones analyzing the degree of lung involvement for each zone: score of 0 (no involvement); 1. <25% involvement; 2. 25% to less than 50% involvement; 3. 50% to less than 75% involvement; and 4. ≥75% involvement. They observed a significant correlation between the CT severity score and rapidity of decline under the clinical condition of time to death, time to ICU admission, and time to intubation. Multivariate regression analysis showed increasing odds of inhospital death associated with a higher CT severity score at admission.

Popadic et al. (2021) studied 160 consecutive critically ill patients with the diagnosis of COVID-19 with moderate to severe ARDS observed in a multivariate analysis that the factors independently associated with mortality were IL-6, serum albumin, D-dimer, and thoracic-computed tomography score at admission.

Recently, Szabó et al. (2021) used artificial intelligence-based thoracic-computed tomography alterations quantification in patients with COVID-19 analyzed five lung regions upper right, middle right, lower right, upper left, and lower left lobes regarding lung volume and % of affected lung. They built a severity score that was calculated by a deep learning model based on the quantitative measurements. They observed that the artificial intelligence severity score was significantly associated with worse clinical outcomes. They concluded that their results provided personalized probabilities of adverse inhospital outcomes that might assist decision making in patients with COVID-19 lungs involvement that was not prospectively validated yet (Corrêa et al., 2021).

CONCLUSION

In conclusion, thoracic tomography of the lungs in ARDS or COVID-19 patients can help to a better diagnosis of pulmonary involvement, classify its severity and make alternative diagnoses and detect possible complications. Thoracic-computed tomography can also help the intensivists adjust PEEP, tidal volume, and patient position during mechanical ventilation and follow-up of the ARDS patients during their hospital stay. Whether severity scores based on thoracic-computed tomography and artificial intelligence may help the clinical prognosis of patients with COVID-19 and ARDS remains to be determined.

AUTHOR CONTRIBUTIONS

CB revised the literature about thoracic-computed tomography to access ARDS and COVID-19 lungs and wrote the manuscript.

REFERENCES

Abbasi, B., Akhavan, R., Ghamari Khameneh, A., Zandi, B., Farrokh, D., Pezeshki Rad, M., et al. (2020). Evaluation of the Relationship between Inpatient COVID-19 Mortality and Chest CT Severity Score. *Am. J. Emerg. Med.* S0735-6757 (20), 30851–30852. doi:10.1016/j.ajem.2020.09.056

Adams, H. J. A., Kwee, T. C., Yakar, D., Hope, M. D., and Kwee, R. M. (2020). Systematic Review and Meta-Analysis on the Value of Chest CT in the Diagnosis of Coronavirus Disease (COVID-19): Sol Scientiae, Illustra Nos. *Am. J. Roentgenology* 215, 1342–1350. doi:10.2214/AJR.20.23391

Amato, M. B. P., Barbas, C. S. V., Medeiros, D. M., Magaldi, R. B., Schettino, G. P., Lorenzi-Filho, G., et al. (1998). Effect of a Protective-Ventilation Strategy on Mortality in the Acute Respiratory Distress Syndrome. *N. Engl. J. Med.* 338 (6), 347–354. doi:10.1056/nejm199802053380602

Aydin, S., Kantarci, M., Karavas, E., Unver, E., Yalcin, S., and Aydin, F. (2021). Lung Perfusion Changes in COVID-19 Pneumonia: a Dual Energy Computerized Tomography Study. *Bjr* 94 (1125), 20201380. doi:10.1259/bjr.20201380

Ball, L., Robba, C., Herrmann, J., Gerard, S., Xin, Y., Mandelli, M., et al. (2021). Lung Distribution of Gas and Blood Volume in Critically Ill COVID-19 Patients: a Quantitative Dual-Energy Computed Tomography Study. *Crit. Care* 25, 214. doi:10.1186/s13054-021-03610-9

Barbas, C. S., Matos, G. F., Amato, M. B., and Carvalho, C. R. (2012). Goal-oriented Respiratory Management for Critically Ill Patients with Acute Respiratory Distress Syndrome. *Crit. Care Res. Pract.* 2012, 952168. doi:10.1155/2012/952168

Barbas, C. S. V., Hoelz, C., and Capellozzi, V. L. (2003). Anesthesia, Pain, Intensive Care and Emergency Medicine. *Gullo* 117, 477–482. doi:10.1007/978-88-470-2215-7

Barbas, C. S. V., and de Matos, G. F. J. (2019). "Recruitment Manoeuvres," in *ERS Practical Handbook. Invasive Mechanical Ventilation*. Editors L. Heunks and M. J. Schultz. Sheffield: European Respiratory Society, 185–194. doi:10.1183/9781849841221.030118

Barbas, C. S. V., Ísola, A. M., and Caser, E. B. (2014). What Is the Future of Acute Respiratory Distress Syndrome after the Berlin Definition? *Curr. Opin. Crit. Care* 20 (1), 10–16. doi:10.1097/mcc.0000000000000058

Barbas, C. S. V., and Nemer, S. N. (2018). Lung Recruitment and Positive End-Expiratory Pressure Titration in Patients with Acute Respiratory Distress Syndrome. *JAMA* 319 (9), 933. doi:10.1001/jama.2017.21840

Berger, J. S., Kunichoff, D., Adhikari, S., Ahuja, T., Amoroso, N., Aphinyanaphongs, Y., et al. (2020). Prevalence and Outcomes of D-Dimer Elevation in Hospitalized Patients with COVID-19. *Atvb* 40 (10), 2539–2547. doi:10.1161/atvbaha.120.314872

Bombino, M., Gattinoni, L., Pesenti, A., Pistolesi, M., and Miniati, M. (1991). The Value of Portable Chest Roentgenography in Adult Respiratory Distress Syndrome. *Chest* 100 (3), 762–769. doi:10.1378/chest.100.3.762

Borges, J. B., Okamoto, V. N., Matos, G. F. J., Caramez, M. P. R., Arantes, P. R., Barros, F., et al. (2006). Reversibility of Lung Collapse and Hypoxemia in Early Acute Respiratory Distress Syndrome. *Am. J. Respir. Crit. Care Med.* 174 (3), 268–278. doi:10.1164/rccm.200506-976oc

Caser, E. B., Zandonade, E., Pereira, E., Gama, A. M. C., and Barbas, C. S. V. (2014). Impact of Distinct Definitions of Acute Lung Injury on its Incidence and Outcomes in Brazilian ICUs. *Crit. Care Med.* 42 (3), 574–582. doi:10.1097/01.ccm.0000435676.68435.56

Cavalcanti, A. B., Cavalcanti, A. B., Suzumura, É. A., Laranjeira, L. N., Paisani, D. M., Damiani, L. P., et al.Writing Group for the Alveolar Recruitment for Acute Respiratory Distress Syndrome Trial (ART) Investigators (2017). Effect of Lung Recruitment and Titrated Positive End-Expiratory Pressure (PEEP) vs Low PEEP on Mortality in Patients with Acute Respiratory Distress Syndrome: A Randomized Clinical Trial. *JAMA* 318 (14), 1335–1345. doi:10.1001/jama.2017.14171

Chiumello, D., Langer, T., Vecchi, V., Luoni, S., Colombo, A., Brioni, M., et al. (2014). Low-dose Chest Computed Tomography for Quantitative and Visual Anatomical Analysis in Patients with Acute Respiratory Distress Syndrome. *Intensive Care Med.* 40, 691–699. doi:10.1007/s00134-014-3264-1

Chung, M., Bernheim, A., Mei, X., Zhang, N., Huang, M., Zeng, X., et al. (2020). CT Imaging Features of 2019 Novel Coronavirus (2019-nCoV). *Radiology* 295, 202–207. doi:10.1148/radiol.2020200230

Corrêa, T. D., Midega, T. D., Timenetsky, K. T., Cordioli, R. L., Barbas, C. S., Silva Júnior, M., et al. (2021). Clinical Characteristics and Outcomes of COVID-19 Patients Admitted to the Intensive Care Unit during the First Year of the Pandemic in Brazil: a Single center Retrospective Cohort Study. *Einstein (São Paulo).* 19, eAO6739. doi:10.31744/einstein_journal/2021AO6739

Cressoni, M., Chiumello, D., Carlesso, E., Chiurazzi, C., Amini, M., Brioni, M., et al. (2014). Compressive Forces and Computed Tomography-Derived Positive End-Expiratory Pressure in Acute Respiratory Distress Syndrome. *Anesthesiology*.121 (3), 572–581. doi:10.1097/aln.0000000000000373

de Matos, G. F., Stanzani, F., Passos, R. H., Fontana, M. F., Albaladejo, R., Caserta, R. E., et al. (2012). How Large Is the Lung Recruitability in Early Acute Respiratory Distress Syndrome: a Prospective Case Series of Patients Monitored by Computed Tomography. *Crit. Care* 16, R4. doi:10.1186/cc10602

Gattinoni, L., Pelosi, P., Crotti, S., and Valenza, F. (1995). Effects of Positive End-Expiratory Pressure on Regional Distribution of Tidal Volume and Recruitment in Adult Respiratory Distress Syndrome. *Am. J. Respir. Crit. Care Med.* 151 (6), 1807–1814. doi:10.1164/ajrccm.151.6.7767524

Gattinoni, L., Pesenti, A., and Carlesso, E. (2013). Body Position Changes Redistribute Lung Computed-Tomographic Density in Patients with Acute Respiratory Failure: Impact and Clinical Fallout through the Following 20 Years. *Intensive Care Med.* 39 (11), 1909–1915. doi:10.1007/s00134-013-3066-x

Gattinoni, L., Taccone, P., Carlesso, E., and Marini, J. J. (2013). Prone Position in Acute Respiratory Distress Syndrome. Rationale, Indications, and Limits. *Am. J. Respir. Crit. Care Med.* 188 (11), 1286–1293. doi:10.1164/rccm.201308-1532ci

Gattinoni, L., Caironi, P., Cressoni, M., Chiumello, D., Ranieri, V. M., Quintel, M., et al. (2006). Lung Recruitment in Patients with the Acute Respiratory Distress Syndrome. *N. Engl. J. Med.* 354, 1775–1786. doi:10.1056/NEJMoa052052

Grillet, F., Busse-Coté, A., Calame, P., Behr, J., Delabrousse, E., and Aubry, S. (2020). COVID-19 Pneumonia: Microvascular Disease Revealed on Pulmonary Dual-Energy Computed Tomography Angiography. *Quant Imaging Med. Surg.* 10 (9), 1852–1862. doi:10.21037/qims-20-708

Guérin, C., Reignier, J., Richard, J. C., Beuret, P., Gacouin, A., Boulain, T., et al.PROSEVA Study Group (2013). Prone Positioning in Severe Acute Respiratory Distress Syndrome. *N. Engl. J. Med.* 368 (23), 2159–2168. doi:10.1056/NEJMoa1214103

Kwee, T. C., and Kwee, R. M. (2020). Chest CT in COVID-19: What the Radiologist Needs to Know. *Radiographics* 40 (7), 1848–1865. doi:10.1148/rg.2020200159

Langer, M., Mascheroni, D., Marcolin, R., and Gattinoni, L. (1988). The Prone Position in ARDS Patients. *Chest* 94 (1), 103–107. doi:10.1378/chest.94.1.103

Lanza, E., Muglia, R., Bolengo, I., Santonocito, O. G., Lisi, C., Angelotti, G., et al. (2020). Quantitative Chest CT Analysis in COVID-19 to Predict the Need for Oxygenation Support and Intubation. *Eur. Radiol.* 30 (12), 6770–6778. doi:10.1007/s00330-020-07013-2

Machado, M., Valerio, M., Álvarez-Uría, A., Olmedo, M., Veintimilla, C., Padilla, B., et al.COVID-19 Study Group (2021). Invasive Pulmonary Aspergillosis in the COVID-19 Era: An Expected New Entity. *Mycoses* 64 (2), 132–143. doi:10.1111/myc.13213

McFadyen, J. D., Stevens, H., and Peter, K. (2020). The Emerging Threat of (Micro) Thrombosis in COVID-19 and its Therapeutic Implications. *Circ. Res.* 127 (4), 571–587. doi:10.1161/circresaha.120.317447

Pelosi, P., Ball, L., Barbas, C. S. V., Bellomo, R., Burns, K. E. A., Einav, S., et al. (2021). Personalized Mechanical Ventilation in Acute Respiratory Distress Syndrome. *Crit. Care* 25 (1), 250. doi:10.1186/s13054-021-03686-3

Pelosi, P., D'Andrea, L., Vitale, G., Pesenti, A., and Gattinoni, L. (1994). Vertical Gradient of Regional Lung Inflation in Adult Respiratory Distress Syndrome. *Am. J. Respir. Crit. Care Med.* 149 (1), 8–13. doi:10.1164/ajrccm.149.1.8111603

Pelosi, P., D'Onofrio, D., Chiumello, D., Paolo, S., Chiara, G., Capelozzi, V. L., et al. (2003). Pulmonary and Extrapulmonary Acute Respiratory Distress Syndrome Are Different. *Eur. Respir. J.* 22:48s–56s. doi:10.1183/09031936.03.00420803

Pesenti, A., Musch, G., Lichtenstein, D., Mojoli, F., Amato, M. B. P., Cinnella, G., et al. (2016). Imaging in Acute Respiratory Distress Syndrome. *Intensive Care Med.* 42, 686–698. doi:10.1007/s00134-016-4328-1

Popadic, V., Klasnja, S., Milic, N., Rajovic, N., Aleksic, A., Milenkovic, M., et al. (2021). Predictors of Mortality in Critically Ill COVID-19 Patients Demanding High Oxygen Flow: A Thin Line between Inflammation, Cytokine Storm, and Coagulopathy. *Oxid Med. Cel Longev* 2021, 6648199. doi:10.1155/2021/6648199

Ranieri, V. M., Ranieri, V. M., Rubenfeld, G. D., Thompson, B. T., Ferguson, N. D., Caldwell, E., et al.ARDS Definition Task Force (2012). Acute Respiratory Distress

Syndrome: the Berlin Definition. *JAMA* 307 (23), 2526–2533. doi:10.1001/jama.2012.5669

Raptis, C. A., Hammer, M. M., Short, R. G., Shah, A., Bhalla, S., Bierhals, A. J., et al. (2020). Chest CT and Coronavirus Disease (COVID-19): a Critical Review of the Literature to Date. *Am. J. Roentgenology* 215, 839–842. doi:10.2214/AJR.20.23202

Rubin, G. D., Ryerson, C. J., Haramati, L. B., Sverzellati, N., Kanne, J. P., Raoof, S., et al. (2020). The Role of Chest Imaging in Patient Management during the COVID-19 Pandemic. *Chest* 158 (1), 106–116. doi:10.1016/j.chest.2020.04.003

Sakr, Y., Giovini, M., Leone, M., Pizzilli, G., Kortgen, A., Bauer, M., et al. (2020). Pulmonary Embolism in Patients with Coronavirus Disease-2019 (COVID-19) Pneumonia: a Narrative Review. *Ann. Intensive Care* 10 (1), 124. doi:10.1186/s13613-020-00741-0

Shi, H., Han, X., Jiang, N., Cao, Y., Alwalid, O., Gu, J., et al. (2020). Radiological Findings from 81 Patients with COVID-19 Pneumonia in Wuhan, China: a Descriptive Study. *Lancet Infect. Dis.* 20, 425–434. doi:10.1016/s1473-3099(20)30086-4

Simon, M., Braune, S., Laqmani, A., Metschke, M., Berliner, C., Kalsow, M., et al. (2016). Value of Computed Tomography of the Chest in Subjects with ARDS: A Retrospective Observational Study. *Respir. Care.* 61 (3), 316–323. doi:10.4187/respcare.04308

Szabó, I. V., Simon, J., Nardocci, C., Kardos, A. S., Nagy, N., Abdelrahman, R. H., et al. (2021). The Predictive Role of Artificial Intelligence-Based Chest CT Quantification in Patients with COVID-19 Pneumonia. *Tomography* 7 (4), 697–710. doi:10.3390/tomography7040058

Yin, Z., Kang, Z., Yang, D., Ding, S., Luo, H., and Xiao, E. (2020). A Comparison of Clinical and Chest CT Findings in Patients with Influenza A (H1N1) Virus Infection and Coronavirus Disease (COVID-19). *Am. J. Roentgenology* 215, 1065–1071. doi:10.2214/AJR.20.23214

Yu, Y., Tu, J., Lei, B., Shu, H., Zou, X., Li, R., et al. (2020). Incidence and Risk Factors of Deep Vein Thrombosis in Hospitalized COVID-19 Patients. *Clin. Appl. Thromb. Hemost.* 26, 107602962095321. doi:10.1177/1076029620953217

Zhang, L., Yan, X., Fan, Q., Liu, H., Liu, X., Liu, Z., et al. (2020). D-dimer Levels on Admission to Predict In-hospital Mortality in Patients with Covid-19. *J. Thromb. Haemost.* 18 (6), 1324–1329. doi:10.1111/jth.14859

Zhou, F., Yu, T., Du, R., Fan, G., Liu, Y., Liu, Z., et al. (2020). Clinical Course and Risk Factors for Mortality of Adult Inpatients with COVID-19 in Wuhan, China: a Retrospective Cohort Study. *The Lancet* 395, 1054–1062. doi:10.1016/s0140-6736(20)30566-3

Conflict of Interest: The author declares that the research was conducted in the absence of any commercial or financial relationships that could be construed as a potential conflict of interest.

Publisher's Note: All claims expressed in this article are solely those of the authors and do not necessarily represent those of their affiliated organizations, or those of the publisher, the editors, and the reviewers. Any product that may be evaluated in this article, or claim that may be made by its manufacturer, is not guaranteed or endorsed by the publisher.

frontiers | Frontiers in Physiology

REVIEW
published: 10 May 2022
doi: 10.3389/fphys.2022.871893

Administration of Drugs/Gene Products to the Respiratory System: A Historical Perspective of the Use of Inert Liquids

Deepthi Alapati[1,2]* *and Thomas H. Shaffer*[1,2,3]*

[1]Nemours Children's Health, Wilmington, DE, United States, [2]Sidney Kimmel School of Medicine, Thomas Jefferson University, Philadelphia, PA, United States, [3]Lewis Katz School of Medicine, Temple University, Philadelphia, PA, United States

The present review is a historical perspective of methodology and applications using inert liquids for respiratory support and as a vehicle to deliver biological agents to the respiratory system. As such, the background of using oxygenated inert liquids (considered a drug when used in the lungs) opposed to an oxygen-nitrogen gas mixture for respiratory support is presented. The properties of these inert liquids and the mechanisms of gas exchange and lung function alterations using this technology are described. In addition, published preclinical and clinical trial results are discussed with respect to treatment modalities for respiratory diseases. Finally, this forward-looking review provides a comprehensive overview of potential methods for administration of drugs/gene products to the respiratory system and potential biomedical applications.

Keywords: drug delivery, gene delivery, partial liquid ventilation, perfluorochemicals, pulmonary

OPEN ACCESS

Edited by:
Andrew John Halayko,
University of Manitoba, Canada

Reviewed by:
Jesus Perez-Gil,
Complutense University of Madrid, Spain
Ian Michael Thornell,
The University of Iowa, United States

***Correspondence:**
Deepthi Alapati
deepthi.alapati@nemours.org
Thomas H. Shaffer
thomas.shaffer@nemours.org

Specialty section:
This article was submitted to Respiratory Physiology and Pathophysiology, a section of the journal Frontiers in Physiology

Received: *08 February 2022*
Accepted: *31 March 2022*
Published: *10 May 2022*

Citation:
Alapati D and Shaffer TH (2022) Administration of Drugs/Gene Products to the Respiratory System: A Historical Perspective of the Use of Inert Liquids. Front. Physiol. 13:871893. doi: 10.3389/fphys.2022.871893

INTRODUCTION

Aerosol drugs have been delivered to the lungs for several thousand years (Stein and Thiel, 2017). The use of aerosol delivery is complex, and deposition of drugs in the respiratory system is influenced by several specific factors: physics of the aerosol (inertia of the aerosol), gravitational factors, diffusion (airflow patterns in the lungs), and pulmonary defense mechanisms. Pulmonary drug delivery has been only partly explored in recent decades even though it could represent an alternative route of administration of drug-based therapies. Pulmonary drug delivery is an attractive route of administration of drugs, since the lungs are an ideal entry point for drugs to the bloodstream because of the large surface area, the very short diffusion distances in the alveolar spaces, and exposure to the entire cardiac output. Today there is an increased need for topical delivery of lung cancer therapy drugs, anti-inflammatory drugs to treat acute respiratory distress (i.e., COVID-19, H1N1 influenza), and gene-targeted lung agents for several relatively uncommon (orphan) diseases and pulmonary arterial hypertension (PAH) (Ali et al., 2015; Muralidharan et al., 2015; Alapati et al., 2019; Keshavarz et al., 2020; Kumar et al., 2020).

During the last 20 years, the combination of nanocrystal technology combined with an inert perfluorochemical vehicle has demonstrated the efficacy of large volume drug delivery to the entire lung because of the vehicle physical-chemical properties (inert properties, low surface tension, and high respiratory gas solubility) (Cullen et al., 1999). Furthermore, based on this combination delivery approach, it has been possible to demonstrate increased lung targeted drug delivery as opposed to systemic delivery. Nanocarriers have been found to be most promising because of their significant advantages (i.e., cell-specific targeted drug delivery and prolonged drug release). Thus, in

TABLE 1 | Physiochemical profile of various perfluorocarbons. Reprinted from Shaffer, T.H., and Wolfson, M.R. (2011). "Liquid Ventilation," in Fetal and Neonatal Physiology, 4th Edition, eds: R. Polin, W.W. Fox, and S. Abman (Philadelphia, PA: WB Saunders), 1063–1081, with permission from Elsevier.

Perfluorocarbon	Formula	Orientation	O_2 Solution (mL/ 100 ml) (25 °C)	Vapor Pressure (mm hg) (37 °C)	Boiling Point (°C)	Viscosity (cSt) (25 °C)	Mol wt (g/mol)	Density (g/ml) (25°C)
PP2	C_7F_{14}	Cyclic	57.2	180	76	0.88	350	1.788
PFOB	$C_8F_{17}Br$	Aliphatic	52.7	11	140.5	1	499	1.89
PCI	$C_7F_{15}Cl$	Aliphatic	52.7	48.5	108	0.82	404.5	1.77
P12F	$C_9F_{20}O$	Aliphatic	52.5	39	121	0.95	504.1	1.721
FC-75F	$C_8F_{16}O$	Cyclic	52.2	51	102	0.85	416.1	1.783
FC-75P	$C_8F_{16}O$	Cyclic	52.2	51	102	0.85	416.1	1.783
PFDMA	$C_{12}F_{18}$	Cyclic	39.4	2.6	177.5	4.35	524.1	2
FC47	$C_{12}F_{27}N$	Aliphatic	38.4	2.5	174	2.52	671.1	1.9
PP9	$C_{11}F_{20}$	Cyclic	38.4	5.2	160	3.32	512.1	1.972
APF-57	C_6F_{14}	Cyclic	70	356.4	57.3	—	338	1.58
APF-100	C_8F_{16}	Cyclic	42.1	64.6	98.6	1.11	400	1.84
APF-125	C_9F_{18}	Cyclic	47.7	30	116.6	1.17	450	1.86
APF-140	$C_{10}F_{18}$	Cyclic	49	13.6	142	2.9	462	1.93
APF-145	$C_{10}F_{20}$	Cyclic	45.3	8.9	142.8	1.44	500	1.9
APF-175	$C_{12}F_{22}$	Cyclic	35	1.4	180	3.5	562	1.98
APF-200	$C_{13}F_{24}$	Cyclic	41	1.26	200	5.3	612	1.99
APF-215	$C_{14}F_{26}$	Cyclic	37	0.2	215	8	662	2.02

combination with inert perfluorochemical vehicles, nanocarriers may provide effective delivery to the entire lung. The advantages offered by pulmonary drug delivery indicate that the challenges of such a delivery approach are worth addressing; if successfully addressed, there are great opportunities to treat unmet clinical needs. The present review focuses on providing a comprehensive historical perspective of the use of inert liquids for respiratory applications.

RESPIRATORY SUPPORT WITH INERT LIQUIDS

The use of liquids for respiratory support is reviewed in this section, as well as the physical properties of fluid used and the rationale for using specific liquids.

The first liquid used as a respiratory medium for lung lavage was saline (Winternitz and Smith, 1920). It debrides the lung and eliminates the gas-liquid interface within it. Early saline studies clarified factors influencing distensibility, alveolar structure, stability, pulmonary blood flow, and ventilation (Neergard, 1929; Mead et al., 1957; Avery and Mead, 1959; Leith and Mead, 1966; Hamosh and Luchsinger, 1968; Davidson et al., 1995; Fournier et al., 1995). Low respiratory gas solubility (O_2; CO_2) and diffusion gradients at atmospheric conditions limited the functional use of saline solution to provide adequate gas exchange (Kylstra et al., 1966; Kylstra, 1967; Kylstra et al., 1973; Wessler et al., 1977; Lynch et al., 1983). The hypothesis that O_2-saturated saline solution dissolved under pressure could possibly sustain submersed mammals was formulated (Stein and Sonnenschein, 1950), and subsequent research revealed that adequately oxygenated liquid could be breathed by and support mammals submerged in hyperbaric oxygenated saline solution (Goodlin, 1962; Kylstra et al., 1962; Pegg et al., 1963; Kylstra et al., 1966). However, CO_2 retention and profound acidosis occurred because of the small gradient between arterial and alveolar CO_2 gradients, thus eliminating saline ventilation for either normobaric or hyperbaric conditions. In addition, it should be noted that although saline has been used to lavage debris and inflammatory mediators from the lungs as noted above, it has also been shown to inactivate pulmonary surfactant and impair lung function (Shaffer and Wolfson, 2011).

Inert Perfluorochemical Liquid Physicochemical Properties

As an alternative to saline as a respiratory medium, the utility of other liquids (silicone, vegetable oils, and animal oils) was investigated as respiratory media; however, these oils, although having high gas solubility, also demonstrated toxic effects (Clark, 1970; Sargent and Seffl, 1970). Perfluorochemicals (PFCs) were initially produced as part of the Manhattan Project during World War II. In 1966, they were used to support normobaric respiration on the basis of their high solubility for respiratory gases (**Table 1**) (Clark and Gollan, 1966), which delineated their use as alternative respiratory mediums. True PFCs are formulated from common organic compounds (e.g., benzene) by substituting carbon-bound hydrogen atoms with fluorine atoms. They provide the advantage of easy storage (indefinitely at room temperature) and can be used under antiseptic conditions without modification (i.e., autoclave, small-pore filtering). They are clear, in most cases, not soluble in aqueous media or nonlipid biologic fluids and are odorless, inert, and transparent—very inoffensive in their use (Shaffer and Wolfson, 2011).

Please refer to **Table 1** (Shaffer and Wolfson, 2011) for details regarding the physicochemical profile and structure of various PFC liquids for PFC ventilation. O_2 and CO_2 are specific to respiratory gas exchange and carried only as dissolved gases with solubilities ranging as much as 16 and three times greater, respectively, in PFC than in saline. Oxygen solubilities range from 35 to 70 ml gas per deciliter at 25°C (Riess, 1992). The carrying capacity for CO_2 is known for only a few PFC compounds, but reported values of CO_2 solubility are approximately four times greater than those for O_2 (122–225 ml/dl [i.e., PFOB; perfluorooctylbromide [PFOB] = 225 ml/dl]). It is noteworthy that perflubron (PFOB; perfluorooctylbromide) is the only medical grade perfluorochemical approved by the FDA for emergency medical use. While many properties of PFC liquids vary, they do provide relatively low surface tension and viscosity, and are more dense than both water and soft tissue.

Variations in specific physicochemical properties of the PFC liquids are significant to their use as respiratory media and as vehicles for the administration of biological agents. Fluids of higher vapor pressure may volatilize from the lung more rapidly than liquids having lower vapor pressure. Fluids with greater spreading coefficients (dependent on surface tension) may distribute more easily in the lung than fluids whose spreading coefficients are lower (i.e., FC-75 > PFOB > APF-140) (Weers and Johnson, 1991; Sekins, 1995). Fluids of higher viscosity or kinematic viscosity may balk at redistribution in the lung, thus remaining in contact with a greater area of the alveolar surface for more time than those stratifying with increased rapidity (Miller et al., 1999; Miller et al., 2001) resulting in greater flow resistance.

NON-CLINICAL AND CLINICAL STUDIES WITH INERT LIQUIDS

The initial preclinical studies in liquid spontaneous breathing and ventilation support were directed at breathing in unusual environments such as deep sea diving, zero gravity, and space travel (Clark and Gollan, 1966; Modell et al., 1973; Moskowitz et al., 1975; Lynch et al., 1983). It was not until the studies with premature lambs (Shaffer et al., 1976; Shaffer et al., 1983a; Shaffer et al., 1983b; Shaffer et al., 1984b; Wolfson et al., 1988) that the application to respiratory distress became evident because of the advantages of low surface tension, improved lung compliance, and gas exchange. As a result of these investigations, the first in extremis FDA-approved total liquid ventilation study in a near-death premature infant with severe respiratory distress was performed (Greenspan et al., 1989). This study and a subsequent study in several critically ill infants (Greenspan et al., 1990) demonstrated that PFC liquid ventilation could support gas exchange and residual improvement in pulmonary function following the return to conventional gas ventilation. The need for a medically approved combination liquid ventilator and medical grade PFC breathing fluid restricted further clinical trials. It is noteworthy, however, that a corporate-sponsored multicenter trial resulted from the success of the neonatal and adult animal trials with PFC liquid-assisted gas ventilation and the initial clinical trials with human subjects.

Subsequently, several separate investigational new drug applications were approved by the FDA to investigate the safety and efficacy of PFCs, mainly PFOB, as a liquid breathing media in neonates. While animal studies over the years showed significant efficacy and safety of liquid breathing, clinical studies using several techniques in humans (infants, children, and adults) had mixed outcomes. The findings from non-clinical and clinical studies are summarized below.

Non-Clinical Studies With Inert Liquids

Over the course of the last 50 years, many animal studies demonstrated liquid ventilation to be an effective approach/treatment for deep sea diving, zero gravity, severe lung injury, and congenital diaphragmatic hernia (CDH). These studies supported the use of liquid ventilation as a superior source of respiratory support when compared with gas media with spontaneous breathing or conventional mechanical ventilation (CMV). Various studies also demonstrated short-term beneficial physiologic responses in lung function because of improved alveolar recruitment and significant preservation of normal histological structure of the lung (Moskowitz et al., 1975; Shaffer et al., 1983a; Shaffer et al., 1983b; Shaffer et al., 1984a; Shaffer et al., 1984b; Wolfson et al., 1992; Leach et al., 1993; Richman et al., 1993; Sekins et al., 1994; Major et al., 1995; Al-Rahmani et al., 2000; Cox et al., 2003). Non-clinical studies in newborn animal models of respiratory distress syndrome (RDS) showed that PFOB enhances uniformity of the lung inflation consistent with PFOB working as an artificial surfactant (Weis et al., 1997; Wolfson et al., 1998; Kandler et al., 2001; Hübler et al., 2002; Merz et al., 2002). Animal studies also showed that PFOB minimizes functional lung impairment because of the high airway pressures and sustained FiO_2 requirements that are characteristics of ventilator-induced lung injury (Greenspan et al., 1990; Wolfson et al., 1992; Bateman et al., 2001; Davies et al., 2002).

Recent studies continue to show PFOB improves oxygenation (Hartog et al., 1997; Bleyl et al., 1999; Al-Rahmani et al., 2000; Bateman et al., 2001; Davies et al., 2002) in animal models of lung injury consistent with earlier findings. Additionally, recent studies report that PFOB increases lung compliance (Bleyl et al., 1999; Al-Rahmani et al., 2000; Kandler et al., 2001; Davies et al., 2002). Findings from earlier studies indicated that PFOB may have potential anti-inflammatory properties. Animal studies showed that administration of PFOB decreased the expression of known inflammatory markers (Kawamae et al., 2000; Haeberle et al., 2002; Merz et al., 2002). Two additional research studies reported PFOB not interfering with cerebral blood flow (Davies et al., 2010; Davies et al., 2013), suggesting partial liquid ventilation (PLV) with PFOB will have limited impact on cardiac output and circulation.

Animal studies consistently support the safety of PFOB, as few negative effects have been reported. Studies show PFOB is not absorbed systemically and causes no long-term harm (Holaday et al., 1972; Shaffer et al., 1996; Cox et al., 2002). Several animal studies reported final concentrations of PFC measured within the

blood and tissue after the end of treatment were considered minimal compared with their baseline control measurements (Holaday et al., 1972; Modell et al., 1973; Shaffer et al., 1996; Cox et al., 2002). Additionally, studies revealed initiation of PLV and removal of PFOB does not produce significant adverse effects. Pneumothorax, a documented adverse event in adult PFOB clinical studies, was not reported with any significance in animal models of severe lung injury employing PFOB.

Clinical Studies in Infants With Inert Liquids

Early clinical studies demonstrated that infants with severe RDS, meconium aspiration, and CDH tolerated liquid PFC in their lungs and were able to effectively exchange gas and maintain cardiovascular stability (Greenspan et al., 1989; Greenspan et al., 1990; Gross et al., 1995; Pranikoff et al., 1996; Henrichsen et al., 2012).

Consistent with those studies and animal studies, additional published reports indicated PFOB increased gas exchange (Hirschl et al., 1995; Gauger et al., 1996; Hirschl et al., 1996; Hirschl et al., 2002) in adults and children. Subsequent studies using PFOB on preterm neonates also reported increases in lung compliance (Greenspan et al., 1990; Hirschl et al., 1995; Hirschl et al., 1996). PFOB rapidly improved lung function and increased survival in a population of neonates with high mortality (Leach et al., 1996).

Most importantly, the utility of PFOB was demonstrated in a multicenter study of premature infants with severe RDS refractory to other available treatments (surfactant therapy, high frequency, too young for extracorporeal membrane oxygenation) (Leach et al., 1996). Thirteen (13) infants were treated with PFOB. Within an hour following the instillation of PFOB, there was an increase in arterial oxygen tension of 138%. Dynamic compliance increased by 61% and continued to climb through the first 24 h (Leach et al., 1996). Furthermore, the mean oxygenation index, markedly elevated at baseline (49 ± 60), fell to 17 ± 16 within the first hour and continued to fall to 9 ± 7 at 24 h. Arterial carbon dioxide tension normalized within 4 h after PFOB treatment. Mean airway pressure decreased from 17 ± 3 to 12 ± 2 cm of water (29%) in the first 24 h despite an increase in tidal volume (5.0 ± 3.4 ml/kg during gas ventilation to 7.8 ± 3.4 ml/kg during PFOB ventilation). It should be noted that no serious adverse events were reported during PFOB-assisted ventilation. It was determined that PFOB-assisted ventilation could be utilized for critically ill infants for several days without serious adverse events. A number of the surviving participants are currently well and in their twenties.

More recently, lavage with PFC has been shown to be safe for treatment of persistent and difficult-to-treat lung atelectasis (Henrichsen et al., 2012). Bronchoalveolar lavage utilizing PFC liquid was performed without incident in infants with severe alveolar proteinosis during conventional mechanical ventilation without necessitating the additional support of extracorporeal membrane oxygenation. Furthermore, recent PFC liquid studies have reported safe imaging studies in bronchopulmonary patients (Degnan et al., 2019).

Follow-up imaging studies up to 20 years after treatment with PFOB in humans demonstrated no negative effects from this treatment (Tiruvoipati et al., 2007; Hagerty et al., 2008; Servaes and Epelman, 2009). The studies demonstrated evidence of residual PFC specs in the lung, thorax, mediastinum, and retroperitoneum. These are also cautionary when interpreting the high-density opacifications associated with Hounsfield unit densities of some PFCs used with intrapulmonary applications such as pulmonary calcification (Tiruvoipati et al., 2007) and stress the necessity of obtaining precise clinical histories in the light of unusual radiographic findings (Hagerty et al., 2008).

Clinical Studies in Adults With Inert Liquids

In early liquid ventilation studies, it was reported that PFOB usage in adults increased lung compliance (Hirschl et al., 1996), which is consistent with preclinical animal studies. However, a randomized clinical trial in adults with acute respiratory distress syndrome (ARDS) randomized to protective conventional mechanical ventilation of the lung, low-dose PFC, or high-dose PFC and partial liquid ventilation did not result in improved mortality. Additional ventilator-free days were realized in the conventional mechanical ventilation group when compared with the low-dose and high-dose PFC groups (Hirschl et al., 2002; Degraeuwe and Zimmermann, 2006; Kacmarek et al., 2006). Improved mortality or ventilator-free days did not result in another randomized clinical trial in spite of decreased progression in respiratory insufficiency to ARDS in patients treated with partial liquid ventilation with PFC.

DRUG/GENE PRODUCT ADMINISTRATION

Systemic administration of therapeutics to target the lung is faced with numerous challenges secondary to potential degradation by serum and hepatic enzymes and rapid renal clearance. Compromised pulmonary blood flow in the injured lung may further limit passive diffusion of the drug from the blood into the lung parenchyma. Retention of the therapeutics in the lung is also often suboptimal. These challenges can be mitigated by local administration of therapeutics through inhalation or airway instillation (Bennett et al., 2002). However, many acute and chronic lung diseases affect distally located alveoli and thus require delivery of biological agents to the distal lung parenchyma for optimal therapeutic effect. Distal delivery of therapeutic agents requires obtaining the correct particle size, which has been challenging. Furthermore, ventilation abnormalities in the impaired lung regions also minimize drug delivery to these target areas.

Drug Delivery With Inert Liquids

Some studies have successfully demonstrated that lungs filled with PFC liquid have the ability to deliver active and inactive agents for the diagnosis and treatment of respiratory disorders.

Respiratory infections affect distally located alveoli with bacteria and viruses multiplying in the alveolar cells. Distal lung distribution of intra-tracheally delivered anti-infective agents is essential to halt disease progression. In a newborn lamb model of acid lung injury, gentamicin administration during tidal liquid ventilation using PFC resulted in

significantly higher lung gentamicin levels compared with intravenous administration (Fox et al., 1997; Zelinka et al., 1997; Cullen et al., 1999; Cox et al., 2001). This technique also resulted in greater pulmonary gentamicin levels and lower serum levels, which are required to achieve therapeutic levels in the lung while mitigating systemic adverse effects of gentamicin. Similarly, when utilizing a piglet model of meconium aspiration, greater pulmonary levels and lower serum levels of vancomycin were achieved after intrapulmonary instillation of vancomycin and PFC followed by partial liquid ventilation, compared with intravenous injection of vancomycin followed by conventional gas ventilation (Jeng et al., 2007).

In an animal model of meconium aspiration syndrome, partial liquid ventilation improved regional distribution of intratracheally administered radio-labelled surfactant compared with conventional mechanical ventilation. There was more uniform distribution of surfactant between the lungs as well as between both ventral and dorsal regions of the lungs. Such uniform distribution was associated with improved systemic oxygenation (Chappell et al., 2001). PFC was also an effective delivery vehicle for pulmonary administration of vasoactive agents (Wolfson et al., 1996).

Inhalational smoke-induced acute lung injury is characterized by airway epithelial injury leading to excess leakage of plasma substrates into large airways and the formation of fibrin casts. Interventions to prevent or treat airway casts are limited. In this regard, PFC has been used for intratracheal administration of plasminogen activators (tissue plasminogen activator [tPA] and single-chain urokinase plasminogen activator [scuPA]) for management of airway clot and fibrinous cast formation associated with smoke-induced acute lung injury. Enzymatic activities of the plasminogen activator following dispersion and storage in PFC were preserved, and PFC administration alone did not impact physiologic or histological differences. In contrast, PFC-facilitated plasminogen activator delivery resulted in significantly better physiologic and histologic outcomes. PFC-facilitated delivery of plasminogen activator demonstrated improved outcomes than achieved by nebulization of plasminogen activators alone (Wolfson et al., 2020).

Drug delivery during PFC PLV respiratory support has been demonstrated with other soluble gases in PFOB such as inspired nitric oxide (NO). NO administration with PLV in surfactant-depleted adult pigs resulted in a significant improvement in gas exchange and decrease in pulmonary artery pressure, most notably without deleterious effects on systemic hemodynamic conditions (Houmes et al., 1997). In a congenital diaphragmatic hernia lamb preparation treated prophylactically with PLV, it was demonstrated that NO improved oxygenation and reduced pulmonary hypertension (Wilcox et al., 1994). As such, the ability to deliver NO during PLV is probably related to distribution of NO in the gas-ventilated regions of the lung, the solubility and diffusion of this gas in the PFC, and recruitment of lung volume. Results on the effective delivery of NO in PFC liquid are consistent with earlier studies showing the use of PFC liquid as a vehicle to deliver biologic agents. Based on transport principles, it appears that the amount of NO delivered to pulmonary structures is dependent on NO concentration in PFC liquid, stratification pattern of gas and PFC liquid in the lung, distribution of pulmonary blood flow, and ventilation-perfusion matching. Finally, the clearance of NO from the partially filled PFC lung and potential formation of NO_2 during liquid ventilation potentially could be different compared with the gas-filled lung.

Gene Delivery to the Respiratory System

Twenty-two percent of all pediatric hospital admissions are due to respiratory illness. Genetic lung diseases account for increased morbidity and mortality (Nogee, 2010; Tanash et al., 2010; Witt et al., 2012). Genetic diseases such as surfactant protein disease, cystic fibrosis, Hermansky-Pudlak syndrome, and neuroendocrine cell hyperplasia of infancy (NEHI) cause severe lung disease and are associated with high mortality and morbidity. No cure currently exists. Pulmonary epithelial cell-specific genetic mutations and abnormal gene regulation play a causal role in many genetic lung diseases and are attractive targets for airway delivery of therapeutic agents. Effective airway-based delivery of gene therapy vectors is a substantial hurdle to successful gene therapy for lung diseases.

CRISPR-Cas9 gene editing provides an unprecedented opportunity to manipulate genes in somatic cells. Editing technologies have demonstrated clear therapeutic promise in non-human primates and early human clinical trials (Komor et al., 2016; Maeder et al., 2019; Frangoul et al., 2021; Musunuru et al., 2021; Rothgangl et al., 2021). New approaches in base editor design enable installation of targeted, single-nucleotide mutations without double strand breaks or the need for donor DNA templates, an exciting advance that paves the way for correction of single nucleotide polymorphisms that comprise the largest class of known pathogenic genetic variants in humans (Landrum et al., 2016; Stenson et al., 2017). Genetic surfactant protein diseases are a particularly attractive target given that the lung is a barrier organ amenable to intratracheal or nasal treatment applications to selectively reach pulmonary cell lineages (Alton et al., 2015; Alapati et al., 2019; Kang et al., 2020).

The postnatal lung presents important limitations to airway delivery because of the substantial mucus and surfactant barrier at the air-epithelial interface, repulsive charge interactions at the cell membrane, and unequal reagent distribution due to the heterogeneity of lung disease with some areas being overinflated and others collapsed (Kim et al., 2016; Alapati and Morrisey, 2017; Roesch and Drumm, 2017). Furthermore, proteinaceous debris and inflammatory fluids contribute to additional physical barriers in diseased lungs. These barriers limit adequate ventilation, particularly to diseased tissues, resulting in limited delivery of inhaled therapies to needed locations. Systemic drug delivery to diseased lung may be affected by the displacement of blood flow away from the injury site. In contrast, any related absence of such immune and physical barriers in the fluid-filled fetal lungs has resulted in systematic gene transfer to the pulmonary epithelial cells

following prenatal viral vector delivery by intra-amniotic injection, taking advantage of fetal breathing movements for lung targeting (Buckley et al., 2005; Endo et al., 2010; Joyeux et al., 2014; Alapati et al., 2019). Additionally, the fluid-filled fetal lung supports relatively uniform targeting of most major pulmonary epithelial cell types, including distal and proximal lineages (Alapati et al., 2019).

Gene Product Delivery With Inert Liquids

The fluid-filled fetal lung physiology could be partially mimicked in postnatal lungs with PFC liquids because of their high spreading coefficients and intriguing properties for pulmonary distribution of biological agents. The high O_2 and CO_2 solubility of PFC liquids allows effective gas exchange, even in lungs filled with fluid. PFCs also reduce surface tension, which assists lung volume recruitment at reduced inspiratory pressures by eliminating the air-liquid interface. Importantly, PFC liquids effectively penetrate collapsed regions of the lung to facilitate access to under-ventilated regions. This is particularly important in non-homogenous lung diseases such as surfactant protein diseases, in which PFC liquids could simultaneously facilitate delivery of therapies, increase gas exchange, and improve pulmonary function. Several groups have exhibited the superior effectiveness of PFC liquids as vehicles for pulmonary distribution of genetic cargo (Lisby et al., 1997; Weiss et al., 1999a; Weiss et al., 1999b; Weiss et al., 2000; Kazzaz et al., 2011). PFC liquids instilled during the intratracheal administration of recombinant viral vector propelled the vector more effectively into the lung. As a result, PFC enhanced airway and alveolar epithelial gene expression in both normal and injured rodent lungs (Weiss et al., 2001). Use of PFC as vehicle for delivery of genetic cargo also resulted in earlier detection of gene expression and need for lesser amounts of vector. In all of these studies, PFC was administered immediately following administration of aqueous vector because of immiscibility of PFC with aqueous solutions. The propulsive effect of PFC resulted in improved delivery and distribution of the vectors. PFC liquids also transiently decreased transepithelial resistance and increased tight junction permeability. This transient increase in epithelial permeability enhanced access to viral vectors and gene expression. The peak effect was observed from 6 h to 1 day following instillation. Notably, alveolar-capillary permeability was not affected (Weiss et al., 2003). Many studies have also demonstrated improvement in lung mechanics and oxygenation in research models of lung injury following administration of PFC liquids in nebulized or aerosolized forms (Bleyl et al., 1999; Ragaller et al., 2001; Kandler et al., 2004; von der Hardt et al., 2004). As such, administration of nebulized perflubron improved resulting recombinant viral vector mediated gene expression (Beckett et al., 2012). By adapting and optimizing PFC liquid strategies demonstrated to be beneficial for viral vector gene delivery, PFC liquids hold promise for enhanced airway delivery of CRISPR systems as therapeutic strategy for a myriad of respiratory disorders.

Considerations for Improving Drug/Gene Delivery With Inert Liquids

The fact that aqueous solutions are not readily soluble in PFCs is an important consideration for PFC drug delivery. Some research projects have circumvented this barrier by relying on bulk flow turbulent mixing (Wolfson et al., 1996; Lisby et al., 1997). However, techniques that improve solubility of the drug or biologic agent in PFC are advantageous to provide stability and equivalent disbursement of the drug within the lung and for more controlled dosing procedures. One such method is generation of nanocrystals that can then be administered during partial liquid ventilation. This approach was successfully utilized by developing gentamicin/perfluorochemical nanocrystal suspension that was delivered using two techniques (Cullen et al., 1999). In the first technique, called the top-fill technique, gentamicin/PFC nanocrystal suspension was instilled through the sideport of an endotracheal tube 29 ± 8 min after initiation of partial liquid ventilation with a bolus of oxygenated perflubron. In the second technique, called the slow-fill technique, the gentamicin/PFC nanocrystal suspension was combined with perflubron, vortexed, and delivered through the sideport of an endotracheal tube. Thus, in the second technique, partial liquid ventilation and gentamicin treatment were initiated simultaneously. Both the techniques resulted in effective distribution of gentamicin into the lung and greater gentamicin levels per gram of dry lung tissue compared with intravenous administration of aqueous gentamicin. The amount of original gentamicin dose left in the lobes of the lungs adjusted for dry weight after 4 h and was greater in the slow-fill technique compared with the top-fill technique.

SUMMARY

When lung parenchymal disease and/or injury are present in the lung, pulmonary ventilation and perfusion are compromised. Ventilation can be irregular and perfusion may be inhibited by ventilation-perfusion mismatch. The route of therapy administration is hindered by these abnormalities, rendering standard intravenous and aerosol/endotracheal tube delivery ineffective in delivering therapeutic agents to the affected area.

Liquid ventilation with an inert respiratory gas solubility is a revolutionary mode for respiratory support, as well as delivery of drug/gene product to the respiratory system. As noted, inert perfluorochemical liquids have low viscosity and high oxygen and carbon dioxide capabilities (Grotberg, 2001). The physical properties of PFC liquids improve lung mechanics and gas exchange and condition the lung parenchymal surface for optimal administration of drug/gene product.

The use of PFC liquid in the respiratory system enhances ventilation and perfusion matching, boosting exposure of the drug/gene product to the circulation, successfully reaching required therapeutic serum drug levels (Fox et al., 1997). Studies have demonstrated the utilization of PFCs as adjuncts for intrapulmonary biological agent delivery both preclinically and clinically as reported herein.

AUTHOR CONTRIBUTIONS

DA and TS conceptualized the idea and prepared the first draft and final manuscript. Both authors approve the final version of the manuscript and agree to be accountable for the content of the work.

FUNDING

This study was supported by NIH K08 HL151760 01 (DA), American Thoracic Society Foundation (DA), Institutional Development Award (IDeA) from the NIH/NGMS COBRE P30GM114736 (TS), and The Nemours Foundation.

REFERENCES

Al-Rahmani, A., Awad, K., Miller, T. F., Wolfson, M. R., and Shaffer, T. H. (2000). Effects of Partial Liquid Ventilation with Perfluorodecalin in the Juvenile Rabbit Lung after Saline Injury. *Crit. Care Med.* 28, 1459–1464. doi:10.1097/00003246-200005000-00034

Alapati, D., Zacharias, W. J., Hartman, H. A., Rossidis, A. C., Stratigis, J. D., Ahn, N. J., et al. (2019). In Utero Gene Editing for Monogenic Lung Disease. *Sci. Transl. Med.* 11, eaav8375. doi:10.1126/scitranslmed.aav8375

Alapati, D., and Morrisey, E. E. (2017). Gene Editing and Genetic Lung Disease. Basic Research Meets Therapeutic Application. *Am. J. Respir. Cel Mol. Biol.* 56, 283–290. doi:10.1165/rcmb.2016-0301ps

Ali, M. E., McConville, J. T., and Lamprecht, A. (2015). Pulmonary Delivery of Anti-Inflammatory Agents. *Expert Opin. Drug Deliv.* 12, 929–945. doi:10.1517/17425247.2015.993968

Alton, E. W. F. W., Armstrong, D. K., Ashby, D., Bayfield, K. J., Bilton, D., Bloomfield, E. V., et al. (2015). Repeated Nebulisation of Non-Viral CFTR Gene Therapy in Patients with Cystic Fibrosis: A Randomised, Double-Blind, Placebo-Controlled, Phase 2b Trial. *Lancet Respir. Med.* 3, 684–691. doi:10.1016/S2213-2600(15)00245-3

Avery, M. E., and Mead, J. (1959). Surface Properties in Relation to Atelectasis and Hyaline Membrane Disease. *Arch. Pediatr. Adolesc. Med.* 97, 517. doi:10.1001/archpedi.1959.02070010519001

Bateman, S. T., Doctor, A., Price, B., Murphy, M. A., Thompson, J. E., Zurakowski, D., et al. (2001). Optimizing Intrapulmonary Perfluorocarbon Distribution: Fluoroscopic Comparison of Mode of Ventilation and Body Position. *Crit. Care Med.* 29, 601–608. doi:10.1097/00003246-200103000-00024

Beckett, T., Bonneau, L., Howard, A., Blanchard, J., Borda, J., Weiner, D. J., et al. (2012). Inhalation of Nebulized Perfluorochemical Enhances Recombinant Adenovirus and Adeno-Associated Virus-Mediated Gene Expression in Lung Epithelium. *Hum. Gene Ther. Methods* 23, 98–110. doi:10.1089/hgtb.2012.014

Bennett, W. D., Brown, J. S., Zeman, K. L., Hu, S.-C., Scheuch, G., and Sommerer, K. (2002). Targeting Delivery of Aerosols to Different Lung Regions. *J. Aerosol Med.* 15, 179–188. doi:10.1089/089426802320282301

Bleyl, J. U., Ragaller, M., Tscho, U., Regner, M., Kanzow, M., Hubler, M., et al. (1999). Vaporized Perfluorocarbon Improves Oxygenation and Pulmonary Function in an Ovine Model of Acute Respiratory Distress Syndrome. *Anesthesiology* 91, 461–469. doi:10.1097/00000542-199908000-00021

Buckley, S. M. K., Waddington, S. N., Jezzard, S., Lawrence, L., Schneider, H., Holder, M. V., et al. (2005). Factors Influencing Adenovirus-Mediated Airway Transduction in Fetal Mice. *Mol. Ther.* 12, 484–492. doi:10.1016/j.ymthe.2005.02.020

Chappell, S. E., Wolfson, M. R., and Shaffer, T. H. (2001). A Comparison of Surfactant Delivery with Conventional Mechanical Ventilation and Partial Liquid Ventilation in Meconium Aspiration Injury. *Respir. Med.* 95, 612–617. doi:10.1053/rmed.2001.1114

Clark, L. C., Jr., and Gollan, F. (1966). Survival of Mammals Breathing Organic Liquids Equilibrated with Oxygen at Atmospheric Pressure. *Science* 152, 1755–1756. doi:10.1126/science.152.3730.1755

Clark, L. C., Jr. (1970). Introduction. *Fed. Proc.* 29, 1698.

Cox, C. A., Cullen, A. B., Wolfson, M. R., and Shaffer, T. H. (2001). Intratracheal Administration of Perfluorochemical-Gentamicin Suspension: A Comparison to Intravenous Administration in Normal and Injured Lungs. *Pediatr. Pulmonol.* 32, 142–151. doi:10.1002/ppul.1100

Cox, C. A., Fox, W. W., Weiss, C. M., Wolfson, M. R., and Shaffer, T. H. (2002). Liquid Ventilation: Gas Exchange, Perfluorochemical Uptake and Biodistribution in an Acute Lung Injury Model. *Pediatr. Crit. Care Med.* 3, 288–296. doi:10.1097/00130478-200207000-00017

Cox, C., Stavis, R. L., Wolfson, M. R., and Shaffer, T. H. (2003). Long-Term Tidal Liquid Ventilation in Premature Lambs: Physiologic, Biochemical and Histological Correlates. *Biol. Neonate.* 84, 232–242. doi:10.1159/000072307

Cullen, A. B., Cox, C. A., Hipp, S. J., Wolfson, M. R., and Shaffer, T. H. (1999). Intra-Tracheal Delivery Strategy of Gentamicin with Partial Liquid Ventilation. *Respir. Med.* 93, 770–778. doi:10.1016/s0954-6111(99)90261-5

Davidson, A., Donner, R., Heckman, J. L., Miller, T. F., Shaffer, T. H., and Wolfson, M. R. (1995). Partial Liquid Ventilation Reduces Left Ventricular Wall Stress in Rescue of Surfactant-Treated Preterm Lambs. *Chest* 3, 108.

Davies, M., Stewart, M., Chavasse, R., Bayley, G., and Butt, W. (2002). Partial Liquid Ventilation and Nitric Oxide in Experimental Acute Lung Injury. *J. Paediatr. Child. Health* 38, 492–496. doi:10.1046/j.1440-1754.2002.00036.x

Davies, M. W., Dunster, K. R., Fraser, J. F., and Colditz, P. B. (2013). Cerebral Blood Flow Is Not Affected during Perfluorocarbon Dosing with Volume-Controlled Ventilation. *J. Paediatr. Child. Health* 49, 1010–1018. doi:10.1111/jpc.12297

Davies, M. W., Dunster, K. R., Wilson, K., and Colditz, P. B. (2010). Perfluorocarbon Dosing when Starting Partial Liquid Ventilation: Haemodynamics and Cerebral Blood Flow in Preterm Lambs. *Neonatology* 97, 144–153. doi:10.1159/000239768

Degnan, A. J., Fox, W. W., Zhang, H., and Saul, D. (2019). Partial Liquid Ventilation for Bronchopulmonary Dysplasia: Visualizing Ventilation Patterns on Chest Radiographs. *Pediatr. Neonatal.* 60, 587–588. doi:10.1016/j.pedneo.2018.10.004

Degraeuwe, P. L. J., and Zimmermann, L. J. I. (2006). Why Partial Liquid Ventilation Did Not Fulfill its Promise. *Am. J. Respir. Crit. Care Med.* 174, 615. doi:10.1164/ajrccm.174.5.615

Endo, M., Henriques-Coelho, T., Zoltick, P. W., Stitelman, D. H., Peranteau, W. H., Radu, A., et al. (2010). The Developmental Stage Determines the Distribution and Duration of Gene Expression after Early Intra-Amniotic Gene Transfer Using Lentiviral Vectors. *Gene Ther.* 17, 61–71. doi:10.1038/gt.2009.115

Fournier, L., Major, D., Cadenas, M., Leclerc, S., Cloutler, R., Wolfson, M. R., et al. (1995). Morphometric and Physiological Differences between Gas and Liquid Ventilated Lung. *Can. J. Anaesth.* 42, A29B.

Fox, W. W., Weis, C. M., Cox, C., Farina, C., Drott, H., Wolfson, M. R., et al. (1997). Pulmonary Administration of Gentamicin during Liquid Ventilation in a Newborn Lamb Lung Injury Model. *Pediatrics* 100, E5. doi:10.1542/peds.100.5.e5

Frangoul, H., Altshuler, D., Cappellini, M. D., Chen, Y.-S., Domm, J., Eustace, B. K., et al. (2021). CRISPR-Cas9 Gene Editing for Sickle Cell Disease and β-Thalassemia. *N. Engl. J. Med.* 384, 252–260. doi:10.1056/nejmoa2031054

Gauger, P. G., Pranikoff, T., Schreiner, R. J., Moler, F. W., and Hirschl, R. B. (1996). Initial Experience with Partial Liquid Ventilation in Pediatric Patients with the Acute Respiratory Distress Syndrome. *Crit. Care Med.* 24, 16–22. doi:10.1097/00003246-199601000-00006

Goodlin, R. (1962). Fœtal Incubator. *Lancet* 1, 1356–1357. doi:10.1016/s0140-6736(62)92469-8

Greenspan, J. S., Wolfson, M. R., Rubenstein, S. D., and Shaffer, T. H. (1990). Liquid Ventilation of Human Preterm Neonates. *J. Pediatr.* 117, 106–111. doi:10.1016/s0022-3476(05)82457-6

Greenspan, J., Wolfson, M., David Rubenstein, S., and Shaffer, T. (1989). Liquid Ventilation of Preterm Baby. *Lancet* 334, 1095. doi:10.1016/s0140-6736(89)91101-x

Gross, G. W., Greenspan, J. S., Fox, W. W., Rubenstein, S. D., Wolfson, M. R., and Shaffer, T. H. (1995). Use of Liquid Ventilation with Perflubron during Extracorporeal Membrane Oxygenation: Chest Radiographic Appearances. *Radiology* 194, 717–720. doi:10.1148/radiology.194.3.7862968

Grotberg, J. B. (2001). Respiratory Fluid Mechanics and Transport Processes. *Annu. Rev. Biomed. Eng.* 3, 421–457. doi:10.1146/annurev.bioeng.3.1.421

Haeberle, H. A., Nesti, F., Dieterich, H.-J., Gatalica, Z., and Garofalo, R. P. (2002). Perflubron Reduces Lung Inflammation in Respiratory Syncytial Virus Infection by Inhibiting Chemokine Expression and Nuclear Factor-κB Activation. *Am. J. Respir. Crit. Care Med.* 165, 1433–1438. doi:10.1164/rccm.2109077

Hagerty, R. D., Phelan, M. P., Morrison, S. C., and Hatem, S. F. (2008). Radiographic Detection of Perflubron Fluoromediastinum and Fluororetroperitoneum 9 Years after Partial Liquid Ventilation. *Emerg. Radiol.* 15, 71–75. doi:10.1007/s10140-007-0673-2

Hamosh, P., and Luchsinger, P. C. (1968). Maximum Expiratory Flow in Isolated Liquid-Filled Lungs. *J. Appl. Physiol.* 25, 485–488. doi:10.1152/jappl.1968.25.5.485

Hartog, A., Houmes, R. J. M., Verbrugge, S. J. C., Erdmann, W., and Lachmann, B. (1997). Partial Liquid Ventilation and Inhaled Nitric Oxide Have a Cumulative Effect in Improving Arterial Oxygenation in Experimental ARDS. *Adv. Exp. Med. Biol.* 428, 281–283. doi:10.1007/978-1-4615-5399-1_39

Henrichsen, T., Lindenskov, P. H., Shaffer, T. H., Loekke, R. J., Fugelseth, D., and Lindemann, R. (2012). Perfluorodecalin Lavage of a Longstanding Lung Atelectasis in a Child with Spinal Muscle Atrophy. *Pediatr. Pulmonol.* 47, 415–419. doi:10.1002/ppul.21565

Hirschl, R. B., Croce, M., Gore, D., Wiedemann, H., Davis, K., Zwischenberger, J., et al. (2002). Prospective, Randomized, Controlled Pilot Study of Partial Liquid Ventilation in Adult Acute Respiratory Distress Syndrome. *Am. J. Respir. Crit. Care Med.* 165, 781–787. doi:10.1164/ajrccm.165.6.2003052

Hirschl, R. B., Pranikoff, T., Gauger, P., Schreiner, R. J., Dechert, R., and Bartlett, R. H. (1995). Liquid Ventilation in Adults, Children and Full-Term Neonates. *Lancet* 346, 1201–1202. doi:10.1016/s0140-6736(95)92903-7

Hirschl, R. B., Pranikoff, T., Wise, C., Overbeck, M. C., Gauger, P., Schreiner, R. J., et al. (1996). Initial Experience with Partial Liquid Ventilation in Adult Patients with the Acute Respiratory Distress Syndrome. *JAMA* 275, 383–389. doi:10.1001/jama.275.5.383

Holaday, D. A., Fiserova-Bergerova, V., and Modell, J. H. (1972). Uptake, Distribution, and Excretion of Fluorocarbon FX-80 (Perfluorobutyl Perfluorotetrahydrofuran) during Liquid Breathing in the Dog. *Anesthesiolog* 37, 387–394. doi:10.1097/00000542-197210000-00005

Houmes, R. J., Hartog, A., Verbrugge, S. J., Böhm, S., and Lachmann, B. (1997). Combining Partial Liquid Ventilation with Nitric Oxide to Improve Gas Exchange in Acute Lung Injury. *Intensive Care Med.* 23, 163–169.

Hübler, M., Souders, J. E., Shade, E. D., Polissar, N. L., Bleyl, J. U., and Hlastala, M. P. (2002). Effects of Perfluorohexane Vapor on Relative Blood Flow Distribution in an Animal Model of Surfactant-Depleted Lung Injury. *Crit. Care Med.* 30, 422–427. doi:10.1097/00003246-200202000-00026

Jeng, M. J., Lee, Y. S., and Soong, W. J. (2007). Effects of Perfluorochemicals for Intrapulmonary Vancomycin Administration and Partial Liquid Ventilation in an Animal Model of Meconium-Injured Lungs. *Acta Paediatr. Taiwan.* 48, 309–316.

Joyeux, L., Danzer, E., Limberis, M. P., Zoltick, P. W., Radu, A., Flake, A. W., et al. (2014). In Utero lung Gene Transfer Using Adeno-Associated Viral and Lentiviral Vectors in Mice. *Hum. Gene Ther. Methods* 25, 197–205. doi:10.1089/hgtb.2013.143

Kacmarek, R. M., Wiedemann, H. P., Lavin, P. T., Wedel, M. K., Tütüncü, A. S., and Slutsky, A. S. (2006). Partial Liquid Ventilation in Adult Patients with Acute Respiratory Distress Syndrome. *Am. J. Respir. Crit. Care Med.* 173, 882–889. doi:10.1164/rccm.200508-1196oc

Kandler, M. A., von der Hardt, K., Gericke, N., Chada, M., Dötsch, J., and Rascher, W. (2004). Dose Response to Aerosolized Perflubron in a Neonatal Swine Model of Lung Injury. *Pediatr. Res.* 56, 191–197. doi:10.1203/01.pdr.0000132667.47744.f4

Kandler, M. A., von der Hardt, K., Schoof, E., Dötsch, J., and Rascher, W. (2001). Persistent Improvement of Gas Exchange and Lung Mechanics by Aerosolized Perfluorocarbon. *Am. J. Respir. Crit. Care Med.* 164, 31–35. doi:10.1164/ajrccm.164.1.2010049

Kang, M. H., van Lieshout, L. P., Xu, L., Domm, J. M., Vadivel, A., Renesme, L., et al. (2020). A Lung Tropic AAV Vector Improves Survival in a Mouse Model of Surfactant B Deficiency. *Nat. Commun.* 11, 3929. doi:10.1038/s41467-020-17577-8

Kawamae, K., Pristine, G., Chiumello, D., Tremblay, L. N., and Slutsky, A. S. (2000). Partial Liquid Ventilation Decreases Serum Tumor Necrosis Factor-Alpha Concentrations in a Rat Acid Aspiration Lung Injury Model. *Crit. Care Med.* 28, 479–483. doi:10.1097/00003246-200002000-00032

Kazzaz, J. A., Strayer, M. S., Wu, J., Malone, D. J., Koo, H. C., Shaffer, T. H., et al. (2011). Perfluorochemical Liquid-Adenovirus Suspensions Enhance Gene Delivery to the Distal Lung. *Pulm. Med.* 2011, 918036. doi:10.1155/2011/918036

Keshavarz, A., Kadry, H., Alobaida, A., and Ahsan, F. (2020). Newer Approaches and Novel Drugs for Inhalational Therapy for Pulmonary Arterial Hypertension. *Expert Opin. Drug Deliv.* 17, 439–461. doi:10.1080/17425247.2020.1729119

Kim, N., Duncan, G. A., Hanes, J., and Suk, J. S. (2016). Barriers to Inhaled Gene Therapy of Obstructive Lung Diseases: a Review. *J. Controlled Release* 240, 465–488. doi:10.1016/j.jconrel.2016.05.031

Komor, A. C., Kim, Y. B., Packer, M. S., Zuris, J. A., and Liu, D. R. (2016). Programmable Editing of a Target Base in Genomic DNA without Double-Stranded DNA Cleavage. *Nature* 533, 420–424. doi:10.1038/nature17946

Kumar, M., Jha, A., Dr, M., and Mishra, B. (2020). Targeted Drug Nanocrystals for Pulmonary Delivery: a Potential Strategy for Lung Cancer Therapy. *Expert Opin. Drug Deliv.* 17, 1459–1472. doi:10.1080/17425247.2020.1798401

Kylstra, J. (1967). "Advantages and Limitations of Liquid Breathing," in *Proceedings of the Third Symposium on Underwater Physiology*. Editor C. J. Lambertsen (Baltimore: Williams & Wilkins), 341–350.

Kylstra, J. A., Paganelli, C. V., and Lanphier, E. H. (1966). Pulmonary Gas Exchange in Dogs Ventilated with Hyperbarically Oxygenated Liquid. *J. Appl. Physiol.* 21, 177–184. doi:10.1152/jappl.1966.21.1.177

Kylstra, J. A., Schoenfisch, W. H., Herron, J. M., and Blenkarn, G. D. (1973). Gas Exchange in Saline-Filled Lungs of Man. *J. Appl. Physiol.* 35, 136–142. doi:10.1152/jappl.1973.35.1.136

Kylstra, J. A., Tissing, M. O., van der Maë'n, A., and de Graaf, R. P. (1962). Of Mice as Fish. *Trans. Am. Soc. Artif. Intern. Organs.* 8, 378–383. doi:10.1097/00002480-196204000-00077

Landrum, M. J., Lee, J. M., Benson, M., Brown, G., Chao, C., Chitipiralla, S., et al. (2016). ClinVar: Public Archive of Interpretations of Clinically Relevant Variants. *Nucleic Acids Res.* 44, D862–D868. doi:10.1093/nar/gkv1222

Leach, C. L., Fuhrman, B. P., Morin, F. C., 3rd, and Rath, M. G. (1993). Perfluorocarbon-associated Gas Exchange (Partial Liquid Ventilation) in Respiratory Distress Syndrome: A Prospective, Randomized, Controlled Study. *Crit. Care Med.* 21, 1270–1278. doi:10.1097/00003246-199309000-00008

Leach, C. L., Greenspan, J. S., Rubenstein, S. D., Shaffer, T. H., Wolfson, M. R., Jackson, J. C., et al. (1996). Partial Liquid Ventilation with Perflubron in Premature Infants with Severe Respiratory Distress Syndrome. The LiquiVent Study Group. *N. Engl. J. Med.* 335, 761–767. doi:10.1056/nejm199609123351101

Leith, D. E., and Mead, J. (1966). Maximum Expiratory Flow in Liquid-Filled Lungs. *Fed. Proc* 25, 506.

Lisby, D. A., Ballard, P. L., Fox, W. W., Wolfson, M. R., Shaffer, T. H., and Gonzales, L. W. (1997). Enhanced Distribution of Adenovirus-Mediated Gene Transfer to Lung Parenchyma by Perfluorochemical Liquid. *Hum. Gene Ther.* 8, 919–928. doi:10.1089/hum.1997.8.8-919

Lynch, P. R., Wilson, J. S., Shaffer, T. H., and Cohen, N. (1983). Decompression Incidence in Air- and Liquid-Breathing Hamsters. *Undersea Biomed. Res.* 10, 1–10. doi:10.1029/gl010i012p01176

Maeder, M. L., Stefanidakis, M., Wilson, C. J., Baral, R., Barrera, L. A., Bounoutas, G. S., et al. (2019). Development of a Gene-Editing Approach to Restore Vision Loss in Leber Congenital Amaurosis Type 10. *Nat. Med.* 25, 229–233. doi:10.1038/s41591-018-0327-9

Major, D., Cadenas, M., Cloutier, R., Fournier, L., Wolfson, M. R., Shaffer, T. H., et al. (1995). Combined Gas Ventilation and Perfluorochemical Tracheal Instillation as an Alternative Treatment for Lethal Congenital Diaphragmatic Hernia in Lambs. *J. Pediatr. Surg.* 30, 1178–1182. doi:10.1016/0022-3468(95)90016-0

Mead, J., Whittenberger, J. L., and Radford, E. P., Jr. (1957). Surface Tension as a Factor in Pulmonary Volume-Pressure Hysteresis. *J. Appl. Physiol.* 10, 191–196. doi:10.1152/jappl.1957.10.2.191

Merz, U., Klosterhalfen, B., Häusler, M., Kellinghaus, M., Peschgens, T., and Hörnchen, H. (2002). Partial Liquid Ventilation Reduces Release of Leukotriene B4 and Interleukin-6 in Bronchoalveolar Lavage in Surfactant-Depleted Newborn Pigs. *Pediatr. Res.* 51, 183–189. doi:10.1203/00006450-200202000-00010

Miller, T. F., Milestone, B., Stern, R., Shaffer, T. H., and Wolfson, M. R. (1999). Effect of Single versus Multiple Dosing on Perfluorochemical Distribution and Elimination during Partial Liquid Ventilation. *Pediatr. Pulmonol.* 27, 410–418. doi:10.1002/(sici)1099-0496(199906)27:6<410::aid-ppul8>3.0.co;2-5

Miller, T. F., Milestone, B., Stern, R., Shaffer, T. H., and Wolfson, M. R. (2001). Effects of Perfluorochemical Distribution and Elimination Dynamics on Cardiopulmonary Function. *J. Appl. Physiol.* 90, 839–849. doi:10.1152/jappl.2001.90.3.839

Modell, J. G., Tham, M. K., Modell, J. H., Calderwood, H. W., and Ruiz, B. C. (1973). Distribution and Retention of Fluorocarbon in Mice and Dogs after Injection or Liquid Ventilation. *Toxicol. Appl. Pharmacol.* 26, 86–92. doi:10.1016/0041-008x(73)90088-4

Moskowitz, G. D., Shaffer, T. H., and Dubin, S. E. (1975). Liquid Breathing Trials and Animal Studies with a Demand-Regulated Liquid Breathing System. *Med. Instrum.* 9, 28–33.

Muralidharan, P., Malapit, M., Mallory, E., Hayes, D., Jr., and Mansour, H. M. (2015). Inhalable Nanoparticulate Powders for Respiratory Delivery. *Nanomedicine* 11, 1189–1199. doi:10.1016/j.nano.2015.01.007

Musunuru, K., Chadwick, A. C., Mizoguchi, T., Garcia, S. P., DeNizio, J. E., Reiss, C. W., et al. (2021). *In Vivo* CRISPR Base Editing of PCSK9 Durably Lowers Cholesterol in Primates. *Nature* 593, 429–434. doi:10.1038/s41586-021-03534-y

Neergard, D. V. (1929). Neue Auffassungen über einen Grundbegriff der Atemmechanic. Die Retraktionkraft der Lunge, abhangig von der Oberfl achenspannung in den Alveolen. *Z. Gesamte. Exp. Med.* 66, 373.

Nogee, L. M. (2010). Genetic Basis of Children's Interstitial Lung Disease. *Pediatr. Allergy Immunol. Pulmonol.* 23, 15–24. doi:10.1089/ped.2009.0024

Pegg, J. H., Horner, T. L., and Wahrenbrock, E. A. (1963). "Breathing of Pressure-Oxygenated Liquids. In: National Academy of Sciences—National Research Council," in *Proceedings of the Second Symposium on Underwater Physiology* (Publication No. 1181) (Washington, D.C.: National Academy of Sciences—National Research Council), 166–170.

Pranikoff, T., Gauger, P. G., and Hirschl, R. B. (1996). Partial Liquid Ventilation in Newborn Patients with Congenital Diaphragmatic Hernia. *J. Pediatr. Surg.* 31, 613–618. doi:10.1016/s0022-3468(96)90659-4

Ragaller, M., Bleyl, J., Tschö, U., Winkler, T., Regner, M., Rasche, S., et al. (2001). Effects of Inhalation of Perfluorocarbon Aerosol on Oxygenation and Pulmonary Function Compared to PGI2 Inhalation in a Sheep Model of Oleic Acid-Induced Lung Injury. *Intensive Care Med.* 27, 889–897. doi:10.1007/s001340100921

Richman, P. S., Wolfson, M. R., and Shaffer, T. H. (1993). Lung Lavage with Oxygenated Perfluorochemical Liquid in Acute Lung Injury. *Crit. Care Med.* 21, 768–774. doi:10.1097/00003246-199305000-00022

Riess, J. G. (1992). Overview of Progress in the Fluorocarbon Approach Toin Vivo Oxygen Delivery. *Biomater. Artif. Cell Immobilization Biotechnol.* 20, 183–202. doi:10.3109/10731199209119635

Roesch, E. A., and Drumm, M. L. (2017). Powerful Tools for Genetic Modification: Advances in Gene Editing. *Pediatr. Pulmonol.* 52, S15–S20. doi:10.1002/ppul.23791

Rothgangl, T., Dennis, M. K., Lin, P. J. C., Oka, R., Witzigmann, D., Villiger, L., et al. (2021). *In Vivo* adenine Base Editing of PCSK9 in Macaques Reduces LDL Cholesterol Levels. *Nat. Biotechnol.* 39, 949–957. doi:10.1038/s41587-021-00933-4

Sargent, J. W., and Seffl, R. J. (1970). Properties of Perfluorinated Liquids. *Fed. Proc.* 29, 1699–1703.

Sekins, K. M., Coalson, J. J., deLemos, R. A., Fields, T. K., Flaim, S. F., Guerra, J. M., et al. (1994). Long-term Partial Liquid Ventilation (PLV) with Perflubron in the Near-Term Baboon Neonate. *Artif. Cell Blood Substitutes, Biotechnol.* 22, 1381–1387. doi:10.3109/10731199409138841

Sekins, K. M. (1995). *Lung Cancer Hyperthermia via Ultrasound and PFC Liquids: Final Report*. Bethesda, MD: National Institutes of Health. National Institutes of Health Grant R43 CA48611-03.

Servaes, S., and Epelman, M. (2009). Perflubron Residua: 12 Years Following Therapy. *Pediatr. Radiol.* 39, 393–395. doi:10.1007/s00247-008-1139-8

Shaffer, T. H., Wolfson, M. R., Greenspan, J. S., Hoffman, R. E., Davis, S. L., and Clark, L. C. (1996). Liquid Ventilation in Premature Lambs: Uptake, Biodistribution and Elimination of Perfluorodecalin Liquid. *Reprod. Fertil. Dev.* 8, 409–416. doi:10.1071/rd9960409

Shaffer, T. H., Douglas, P. R., Lowe, C. A., and Bhutani, V. K. (1983a). The Effects of Liquid Ventilation on Cardiopulmonary Function in Preterm Lambs. *Pediatr. Res.* 17, 303–306. doi:10.1203/00006450-198304000-00017

Shaffer, T. H., Forman, D. L., and Wolfson, M. R. (1984a). Physiological Effects of Ventilation with Liquid Fluorocarbon at Controlled Temperatures. *Undersea Biomed. Res.* 11, 287–298.

Shaffer, T. H., Lowe, C. A., Bhutani, V. K., and Douglas, P. R. (1984b). Liquid Ventilation: Effects on Pulmonary Function in Distressed Meconium-Stained Lambs. *Pediatr. Res.* 18, 47–52.

Shaffer, T. H., Rubenstein, D., Moskowitz, G. D., and Delivoria-Papadopoulos, M. (1976). Gaseous Exchange and Acid-Base Balance in Premature Lambs during Liquid Ventilation since Birth. *Pediatr. Res.* 10, 227–231. doi:10.1203/00006450-197604000-00005

Shaffer, T. H., Tran, N., Bhutani, V. K., and Sivieri, E. M. (1983b). Cardiopulmonary Function in Very Preterm Lambs during Liquid Ventilation. *Pediatr. Res.* 17, 680–684. doi:10.1203/00006450-198308000-00016

Shaffer, T. H., and Wolfson, M. R. (2011). "Liquid Ventilation," in *Fetal and Neonatal Physiology*. Editors R. Polin, W. W. Fox, and S. Abman. 4th Edition (Philadelphia, PA: WB Saunders), 1063–1081. doi:10.1016/b978-1-4160-3479-7.10098-9

Stein, S. N., and Sonnenschein, R. R. (1950). Electrical Activity and Oxygen Tension of Brain during Hyperoxie Convulsions. *J. Aviat. Med.* 21, 401–405.

Stein, S. W., and Thiel, C. G. (2017). The History of Therapeutic Aerosols: A Chronological Review. *J. Aerosol Med. Pulm. Drug Deliv.* 30, 20–41. doi:10.1089/jamp.2016.1297

Stenson, P. D., Mort, M., Ball, E. V., Evans, K., Hayden, M., Heywood, S., et al. (2017). The Human Gene Mutation Database: towards a Comprehensive Repository of Inherited Mutation Data for Medical Research, Genetic Diagnosis and Next-Generation Sequencing Studies. *Hum. Genet.* 136, 665–677. doi:10.1007/s00439-017-1779-6

Tanash, H. A., Nilsson, P. M., Nilsson, J.-Å., and Piitulainen, E. (2010). Survival in Severe Alpha-1-Antitrypsin Deficiency (PiZZ). *Respir. Res.* 11, 44–50. doi:10.1186/1465-9921-11-44

Tiruvoipati, R., Balasubramanian, S. K., Entwisle, J. J., Firmin, R. K., and Peek, G. J. (2007). Pseudocalcification on Chest CT Scan. *Br. J. Radiol.* 80, e125–e127. doi:10.1259/bjr/61486305

von der Hardt, K., Kandler, M. A., Brenn, G., Scheuerer, K., Schoof, E., Dötsch, J., et al. (2004). Comparison of Aerosol Therapy with Different Perfluorocarbons in Surfactant-Depleted Animals. *Crit. Care Med.* 32, 1200–1206. doi:10.1097/01.ccm.0000124876.31138.f6

Weers, J., and Johnson, C. (1991). *Equilibrium Spreading Coefficients of Perfluorocarbons*. San Diego, CA: Alliance Pharmaceutical Corporation. Research and Development Report.

Weis, C. M., Wolfson, M. R., and Shaffer, T. H. (1997). Liquid-Assisted Ventilation: Physiology and Clinica Application. *Ann. Med.* 29, 509–517. doi:10.3109/07853899709007475

Weiss, D. J., Beckett, T., Bonneau, L., Young, J., Kolls, J. K., and Wang, G. (2003). Transient Increase in Lung Epithelial Tight junction Permeability: An Additional Mechanism for Enhancement of Lung Transgene Expression by Perfluorochemical Liquids. *Mol. Ther.* 8, 927–935. doi:10.1016/j.ymthe.2003.09.003

Weiss, D. J., Bonneau, L., Allen, J. M., Miller, A. D., and Halbert, C. L. (2000). Perfluorochemical Liquid Enhances Adeno-Associated Virus-Mediated Transgene Expression in Lungs. *Mol. Ther.* 2, 624–630. doi:10.1006/mthe.2000.0207

Weiss, D. J., Bonneau, L., and Liggitt, D. (2001). Use of Perfluorochemical Liquid Allows Earlier Detection of Gene Expression and Use of Less Vector in normal Lung and Enhances Gene Expression in Acutely Injured Lung. *Mol. Ther.* 3, 734–745. doi:10.1006/mthe.2001.0321

Weiss, D. J., Strandjord, T. P., Jackson, J. C., Clark, J. G., and Liggitt, D. (1999a). Perfluorochemical Liquid-Enhanced Adenoviral Vector Distribution and Expression in Lungs of Spontaneously Breathing Rodents. *Exp. Lung Res.* 25, 317–333. doi:10.1080/019021499270222

Weiss, D. J., Strandjord, T. P., Liggitt, D., and Clark, J. G. (1999b). Perflubron Enhances Adenovirus-Mediated Gene Expression in Lungs of Transgenic Mice

with Chronic Alveolar Filling. *Hum. Gene Ther.* 10, 2287–2293. doi:10.1089/10430349950016933

Wessler, E. P., Iltis, R., and Clark, L. C., Jr. (1977). The Solubility of Oxygen in Highly Fluorinated Liquids. *J. Fluorine Chem.* 9, 137. doi:10.1080/00091383.1977.10569184

Wilcox, D. T., Glick, P. L., Karamanokian, H. L., Leach, C., Morin, F. C., 3rd, and Fuhrman, B. P. (1994). Perfluorocarbon Associated Gas Exchange (PAGE) and Nitric Oxide in the Lamb with Congenital Diaphragmatic Hernia Model. *Pediatr. Res.* 35, A260.

Winternitz, M. C., and Smith, G. H. (1920). *Preliminary Studies in Intratracheal Therapy*. New Haven, CT: Yale University Press, 144–160.

Witt, W. P., Weiss, A. J., and Elixhauser, A. (2012). Overview of Hospital Stays for Children in the United States, 2012. Statistical Brief #187. Healthcare Cost and Utilization Project (HCUP) Statistical Briefs [online]. Agency for Healthcare Research and Quality (US). 2006-2014 Dec. Available at: http://www.hcup-us.ahrq.gov/reports/statbriefs/sb187-Hospital-Stays-Children-2012.pdf (Accessed February 5, 2022).

Wolfson, M. R., Enkhbaatar, P., Fukuda, S., Nelson, C. L., Williams, R. O., III, Surasarang, S. H., et al. (2020). Perfluorochemical-facilitated Plasminogen Activator Delivery to the Airways: A Novel Treatment for Inhalational Smoke-Induced Acute Lung Injury. *Clin. Transl. Med.* 10, 258–274. doi:10.1002/ctm2.26

Wolfson, M. R., Greenspan, J. S., Deoras, K. S., Rubenstein, S. D., and Shaffer, T. H. (1992). Comparison of Gas and Liquid Ventilation: Clinical, Physiological, and Histological Correlates. *J. Appl. Physiol.* 72, 1024–1031. doi:10.1152/jappl.1992.72.3.1024

Wolfson, M. R., Greenspan, J. S., and Shaffer, T. H. (1996). Pulmonary Administration of Vasoactive Substances by Perfluorochemical Ventilation. *Pediatrics* 97, 449–455. doi:10.1542/peds.97.4.449

Wolfson, M. R., Kechner, N. E., Roache, R. F., DeChadarevian, J.-P., Friss, H. E., Rubenstein, S. D., et al. (1998). Perfluorochemical rescue after Surfactant Treatment: Effect of Perflubron Dose and Ventilatory Frequency. *J. Appl. Physiol.* 84, 624–640. doi:10.1152/jappl.1998.84.2.624

Wolfson, M. R., Tran, N., Bhutani, V. K., and Shaffer, T. H. (1988). A New Experimental Approach for the Study of Cardiopulmonary Physiology during Early Development. *J. Appl. Physiol.* 65, 1436–1443. doi:10.1152/jappl.1988.65.3.1436

Zelinka, M. A., Wolfson, M. R., Calligaro, I., Rubenstein, S. D., Greenspan, J. S., and Shaffer, T. H. (1997). A Comparison of Intratracheal and Intravenous Administration of Gentamicin during Liquid Ventilation. *Eur. J. Pediatr.* 156, 401–404. doi:10.1007/s004310050625

Conflict of Interest: The authors declare that the research was conducted in the absence of any commercial or financial relationships that could be construed as a potential conflict of interest.

Publisher's Note: All claims expressed in this article are solely those of the authors and do not necessarily represent those of their affiliated organizations, or those of the publisher, the editors and the reviewers. Any product that may be evaluated in this article, or claim that may be made by its manufacturer, is not guaranteed or endorsed by the publisher.

frontiers | Frontiers in Physiology

SYSTEMATIC REVIEW
published: 14 June 2022
doi: 10.3389/fphys.2022.838414

Methods and Applications in Respiratory Physiology: Respiratory Mechanics, Drive and Muscle Function in Neuromuscular and Chest Wall Disorders

*Nina Patel, Kelvin Chong and Ahmet Baydur**

[1]*Dornsife College of Letters, Arts and Sciences, Division of Pulmonary, Critical Care and Sleep Medicine, Keck School of Medicine and University of Southern California, Los Angeles, CA, United States*

Individuals with neuromuscular and chest wall disorders experience respiratory muscle weakness, reduced lung volume and increases in respiratory elastance and resistance which lead to increase in work of breathing, impaired gas exchange and respiratory pump failure. Recently developed methods to assess respiratory muscle weakness, mechanics and movement supplement traditionally employed spirometry and methods to evaluate gas exchange. These include recording postural change in vital capacity, respiratory pressures (mouth and sniff), electromyography and ultrasound evaluation of diaphragmatic thickness and excursions. In this review, we highlight key aspects of the pathophysiology of these conditions as they impact the patient and describe measures to evaluate respiratory dysfunction. We discuss potential areas of physiologic investigation in the evaluation of respiratory aspects of these disorders.

Keywords: neuromuscular disease, respiratory mechanics, dyspnea, control of ventilation, expiratory flow limitation, diaphragmatic fatigue, gas exchange, respiratory pressures

OPEN ACCESS

Edited by:
Andrew T. Lovering, University of Oregon, United States

Reviewed by:
Matthew J. Fogarty, Mayo Clinic, United States
Nicolle Jasmin Domnik, Western University, Canada

****Correspondence:***
Ahmet Baydur
baydur@usc.edu

Specialty section:
This article was submitted to Respiratory Physiology and Pathophysiology, a section of the journal Frontiers in Physiology

Received: *17 December 2021*
Accepted: *10 May 2022*
Published: *14 June 2022*

Citation:
Patel N, Chong K and Baydur A (2022) Methods and Applications in Respiratory Physiology: Respiratory Mechanics, Drive and Muscle Function in Neuromuscular and Chest Wall Disorders. Front. Physiol. 13:838414. doi: 10.3389/fphys.2022.838414

1 INTRODUCTION

Neuromuscular and chest wall disorders impact breathing in a manner different from injury to the lungs. Respiratory muscle weakness, reduced lung volume and increases in respiratory elastance and resistance lead to increase in work of breathing, respiratory pump failure and impaired gas exchange (Campbell, 1965). The main objective of this review is to highlight key aspects of the pathophysiology of these conditions as they impact the patient and describe recently developed measures to evaluate respiratory dysfunction. We describe key aspects of normal respiratory muscle structure and function, how they are affected in neuromuscular disorders (NMDs), current methods of functional evaluation, and recent advances in their assessment. We finish with suggestions for potential applications of newer techniques that may be considered for their evaluation. We focus primarily on the pathophysiology of NMDs as they impact adults but will refer to changes in children where relevant.

2 PATHOPHYSIOLOGY

2.1 Normal Respiratory Muscle Function

The respiratory system functions to secure gas exchange between ambient air and blood to maintain arterial blood gas pressures within certain acceptable values. It consists of the lungs, chest wall

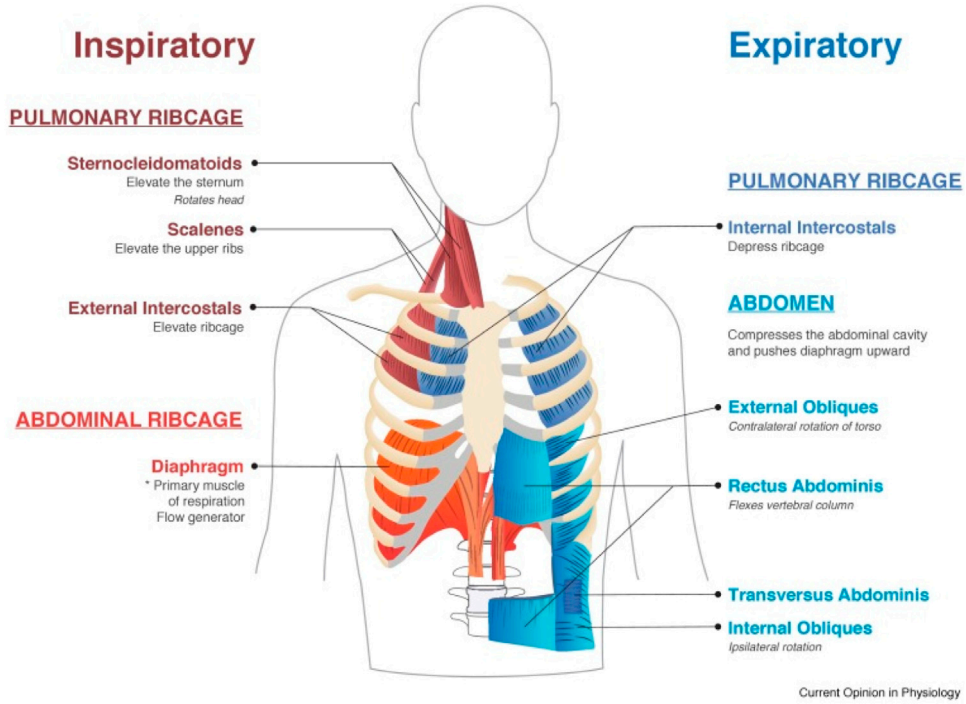

FIGURE 1 | Muscles involved in normal inspiration and expiration. From Welch et al., 2019.

(including respiratory muscles), controllers of breathing, and spinal cord and peripheral nerves that communicate with the respiratory system. Neuromuscular and chest wall disorders affect these structures in varied ways, depending on the age of onset, distribution of neuro/myopathic involvement and rate of progression of the disorder.

Respiratory muscles are classified into those with inspiratory and expiratory function (**Figure 1**) (Campbell, 1965; Benditt, 2019; Welch et al., 2019). In healthy individuals during quiet breathing, the diaphragm is the only active inspiratory muscle; expiration is achieved by passive relaxation of the lungs. During increased demand such as exercise, other muscles become selectively active depending on the relative increase in inspiratory or expiratory requirements, or both. Upper airway dilator muscles maintain patency of the pharynx and larynx, preventing upper airway occlusion, an event occuring frequently with bulbar dysfunction and exacerbated during sleep-disordered breathing.

2.2 Diaphragm

The diaphragm is a thin sheet of muscle acting as a piston, decreasing intrathoracic pressure and drawing air into the lungs. It enables the ribs to move up and outwards ("bucket handle" action), increasing their transverse span (Benditt, 2019). It is configured like an elliptical cylindroid with a dome cap. The cylindrical portion of the diaphragm shortens during inspiration while the dome changes little. Two components counterbalance the

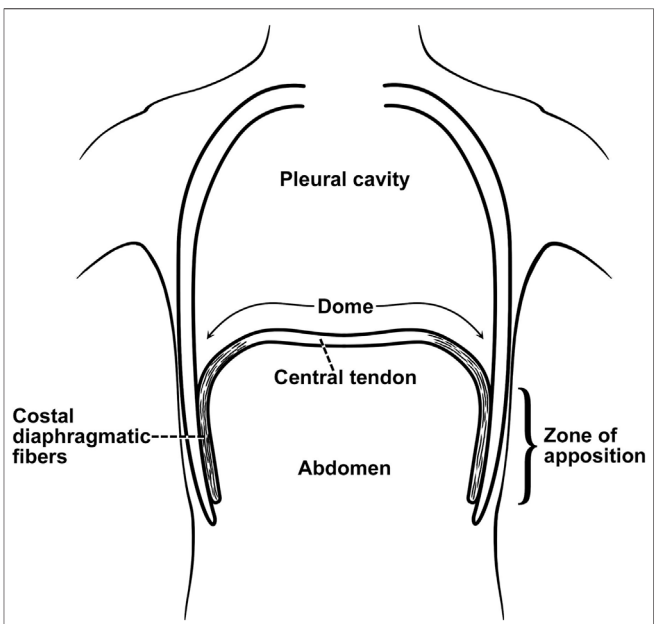

FIGURE 2 | Zone of apposition of the diaphragm. The muscle fibers of the diaphragm originate from the circumference of the thoracic outlet, in particular the lower ribs, and converge to insert into a central tendon). From their origins on the lower ribs the fibers run mainly cranially and are directly parallel (apposed) to the inner aspect of the lower rib cage, constituting the "zone of apposition." From (Troyer and Wilson, 2016).

inspiratory action: the appositional and insertional components. The zone of apposition is represented by the muscular portion inserted into and parallel to posterolateral aspect of the abdominal wall (**Figure 2**). The increase in abdominal pressure on the lower rib cage constitutes the appositional portion while the action of the diaphragm in relation to the rib cage constitutes the insertion portion (Mead, 1979; Loring and Mead, 1982; Troyer and Wilson, 2016). During tidal breathing in upright position the diaphragm and intercostal muscles contribute to 70% and 30% of the Vt, respectively (Druz and Sharp, 1981). In supine posture the contribution of diaphragm increases to 90% (Mognoni et al., 1969; Druz and Sharp, 1981), predisposing to orthopnea. The diaphragm generates only 10–20% of its maximum force generation during quiet breathing (Benditt, 2019; Welch et al., 2019).

2.3 Intercostal muscles

Intercostal muscles span the intercostal space as two thin layers. The inner intercostal fibers run in the caudal-dorsal direction from the sternocostal junction to near the tubercles of the ribs (De Troyer and Estenne, 1984). Fibers of the external intercostals run caudal-ventrally, extending from the tubercles of the ribs to the costochondral junction.

The functions of intercostal muscles have been controversial, particularly because they cannot be activated individually and are inaccessible. De Troyer et al. (De Troyer and Estenne, 1984) found that external intercostal muscles possess a substantial inspiratory mechanical advantage that decreases in the caudal and ventral directions until it is reversed into an expiratory mechanical advantage. The internal intercostals primarily exhibit an expiratory mechanical advantage (Benditt, 2019) while the intertriginous portion of the internal (parasternal) intercostals also possess an inspiratory advantage (De Troyer and Estenne, 1984; Benditt, 2019). External intercostal muscles additionally stabilize (stiffen) the rib cage, minimizing its inward collapse during inspiration while maintaining ventilation-perfusion relationships (Roussos).

2.4 Accessory Inspiratory Muscles

The accessory inspiratory muscles consist of the sternocleidomastoids (SCM), scalenes, pectoralis major and minor, and inferior fibers of serratus anterior and latissimus dorsi. The sternocleidomastoids elevate the clavicles and first rib, reducing pleural pressure and cause the abdomen and lateral ribcage to expand outward (De Troyer and Estenne, 1984; Roussos). They become active at high tidal volume generation, such as during exercise (Roussos). Sternocleidomastoid activity increases during respiratory distress from any cause, but has been mainly documented in patients with chronic obstructive pulmonary disease (COPD) (Sarkar et al., 2019): more than a 5 mm upward movement of the clavicle is associated with severe airflow limitation, reflected by an FEV_1 of 0.6 L or less (Sarkar et al., 2019). The scalenes arise from the transverse processes of the lower cervical vertebra and insert into the first 2 ribs. They contract under increased stress and metabolic demand, expanding the upper rib cage to augment tidal breathing.

Bastir et al. (Bastir et al., 2017) showed that expansion and contraction (kinematics) of the pulmonary and diaphragmatic parts of the thorax differed in their modes of shape change during breathing while the degree of shape change was similar in both compartments. The diaphragmatic part exhibited expansion more than the pulmonary part, therefore the upper thorax has to undergo greater deformation to expand to the same degree as the lower thorax. This has important implications with regard to respiratory muscles weakened at different times. For example, in ascending paralysis, the lower rib cage is likely to exhibit inward retraction and collapse as the intercostals weaken, while the diaphragm and accessory neck muscles assume increasing inspiratory activity. Thus, variability in regional lung expansion, ventilation-perfusion matching and gas exchange ensue depending on which thoracic muscles are impaired and the time over which these changes evolve (Roussos).

2.5 Abdominal Muscles

Four primary abdominal muscles augment expiratory force—the rectus abdominus, transverse abdominus, internal abdominal oblique and external abdominal oblique (Welch et al., 2019; Roussos). They increase intraabdominal pressure by pulling the abdominal wall inwards and displacing the diaphragm up into the thoracic cavity. In addition they lower the ribs, pulling them medially thereby deflating the ribcage, key during forced expiration such as coughing.

Abdominal muscles indirectly aid with inspiration. They compress the lungs to below their normal end-expiratory volume, storing elastic energy in the chest wall during expiration, facilitating passive inspiration. This action increases the curvature of the diaphragm and its force generation (based on Laplace's Law) (Roussos).

2.6 Upper Airway Dilator Muscles

Dilator muscles of the pharynx and larynx facilitate air flow by minimizing upper airway resistance during inspiration, an important function compromised in patients with bulbar dysfunction, and more so in individuals with obstructive sleep apnea (Oliven et al., 2018). Airway patency is maintained by coordinated co-activation of inspiratory and upper airway muscles, including the genioglossus, and preventing collapse of pharyngeal soft tissues (Van de Graaff et al., 1984; Kobayashi et al., 1996; Malhotra et al., 2000; Eckert et al., 2007; Fauroux and Khirani, 2014; Oliven et al., 2018). Posterior movement of the hyoid during inspiration can increase airway resistance and limit airflow, especially during sleep, an action opposed by contraction of the sternothyroid, thyrohyoid, sternohyoid, and geniohyoid muscles to preserve upper airway patency (Van de Graaff et al., 1984).

3 REDUCTIONS IN RESPIRATORY SYSTEM COMPLIANCE AND VOLUMES

Patients with NMD exhibit reduced vital capacity (Fauroux and Khirani, 2014; Lo Mauro and Aliverti, 2016) and respiratory (lung + chest wall) compliance (increase in respiratory elastance) (**Figure 3**), in part due to alveolar collapse and, when present, scoliosis. Recurrent aspiration contributes to further reduction in

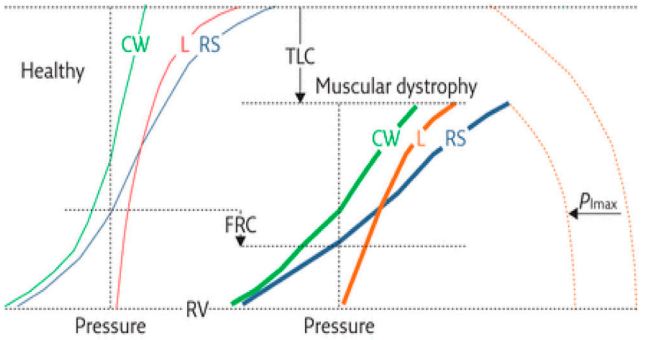

FIGURE 3 | Respiratory mechanics in individual with muscular dystrophy compared to that of a healthy individual. Shown are the presumed pressure–volume curves of the respiratory system (RS, blue curves) and its two components, the chest wall (CW, green curves) and lung (L, red curves), for healthy subjects (thin curves on the left panel) and patients with muscular dystrophy (thick curves on the right panel). The maximal inspiratory pressure (PImax) is also shown (dashed curves). Key features include 1) decreased total lung capacity (TLC); 2) decreased compliance of chest wall (CCW), lungs (CL) and respiratory system, a consequence of reduced thoracic volume (slopes of the corresponding pressure–volume curves); 3) reduced PImax; 4) decreased inspiratory capacity (IC = TLC–FRC); and 5) reduced expiratory reserve volume (ERV = FRC–RV). Functional residual capacity (FRC) may be reduced or even normal. Residual volume (RV) is usually preserved. PImax represents the force of inspiratory muscles, while the volume variations are the resulting action of their contraction. The compliance of the respiratory system is decreased because of **(A)** lung atelectasis and fibrosis, the former a consequence of hypoventilation, and the latter from recurrent aspirations; and **(B)** scoliosis, induced by assymmetric involvement of trunk muscles. Figure caption modified from (Lo Mauro and Aliverti, 2016).

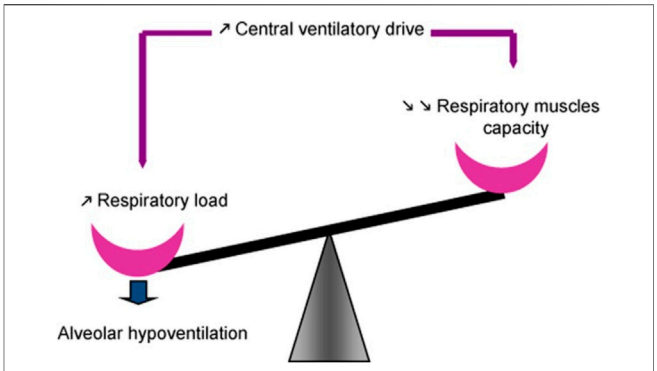

FIGURE 4 | Maintenance of spontaneous ventilation depends on balance between function of the respiratory muscles on one side and the respiratory load, determined by respiratory mechanics, on the other. Central respiratory drive is regulated such that work of breathing is minimized by adjusting tidal volume and respiratory rate to compensate for the load. Alveolar hypoventilation ensues when the respiratory load exceeds the ability of the central drive and respiratory muscles to maintain adequate gas exchange, often associated with respiratory muscle fatigue. From (Fauroux and Khirani, 2014).

lung compliance with loss of aerated alveolar volume, as seen with acute respiratory distress syndrome, and a serious complication of aspiration (Zaloga, 2002). Upper airway collapse from bulbar dysfunction further increases resistance to breathing (Benditt, 2019). Such changes in compliance contribute to increase in work of breathing. Work of breathing is kept at the lowest level by adjusting tidal volume and respiratory rate to compensate for the load. Alveolar hypoventilation results from the respiratory load exceeding the ability of the central drive and respiratory muscles to maintain adequate gas exchange (**Figure 4**).

In supine posture gravitational pressure from abdominal contents impairs tidal excursions of the diaphragm. In most NMDs a decrease in VC upon assuming supine posture (by 25% or more) is a sensitive index of diaphragmatic weakness (Fromageot et al., 2001; Lechtzin et al., 2002; Prigent et al., 2012; Chen et al., 2013). In this connection, in the upright position, application of an abdominal wrap below the lower rib margin displaces the diaphragm cephalad, lengthening its fibers, increasing its force generation and reducing dyspnea, a technique widely adopted by poliomyelitis patients during the epidemic of the 1940s and 1950s to improve activities of daily living and quality of life (Bach, 2017). Individuals with high cervical cord injury and others with weak abdominal musculature also find abdominal wraps to be helpful with breathing (Goldman et al., 1986; McCool et al., 1986; Scott et al., 1993; Berlowitz et al., 2016). Their VC increases as diaphragmatic fibers lengthen with increase in force generation and reversal of platypnea (Fugl-Meyer and Grimby, 1984; Baydur et al., 2001; Terson de Paleville et al., 2014). This finding is in line with studies in able-bodied individuals in which maximal force generation of the transdiaphragmatic pressure (Pdi) decreases as lung volume increases (Beck et al., 1998) and would explain the increase in diaphragmatic strength in the supine spinal cord-injured patient.

4 EFFECTS OF OBESITY

Similar to able-bodied people, individuals with NMD are at risk for developing chronic diseases resulting from obesity and a sedentary lifestyle. Aitkens et al. (Aitkens et al., 2005) found that 55% of their NMD patients met criteria for metabolic syndrome. Bauman et al. (Bauman et al., 1992) determined that cardiovascular disease was the leading cause of death in individuals with spinal cord injury and occurred at a younger age than in able-bodied persons.

Changes in respiratory mechanics occurring in NMD are augmented with obesity. Oxygen cost and work of breathing are increased to overcome respiratory resistance or inertance (Dempsey et al., 1966; Sharp et al., 1986; Kress et al., 1999). Despite the increase in gravitational load of the chest wall in the supine position, functional residual capacity (FRC) does not fall below seated values in obese subjects with reduced FRC when seated. In supine position inspiratory muscle activity maintains dynamic hyperinflation above relaxation volume presumably because of greater muscle length and force generation (Yap et al., 1995).

In a retrospective study of 34 patients with Duchenne muscular dystrophy (DMD, mean age 13.7 years) Chew et al. (Chew et al., 2016) found that BMI was positively related to FVC, contrary to what one might expect in obese individuals (Sharp

et al., 1964; Thomas et al., 1989; Salome et al., 2010). The observed association may have been the result of corticosteroid therapy resulting in greater muscle mass and strength, although the study did not take into account changes in muscle and fat mass, edema or growth, also known to occur in DMD (Durnin and Rahaman, 1967; Stanbury and Graham, 1998; Pessolano et al., 2003).

5 CONTROL OF VENTILATION AND ITS RELATION TO RESPIRATORY LOAD COMPENSATION

The link between the nervous system and respiratory muscles are the motor neurons located in the brain stem. The ventral medulla regulates exhalation while the dorsal medulla is responsible for inhalation. Communication between the two parts of the medulla is through integration of input from peripheral and central respiratory muscles to generate a cyclical respiratory rhythm. The pontine group allows for regulation of the medullary signals to ensure smooth inspiration and expiration transition. Central chemoreceptors located within the medulla and retrotrapezoid nucleus to sense pH changes related to carbon dioxide concentrations in the cerebrospinal fluid (Panitch, 2009). Peripheral chemoreceptors (carotid and aortic bodies) respond primarily to changes in arterial oxygen tension.

As early as the poliomyelitis epidemic (Whittenberger and Sarnoff, 1950; Plum and Swanson, 1958), changes in central control of ventilation have been described in various NMDs (Kilburn et al., 1959; Carroll et al., 1976; Rosenow and Engel, 1978a; Borel et al., 1993; Rialp et al., 2013). A blunting of the ventilatory response to hypercapnia implies a decrease in chemoreceptor sensitivity; however, in the presence of diffuse muscle weakness and abnormal respiratory mechanics, determining the exact contribution of the medullary motoneurons to a decrease in ventilatory response can be a challenge (Borel et al., 1993; Rialp et al., 2013). Measurement of occlusion pressure ($P_{0.1}$) provides a more reliable assessment of central drive as it is not influenced by change in lung volume and flow resistance (Whitelaw et al., 1975). Indeed, some studies have demonstrated normal or increased $P_{0.1}$ (McCool et al., 1988; Baydur, 1991), indicating that central drive is intact. In many cases, sleep-disordered breathing contributes to nocturnal hypoventilation even as the patient is able to maintain normal daytime gas exchange (Aboussouan, 2015; Fermin et al., 2016). An inspiratory vital capacity of less than 60% predicts sleep disordered breathing in children and adolescents with NMD [59 Fermin]. Overnight polysomnography confirms presence of sleep-disordered breathing. Sleep abnormalities of central origin can be seen in myotonic dystrophy, which may be separate from the muscular deficit. We refer the reader to excellent reviews on sleep-disordered breathing for in-depth discussions of their diagnosis and management (Aboussouan, 2015; Fermin et al., 2016).

Axen (Axen, 1982) described variable changes in ventilatory control (tidal volume and inspiratory duration) in cervical cord-injured men in response to elastic and resistive loads, assuming identical respiratory muscle pressure (Pmus) wave forms in the unloaded and loaded states. Afferent pathways from the mouth, lung, and/or diaphragm modulated the phrenic discharge during the first loaded breath. In chest wall disorders such as kyphoscoliosis (KS), respiratory elastance and resistance are increased, and breathing pattern is rapid and shallow, resulting in defense of tidal volume (Vt) in the face of inspiratory resistive loading. Baydur and Carlson (Baydur and Carlson, 1996) computed passive elastance (Ers) and active elastance and resistance (E′rs and R′rs, respectively) in anesthetized patients according to previously described techniques (Behrakis et al., 1983; Baydur et al., 1989). The difference between passive and active respiratory elastance represents changes in thoracic mechanical properties (stiffening) related to chest wall distortion during added loads. With resistive loading, driving pressure and inspiratory time were prolonged compared to healthy subjects, while percent reduction in Vt and minute ventilation was less in KS. Increased intrinsic impedance, Pmus, and differences in changes in neural timing in anesthetized kyphoscoliotics contributed to modestly greater Vt defense, compared to that of anesthetized subjects free of cardiorespiratory disease.

5.1 Elastic Load Compensation

If someone were to hold a 20-lb weight with arm outstretched and had a 1-lb weight added to the load, they are not likely to feel the added weight as afferent sensory receptors adapt to the high muscle tension; by contrast, they are more likely to feel the addition of a 10-lb weight which noticeably adds to the tension. A similar analogy can be applied in individuals with increased elastic respiratory loads. To evaluate the effects of abnormal respiratory mechanics and neuromuscular drive on the various components of elastic load compensation, Baydur et al. (Baydur et al., 1989) studied anesthetized patients with KS whose mean passive and active respiratory elastance, active respiratory resistance, and peak inspiratory occlusion pressure were, respectively, 89%, 84%, 100%, and 37% greater, and inspiratory duration (Ti) 13% less than corresponding values in anesthetized control subjects. The increased intrinsic elastance and resistance and decreased Ti contributed to Vt defense in KS in the absence of vagal modulation. Characteristics of elastic load compensation in anesthetized KS patients are nevertheless similar to those of anesthetized normal subjects.

5.2 Post-Inspiratory Diaphragmatic Braking Activity

The diaphragm has been shown to exhibit post-inspiratory activity during passive expiration (pliometric activity) (Muller et al., 1979; Muller et al., 1980; Zin et al., 1983; Baydur, 1992; Easton et al., 1999) resulting in preservation of lung volume. Such activity may be of benefit in patients with chest wall disorders in preventing airway collapse (Muller et al., 1980; Baydur, 1992). Absence of pliometric activity may result in reduction in lung volume and atelectasis.

6 DYSPNEA IN PATIENTS WITH NEUROMUSCULAR DISEASE: CONCEPT OF AIR HUNGER VS. PERCEPTION OF RESPIRATORY WORK AND EFFORT

The sensation of an urge to breathe is referred to as "air hunger", for example, when it develops during a long breath hold (Banzett et al., 2021) it occurs when urgent homeostatic needs to maintain gas exchange are not met. Stimuli that increase air hunger include hypercapnia, hypoxia, exercise, and acidosis; tidal expansion of the lungs (spontaneous or assisted) reduces air hunger. As such, it is not affected by respiratory muscle activity and is thought to be regulated by central chemoreceptors in the brain stem (Banzett et al., 1990). By contrast, when respiratory muscle fatigue or an increase in breathing load (such as occurs with pneumonia) calls for increase in muscle contraction, a sensation of increased work or effort is described; it likely arises from respiratory muscle afferents or from the brainstem or cerebral cortex.

A striking example of these events is that of a chronically over-ventilated muscular dystrophy patient whose $PaCO_2$ has gradually decreased to the 20–30 mm Hg range (a common issue as patients feels better with sensation of increase in chest wall expansion with increase in Vt. Patients receiving nocturnal ventilation often maintain a lower PCO_2 during the following day. Possible explanations include: 1) Reducing daytime work of breathing by resting respiratory muscles at night, and 2) CO_2 elimination at night promotes bicarbonate excretion with a lower set point for ventilatory control as metabolic alkalosis is corrected. Allowing the PCO_2 to increase by intermittently reducing the delivered Vt (even by 30–50 ml at a time) or respiratory rate become uncomfortable for the patient, increasing demand that ventilator settings be restored to their original state (personal observation). These symptoms suggest a re-set of the threshold for CO_2 sensitivity such that even a slight rise in PCO_2 induces air hunger despite (or because of) the chronic hypocapnia. Coughing induced by airway irritation can aggravate the sensation of air hunger and might be vagally mediated but central mechanisms cannot be ruled out (Nishino et al., 2008).

By contrast, individuals will describe a sensation of feeling "hard to breathe" when experiencing a respiratory infection because of alterations in respiratory compliance and resistance (with little or no change in blood gases). Changing ventilator settings by increasing the Vt or respiratory rate relieves their symptoms, but at the cost of inducing a chronic respiratory alkalosis. The resulting reduction in plasma bicarbonate stores increases vulnerability to metabolic acidosis resulting from sepsis, shock and other causes.

7 RESPIRATORY MUSCLE FATIGUE

Respiratory muscle fatigue is defined by loss in capacity for developing force against a constant load (Roussos and Koutsoukou, 2003). The higher the diaphragmatic force generation is as a function of maximal pressure the diaphragm can sustain, the greater the chance the diaphragm is likely to fatigue. Multiple factors contribute depending on how the NMD affects the central nervous system, transmission of signals between the CNS and muscle (central fatigue) or even the muscle itself (peripheral fatigue). Central muscle fatigue results from a deficit in the capacity to recruit all muscle units, while peripheral fatigue is due to a failure of muscle fibers to respond maximally during full activation (Edwards, 1979). Weakening of respiratory muscles produces paradoxical breathing (asynchronous movement) between abdomen and ribcage (Troyer and Wilson, 2016). As the diaphragm fatigues, inspiratory action assumed by the accessory muscles of the neck results in inward retraction of the ribcage and outward displacement of the abdominal wall (Benditt, 2019).

Measurement of transdiaphragmatic pressure (Pdi) (using esophageal and gastric balloons) is a more precise means of recording diaphragmatic force generation (Pdi) and endurance (Roussos et al., 1979a; Bellemare and Grassino, 1982). It is, however, invasive and requires coaching for naïve individuals, and therefore primarily used in research. The individual is asked to breathe through a series of inspiratory flow resistors to achieve a target pressure on an oscilloscope or computer screen. From these measurements, the tension-time index [TTdi = (Pdi/Pdimax) (Ti/Ttot), where Ti is the inspiratory time and Ttot is the duration of respiratory cycle] can be computed. TTdi values of >0.18 are associated with respiratory muscle fatigue and reduced endurance (Roussos et al., 1979a; Bellemare and Grassino, 1982). The technique is capable of producing inspiratory pressures generated by rib cage muscles in the absence of diaphragmatic contribution. A potential clinical application of Pdi in individuals with NMD is to determine which inspiratory muscles contribute to respiratory insufficiency and cough impairment (as a result of loss of lung volume and elastic recoil): Alternating amplitude of Pdi and gastric pressure (Pga) indicates recruitment and derecruitment of different groups of inspiratory muscles (Roussos et al., 1979a).

A non-invasive alternative is to measure the tension-time index of the inspiratory muscles as a whole (TTlim) during mouth breathing without the use of esophageal and gastric balloons (Ramonatxo et al., 1995). An increase in mean inspiratory pressure in relation to the maximal inspiratory pressure produces an increase in TTlim. Another noninvasive tool analogous to the TTdi is the breathing intolerance index (BIT), used to assess the ability of patients with NMD and other conditions to wean off ventilation (Koga et al., 2206). It makes use of the relation of breathing pattern to vital capacity (VC) [(Vt/VC) (Ti/Ttot)]. In this analysis, lung volumes replace respiratory muscle pressures so that the ratios comprising BIT can be affected by lung and chest wall mechanics in addition to respiratory muscle strength. Later, Baydur and Chen (Baydur and Chen, 2013) found BIT in patients with obesity (a chest wall disorder) tended to be higher than in healthy controls in contrast to patients with chronic obstructive pulmonary disease.

Sarmento and colleagues (Sarmento et al., 2021) found that *1)* inspiratory rib cage muscles (sternocleidomastoids, scalenes and parasternals) differed in their responses to fatigue and recovery, as reflected by changes in spectral surface EMG variables, *2)* loss of mechanical power in rib cage muscles resulted from reduced shortening velocity, and *3)* relaxation properties recovered better

from fatigue than do contractile characteristics. Recovery of fatigue varied, with median frequency returning to pre-fatigue values faster than the high/low (H/L) frequency spectrum suggesting that mechanisms of fatigue differed depending on the specific inspiratory muscle. Furthermore, changes in relaxation rates were strongly associated with the H/L frequency spectrum and predicted inspiratory ribcage muscle recovery. Again, the rate of progression of respiratory impairment (or stabilization) will vary depending on which groups of muscles are involved and their characteristics of fatigability. In addition to twitch characteristics assessed by EMG (Bellemare and Roussos, 1995), muscle fatigue characteristics may be presaged by periodic analysis of their H/L frequency spectrum.

8 PHYSIOLOGY OF COUGH: NEUROMECHANICAL COUPLING

Patients with NMD experience difficulty clearing airway secretions due to ineffective cough (Perrin et al., 2204; Yang and Finkel, 2010; Sahni and Wolfe, 2018; Allen, 2010). For an effective cough, one needs to take a deep breath, while the glottis closes to increase intrathoracic pressure, followed by its opening explosively in conjunction with abdominal contraction to expel air. Peak cough flows below 160 L/min are considered ineffective (Bach, 2017). Glottic and bulbar dysfunction lead to accumulation of saliva in the valleculae and pyriform sinuses (Silbergleit et al., 1991; Sonies and Dalakas, 1991). As a result, ineffective airway clearance predispose to recurrent pneumonia a major cause of mortality and morbidity (Chatwin et al., 2018).

The cough reflex is chiefly mediated by vagal afferent nerve fibers innervating the larynx, large airways and parenchyma; its components comprise both myelinated (rapidly and slowly adapting receptors) and unmyelinated rapidly adapting and noniceptive pulmonary fiber (C-fiber) receptors (Widdicombe, 1954; Paintal et al., 1986). The latter fibers assume a major role in cough and related reflexes. Deep inspiration stimulates airway irritant receptors, therefore an impaired inspiratory effort will diminish triggers to cough as well as the effort. Other neural pathways regulating the cough reflex include the glossopharyngeal and phrenic nerves which have many sensory as well as motor fibers. Efferent pathways include (again) the *1)* vagus (motor nerve for the muscles of the pharynx and larynx); *2)* the spinal motor nerves of which the thoracic supply the intercostal muscles and the lumbar nerves the abdominal muscles; and *3)* the trigeminal, facial, hypoglossal and accessory nerves innervating the upper airway and accessory muscles, called into play during cough (Bouros and Green, 1971).

Patients with spinal cord injury exhibit respiratory muscle dysfunction to the extent reflected by the level of cord injury (Ledsome and Sharp, 1981; Fugl-Meyer and Grimby, 1984; Baydur et al., 2001). High cord injuries leave intact residual action by the diaphragm and accessory muscles with cough generation dependent on high lung elastic recoil. Even with such injuries, however, active expiration in quadriplegic individuals can be augmented by contraction of the clavicular portion of the pectoralis major (innervated by the 5th through 7th cervical segments) which displaces the manubrium and upper ribs downward, contracting the upper rib cage (De Troyer et al., 1986), an important consideration for cough generation. By contrast, the lower rib cage expanded, at least in early inspiration, as a result of increase in abdominal pressure. Estenne et al. (Estenne et al., 1994) later showed that despite weak expiratory muscles, quadriplegic individuals were able to enhance their cough ability as a result of dynamic compression of tracheal and large airways enabling marked increase in expiratory flow, even though peak pleural pressures were 74–92% less than in normal subjects.

9 RESPIRATORY FAILURE

Respiratory failure develops from impairment of ventilation and gas exchange due to lung or chest wall dysfunction. Increases in respiratory elastance and resistance due to lung volume reduction and thoracic cage distortion lead to increase in work of breathing and respiratory muscle fatigue. Typically, arterial oxygen tensions lower than 8.0 kPa and arterial carbon dioxide tensions above 6.0 kPa define respiratory failure. These values should serve as guides to identifying respiratory failure, not as rigid cut-offs (Roussos and Koutsoukou, 2003; Welch et al., 2019).

There are two types of respiratory failure—hypoxemia with and without hypercapnia (Roussos and Koutsoukou, 2003). The former is a result of inadequate ventilation due to reduced neural drive and muscular power as occurs with progressive NMDs. Hypercapnic failure reflects increase in physiological dead space, manifested during rapid, shallowing breathing due to abnormal chest wall mechanics (Welch et al., 2019). Hypoxemia without hypercapnia results from impaired oxygen transfer, a consequence of atelectasis and chest wall distortion (Campbell, 1965; Welch et al., 2019). Microatelectasis results in an increase in the alveolar-arterial oxygen difference (AaDO2), reflected by a normal PaO_2, sometimes in conjunction with a reduced $PaCO_2$ while breathing room air. In individuals with sleep apnea, loss of upper airway muscle tone and collapse coupled with weakening thoracic cage muscles lead to impaired gas exchange, exaggerated during REM sleep (Benditt, 2019). As sleep disordered breathing worsens, hypercapnia persists throughout day and night.

Acute decompensation may result from aspiration due to bulbar dysfunction-induced dysphagia or gastroesophageal reflux (Allen, 2010; Wijdicks, 2017; Welch et al., 2019), requiring assisted ventilation. In this connection, long-term ventilatory support can result in further weakening of the diaphragm due to muscle atrophy (Roussos et al., 1979b; Jaber et al., 2011) and passive increase in end-expiratory volume by application of positive end-expiratory pressure (PEEP) (Jansen et al., 2021).

10 EVALUATION OF RESPIRATORY MUSCLE FUNCTION AND PHYSIOLOGIC CHANGES IN NMD

10.1 Electrophysiologic Techniques

Relating the electrical activity of the diaphragm to its force generation during quiet breathing or maximal respiratory efforts is used to assess diaphragmatic weakness and its

propensity to fatigue under conditions of increased load (Bellemare and Grassino, 1982; Bellemare and Roussos, 1995; Sarmento et al., 2021). Assessing the ratio of diaphragm compound muscle action potential (CMAP) amplitude to transdiaphragmatic twitch pressure is also used to distinguish between defects in neuromuscular transmission defects (when both quantities decrease) and defects in muscle contractility (when twitch pressure is decreased in presence of a normal CMAP) (Aldrich et al., 1986).

10.2 Respiratory Pressures

Traditionally, respiratory muscle strength has been measured with maximal inspiratory and expiratory mouth pressures (Black and Hyatt, 1971; Leech et al., 1983; Vincken et al., 1987). Padkao and Boonla (Padkao and Boonla, 2020) showed that Pimax and Pemax were significantly related to middle and lower thoracic wall expansion, suggesting that respiratory muscle strength was more closely associated with chest wall expansion and diaphragmatic descent than with expiratory muscle strength. If thoracic cage muscles are weakened by disease, rib cage expansion is impaired and the rib cage fails to expand, these maneuvers are, however, difficult to perform by patients with weak muscles, as they require cooperation and coordination, Pimax (MIP) and Pemax (MEP) are ideally generated at residual volume and total capacity, respectively, and need to be maintained for 4 s, a challenge even for able-bodied individuals (Aldrich and Spiro, 1995).

As alluded to earlier, respiratory impairment depends on the pattern of muscle and/or nerve involvement and on the rate of progression of disease. Respiratory muscles are often involved in patients with proximal limb weakness, as in certain myopathies (Rosenow and Engel, 1978b; Braun et al., 1983; Mellies et al., 2005; Bi et al., 2021). Braun et al. (Braun et al., 1983) studied 53 patients with proximal myopathy (16 with lung disease). Hypercapnia was inversely related to VC (which, however, could be as high as 55% predicted), as well as to respiratory muscle strength (RMS, average of Pimax and Pemax). The latter relationship (an occlusive maneuver devoid of airflow and with negligible change in lung volume) reflected respiratory muscle weakness more than a decrease in VC which is affected by lung disease. Carbon dioxide retention did not occur until RMS was less than 50% predicted (Braun et al., 1983).

More recently, measurement of sniff nasal inspiratory pressures (SNIP) have been found to be better tolerated and reproducible (Ti and Fit Ting, 1999; Sarmento et al., 2021). Nasal pressure is measured in an occluded nostril as the patient sniffs through the opposite nasal passage and is closely associated with and easier to perform than Pimax (Laroche et al., 1988; Ti and Fit Ting, 1999) and FVC (Nicot et al., 2006) measurements. In a study of 61 patients with NMD and COPD, recording of esophageal pressure during a maximal sniff was found to be useful in assessing inspiratory muscle strength and easier to perform than the MIP (Sarmento et al., 2021). Many patients had normal sniff Pes despite low MIPs, suggesting that performing MIP was challenging because of dyspnea and weakness of facial muscles with difficulty in maintaining static pressures.

Transdiaphragmatic pressure (Pdi) can be recorded while breathing spontaneously or during maximal inspiratory maneuvers, such as a sniff (Perrin et al., 2204; Yang and Finkel, 2010). It can also be measured during magnetic stimulation of the phrenic nerve and has the advantage of greater accuracy for measuring diaphragm strength, especially in individuals with airflow limitation in whom airway opening pressure or SNIP would not accurately reflect esophageal pressure because of reduced lung elastic recoil and gas decompression. Measurement of Pdi and its role in the evaluation of diaphragmatic fatigue is described in detail in **section 7**.

10.3 Spirometry and Lung Volumes

Spirometry is essential in the diagnosis and management of pulmonary diseases and can be performed in children as young as 6 years old (**Table 1**) (Steier et al., 2007; Sharma, 2009; Caruso et al., 2015; Chiang et al., 2018). It facilitates assessment of functional capacity, following the course of illness, and response to management.

The forced expiratory volume in one second (FEV_1) and FVC will show different rates of decline, depending on the course of illness. However, the ratio FEV1/FVC remains within normal range (80–100%). Using FEV1, respiratory health can be graded from mild to very severe: mild >70% predicted; moderate 60–69%; moderately severe 50–59%; severe ranging 35–49%; and very severe <35% (Sahni and Wolfe, 2018; Allen, 2010). **Table 1** lists tests useful for evaluating respiratory function in patients with NMD and chest wall disorders. In a study of 60 patients with Duchenne muscular dystrophy, FVC and peak expiratory flow (PEF or Pemax) decreased linearly by 5 percent per year (Mayer et al., 2015). An FVC of <40% predicted was associated with a PaCO2 ≥45 mm Hg and a base excess of >4 mmol/L. Some have reported the value of determining the plateau VC which correlates with severity of Duchenne dystrophy (DMD) and risk of developing severe scoliosis (Welch et al., 2019). Following the VC plateau may indicate the best point to initiate air stacking to maximum lung insufflations (Benditt, 2019). Inspiratory muscle weakness is detected by a 20% or more reduction in VC upon assuming supine posture (Fromageot et al., 2001; Lechtzin et al., 2002; Prigent et al., 2012; Chen et al., 2013) and indicates need for assisted ventilation (Chen et al., 2013) (**Figure 5**). The reduction in lung volume also results in a decrease in maximal transdiaphragmatic sniff pressure (Pdimax sniff) (**Figure 6**). In general, assisted ventilation is indicated for patients whose VC has decreased below 1 L or 30% predicted (Steier et al., 2007; Sharma, 2009; Mayer et al., 2015; Chiang et al., 2018). Decline in FVC can be variable in patients with amyotrophic lateral sclerosis (ALS) (Ackrivo et al., 2019a), indicating phenotypes with differing prognostic implications (Elamin et al., 2015; Ackrivo et al., 2019b) (**Figure 7**).

Lung volume subdivisions can be measured using body plethysmography, gas dilution, or washout techniques (**Table 1**). If airflow limitation is suspected, plethysmography is the preferred method to avoid underestimating volume of trapped gas (Sharma, 2009; Mayer et al., 2015; Chiang et al., 2018). The method distinguishes air trapping from effects of obesity; both conditions result in reduction of expiratory reserve volume, while inspiratory capacity is reduced with air trapping but is increased with obesity. In advanced stages, preferential weakening of abdominal muscles with decrease in maximal

TABLE 1 | Respiratory function tests commonly used to evaluate individuals with neuromuscular disorders.

Lung Volumes
Total lung capacity (TLC)
Residual volume (RV)
Spirometry
Peak flow rate (PFR)
Cough peak flow (CPF)
Forced vital capacity (FVC) (preferably in seated and supine positions)
Forced expiratory volume in 1 s (FEV_1)
Maximum insufflation capacity (MIC)
Respiratory muscle strength
Maximal expiratory pressure (MEP) (preferably in seated and supine positions)
Maximal inspiratory pressure (MIP) (preferably in seated and supine positions)
Sniff test (SNIP)
Gas exchange
Oxyhemoglobin saturation by pulse oximetry
Capnography: end-tidal CO_2 (PetCO2) measurement
Arterial or venous blood gas profile

Modified from (Sharma, 2009).

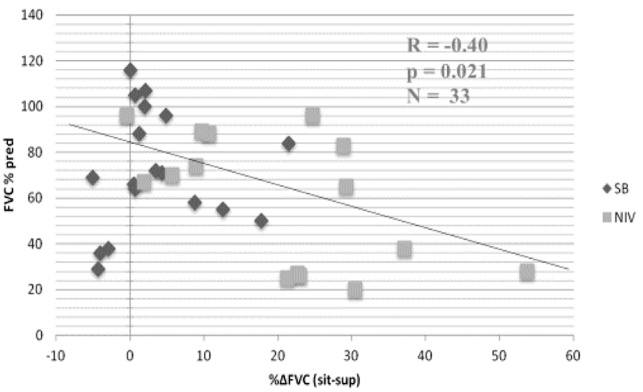

FIGURE 5 | Relationship between % change in forced vital capacity (FVC) from seated (sit) to supine (sup) posture and baseline FVC in seated position in patients with neuromuscular disease (FVCsit, % predicted). Black diamonds, spontaneous breathing (SB); grey squares, noninvasive ventilation (NIV). Patients with greater than 20% decrease in FVC when supine required NIV. From (Chen et al., 2013).

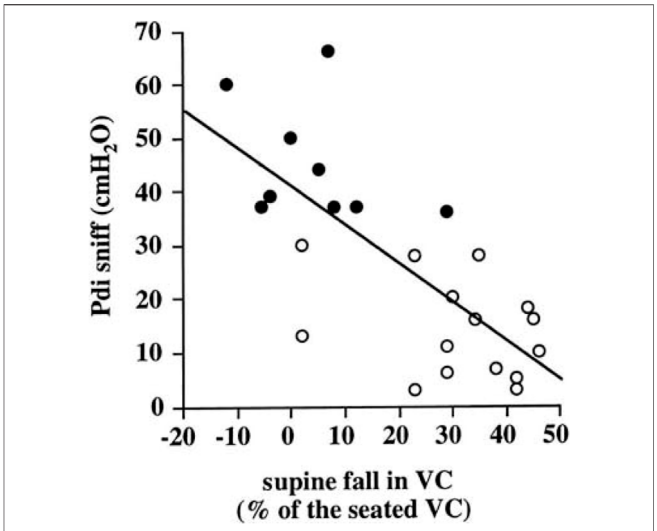

FIGURE 6 | Relation between transdiaphragmatic sniff pressure (Pdi sniff) and supine fall in VC. Open symbols indicate patients with paradoxical diaphragmatic motion and closed symbols indicate patients without paradoxical diaphragmatic motion. From (Fromageot et al., 2001).

expiratory pressure (Pemax) may explain the preservation or increase in residual volume. Spasticity of rib cage muscles prevents outward recoil of the chest wall from being reduced further helping to maintain FRC and preserve residual volume (RV). Patients may experience difficulty in performing panting maneuvers in the body box because of bulbar weakness. Excessive upper airway and cheek compliance may also result in underestimation of FRC and RV (Jaeger, 1982).

10.4 Measurement of Flow Limitation and Airway Resistance--Old and New Techniques

The presence of intrathoracic airflow limitation has been determined using the negative expiratory pressure (NEP) technique (**Figure 8**) in patients with NMDs (Baydur, 2013). It avoids technical challenges posed by spirometry such as lung history and inhomogeneity, forced expiratory maneuvers, and the speed of forced expiration, all influenced by viscoelastic properties of the lung and chest wall. NEP consists of comparing the tidal expiratory flow during application of gentle negative pressure (about −5 cm H_2O) at the onset of expiration to the immediately preceding tidal expiratory flow. Expiratory flow should increase in healthy individuals while it changes little or not all in airflow limitation. Obese individuals or those with weakened bulbar musculature may exhibit transient decreases in tidal expiratory flow as upper airway soft tissues appose each other during application of NEP (**Figure 8C**). Such patients may be at risk for obstructive apneas during sleep as the upper airway may collapse during inspiratory efforts.

The forced oscillation technique (FOT) or impulse oscillometry (IOS) until recently was employed in infants and young children as a useful alternative to spirometry to assess airway mechanics. More recently, it has been increasingly used to assess respiratory resistance and impedance in older individuals with obstructive and restrictive disorders (Lappas et al., 2016). Even fewer studies have evaluated respiratory mechanics in individuals with neuromuscular disorders. Impedance measurements can be easily obtained as they require little cooperation and no forced respiratory maneuvers. In one study normal respiratory impedance (Xrs) characteristics were found, while respiratory resistance (Rrs) was somewhat higher than those found in normal subjects (Wesseling et al., 1992). Van Noord et al. (Van Noord et al., 1991) found that patients with kyphoscoliosis (TLC 41% based on arm span) exhibited an increase in total respiratory resistance and elastance.

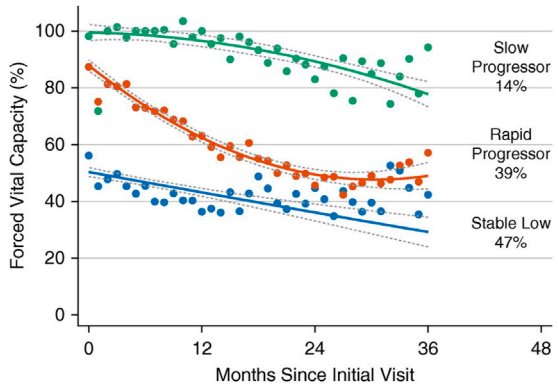

FIGURE 7 | The Penn Comprehensive ALS Center cohort trajectories of forced vital capacity (FVC) percent predicted with 95% confidence intervals. Three groups of patients with amyotrophic lateral sclerosis (ALS) are indicated by slow progressors (green), rapid progressors (red), and stable low (blue). Percentages represent proportion of the cohort with the corresponding group number as the highest predicted posterior probability. From (Ackrivo et al., 2019a).

10.5 Assessment of Control of Ventilation

The measurement of ventilatory drive by occlusion pressure recorded 100 msec after the onset of inspiratory effort ($P_{0.1}$) is a noninvasive method that assesses central drive and has been measured in NMD(Whitelaw et al., 1975; Baydur, 1991). Several factors, however, can alter the relation between P0. 1 and central drive, including presence of dynamic hyperinflation, expiratory muscle activity, chest wall distortion, respiratory muscle weakness, neuromuscular junction blockade, and the shape of the inspiratory pressure waveform (Whitelaw and Derenne, 1993). Central respiratory drive is blunted in patients with hypercapnic respiratory failure associated with NMD. In one study, NMD patients exhibited a hypercapnic drive response of only 30% that of normal subjects (García Río et al., 1994). The difference could be attributed to the reduced sensitivity of the chemoreceptors to chemical CO_2.

10.6 Peak Expiratory and Cough Flows

Peak expiratory flow and cough flow (PEF and PCF, respectively) are used to assess ability to cough and clear airway secretions. Values of PEF less than 160 L/min are associated with increased risk for retained secretions, atelectasis and pneumonia (Bach and Saporito, 1996; Bach et al., 1997; Bach, 2017). Suarez and colleagues (Suárez et al., 2002) found differences between PEF and PCF to be 46%, 43% and 11% in normal subjects, patients with DMD and those with ALS, respectively, the last finding because of poor glottic closure. Determination of PEF and PCF can be applied to estimate respiratory muscle strength if maximal static mouth pressures cannot be performed (Suárez et al., 2002). Patients with PCF below 160 L/min benefit from mechanical in-exsufflation (Bach and Saporito, 1996; Bach et al., 1997; Polkey and Moxham, 2001; Suárez et al., 2002; Miller and Mayer, 2021).

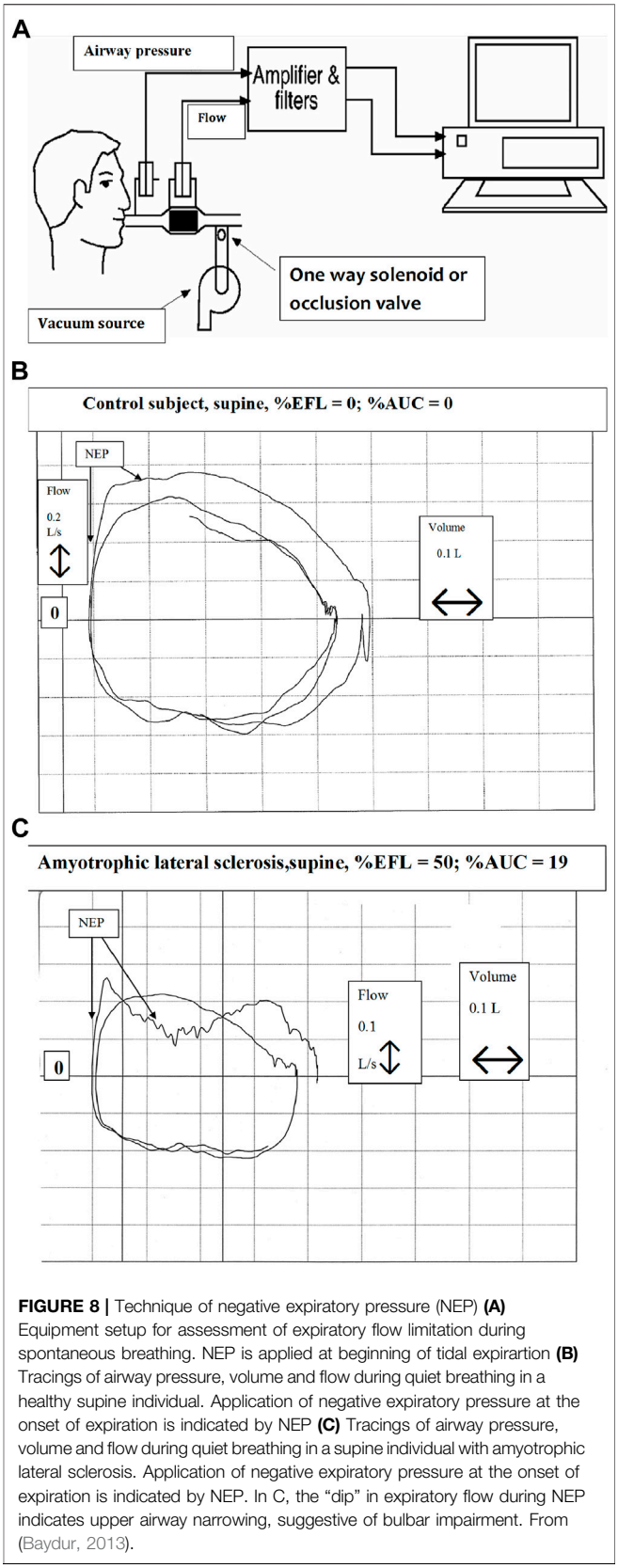

FIGURE 8 | Technique of negative expiratory pressure (NEP) **(A)** Equipment setup for assessment of expiratory flow limitation during spontaneous breathing. NEP is applied at beginning of tidal expirartion **(B)** Tracings of airway pressure, volume and flow during quiet breathing in a healthy supine individual. Application of negative expiratory pressure at the onset of expiration is indicated by NEP **(C)** Tracings of airway pressure, volume and flow during quiet breathing in a supine individual with amyotrophic lateral sclerosis. Application of negative expiratory pressure at the onset of expiration is indicated by NEP. In C, the "dip" in expiratory flow during NEP indicates upper airway narrowing, suggestive of bulbar impairment. From (Baydur, 2013).

10.7 Dyspnea and Sleep Quality

The reporting of dyspnea in patients with NMD may be related to sleep deprivation. Rault et al. (Rault et al., 2020) recently reported that a single night of sleep deprivation in a cohort of 20 healthy subjects reduced respiratory endurance during an inspiratory loading trial, accompanied by an increased sensation of dyspnea. More recently, using a questionnaire survey, the same group showed that the same individuals described a sensation of smothering more often than in a non-sleep-deprived control group (Rault et al., 2021). Thus, sleep deprivation modifies the sensation of dyspnea. While similar studies have yet to be done in individuals with NMD, increased respiratory elastance, and resistance, sleep deprivation should result in an increased sensation of breathlessness.

10.8 Oximetry and Capnography

Oximetry and capnography are useful to monitor gas exchange during studies of sleep disordered breathing. In patients with OSA (a chest wall disorder), oximetry may exhibit a sawtooth pattern during oxygen desaturation (Won et al., 2016) which represents cyclical variation in chemoreceptor response to fluctuations in ventilation or cardiac output (slow circulation time). Oximetry is more reliable when used in junction with capnography. While not as reliable as arterial blood gas analysis (because of changes in pH and CO_2), the latter is invasive and increases work for the technologist and/or nursing. Capnography records CO_2 tensions continuously using an end-tidal sensor or transcutaneous sensor. Disadvantages include expense, need for repeated calibration and susceptibility to external influences. A study simultaneously recording end-tidal and transcutaneous CO_2 found that transcutaneous capnometry registered higher values of CO_2 than the end-tidal method (Won et al., 2016). Using only end-tidal capnometry, the patient would not have been considered hypercapnic and thereby not offered assisted ventilation. Differences in recorded values should be considered when deciding to give a patient end-tidal or transcutaneous capnometry.

11 RECENT AND FUTURE DEVELOPMENTS

A number of recent molecular and physiologic approaches have demonstrated potential roles in further evaluation of respiratory function and treatment in NMD. Their continued role in clinical evaluation and management of neuromuscular-respiratory issues remains to be determined with more extended trials and clinical experience.

11.1 Gene Therapy

Recent developments in gene therapy have markedly improved care for NMDs (Markham et al., 2015; Harada et al., 2020; Oechsel and Cartwright, 2021; Paul et al., 2021). For instance, a new therapy called Poloxamer 188 NF improved respiratory function and measurements in dystrophic mice by targeting cardiomyocytes and improving intracellular calcium concentrations (Vincken et al., 1987). Plethysmographic measurements of dystrophic mice were similar to wild-type mice showing that the effects of muscular dystrophy could be minimized with the Poloxamer. Nusinersen, and onasemnogene aveparvovec (AVCS-101), a gene replacement therapy, have resulted in promising improvements in respiratory function and quality of life (Harada et al., 2020; Oechsel and Cartwright, 2021; Paul et al., 2021).

11.2 Electrical Stimulation of Muscles

In ALS reinnervation of denervated muscle fibers is crucial for preserving motor function as a means of compensating for motor neuron degeneration in long-term survivors. Diaphragm pacing has been advocated as a means of preserving respiratory muscle function, or at least, slowing its deterioration, but remains controversial (DiPALS, writing committee, DiPALS, Study Group Collaborators, 2015; Bermejo et al., 2016). Its mechanism was originally thought to be related to an increase in muscle fiber tone, thereby increasing its contractile properties.

Electrical stimulation of motor nerves leads to a reverse recruitment of motor units, in which larger fibers with less input resistance are activated before the smaller fibers. Recent studies in ALS have shown the opposite effect with an accelerated deterioration in respiratory function and increase in mortality (Bermejo et al., 2016). The RespistimALS group (Bermejo et al., 2016) reported that pacing in individuals with ALS failed to exhibit, over time, a significant increase in maximal amplitude of motor unit potentials (MUPs). These patients eventually required noninvasive ventilation and experienced decreased survival. By contrast, those who did not receive muscle stimulation showed a progressive increase in MUPs over time. Because efficient reinnervation leads to motor unit enlargement with an increase in muscle fiber content of surviving units, the authors concluded that the absence of increase in MUP amplitude over time in the active stimulation group supported the concept of a pacing-induced defective reinnervation.

In contrast to directly stimulating the muscle, the phrenic nerve can also be stimulated in cases of muscle deterioration to strengthen the diaphragm. However, the efficacy of this technique is disputed by some. In a study assessing the effects of phrenic nerve stimulation in 13 patients with myasthenia gravis, Mier et al. (Mier et al., 1992) demonstrated absence of change in diaphragmatic action potentials and even a reduction in 5 of the patients' action potentials. A study testing phrenic nerve stimulation in humans with ALS was terminated early because of an excessive mortality rate and complications such as pneumothorax and acute respiratory failure occurring in the test group (Gonzalez-Bermejo et al., 2016).

11.3 Magnetic Stimulation of Respiratory Muscles

Contrary to electrical stimulation, magnetic stimulation is more of a diagnostic tool. Through different positions and placements of electrodes, the phrenic nerve can be stimulated by cervical, anterior pre-sternal and unilateral/bilateral anterolateral magnetic stimulation, and CMAP can be recorded (Man et al., 2004). These assessments indicate which parts of the diaphragm

would benefit from rehabilitation and prognosticate the muscle's recovery.

11.4 Imaging of Respiratory Muscles

Ultrasound imaging of the diaphragm is a non-invasive means of measuring diaphragm thickness and inspiratory thickening because an increase in diaphragm thickness leads to inspiratory strength (Roussos et al., 1979b; Boussuges et al., 2021). When applied by experienced users it provides reproducible results, with good inter- and intra-observer reliability (Cohn et al., 1997; Schepens et al., 2015). The thickness of the diaphragm can be determined in more than 85% of measurements, with a low coefficient of variation (0.09–0.14). Goligher et al. (Roussos et al., 1979b) assessed the validity of ultrasound in assessing diaphragm thickness and function in patients on mechanical ventilation. They found that only the right hemidiaphragm thickness is able to be measured, not the left, to help track the patient's status while on mechanical ventilation unless the patent had a unilateral injury. Thickness of the right hemidiaphragm is also related to the degree of contractile activation of muscle during ventilation, so this technique can be used to assess diaphragm atrophy (Roussos et al., 1979b). The technique has the potential to be applied in NMD to assess changes in diaphragm thickness and motion over time, but requires skill and experience. It would be best applied in individuals who have not received assisted ventilation in order to monitor any progressive muscle loss from the NMD itself.

More recently kinematic analysis of the diaphragm from three-dimensional magnetic resonance images has been able to assess diaphragm mechanics (Mogalle et al., 2016) and is more sensitive than lung function testing in detecting weakness of the muscle; individuals with Pompé disease compensate for impaired diaphragm function with increase in chest wall movement.

11.5 Evaluation of Respiratory Mechanics During Mechanical Ventilation in NMD and Chest Wall Disorders

An interesting concept to consider is the phenomenon of airway opening pressure (AOP) during inspiration from FRC to total lung capacity (TLC) in individuals with restrictive respiratory disorders such as NMD and chest wall deformities receiving mechanical ventilation. As noted above, such patients may exhibit expiratory flow limitation (EFL) (Baydur, 2013). In such situations, it is possible to record the pressure-volume relationships to assess respiratory compliance and the AOP to facilitate adjustment of tidal volume and positive end-expiratory pressure (PEEP) and optimize gas exchange.

The question arises as to the relation of AOP to expiratory flow limitation (EFL): do they correspond? An analogy of this feature can be made with acute respiratory distress syndrome (ARDS). Using the airway occlusion technique, Guerin et al. (Guérin et al., 2020) showed that in semi-recumbent ARDS patients at PEEP 5 cm H_2O, EFL and AOP did not occur simultaneously. While most patients with EFL exhibited an AOP, nearly half of patients with AOP did not have EFL. The additional tissue resistance measured at the end of inspiration was higher in patients with EFL than in those without EFL but did not differ amongst patients with and without AOP. Meanwhile, the interrupter resistance (of the conducting airways) did not differ between EFL and non-EFL patients, suggesting that EFL occurred in small airways. Thus, applying increasing levels of PEEP results in higher AOP without abolishing EFL. In addition, lung dynamic elastance was higher in FL than in non-FL patients and had a good accuracy for detecting EFL.

While the histopathologic features of ARDS are different from that of the microatelectatic changes seen with thoracic cage disorders, the lung mechanical properties of the latter conditions should be similar to that of ARDS with increases in respiratory resistance and elastance. If the curve depicting the lung transpulmonary pressure-volume relationship in a ventilated neuromuscular or scoliotic patient shown in **Figure 3** were recorded at lower lung volumes, a discreet inflection point and its relationship to the presence or absence of EFL could be detected. Thus, application of PEEP would be expected to shift AOP towards higher airway pressures. In turn, determination of the location of AOP would optimize ventilator settings to improve gas exchange while avoiding volutrauma. It is not known how differences in lung mechanics between ARDS and NMD/chest wall disorder patients would influence the relation between EFL and AOP. This aspect of respiratory mechanics is a suggested opportunity for further study.

12 OPPORTUNITIES FOR FUTURE RESEARCH

12.1 Serum Biomarkers for Inflammation

COPD causes inflammation resulting in skeletal muscle dysfunction. COPD increases inflammatory factors such as IL-6, TNF-α, IL-8, and C-reactive protein, as well as an increase in the generation of reactive oxygen species (ROS) (Kim et al., 2008). The combination of inflammatory factors and ROS may be the cause of muscle wasting in COPD. Muscle atrophy from COPD can also severely affect inspiratory muscles, limiting their function. These events are similar in patients with NMDs depending on the etiologic origin of muscle weakness, so in both diseases, serum biomarkers can be used to noninvasively evaluate muscle breakdown and effects on the inspiratory muscles. Therefore, future research could evaluate the association between respiratory impairment and these biomarkers.

The neurodegenerative changes associated with NMD are, in some ways, similar to the myriad changes documented with COPD and aging (Kim et al., 2008; Dobrowolny et al., 2021). Neuromuscular junctions (NMJ) undergo functional, morphological, and molecular alterations during aging, resulting in a progressive decrease in skeletal muscle mass and strength (sarcopenia), changes common in NMD. In addition to the intrinsic myoneural changes inherent of NMDs, ROS homeostasis can contribute to changes in the neuromuscular junction morphology and stability, leading to reduction in fiber

number and innervation. For example, Puig-Vilanova et al. (Puig-Vilanova et al., 2014) found that in the diaphragm of COPD patients, compared to control subjects, muscle-specific microRNA expression was downregulated, while histone acetyltransferases (HATs) and deacetylases and myocyte enhancer factor 2C protein levels were higher; by contrast, DNA methylation levels, muscle fiber types and sizes did not differ between patients and controls. The authors concluded that these epigenetic events act as adaptive mechanisms used to overcome the continuous inspiratory loads of the respiratory system in COPD. As respiratory muscles in NMDs are subject to mechanical and oxidative stresses similar to those observed in COPD, epigenetic events may also regulate respiratory muscle dysfunction and are a potential fertile area of investigation in this group of disorders.

12.2 Changes in Respiratory Pressures Influenced by Inspiratory Maneuvers

The updated guidelines by the ERS in 2019 (Laveneziana et al., 2019) do not provide much detail about performance of the SNIP test, limiting the instructions to: "the test is performed at FRC and the subject is instructed to sniff quickly and deeply". Although considered a more physiological maneuver, an individual can perform a sniff test suboptimally when not appropriately instructed. In the evaluation of respiratory muscle strength, the diaphragmatic control performed during the SNIP test influences the inspiratory pressure and contractile properties of inspiratory muscles This occurs due to changes in the pattern of muscle recruitment, which change the force velocity characteristics of muscles. Benicio et al. instructed patients to perform a maximal effort starting from relaxed FRC according to ATS/ERS guidelines (Laveneziana et al., 2019). Participants were initially trained to breathe with a slow diaphragmatic breathing pattern, allowing bulging of the anterior abdominal wall (also known as ballistic contraction, diaphC). They were then instructed to inhale deeply through the nose, while simultaneously moving the abdominal wall outward (ballistic inspiratory maneuver). The main findings of this study showed that the maneuver with diaphC compared to without diaphC 1) significantly reduced the SNIP value, 2) reduced contraction times and electrical activity of accessory inspiratory muscles, and 3) decreased absolute values of maximum relaxation rate ($p < 0.01$), maximum rate of pressure development (MRPD). These findings confirmed that SNIP values diminish when a ballistic contraction of the diaphragm muscle is performed during a sniff maneuver. Thus, instructions on diaphC are recommended for specifically targeting diaphragm activity and better performance of the SNIP test.

12.3 Power Spectrum of EMG

Analysis of the power spectrum of EMG is a relatively old technique to assess muscle fatigue in patients during and after exercise with and without COPD and has not been employed in NMDs. Casabona et al. (Casabona et al., 2021) studied the possibility of using the power spectrum of EMG with non-fatigueable exercises to estimate muscle fiber composition in patients with COPD due to the different spectral content of the sEMG signal, which depends on the fiber type composition. The conclusion was that the power spectrum of COPD patients was at higher frequencies, which aligned with the severity of the disease. Even though this experiment was done on leg muscles, the same principle may be applied to the diaphragm and other inspiratory muscles by using surface electrodes, or better, esophageal electrodes situated at the cardia. Profiles of electromyographic power spectrum can be generated during repetitive maximal diaphragmatic contractions during deep breathing maneuvers. Future research could focus on this potential for detecting respiratory muscle fatigue before it affects VC, Pimax or Pdi.

12.4 Muscle Fiber Type

Changes in fiber type composition occur in NMDs (Glaser et al., 2018). New investigational approaches may elucidate how muscle fiber type specification occurs during disease conditions. For example, skeletal muscle cell culture from human pluripotent cell resources can provide a new instrument to study differentiation of human skeletal myocytes into myotubes with specific fiber types in culture (Hosoyama et al., 2014; Jiwlawat et al., 2017). Such studies could elucidate mechanisms involved in changes of fiber composition and ratio in the skeletal muscle of certain NMDs, and how they influence respiratory muscle kinematics and pathology. Such work carries the potential to create an *in vitro* model of contractile sarcomeric myofibrils for disease modeling and drug screening to study neuromuscular diseases.

13 CONCLUSION

Thoracic cage disorders are characterized by reduced lung volumes and respiratory compliance. Both upper and lower airway changes contribute to increase in airway resistance. While respiratory muscle weakness is a key feature that contributes to respiratory failure, central drive may be increased as characterized by increase in P0.1. Changes in respiratory mechanics contribute to elastic and resistive load compensation. Diaphragmatic braking action during expiration helps prevent further reduction in lung volume and atelectasis. Diagnostic studies focus on the evaluation of lung volumes and flows, respiratory muscle strength, ventilatory drive and recording of electromechanical dissociation of respiratory muscles. Ultrasound evaluation of diaphragmatic thickness and motion may prove useful in predicting respiratory muscle fatigue and failure. Mechanical ventilation affords an opportunity for further assessment of diaphragmatic function and airway properties such as expiratory flow limitation and airway opening pressure, which may provide guidance in applying appropriate ventilator settings. Finally, utilizing biochemical, genetic modeling and cell culture techniques have the potential to elucidate mechanisms of neuromuscular degeneration and the potential for discovering therapeutic

approaches to halting or even stabilizing the loss of skeletal muscle, including respiratory muscles.

DATA AVAILABILITY STATEMENT

The original contributions presented in the study are included in the article/Supplementary Materials, further inquiries can be directed to the corresponding author.

AUTHOR CONTRIBUTIONS

AB searched and selected the literature, conceived of the structure of the paper, guided the students who wrote the major portion of the paper, contributed to and revised the text and figures. NP searched and selected the literature, wrote most of the text, selected some of the figures. KC searched and selected appropriate literature, contributed to the text and created the table.

REFERENCES

Aboussouan, L. S. (2015). Sleep-disordered Breathing in Neuromuscular Disease. Am. J. Respir. Crit. Care *Med.* 191, 979–989. doi:10.1164/rccm.201412-2224ci

Ackrivo, J., Hansen-Flaschen, J., Jones, B. L., Wileyto, E. P., Schwab, R. J., Elman, L., et al. (2019). Classifying Patients with Amyotrophic Lateral Sclerosis by Changes in FVC. A Group-Based Trajectory Analysis. *Am. J. Respir. Crit. Care. Med.* 200 (2), 1513–1521. doi:10.1164/rccm.201902-0344OC

Ackrivo, J., Hansen-Flaschen, J., Wileyto, E. P., Schwab, R. J., Elman, L., and Kawut, S. M. (2019). Development of a Prognostic Model of Respiratory Insufficiency or Death in Amyotrophic Lateral Sclerosis. *Eur. Respir. J.* 53, 1802237. doi:10.1183/13993003.02237-2018

Aitkens, S., Kilmer, D. D., Wright, N. C., and McCrory, M. A. (2005). Metabolic Syndrome in Neuromuscular Disease. *Archives Phys. Med. Rehabilitation* 86 (5), 1030–1036. doi:10.1016/j.apmr.2004.09.012

Aldrich, T. K., Shander, A., Chaudhry, I., and Nagashima, H. (1986). Fatigue of Isolated Rat Diaphragm: Role of Impaired Neuromuscular Transmission. *J. Appl. Physiology* 61 (3), 1077–1083. doi:10.1152/jappl.1986.61.3.1077

Aldrich, T. K., and Spiro, P. (1995). Maximal Inspiratory Pressure: Does Reproducibility Indicate Full Effort? *Thorax* 50 (1), 40–43. doi:10.1136/thx.50.1.40

Allen, J. (2010). Pulmonary Complications of Neuromuscular Disease: A Respiratory Mechanics Perspective. *Paediatr. Respir. Rev.* 11 (1), 18–23. doi:10.1016/j.prrv.2009.10.002

Axen, K. (1982). Ventilatory Responses to Mechanical Loads in Cervical Cord-Injured Humans. *J. Appl. Physiology* 52 (3), 748–756. doi:10.1152/jappl.1982.52.3.748.48

Bach, J. R., Ishikawa, Y., and Kim, H. (1997). Prevention of Pulmonary Morbidity for Patients with Duchenne Muscular Dystrophy. *Chest* 112 (4), 1024–1028. doi:10.1378/chest.112.4.1024

Bach, J. R. (2017). Noninvasive Respiratory Management of Patients with Neuromuscular Disease. *Ann. Rehabil. Med.* 41 (4), 519–538. doi:10.5535/arm.2017.41.4.519

Bach, J. R., and Saporito, L. R. (1996). Criteria for Extubation and Tracheostomy Tube Removal for Patients with Ventilatory Failure. *Chest* 110 (6), 1566–1571. doi:10.1378/chest.110.6.1566

Banzett, R. B., Lansing, R. W., and Binks, A. P. (2021). Air Hunger: A Primal Sensation and a Primary Element of Dyspnea. *Compr. Physiol.* 11 (2), 1449–1483. doi:10.1002/cphy.c200001

Banzett, R. B., Lansing, R. W., Brown, R., Topulos, G. P., Yager, D., Steele, S. M., et al. (1990). 'Air Hunger' from Increased PCO2 Persists after Complete Neuromuscular Block in Humans. *Respir. Physiol.* 81, 1–17. doi:10.1016/0034-5687(90)90065-7

Bastir, M., García-Martínez, D., Torres-Tamayo, N., Sanchis-Gimeno, J. A., O'Higgins, P., Utrilla, C., et al. (2017). *In Vivo* 3D Analysis of Thoracic Kinematics: Changes in Size and Shape during Breathing and Their Implications for Respiratory Function in Recent Humans and Fossil Hominins. *Anat. Rec.* 300 (2), 255–264. doi:10.1002/ar.23503

Bauman, W. A., Spungen, A. M., Raza, M., Rothstein, J., Zhang, R. L., Zhong, Y. G., et al. (1992). Coronary Artery Disease: Metabolic Risk Factors and Latent Disease in Individuals with Paraplegia. *Mt. Sinai J. Med.* 59, 163–168.

Baydur, A., and Carlson, M. (1996). Immediate Response to Inspiratory Resistive Loading in Anesthetized Patients with Kyphoscoliosis: Spirometric and Neural Effects. *Lung* 174, 99–118. doi:10.1007/BF00177704

Baydur, A., Adkins, R. H., and Milic-Emili, J. (2001). Lung Mechanics in Individuals with Spinal Cord Injury: Effects of Injury Level and Posture. *J. Appl. Physiology* 90 (2), 405–411. doi:10.1152/jappl.2001.90.2.405

Baydur, A., and Chen, Z. (2013). Breathing Intolerance Index in COPD and Obesity: A Comparative Observational Study. *Ojrd* 03, 119–127. doi:10.4236/ojrd.2013.33019

Baydur, A. (1992). Decay of Inspiratory Muscle Pressure during Expiration in Anesthetized Kyphoscoliosis Patients. *J. Appl. Physiology* 72 (2), 712–720. doi:10.1152/jappl.1992.72.2.712

Baydur, A. (2013). Expiratory Flow Limitation in Intra and Extrathoracic Respiratory Disorders: Use of the Negative Expiratory Pressure Technique - Review and Recent Developments. *InTechOpen*. doi:10.5772/53270

Baydur, A. (1991). Respiratory Muscle Strength and Control of Ventilation in Patients with Neuromuscular Disease. *Chest* 99 (2), 330–338. doi:10.1378/chest.99.2.330

Baydur, A., Swank, S. M., Stiles, C. M., and Sassoon, C. S. (1989). Respiratory Elastic Load Compensation in Anesthetized Patients with Kyphoscoliosis. *J. Appl. Physiology* 67, 1024–1031. doi:10.1152/jappl.1989.67.3.1024

Beck, J., Sinderby, C., Lindström, L., and Grassino, A. (1998). Effects of Lung Volume on Diaphragm EMG Signal Strength during Voluntary Contractions. *J. Appl. Physiology* 85 (3), 1123–1134. doi:10.1152/jappl.1998.85.3.1123

Behrakis, P. K., Higgs, B. D., Baydur, A., Zin, W. A., and Milic-Emili, J. (1983). Active Inspiratory Impedance in Halothane-Anesthetized Humans. *J. Appl. Physiology* 54, 1477–1481. doi:10.1152/jappl.1983.54.6.1477

Bellemare, F., and Grassino, A. (1982). Effect of Pressure and Timing of Contraction on Human Diaphragm Fatigue. *J. Appl. Physiology* 53, 1190–1195. doi:10.1152/jappl.1982.53.5.1190

Bellemare, F. (1995). "Strength of the Respiratory Muscles," in *The ThoraxLung Biology Biology in Health and Disease*. Editor Ch. Roussos, 85, 1161–1197. part B, ch. 40.

Benditt, J. O. (2019). Respiratory Care of Patients with Neuromuscular Disease. *Respir. Care* 64 (6), 679–688. doi:10.4187/respcare.06827

Berlowitz, D. J., Wadsworth, B., and Ross, J. (2016). Respiratory Problems and Management in People with Spinal Cord Injury. *Breathe* 12, 328–340. doi:10.1183/20734735.012616

Bermejo, J. G., Morélot-Panzini, C., Tanguy, M. L., Meininger, V., Pradat, P. F., Lenglet, T., et al. (2016). Early Diaphragm Pacing to Delay Non-invasive Ventilation in Patients with Amyotrophic Lateral Sclerosis (RespiStimALS): A Multicenter, Triple-Blind, Randomized Controlled Trial. *Eur. Respir. J.* 48, OA270. doi:10.1183/13993003.congress-2016.oa270

Bi, T., Zhang, J., Strohl, K. P., and Han, F. (2021). Hypercapnia and Hypoxemia in a Young Woman. *Ann. ATS* 18 (3), 527–533. doi:10.1513/annalsats.202006-699cc

Black, L. F., and Hyatt, R. E. (1971). Maximal Static Respiratory Pressures in Generalized Neuromuscular Disease. *Am. Rev. Respir. Dis.* 103 (5), 641–650. doi:10.1164/arrd.1971.103.5.641

Borel, C. O., Teitelbaum, J. S., and Hanley, D. F. (1993). Ventilatory Drive and Carbon Dioxide Response in Ventilatory Failure Due to Myasthenia Gravis and Guillain-Barré Syndrome. *Crit. Care Med.* 21 (11), 1717–1726. doi:10.1097/00003246-199311000-00022

Bouros, D., and Green, M. (1971). "Cough. "Physiological and Pathophysiological Considerations," in *The Thorax, Part B: Applied Physiology*. Editor Ch. Roussos (New York: Lung Biology in Health and Disease, Marcel Dekker, Inc.), 85, 1335–1354.

Boussuges, A., Rives, S., Finance, J., Chaumet, G., Vallée, N., Risso, J.-J., et al. (2021). Ultrasound Assessment of Diaphragm Thickness and Thickening: Reference Values and Limits of Normality when in a Seated Position. *Front. Med.* 8, 742703. doi:10.3389/fmed.2021.742703

Braun, N. M., Arora, N. S., and Rochester, D. F. (1983). Respiratory Muscle and Pulmonary Function in Polymyositis and Other Proximal Myopathies. *Thorax* 38, 616–623. doi:10.1136/thx.38.8.616

Campbell, E. J. M. (1965). Respiratory Failure. *Bmj* 1 (5448), 1451–1460. doi:10.1136/bmj.1.5448.1451

Carroll, J. E., Zwillich, C., Weil, J. V., and Brooke, M. H. (1976). Depressed Ventilatory Response in Oculocraniosomatic Neuromuscular Disease. *Neurology* 26, 140. doi:10.1212/wnl.26.2.140

Caruso, P., Albuquerque, A. L. P. d., Santana, P. V., Cardenas, L. Z., Ferreira, J. G., Prina, E., et al. (2015). Diagnostic Methods to Assess Inspiratory and Expiratory Muscle Strength. *J. Bras. Pneumol.* 41 (2), 110–123. doi:10.1590/s1806-37132015000004474

Casabona, A., Valle, M. S., Laudani, L., Crimi, C., Russo, C., Malaguarnera, L., et al. (2021). Is the Power Spectrum of Electromyography Signal a Feasible Tool to Estimate Muscle Fiber Composition in Patients with COPD? *Jcm* 10 (17), 3815. doi:10.3390/jcm10173815

Chatwin, M., Toussaint, M., Gonçalves, M. R., Sheers, N., Mellies, U., Gonzales-Bermejo, J., et al. (2018). Airway Clearance Techniques in Neuromuscular Disorders: A State of the Art Review. *Respir. Med.* 136, 98–110. doi:10.1016/j.rmed.2018.01.012

Chen, J., Nguyen, N., and Soong, M. (2013). Postural Change of FVC in Patients with Neuromuscular Disease: Relation to Initiating Non-invasive Ventilation. *J. Pulmon Resp. Med.* 3, 2. doi:10.4172/2161-105X.1000147

Chew, K., carey, K., Ho, G., Mallitt, K.-A., Widger, J., and Farrar, M. (2016). The Relationship of Body Habitus and Respiratory Function in Duchenne Muscular Dystrophy. *Respir. Med.* 119, 35–40. doi:10.1016/j.rmed.2016.08.018

Chiang, J., Mehta, K., and Amin, R. (2018). Respiratory Diagnostic Tools in Neuromuscular Disease. *Children* 5 (6), 78. doi:10.3390/children5060078

Cohn, D., Benditt, J. O., Eveloff, S., and McCool, F. D. (1997). Diaphragm Thickening during Inspiration. *J. Appl. Physiology* 83, 291–296. doi:10.1152/jappl.1997.83.1.291

De Troyer, A., and Estenne, M. (1984). Coordination between Rib Cage Muscles and Diaphragm during Quiet Breathing in Humans. *J. Appl. Physiology* 57 (3), 899–906. doi:10.1152/jappl.1984.57.3.899

De Troyer, A., Estenne, M., and Heilporn, A. (1986). Mechanism of Active Expiration in Tetraplegic Subjects. *N. Engl. J. Med.* 314, 740–744. doi:10.1056/nejm198603203141203

Dempsey, J. A., Reddan, W., Balke, B., and Rankin, J. (1966). Work Capacity Determinants and Physiologic Cost of Weight-Supported Work in Obesity. *J. Appl. Physiology* 21, 1815–1820. doi:10.1152/jappl.1966.21.6.1815

DiPALS, writing committee, DiPALS, Study Group Collaborators (2015). Safety and Efficacy of Diaphragm Pacing in Patients with Respiratory Insufficiency Due to Amyotrophic Lateral Sclerosis (DiPALS): a Multicentre, Open-Label, Randomised Controlled Trial. *Lancet Neurol.* 14, 883–892. doi:10.1016/S1474-4422(15)00152-0

Dobrowolny, G., Barbiera, A., Sica, G., and Scicchitano, B. M. (2021). Age-related Alterations at Neuromuscular Junction: Role of Oxidative Stress and Epigenetic Modifications. *Cells* 10 (6), 1307. doi:10.3390/cells10061307

Druz, W. S., and Sharp, J. T. (1981). Activity of Respiratory Muscles in Upright and Recumbent Humans. *J. Appl. Physiology* 51 (6), 1552–1561. doi:10.1152/jappl.1981.51.6.1552

Durnin, J. V. G. A., and Rahaman, M. M. (1967). The Assessment of the Amount of Fat in the Human Body from Measurements of Skinfold Thickness. *Br. J. Nutr.* 21, 681–689. doi:10.1079/bjn19670070

Easton, P. A., Katagiri, M., Kieser, T. M., and Platt, R. S. (1999). Postinspiratory Activity of Costal and Crural Diaphragm. *J. Appl. Physiology* 87, 582–589. doi:10.1152/jappl.1999.87.2.582

Eckert, D. J., McEvoy, R. D., George, K. E., Thomson, K. J., and Catcheside, P. G. (2007). Genioglossus Reflex Inhibition to Upper-Airway Negative-Pressure Stimuli during Wakefulness and Sleep in Healthy Males. *J. Physiol.* 581 (Pt 3), 1193–1205. doi:10.1113/jphysiol.2007.132332

Edwards, R. H. (1979). The Diaphragm as a Muscle. Mechanisms Underlying Fatigue. *Am. Rev. Respir. Dis.* 119, 81–84. doi:10.1164/arrd.1979.119.2P2.81

Elamin, M., Bede, P., Montuschi, A., Pender, N., Chio, A., and Hardiman, O. (2015). Predicting Prognosis in Amyotrophic Lateral Sclerosis: a Simple Algorithm. *J. Neurol.* 262, 1447–1454. doi:10.1007/s00415-015-7731-6

Estenne, M., Van Muylem, A., Gorini, M., Kinnear, W., Heilporn, A., and De Troyer, A. (1994). Evidence of Dynamic Airway Compression during Cough in Tetraplegic Patients. *Am. J. Respir. Crit. Care Med.* 150 (4), 1081–1085. doi:10.1164/ajrccm.150.4.7921440

Fauroux, B., and Khirani, S. (2014). Neuromuscular Disease and Respiratory Physiology in Children: Putting Lung Function into Perspective. *Respirology* 19 (6), 782–791. doi:10.1111/resp.12330

Fermin, A. M., Afzal, U., and Culebras, A. (2016). Sleep in Neuromuscular Diseases. *Sleep. Med. Clin.* 11 (1), 53–64. doi:10.1016/j.jsmc.2015.10.005

Fromageot, C., Lofaso, F., Annane, D., Falaize, L., Lejaille, M., Clair, B., et al. (2001). Supine Fall in Lung Volumes in the Assessment of Diaphragmatic Weakness in Neuromuscular Disorders. *Archives Phys. Med. Rehabilitation* 82 (1), 123–128. doi:10.1053/apmr.2001.18053

Fugl-Meyer, A. R., and Grimby, G. (1984). Respiration in Tetraplegia and in Hemiplegia: a Review. *Int. Rehabil. Med.* 6 (4), 186–190. doi:10.3109/03790798409165962

García Río, F., Prados, C., Diez Tejedor, E., Diaz Lobato, S., Alvarez-Sala, R., Villamor, J., et al. (1994). Breathing Pattern and Central Ventilatory Drive in Mild and Moderate Generalised Myasthenia Gravis. *Thorax* 49 (7), 703–706. doi:10.1136/thx.49.7.703

Glaser, J., and Suzuki, M. (2018). "Skeletal Muscle Fiber Types in Neuromuscular Diseases." In *Muscle Cell and Tissue*. Ed by K. Sakuma. In London, United Kingdom: In Tech. doi:10.5772/intechopen.79474

Goldman, J. M., Rose, L. S., Williams, S. J., Silver, J. R., and Denison, D. M. (1986). Effect of Abdominal Binders on Breathing in Tetraplegic Patients. *Thorax* 41, 940–945. doi:10.1136/thx.41.12.940

Gonzalez-Bermejo, J., Morélot-Panzini, C., Tanguy, M.-L., Meininger, V., Pradat, P.-F., Lenglet, T., et al. (2016). Early Diaphragm Pacing in Patients with Amyotrophic Lateral Sclerosis (RespiStimALS): a Randomised Controlled Triple-Blind Trial. *Lancet Neurology* 15 (12), 1217–1227. doi:10.1016/s1474-4422(16)30233-2

Guérin, C., Terzi, N., Galerneau, L.-M., Mezidi, M., Yonis, H., Baboi, L., et al. (2020). Lung and Chest Wall Mechanics in Patients with Acute Respiratory Distress Syndrome, Expiratory Flow Limitation, and Airway Closure. *J. Appl. Physiology* 128, 1594–1603. doi:10.1152/japplphysiol.00059.2020

Harada, Y., Rao, V. K., Arya, K., Kuntz, N. L., DiDonato, C. J., Napchan-Pomerantz, G., et al. (2020). Combination Molecular Therapies for Type 1 Spinal Muscular Atrophy. *Muscle Nerve* 62 (4), 550–554. doi:10.1002/mus.27034

Hosoyama, T., McGivern, J. V., Van Dyke, J. M., Ebert, A. D., and Suzuki, M. (2014). Derivation of Myogenic Progenitors Directly from Human Pluripotent Stem Cells Using a Sphere-Based Culture. *Stem Cells Transl. Med.* 3, 564–574. doi:10.5966/sctm.2013-0143

Jaber, S., Petrof, B. J., Jung, B., Chanques, G., Berthet, J.-P., Rabuel, C., et al. (2011). Rapidly Progressive Diaphragmatic Weakness and Injury during Mechanical Ventilation in Humans. *Am. J. Respir. Crit. Care Med.* 183, 364–371. doi:10.1164/rccm.201004-0670oc

Jaeger, M. J. (1982). Effect of the Cheeks and the Compliance of Alveolar Gas on the Measurement of Respiratory Variables. *Respir. Physiol.* 47 (3), 325–340. doi:10.1016/0034-5687(82)90061-5

Jansen, D., Jonkman, A. H., Vries, H. J. d., Wennen, M., Elshof, J., Hoofs, M. A., et al. (2021). Positive End-Expiratory Pressure Affects Geometry and Function of the Human Diaphragm. *J. Appl. Physiology* 131, 1328–1339. doi:10.1152/japplphysiol.00184.2021

Jiwlawat, S., Lynch, E., Glaser, J., Smit-Oistad, I., Jeffrey, J., Van Dyke, J. M., et al. (2017). Differentiation and Sarcomere Formation in Skeletal Myocytes Directly Prepared from Human Induced Pluripotent Stem Cells Using a Sphere-Based Culture. *Differentiation* 96, 70–81. doi:10.1016/j.diff.2017.07.004

Benício, K. (2021). Effects of Diaphragmatic Control on Multiparametric Analysis of the Sniff Nasal Inspiratory Pressure Test and Inspiratory Muscle Activity in Healthy Subjects. *PLoS One* 16 (7), e0253132. doi:10.1371/journal.pone.0253132

Kilburn, K. H., Eagan, J. T., Sieker, H. O., and Heyman, A. (1959). Cardiopulmonary Insufficiency in Myotonic and Progressive Muscular Dystrophy. *N. Engl. J. Med.* 261, 1089–1096. doi:10.1056/nejm195911262612201

Kim, H. C., Mofarrahi, M., and Hussain, S. N. (2008). Skeletal Muscle Dysfunction in Patients with Chronic Obstructive Pulmonary Disease. *Int. J. Chron. Obstruct Pulmon Dis.* 3 (4), 637–658. doi:10.2147/copd.s4480

Kobayashi, I., Perry, A., Rhymer, J., Wuyam, B., Hughes, P., Murphy, K., et al. (1996). Inspiratory Coactivation of the Genioglossus Enlarges Retroglossal Space in Laryngectomized Humans. *J. Appl. Physiology* 80, 1595–1604. doi:10.1152/jappl.1996.80.5.1595

Koga, T., Watanabe, K., Sano, M., Ishikawa, Y., and Bach, J. R. (2206). Breathing Intolerance Index: A New Indicator for Ventilator Use. *Am. J. Phys. Med. Rehabil.* 85 (1), 24–30. doi:10.1097/01.phm.0000184237.62628.e1

Kress, J. P., Pohlman, A. S., Alverdy, J., and Hall, J. B. (1999). The Impact of Morbid Obesity on Oxygen Cost of Breathing (Vo2RESP) at Rest. *Am. J. Respir. Crit. Care Med.* 160, 883–886. doi:10.1164/ajrccm.160.3.9902058

Lappas, A. S., Tzortzi, A. S., and Behrakis, P. K. (2016). Forced Oscillations in Applied Respiratory Physiology: Clinical Applications. *Clin. Res. Pulmonol.* 2 (2), 1016.

Laroche, C. M., Mier, A. K., Moxham, J., and Green, M. (1988). The Value of Sniff Esophageal Pressures in the Assessment of Global Inspiratory Muscle Strength. *Am. Rev. Respir. Dis.* 138, 598–603. doi:10.1164/ajrccm/138.3.598

Laveneziana, P., Albuquerque, A., Aliverti, A., Babb, T., Barreiro, E., Dres, M., et al. (2019). ERS Statement on Respiratory Muscle Testing at Rest and during Exercise. *Eur. Respir. J.* 53 (6), 1801214. doi:10.1183/13993003.01214-2018

Lechtzin, N., Wiener, C. M., Shade, D. M., Clawson, L., and Diette, G. B. (2002). Spirometry in the Supine Position Improves the Detection of Diaphragmatic Weakness in Patients with Amyotrophic Lateral Sclerosis. *Chest* 121 (2), 436–442. doi:10.1378/chest.121.2.436

Ledsome, J. R., and Sharp, J. M. (1981). Pulmonary Function in Acute Cervical Cord Injury. *Am. Rev. Respir. Dis.* 124, 41–44. doi:10.1164/arrd.1981.124.1.41

Leech, J. A., Ghezzo, H., Stevens, D., and Becklake, M. R. (1983). Respiratory Pressures and Function in Young Adults1-4. *Am. Rev. Respir. Dis.* 128 (1), 17–23. doi:10.1164/arrd.1983.128.1.17

Lo Mauro, A., and Aliverti, A. (2016). Physiology of Respiratory Disturbances in Muscular Dystrophies. *Breathe* 12 (4), 318–327. doi:10.1183/20734735.012716

Loring, S. H., and Mead, J. (1982). Action of the Diaphragm on the Rib Cage Inferred from a Force-Balance Analysis. *J. Appl. Physiology* 53 (3), 756–760. doi:10.1152/jappl.1982.53.3.756

Malhotra, A., Fogel, R. B., Edwards, J. K., Shea, S. A., and White, D. P. (2000). Local Mechanisms Drive Genioglossus Activation in Obstructive Sleep Apnea. *Am. J. Respir. Crit. Care Med.* 161, 1746–1749. doi:10.1164/ajrccm.161.5.9907109

Man, W. D.-C., Moxham, J., and Polkey, M. I. (2004). Magnetic Stimulation for the Measurement of Respiratory and Skeletal Muscle Function. *Eur. Respir. J.* 24 (5), 846–860. doi:10.1183/09031936.04.00029004

Markham, B. E., Kernodle, S., Nemzek, J., Wilkinson, J. E., and Sigler, R. (2015). Chronic Dosing with Membrane Sealant Poloxamer 188 NF Improves Respiratory Dysfunction in Dystrophic *Mdx And Mdx/Utrophin-/-* Mice. *PLoS ONE* 10 (8), e0134832. doi:10.1371/journal.pone.0134832

Mayer, O. H., Finkel, R. S., Rummey, C., Benton, M. J., Glanzman, A. M., Flickinger, J., et al. (2015). Characterization of Pulmonary Function in Duchenne Muscular Dystrophy. *Pediatr. Pulmonol.* 50 (5), 487–494. doi:10.1002/ppul.23172

McCool, F. D., Brown, R., Mayewski, R. J., and Hyde, R. W. (1988). Effects of Posture on Stimulated Ventilation in Quadriplegia. *Am. Rev. Respir. Dis.* 138 (1), 101–105. doi:10.1164/ajrccm/138.1.101

McCool, F. D., Pichurko, B. M., Slutsky, A. S., Sarkarati, M., Rossier, A., and Brown, R. (1986). Changes in Lung Volume and Rib Cage Configuration with Abdominal Binding in Quadriplegia. *J. Appl. Physiology* 60, 1198–1202. doi:10.1152/jappl.1986.60.4.1198

Mead, J. (1979). Functional Significance of the Area of Apposition of Diaphragm to Rib Cage [proceedings]. *Am. Rev. Respir. Dis.* 119 (2), 31–32. doi:10.1164/arrd.1979.119.2P2.31

Mellies, U., Dohna-Schwake, C., and Voit, T. (2005). Respiratory Function Assessment and Intervention in Neuromuscular Disorders. *Curr. Opin. Neurol.* 18, 543–547. doi:10.1097/01.wco.0000180662.03544.5f

Mier, A., Brophy, C., Moxham, J., and Green, M. (1992). Repetitive Stimulation of Phrenic Nerves in Myasthenia Gravis. *Thorax* 47 (8), 640–644. doi:10.1136/thx.47.8.640

Miller, K., and Mayer, O. H. (2021). Pulmonary Function Testing in Patients with Neuromuscular Disease. *Pediatr. Pulmonol.* 56 (4), 693–699. doi:10.1002/ppul.25182

Mogalle, K., Perez-Rovira, A., Ciet, P., Wens, S. C. A., van Doorn, P. A., Tiddens, H. A. W. M., et al. (2016). Quantification of Diaphragm Mechanics in Pompe Disease Using Dynamic 3D MRI. *PloS ONE* 11 (7), e0158912. doi:10.1371/journal.pone.0158912

Mognoni, P., Saibene, F., and Sant'Ambrogio, G. (1969). Contribution of the Diaphragm and the Other Inspiratory Muscles to Different Levels of Tidal Volume and Static Inspiratory Effort in the Rabbit. *J. Physiol.* 202, 517–534. doi:10.1113/jphysiol.1969.sp008825

Muller, N., Bryan, A. C., and Zamel, N. (1980). Tonic Inspiratory Muscle Activity as a Cause of Hyperinflation in Histamine-Induced Asthma. *J. Appl. Physiology* 49, 869–874. doi:10.1152/jappl.1980.49.5.869

Muller, N., Volgyesi, G., Becker, L., Bryan, M. H., and Bryan, A. C. (1979). Diaphragmatic Muscle Tone. *J. Appl. Physiology* 47, 279–284. doi:10.1152/jappl.1979.47.2.279

Nicot, F., Hart, N., Forin, V., Boulé, M., Clément, A., Polkey, M. I., et al. (2006). Respiratory Muscle Testing. *Am. J. Respir. Crit. Care Med.* 174 (1), 67–74. doi:10.1164/rccm.200512-1841oc

Nishino, T., Isono, S., Shinozuka, N., and Ishikawa, T. (2008). Coughing Induced by Airway Irritation Modulates the Sensation of Air Hunger. *J. Physiol.* 586 (2), 649–658. doi:10.1113/jphysiol.2007.145276

Oechsel, K. F., and Cartwright, M. S. (2021). Combination Therapy with Onasemnogene and Risdiplam in Spinal Muscular Atrophy Type 1. *Muscle Nerve* 64 (4), 487–490. doi:10.1002/mus10.1002/mus.27375

Oliven, R., Cohen, G., Dotan, Y., Somri, M., Schwartz, A. R., and Oliven, A. (2018). Alteration in Upper Airway Dilator Muscle Coactivation during Sleep: Comparison of Patients with Obstructive Sleep Apnea and Healthy Subjects. *J. Appl. Physiology* 124, 421–429. doi:10.1152.japplphysiol.01067.201610.1152/japplphysiol.01067.2016

Padkao, T., and Boonla, O. (2020). Relationships between Respiratory Muscle Strength, Chest Wall Expansion, and Functional Capacity in Healthy Nonsmokers. *J. Exerc Rehabil.* 16 (2), 189–196. doi:10.12965/jer.2040080.040

Paintal, A. S. (1986). "Chapter 1 the Visceral Sensations - Some Basic Mechanisms," in *Progress in Brain Research*. Editors F. Gervero and J. F. B. Morrison (Amsterdam: Elsevier Scientific Publishers), 3–19. doi:10.1016/s0079-6123(08)62752-1

Panitch, H. B. (2009). Diurnal Hypercapnia in Patients with Neuromuscular Disease. *Paediatr. Respir. Rev.* 11 (1), 3–8. doi:10.1016/j.prrv.2009.10.0010.1016/j.prrv.2009.10.005

Paul, G. R., Gushue, C., Kotha, K., and Shell, R. (2021). The Respiratory Impact of Novel Therapies for Spinal Muscular Atrophy. *Pediatr. Pulmonol.* 56 (4), 721–728. doi:10.1002/ppul.25135

Perrin, C., Unterborn, J. N., Ambrosio, C. D., and Hill, N. S. (2204). Pulmonary Complications of Chronic Neuromuscular Diseases and Their Management. *Muscle Nerve* 29 (1), 5–27. doi:10.1002/mus.10487

Pessolano, F., Suarez, A., Monteiro, S., Mesa, L., Dubrovsky, A., Roncoroni, A., et al. (2003). Nutritional Assessment of Patients with Neuromuscular Diseases. *Am. J. Phys. Med. Rehabil.* 82, 182–185. doi:10.1097/00002060-200303000-00005

Plum, F., and Swanson, A. G. (1958). Abnormalities in Central Regulation of Respiration in Acute and Convalescent Poliomyelitis. *Arch. NeurPsych* 80, 267–285. doi:10.1001/archneurpsyc.1958.02340090003001

Polkey, M. I., and Moxham, J. (2001). Clinical Aspects of Respiratory Muscle Dysfunction in the Critically Ill. *Chest* 119 (3), 926–939. doi:10.1378/chest.119.3.926

Prigent, H., Orlikowski, D., Laforêt, P., Letilly, N., Falaize, L., Pellegrini, N., et al. (2012). Supine Volume Drop and Diaphragmatic Function in Adults with Pompe Disease: Table 1-. *Eur. Respir. J.* 39, 1545–1546. doi:10.1183/09031936.00169011

Puig-Vilanova, E., Aguiló, R., Rodríguez-Fuster, A., Martínez-Llorens, J., Gea, J., and Barreiro, E. (2014). Epigenetic Mechanisms in Respiratory Muscle Dysfunction of Patients with Chronic Obstructive Pulmonary Disease. *PLoS One* 9 (11), e111514. doi:10.1371/journal.pone.0111514

Ramonatxo, M., Boulard, P., and Prefaut, C. (1995). Validation of a Noninvasive Tension-Time Index of Inspiratory Muscles. *J. Appl. Physiology* 78 (2), 646–653. doi:10.1152/jappl.1995.78.2.646

Rault, C., Heraud, Q., Ragot, S., Robert, R., and Drouot, X. (2021). Sleep Deprivation Increases Air Hunger rather Than Breathing Effort. *Am. J. Respir. Crit. Care Med.* 203 (5), 642–645. doi:10.1164/rccm.202004-1478le

Rault, C., Sangaré, A., Diaz, V., Ragot, S., Frat, J.-P., Raux, M., et al. (2020). Impact of Sleep Deprivation on Respiratory Motor Output and Endurance. A Physiological Study. *Am. J. Respir. Crit. Care Med.* 201, 976–983. doi:10.1164/rccm.201904-0819oc

Rialp, G., Raurich, J. M., Llompart-Pou, J. A., Ayestaran, I., and Ibanez, J. (2013). Central Respiratory Drive in Patients with Neuromuscular Diseases. *Respir. Care* 58 (3), 450–457. doi:10.4187/respcare.01873

Rosenow, E. C., and Engel, A. G. (1978). Acid Maltase Deficiency in Adults Presenting as Respiratory Failure. *Am. J. Med.* 64, 485–491. doi:10.1016/0002-9343(78)90235-8

Rosenow, E. C., and Engel, A. G. (1978). Acid Maltase Deficiency in Adults Presenting as Respiratory Failure. *Am. J. Med.* 64 (3), 485–491. doi:10.1016/0002-9343(78)90235-8

Roussos, C. (1978). Function and Fatigue of Respiratory Muscles. *Chest* 88 (2), 124S–132S. doi:10.1378/chest.88.2.124s

Roussos, C., Fixley, M., Gross, D., and Macklem, P. T. (1979). Fatigue of Inspiratory Muscles and Their Synergic Behavior. *J. Appl. Physiology* 46 (5), 897–904. doi:10.1152/jappl.1979.46.5.897

Roussos, C., Fixley, M., Gross, D., and Macklem, P. T. (1979). Fatigue of Inspiratory Muscles and Their Synergic Behavior. *J. Appl. Physiology* 46 (5), 897–904. doi:10.1152/jappl.1979.46.5.897

Roussos, C., and Koutsoukou, A. (2003). Respiratory Failure. *Eur. Respir. J.* 22 (Suppl. 47), 3s–14s. doi:10.1183/09031936.03.00038503

Sahni, A. S., and Wolfe, L. (2018). Respiratory Care in Neuromuscular Diseases. *Respir. Care* 63 (5), 601–608. doi:10.4187/respcare.06210

Salome, C. M., King, G. G., and Berend, N. (2010). Physiology of Obesity and Effects on Lung Function. *J. Appl. Physiology* 108, 206–211. doi:10.1152/japplphysiol.00694.2009

Sarkar, M., Bhardwaz, R., and Madabhavi, I. (2019). Physical Signs in Patients with Chronic Obstructive Pulmonary Disease. *Lung India* 36 (1), 38–47. doi:10.4103/lungindia.lungindia_145_1810.1378/chest.88.2_supplement.124s

Sarmento, A., Fregonezi, G., Lira, M., Marques, L., Pennati, F., Resqueti, V., et al. (2021). Changes in Electromyographic Activity, Mechanical Power, and Relaxation Rates Following Inspiratory Ribcage Muscle Fatigue. *Sci. Rep.* 11, 12475. doi:10.1038/s41598-021-92060-y

Schepens, T., Verbrugghe, W., Dams, K., Corthouts, B., Parizel, P. M., and Jorens, P. G. (2015). The Course of Diaphragm Atrophy in Ventilated Patients Assessed with Ultrasound: a Longitudinal Cohort Study. *Crit. Care.* 19, 422–430. doi:10.1186/s13054-015-1141-0

Scott, M., Frost, F., and Supinski, G. (1993). The Effect of Body Position and Abdominal Binders in Chronic Tetraplegic Subjects More Than 15 Years Post-injury. *J. Am. Paraplegia Soc.* 16, 117.

Sharma, G. D. (2009). Pulmonary Function Testing in Neuromuscular Disorders. *Pediatrics* 123, S219–S221. doi:10.1542/peds.2008-2952d

Sharp, J. T., Druz, W. S., and Kondragunta, V. R. (1986). Diaphragmatic Responses to Body Position Changes in Obese Patients with Obstructive Sleep Apnea1-3. *Am. Rev. Respir. Dis.* 133 (1), 32–37. doi:10.1164/arrd.1986.133.1.32

Sharp, J. T., Henry, J. P., Sweany, S. K., Meadows, W. R., and Pietras, R. J. (1964). The Total Work of Breathing in Normal and Obese Men*. *J. Clin. Investig.* 43 (4), 728–739. doi:10.1172/JCI104957

Silbergleit, A. K., Waring, W. P., Sullivan, M. J., and Maynard, F. M. (1991). Evaluation, Treatment, and Follow-Up Results of Post Polio Patients with Dysphagia. *Otolaryngol. Head. Neck Surg.* 104, 333–338. doi:10.1177/019459989110400308

Sonies, B. C., and Dalakas, M. C. (1991). Dysphagia in Patients with the Post-Polio Syndrome. *N. Engl. J. Med.* 324, 1162–1167. doi:10.1056/nejm199104253241703

Stanbury, R. M., and Graham, E. M. (1998). Systemic Corticosteroid Therapy---side effects and their management. *Br. J. Ophthalmol.* 82, 704–708. doi:10.1136/bjo.82.6.704

Steier, J., Kaul, S., Seymour, J., Jolley, C., Rafferty, G., Man, W., et al. (2007). The value of multiple tests of respiratory muscle strength. *Thorax* 62 (11), 975–980. doi:10.1136/thx.2006.072884

Suárez, A. A., Pessolano, F. A., Monteiro, S. G., Ferreyra, G., Capria, M. E., Mesa, L., et al. (2002). Peak flow and peak cough flow in the evaluation of expiratory muscle weakness and bulbar impairment in patients with neuromuscular disease. *Am. J. Phys. Med. Rehabilitation* 81 (7), 506–511. doi:10.1097/00002060-200207000-00007

Terson de Paleville, D. G. L., Sayenko, D. G., Aslan, S. C., Folz, R. J., McKay, W. B., and Ovechkin, A. V. (2014). Respiratory motor function in seated and supine positions in individuals with chronic spinal cord injury. *Respir. Physiology Neurobiol.* 203, 9–14. doi:10.1016/j.resp.2014.08.013

Thomas, P. S., Cowen, E. R., Hulands, G., and Milledge, J. S. (1989). Respiratory function in the morbidly obese before and after weight loss. *Thorax* 44, 382–386. doi:10.1136/thx.44.5.382

Ti, D. S., and Fit Ting, J.-W. (1999). Sniff Nasal Inspiratory Pressure. *Am. J. Respir. Crit. Care Med.* 159 (1), 107–111. doi:10.1164/ajrccm.159.1.9804052

Troyer, A. D., and Wilson, T. A. (2016). Action of the diaphragm on the rib cage. *J. Appl. Physiology* 121 (2), 391–400. doi:10.1152/japplphysiol.00268.2016

Van de Graaff, W. B., Gottfried, S. B., Mitra, J., van Lunteren, E., Cherniack, N. S., and Strohl, K. P. (1984). Respiratory function of hyoid muscles and hyoid arch. *J. Appl. Physiology* 57, 197–204. doi:10.1152/jappl.1984.57.1.197

Van Noord, J. A., Cauberghs, M., Van De Woestijne, K. P., and Demedts, M. (1991). Total respiratory resistance and reactance in ankylosing spondylitis and kyphoscoliosis. *Eur. Respir. J.* 4 (8), 945–951.

Vincken, W., Ghezzo, H., and Cosio, M. G. (1987). Maximal static respiratory pressures in adults: normal values and their relationship to determinants of respiratory function. *Bull. Eur. Physiopathol. Respir.* 23 (5), 435–439.

Welch, J. F., Kipp, S., and Sheel, A. W. (2019). Respiratory muscles during exercise: mechanics, energetics, and fatigue. *Curr. Opin. Physiology* 10, 102–109. doi:10.1016/j.cophys.2019.04.023

Wesseling, G., Quaedvlieg, F. C. M., and Wouters, E. F. M. (1992). Oscillatory mechanics of the respiratory system in neuromuscular disease. *Chest* 102, 1752–1757. doi:10.1378/chest.102.6.1752

Whitelaw, W. A., Derenne, J.-P., and Milic-Emili, J. (1975). Occlusion pressure as a measure of respiratory center output cm conscious man. *Respir. Physiol.* 23 (2), 181–199. doi:10.1016/0034-5687(75)90059-6

Whitelaw, W. A., and Derenne, J. P. (1993). Airway occlusion pressure. *J. Appl. Physiology* 74, 1475–1483. doi:10.1152/jappl.1993.74.4.1475

Whittenberger, J. L., and Sarnoff, S. J. (1950). Physiologic principles in the treatment of respiratory failure. *Med. Clin. N. Am.* 34, 1335–1362. doi:10.1016/s0025-7125(16)35367-6

Widdicombe, J. G. (1954). Receptors in the trachea and bronchi of the cat. *J. Physiol. Lond.* 123, 71–104. doi:10.1113/jphysiol.1954.sp005034

Wijdicks, E. F. M. (2017). The neurology of acutely failing respiratory mechanics. *Ann. Neurol.* 81 (4), 485–494. doi:10.1002/ana.24908

Won, Y. H., Choi, W. A., Lee, J. W., Bach, J. R., Park, J., and Kang, S.-W. (2016). Sleep transcutaneous vs. end-tidal CO2 monitoring for patients with neuromuscular disease. *Am. J. Phys. Med. Rehabil.* 95 (2), 91–95. doi:10.1097/phm.0000000000000345

Yang, M. L., and Finkel, R. S. (2010). Overview of paediatric neuromuscular disorders and related pulmonary issues: diagnostic and therapeutic considerations. *Paediatr. Respir. Rev.* 11 (1), 9–17. doi:10.1016/j.prrv.2009.10.009

Yap, J. C., Watson, R. A., Gilbey, S., and Pride, N. B. (1995). Effects of posture on respiratory mechanics in obesity. *J. Appl. Physiology* 79, 1199–1205. doi:10.1152/jappl.1995.79.4.1199

Zaloga, G. P. (2002). Aspiration-related illnesses: Definitions and diagnosis. *JPEN J. Parenter. Enter. Nutr.* 26, S2–S8. doi:10.1177/014860710202600602

Zin, W. A., Pengelly, L. D., and Milic-Emili, J. (1983). Decay of inspiratory muscle pressure during expiration in anesthetized cats. *J. Appl. Physiology* 54 (2), 408–413. doi:10.1152/jappl.1983.54.2.408

Conflict of Interest: The authors declare that the research was conducted in the absence of any commercial or financial relationships that could be construed as a potential conflict of interest.

frontiers | Frontiers in Physiology

REVIEW
published: 13 July 2022
doi: 10.3389/fphys.2022.817263

Lung Mechanics Over the Century: From Bench to Bedside and Back to Bench

Paolo Jose Cesare Biselli[1], Fernanda Degobbi Tenorio Quirino Dos Santos Lopes[2], Renato Fraga Righetti[2,3], Henrique Takachi Moriya[4], Iolanda Fátima Lopes Calvo Tibério[2] and Milton Arruda Martins[2]*

[1]Intensive Care Unit, University Hospital, University of Sao Paulo, Sao Paulo, Brazil, [2]Laboratory of Experimental Therapeutics, Department of Clinical Medicine, School of Medicine, University of Sao Paulo, Sao Paulo, Brazil, [3]Hospital Sírio-Libanês, Serviço de Reabilitação, São Paulo, Brazil, [4]Biomedical Engineering Laboratory, Escola Politecnica, University of Sao Paulo, Sao Paulo, Brazil

OPEN ACCESS

Edited by:
Andrew John Halayko, University of Manitoba, Canada

Reviewed by:
Franco Laghi, Loyola University Chicago, United States
Man-Ju Ting, Far Eastern Memorial Hospital, Taiwan
Gamal Agmy, Assiut University, Egypt
Rebecca Heise, Virginia Commonwealth University, United States

***Correspondence:**
Paolo Jose Cesare Biselli
p_biselli@hotmail.com

Specialty section:
This article was submitted to Respiratory Physiology and Pathophysiology, a section of the journal Frontiers in Physiology

Received: *17 November 2021*
Accepted: *17 June 2022*
Published: *13 July 2022*

Citation:
Biselli PJC, Degobbi Tenorio Quirino Dos Santos Lopes F, Righetti RF, Moriya HT, Tibério IFLC and Martins MA (2022) Lung Mechanics Over the Century: From Bench to Bedside and Back to Bench. Front. Physiol. 13:817263. doi: 10.3389/fphys.2022.817263

Lung physiology research advanced significantly over the last 100 years. Respiratory mechanics applied to animal models of lung disease extended the knowledge of the workings of respiratory system. In human research, a better understanding of respiratory mechanics has contributed to development of mechanical ventilators. In this review, we explore the use of respiratory mechanics in basic science to investigate asthma and chronic obstructive pulmonary disease (COPD). We also discuss the use of lung mechanics in clinical care and its role on the development of modern mechanical ventilators. Additionally, we analyse some bench-developed technologies that are not in widespread use in the present but can become part of the clinical arsenal in the future. Finally, we explore some of the difficult questions that intensive care doctors still face when managing respiratory failure. Bringing back these questions to bench can help to solve them. Interaction between basic and translational science and human subject investigation can be very rewarding, as in the conceptualization of "Lung Protective Ventilation" principles. We expect this interaction to expand further generating new treatments and managing strategies for patients with respiratory disease.

Keywords: lung mechanics modelling, equation of motion, constant-phase model, respiratory diseases, animal models—rodent, critical care, mechanical ventilalion, lung physiology

INTRODUCTION

Respiratory mechanics has been extensively studied during the last century (RAHN et al., 1946; Otis, 1977; Collett et al., 1985; Bates, 2005) with resultant improvement in our understanding of the function of the respiratory system in health and disease states (MEAD et al., 1955; Reinert and Trendelenburg, 1972; Dodd et al., 1988; Mador, 1991). Newfound knowledge of respiratory mechanics has also been applied to different animal models of respiratory disease (Wanner and Abraham, 1982; Wanner et al., 1990; Irvin and Bates, 2003).

Over the years, accumulated knowledge in respiratory mechanics has been incorporated into mechanical ventilators and respiratory functional assessment of patients (Younes, 1992; Sinderby et al., 1999; Jonkman et al., 2020). Respiratory mechanics became not only a tool for investigating lung disorders. It was also used in developing treatments for failing respiratory system and in designing strategies to prevent lung injury (Henderson et al., 2017).

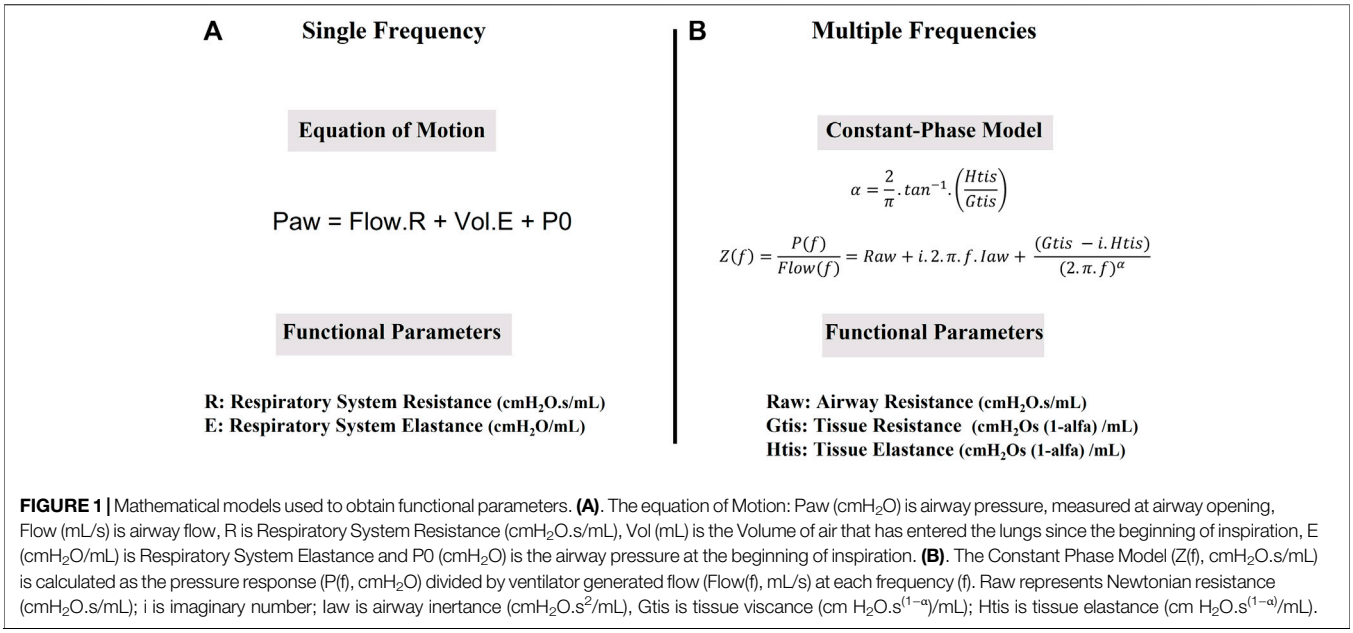

FIGURE 1 | Mathematical models used to obtain functional parameters. **(A)**. The equation of Motion: Paw (cmH_2O) is airway pressure, measured at airway opening, Flow (mL/s) is airway flow, R is Respiratory System Resistance ($cmH_2O.s/mL$), Vol (mL) is the Volume of air that has entered the lungs since the beginning of inspiration, E (cmH_2O/mL) is Respiratory System Elastance and P0 (cmH_2O) is the airway pressure at the beginning of inspiration. **(B)**. The Constant Phase Model (Z(f), $cmH_2O.s/mL$) is calculated as the pressure response (P(f), cmH_2O) divided by ventilator generated flow (Flow(f), mL/s) at each frequency (f). Raw represents Newtonian resistance ($cmH_2O.s/mL$); i is imaginary number; Iaw is airway inertance ($cmH_2O.s^2/mL$), Gtis is tissue viscance (cm $H_2O.s^{(1-\alpha)}/mL$); Htis is tissue elastance (cm $H_2O.s^{(1-\alpha)}/mL$).

In this review, we describe some of the mathematical approaches used in respiratory mechanics in animal models and in patients and their application in the development of mechanical ventilation. Finally, we will discuss how respiratory mechanics is still important for both research and clinical care and how it can provide insightful information moving respiratory science forward.

RESPIRATORY MECHANICS IN ANIMAL MODELS

Animal models have been extensively used to elucidate different physiological mechanisms leading to respiratory disease development, such as asthma and chronic obstructive pulmonary disease (COPD).

Generally, the assessment of respiratory mechanics in animal models is based on the acquisition of pressure and volume/flow data. From these data, mathematical models whose parameters have physiological significance are applied (Bates, 2005).

The most used model for evaluating respiratory mechanics is known as the "equation of motion." It is a linear one-compartment model that assumes the respiratory system is excited at a single frequency, usually very close to the respiratory rate (**Figure 1**) (Bates, 2005). The parameters of this model are respiratory system resistance, representing the amount of pressure required to generate flows; and respiratory system elastance, which is the amount of pressure required to maintain volume changes in the respiratory system.

The equation of motion does not contemplate viscoelastic phenomenon. Viscoelasticity is the property to accommodate stress following changes in volume (stress relaxation) (Faffe and Zin, 2009). It can be observed in pressure-time graph once inspiratory flow is abruptly stopped. The slow pressure decrease after inspiratory pause reveals stress relaxation (**Figure 2A**). It results from parenchymal fiber conformational adaptation (Faffe and Zin, 2009), changes in surface tension in water-air interfaces or redistribution of air within lung regions (Bates, 2009). Measurements in viscoelasticity add complexity to equation of motion model.

The respiratory system has a high frequency dependence. This led to the use of excitations with more than one frequency in order to calculate the respiratory impedance that basically characterizes the biomechanical behaviour of the respiratory system in the frequencies contained in the excitation (**Figure 1**) (Hantos et al., 1992).

For a better physiological understanding of respiratory impedance, models are used whose parameters are correlated with dissipative (airway resistance and tissue viscosity) and conservative (elastance or tissue compliance) components. The most used model for understanding respiratory impedance in small rodents is the constant-phase model (Bates and Irvin, 2003). This model provides more detailed information on lung mechanics comparing to equation of motion. It describes proximal and distal airways with different parameters, which can be useful to evaluate obstructive diseases.

Respiratory Mechanics in Animal Models of Lung Disease

Respiratory mechanics have been studied in several animal models of respiratory diseases. In experimental emphysema, researchers observed a decrease in tissue elastance and viscosity (see section "Respiratory mechanics in animal

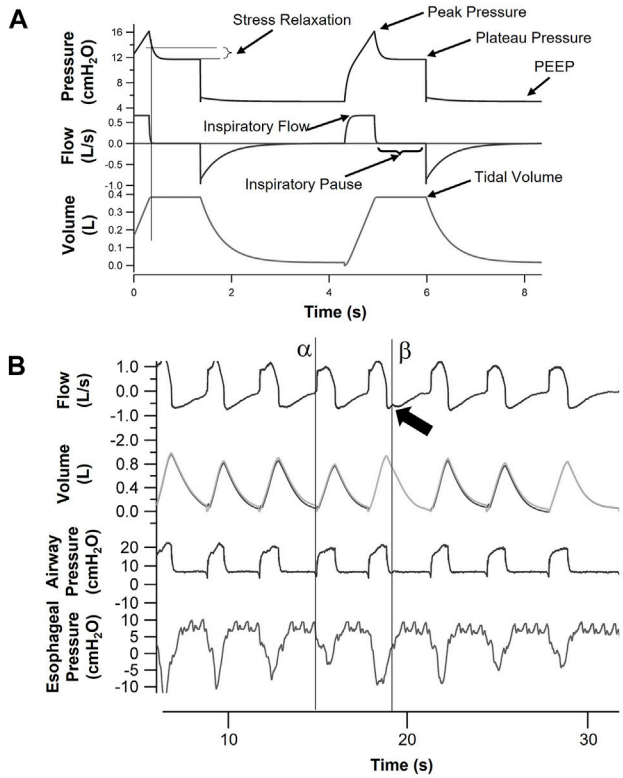

$$Airway\ Pressure = Po + Resistance * Flow + \frac{Tidal\ Volme}{Compliance}$$

$$Static\ Compliance = \frac{Tidal\ Volme}{Plateau\ Pressure - PEEP}$$

$$Resistance = \frac{Peak\ Pressure - Plateau\ Pressure}{Inspiratory\ Flow}$$

$$Airway\ Pressure + Pmus = Po + Resistance * Flow + \frac{Tidal\ Volme}{Compliance}$$

FIGURE 2 | Respiratory mechanics in paralyzed and spontaneously breathing patients. **(A)**. This is a representation of Flow, Volume and Pressure signals over time for a patient under sedation and neuromuscular blockage. Since there is no respiratory muscle activity, equation of motion (see **Figure 1A**) can be applied. Compliance (inverse of Elastance, displayed in **Figure 1**) and Resistance can be found using minimum square method or by the inspiratory pause special case displayed in **(A)**. Applying an inspiratory pause will simplify the equation allowing measurement of Static Compliance and Resistance. It also allows observation of viscoelastic properties of the respiratory system, with the slow decrease in pressure (Stress Relaxation) once flow is abruptly stopped. **(B)**. In non-sedated patients, respiratory muscles interact with the ventilator. In this example, we show Pressure, Flow, Volume and Esophageal Pressure signal over time in a patient ventilated in Pressure Support Mode. Muscle activity can be measured with an esophageal catheter. In this scenario, equation of motion needs to be adapted to include pressure generated by respiratory muscles (Pmus). The model becomes less stable but esophageal pressure reveals several features of patient ventilator interaction. The observed changes in tidal volumes over several breaths is caused by a change in patient's effort detected by esophageal pressure. Additionally, we can observe the inspiratory effort triggering mechanical ventilator (line α) and the prolongation of patient's inspiratory effort into ventilator expiration (line β), distorting expiratory flow curve (arrow).

models") related to alveolar destruction and loss of viscoelastic properties (Bates, 2009; Ito et al., 2019a, 2019b). On the other hand, repairing lung tissue with different components of extracellular matrix also alters lung function. Changes in collagen fibers types I and III and elastin in lung parenchyma leads to loss of lung elasticity (Fietzek and Kuehn, 1976; Shifren et al., 2007; Suki and Bates, 2008; Koenders, 2009).

Airway resistance increase is usually detected in experimental models of asthma where structural changes in airways are the major histological finding (Bates, 2009). Edema in peribronchovascular areas also increases viscoelastic properties. Airway hyperresponsiveness can be detected with a dose-response curve to methacholine or the antigen itself (Wang et al., 1986). Both constant phase model and equation of motion can be used to describe respiratory function in these animals (Bates, 2009) (see **Figure 1** and section "Respiratory mechanics in animal models" above).

Camargo et al. (2020) showed in an experimental model of asthma in mice sensitized with ovalbumin that there was an increased response of airway resistance when compared to the control group. In addition, Possa et al. (2012); Righetti et al. (2014) and Pigati et al. (2015), in an experimental model of asthma showed that the worsening in mechanical parameters had a positive correlation with markers of eosinophilic inflammation, Th2 profile cytokines, oxidative stress (iNOS and 8- iso-PGF2alpha), and extracellular matrix remodelling.

Oscillatory mechanics and the constant phase model (see **Figure 1** and section "Respiratory mechanics in animal models" above) can be applied not only to whole lung, but also to lung tissue *in vitro*. Using this technique, it is possible to calculate resistance and elastance of lung tissue strips (Leite-Júnior et al., 2003). For oscillatory mechanics, subpleural parenchyma strips of the lower lobes are cut and the resting length (Lr) and wet weight (W0) of each strip are measured (Aristoteles et al., 2013; Righetti et al., 2014). Lung tissue strips are composed of 86–90% alveoli, 5–8% blood vessels and 0.4–5% airways (Ludwig and Dallaire, 1994; Aristoteles et al., 2013). The tissue lungs are infused with Krebs solution (in mM: NaCl, 118;

KCl, 4.5; $NaHCO_3$, 25.5; $CaCl_2$, 2.5; $MgSO_4$, 1.2; KH_2PO_4, 1.2; glucose 10) and metal clips are glued to either end of the tissue strips with cyanoacrylate. Steel wires are attached to the clips; one side is connected to a force transducer and the other side is connected to a servo-controlled lever arm. The lever arm is capable of peak-to-peak length excursions. It is connected to a function generator, which controlled the frequency, amplitude, and waveform of the device oscillation (Ebihara et al., 2000; Pigati et al., 2015). The resting tension (T) is set by the movement of a screw thumb wheel system, which effected slow vertical displacements of the force transducer. Length and force signals are converted from analog to digital with an analog-to-digital converter and recorded by a compatible computer. The resistance (R) and elastance (E) of the lung tissue strip are estimate by the recursive least-squares algorithm to the equation of motion (Ludwig and Dallaire, 1994; Aristoteles et al., 2013; Righetti et al., 2014; Pigati et al., 2015).

$$T = E\Delta 1 + R\left(\Delta 1/\Delta t\right) + K$$

Where T is tension, l is length, $\Delta l/\Delta t$ is the length change per unit of time, and K is a constant reflecting resting tension. The unstressed cross-sectional area ($A0$) of the strip was obtained from the formula:

$$A0\ (cm^2) = W0/(p \times Lr)$$

In this sense, Nakashima et al. (Nakashima et al., 2008) evaluated the active process of lung immune unresponsiveness with oral ingestion of ovalbumin (oral tolerance) in guinea pigs sensitized with ovalbumin and Starling (Starling et al., 2009) evaluated the use of nitric oxide synthetase inhibitor in an experimental model of asthma. In both studies oscillatory mechanics identified the improvement in lung tissue resistance and elastance parameters as a result of treatment. Furthermore, changes in lung resistance and elastance also correlate with changes in inflammation, oxidative stress, and remodelling in the lung parenchyma (Righetti et al., 2014; Pigati et al., 2015). Pigati et al. 2015 showed similar changes in resistance and elastance of the respiratory system and lung tissue strip. Moreover, tissue strip oscillatory mechanics can also include dose-response curves after challenges with antigen or methacholine. (Lanças et al., 2006). In recent decades, several studies used this technique for measuring lung tissue resistance and elastance *in vitro* (Xisto et al., 2005; Santos et al., 2008; Starling et al., 2009; Aristoteles et al., 2013; Righetti et al., 2014; Pigati et al., 2015) and these studies helped to support the importance of alterations in the lung parenchyma of asthmatic patients (Tulić and Hamid, 2003; Mauad et al., 2004; Martin, 2008).

Lung mechanics produces a simple description of the function of the lungs and can be used to detect diseases and to analyse the effects of potential treatments. The new methodologies (lung strip mechanics and oscillatory mechanics) described above allowed a more complex and accurate description of lung function (Bates and Irvin, 2003; Leite-Júnior et al., 2003; Lanças et al., 2006). In the decades to come, lung mechanics will continue to play a fundamental role in respiratory research and clinical care.

LUNG PHYSIOLOGY IN HUMAN SUBJECTS: MECHANICAL VENTILATION AND LUNG ASSESSMENT

Lung Physiology and Evolution of Mechanical Ventilators

Besides allowing mechanistic investigation on several lung diseases, respiratory physiology largely contributed to evolution of mechanical ventilation. In the past century, mechanical ventilation evolved from bulky and cumbersome negative pressure chambers (iron lungs) to modern positive pressure ventilators (Kacmarek, 2011). Over decades, many features and ventilatory modes were added to ventilators. This process was greatly assisted by knowledge gained in basic lung physiology.

Incorporation of positive end expiratory pressure (PEEP) to mechanical ventilators became widespread after the description of Acute Respiratory Distress Syndrome (ARDS) in 1967 (Ashbaugh et al., 1967) and observations of hypoxemia improvement with the use of PEEP (Ashbaugh et al., 1969). Measurements of lung compliance using equation of motion and responses to PEEP were important for defining the new syndrome. Although compliance is not part of current ARDS definition (Ranieri et al., 2012), it has been used in initial characterizations of the syndrome (Ashbaugh et al., 1967; Murray et al., 1988). Later, investigations on the role of PEEP and tidal volume in ARDS contributed to understanding Ventilation Induced Lung Injury (VILI) (Parker et al., 1990a; Corbridge et al., 1990; Dreyfuss and Saumon, 1993); and were the basis for developing Lung Protective Ventilation (Amato et al., 1998; The Acute Respiratory Distress Syndrome Network, 2000).

Some ventilatory modes added in time to ventilators were largely based on lung physiology. In Proportional Assist Ventilation (PAV), lung compliance and resistance are used to determine the amount of airway pressure delivered by the ventilator (Younes, 1992). In Neurally-Adjusted Ventilatory Assist (NAVA), electrical impulses generated by depolarization of diaphragm fibers are captured and control the level of ventilatory support (Sinderby et al., 1999). In Automatic Tube Compensation (ATC), mechanical ventilators provide additional pressure proportional to flow and endotracheal tube resistance (Guttmann et al., 1993; L'Her, 2012).

Respiratory Mechanics Applied to Clinical Care

Assessment of lung mechanics is used in daily clinical care. In patients receiving invasive mechanical ventilation, the equation of motion is used to describe lung mechanics and to assist in the characterization of respiratory failure (Pham et al., 2017). Physicians can measure increases in resistance (**Figure 2**) in respiratory failure in patients with obstructive disease. Changes

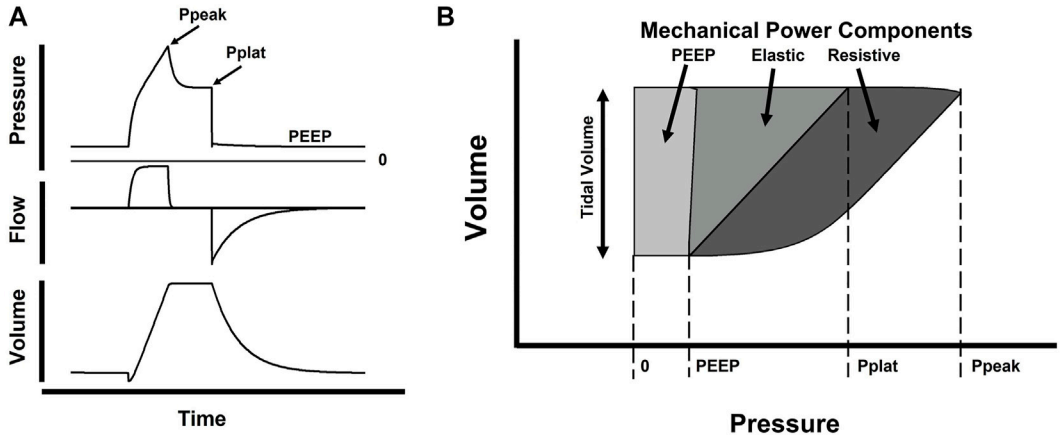

FIGURE 3 | Schematic representation of Mechanical Power. In panel **(A)** we display a single breath of a patient ventilated with Volume Assist Control. Graphs show changes in Pressure, Flow and Volume over time and highlight points of interest: PEEP, peak pressure (Ppeak) and plateau pressure (Pplat, at end of inspiratory pause). In figure **(B)**, we display a Volume-Pressure loop with the same points of interest observed in panel **(A)**. Dark gray area represents Resistive Mechanical Power, change in pressure to overcome resistive respiratory forces integrated over change in volume (tidal volume); middle gray area represents Elastic mechanical power, change in pressure to overcome elastic respiratory forces integrated over change in volume; light gray area represents PEEP mechanical power, a static component of pressure representing baseline tension on the respiratory system also integrated over change in tidal volume. (Adapted from Silva et al., 2019).

in resistance over the course of treatment can indicate worsening or improvement of disease status and guide ventilatory support.

In ARDS, measurements of lung compliance (**Figure 2**) inform the clinician about disease severity (Morales-Quinteros et al., 2019; Panwar et al., 2020; Boscolo et al., 2021). In COVID pandemic, lung compliance was employed to describe specific phenotypes: patients with hypoxemia but little amount of lung collapse and high compliance versus very low compliant lungs with large amount of lung collapse (Gattinoni et al., 2020b). The authors suggested different phenotypes could benefit from different ventilatory strategies (Gattinoni et al., 2020a). This approach was disputed by other researchers, who demonstrated respiratory compliance in COVID patients were similar to values previously reported in ARDS (Tobin, 2020; Ziehr et al., 2020; Sjoding et al., 2021) and treatment should not be changed. Early findings during a pandemic should be carefully evaluated before changing current practice (Meyer et al., 2021). Despite the controversy, use of physiological parameters to further classify ARDS patients highlights the heterogeneity of the disease (Khan et al., 2021). In the future, we might be able to learn what parameters could determine changes in treatment strategies.

Over decades, different physiological approaches have been proposed to properly set PEEP levels in ARDS patients. Obtaining lung pressure-volume curve and selecting PEEP levels according to best compliance was initially used by Amato (Amato et al., 1998). This is rather laborious and measuring lung compliance at different PEEP levels after lung recruitment could be a suitable simplification of this method. Calculating dead space and shunt fraction was also used for PEEP selection (Ferluga et al., 2018; Karbing et al., 2020; Tusman et al., 2020). Recently, measuring potential recruitment has also been proposed (Chen et al., 2020). And Talmor et al. (2008) proposed setting PEEP levels to maintain a positive transpulmonary pressure, measured using an esophageal catheter. They have shown improvements in oxygenation but failed to demonstrate decrease in mortality with this technique (Beitler et al., 2019). Unfortunately, an ideal method for PEEP selection has not been found. Some authors have used a FiO_2-based table to guide PEEP setting. This method can be suitable in the busy ICU environment but did not reduce ARDS mortality (Brower et al., 2004). Additionally, setting PEEP based on FiO_2 level ignores that patients might respond very differently. Physiological approaches could still be useful in addressing this problem.

More recently, Gattinoni proposed the use of Mechanical power, a new measurement of stress applied to lungs based on energy delivered during mechanical ventilation (Gattinoni et al., 2016). Mechanical power was based on equation of motion and incorporated concepts of mechanical work displayed on Campbell's diagram (Cabello and Mancebo, 2006). Each component of the equation of motion was multiplied by the change in volume and Respiratory rate (**Figure 3**) to evaluate the individual contribution to lung injury (Silva et al., 2019). The usefulness of this new analysis is still under investigation. Some authors believe it does not add substantial new information to mechanical ventilation management (Costa et al., 2021). On the other hand, mechanical power can be associated to biomarkers of lung deterioration (Rocco et al., 2020). At a minimum, it underscored the importance of respiratory rate as a source of stress to lungs during ventilation.

The assessment of respiratory mechanics in spontaneously breathing patients has always been a challenge. Respiratory effort should be accounted for when applying equation of motion (Grinnan and Truwit, 2005). Esophageal catheters can be used to measure patients' effort (Baydur et al., 1982), allowing the use of equation of motion even in non-paralyzed patients (**Figure 2**). On the other hand, new lung mechanics techniques evolving from experimental physiology can be used in spontaneously ventilated

patients. Notably, forced oscillation technique, or oscillometry, has contributed to a better understanding of lung function in clinical routine and in research, particularly in patients with obstructive disease (Peterson-Carmichael et al., 2016; Hantos, 2021; Lundblad and Robichaud, 2021).

Lung Protective Ventilation. Tidal Volume Challenge

Initial basic research on the effects of PEEP and tidal volume in ARDS (Parker et al., 1990b; Carlton et al., 1990; Corbridge et al., 1990; Dreyfuss and Saumon, 1993) later translated in trials investigating mechanical ventilation management strategies (Amato et al., 1998; The Acute Respiratory Distress Syndrome Network, 2000). Current guidelines for ARDS management suggest limiting tidal volume to 6 ml/kg and plateau pressure to 30 cm H_2O (Griffiths et al., 2019; Papazian et al., 2019). This strategy was named lung protective ventilation. It revealed that mechanical ventilation can be harmful to lungs and defined new targets for the health team. It also introduced the challenging idea that aiming normal blood gas values during mechanical ventilation could lead to worse outcomes. Higher pCO_2 levels (permissive hypercapnia) generated by reduction tidal volume were initially regarded as benign. Later, some authors recognized hypercapnia was associated to impaired immunologic response and vascular tonus dysfunction. Hypercapnia increases pulmonary resistance and can contribute to acute cor pulmonale (Repessé and Vieillard-Baron, 2017; Barnes et al., 2018). Nevertheless, the best current evidence still recommends limiting tidal volume for ARDS patients despite CO_2 elevation. Patients with hypercapnia in this setting could be managed with additional rescue strategies (Repessé and Vieillard-Baron, 2017).

Lung protective ventilation concepts were further explored in a later reanalysis of the initial ARDS trials (Amato et al., 2015). The authors used a multilevel mediation analysis to conclude that driving pressure (plateau pressure—PEEP) was the variable most significantly associated to mortality. Although ARDS guidelines advised against the use of targets of driving pressure (Papazian et al., 2019), this measurement integrates the concepts of disease severity (lung compliance) and ventilator management (tidal volume). Further prospective trials are required but driving pressure could become an essential parameter to monitor in the future.

The success of managing mechanical ventilation during ARDS led several authors to suggest the use of lung protective ventilation in all patients receiving mechanical ventilation. Indeed, initial observational studies suggested better outcomes or decreased inflammatory cytokine production when limiting tidal volume in non-ARDS patients (Determann et al., 2010; Neto et al., 2012; Fuller et al., 2013). The initial observations were not confirmed in a properly conducted clinical trial (Simonis et al., 2018). As surprising this might look, one must remember that patients with ARDS have lungs very different from normal and from other patients on mechanical ventilation. Limiting tidal volume can be useful in some scenarios, as operating rooms, but can be very challenging in ICU. Some individuals would require deep sedation and muscle paralysis to limit tidal volume regardless of the ventilatory mode selected, adding significant morbidity to patient care. Patients waking from sedation after uneventful surgery that develop large tidal volume on spontaneous breathing should probably be extubated and not deeply sedated. COPD patients could benefit from lowering tidal volume and minute ventilation, but probably would handle very poorly high respiratory rates that might be required if tidal volumes are greatly reduced (Marini, 2011).

Even in ARDS patients, duration of strict protective ventilation can bring challenges to caring team. Although essential in the beginning of care, limiting tidal volumes can be difficult in some patients once sedation and muscle paralysis are withdrawn. Maintaining long periods of sedation and paralysis can lead to muscle weakening and prolong time on mechanical ventilation (Kress et al., 2000; Girard et al., 2008; Reade and Finfer, 2014). On the other hand, patients with high ventilatory drive will produce large tidal volumes regardless of ventilatory mode selected (Yoshida et al., 2013; Papazian et al., 2019).

The importance of ventilatory drive and its contribution to lung injury is still under investigation. It has been recognized that patients can generate significant amount of inspiratory pressure during respiratory failure, both before and after being intubated. Large inspiratory pressure swings will translate into large transpulmonary pressure irrespective of the settings on non-invasive ventilation device (before intubation) or mechanical ventilator (after intubation) (Brochard et al., 2017). Even when volume assist control mode is selected, patients with large swings generate intrathoracic pressure reduction that can produce lung edema, increases in left ventricle afterload and double triggering in ventilator, which doubles or triples tidal volumes (Pohlman et al., 2008; Pinsky, 2018; Sottile et al., 2020). The contribution or spontaneous breathing patterns to lung injury has been named P-SILI (Patient Self Inflicted Lung Injury). Although some authors have advised against using those new concepts to manage ventilator at this stage due to lack of experimental and clinical data (Tobin et al., 2020), this will be an important topic to explore. The relative importance of spontaneous effort in producing lung injury will need to be balanced against the deleterious effects of extending sedation and muscle paralysis.

Guidelines for properly managing those patients are still missing. We will need further cooperation between basic and clinical science to understand the limits of lung protective ventilation. We need to understand when this strategy is absolutely required warranting muscle paralysis; and when we can be more flexible on these rules. We also need to understand what other lung disorders require limiting tidal volume.

Respiratory Mechanics in Obstructive Lung Diseases

Patients with respiratory failure secondary to obstructive lung disease can require mechanical ventilation. Ventilatory strategies for these patients are designed to avoid air trapping and intrinsic PEEP (PEEPi) generation (Reddy and Guntupalli, 2007). PEEPi is produced when expiratory time is insufficient to allow complete

tidal volume exhalation, usually when both airway resistance and respiratory rate increase. Air is trapped inside the lungs, increasing intrathoracic pressure, decreasing venous return and increasing patients' effort to trigger the ventilator and generate inspiratory flows (Pepe and Marini, 1982; Marini, 2011). Mechanical ventilator settings should allow enough expiratory time to minimize the impact of PEEPi. Although limiting tidal volume can be beneficial, low minute ventilation and high expiratory time should be main targets (Reddy and Guntupalli, 2007).

In obstructive patients, equation of motion can be used to measure lung resistance and monitor the response to treatments: bronchodilators, antibiotics and management of airway secretion. PEEPi can be measured with expiratory pause, informing bedside decisions on setting ventilator parameters.

However, there are limitations for the use of lung mechanics in those patients. Equation of motion is usually applied only to inspiratory phase, where airway pressure variation is significant. Measurement of airway resistance during expiration is often neglected despite its importance in generating PEEPi. Some patients in respiratory failure reach a condition of expiratory flow limitation, where airways collapse at the mid-end expiration (Bates, 2009). In this scenario, expiratory flow becomes independent of pressure gradient and expiratory airway resistance cannot be defined using equation of motion.

Additionally, patients on mechanical ventilators are often awake and have spontaneous breathing. In this setting, if pressure generated by respiratory muscles is not measured (**Figure 2B**), lung mechanics cannot be properly assessed. PEEPi measurement requires long expiratory pause which is usually not possible in patients with spontaneous breathing (Grinnan and Truwit, 2005). And since PEEPi is highly dependent on respiratory rate, values of PEEPi obtained during neuromuscular block are hardly valid when patients resume respiratory effort.

In the future, widespread use of esophageal pressure catheters can allow monitoring of respiratory effort and assessment of lung mechanics in patients with spontaneous breathing (Grinnan and Truwit, 2005). PEEPi can also be measured using esophageal pressure monitoring (Marini, 2011). Methods for measuring expiratory resistance and detecting expiratory flow limitation can become easier. Finally, oscillatory mechanics at the bedside can provide information on dissipative forces of the respiratory system even in patients with spontaneous breathing (see section Oscillometry). It could then allow the analysis of lung resistance in patients with obstructive lung disease without the requirement of deep sedation.

LUNG PHYSIOLOGY STILL NOT AT BEDSIDE PRIMETIME

For different reasons, several physiological approaches developed in the lab did not reach bedside yet and will be discussed in the paragraphs below. Some of these techniques are laborious or provide data clinicians are not ready to use. Some techniques, on the other hand, did become commercially available but are still seldom employed.

Multiple inert gas elimination technique (MIGET) was designed for determining ventilation/perfusion distribution throughout the lungs using several gases with different solubility on blood. MIGET advanced knowledge of respiratory physiology in different species and elucidated mechanisms of hypoxia in different disorders (Wagner, 2008). The technique is very laborious and requires not only injection of several gases but also a pulmonary catheter for measuring cardiac output and gas detector. It provides useful clinical information and could be used to select PEEP levels or describe functional lung behaviour during treatment. Its complexity, however, prevented widespread clinical application.

Electrical Impedance Tomography (EIT) evolved from very simple and inaccurate devices to monitor respiratory rate into complex continuous monitors of lung ventilation. Recent advances in the technique also included perfusion and V/Q distribution measurement using electrocardiography-gated impedance signals or following hypertonic saline infusion (Costa et al., 2009; Nguyen et al., 2012). There should be some caution in interpreting perfusion measured by impedance technique. Impedance signals should not be able to detect perfusion defects in small capillaries if pulmonary blood flow to major arteries remains unchanged (Deibele et al., 2008). Therefore, some authors believe perfusion EIT will be more useful as a non-invasive tool for diagnosing pulmonary embolism rather than small V/Q mismatch (Maciejewski et al., 2021). However, the technology is still evolving and methods for diagnosing small perfusion defects could arise.

Although not used in many ICUs, EIT became commercially available and can provide useful information on ventilation during patient care. It can be used to improve PEEP titration since it displays both overdistention and lung collapse. It also provides a visual and numerical analysis of ventilation homogeneity, can detect pneumothorax in real time and displays patterns of ventilation during spontaneous efforts (Coppadoro et al., 2020; Maciejewski et al., 2021). In the present, there is not enough supporting evidence for the use of EIT, but it can become an important monitoring device in the future.

Measuring resting lung volumes has always been difficult in clinical and research settings. Nitrogen-washout measurements have been proposed by some authors. The technique uses changes in FiO_2 concentrations and nitrogen dilution to estimate lung volumes (Olegård et al., 2005; Dellamonica et al., 2011). The process, however, is time-consuming and cannot be applied continuously in a busy ICU. Nevertheless, measuring resting lung volumes can be used to properly set tidal volumes. Guidelines for ARDS management suggest limiting tidal volumes to 6 ml/kg of ideal body weight, which is calculated based on patient height to correct for different lung sizes (Papazian et al., 2019). However, ARDS patients have different lung volumes not only because of different body constitution but also because of extension of the disease (Chiumello et al., 2008; Mattingley et al., 2011). Scaling tidal volume to actual size of lungs

could allow settings targeted not only to each patient, but also to each phase of the disease (Chiumello et al., 2008; Macintyre, 2016; Umbrello et al., 2017; Pelosi et al., 2021).

Patients' effort monitoring has been possible to measure for decades using esophageal catheters (Baydur et al., 1982). Although commercially available and proposed by many different research groups, the technique is seldom employed (Akoumianaki et al., 2014). Misplacement of the catheter, patients' discomfort and lack of clear clinical benefit could explain the low enthusiasm for the approach. On the other hand, as we manage patients with less sedation and greater levels of interaction with ventilators, measuring effort can become important. If future research relates respiratory effort to lung injury, spontaneous breathing should be carefully handled.

Oscillometry

Oscillometry or forced oscillation technique consists of applying flow or pressure oscillations at the entrance of the airways and monitoring the response obtained with the oscillations in order to calculate the impedance of the respiratory system. Impedance is the mechanical load of the respiratory system to ventilation.

Initially, the forced oscillation technique was used in apnea situations so that voluntary respiratory efforts did not mask the actual physiological condition of the respiratory system. However, with signal processing techniques, it became possible to use oscillometry in spontaneously ventilating patients by superimposing a high-frequency pressure waveform on the tidal breathing pattern (Peterson-Carmichael et al., 2016) and still calculate the impedance of the respiratory system with the effects of breathing minimized.

The constant-phase model (see section 'Respiratory mechanics in animal models' and **Figure 1**) applied in small rodents is not suitable for patients because of the low frequency broadband excitation needed (Lundblad and Robichaud, 2021). So, the analysis of the human respiratory impedance is based mostly on the frequency response behaviour of impedance, a complex mathematical function with real and imaginary components. This analysis strongly helps the understanding of respiratory physiology, as the real component is related to dissipative energy (resistance) and the imaginary component is related to conservative energy (elastance) of the respiratory system (Lundblad and Robichaud, 2021).

According to Hantos (Hantos, 2021), manoeuvres using oscillometry involving large but slow changes in lung volume allows for fine mapping of respiratory mechanics exceeding the tidal range and a novel intra-breath modality is capable of tracking the dynamic changes in respiratory system.

Technical standards for respiratory oscillometry have been published (King et al., 2020) and commercial devices are becoming popular.

BACK TO BENCH

Basic science and lung physiology helped to develop and advance mechanical ventilation at bedside and they still can be very important for the challenges ahead.

Lung protective ventilation does not answer all questions in respiratory failure. It was crafted long ago, when mechanical ventilation care was substantially different. Awake patients interacting with ventilators bring additional challenges. How far should we go to limit tidal volume? Should we continue to keep low levels of sedation in patients with high respiratory drive? Should we tolerate higher tidal volumes once the initial inflammatory phase of ARDS is over and oxygenation starts to improve? And how should we handle patients without ARDS with high respiratory drive and tidal volumes?

Measuring effort, lung volumes, lung inhomogeneities, pattern of ventilation and V/Q distribution or mechanical power can provide some of these answers. At the same time, ventilators used for small animals incorporated some of the technologies developed at the bedside, as pressure support ventilation. P-SILI and the effects of respiratory effort can be further investigated in animal models.

The advent of ECMO (extracorporeal membrane oxygenation) has brough additional complexity to the field. Once limited to operating rooms, ECMO use in ICU became more popular after influenza (H1N1 in 2009) and COVID (2020) pandemics (Combes et al., 2018; Barbaro et al., 2020). Although very expensive and invasive, ECMO can provide all the respiratory support required by some patients. Ventilators can then be adjusted to provide very minimum ventilation. The optimal setting and how long a patient should be maintained in ECMO are still under investigation (Tonna et al., 2021).

CONCLUSION

The study of lung mechanics has substantially contributed to development of knowledge of respiratory diseases. It was also a cornerstone in the creation and evolution of mechanical ventilation. The combination of basic, translational and applied sciences has proved very useful in respiratory physiology leading not only to better understanding physiopathology but also to designing supportive treatment. In the years to come, we expect this partnership to continue as we face new challenges in managing patients with respiratory failure.

AUTHOR CONTRIBUTIONS

PB, FD, IT, and MM contributed to conception and design of the study. HM and RR wrote sections of the manuscript. All authors contributed to manuscript revision, read, and approved the submitted version.

REFERENCES

Akoumianaki, E., Maggiore, S. M., Valenza, F., Bellani, G., Jubran, A., and Loring, S. H. (2014). The Application of Esophageal Pressure Measurement in Patients with Respiratory Failure. *Am. J. Respir. Crit. Care Med.* 189, 520–531. doi:10.1164/rccm.201312-2193CI

Amato, M. B., Barbas, C. S., Medeiros, D. M., Magaldi, R. B., Schettino, G. P., Lorenzi-Filho, G., et al. (1998). Effect of a Protective-Ventilation Strategy on Mortality in the Acute Respiratory Distress Syndrome. *N. Engl. J. Med.* 338, 347–354. doi:10.1056/NEJM199802053380602

Amato, M. B. P., Meade, M. O., Slutsky, A. S., Brochard, L., Costa, E. L. v., Schoenfeld, D. A., et al. (2015). Driving Pressure and Survival in the Acute Respiratory Distress Syndrome. *N. Engl. J. Med.* 372, 747–755. doi:10.1056/NEJMsa1410639

Aristoteles, L. R. C. R. B., Righetti, R. F., Pinheiro, N. M., Franco, R. B., Starling, C. M., da Silva, J. C. P., et al. (2013). Modulation of the Oscillatory Mechanics of Lung Tissue and the Oxidative Stress Response Induced by Arginase Inhibition in a Chronic Allergic Inflammation Model. *BMC Pulm. Med.* 13, 52. doi:10.1186/1471-2466-13-52

Ashbaugh, D. G., Petty, T. L., Bigelow, D. B., and Harris, T. M. (1969). Continuous Positive-Pressure Breathing (CPPB) in Adult Respiratory Distress Syndrome. *J. Thorac. Cardiovasc Surg.* 57, 31–41. doi:10.1016/s0022-5223(19)42760-8

Ashbaugh, D. G., Boyd Bigelow, D., Petty, T. L., and Levine, B. E. (1967). Acute Respiratory Distress in Adults. *Lancet* 290. doi:10.1016/S0140-6736(67)90168-7

Barbaro, R. P., MacLaren, G., Boonstra, P. S., Iwashyna, T. J., Slutsky, A. S., Fan, E., et al. (2020). Extracorporeal Membrane Oxygenation Support in COVID-19: an International Cohort Study of the Extracorporeal Life Support Organization Registry. *Lancet* 396, 1071–1078. doi:10.1016/S0140-6736(20)32008-0

Barnes, T., Zochios, V., and Parhar, K. (2018). Re-examining Permissive Hypercapnia in ARDS: A Narrative Review. *Chest* 154. doi:10.1016/j.chest.2017.11.010

Bates, J. H. T., and Irvin, C. G. (2003). Measuring Lung Function in Mice: The Phenotyping Uncertainty Principle. *J. Appl. Physiology* 94, 1297–1306. doi:10.1152/japplphysiol.00706.2002

Bates, J. H. T. (2009). *Lung Mechanics: An Inverse Modeling Approach*. Cambridge University Press. doi:10.1017/CBO9780511627156

Bates, J. (2005). "Measuring Techniques in Respiratory Mechanics," in *Physiologic Basis of Respiratory Disease*. Editors Q. Hamid, J. Shannon, and J. Martin, 623–637.

Baydur, A., Behrakis, P. K., Zin, W. A., Jaeger, M. J., and Milic-Emili, J. (1982). Simple Method for Assessing the Validity of the Esophageal Balloon Technique. *Am. Rev. Respir. Dis.*, 126788–791. doi:10.1164/arrd.1982.126.5.788

Beitler, J. R., Sarge, T., Banner-Goodspeed, V. M., Gong, M. N., Cook, D., Novack, V., et al. (2019). Effect of Titrating Positive End-Expiratory Pressure (PEEP) with an Esophageal Pressure-Guided Strategy vs an Empirical High PEEP-F Io 2 Strategy on Death and Days Free from Mechanical Ventilation Among Patients with Acute Respiratory Distress Syndrome: A Randomized Clinical Trial. *JAMA - J. Am. Med. Assoc.* 321 (9), 846–857. doi:10.1001/jama.2019.0555

Boscolo, A., Sella, N., Lorenzoni, G., Pettenuzzo, T., Pasin, L., Pretto, C., et al. (2021). Static Compliance and Driving Pressure Are Associated with ICU Mortality in Intubated COVID-19 ARDS. *Crit. Care* 25, 263. doi:10.1186/s13054-021-03667-6

Brochard, L., Slutsky, A., and Pesenti, A. (2017). Mechanical Ventilation to Minimize Progression of Lung Injury in Acute Respiratory Failure. *Am. J. Respir. Crit. Care Med.* 195, 438–442. doi:10.1164/rccm.201605-1081CP

Brower, R. G., Hopkins Uni-versity, J., Lanken, P. N., MacIntyre, N., Matthay, M. A., Morris, A., et al. (2004). Higher versus Lower Positive End-Expiratory Pressures in Patients with the Acute Respiratory Distress Syndrome the Members of the Writing Committee. *N. Engl. J. Med.* 351 (4), 327–336. Available at: www.ardsnet.org. doi:10.1056/NEJMoa032193

Cabello, B., and Mancebo, J. (2006). Work of Breathing. *Intensive Care Med.* 32, 1311–1314. doi:10.1007/s00134-006-0278-3

Camargo, L. do N., Santos, T. M. dos, Andrade, F. C. P. de, Fukuzaki, S., dos Santos Lopes, F. D. T. Q., de Arruda Martins, M., et al. (2020). Bronchial Vascular Remodeling Is Attenuated by Anti-IL-17 in Asthmatic Responses Exacerbated by LPS. *Front. Pharmacol.* 11. doi:10.3389/fphar.2020.01269

Carlton, D. P., Cummings, J. J., Scheerer, R. G., Poulain, F. R., and Bland, R. D. (1990). Lung Overexpansion Increases Pulmonary Microvascular Protein Permeability in Young Lambs. *J. Appl. Physiology* 69, 577–583. doi:10.1152/jappl.1990.69.2.577

Chen, L., del Sorbo, L., Grieco, D. L., Junhasavasdikul, D., Rittayamai, N., Soliman, I., et al. (2020). Potential for Lung Recruitment Estimated by the Recruitment-To-Inflation Ratio in Acute Respiratory Distress Syndrome a Clinical Trial. *Am. J. Respir. Crit. Care Med.* 201, 178–187. doi:10.1164/rccm.201902-0334OC

Chiumello, D., Carlesso, E., Cadringher, P., Caironi, P., Valenza, F., Polli, F., et al. (2008). Lung Stress and Strain during Mechanical Ventilation for Acute Respiratory Distress Syndrome. *Am. J. Respir. Crit. Care Med.* 178, 346–355. doi:10.1164/rccm.200710-1589OC

Collett, P. W., Perry, C., and Engel, L. A. (1985). Pressure-time Product, Flow, and Oxygen Cost of Resistive Breathing in Humans. *J. Appl. Physiology* 58, 1263–1272. doi:10.1152/jappl.1985.58.4.1263

Combes, A., Hajage, D., Capellier, G., Demoule, A., Lavoué, S., Guervilly, C., et al. (2018). Extracorporeal Membrane Oxygenation for Severe Acute Respiratory Distress Syndrome. *N. Engl. J. Med.* 378. doi:10.1056/nejmoa1800385

Coppadoro, A., Grassi, A., Giovannoni, C., Rabboni, F., Eronia, N., Bronco, A., et al. (2020). Occurrence of Pendelluft under Pressure Support Ventilation in Patients Who Failed a Spontaneous Breathing Trial: an Observational Study. *Ann. Intensive Care* 10. doi:10.1186/s13613-020-00654-y

Corbridge, T. C., Wood, L. D. H., Crawford, G. P., Chudoba, M. J., Yanos, J., and Sznajder, J. I. (1990). Adverse Effects of Large Tidal Volume and Low PEEP in Canine Acid Aspiration. *Am. Rev. Respir. Dis.* 142. doi:10.1164/ajrccm/142.2.311

Costa, E. L. V., Lima, P. G., and Amato, M. B. R. (2009). Electrical Impedance Tomography. *Curr. Opin. Crit. Care* 15. doi:10.1097/MCC.0b013e3283220e8c

Costa, E. L. V., Slutsky, A. S., Brochard, L. J., Brower, R., Serpa-Neto, A., Cavalcanti, A. B., et al. (2021). Ventilatory Variables and Mechanical Power in Patients with Acute Respiratory Distress Syndrome. *Am. J. Respir. Crit. Care Med.* 204, 303–311. doi:10.1164/rccm.202009-3467OC

Deibele, J. M., Luepschen, H., and Leonhardt, S. (2008). Dynamic Separation of Pulmonary and Cardiac Changes in Electrical Impedance Tomography. *Physiol. Meas.* 29. doi:10.1088/0967-3334/29/6/S01

Dellamonica, J., Lerolle, N., Sargentini, C., Beduneau, G., di Marco, F., Mercat, A., et al. (2011). Accuracy and Precision of End-Expiratory Lung-Volume Measurements by Automated Nitrogen Washout/washin Technique in Patients with Acute Respiratory Distress Syndrome. *Crit. Care* 15. doi:10.1186/cc10587

Determann, R. M., Royakkers, A., Wolthuis, E. K., Vlaar, A. P., Choi, G., Paulus, F., et al. (2010). Ventilation with Lower Tidal Volumes as Compared with Conventional Tidal Volumes for Patients without Acute Lung Injury: A Preventive Randomized Controlled Trial. *Crit. Care* 14. doi:10.1186/cc8230

Dodd, D. S., Yarom, J., Loring, S. H., and Engel, L. A. (1988). O2 Cost of Inspiratory and Expiratory Resistive Breathing in Humans. *J. Appl. Physiology* 65. doi:10.1152/jappl.1988.65.6.2518

Dreyfuss, D., and Saumon, G. (1993). Role of Tidal Volume, FRC, and End-Inspiratory Volume in the Development of Pulmonary Edema Following Mechanical Ventilation. *Am. Rev. Respir. Dis.* 148. doi:10.1164/ajrccm/148.5.1194

Ebihara, T., Venkatesan, N., Tanaka, R., and Ludwig, M. S. (2000). Changes in Extracellular Matrix and Tissue Viscoelasticity in Bleomycin-Induced Lung Fibrosis: Temporal Aspects. *Am. J. Respir. Crit. Care Med.* 162. doi:10.1164/ajrccm.162.4.9912011

Faffe, D. S., and Zin, W. A. (2009). Lung Parenchymal Mechanics in Health and Disease. *Physiol. Rev.* 89. doi:10.1152/physrev.00019.2007

Ferluga, M., Lucangelo, U., and Blanch, L. (2018). Dead Space in Acute Respiratory Distress Syndrome. *Ann. Transl. Med.* 6. doi:10.21037/atm.2018.09.46

Fietzek, P. P., and Kuehn, K. (1976). The Primary Structure of Collagen. *Int. Rev. Connect. Tissue Res.* 7. doi:10.1016/b978-0-12-363707-9.50007-1

Fuller, B. M., Mohr, N. M., Drewry, A. M., and Carpenter, C. R. (2013). Lower Tidal Volume at Initiation of Mechanical Ventilation May Reduce Progression to Acute Respiratory Distress Syndrome: A Systematic Review. *Crit. Care* 17. doi:10.1186/cc11936

Gattinoni, L., Chiumello, D., Caironi, P., Busana, M., Romitti, F., Brazzi, L., et al. (2020a). COVID-19 Pneumonia: Different Respiratory Treatments for

Different Phenotypes? *Intensive Care Med.* 46. doi:10.1007/s00134-020-06033-2

Gattinoni, L., Coppola, S., Cressoni, M., Busana, M., Rossi, S., and Chiumello, D. (2020b). COVID-19 Does Not Lead to a "Typical" Acute Respiratory Distress Syndrome. *Am. J. Respir. Crit. Care Med.* 201, 1299–1300. doi:10.1164/rccm.202003-0817LE

Gattinoni, L., Tonetti, T., Cressoni, M., Cadringher, P., Herrmann, P., Moerer, O., et al. (2016). Ventilator-related Causes of Lung Injury: the Mechanical Power. *Intensive Care Med.* 42, 1567–1575. doi:10.1007/s00134-016-4505-2

Girard, T. D., Kress, J. P., Fuchs, B. D., Thomason, J. W., Schweickert, W. D., Pun, B. T., et al. (2008). Efficacy and Safety of a Paired Sedation and Ventilator Weaning Protocol for Mechanically Ventilated Patients in Intensive Care (Awakening and Breathing Controlled Trial): a Randomised Controlled Trial. *Lancet* 371, 126–134. doi:10.1016/S0140-6736(08)60105-1

Griffiths, M. J. D., McAuley, D. F., Perkins, G. D., Barrett, N., Blackwood, B., Boyle, A., et al. (2019). Guidelines on the Management of Acute Respiratory Distress Syndrome. *BMJ Open Respir. Res.* 6, e000420. doi:10.1136/bmjresp-2019-000420

Grinnan, D. C., and Truwit, J. D. (2005). Clinical Review: Respiratory Mechanics in Spontaneous and Assisted Ventilation. *Crit. Care* 9, 472–484. doi:10.1186/cc3516

Guttmann, J., Eberhard, L., Fabry, B., Bertschmann, W., and Wolff, G. (1993). Continuous Calculation of Intratracheal Pressure in Tracheally Intubated Patients. *Anesthesiology* 79. doi:10.1097/00000542-199309000-00014

Hantos, Z., Daroczy, B., Suki, B., Nagy, S., and Fredberg, J. J. (1992). Input Impedance and Peripheral Inhomogeneity of Dog Lungs. *J. Appl. Physiology* 72. doi:10.1152/jappl.1992.72.1.168

Hantos, Z. (2021). Intra-breath Oscillometry for Assessing Respiratory Outcomes. *Curr. Opin. Physiology* 22. doi:10.1016/j.cophys.2021.05.004

Henderson, W. R., Chen, L., Amato, M. B. P., and Brochard, L. J. (2017). Fifty Years of Research in ARDS: Respiratory Mechanics in Acute Respiratory Distress Syndrome. *Am. J. Respir. Crit. Care Med.* 196, 822–833. doi:10.1164/rccm.201612-2495CI

Irvin, C. G., and Bates, J. H. T. (2003). Measuring the Lung Function in the Mouse: The Challenge of Size. *Respir. Res.* 4. doi:10.1186/rr199

Ito, J. T., de Brito Cervilha, D. A., Lourenço, J. D., Gonçalves, N. G., Volpini, R. A., Caldini, E. G., et al. (2019a). Th17/Treg Imbalance in COPD Progression: A Temporal Analysis Using a CS-Induced Model. *PLoS ONE* 14. doi:10.1371/journal.pone.0209351

Ito, J. T., Lourenço, J. D., Righetti, R. F., Tibério, I. F. L. C., Prado, C. M., and Lopes, F. D. T. Q. S. (2019b). Extracellular Matrix Component Remodeling in Respiratory Diseases: What Has Been Found in Clinical and Experimental Studies? *Cells* 8, 342. doi:10.3390/cells8040342

Jonkman, A. H., Rauseo, M., Carteaux, G., Telias, I., Sklar, M. C., Heunks, L., et al. (2020). Proportional Modes of Ventilation: Technology to Assist Physiology. *Intensive Care Med.* 46. doi:10.1007/s00134-020-06206-z

Kacmarek, R. M. (2011). The Mechanical Ventilator: Past, Present, and Future. *Respir. Care* 56, 1170–1180. doi:10.4187/respcare.01420

Karbing, D. S., Panigada, M., Bottino, N., Spinelli, E., Protti, A., Rees, S. E., et al. (2020). Changes in Shunt, Ventilation/perfusion Mismatch, and Lung Aeration with PEEP in Patients with ARDS: A Prospective Single-Arm Interventional Study. *Crit. Care* 24. doi:10.1186/s13054-020-2834-6

Khan, Y. A., Fan, E., and Ferguson, N. D. (2021). Precision Medicine and Heterogeneity of Treatment Effect in Therapies for ARDS. *Chest* 160. doi:10.1016/j.chest.2021.07.009

King, G. G., Bates, J., Berger, K. I., Calverley, P., de Melo, P. L., Dellacà, R. L., et al. (2020). Technical Standards for Respiratory Oscillometry. *Eur. Respir. J.* 55. doi:10.1183/13993003.00753-2019

Koenders, C. M. A. (2009). Wave Propagation through Elastic Granular and Granular Auxetic Materials. *Phys. Status Solidi (B) Basic Res.* 246. doi:10.1002/pssb.200982039

Kress, J. P., Pohlman, A. S., O'Connor, M. F., and Hall, J. B. (2000). Daily Interruption of Sedative Infusions in Critically Ill Patients Undergoing Mechanical Ventilation. *N. Engl. J. Med.* 342, 1471–1477. doi:10.1056/NEJM200005183422002

Lanças, T., Kasahara, D. I., Prado, C. M., Tibério, I. F. L. C., Martins, M. A., and Dolhnikoff, M. (2006). Comparison of Early and Late Responses to Antigen of Sensitized guinea Pig Parenchymal Lung Strips. *J. Appl. Physiology* 100. doi:10.1152/japplphysiol.00828.2005

Leite-Júnior, J. H., Rocco, P. R. M., Faffe, D. S., Romero, P. v., and Zin, W. A. (2003). On the Preparation of Lung Strip for Tissue Mechanics Measurement. *Respir. Physiology Neurobiol.* 134. doi:10.1016/S1569-9048(02)00217-3

L'Her, E. (2012). Automatic Tube Compensation: Is it Worthwhile? *Respir. Care* 57. doi:10.4187/respcare.01865

Ludwig, M. S., and Dallaire, M. J. (1994). Structural Composition of Lung Parenchymal Strip and Mechanical Behavior during Sinusoidal Oscillation. *J. Appl. Physiology* 77. doi:10.1152/jappl.1994.77.4.2029

Lundblad, L. K. A., and Robichaud, A. (2021). Oscillometry of the Respiratory System. A Translational Opportunity Not to be missed. *Am. J. Physiology - Lung Cell. Mol. Physiology* 320. doi:10.1152/AJPLUNG.00222.2020

Maciejewski, D., Putowski, Z., Czok, M., and Krzych, Ł. J. (2021). Electrical impedance tomography as a tool for monitoring mechanical ventilation. An introduction to the technique. *Adv. Med. Sci.* 66. doi:10.1016/j.advms.2021.07.010

Macintyre, N. R. (2016). Lung protective ventilator strategies: Beyond scaling tidal volumes to ideal lung size. *Crit. Care Med.* 44. doi:10.1097/CCM.0000000000001454

Mador, M. J. (1991). Respiratory muscle fatigue and breathing pattern. *Chest* 100. doi:10.1378/chest.100.5.1430

Marini, J. J. (2011). Dynamic hyperinflation and auto-positive end-expiratory pressure lessons learned over 30 years. *Am. J. Respir. Crit. Care Med.* 184, 756–762. doi:10.1164/rccm.201102-0226PP

Martin, R. J. (2008). Exploring the distal lung: New direction in asthma. *Israel Med. Assoc. J.* 10 (12), 846–849.

Mattingley, J. S., Holets, S. R., Oeckler, R. A., Stroetz, R. W., Buck, C. F., and Hubmayr, R. D. (2011). Sizing the lung of mechanically ventilated patients. *Crit. Care* 15, R60. doi:10.1186/cc10034

Mauad, T., Silva, L. F. F., Santos, M. A., Grinberg, L., Bernardi, F. D. C., Martins, M. A., et al. (2004). Abnormal alveolar attachments with decreased elastic fiber content in distal lung in fatal asthma. *Am. J. Respir. Crit. Care Med.* 170. doi:10.1164/rccm.200403-305OC

Mead, J., Lindgren, I., and Gaensler, E. A. (1955). The mechanical properties of the lungs in emphysema. *J. Clin. Investig.* 34. doi:10.1172/jci103150

Meyer, N. J., Gattinoni, L., and Calfee, C. S. (2021). Acute respiratory distress syndrome. *Lancet* 398, 622–637. doi:10.1016/S0140-6736(21)00439-6

Morales-Quinteros, L., Schultz, M. J., Bringué, J., Calfee, C. S., Camprubí, M., Cremer, O. L., et al. (2019). Estimated dead space fraction and the ventilatory ratio are associated with mortality in early ARDS. *Ann. Intensive Care* 9, 128. doi:10.1186/s13613-019-0601-0

Murray, J. F., Matthay, M. A., Luce, J. M., and Flick, M. R. (1988). An expanded definition of the adult respiratory distress syndrome. *Am. Rev. Respir. Dis.* 138, 720–723. doi:10.1164/ajrccm/138.3.720

Nakashima, A. S., Prado, C. M., Lanças, T., Ruiz, V. C., Kasahara, D. I., Leick-Maldonado, E. A., et al. (2008). Oral tolerance attenuates changes in *In Vitro* lung tissue mechanics and extracellular matrix remodeling induced by chronic allergic inflammation in guinea pigs. *J. Appl. Physiology* 104, 1778–1785. doi:10.1152/japplphysiol.00830.2007

Neto, A. S., Cardoso, S. O., Manetta, J. A., Pereira, V. G. M., Espósito, D. C., Pasqualucci, M. D. O. P., et al. (2012). Association between use of lung-protective ventilation with lower tidal volumes and clinical outcomes among patients without acute respiratory distress syndrome: A meta-analysis. *JAMA - J. Am. Med. Assoc.* 308. doi:10.1001/jama.2012.13730

Nguyen, D. T., Jin, C., Thiagalingam, A., and McEwan, A. L. (2012). A review on electrical impedance tomography for pulmonary perfusion imaging. *Physiol. Meas.* 33. doi:10.1088/0967-3334/33/5/695

Olegård, C., Söndergaard, S., Houltz, E., Lundin, S., and Stenqvist, O. (2005). Estimation of functional residual capacity at the bedside using standard monitoring equipment: A modified nitrogen washout/washin technique requiring a small change of the inspired oxygen fraction. *Anesth. Analgesia* 101. doi:10.1213/01.ANE.0000165823.90368.55

Otis, A. B. (1977). Pressure-flow relationships and power output of breathing. *Respir. Physiol.* 30. doi:10.1016/0034-5687(77)90017-2

Panwar, R., Madotto, F., Laffey, J. G., and van Haren, F. M. P. (2020). Compliance phenotypes in early acute respiratory distress syndrome before the COVID-19

pandemic. *Am. J. Respir. Crit. Care Med.* 202. doi:10.1164/rccm.202005-2046OC

Papazian, L., Aubron, C., Brochard, L., Chiche, J. D., Combes, A., Dreyfuss, D., et al. (2019). Formal guidelines: management of acute respiratory distress syndrome. *Ann. Intensive Care* 9. doi:10.1186/s13613-019-0540-9

Parker, J. C., Hernandez, L. A., Longenecker, G. L., Peevy, K., and Johnson, W. (1990a). Lung edema caused by high peak inspiratory pressures in dogs. Role of increased microvascular filtration pressure and permeability. *Am. Rev. Respir. Dis.* 142. doi:10.1164/ajrccm/142.2.321

Parker, J. C., Hernandez, L. A., Longenecker, G. L., Peevy, K., and Johnson, W. (1990b). Lung edema caused by high peak inspiratory pressures in dogs. Role of increased microvascular filtration pressure and permeability. *Am. Rev. Respir. Dis.* 142. doi:10.1164/ajrccm/142.2.321

Pelosi, P., Ball, L., Barbas, C. S. V., Bellomo, R., Burns, K. E. A., Einav, S., et al. (2021). Personalized mechanical ventilation in acute respiratory distress syndrome. *Crit. Care* 25. doi:10.1186/s13054-021-03686-3

Pepe, P. E., and Marini, J. J. (1982). Occult positive end-expiratory pressure in mechanically ventilated patients with airflow obstruction: the auto-PEEP effect. *Am. Rev. Respir. Dis.* 126, 166–170. doi:10.1164/arrd.1982.126.1.166

Peterson-Carmichael, S., Seddon, P. C., Cheifetz, I. M., Frerichs, I., Hall, G. L., Hammer, J., et al. (2016). An official American thoracic society/european respiratory society workshop report: Evaluation of respiratory mechanics and function in the pediatric and neonatal intensive care units. *Ann. Am. Thorac. Soc.* 13, S1–S11. doi:10.1513/AnnalsATS.201511-730ST

Pham, T., Brochard, L. J., and Slutsky, A. S. (2017). Mechanical Ventilation: State of the Art. *Mayo Clin. Proc.* 92, 1382–1400. doi:10.1016/j.mayocp.2017.05.004

Pigati, P. A., Righetti, R. F., Possa, S. S., Romanholo, B. S., Rodrigues, A. P. D., dos Santos, A. S. A., et al. (2015). Y-27632 is associated with corticosteroid-potentiated control of pulmonary remodeling and inflammation in guinea pigs with chronic allergic inflammation. *BMC Pulm. Med.* 15. doi:10.1186/s12890-015-0073-4

Pinsky, M. R. (2018). Cardiopulmonary interactions: Physiologic basis and clinical applications. *Ann. Am. Thorac. Soc.* doi:10.1513/AnnalsATS.201704-339FR

Pohlman, M. C., McCallister, K. E., Schweickert, W. D., Pohlman, A. S., Nigos, C. P., Krishnan, J. A., et al. (2008). Excessive tidal volume from breath stacking during lung-protective ventilation for acute lung injury. *Crit. Care Med.* 36. doi:10.1097/CCM.0b013e31818b308b

Possa, S. S., Charafeddine, H. T., Righetti, R. F., da Silva, P. A., Almeida-Reis, R., Saraiva-Romanholo, B. M., et al. (2012). Rho-kinase inhibition attenuates airway responsiveness, inflammation, matrix remodeling, and oxidative stress activation induced by chronic inflammation. *Am. J. Physiology - Lung Cell. Mol. Physiology* 303. doi:10.1152/ajplung.00034.2012

Rahn, H., Otis, A., and Fenn, W. O. (1946). The pressure-volume diagram of the thorax and lung. *Fed. Proc.* 5. doi:10.1152/ajplegacy.1946.146.2.161

Ranieri, V. M., Rubenfeld, G. D., Thompson, B. T., Ferguson, N. D., Caldwell, E., Fan, E., et al. (2012). Acute respiratory distress syndrome: The Berlin definition. *JAMA - J. Am. Med. Assoc.* 307. doi:10.1001/jama.2012.5669

Reade, M. C., and Finfer, S. (2014). Sedation and Delirium in the Intensive Care Unit. *N. Engl. J. Med.* 370, 444–454. doi:10.1056/nejmra1208705

Reddy, R. M., and Guntupalli, K. K. (2007). Review of ventilatory techniques to optimize mechanical ventilation in acute exacerbation of chronic obstructive pulmonary disease. *Int. J. COPD* 2.

Reinert, M., and Trendelenburg, F. (1972). Correlation between parameters of breathing mechanics, respiratory gases and blood gases in patients with chronic bronchial obstruction. *Respiration* 29. doi:10.1159/000192889

Repessé, X., and Vieillard-Baron, A. (2017). Hypercapnia during acute respiratory distress syndrome: The tree that hides the forest. *J. Thorac. Dis.* 9. doi:10.21037/jtd.2017.05.69

Righetti, R. F., Pigati, P. A. da S., Possa, S. S., Habrum, F. C., Xisto, D. G., Antunes, M. A., et al. (2014). Effects of Rho-kinase inhibition in lung tissue with chronic inflammation. *Respir. Physiology Neurobiol.* 192. doi:10.1016/j.resp.2013.12.012

Rocco, P. R. M., Silva, P. L., Samary, C. S., Hayat Syed, M. K., and Marini, J. J. (2020). Elastic power but Not driving power is the key promoter of ventilator-induced lung injury in experimental acute respiratory distress syndrome. *Crit. Care* 24. doi:10.1186/s13054-020-03011-4

Santos, F. B., Garcia, C. S. N. B., Xisto, D. G., Negri, E. M., Capelozzi, V. L., Faffe, D. S., et al. (2008). Effects of amiodarone on lung tissue mechanics and parenchyma remodeling. *Respir. Physiology Neurobiol.* 162. doi:10.1016/j.resp.2008.05.004

Shifren, A., Woods, J. C., Rosenbluth, D. B., Officer, S., Cooper, J. D., and Pierce, R. A. (2007). Upregulation of elastin expression in constrictive bronchiolitis obliterans. *Int. J. COPD* 2.

Silva, P. L., Ball, L., Rocco, P. R. M., and Pelosi, P. (2019). Power to mechanical power to minimize ventilator-induced lung injury? *Intensive Care Med. Exp.* 7. doi:10.1186/s40635-019-0243-4

Simonis, F. D., Serpa Neto, A., Binnekade, J. M., Braber, A., Bruin, K. C. M., Determann, R. M., et al. (2018). Effect of a Low vs Intermediate Tidal Volume Strategy on Ventilator-Free Days in Intensive Care Unit Patients Without ARDS: A Randomized Clinical Trial. *JAMA - J. Am. Med. Assoc.* 320, 1872–1880. doi:10.1001/jama.2018.14280

Sinderby, C., Navalesi, P., Beck, J., Skrobik, Y., Comtois, N., Friberg, S., et al. (1999). Neural control of mechanical ventilation in respiratory failure. *Nat. Med.* 5. doi:10.1038/71012

Sjoding, M. W., Admon, A. J., Saha, A. K., Kay, S. G., Brown, C. A., Co, I., et al. (2021). Comparing Clinical Features and Outcomes in Mechanically Ventilated Patients with COVID-19 and the Acute Respiratory Distress Syndrome. *Ann. Am. Thorac. Soc.* 18 (11), 1876–1885. doi:10.1513/annalsats.202008-1076oc

Sottile, P. D., Albers, D., Smith, B. J., and Moss, M. M. (2020). Ventilator dyssynchrony-Detection, pathophysiology, and clinical relevance: A Narrative review. *Ann. Thorac. Med.* 15, 190–198. doi:10.4103/atm.ATM_63_20

Starling, C. M., Prado, C. M., Leick-Maldonado, E. A., Lanças, T., Reis, F. G., Aristóteles, L. R. C. B. R., et al. (2009). Inducible nitric oxide synthase inhibition attenuates lung tissue responsiveness and remodeling in a model of chronic pulmonary inflammation in guinea pigs. *Respir. Physiology Neurobiol.* 165. doi:10.1016/j.resp.2008.11.011

Suki, B., and Bates, J. H. T. (2008). Extracellular matrix mechanics in lung parenchymal diseases. *Respir. Physiology Neurobiol.* 163. doi:10.1016/j.resp.2008.03.015

Talmor, D., Sarge, T., Malhotra, A., O'Donnell, C. R., Ritz, R., Lisbon, A., et al. (2008). Mechanical Ventilation Guided by Esophageal Pressure in Acute Lung Injury. *N. Engl. J. Med.* 359, 2095–2104. doi:10.1056/nejmoa0708638

The Acute Respiratory Distress Syndrome Network (2000). Ventilation with lower tidal volumes as compared with traditional tidal volumes for acute lung injury and the acute respiratory distress syndrome. The Acute Respiratory Distress Syndrome Network. *N. Engl. J. Med.* 342, 1301–1308. doi:10.1056/NEJM200005043421801

Tobin, M. J. (2020). Does Making a Diagnosis of ARDS in Patients With Coronavirus Disease 2019 Matter? *Chest* 158, 2275–2277. doi:10.1016/j.chest.2020.07.028

Tobin, M. J., Laghi, F., and Jubran, A. (2020). Caution about early intubation and mechanical ventilation in COVID-19. *Ann. Intensive Care* 10, 78. doi:10.1186/s13613-020-00692-6

Tonna, J. E., Abrams, D., Brodie, D., Greenwood, J. C., Rubio Mateo-Sidron, J. A., Usman, A., et al. (2021). Management of Adult Patients Supported with Venovenous Extracorporeal Membrane Oxygenation (VV ECMO): Guideline from the Extracorporeal Life Support Organization (ELSO). *ASAIO J.* doi:10.1097/MAT.0000000000001432

Tulić, M. K., and Hamid, Q. (2003). Contribution of the distal lung to the pathologic and physiologic changes in asthma: Potential therapeutic target - Roger S. Mitchell Lecture. *Chest* 123 348S–355S. doi:10.1378/chest.123.3_suppl.348S

Tusman, G., Gogniat, E., Madorno, M., Otero, P., Dianti, J., Ceballos, I. F., et al. (2020). Effect of PEEP on dead space in an experimental model of ARDS. *Respir. Care* 65, 11–20. doi:10.4187/respcare.06843

Umbrello, M., Marino, A., and Chiumello, D. (2017). Tidal volume in acute respiratory distress syndrome: How best to select it. *Ann. Transl. Med.* 5, 287. doi:10.21037/atm.2017.06.51

Wagner, P. D. (2008). The multiple inert gas elimination technique (MIGET). *Intensive Care Med.* 34. doi:10.1007/s00134-008-1108-6

Wang, C. G., Dimaria, G., Bates, J. H. T., Guttmann, R. D., and Martin, J. G. (1986). Methacholine-induced airway reactivity of inbred rats. *J. Appl. Physiology* 61. doi:10.1152/jappl.1986.61.6.2180

Wanner, A., Abraham, W. M., Douglas, J. S., Drazen, J. M., Richerson, H. B., and Ram, J. S. (1990). Models of airway hyperresponsiveness. in American Review of Respiratory Disease. doi:10.1164/ajrccm/141.1.253

Wanner, A., and Abraham, W. M. (1982). Experimental models of asthma. *Lung* 160, 231–243. doi:10.1007/BF02719297

Xisto, D. G., Farias, L. L., Ferreira, H. C., Picanço, M. R., Amitrano, D., Lapa E Silva, J. R., et al. (2005). Lung parenchyma remodeling in a murine model of chronic allergic inflammation. *Am. J. Respir. Crit. Care Med.* 171. doi:10.1164/rccm.200408-997OC

Yoshida, T., Torsani, V., Gomes, S., Santis, R. R. D., Beraldo, M. A., Costa, E. L. V., et al. (2013). Spontaneous effort causes occult pendelluft during mechanical ventilation. *Am. J. Respir. Crit. Care Med.* 188. doi:10.1164/rccm.201303-0539OC

Younes, M. (1992). Proportional assist ventilation, a new approach to ventilatory support: Theory. *Am. Rev. Respir. Dis.* 145. doi:10.1164/ajrccm/145.1.114

Ziehr, D. R., Alladina, J., Petri, C. R., Maley, J. H., Moskowitz, A., Medoff, B. D., et al. (2020). Respiratory pathophysiology of mechanically ventilated patients with COVID-19: A cohort study. *Am. J. Respir. Crit. Care Med.* 201. doi:10.1164/rccm.202004-1163LE

Conflict of Interest: The authors declare that the research was conducted in the absence of any commercial or financial relationships that could be construed as a potential conflict of interest.

frontiers | Frontiers in Physiology

SYSTEMATIC REVIEW
published: 15 July 2022
doi: 10.3389/fphys.2022.858046

Pooled Analysis of Central Venous Pressure and Brain Natriuretic Peptide Levels in Patients With Extubation Failure

Jianghong Cao[1]*, *Beibei Wang*[2], *Lili Zhu*[1] and *Lu Song*[1]

[1]Department of Intensive Care Unit, Shanxi Provincial People's Hospital, Taiyuan, China, [2]Department of Cardiology, The First People's Hospital of Jinzhong, Jinzhong, China

Purpose: Cardiac insufficiency has been considered to be a common cause of extubation failure. Some studies have shown that central venous pressure (CVP) and brain natriuretic peptide (BNP) are able to predict extubation outcomes. Therefore, we conducted a pooled analysis to evaluate the potential of CVP and BNP levels as predictors of extubation outcomes, using a cohort of critically ill patients who were on mechanical ventilation (MV).

Methods: We searched three online electronic databases up to October 2021. All data were analyzed using Review Manager 5.4. For each study, the analysis was performed using standardized mean differences (SMD) with 95% confidence intervals (CI).

Results: The pooled analysis of seven studies on CVP levels and extubation outcomes showed that elevated CVP levels were significantly associated with extubation failure (SMD:0.47, 95% CI: 0. 43–0.51, $p < 0.00001$). This association also appeared before extubation (SMD:0.47, 95% CI: 0. 43–0.51, $p < 0.00001$), but it did not appear after extubation (SMD: 0.63, 95% CI: –0.05–1.31, p=0.07). Similarly, pooled analysis of eight studies on BNP levels and extubation outcomes showed that increased BNP levels are closely related to extubation failure (SMD:0.68, 95% CI: 0.49–0.86, $p < 0.00001$). This relationship also occurs before (SMD: 0.57, 95% CI: 0.35–0.79, $p < 0.00001$) and after (SMD: 0.91, 95% CI: 0.59–1.23, $p < 0.00001$) extubation.

Conclusions: This study showed that elevated CVP and BNP levels are associated with extubation failure in critically ill patients. However, BNP levels are more valuable than CVP levels in predicting extubation outcomes.

Keywords: central venous pressure, brain natriuretic peptide, extubation failure, pooled-analysis, cardiac insufficiency

OPEN ACCESS

Edited by:
Andrew John Halayko, University of Manitoba, Canada

Reviewed by:
Moacir Fernandes Godoy, Faculdade de Medicina de São José do Rio Preto, Brazil
Jean Deschamps, Cleveland Clinic, United States

***Correspondence:**
Jianghong Cao
jianghongcao1014@163.com

Specialty section:
This article was submitted to Respiratory Physiology and Pathophysiology, a section of the journal Frontiers in Physiology

Received: *19 January 2022*
Accepted: *09 June 2022*
Published: *15 July 2022*

Citation:
Cao J, Wang B, Zhu L and Song L (2022) Pooled Analysis of Central Venous Pressure and Brain Natriuretic Peptide Levels in Patients With Extubation Failure. Front. Physiol. 13:858046. doi: 10.3389/fphys.2022.858046

INTRODUCTION

Liberation from mechanical ventilation (MV) is a very challenging process for clinicians in the Intensive Care Unit (ICU). Premature extubation is associated with the probability of reintubation, extended ICU stay, and mortality (Harrison et al., 2002; Perren et al., 2010). Delayed extubation may lead to ventilator-acquired pneumonia, prolonged hospital stay, and high mortality (Esteban et al.,

2002; Thille et al., 2011; Fernandez-Zamora et al., 2018). Therefore, it is extremely important to identify reliable and accurate markers for predicting extubation outcomes.

Traditionally, respiratory failure was considered to be the main cause of extubation failure. Consequently, predictive markers for extubation outcomes have focused primarily on breathing-related parameters, including rapid shallow breathing index (f/Vt), respiratory rate, minute ventilation, and cough intensity (Khamiees et al., 2001; Frutos-Vivar et al., 2006). Unfortunately, these predictors do not accurately predict extubation outcomes (Hsieh et al., 2018). Recently, other studies have shown that cardiac dysfunction plays an important role in extubation outcomes, and respiratory diseases have a certain impact on cardiac function (Chatila et al., 1996; Frazier et al., 2006). Moreover, some reports have shown that cardiac insufficiency is a cause of failure in as many as 50% of patients who have failed extubation. Thus, a simple and effective method is urgently needed to predict extubation outcomes for those with cardiac dysfunction.

Central venous pressure (CVP) reflects right atrial force, which is influenced by cardiac function, blood volume and vascular tension. Brain natriuretic peptide (BNP) is mainly secreted by cardiomyocytes to compensate for myocardial stretch and volume overload. Both CVP and BNP are important markers for monitoring cardiac function and volume, which can be affected by disconnection from MV. Previous studies have shown that the predictive value of BNP levels on extubation outcomes is controversial. There are few studies on the predictive value of CVP levels on extubation outcomes. Thus, we systematically reviewed the literature and conducted a pooled analysis to determine the association and predictive value of BNP and CVP levels on extubation outcomes.

MATERIALS AND METHODS

Search Strategy

To identify qualified published studies, two independent researchers (ZLL and SL) systematically searched the Web of Science, EMBASE, and Cochrane Library, using the following keywords: "extubation," "weaning," "disconnect of mechanical ventilation," "discontinuation of mechanical ventilation," "central venous pressure," "CVP," "Brain natriuretic peptide," "BNP," and "brain natriuretic peptide". The searches encompassed studies up to October 2021 and were limited to those published in English. In addition, we manually searched relevant reviews and references within those publications to identify potentially relevant studies. If there was a disagreement about inclusion, a third researcher (CJH) was called to discuss the decision.

Inclusion and Exclusion Criteria

The inclusion criteria were as follows: patients were adults hospitalized in the ICU for underlying cardiovascular or respiratory disease who received MV for no less than 24 h. Patients were extubated after adequate evaluation and followed for at least 24 h after weaning from MV. CVP or BNP levels were monitored before or after extubation. Extubation failure was defined as re-intubation within 48 h, spontaneous respiratory failure, noninvasive or invasive ventilation within 48 h after extubation, or death within 48 h. The exclusion criteria were as follows: potential confounding variables for CVP, such as lax measurement of CVP, potential confounding factors for BNP such as renal insufficiency, studies lacking the necessary data, duplicate studies, reviews, case reports, abstracts or letters.

Data Extraction and Quality Assessment

Two researchers (ZLL and SL) independently screened the titles and abstracts using set keywords, and then checked the full text according to inclusion and exclusion criteria. The following information was extracted: the first author's name, publication year, age, sex (%), country, sample size, timing of BNP and CVP measurement, methods and durations of SBT and definition of extubation failure. When there were differences in data extraction, it was discussed with the third researcher (CJH). The Newcastle-Ottawa scale (NOS) was used to assess the quality of the included studies (Stang, 2010). Studies that had a score ≥6 points were considered a "high-quality study." This study was approved by the Ethics Committee of Shanxi Provincial People's Hospital (No. 223, 2022).

Statistical Analysis

The pooled analysis was analyzed by Review Manager 5.4. Standardized mean differences (SMD) and corresponding 95% confidence intervals (CIs) of the CVP and BNP levels were collected and calculated for each study. When the median and interquartile range (IQR) was provided, the mean and standard deviation (M ± SD) was estimated using Luo's approach and Wan's method, respectively (Wan et al., 2014; Luo et al., 2018). Heterogeneity is evaluated by calculating the *I*- squared (I^2) index. I^2 values of 75%–100%, 50%–75%, 25%–50% and < 25% were considered as high, moderate, low heterogeneous and homogeneous, respectively. If there was significant heterogeneity (I^2 > 50% or p < 0.05), a random effect model was used, otherwise, a fixed effect model was applied.

In order to identify the potential heterogeneity, we performed subgroup analysis based on the levels of CVP and BNP before and after extubation. Moreover, we deleted one study at a time and repeated the analysis, namely the leave-one-out method for sensitivity analysis. Egger's and Begg's tests were used to find potential publication bias. When the p value was less than 0.05, it was considered statistically significant.

RESULTS

Study Processing

Using our search strategy, a total of 1,234 potentially original studies were identified and excluding duplications, 874 studies remained. Careful screening of titles and abstracts, identified 841 studies that did not meet the inclusion and exclusion criteria, and these were also excluded. Finally, after carefully reading the main body of the remaining 33 studies, 20 studies were eventually excluded. In the end, 12 qualified studies were inclued (Chien

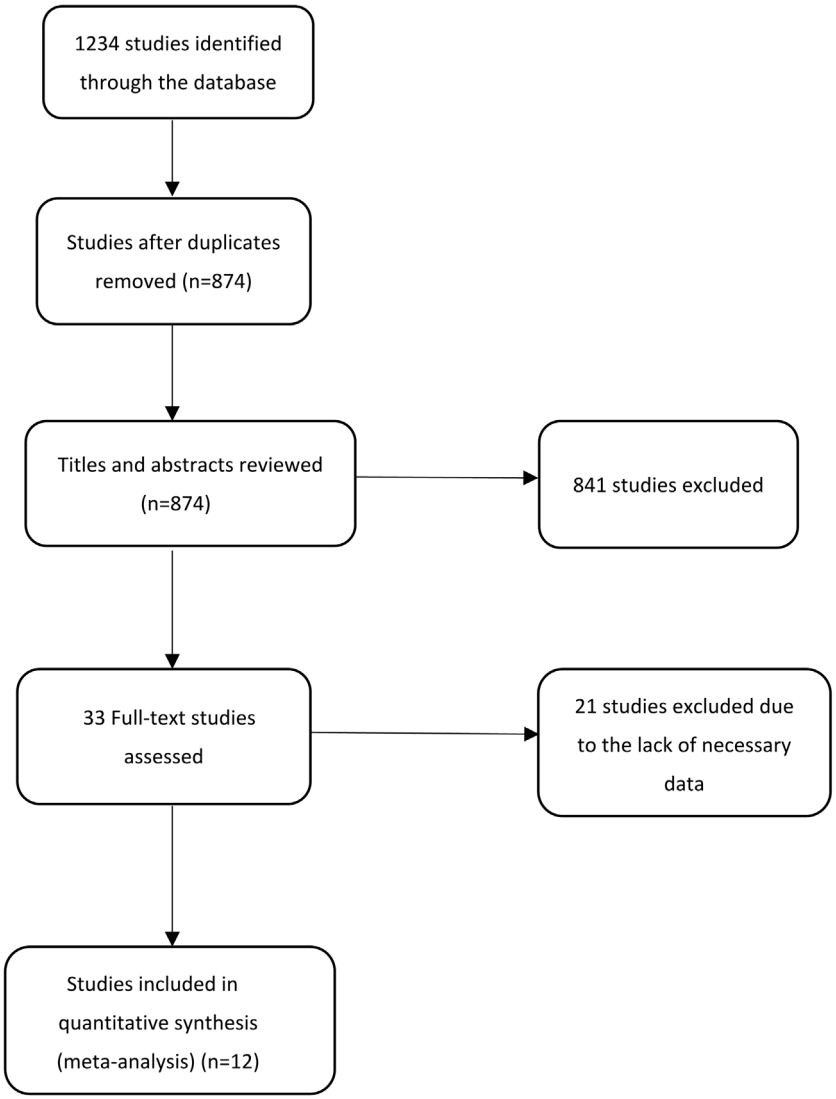

FIGURE 1 | Selection process for studies included in the pooled- analysis.

et al., 2008; Zapata et al., 2011; Saugel et al., 2012; Soummer et al., 2012; Ma et al., 2013; Maraghi et al., 2014; Farghaly et al., 2015; Konomi et al., 2016; Tanios et al., 2016; Haji et al., 2018; Dubo et al., 2019; Zhao et al., 2021). The screening process of these studies is shown in **Figure 1**. Meanwhile, **Table 1** listed the basic characteristics of the included studies. As NOS scores of these studies were at least 6, all were considered of high quality.

Central Venous Pressure Levels and Extubation Outcomes

We found seven studies that described a relationship between the CVP levels and extubation outcomes. Since there was no significant heterogeneity (I^2 < 50%), the fixed effect model was applied. The fixed effect pooled SMD was 0.47 (95% CI: 0.43–0.51, p < 0.00001) (**Figure 2**). Subgroup analysis based on extubation time showed that the results of pooled analysis were consistent with the association between elevated CVP levels and extubation failure before extubation (SMD:0.47,95% CI: 0.43–0.51, p < 0.00001). However, this association had no significant correlation after extubation (SMD: 0.63, 95% CI: −0.05–1.31, p=0.07).

Due to the limited studies included, potential publication bias was not carried out. Since none of the studies had a significant influence on the pooled results, the leave-one-out sensitivity analyses suggested robust results.

Brain Natriuretic Peptide Levels and Extubation Outcomes

We also found eight studies that contained information about the association between the BNP levels and extubation outcomes.

TABLE 1 | Characteristics of studies.

Study	Country	Age (ES/EF)	Male (%)	Setting	N (ES/EF)	Indicator	Timing of extubation	Methods and durations of SBT	Definition of EF	NOS
Chien2008 testing group (Chien et al., 2008)	China	79.1 ± 8.6/ 81.5 ± 7.4	53	ICU	33/8	BNP	Before extubation	2 h SBT	SBT failure or reintubation within 48 h	7
Chien2008 validation group (Chien et al., 2008)	China	79.7 ± 9.2/ 76.3 ± 7.3	57	ICU	38/11	BNP	Before extubation	2 h SBT	SBT failure or reintubation within 48 h	7
Dubo 2019 (Dubo et al., 2019)	Chile	54 ± 21/ 47 ± 24	81	medical-surgical ICU	154/11	CVP	Before and after extubation	T- piece and 60–120 min SBT	Reintubation within 48 h	7
Konomi 2016 (Konomi et al., 2016)	Greece	54 ± 21/ 69 ± 16	40	Multidisciplinary ICU	27/15	CVP and BNP	Before and after extubation	T- piece and 2 h SBT	SBT failure or reintubation within 48 h	6
Ma 2013 (Ma et al., 2013)	China	62.3 ± 12.0/ 59.1 ± 3.9	85.7	ICU	22/7	CVP	Before extubation	T- piece and 120 min SBT	Reintubation within 48 h	6
Saugel 2012 (Saugel et al., 2012)	Germany	63.5 ± 14.5/ 64.6 ± 8.4	86	medical ICU	54/7	CVP	Before extubation	NG	Reintubation within 48 h	7
Zapata 2011 (Zapata et al., 2011)	Spain	61.6 ± 14.7/ 66.7 ± 9.7	68	ICU	58/10	CVP and BNP	Before and after extubation	T- piece and 30–120 min SBT	Reintubation within 48 h	8
Zhao 2021 MIMIC-IV (Zhao et al., 2021)	NG	64 ± 16/ 68 ± 15	NG	ICU	13,433/ 2,756	CVP	Before extubation	NG	Reintubation	7
Zhao 2021 ZS (Zhao et al., 2021)	China	60 ± 13/ 63 ± 12	NG	ICU	451/51	CVP	Before extubation	NG	NIV、reintubation or death within 48 h	8
Farghaly 2015 (Farghaly et al., 2015)	Australia	53.81 ± 18.9/ 57.14 ± 12.9	43	Respiratory ICU	16/14	BNP	Before and after extubation	PSV and 2 h SBT	SBT failure or reintubation within 48 h	8
Maraghi 2014 (Maraghi et al., 2014)	Egypt	46 ± 10.35/ 54 ± 9.25	32	ICU	25/7	BNP	Before and after extubation	T-piece and 2 h SBT	SBT failure or reintubation within 48 h	6
Soummer 2012 (Soummer et al., 2012)	France	59 ± 14± 15	59	Multidisciplinary ICU	57/29	BNP	Before and after extubation	T- piece and 60- min SBT	Noninvasive or invasive ventilation) within 48 h after extubation	7
Tanios 2016 (Tanios et al., 2016)	United States	NA	48	ICU	56/29	BNP	Before extubation	PSV and 2 h SBT	SBT failure	6
Haji 2018 (Haji et al., 2018)	Australia	63.5 ± 4.6/ 77 ± 2.7	64	ICU	42/11	BNP	after extubation	PSV and 60min SBT	Nonscheduled NIVM, or death within 48 h	7

Abbreviations: EF, extubation failure; ES, extubation successl; ICU, intensive care unit; SBT, spontaneous breathing trail; BNP, brain natriuretic peptide; CVP: central venous pressure; NG: not given.

Since there was no significant heterogeneity ($I^2 < 50\%$), the fixed effect model was applied. The fixed effect pooled SMD was 0.68 (95% CI: 0.49–0.86, $p < 0.00001$) (**Figure 3**). Based on the subgroup analysis of extubation time, we found that the pooled results were consistent with the relationship between high BNP levels and extubation failure before extubation (SMD: 0.57, 95% CI: 0.35–0.79, $p < 0.00001$) and after extubation (SMD: 0.91, 95% CI: 0.59–1.23, $p < 0.00001$).

No potential publication bias was observed with respect to the relationship between BNP levels and extubation outcomes, according to the results of the Egger's test ($P > 0.05$) and Begg's test ($P > 0.05$). The leave-one-out sensitivity also showed robust results, as none of the studies had a significant effect on the overall outcomes.

DISCUSSION

In this study, we identified an association between high CVP and BNP levels with extubation failure in critically ill patients. An association was also found with both elevated BNP and CVP levels before extubation and elevated BNP levels after extubation.

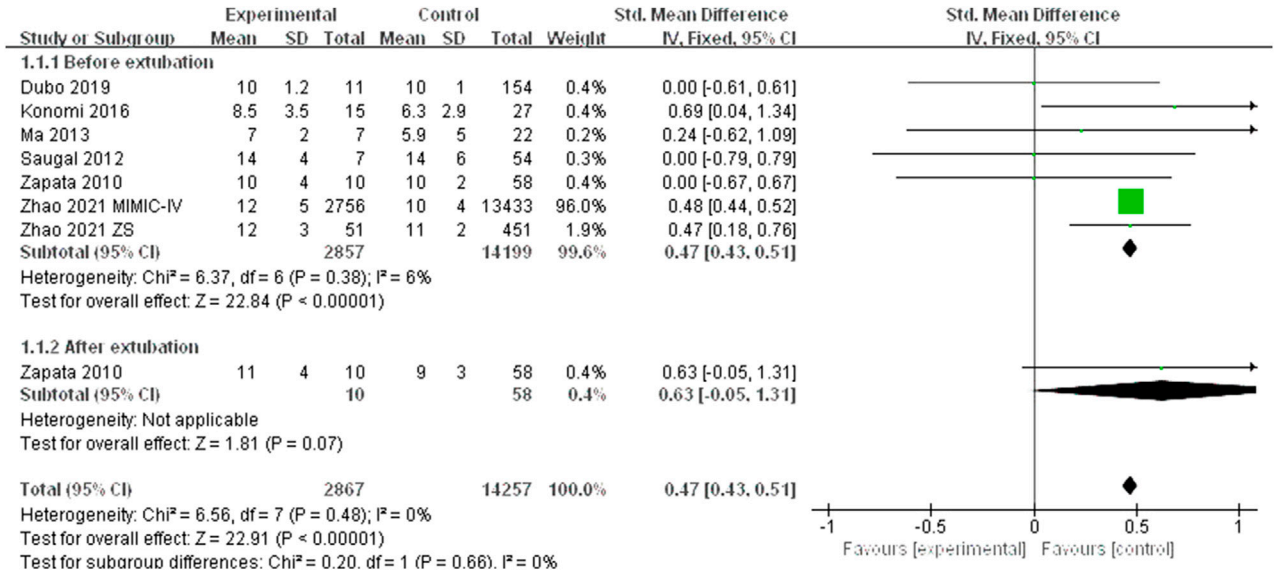

FIGURE 2 | The CVP levels standard mean difference between extubation failure and extubation success groups.

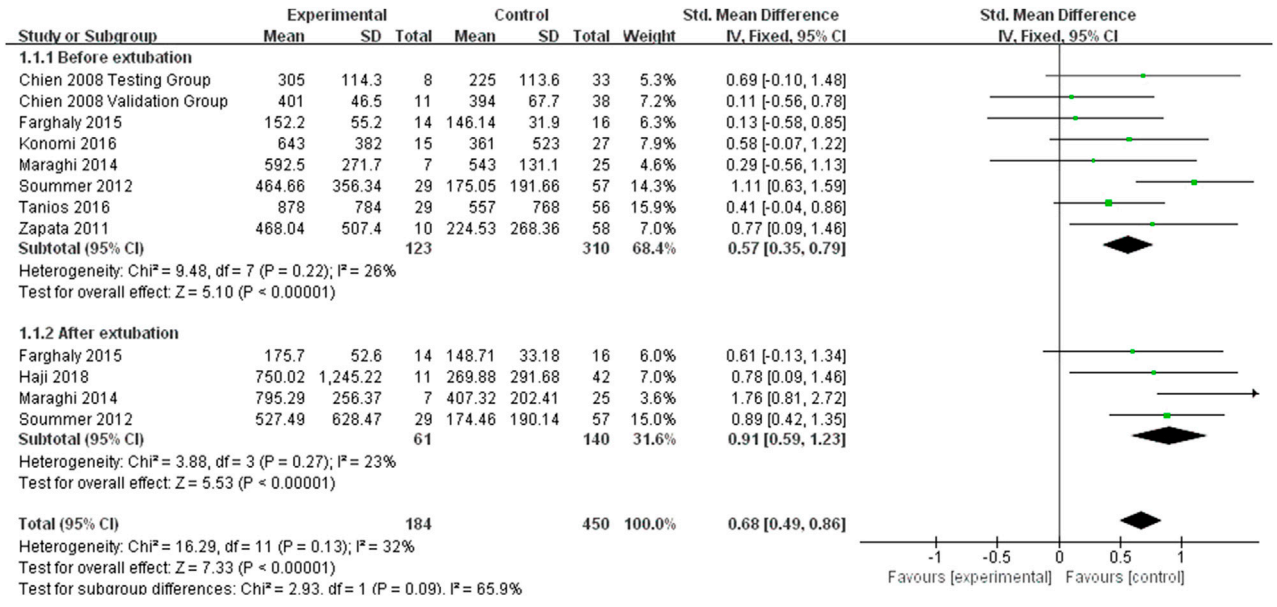

FIGURE 3 | The BNP levels standard mean difference between extubation failure and extubation success groups.

However, this association did not appear in elevated CVP levels after extubation. Thus, these results suggested that the measurement of CVP and BNP levels may be useful indicators for patients undergoing extubation from MV. Moreover, compared with CVP levels, BNP levels are a more valuable predictor of extubation outcomes. The values of I^2 = 0% for CVP and I^2 = 23% for BNP showed that our pooled analysis was homogeneous, and the leave-one-out sensitivity showed our results are robust.

In the process of liberation from MV, the intrathoracic pressure develops from positive to negative. This promotes the systemic venous blood reflux increases the right ventricular preload and augmented left ventricular transmural pressure and afterload (Buda et al., 1979). Moreover, emotional stress and potential hypoxia during extubation may lead to sympathetic excitation. Many critically ill patients have undiagnosed or subclinical cardiovascular diseases, which often hiderfluid management and cardiovascular compensation. Thus,

insufficient cardiac reserve may lead to subsequent respiratory insufficiency and failed extubation (Jubran et al., 1998). In particular, marked or even asymptomatic, diastolic or systolic dysfunction, as well as arrhythmias, coronary heart disease, and other heart conditions increase the likelihood of extubation failure.

Both CVP and BNP levels are able to monitor heart function and volume. Critically ill patients in the ICU often require an indwelling central venous catheter to monitor cardiac function and fluid replacement. There are only a few studies describing the association between CVP levels and extubation outcomes. Our analysis suggested that elevated CVP levels are associated with extubation failure, and that this association was observed before extubation. This result is consistent with the results of Dubo et al. (2019), which demonstrated that an early rise in CVP levels before extubation, increased the risk of extubation failure. However, this association was not observed after extubation. We believe that this conclusion is controversial for two main reasons: first, after adequate treatment, most patients' cardiac function improved significantly after extubation. Potential cardiac insufficiency could not be detected due to the poor sensitivity of CVP in monitoring cardiac function and volume. Second, the lack of data may be one reason for conflicting results, as only one studies were included. Therefore, more well-designed studies should be carried out.

BNP has been proven to be a sensitive serum marker of cardiac dysfunction (Win et al., 2005). Zapata et al. (2011) and Lara et al. (2013) found compared with patients with successful extubation, patients with extubation failure had higher BNP levels before and after extubation. Our study also confirmed that elevated BNP levels were significantly associated with extubation failure. Our anlaysis also showed that elevated BNP levels before extubation were closely related to extubation failure, consistent with studies by Chien et al. and Konomi et al. Unlike CVP, this association also appeared after extubation. Some studies have shown that increased BNP levels after extubation are a predictive factor for extubation failure (Lemaire et al., 1988; Jubran et al., 1998). Since BNP is a sensitive indicator of cardiac insufficiency, potential cardiac insufficiency can be detected early on.

Strengths and Limitations

The measurement of CVP levels is affected by the observer's mode of measurement and the patient's condition. For example, intra-thoracic pressure, intra-abdominal pressure, position, or depth of venous catheter placement can affect the results. Although we can standardize the observer's measurement and try to avoid a patient influence on the CVP measurements, there is poor predictive value for extubation outcomes. As ICU patients often have in-dwelling central venous catheters, CVP could easily and quickly be evaluated at the bedside. BNP is a sensitive marker for monitoring cardiac insufficiency and accurately predicts extubation outcomes. However, the utility of BNP as a marker also has its limitations. The detection of BNP is affected by age, renal insufficiency, drugs and other unavoidable factors. In conclusion, although CVP is able to identify early extubation outcomes, its predictive value is poor. In contrast, BNP has high predictive value, but the detection of extubation outcomes is inferior. Finally, the accuracy of our results may be affected by the limited number of studies we included. Since we do not have access to the original data for drawing ROC curves, we cannot determine a reliable cut-off point fot the CVP and BNP tests.

CONCLUSION

Our study showed that elevated CVP and BNP levels are related to the risk of extubation failure. More importantly, compared with CVP levels, BNP levels are more valuable than CVP levels in predicting extubation outcomes.

DATA AVAILABILITY STATEMENT

The original contributions presented in the study are included in the article/Supplementary Material, further inquiries can be directed to the corresponding author.

AUTHOR CONTRIBUTIONS

JC and BW wrote the main manuscript text. LZ and LS prepared Figures 1, 2, 3, and Table 1. All authors reviewed the manuscript.

REFERENCES

Buda, A. J., Pinsky, M. R., Ingels, N. B., Daughters, G. T., Stinson, E. B., and Alderman, E. L. (1979). Effect of Intrathoracic Pressure on Left Ventricular Performance. *N. Engl. J. Med.* 301 (9), 453–459. doi:10.1056/NEJM197908303010901

Chatila, W., Ani, S., Guaglianone, D., Jacob, B., Amoateng-Adjepong, Y., and Manthous, C. A. (1996). Cardiac Ischemia during Weaning from Mechanical Ventilation. *Chest* 109 (6), 1577–1583. doi:10.1378/chest.109.6.1577

Chien, J.-Y., Lin, M.-S., Huant, Y. C. T., Chien, Y.-F., Yu, C.-J., and Yang, P.-C. (2008). Changes in B-type Natriuretic Peptide Improve Weaning Outcome Predicted by Spontaneous Breathing Trial. *Crit. care Med.* 36 (5), 1421–1426. doi:10.1097/CCM.0b013e31816f49ac

Dubo, S., Valenzuela, E. D., Aquevedo, A., Jibaja, M., Berrutti, D., Labra, C., et al. (2019). Early Rise in Central Venous Pressure during a Spontaneous Breathing Trial: A Promising Test to Identify Patients at High Risk of Weaning Failure? *PloS one* 14 (12), e0225181. doi:10.1371/journal.pone.0225181

Esteban, A., Anzueto, A., Frutos, F., Inmaculada, A., Laurent, B., Thomas, E. S., et al. (2002). Characteristics and Outcomes in Adult Patients Receiving Mechanical VentilationA 28-Day International Study. *JAMA* 287, 345–355. doi:10.1001/jama.287.3.345

Farghaly, S., Galal, M., Hasan, A. A., and Nafady, A. (2015). Brain Natriuretic Peptide as a Predictor of Weaning from Mechanical Ventilation in Patients with Respiratory Illness. *Aust. Crit. Care* 28 (3), 116–121. doi:10.1016/j.aucc.2014.12.002

Fernandez-Zamora, M. D., Gordillo-Brenes, A., Banderas-Bravo, E., Arboleda-Sánchez, J. A., Hinojosa-Pérez, R., Aguilar-Alonso, E., et al. (2018). Prolonged Mechanical Ventilation as a Predictor of Mortality after Cardiac Surgery. *Respir. Care* 63 (5), 550–557. doi:10.4187/respcare.04915

Frazier, S. K., Brom, H., Widener, J., Pender, L., Stone, K. S., and Moser, D. K. (2006). Prevalence of Myocardial Ischemia during Mechanical Ventilation and Weaning and its Effects on Weaning Success. *Heart & Lung* 35 (6), 363–373. doi:10.1016/j.hrtlng.2005.12.006

Frutos-Vivar, F., Ferguson, N. D., Esteban, A., EpsteinEpstein, S. K., Arabi, Y., Apezteguía, C., et al. (2006). Risk Factors for Extubation Failure in Patients Following a Successful Spontaneous Breathing Trial. *Chest* 130 (6), 1664–1671. doi:10.1378/chest.130.6.1664

Haji, K., Haji, D., Canty, D. J., Royse, A. G., Green, C., and Royse, C. F. (2018). The Impact of Heart, Lung and Diaphragmatic Ultrasound on Prediction of Failed Extubation from Mechanical Ventilation in Critically Ill Patients: a Prospective Observational Pilot Study. *Crit. Ultrasound J.* 10 (1), 13. doi:10.1186/s13089-018-0096-1

Harrison, A. M., Cox, A. C., Davis, S., Piedmonte, M., Drummond-Webb, J. J., Mee, R. B. B., et al. (2002). Failed Extubation after Cardiac Surgery in Young Children: Prevalence, Pathogenesis, and Risk Factors*. *Pediatr. Crit. Care Med.* 3 (2), 148–152. doi:10.1097/00130478-200204000-00011

Hsieh, M.-H., Hsieh, M.-J., Chen, C.-M., Hsieh, C.-C., Chao, C.-M., and Lai, C.-C. (2018). An Artificial Neural Network Model for Predicting Successful Extubation in Intensive Care Units. *J. Clin. Med.* 7 (9), 240. doi:10.3390/jcm7090240

Jubran, A., Mathru, M., Dries, D., and Tobin, M. J. (1998). Continuous Recordings of Mixed Venous Oxygen Saturation during Weaning from Mechanical Ventilation and the Ramifications Thereof. *Am. J. Respir. Crit. Care Med.* 158 (6), 1763–1769. doi:10.1164/ajrccm.158.6.9804056

Khamiees, M., Raju, P., DeGirolamo, A., Amoateng-Adjepong, Y., and Manthous, C. A. (2001). Predictors of Extubation Outcome in Patients Who Have Successfully Completed a Spontaneous Breathing Trial. *Chest* 120 (4), 1262–1270. doi:10.1378/chest.120.4.1262

Konomi, I., Tasoulis, A., Kaltsi, I., Karatzanos, E., Vasileiadis, I., Temperikidis, P., et al. (2016). Left Ventricular Diastolic Dysfunction-An Independent Risk Factor for Weaning Failure from Mechanical Ventilation. *Anaesth. Intensive Care* 44 (4), 466–473. doi:10.1177/0310057X1604400408

Lara, T. M., Hajjar, L. A., de Almeida, J. P., Fukushima, J. T., Barbas, C. S. V., Rodrigues, A. R. B., et al. (2013). High Levels of B-type Natriuretic Peptide Predict Weaning Failure from Mechanical Ventilation in Adult Patients after Cardiac Surgery. *Clinics* 68 (1), 33–38. doi:10.6061/clinics/2013(01)oa05

Lemaire, F., Teboul, J.-L., Cinotti, L., Giotto, G., Abrouk, F., Steg, G., et al. (1988). Acute Left Ventricular Dysfunction during Unsuccessful Weaning from Mechanical Ventilation. *Anesthesiology* 69 (2), 171–179. doi:10.1097/00000542-198808000-00004

Luo, D., Wan, X., Liu, J., and Tong, T. (2018). Optimally Estimating the Sample Mean from the Sample Size, Median, Mid-range, And/or Mid-quartile Range. *Stat. Methods Med. Res.* 27 (6), 1785–1805. doi:10.1177/0962280216669183

Ma, G., Liao, W., Qiu, J., Su, Q., Fang, Y., and Gu, B. (2013). N-terminal Prohormone B-type Natriuretic Peptide and Weaning Outcome in Postoperative Patients with Pulmonary Complications. *J. Int. Med. Res.* 41 (5), 1612–1621. doi:10.1177/0300060513490085

Maraghi, S. E., Hosny, M., Samir, M., and Radwan, W. (2014). Usage of B-type Natriuretic Peptide for Prediction of Weaning Outcome by Spontaneous Breathing Trial. *Egypt. J. Chest Dis. Tuberc.* 63, 671–678. doi:10.1016/j.ejcdt.2014.04.003

Perren, A., Previsdomini, M., Llamas, M., Cerutti, B., Györik, S., Merlani, G., et al. (2010). Patients' Prediction of Extubation Success. *Intensive Care Med.* 36 (12), 2045–2052. doi:10.1007/s00134-010-1984-4

Saugel, B., Rakette, P., Hapfelmeier, A., Schultheiss, C., Phillip, V., Thies, P., et al. (2012). Prediction of Extubation Failure in Medical Intensive Care Unit Patients. *J. Crit. care* 27 (6), 571–577. doi:10.1016/j.jcrc.2012.01.010

Soummer, A., Perbet, S., Brisson, H., Arbelot, C., Constantin, J.-M., Lu, Q., et al. (2012). Ultrasound Assessment of Lung Aeration Loss during a Successful Weaning Trial Predicts Postextubation Distress*. *Crit. care Med.* 40 (7), 2064–2072. doi:10.1097/ccm.0b013e31824e68ae

Stang, A. (2010). Critical Evaluation of the Newcastle-Ottawa Scale for the Assessment of the Quality of Nonrandomized Studies in Meta-Analyses. *Eur. J. Epidemiol.* 25 (9), 603–605. doi:10.1007/s10654-010-9491-z

Tanios, M., Epstein, S., Sauser, S., and Chi, A. (2016). Noninvasive Monitoring of Cardiac Output during Weaning from Mechanical Ventilation: A Pilot Study. *Am. J. Crit. Care* 25 (3), 257–265. doi:10.4037/ajcc2016921

Thille, A. W., Harrois, A., Schortgen, F., Brun-Buisson, C., and Brochard, L. (2011). Outcomes of Extubation Failure in Medical Intensive Care Unit Patients*. *Crit. care Med.* 39 (12), 2612–2618. doi:10.1097/ccm.0b013e3182282a5a

Wan, X., Wang, W., Liu, J., and Tong, T. (2014). Estimating the Sample Mean and Standard Deviation from the Sample Size, Median, Range And/or Interquartile Range. *BMC Med. Res. Methodol.* 14, 135. doi:10.1186/1471-2288-14-135

Win, H. K., Chang, S.-M., Raizner, M., Shah, G., Basky, F. A., Desai, U., et al. (2005). Percent Change in B-type Natriuretic Peptide Levels during Treadmill Exercise as a Screening Test for Exercise-Induced Myocardial Ischemia. *Am. heart J.* 150 (4), 695–700. doi:10.1016/j.ahj.2004.12.003

Zapata, L., Vera, P., Roglan, A., Gich, I., Ordonez-Llanos, J., and Betbesé, A. J. (2011). B-type Natriuretic Peptides for Prediction and Diagnosis of Weaning Failure from Cardiac Origin. *Intensive Care Med.* 37 (3), 477–485. doi:10.1007/s00134-010-2101-4

Zhao, Q.-Y., Wang, H., Luo, J.-C., Luo, M.-H., Liu, L.-P., Yu, S.-J., et al. (2021). Development and Validation of a Machine-Learning Model for Prediction of Extubation Failure in Intensive Care Units. *Front. Med.* 8, 676343. doi:10.3389/fmed.2021.676343

Conflict of Interest: The authors declare that the research was conducted in the absence of any commercial or financial relationships that could be construed as a potential conflict of interest.

Publisher's Note: All claims expressed in this article are solely those of the authors and do not necessarily represent those of their affiliated organizations, or those of the publisher, the editors and the reviewers. Any product that may be evaluated in this article, or claim that may be made by its manufacturer, is not guaranteed or endorsed by the publisher.

frontiers | Frontiers in Physiology

ORIGINAL RESEARCH
published: 18 July 2022
doi: 10.3389/fphys.2022.803641

Resting Physiologic Dead Space as Predictor of Postoperative Pulmonary Complications After Robotic-Assisted Lung Resection: A Pilot Study

Rohit Godbole[1], *Sanford B. Church*[1], *Amir Abolhoda*[1,2], *Janos Porszasz*[3] *and Catherine S. H. Sassoon*[1,2]*

[1]*Department of Medicine, Division of Pulmonary and Critical Care Medicine, University of California, Irvine, CA, United States,* [2]*Department of Medicine, Division of Pulmonary and Critical Care Medicine, VA Long Beach Healthcare System, Long Beach, CA, United States,* [3]*The Lundquist Institute for Biomedical Innovation at Harbor-UCLA Medical Center, Torrance, CA, United States*

Lung resection surgery carries significant risks of postoperative pulmonary complications (PPC). Cardiopulmonary exercise testing (CPET) is performed to predict risk of PPC in patients with severely reduced predicted postoperative forced expiratory volume in one second (FEV1) and diffusion of carbon monoxide (DLCO). Recently, resting end-tidal partial pressure of carbon dioxide ($PETCO_2$) has been shown as a good predictor for increased risk of PPC. However, breath-breath breathing pattern significantly affects $PETCO_2$. Resting physiologic dead space (VD), and physiologic dead space to tidal volume ratio (VD/VT), may be a better predictor of PPC than $PETCO_2$. The objective of this study was to prospectively determine the utility of resting measurements of VD and VD/VT in predicting PPC in patients who underwent robotic-assisted lung resection for suspected or biopsy-proven lung malignancy. Thirty-five consecutive patients were included in the study. Patients underwent preoperative pulmonary function testing, symptom-limited CPET, and a 6-min walk test. In the first 2 min prior to the exercise portion of the CPET, we obtained resting VT, minute ventilation ($\dot{V}E$), VD (less instrument dead space), VD/VT, $PETCO_2$, and arterial blood gases. PPC within 90 days were recorded. Fourteen (40%) patients had one or more PPC. Patients with PPC had significantly elevated resting VD compared to those without (0.318 ± 0.028 L vs. 0.230 ± 0.017 L (± SE), $p < 0.006$), and a trend toward increased VD/VT (0.35 ± 0.02 vs. 0.31 ± 0.02, $p = 0.051$). Area under the receiver operating characteristic (ROC) for VD was 0.81 ($p < 0.002$), VD/VT was 0.68 ($p = 0.077$), and $PETCO_2$ was 0.52 ($p = 0.840$). Peak $\dot{V}O_2$, $\dot{V}E/\dot{V}CO_2$ slope, pulmonary function tests, 6-min walk distance and arterial blood gases were similar between the two groups. Intensive care unit and total hospital length of stay was significantly longer in those with PPC. In conclusion, preoperative resting VD was significantly elevated in patients with PPC. The observed increase in resting VD may be a potentially useful predictor of PPC in patients undergoing robotic-assisted lung resection surgery for suspected or biopsy-proven lung malignancy. A large prospective study is needed for confirmation.

Keywords: physiologic dead space, postoperative predictor, pulmonary complications, robotic-assisted lung resection, lung cancer

OPEN ACCESS

Edited by:
Andrew John Halayko, University of Manitoba, Canada

Reviewed by:
Devin B. Phillips, Queen's University, Canada
Marta Guðjónsdóttir, University of Iceland, Iceland

***Correspondence:**
Catherine S. H. Sassoon
csassoon@uci.edu

Specialty section:
This article was submitted to Respiratory Physiology and Pathophysiology, a section of the journal Frontiers in Physiology

Received: *28 October 2021*
Accepted: *17 June 2022*
Published: *18 July 2022*

Citation:
Godbole R, Church SB, Abolhoda A, Porszasz J and Sassoon CSH (2022) Resting Physiologic Dead Space as Predictor of Postoperative Pulmonary Complications After Robotic-Assisted Lung Resection: A Pilot Study. Front. Physiol. 13:803641. doi: 10.3389/fphys.2022.803641

INTRODUCTION

Preoperative evaluation of lung function is the standard of care to estimate the risks of postoperative pulmonary complications (PPC) following lung resection for lung nodules, either biopsy-proven, or suspicious for cancer. Lung resection surgery carries significant risks, including postoperative respiratory failure, pneumonia, and atelectasis, resulting in prolonged hospital length of stay and mortality. Preoperatively, cardiopulmonary exercise testing (CPET), stair climb or shuttle-walk tests, as well as forced expiratory volume in 1 s (FEV_1), diffusion capacity for carbon monoxide (DLCO) have been utilized to assess patients' risks of PPC. If there is no increased cardiac risk for lung resection surgery, but severely reduced postoperative predicted FEV_1 and/or DLCO, or poor performance of stair climb or shuttle-walk test, current guidelines recommend CPET (Brunelli et al., 2013). With CPET, subjects who underwent lobectomy or pneumonectomy, maximum oxygen utilization or peak oxygen uptake (Peak $\dot{V}O_2$) has been shown as a good predictor of morbidity and mortality (Brunelli et al., 2009). Subsequently, the same group of investigators reported the advantage of minute ventilation to carbon dioxide production ($\dot{V}E/\dot{V}CO_2$) slope as predictor of PPC risks independent of Peak $\dot{V}O_2$ (Brunelli et al., 2012). Patients with $\dot{V}E/\dot{V}CO_2$ slope greater than 35 had high morbidity and mortality.

In healthy individuals, $\dot{V}E/\dot{V}CO_2$ ratio decreases during exercise with increasing workload (Wasserman et al., 1967). The ratio increases when $\dot{V}E$ is greater than $\dot{V}CO_2$ in response to metabolic acidosis. $\dot{V}E/\dot{V}CO_2$ is also dependent on physiologic dead space to tidal volume ratio (VD/VT) (Roman et al., 2013). According to balance of masses (Whipp, 2006), this can be demonstrated from the relationship between arterial partial pressure of carbon dioxide ($PaCO_2$), $\dot{V}CO_2$, and $\dot{V}E/\dot{V}CO_2$ in which:

$$\dot{V}E/\dot{V}CO_2 = \frac{k}{[PaCO_2 x (1 - VD/VT)]} \quad (1)$$

where k is constant, equals to 863. From **Eq. 1**, as Roman et al. (2013) demonstrated, high resting $\dot{V}E/\dot{V}CO_2$ is associated with high VD/VT, low $PaCO_2$, end-tidal PCO_2 ($PETCO_2$), or both.

In a recent retrospective study, Brat et al. (2016) demonstrated elevated $\dot{V}E/\dot{V}CO_2$ slope and reduced end-tidal PCO_2 ($PETCO_2$) at both peak exercise and rest in patients with PPC, with resting $PETCO_2$ as the strongest independent predictor. However, $PETCO_2$, is affected by regional ventilation-perfusion mismatch and breathing pattern (Lewis et al., 1994). Resting VD or VD/VT has not been explored as a predictor of PPC risk after lung resection. Whereas the safety of symptom-limited CPET has been well documented, there is a substantial number of patients who are unable or unwilling to perform CPET (Keteyian et al., 2009). In this regard, the addition of resting test(s) that can effectively predict risks of PPC after lung resection will be beneficial.

The primary objective of our study was to determine if resting VD or VD/VT could reliably predict the risk of PPC within 90 days of robotic-assisted lung resection surgery in patients with a suspicious or biopsy-proven lung malignancy. The secondary objective was to compare the utility of resting VD or VD/VT with resting $PETCO_2$ as a predictor of PPC in our population. We hypothesized that elevated resting VD or VD/VT will be useful and a better predictor of PPC risk than $PETCO_2$.

MATERIALS AND METHODS

Participants

Seventy-four patients with suspected or biopsy-proven lung malignancy were referred for lobectomy or segmentectomy by the multi-disciplinary team for lung cancer management at the Veteran Affairs Healthcare System, Long Beach, from January 2018 to January 2019. Thirty-nine patients were excluded for the following reasons: 1) declined to consent for the study (n = 11), declined or unable to perform CPET (n = 22), declined lung resection (n = 4), or had lung resection at another institution (n = 2). We studied the remaining 35 patients consecutively. Prior to the study each patient signed a written informed consent. Patients had to meet the following criteria: age greater than 18 years, non-pregnant, and ability to perform pulmonary function tests, six-minute walk test (6MWT), and CPET with no contraindications (Datta et al., 2015).

Study Design

This was a prospective observational study approved by the institutional review board of the Veteran Affairs Healthcare System, Long Beach. Patients underwent preoperative pulmonary function testing, 6MWT, and CPET.

Spirometry and breath-by-breath gas analysis during CPET was performed using Vmax Encore^{TM} System (Vyaire Medical, Irvine, CA, United States). CPET was performed on average 12 days prior to surgery on incremental cycle ergometer (VIAsprint 150P^{TM}, AIM, Sylmar, CA, United States). All equipment was calibrated prior to every test. After allowing the patient to adapt to the breathing apparatus and seated quietly on the cycle ergometer for at least 15 min, CPET commenced. CPET involved 2 min of rest, followed by 2 min of unloaded pedaling, then continued with application of ramp-incremental work-rate profile (5–15 W/min) to the point of symptom limitation (Datta et al., 2015). During CPET an average of 10 s data points were displayed. No patients discontinued CPET for cardiac events. Single arterial blood sample was obtained from each patient proximate to the CPET 2-min rest period via radial artery puncture using standard technique, and immediately analyzed via blood gas analyzer (RapidPoint 400 Series, Bayer Healthcare Systems, Oxnard, CA). Samples were obtained at room temperature and corrected for body temperature of 37°C. From **Eq. 1**, utilizing resting $\dot{V}E/\dot{V}CO_2$ averaged over 2-min and $PaCO_2$ obtained from arterial blood gases, resting VD and VD/VT were calculated. Instrument dead-space measured by water displacement method three times, and the average value amounted to 169 ml was subtracted from the calculated VD. $\dot{V}E/\dot{V}CO_2$ slope was calculated using linear regression with $\dot{V}E$ as the dependent, and $\dot{V}CO_2$ the independent variable with onset of

TABLE 1 | Subjects characteristics.

Characteristics	Subjects with post-operative pulmonary complications (n = 14)	Subjects without post-operative pulmonary complications (n = 21)	p
Age (years)	70.3 ± 1.8	70.7 ± 1.5	0.859
Male (%)	100	100	
Height (m)	1.78 ± 0.02	1.78 ± 0.01	0.753
Weight (Kg)	84.4 ± 4.1	82.0 ± 3.0	0.626
Tobacco Use (packyears) †	40 (15, 80)	25 (1, 50)	0.181
COPD, n (%)	11 (78.6)	10 (52.4)	0.163
CHF, n (%)	2 (14.3)	2 (9.5)	1.00

Values are mean ± SE, † is median with 25 and 75 percentiles in parenthesis.
Definition of abbreviations: COPD, chronic obstructive pulmonary disease; CHF, congestive heart failure.

workload as the initial point to the peak workload as the end point. Nadir $\dot{V}E/\dot{V}CO_2$ was calculated, when available, at the ventilatory compensation threshold and average over 30 s (Mezzani, 2017). Finally, the 6MWT was conducted following complete resolution of symptoms from CPET.

One board-certified cardiothoracic surgeon (AA) performed all lung resections using robotic-assisted surgery. The surgical team managed patients postoperatively with patients mobilized as soon as tolerated. PPCs were recorded after a thorough chart review and included events immediately after surgery up to 90 days post-surgery. The PPCs included 1) pneumonia defined as increased sputum production, leukocytosis, fever, positive sputum culture, and consolidation on chest x-ray, 2) respiratory failure requiring invasive or non-invasive mechanical ventilation, or 3) atelectasis requiring bronchoscopy.

Statistical Analysis

For this pilot study, a sample size of 24 subjects was required as determined using a mean difference of 25% according to the morbidity of postoperative lung resection reported by Brunelli et al. (2012), standard deviation of 30%, power of 0.80, and alpha of 0.05. Patients were grouped into those with and without PPC. Continuous variables were expressed as mean and standard deviation or standard error of the mean as appropriate; and compared using the unpaired two-tailed Student's t test. Categorical variables, or those that did not pass the normality test and/or equal variance test, were compared using the Mann-Whitney Rank Sum test, and median with interquartile range values are reported. Differences in proportion were evaluated using the Fisher exact test. Receiver operating characteristic (ROC) curves were evaluated for threshold values for variables of interest, i.e., VD, VD/VT and $PETCO_2$. In ROC, sensitivity, the dependent variable is the ability of a test to correctly identify patients with PPC, while specificity is the ability of a test to correctly identify those without PPC. Ideally, the threshold value has a sensitivity proximate 1.0 and 1-specificity (the independent variable) proximate 0, or the area under the ROC curve is close to 1.0. When the area under the ROC is statistically significant, the threshold value was determined from the highest sum of sensitivity and specificity according to the Youden approach (Bewick et al., 2004). Data were analyzed using Sigmaplot v.14 software (Systat Software Inc., San Jose, CA, United States).

RESULTS

Postoperative pulmonary complications occurred in 14 (40%) out of 35 patients with one or more complications occurring in the same patient. There was no mortality. All patients underwent lobectomy, except one patient in each group, with and without PPC, had segmentectomy.

Table 1 shows the baseline characteristics of patients in both groups with and without PPC. Average age in both groups was 70 years, and all patients were male Veterans. Tobacco use did not differ between groups, but was somewhat higher in those with (40 packyears) than without (25 packyears) PPC. A similar trend was shown in the prevalence of COPD with 79% of those having PPC compared to 52% in those without PPC. The prebronchodilator spirometry, DLCO, and 6-min Walk distance were similar in both groups (**Table 2**).

Table 3 demonstrates the measured variables at rest and with exercise during CPET. At rest, the PPC group had significantly elevated VD, average was 0.318 L versus 0.230 L in those without PPC ($p < 0.006$). VD/VT tended to be greater ($p = 0.051$) in the PPC group, while $PETCO_2$, other ventilatory variables, and arterial blood gases were not significantly different from those without PPC (**Table 3**). Resting hyperventilation was not observed during CPET as corroborated by the pH and $PaCO_2$.

With exercise, peak $\dot{V}O_2$, $\dot{V}O_2$ at lactate threshold, peak power, $\dot{V}E/\dot{V}CO_2$ slope, and nadir $\dot{V}E/\dot{V}CO_2$ were similar in both groups. Nadir $\dot{V}E/\dot{V}CO_2$ was estimated in only those who attained ventilator compensation threshold, 12 and 15 patients in the group with and without PPC, respectively.

Postoperative pneumonia and atelectasis requiring therapeutic bronchoscopy were the most common PPCs (**Table 4**). As expected, patients with PPCs had significantly extended ICU and hospital length of stay compared with the group without PPC.

Figure 1 shows the ROC analysis for VD, VD/VT and $PETCO_2$. The area under the ROC curve (AUC) was statistically significant for VD only (0.81, $p = 0.002$). The AUC for VD/VT and $PETCO_2$ was 0.68 ($p = 0.077$) and 0.53

TABLE 2 | Pulmonary function and six-minute walk tests.

Variables	Subjects with post-operative pulmonary complications (*n* = 14)	Subjects without post-operative pulmonary complications (*n* = 21)	*p*
FEV1/FVC (%)	65.8 ± 3.3	70.0 ± 2.9	0.352
FEV1 (L)	2.33 ± 0.22	2.73 ± 0.15	0.120
FEV1 (% predicted)	73.5 ± 7.2	85.1 ± 4.1	0.143
FVC (L)	3.65 ± 0.27	3.96 ± 0.19	0.342
FVC (% predicted)	83.4 ± 5.7	92.0 ± 3.1	0.166
DLCO (ml/min/mm Hg)	20.3 ± 2.0	22.1 ± 1.8	0.517
DLCO (% predicted)	77.6 ± 8.6	83.5 ± 6.9	0.598
6 MWT (m)	400.4 ± 21.5	408.0 ± 14.8	0.766

Values are mean ± SE.

Definition of abbreviations: FEV1, forced expiratory volume in 1 s; FVC, forced expiratory vital capacity; DLCO, diffusing capacity for carbon monoxide; 6 MWT, six-minute walk test.

TABLE 3 | Cardiopulmonary exercise test at rest and exercise.

At rest			
Variables	**Subjects with post-operative pulmonary complications (*n* = 14)**	**Subjects without post-operative pulmonary complications (*n* = 21)**	***p***
VT (L)	0.904 ± 0.071	0.764 ± 0.043	0.084
Frequency (breaths/min)	20.1 ± 1.4	19.7 ± 0.9	0.816
$\dot{V}E$ (L/min)	17.4 ± 1.1	14.9 ± 1.0	0.110
$\dot{V}CO_2$ (L/min)	0.382 ± 0.03	0.348 ± 0.02	0.376
$\dot{V}O_2$ (L/min)	0.470 ± 0.04	0.395 ± 0.03	0.097
Respiratory Quotient	0.82 ± 0.02	0.81 ± 0.01	0.735
$\dot{V}E/\dot{V}CO_2$	47.0 ± 2.6	43.6 ± 1.6	0.250
VD (L)	0.318 ± 0.03	0.230 ± 0.02	0.006*
VD/VT	0.35 ± 0.02	0.31 ± 0.02	0.051
$PETCO_2$ (mm Hg)	32.0 ± 1.4	31.5 ± 1.0	0.763
pH (unit)	7.43 ± 0.01	7.43 ± 0.01	0.666
$PaCO_2$ (mm Hg)	37.9 ± 1.9	35.6 ± 1.3	0.312
PaO_2 (mm Hg)	78.5 ± 3.3	86.0 ± 3.5	0.153
SaO_2 (%)	92.7 ± 0.7	92.8 ± 1.3	0.977
$PETCO_2$-$PaCO_2$	5.9 ± 0.9	4.02 ± 0.7	0.134
With Exercise			
Peak $\dot{V}O_2$ (L/min)	1.646 ± 0.127	1.686 ± 0.090	0.792
Peak $\dot{V}O_2$ (% PRED)	77.9 ± 5.6	77.7 ± 3.8	0.969
Peak $\dot{V}O_2$ (L/min/Kg)	19.6 ± 1.3	20.2 ± 1.1	0.494
$\dot{V}O_2$ at LT (L/min)	1.29 ± 0.10	1.38 ± 0.07	0.446
$\dot{V}O_2$ at LT (% of Peak $\dot{V}O_2$)	78.9 ± 2.5	81.2 ± 1.9	0.334
Peak Power (watts/min)	84.0 ± 6.3	95.0 ± 5.9	0.222
$\dot{V}E/\dot{V}CO_2$ slope	33.0 ± 2.3	31.2 ± 1.1	0.446
Nadir $\dot{V}E/\dot{V}CO_2$†	34.3 ± 1.1	32.4 ± 1.4	0.333

Values are mean ± SE. *p < 0.05.

*Definition of abbreviations: VT, tidal volume; $\dot{V}E$, minute ventilation; $\dot{V}O_2$, oxygen consumption; $\dot{V}CO_2$, carbon dioxide production; $PETCO_2$, end-tidal carbon dioxide; VD, physiologic dead space volume; VD/VT, physiologic dead space to tidal volume ratio; LT, lactate threshold. † Measured at ventilatory compensation threshold, subjects with post-operative pulmonary complications (*n = 12); without post-operative pulmonary complications (*n = 16). See text for further explanation.*

TABLE 4 | ICU, hospital length of stay, and types of post-surgical complications.

	Subjects with post-operative pulmonary complications (*n* = 14)	Subjects without post-operative pulmonary complications (*n* = 21)	*p*
Pneumonia, n (%)	8 (57.1)	0 (0.0)	< 0.001
Atelectasis Requiring Bronchoscopy, n (%)	5 (35.7)	0 (0.0)	< 0.01
Respiratory Failure Requiring IMV, n (%)	3 (21.4)	0 (0.0)	0.06
Respiratory Failure Requiring NIV, n (%)	2 (14.3)	0 (0.0)	0.153
ICU Length of Stay (days) †	4 (4, 7)	2 (1, 3)	< 0.001
Hospital Length of Stay (days)†	9 (7, 13)	4 (4, 8)	< 0.001

†Values are median with 25 and 75 percentiles in parenthesis.

Definition of abbreviations: ICU, intensive care unit; IMV, invasive mechanical ventilation; NIV, noninvasive mechanical ventilation.

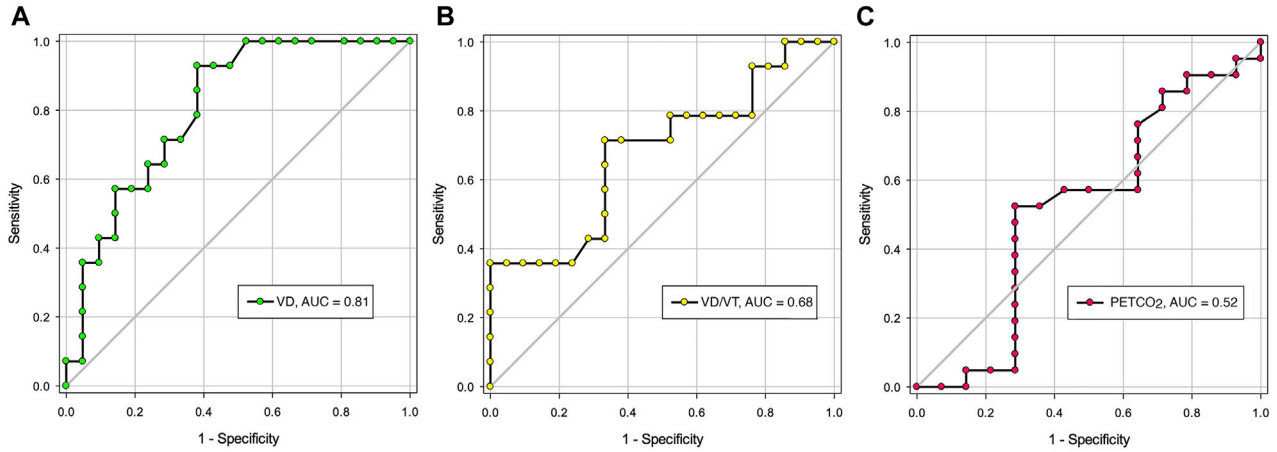

FIGURE 1 | The area under the Receiver Operating Characteristic Curves for resting VD, VD/VT and $PETCO_2$. **(A)**. Area under the curve (AUC) for VD: 0.81 (p = 002); **(B)**. AUC for VD/VT: 0.68 (p = 0.077); **(C)**. AUC for $PETCO_2$: 0.52 (p = 0.839). Definition of abbreviations: VD, dead space volume; VD/VT, dead space to tidal volume ratio; $PETCO_2$, end-tidal CO_2 pressure. NS, not significant.

(p = 0.839), respectively. A threshold value for VD at or below 0.229 L appears to be an acceptable predictor for the lack of PPC with sensitivity of 62% (95% Confidence Interval (CI): 38%–82%), and specificity of 93% (95% CI: 66%–100%). The positive and negative likelihood ratio was 8.7 and 0.4, respectively.

DISCUSSION

In this pilot study, our major findings were, 1) the preoperatively measured resting physiological dead space volume (VD) was the only variable separating groups of patients with and without PPC; 2) resting VD was also a significant predictor of PPC after robotic-assisted lung cancer resection surgery with a threshold value of 0.229 L; 3) resting end-tidal PCO_2 was not useful in predicting the frequency of PPC; and 4) the PPC following robotic-assisted lung resection surgery was relatively high of 40%.

Resting Physiological Dead Space

Resting VD, the sum of anatomical and alveolar dead space, was obtained from ventilatory efficiency ($\dot{V}E/\dot{V}CO2$) via breath-by-breath gas analysis and arterial PCO_2 rather than $PETCO_2$, and therefore, avoiding inaccurate estimate (Lewis et al., 1994). The elevated resting VD in the PPC group might be accounted for by an increase in ventilation-perfusion inequalities despite similar spirometry and DLCO indices (Sinha et al., 2011; Robertson, 2015). A crude estimate of ventilation-perfusion inequalities, $PaCO_2$-$PETCO_2$ difference was similar in both groups (**Table 3**). However, on a closer observation there were subtle differences in the measures of airflow limitation (FEV_1/FVC, FEV_1 and FVC) between those with and without PPC; with a higher prevalence of patients with COPD in the PPC group (79% vs. 52% without PPC). The underlying COPD cannot be dismissed to account for the high VD in the PPC group (**Table 1**).

While VD differed significantly between groups with and without PPC, VD/VT did not. The lack of significant difference in VD/VT was possibly related to the mildly elevated VT in the PPC group despite statistically insignificant (**Table 3**). Patients with a high resting VD may require higher compensatory VT to achieve effective ventilation and removal of CO_2. Thus, the VD/VT ratio was similar for both groups with and without PPC. There have been several studies in healthy subjects describing this phenomenon of elevated VT in response to elevated VD during exercise (Wasserman et al., 1967), and at rest (Krishnan et al., 1997). The possible mechanisms may include alterations in the PCO_2 time profile or oscillations sensed by airway and/or pulmonary receptors, carotid chemoreceptors, or the central chemoreceptors (McParland et al., 1991). However, studies have shown that airway receptors (Krishnan et al., 1997) and carotid chemoreceptors (Syabbalo et al., 1993) do not play a major role in the mechanism of increased VT in response to elevated VD. Central chemoreceptors may possibly have a predominant role.

As shown in **Table 2**, a large percentage of our patients with PPC had mild COPD (prebronchodilator FEV_1/FVC of 65.8%) with an average resting VD/VT of 0.35. Our findings were comparable to that of Elbehairy et al. (2015) with their mild COPD patients. The average prebronchodilator FEV_1/FVC was 59.5% and resting VD/VT of 0.37. VT and frequency were not reported; however, minute ventilation ($\dot{V}E$) was lower, 11.8 L/min compared to 17.4 L/min in our patients. The lack of increased $\dot{V}E$ in their study was not apparent, however, altered breathing pattern with ventilatory constraint such as low VT and high frequency would increase VD/VT (Whipp, 2006; Smith and Olson, 2019).

In this trial or experimental cohort, resting VD appears a useful predictor of PPC following lung resection surgery at a threshold value of 0.229 L, with area under ROC curve of 0.81 (**Figure 1**). This confers the advantage for those patients who cannot or decline to perform CPET in the preoperative evaluation of postoperative complications risk after lung resection surgery. The positive likelihood ratio was 8.7, suggesting that a positive result is

8.7 times as likely for a patient who experienced PPC as one who did not. At the above threshold value, we obtained a sensitivity of 62% and specificity of 93%. The Youden index is 55% [(62% + 93%)−100%] suggesting that the resting VD threshold value yields an appreciable fraction that may be misclassified (Bewick et al., 2004). For this reason, this threshold value needs to be prospectively validated in a large number of patients.

Resting End-Tidal PCO_2

A recent study of Brat et al. (2016) demonstrated that resting $PETCO_2$ was a strong predictor of PPC following lung resection surgery. In contrast, our results differed in that resting $PETCO_2$ was similar for both groups with and without PPC (**Table 3**). Differences might be related to patient characteristics such as 36% of their cohort were female; and/or variability in $PETCO_2$ estimate. $PETCO_2$ is critically influenced by breath-by-breath changes in the pattern of breathing. It is determined by the timing of end-exhalation during the alveolar phase-III of CO_2 of each breath. In patients with airflow limitation a plateau of alveolar phase-III could not be attained resulting in large variability of its measurement and a large gradient between $PaCO_2$ and $PETCO_2$ (Sinha et al., 2011). Furthermore, particularly in COPD patients, wasted ventilation contaminates the measurements, as inhaled CO_2 that doesn't take part in gas-exchange is exhaled and dilutes the mixed expired CO_2. Our study did not show significant difference in $PaCO_2$-$PETCO_2$ between both groups, probably related to variability of $PETCO_2$.

Postoperative Pulmonary Complications Following Robotic-Assisted Lung Surgery

CPET has been considered as the gold standard in the evaluation of PPC following lung resection (Brunelli et al., 2013). Interestingly, neither Peak $\dot{V}O_2$ nor $\dot{V}E/\dot{V}CO_2$ slope were able to preoperatively distinguish patients with and without PPC. Peak $\dot{V}O_2$ for both groups averaged 20 L/min/Kg and $\dot{V}E/\dot{V}CO_2$ averaged less than 34 (**Table 3**). Most likely this was due to our patients' absence of, or mild airflow limitation; or compensated stable heart failure. The PPC rate in our cohort was considered relatively high of 40%. However, this complication rate in the older patients as in our cohort, were within the range of others, 33%–44% (Velez-Cubian, et al., 2015; Veluswamy et al., 2020).

Study Strength and Limitation

The strength of our study is the prospective design of the study and the use of $PaCO_2$ rather than $PETCO_2$ in the calculation of VD. However, our study has several shortcomings. First, our population consists of only male gender from a single institution, the Veterans Affairs Healthcare System. The results of this study, therefore, may not be applicable to the female population and a multi-center study would be desirable. Second, although the number of subjects studied exceeded the calculated sample size, the present study is relatively small involving a trial cohort and will require a validation cohort to test whether resting VD will hold as a reliable predictor of PPC risk. Furthermore, a multivariate analysis to assess the confounding effects of COPD cannot be performed. Nonetheless, resting VD stood out as a potentially useful predictor of PPC risk after robotic-assisted lung surgery. Third, all lung resections involved lobectomy except for two segmentectomies, and no pneumectomy was performed. Hence, resting VD as predictor of PPC is only applicable in those patients with lobectomies.

Conclusion

In summary, our prospective study demonstrated that following robotic-assisted lung resection for suspected or biopsy-proven lung cancer, resting VD obtained preoperatively separated those patients with and without postoperative pulmonary complications. Resting VD is also a potential predictor for postoperative pulmonary complications risk. However, this will have to be further validated with a large number of patients.

DATA AVAILABILITY STATEMENT

The original contributions presented in the study are included in the article, further inquiries can be directed to the corresponding author.

ETHICS STATEMENT

The studies involving human participants were reviewed and approved by Institutional Review Board of the VA Long Beach Healthcare System. The patients/participants provided their written informed consent to participate in this study.

AUTHOR CONTRIBUTIONS

RG designed the study, conducted the experiments, analyzed and critically interpreted the data and drafted the manuscript; SC conducted the experiments, and analyzed the data; AA designed the study and performed the robotic-assisted surgery; JP provided consultation for CPET, dead space calculation, and critically reviewed the manuscript; CS designed the study, critically analyzed, interpreted the data, drafted and revised the manuscript. All authors had full access to all of the study data, critically revised the manuscript for important intellectual content, approved the final version of the manuscript, and took responsibility for the integrity of the data and the accuracy of the data analysis.

FUNDING

Southern California Institute for Research and Education (SCIRE).

ACKNOWLEDGMENTS

The authors thank the contributions of Thomas Clevenger and Angela Tadeo for performing the pulmonary function and cardiopulmonary exercise testing.

REFERENCES

Bewick, V., Cheek, L., and Ball, J. (2004). Statistics Review 13: Receiver Operating Characteristic Curves. *Crit. Care.* 8 (6), 508–512. doi:10.1186/cc3000

Brat, K., Tothova, Z., Merta, Z., Taskova, A., Homolka, P., Vasakova, M., et al. (2016). Resting End-Tidal Carbon Dioxide Predicts Respiratory Complications in Patients Undergoing Thoracic Surgical Procedures. *Ann. Thorac. Surg.* 102 (5), 1725–1730. doi:10.1016/j.athoracsur.2016.05.070

Brunelli, A., Belardinelli, R., Pompili, C., Xiumé, F., Refai, M., Salati, M., et al. (2012). Minute Ventilation-to-Carbon Dioxide Output (e/co2) Slope Is the Strongest Predictor of Respiratory Complications and Death After Pulmonary Resection. *Ann. Thorac. Surg.* 93, 1802–1806. doi:10.1016/j.athoracsur.2012.03.022

Brunelli, A., Belardinelli, R., Refai, M., Salati, M., Socci, L., Pompili, C., et al. (2009). Peak Oxygen Consumption during Cardiopulmonary Exercise Test Improves Risk Stratification in Candidates to Major Lung Resection. *Chest* 135, 1260–1267. doi:10.1378/chest.08-2059

Brunelli, A., Kim, A. W., Berger, K. I., and Addrizzo-Harris, D. J. (2013). Physiologic Evaluation of the Patient with Lung Cancer Being Considered for Resectional Surgery. *Chest* 143 (5 Suppl. l), e166S–e190S. doi:10.1378/chest.12-2395

Datta, D., Normandin, E., and ZuWallack, R. (2015). Cardiopulmonary Exercise Testing in the Assessment of Exertional Dyspnea. *Ann. Thorac. Med.* 10 (2), 77–86. doi:10.4103/1817-1737.151438

Elbehairy, A. F., Ciavaglia, C. E., Webb, K. A., Guenette, J. A., Jensen, D., Mourad, S. M., et al. (2015). Pulmonary Gas Exchange Abnormalities in Mild Chronic Obstructive Pulmonary Disease. Implications for Dyspnea and Exercise Intolerance. *Am. J. Respir. Crit. Care Med.* 191 (12), 1384–1394. doi:10.1164/rccm.201501-0157OC

Keteyian, S. J., Isaac, D., Thadani, U., Roy, B. A., Bensimhon, D. R., McKelvie, R., et al. (2009). Safety of Symptom-Limited Cardiopulmonary Exercise Testing in Patients with Chronic Heart Failure Due to Severe Left Ventricular Systolic Dysfunction. *Am. Heart J.* 158 (4 Suppl. l), S72–S77. doi:10.1016/j.ahj.2009.07.014

Krishnan, B. S., Stockwell, M. J., Clemens, R. E., and Gallagher, C. G. (1997). Airway Anesthesia and Respiratory Adaptations to Dead Space Loading and Exercise. *Am. J. Respir. Crit. Care Med.* 155 (2), 459–465. doi:10.1164/ajrccm.155.2.9032179

Lewis, D. A., Sietsema, K. E., Casaburi, R., and Sue, D. Y. (1994). Inaccuracy of Noninvasive Estimates of VD/VT in Clinical Exercise Testing. *Chest* 106 (5), 1476–1480. doi:10.1378/chest.106.5.1476

McParland, C., Mink, J., and Gallagher, C. G. (1991). Respiratory Adaptations to Dead Space Loading during Maximal Incremental Exercise. *J. Appl. Physiology* 70 (1), 55–62. doi:10.1152/jappl.1991.70.1.55

Mezzani, A. (2017). Cardiopulmonary Exercise Testing: Basics of Methodology and Measurements. *Ann. ATS* 14 (Suppl. 1), S3–S11. doi:10.1513/AnnalsATS.201612-997FR

Robertson, H. T. (2015). Dead Space: the Physiology of Wasted Ventilation. *Eur. Respir. J.* 45 (6), 1704–1716. doi:10.1183/09031936.00137614

Roman, M. A., Casaburi, J. D., Porszasz, J., and Casaburi, R. (2013). Noninvasive Assessment of Normality of V D/V T in Clinical Cardiopulmonary Exercise Testing Utilizing Incremental Cycle Ergometry. *Eur. J. Appl. Physiol.* 113 (1), 33–40. doi:10.1007/s00421-012-2407-8

Sinha, P., Flower, O., and Soni, N. (2011). Deadspace Ventilation: a Waste of Breath!. *Intensive Care Med.* 37 (5), 735–746. doi:10.1007/s00134-011-2194-4

Smith, J. R., and Olson, T. P. (2019). Ventilatory Constraints Influence Physiological Dead Space in Heart Failure. *Exp. Physiol.* 104 (1), 70–80. doi:10.1113/EP087183

Syabbalo, N. C., Zintel, T., Watts, R., and Gallagher, C. G. (1993). Carotid Chemoreceptors and Respiratory Adaptations to Dead Space Loading during Incremental Exercise. *J. Appl. Physiology* 75 (3), 1378–1384. doi:10.1152/jappl.1993.75.3.1378

Velez-Cubian, F. O., Ng, E. P., Fontaine, J. P., and Toloza, E. M. (2015). Robotic-Assisted Videothoracoscopic Surgery of the Lung. *Cancer control.* 22 (3), 314–325. doi:10.1177/107327481502200309

Veluswamy, R. R., Whittaker Brown, S.-A., Mhango, G., Sigel, K., Nicastri, D. G., Smith, C. B., et al. (2020). Comparative Effectiveness of Robotic-Assisted Surgery for Resectable Lung Cancer in Older Patients. *Chest* 157 (5), 1313–1321. doi:10.1016/j.chest.2019.09.017

Wasserman, K., Van Kessel, A. L., and Burton, G. G. (1967). Interaction of Physiological Mechanisms during Exercise. *J. Appl. Physiology* 22 (1), 71–85. doi:10.1152/jappl.1967.22.1.71

Whipp, B. J. (2006). *Exercise Physiology*. Wiley Encyclopedia of Biomedical Engineering, 1–14. Available at: https://onlinelibrary.wiley.com/doi/epdf/10.1002/9780471740360.ebs0464.

Conflict of Interest: The authors declare that the research was conducted in the absence of any commercial or financial relationships that could be construed as a potential conflict of interest.

frontiers | Frontiers in Physiology

TYPE Original Research
PUBLISHED 04 October 2022
DOI 10.3389/fphys.2022.867473

OPEN ACCESS

EDITED BY
Lorenzo Ball,
University of Genoa, Italy

REVIEWED BY
Robert Huhle,
University Hospital Carl Gustav Carus, Germany
Alfredo Maria Lurati,
Fornaroli hospital Magenta, Italy

*CORRESPONDENCE
Chang Hyun Lee,
changhyun.lee@snu.ac.kr

SPECIALTY SECTION
This article was submitted to Respiratory Physiology and Pathophysiology, a section of the journal Frontiers in Physiology

RECEIVED 14 February 2022
ACCEPTED 19 August 2022
PUBLISHED 04 October 2022

CITATION
Choi J, Chae KJ, Jin GY, Lin C-L, Laroia AT, Hoffman EA and Lee CH (2022), CT-based lung motion differences in patients with usual interstitial pneumonia and nonspecific interstitial pneumonia.
Front. Physiol. 13:867473.
doi: 10.3389/fphys.2022.867473

CT-based lung motion differences in patients with usual interstitial pneumonia and nonspecific interstitial pneumonia

Jiwoong Choi[1,2,3], Kum Ju Chae[4], Gong Yong Jin[4], Ching-Long Lin[3,5,6], Archana T. Laroia[7], Eric A. Hoffman[7] and Chang Hyun Lee[7,8]*

[1]Department of Internal Medicine, University of Kansas School of Medicine, Kansas City, KS, United States, [2]Department of Bioengineering, University of Kansas, Lawrence, KS, United States, [3]Department of Mechanical Engineering, University of Iowa, Iowa City, IA, United States, [4]Department of Radiology, Research Institute of Clinical Medicine of Jeonbuk National University-Biomedical Research Institute of Jeonbuk National University Hospital, Jeonbuk National University and Medical School, Jeonju, South Korea, [5]IIHR-Hydroscience & Engineering, University of Iowa, Iowa City, IA, United States, [6]Department of Biomedical Engineering, University of Iowa, Iowa City, IA, United States, [7]Department of Radiology, University of Iowa, University of Iowa Hospitals and Clinics, Iowa, IA, United States, [8]Department of Radiology, Seoul National University College of Medicine, Seoul National University Hospital, Seoul, South Korea

We applied quantitative CT image matching to assess the degree of motion in the idiopathic ILD such as usual interstitial pneumonia (UIP) and nonspecific interstitial pneumonia (NSIP). Twenty-one normal subjects and 42 idiopathic ILD (31 UIP and 11 NSIP) patients were retrospectively included. Inspiratory and expiratory CT images, reviewed by two experienced radiologists, were used to compute displacement vectors at local lung regions matched by image registration. Normalized three-dimensional and two-dimensional (dorsal-basal) displacements were computed at a sub-acinar scale. Displacements, volume changes, and tissue fractions in the whole lung and the lobes were compared between normal, UIP, and NSIP subjects. The dorsal-basal displacement in lower lobes was smaller in UIP patients than in NSIP or normal subjects (p = 0.03, p = 0.04). UIP and NSIP were not differentiated by volume changes in the whole lung or upper and lower lobes (p = 0.53, p = 0.12, p = 0.97), whereas the lower lobe air volume change was smaller in both UIP and NSIP than normal subjects (p = 0.02, p = 0.001). Regional expiratory

Abbreviations: IPF, idiopathic pulmonary fibrosis; CT, computed tomography; FVC, forced vital capacity; DL_{CO}, diffusion capacity of carbon monoxide; MRI, magnetic resonance imaging; COPD, chronic obstructive pulmonary disease; ILD, interstitial lung disease; UIP, usual interstitial pneumonia; NSIP, nonspecific interstitial pneumonia; ATS, American Thoracic Society; ERS, European Respiratory Society; GGO, ground glass opacity; 3D, three-dimensional; PFT, pulmonary function test; FEV_1, forced expiratory volume in 1 s; SSTVD, sum of squared tissue volume difference; 2D, two-dimensional; DB, dorso-basal; $s*$, normalized 3D local displacement magnitude; s, 3D local displacement magnitude; V^{IN}, inspiratory lung volume; V^{EX}, expiratory lung volume; x^{IN}, inspiratory position of the local lung region; x^{EX}, expiratory position of the local lung region; θ, displacement angle; LAA, low attenuation area; HU, Hounsfield unit; HRCT, high-resolution CT.

tissue fractions and displacements showed positive correlations in normal and UIP subjects but not in NSIP subjects. In summary, lung motionography quantified by image registration-based lower lobe dorsal-basal displacement may be used to assess the degree of motion, reflecting limited motion due to fibrosis in the ILD such as UIP and NSIP.

KEYWORDS

interstitial lung disease, idiopathic pulmonary fibrosis, usual interstitial pneumonia, computed tomography, lung motionography, quantitative computed tomography image matching, image registration, computational biomechanics

1 Introduction

Idiopathic pulmonary fibrosis (IPF) is a chronic, progressive fibrosing interstitial pneumonia of unknown cause in adults characterized by the progressive worsening of dyspnea and lung function and is associated with poor prognosis. CT features of fibrosis and honeycombing are strongly correlated with forced vital capacity (FVC) and diffusion capacity of carbon monoxide (DL_{CO}) measurements (Lynch et al., 2005). It has been known that the extent of fibrosis and honeycombing on CT is predictive of survival in IPF (Flaherty et al., 2003; Jeong et al., 2005; Best et al., 2008; Shin et al., 2008; Sumikawa et al., 2008; Raghu et al., 2018, 2022).

Elastography is a technique that uses the fact that a pathological process alters the elastic properties of the involved tissue or organ and is applied for the non-invasive evaluation of the stiffness of a lesion in the breast and fibrosis in the liver (Goddi et al., 2012; Barr et al., 2015). The degree of fibrosis in the lung parenchyma is also critical for the survival, prognosis, and treatment of interstitial lung disease (ILD) (Raghu et al., 2022). Elastography has been used with ultrasonography and MRI for the breast and liver; however, the lung parenchyma is not easily evaluated with this application due to the presence of air and respiratory motion artifacts. In the lung, the local lung motion can be computed using the image registration of volumetric CT images at different lung volumes (Yin et al., 2009; Choi, 2011; Yin et al., 2013; Jahani et al., 2014; Jahani et al., 2015; Jahani et al., 2017; Shin et al., 2020; Kang et al., 2021).

Recent advances in quantitative CT imaging and image matching techniques enabled the utilization of local lung information of inspiration and expiration CT scans in the computation of changes between the scans (Choi et al., 2010; Yin et al., 2010; Galban et al., 2012). Quantitative analysis of regional lung structures and functions of airway segments and lung parenchyma have been utilized to assess the regional lung characteristics, mostly for obstructive lung diseases such as asthma and chronic obstructive pulmonary disease (COPD) (Chae et al., 2020; Choi J et al., 2017; Choi et al., 2013; Choi et al., 2015; Galban et al., 2012; Jahani et al., 2017). Attempts to utilize these quantification methods for ILD are also increasing (Flaherty et al., 2003; Jeong et al., 2005; Best et al., 2008; Shin et al., 2008; Sumikawa et al., 2008). A mass preserving non-rigid image registration technique (Yin et al., 2009) can provide the matching of local lung regions between CT images at two different lung volumes. The method has been utilized to compute the regional displacement of local lung parenchyma between inspiration and expiration (Yin et al., 2013). The recent application of the cross-volume (inspiratory-expiratory) CT image matching-derived three-dimensional (3D) lung motion map differentiated regional lung motions between supine and prone positing in healthy subjects (Shin et al., 2020) and impaired diaphragm motion in patients with COPD and idiopathic pulmonary fibrosis (IPF) compared to healthy controls (Kang et al., 2021).

In this study, we applied this local lung "motionography" information based on cross-volume image matching technique to investigate if it can differentiate between the usual interstitial pneumonia (UIP) and nonspecific interstitial pneumonia (NSIP).

2 Materials and methods

2.1 Patient selection and data acquisition

This study was retrospectively designed and approved by the institutional review board, and informed consent was waived. From January 2013 to December 2017, we retrieved 361 idiopathic interstitial pneumonia (IIP) patients who underwent CT scans and pulmonary function tests (PFTs) from the hospital information system. Two chest radiologists (K.J.C. and C.H.L. with 5 and 20 years of experiences, respectively) reviewed CT images with four categories (UIP, probable UIP, indeterminate UIP, and alternative diagnosis) for UIP diagnosis according to the ATS/ERS guideline in consensus (Raghu et al., 2018). Twenty patients with definite UIP pattern on the CT scan and 11 patients with pathologic UIP were regarded as IPF on multidisciplinary diagnosis (age = 71.6 ± 6.7, M:F = 19:12). Pathologic confirmed NSIP patients were included as the NSIP group (age = 61.9 ± 8.6, M:F = 3:8) (Supplementary Figure S1). For the comparison, data of additional 21 normal subjects (age = 58.0 ± 13.4, M:F = 10:11) who participated in a previous study (Kim et al., 2017) were included in our analysis. The normal subjects had normal PFT results, normal chest CT scans, and no known history of lung disease or surgery.

Imaging was performed using a 128 multi-detector CT scanner (Ingenuity, Philips Healthcare, Best, Netherlands) under full inspiration and full expiration of the patients. The patients were coached by the radiology technician to take a full inhalation and full exhalation, respectivley. CT parameters were as follows: 120 kVp tube voltage, 170 reference mAs tube current-time product, z-dome, 3D dose modulation, 1.0 mm slice thickness, 1.0 mm reconstruction increment, YC 0 reconstruction filter, 0.5 s rotation time. The average voxel volume was 0.294 mm^3. PFTs were performed according to the American Thoracic Society (ATS)/European Respiratory Society (ERS) guidelines (Miller et al., 2005). Dynamic study was first done. Then, static lung volumes were measured, followed by a bronchodilator test. Finally, DL_{CO} was measured. From the spirometry data, forced expiratory volume in 1 s (FEV_1), FVC, and the FEV_1/FVC ratio were assessed.

2.2 Inspiratory and expiratory CT image segmentation and registration

Supplementary Figure S2 shows the flow chart to compute the displacement at local lung regions from a pair of volumetric CT images at inspiration and expiration. First, individual volumetric CT images at inspiration and expiration were segmented and measured for the airway, vessels, lungs, and lobes, utilizing Apollo 2.0 (VIDA Diagnostics, Coralville, Iowa, United States). Then, a mass preserving non-rigid image registration method (Yin et al., 2009) was employed to obtain the local-to-local image matching between inspiration and expiration. The method determines a spatial transformation that matches the two images by minimizing a cost function that is the sum of the squared tissue volume difference (SSTVD). The cost function serves to minimize the local tissue volume difference within the lungs between matched regions, preserving the tissue mass of the lungs if the tissue density is assumed to be constant in the lung. This is particularly appropriate because air changes in the lung while the change of tissue components is minimal. The multiresolution approach adds the quality of local lung matching.

2.3 Local lung displacement

From matched local lung parenchymal units at a sub-acinar scale, 3D displacement vectors from expiration to inspiration were computed by the voxel-wise subtraction of the position vector on expiratory CT $\boldsymbol{x}^{EX}$ from the matched position vector on inspiratory CT $\boldsymbol{x}^{IN}$, where $\boldsymbol{x}$, EX, and IN denote the position vector, expiratory CT, and inspiratory CT, respectively. Two-dimensional (2D) dorso-basal (DB) displacements were also computed using only dorso-ventral and apico-basal components and neglecting transverse changes. 3D displacements and DB displacement magnitudes were both normalized by the cubic root of the global lung volume change from expiration to inspiration CT scans (ΔV) (Eq. 1), in order to reduce the effect of inter-subject variability by inspiration and expiration lung volumes in quantification. Normalized 3D local displacement was denoted by s^*

$$s^* = s \Big/ \sqrt[3]{\Delta V} = \left| x^{IN} - x^{EX} \right| \Big/ \sqrt[3]{\Delta V} \quad (1)$$

DB displacement that excludes the transverse direction was denoted by $s_{yz}{}^*$, where the y and z directions are ventral to the dorsal and apical to basal directions, respectively, as indicated in Supplementary Figure S3. From DB vector, the displacement angle from y axis, θ, was computed. For visual interpretation, 3D displacement vectors were plotted on inspiration image color-coded by s^*.

2.4 Other functional imaging metrics

As imaging-based large-scale functional indicators, air volumes in the whole lung and the lobes were measured on inspiration and expiration. Mean local tissue fractions (TFs) on inspiration and expiration, which may also indicate the degree of fibrosis, were computed and compared with displacement variables. TFs in individual parenchymal units were averaged in the five lobes and combined regions.

2.5 Statistical analysis

Student's t-tests were conducted for comparison between the groups of normal and ILD patients. When categorizing the ILD patients into NSIP and UIP, and comparing between the groups of normal, NSIP, and UIP, the analysis of variance (ANOVA) was done along with Tukey's post hoc test to determine significant pairwise comparisons. Statistical analyses were performed using the R statistical programming environment, version 3.0.2 (the R Foundation, Vienna, Austria). p values <0.05 were considered significant.

3 Results

3.1 Global and regional lung functions

Lung function test values and CT-based volumetric parameters were compared between normal, NSIP, and UIP subjects. ILD (both NSIP and UIP) patients were differentiated from normal subjects. In ILD, FEV_1 and FVC were decreased ($p < 0.001$, both), while FEV_1/FVC was not different. DL_{CO} was also decreased ($p = 0.001$) (Table 1). The static air volumes at inspiration were decreased in the whole lung ($p < 0.001$), the upper lobes ($p = 0.011$), and the lower lobes ($p < 0.001$). In regard to the dynamics

TABLE 1 Comparison of the lung function test results and volumetric parameters between normal, NSIP, and UIP patients.

	Normal (n = 21)	NSIP (n = 11)	UIP (n = 31)	NSIP + UIP vs. Normal[a]	NSIP vs. Normal[b]	UIP vs. Normal[b]	UIP vs. NSIP[b]
FEV_1 (%pred)	110.1 ± 16.2	97.7 ± 20.0	84.9 ± 21.0	< 0.001	0.230	< 0.001	NA
FEV_1/FVC (%pred)	80.9 ± 4.6	80.5 ± 3.9	83.1 ± 7.6	0.290	NA	NA	NA
FVC (%pred)	99.6 ± 13.5	87.4 ± 18.7	69.3 ± 16.6	< 0.001	0.120	< 0.001	0.009
DL_{CO} (%pred)	86.6 ± 24.3	66.9 ± 15.6	57.1 ± 21.4	0.001	0.130	0.003	0.420
Air volume, IN, whole (ml)	3792 ± 1194	2373 ± 906	2415 ± 894	< 0.001	0.001	< 0.001	NA
Air volume, IN, upper (ml)	1993 ± 639	1644 ± 559	1516 ± 564	0.011	NA	0.0160	NA
Air volume, IN, lower (ml)	1799 ± 596	729 ± 396	899 ± 430	< 0.001	< 0.001	< 0.001	NA
Air volume change, upper (%TLC)	19.2 ± 6.1	19.3 ± 9.9	16.3 ± 7.6	0.270	NA	NA	NA
Air volume change, lower (%TLC)	27.6 ± 8.1	15.2 ± 7.1	15.8 ± 6.7	< 0.001	< 0.001	< 0.001	NA

[a]p –values of Student's t-test.
[b]p –values of ANOVA post hoc test (NA stands for "not applicable" and denotes p > 0.05 by ANOVA).

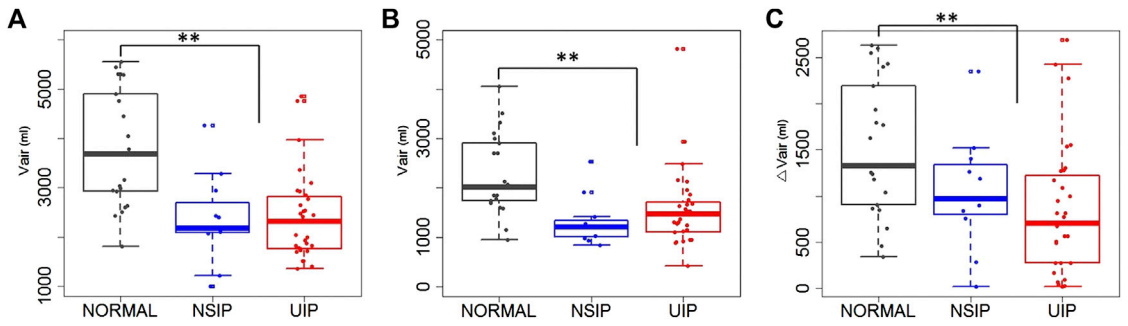

FIGURE 1
Air volumes at **(A)** inspiration and at **(B)** expiration, and **(C)** air volume changes between inspiration and expiration in the whole lung of normal, NSIP, and UIP subjects. ** denotes $p < 0.05$.

between inspiration and expiration, the air volume change was decreased in the whole lung ($p < 0.001$) and in the lower lobes ($p < 0.001$) but not in the upper lobes (Figure 1). Noticeably, only FVC differentiated between NSIP and UIP within ILD and no other parameters in PFT or volumetric lung did. Only the inter-subject variability of the upper lobe air volumes was found greater among UIP subjects than normal or NSIP subjects.

3.2 Displacement magnitude and vectors

Local lung displacements are presented for the normal, NSIP, and UIP subjects in Figure 2, demonstrating a hundred DB displacement vectors and magnitude maps in the entire conducting airway models, as well as CT axial views. In the normal subject, the local displacement of the lower lobe near the posterior costophrenic angle was the highest with the dorso-basal distribution. We speculated that the DB displacement is greater in the more gravitationally dependent lung regions and directions of the displacement vectors reflected regional lung deformation characteristics, similar to regional relative ventilation. In the UIP pattern, the local displacement of the lower lobe was significantly decreased near the posterior costophrenic angle and basal lung, which may represent the advanced fibrosis showing limited lung motions in the lung parenchyma. Lung regions moved more in the ventral direction, which could be attributable to a significant decrease in the movement toward the basal direction. The NSIP subject shows the intermediate characteristics of the displacement distribution toward the posterior costophrenic angle in between the normal and UIP subjects.

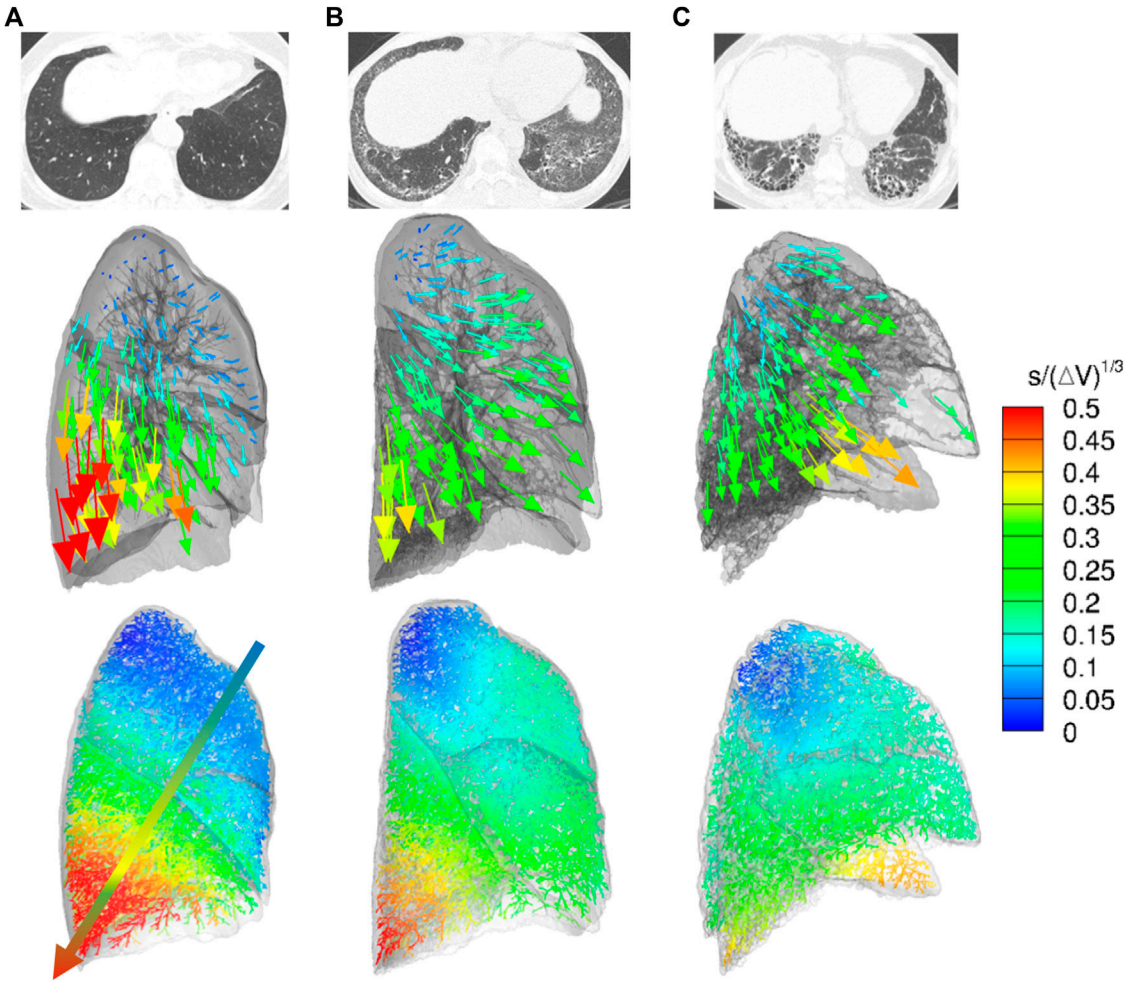

FIGURE 2
CT axial views (top), displacement vectors from expiration to inspiration (middle), and normalized dorsal and basal displacement magnitude maps on the entire conducting airway model (bottom) in representative **(A)** normal, **(B)** NSIP, and **(C)** UIP subjects.

3.3 Displacement and angle

Local lung displacements between inspiration and expiration for all 3D components and for DB motions were compared in the whole lung, the upper lobes, and the lower lobes between normal, NSIP, and UIP patients (Table 2; Figure 3). DB (2D) relative displacement magnitudes in the lower lobes were found smaller in UIP lungs than not only normal lungs (p = 0.007) but also NSIP lungs (p = 0.036). The local displacement magnitude of the lower lobes near the posterior costophrenic angle noticeably decreased in the UIP subjects than NSIP (p = 0.040). ILD patients had a decreased DB displacement angle, θ, in the whole lung (p = 0.008) and in the lower lobes (p < 0.001) than normal subjects. UIP subjects show the same results that θ decreased in the whole lung (p = 0.012) and in the lower lobes (p < 0.001), which reflects limited lung motions toward the basal (z) direction. In the upper lobes, DB displacement increased in NSIP lungs than in UIP lungs (p = 0.032), while it is similar between normal and UIP lungs.

3.4 Tissue fractions

Mean local TFs were also compared (Table 3 and Figure 4). TFs increased in ILD (both NSIP and UIP) patients compared to those in normal subjects in the upper and the lower lobes and consequently in the whole lung on both inspiration and expiration (p < 0.001 for all). Between NSIP and UIP, TFs do not significantly differ in all individual lung regions. However, the upper lobe to lower lobe ratio is significantly smaller in NSIP than in UIP and also than normal subjects both on inspiration (p = 0.002) and on expiration (p < 0.001). The upper–lower ratio is significantly

TABLE 2 Comparison of the motionographic variables between normal, NSIP, and UIP patients.

	Normal (n = 21)	NSIP (n = 11)	UIP (n = 31)	NSIP + UIP vs. Normal[a]	NSIP vs. Normal[b]	UIP vs. Normal[b]	UIP vs. NSIP[b]
s^*	0.21 ± 0.06	0.22 ± 0.07	0.17 ± 0.08	0.048	0.920	0.030	0.040
s^*, upper	0.10 ± 0.03	0.15 ± 0.05	0.10 ± 0.06	0.770	0.140	0.830	0.037
s^*, lower	0.29 ± 0.09	0.32 ± 0.11	0.23 ± 0.11	0.015	1.000	0.009	0.038
s^*_{yz}	0.20 ± 0.06	0.21 ± 0.07	0.15 ± 0.07	0.031	0.950	0.018	0.032
s^*_{yz}, upper	0.10 ± 0.03	0.14 ± 0.05	0.09 ± 0.06	0.950	0.140	0.690	0.024
s^*_{yz}, lower	0.27 ± 0.09	0.29 ± 0.11	0.20 ± 0.10	0.012	1.000	0.007	0.036
θ	37.6 ± 13.5	33.7 ± 14.8	23.7 ± 18.9	0.008	NA	0.012	NA
θ, upper	17.6 ± 20.5	22.0 ± 17.1	12.4 ± 20.8	0.630	NA	NA	NA
θ, lower	52.9 ± 10.3	47.4 ± 16.9	32.4 ± 21.9	< 0.001	0.680	< 0.001	NA

[a]p –values of Student's t-test.
[b]p –values of ANOVA post hoc test (NA denotes p > 0.05 by ANOVA).
Values in columns 2–4 are means ± SD. Values in columns 5–8 are the p values.
s^*: 3D displacement magnitude calculated from the x, y, and z components.
s^*_{yz}: DB displacement magnitude from the y and z components indicatinghe tdorsal and basal lung motion.
upper: upper and middle lobes; lower: lower lobes

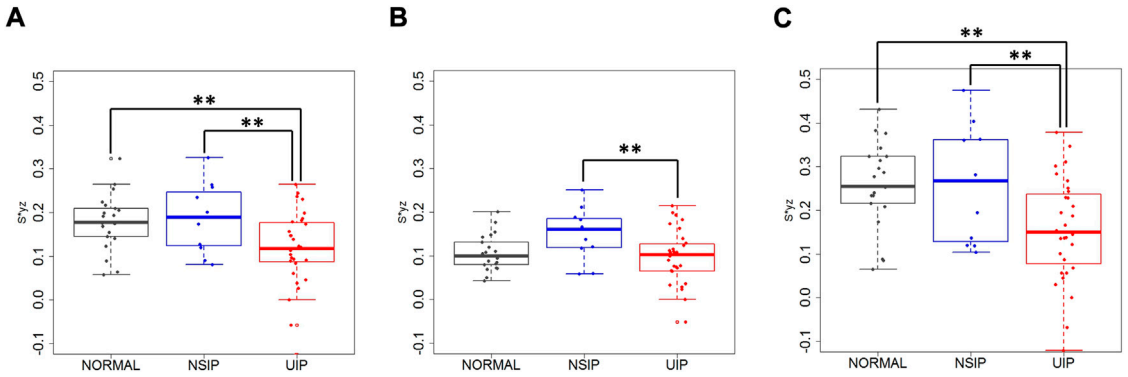

FIGURE 3
Dorsal basal displacement in **(A)** the whole lung, **(B)** the upper lobes, and **(C)** the lower lobes of normal, NSIP, and UIP subjects. ** denotes $p < 0.05$.

smaller in IPF than normal subjects on inspiration ($p < 0.001$) but not on expiration ($p = 0.240$). In NSIP, the upper–lower ratio of local TF is significantly smaller than normal subjects both on inspiration ($p < 0.001$) and expiration ($p < 0.001$).

3.5 Correlation between displacement and tissue fraction

Correlations of the TFs with displacements (3D and DB) were analyzed in normal subjects, NSIP, UIP, ILD (UIP + NSIP), and the entire subjects. In normal subjects, TFs on expiration showed high positive correlations with both 3D and DB displacements in all regions (Table 4). The correlations were slightly higher with 3D displacement ($r = 0.72$ for the whole lung) than with DB displacement ($r = 0.71$ for the whole lung). In four lobes, the left upper lobe (LUL), the right upper lobe (RUL), the right middle lobe (RML), and the right lower lobe (RLL), the correlations range between 0.68 and 0.71, while it is relatively lower in the left lower lobe (LLL) ($r = 0.51$) than the other lobes. Correlations between upper–lower ratios of TF and displacement (3D and DB) also show positive correlation ($r = 0.59$ and $r = 0.58$, respectively). On inspiration, no significant correlation between TFs and displacements was found in any region. Compared to the normal subjects, the correlations decreased in UIP lungs, particurly in the RML ($r = 0.71$ and $r = 0.42$ in normal and UIP, respectively, with 3D displacement). In contrast to normal subjects, the correlation with DB displacement became greater

TABLE 3 Comparison of TFs between normal, NSIP, and UIP patients.

	Normal (n = 21)	NSIP (n = 11)	UIP (n = 31)	NSIP + UIP vs. Normal[b]	NSIP vs. Normal[b]	UIP vs. Normal[b]	UIP vs. NSIP[b]
IN, all lobes (%)	14.6 ± 2.7	20.0 ± 5.6	20.9 ± 4.3	< 0.001	0.011	< 0.001	0.660
IN, upper lobes (%)	13.8 ± 2.5	17.5 ± 5.3	19.1 ± 4.1	< 0.001	0.050	< 0.001	0.380
IN, lower lobes (%)	15.6 ± 3.1	25.5 ± 6.9	24.3 ± 5.4	< 0.001	< 0.001	< 0.001	0.590
IN, upper/lower lobes	0.896 ± 0.076	0.690 ± 0.080	0.797 ± 0.109	< 0.001	< 0.001	< 0.001	0.002
EX, all lobes (%)	24.6 ± 5.2	34.1 ± 4.9	33.1 ± 9.8	< 0.001	< 0.001	< 0.001	0.640
EX, upper lobes (%)	20.9 ± 4.5	27.9 ± 4.5	28.5 ± 8.3	< 0.001	< 0.001	< 0.001	0.770
EX, lower lobes (%)	28.6 ± 6.2	47.7 ± 8.7	41.5 ± 13.4	< 0.001	< 0.001	< 0.001	0.094
EX, upper/lower lobes	0.737 ± 0.090	0.591 ± 0.067	0.704 ± 0.108	0.020	< 0.001	0.240	< 0.001

[a]p –values of Student's t-test.
[b]p –values of ANOVA post hoc test.
Values in columns 2–4 are means ± SD. Values in columns 5–8 are the p values.

than with 3D displacement in all five lobes of UIP patients. Upper–lower ratios were not linearly correlated with displacements in either UIP or NSIP.

4 Discussion

This study shows that imaging-based regional lung DB displacement can distinguish mechanical behaviors between UIP and NSIP. The gross measurement of the degree or extent of fibrosis on the CT scan could be an important biomarker for the assessment of idiopathic interstitial pneumonia. Although honeycombing on CT is one of the prognostic factors in IPF, the concordance rate between radiologists is not high (Watadani et al., 2013). Additionally, the high-resolution CT (HRCT) scan alone does not accurately reveal micro-honeycombing that could be one of the findings to make a diagnosis as UIP classified as a possible UIP on the CT scan (Travis et al., 2013). The lung motionography using the cross-volume imaging registration technique used in the present study may be one of the unique methods to reflect the degree and extent of lung motion limitations, which may enable the detection of the early stage of fibrosis and reflect the whole lung fibrosis or restricted lung function for the assessment of interstitial fibrotic lung disease.

4.1 Normalized displacement

CT findings of ILD could be affected by the lung volumes at the level of inspiration and expiration. In a clinical environment, inflation levels at which inspiration and expiration CT images are acquired may vary for many reasons, which could add uncertainty to the CT reading of individual images or quantitative analysis of changes between the two images. We propose a normalization of displacement by a cubic root of the lung volume change between two images, to minimize the effect of uncertainty due to lung inflation level, and to conduct standardized relative regional characteristics of local lung motion. We used the length scale for normalization to nondimensionalize the measure. The parenchymal unit volume to measure the local lung motion is at an acinar scale, which may reflect characteristics at the scale of the functional unit of the lung in addition to the smooth possible noise of information from smaller voxels. It has been shown that the normalization of image-registration-based regional lung functions using the global lung volumes has shown successful inter-subject quantitative CT analysis (Chae et al., 2020; Choi S et al., 2017; Shin et al., 2020; Kang et al., 2021).

4.2 Lower lobe functional limitation

As expected, the limitation of motion in the lower lobes corresponded to the distribution of honeycombing on CT scan. Dorsal-basal movement of the lung in the supine position for the CT scan is highest in the normal subjects and accordingly the dorsal-basal movement of the lung was mostly restricted in the patients with ILD. In addition to the motion limitation, the air volume change also decreased in the lower lobes in patients with ILD. All the patients were scanned in the supine position in this study. However, the lung motion and air volume change between inspiration and expiration in prone position could be interesting because the prone position improves arterial oxygenation, reduces shunts, and can affect diaphragmatic motions (Albert et al., 1987; Tomita et al., 2004). It is speculated that the increased stiffness due to excessive

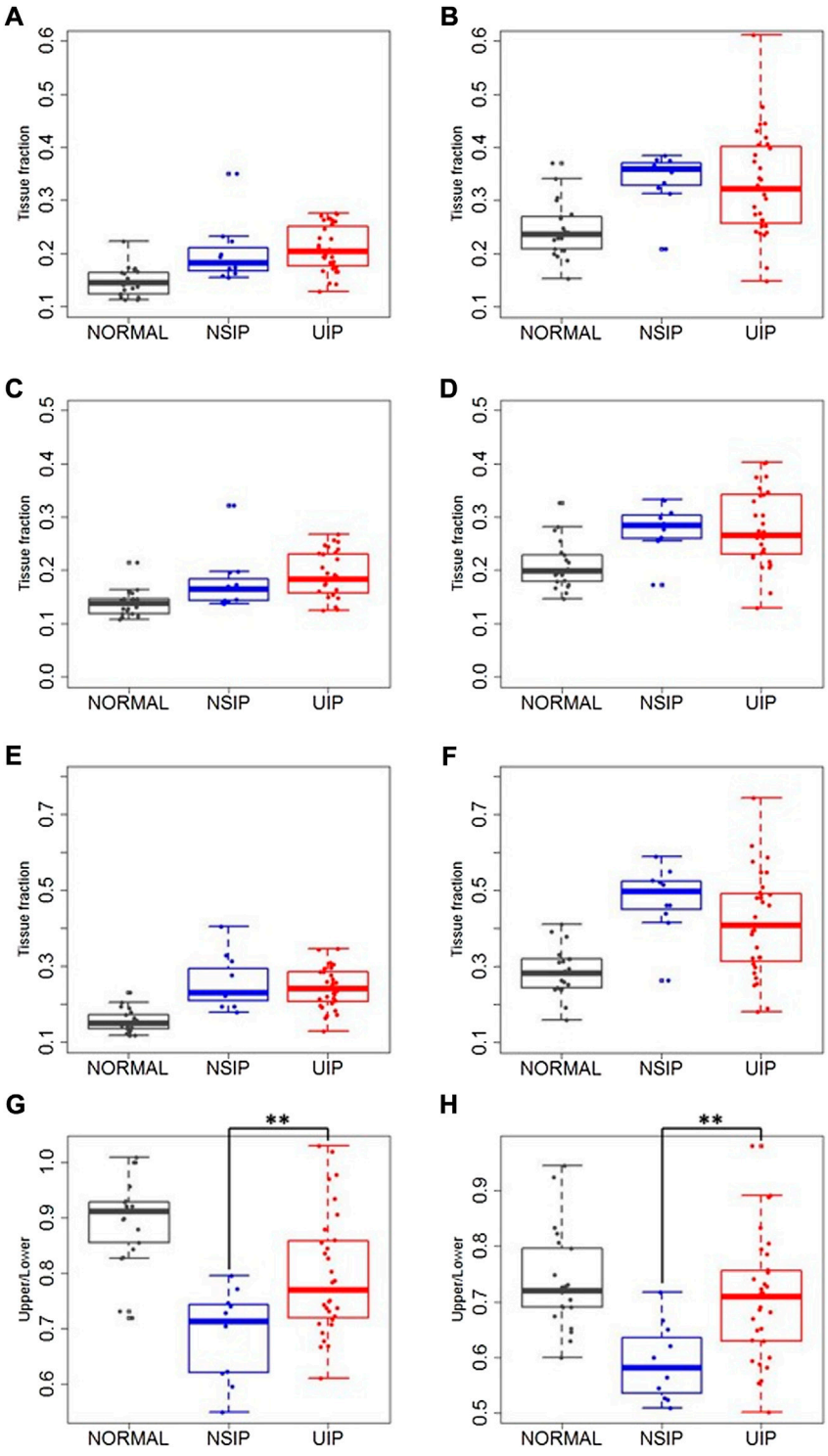

FIGURE 4
Local TFs on **(A,C,E,G)** inspiration and on **(B,D,F,H)** expiration in the whole lung **(A,B)**, upper and middle lobes **(C,D)**, lower lobes **(E,F)**, and upper–lower ratio **(G,H)** in normal, NSIP, and UIP subjects. ** denotes $p < 0.05$.

TABLE 4 Regional correlation of TF with 3D and dorso-basal displacements.

	Normal, 3D	Normal, DB	UIP, 3D	UIP, DB
LUL	0.71	0.69	0.62	0.66
LLL	0.51	0.5	0.46	0.47
RUL	0.68	0.64	0.54	0.62
RML	0.71	0.7	0.42	0.47
RLL	0.7	0.69	0.6	0.62
Upper lobes	0.75	0.73	0.58	0.64
Lower lobes	0.66	0.65	0.56	0.57
All lobes	0.72	0.71	0.59	0.62
upper/lower lobes	0.59	0.58	0.06	−0.05

Values are Pearson's correlation coefficients.

fibrosis with honeycombing limited regional lung motions in the lower lobes of UIP patients compared to normal and even to NSIP, as demonstrated in Figure 2.

4.3 Direction of lung movement

The motivation of using 3D and 2D displacements originated from the idea that the degree of fibrosis in the lung may be associated with the reduced capability of lung motion, because regional lung motion is based upon the cumulative deformation of local lung regions, which are limited in the restrictive changes in UIP and NSIP. Since the 3D volumetric analysis is available and the nature of lung deformation is three-dimensional, we used 3D displacement. Considering that the regional lung deformation primarily varies through dorsoventral and apicobasal axes, but not necessarily through the lateromedial axis, with gravitational dependency, we used 2D formulation as well.

From normal to NSIP and UIP, the direction of the lung movement also changes from the posterior costophrenic angle direction to the anterior costophrenic angle direction with the deformation of the lung morphology. This may mainly be attributable to the distribution of honeycombing or lung fibrosis in the dorsal and basal regions of the lung. As demonstrated in Figure 2, the proposed method can illustrate the morphologic deformation of the whole lung in patients with restricted lung function compared to the normal subjects.

4.4 Association with pulmonary function test analysis

Among the PFT results presented in Table 1, only FVC (% pred) differentiated UIP against NSIP. However, other measures including DL_{CO} were not significantly different between UIP and NSIP. This may imply that the earlier stage of fibrosis, septal thickening, or inflammatory process may all contribute to a decrease in DL_{CO}, and the progression of fibrosis decreases the lung motion, in association with the decline of the full ventilation capacity (decreased FVC). A lower lobe predominance of air volume change between inspiration and expiration also supports this argument. With this interpretation, the proposed CT-based lung motionography is considered useful for capturing the progression of the fibrotic disease, since the contribution of CT imaging in the characterization of IPF is gaining more attention and acceptance in clinical use (Raghu et al., 2018, 2022) and the proposed method provides regional alteration of lung motion at such small scales as acini or voxels.

4.5 Tissue fraction

Regional TF analysis results support the above discussion. Regional characteristics of local TFs on inspiration and on expiration can be interpreted as indicators of small-scale structural alteration, and regional characteristics of local displacements serve as indicators of small-scale functional alteration. We speculated that the increase of TF seen in NSIP might be explained by the structural alteration with the early stage of fibrosis and relatively lower functional decrease compensated by regional hyperinflations in contrast to UIP with advanced fibrosis and restricted lung function. In this study, the result of increased expiratory TF in UIP is also in agreement with the report of a previous study (Petroulia et al., 2018). The correlation of the results between displacements and TFs suggests the following interpretation. In normal subjects, the positive correlation of displacements only with expiratory TF and not with inspiratory TF reflects deformation characteristics of healthy lungs. On inspiration near the total lung capacity (TLC), TFs are relatively uniform due to the full recruitment of alveoli; the deflation from TLC is greater in more dorsal and basal regions along with more displacement and more expiratory TFs (less air fractions) in these regions. This may imply that the mechanical property of local lung structure is presumably homogeneous in normal subjects. TF increase in NSIP and UIP patients may indicate the presence of fibrosis or

thickening of the interlobular septum and/or intralobular septum in the lung parenchyma. TF was better correlated with DB displacement than 3D displacement in all five lobes of UIP patients. This supports that DB displacement may better characterize the UIP-associated structural alteration such as fibrosis or intra- and interlobular septal thickening than 3D displacement.

4.6 Study limitations

One of the limitations of the current study is that the inspiration to expiration volume change could be affected by the level of respiration of the patients. This may limit the accurate assessment of the ILD. However, the disease itself may manifest a decreased volume change between inspiration and expiration and also due to the decreased lung volume with fibrosis. We tried to minimize the effect of variability in lung volumes between inspiration and expiration. Further studies may be needed to better understand the relationship of the degree of fibrosis and lung volumes and to compare normalization based on other quantities, which requires more subjects. The clinically diagnosed NSIP group without CT honeycombing may have pathological UIP with micro-honeycombing or atypical UIP. But the purpose of this study was to assess the lung motion related to the degree of fibrosis presented as honeycombing on CT scan, which represents a more advanced stage of interstitial fibrosis compared to reticular opacity or ground-glass opacity on CT scan.

The focus of the current study is limited to the discriminative characterization of lung motionography between UIP and NSIP. Characterization of the associated nature between impaired lung motionography with common clinical measures including PFTs, such as linear or nonlinear relationship, is not fully understood and remains for future study with a greater sample size. The scope of the current work does not include the connected tissue disease (CTD)-associated ILD. It may be worth applying the regional lung motionography analysis for RA-ILD, SSc-ILD, and Sjogren disease, which remains for future studies. Also, the methods for the analysis of lung motion in the current study is limited to CT-based approaches. However, further investigation of lung motion in ILD associating with other radiological methods such as ultrasound B-lines (Manolescu et al., 2020, Tardella et al., 2018) may provide additional understanding of impaired lung motionography that can expand the lung motion assessment for more clinical applications.

4.7 Concluding remarks

In conclusion, CT-based regional lung motionography may be used to illustrate the restricted lung motion or indirectly reflect the degree or extent of lung fibrosis. Lower lobe lung motions using image registration technique were significantly different between normal, NSIP, and UIP patterns on CT scans.

Data availability statement

The raw data supporting the conclusions of this article will be made available by the authors without undue reservation, under consideration of the terms that participants were not asked for consent to make individual data available. Requests to access the datasets should be directed to changhyun.lee@snu.ac.kr.

Ethics statement

The studies involving human participants were reviewed and approved by Institutional Review Boards of Seoul National University Hospital and Jeonbuk National University Hospital. Written informed consent for participation was not required for this study in accordance with the national legislation and the institutional requirements.

Author contributions

Conception and design: JC and CHL; acquisition of data: KJC, GYJ, CHL; analysis and interpretation of data: all authors; drafting the article or revising it critically for important intellectual content: JC, KJC, EAH, ATL, CHL; final approval of the version to be published: all authors.

Funding

Basic Science Research Program through the National Research Foundation of Korea (NRF) funded by the Ministry of Education (2016R1D1A1B03936078 and 2017R1D1A1A09082160) and the Korea Environment Industry & Technology Institute (KEITI) through Environmental Health Action Program funded by the Korea Ministry of Environment (MOE) (2018001360001).

Acknowledgments

The authors would like to thank Margaret Park and Sara Park, Department of Radiology, Seoul National University Hospital, Seoul, Korea, for the assistance with statistical analysis and also thank Kyung Min Shin, Department of Radiology, Kyungpook National University Chilgok Hospital, Chilgok, Korea, for providing valuable discussions.

Conflict of interest

EAH is a founder and shareholder of VIDA (Coralville, IA, United States).

The remaining authors declare that the research was conducted in the absence of any commercial or financial relationships that could be construed as a potential conflict of interest.

Publisher's note

All claims expressed in this article are solely those of the authors and do not necessarily represent those of their affiliated organizations, or those of the publisher, the editors, and the reviewers. Any product that may be evaluated in this article, or claim that may be made by its manufacturer, is not guaranteed or endorsed by the publisher.

Supplementary material

The Supplementary Material for this article can be found online at: https://www.frontiersin.org/articles/10.3389/fphys.2022.867473/full#supplementary-material

References

Albert, R. K., Leasa, D., Sanderson, M., Robertson, H. T., Hlastala, M. P., Kirk, W., et al. (1987). The prone position improves arterial oxygenation and reduces shunt in oleic-acid-induced acute lung injury. *Am. Rev. Respir. Dis.* 135, 628–633. doi:10.1164/arrd.1987.135.3.628

Barr, R. G., Ferraioli, G., Palmeri, M. L., Goodman, Z. D., Garcia-Tsao, G., Rubin, J., et al. (2015). Elastography assessment of liver fibrosis: Society of radiologists in ultrasound consensus conference statement. *Radiology* 276, 845–861. doi:10.1148/radiol.2015150619

Best, A. C., Meng, J., Lynch, A. M., Bozic, C. M., Miller, D., Grunwald, G. K., et al. (2008). Idiopathic pulmonary fibrosis: Physiologic tests, quantitative CT indexes, and CT visual scores as predictors of mortality. *Radiology* 246, 935–940. doi:10.1148/radiol.2463062200

Chae, K. J., Choi, J., Jin, G. Y., Hoffman, E. A., Laroia, A. T., Park, M., et al. (2020). Relative regional air volume change maps at the acinar scale reflect variable ventilation in low lung attenuation of COPD patients. *Acad. Radiol.* 27 (11), 1540–1548. doi:10.1016/j.acra.2019.12.004

Choi, J., Hoffman, E. A., Lin, C. L., Milhem, M. M., Tessier, J., and Newell, J. D. (2017). Quantitative computed tomography determined regional lung mechanics in normal nonsmokers, normal smokers and metastatic sarcoma subjects. *Plos One* 12, e0179812. doi:10.1371/journal.pone.0179812

Choi, J., Xia, G., Tawhai, M. H., Hoffman, E. A., and Lin, C. L. (2010). Numerical study of high-frequency oscillatory air flow and convective mixing in a CT-based human airway model. *Ann. Biomed. Eng.* 38, 3550–3571. doi:10.1007/s10439-010-0110-7

Choi, J. Multiscale numerical analysis of airflow in CT-based subject specific breathing human lungs. In: *Mechanical engineering*, University of Iowa. Iowa City, IA, USA: University of Iowa, 2011, p. xviii, 236 pages.

Choi, S., Hoffman, E. A., Wenzel, S. E., Castro, M., Fain, S., Jarjour, N., et al. (2017). Quantitative computed tomographic imaging-based clustering differentiates asthmatic subgroups with distinctive clinical phenotypes. *J. Allergy Clin. Immunol.* 140, 690–700. doi:10.1016/j.jaci.2016.11.053

Choi, S., Hoffman, E. A., Wenzel, S. E., Castro, M., Fain, S. B., Jarjour, N. N., et al. (2015). Quantitative assessment of multiscale structural and functional alterations in asthmatic populations. *J. Appl. Physiol.* 118, 1286–1298. doi:10.1152/japplphysiol.01094.2014

Choi, S., Hoffman, E. A., Wenzel, S. E., Tawhai, M. H., Yin, Y. B., Castro, M., et al. (2013). Registration-based assessment of regional lung function via volumetric CT images of normal subjects vs. severe asthmatics. *J. Appl. Physiol.* 115, 730–742. doi:10.1152/japplphysiol.00113.2013

Flaherty, K. R., Thwaite, E. L., Kazerooni, E. A., Gross, B. H., Toews, G. B., Colby, T. V., et al. (2003). Radiological versus histological diagnosis in UIP and NSIP: Survival implications. *Thorax* 58, 143–148. doi:10.1136/thorax.58.2.143

Galban, C. J., Han, M. K., Boes, J. L., Chughtai, K. A., Meyer, C. R., Johnson, T. D., et al. (2012). Computed tomography-based biomarker provides unique signature for diagnosis of COPD phenotypes and disease progression. *Nat. Med.* 18, 1711–1715. doi:10.1038/nm.2971

Goddi, A., Bonardi, M., and Alessi, S. (2012). Breast elastography: A literature review. *J. Ultrasound* 15, 192–198. doi:10.1016/j.jus.2012.06.009

Jahani, N., Choi, S., Choi, J., Haghighi, B., Hoffman, E. A., Comellas, A. P., et al. (2017). A four-dimensional computed tomography comparison of healthy and asthmatic human lungs. *J. Biomech.* 56, 102–110. doi:10.1016/j.jbiomech.2017.03.012

Jahani, N., Choi, S., Choi, J., Iyer, K., Hoffman, E. A., and Lin, C. L. (2015). Assessment of regional ventilation and deformation using 4D-CT imaging for healthy human lungs during tidal breathing. *J. Appl. Physiol.* 119, 1064–1074. doi:10.1152/japplphysiol.00339.2015

Jahani, N., Yin, Y. B., Hoffman, E. A., and Lin, C. L. (2014). Assessment of regional non-linear tissue deformation and air volume change of human lungs via image registration. *J. Biomech.* 47, 1626–1633. doi:10.1016/j.jbiomech.2014.02.040

Jeong, Y. J., Lee, K. S., Muller, N. L., Chung, M. P., Chung, M. J., Han, J., et al. (2005). Usual interstitial pneumonia and non-specific interstitial pneumonia: Serial thin-section CT findings correlated with pulmonary function. *Korean J. Radiol.* 6, 143–152. doi:10.3348/kjr.2005.6.3.143

Kang, J. H., Choi, J., Chae, K. J., Shin, K. M., Lee, C. H., Guo, J., et al. (2021). CT-derived 3D-diaphragm motion in emphysema and IPF compared to normal subjects. *Sci. Rep.* 11 (1), 14923. doi:10.1038/s41598-021-93980-5

Lynch, D. A., Godwin, J. D., Safrin, S., Starko, K. M., Hormel, P., Brown, K. K., et al. (2005). High-resolution computed tomography in idiopathic pulmonary fibrosis: Diagnosis and prognosis. *Am. J. Respir. Crit. Care Med.* 172, 488–493. doi:10.1164/rccm.200412-1756OC

Manolescu, D., Oancea, C., Timar, B., Traila, D., Malita, D., Birsasteanu, F., et al. (2020). Ultrasound mapping of lung changes in idiopathic pulmonary fibrosis. *Clin. Respir. J.* 14 (1), 54–63. Epub 2019 Nov 14. PMID: 31675455. doi:10.1111/crj.13101

Petroulia, V., Funke, M., Zumstein, P., Berezowska, S., Ebner, L., Geiser, T., et al. (2018). Increased expiratory computed tomography density reveals possible abnormalities in radiologically preserved lung parenchyma in idiopathic pulmonary fibrosis. *Invest. Radiol.* 53, 45–51. doi:10.1097/RLI.0000000000000405

Raghu, G., Remy-Jardin, M., Myers, J. L., Richeldi, L., Ryerson, C. J., Lederer, D. J., et al. (2018). Diagnosis of idiopathic pulmonary fibrosis. An official ATS/ERS/JRS/ALAT clinical practice guideline. *Am. J. Respir. Crit. Care Med.* 198, e44–e68. doi:10.1164/rccm.201807-1255ST

Raghu, G., Remy-Jardin, M., Richeldi, L., Thomson, C. C., Inoue, Y., Johkoh, T., et al. (2022). Idiopathic pulmonary fibrosis (an update) and progressive pulmonary fibrosis in adults: An official ATS/ERS/JRS/ALAT clinical practice guideline. *Am. J. Respir. Crit. Care Med.* 205 (9), e18–e47. doi:10.1164/rccm.202202-0399ST

Shin, K. M., Choi, J., Chae, K. J., Jin, G. Y., Eskandari, A., Hoffman, E. A., et al. (2020). Quantitative CT-based image registration metrics provide different ventilation and lung motion patterns in prone and supine positions in healthy subjects. *Respir. Res.* 21 (1), 254. doi:10.1186/s12931-020-01519-5

Shin, K. M., Lee, K. S., Chung, M. P., Han, J., Bae, Y. A., Kim, T. S., et al. (2008). Prognostic determinants among clinical, thin-section CT, and histopathologic findings for fibrotic idiopathic interstitial pneumonias: Tertiary hospital study. *Radiology* 249, 328–337. doi:10.1148/radiol.2483071378

Sumikawa, H., Johkoh, T., Colby, T. V., Ichikado, K., Suga, M., Taniguchi, H., et al. (2008). Computed tomography findings in pathological usual interstitial pneumonia: Relationship to survival. *Am. J. Respir. Crit. Care Med.* 177, 433–439. doi:10.1164/rccm.200611-1696OC

Tomita, K., Sakai, Y., Monma, M., Ohse, H., and Imura, S. (2004). Analysis of diaphragmatic motion with prone positioning using dynamic MRI. *J. Phys. Ther. Sci.* 16, 85–89. doi:10.1589/jpts.16.85

Travis, W. D., Costabel, U., Hansell, D. M., King, T. E., Lynch, D. A., Nicholson, A. G., et al. (2013). An official American thoracic society/European respiratory society statement: Update of the international multidisciplinary classification of the idiopathic interstitial pneumonias. *Am. J. Respir. Crit. Care Med.* 188, 733–748. doi:10.1164/rccm.201308-1483ST

Watadani, T., Sakai, F., Johkoh, T., Noma, S., Akira, M., Fujimoto, K., et al. (2013). Interobserver variability in the CT assessment of honeycombing in the lungs. *Radiology* 266, 936–944. doi:10.1148/radiol.12112516

Yin, Y., Choi, J., Hoffman, E. A., Tawhai, M. H., and Lin, C. L. (2013). A multiscale MDCT image-based breathing lung model with time-varying regional ventilation. *J. Comput. Phys.* 244, 168–192. doi:10.1016/j.jcp.2012.12.007

Yin, Y., Choi, J., Hoffman, E. A., Tawhai, M. H., and Lin, C. L. (2010). Simulation of pulmonary air flow with a subject-specific boundary condition. *J. Biomech.* 43, 2159–2163. doi:10.1016/j.jbiomech.2010.03.048

Yin, Y., Hoffman, E. A., and Lin, C. L. (2009). Mass preserving nonrigid registration of CT lung images using cubic B-spline. *Med. Phys.* 36, 4213–4222. doi:10.1118/1.3193526

Advantages of publishing in Frontiers

OPEN ACCESS
Articles are free to read for greatest visibility and readership

FAST PUBLICATION
Around 90 days from submission to decision

HIGH QUALITY PEER-REVIEW
Rigorous, collaborative, and constructive peer-review

TRANSPARENT PEER-REVIEW
Editors and reviewers acknowledged by name on published articles

Frontiers
Avenue du Tribunal-Fédéral 34
1005 Lausanne | Switzerland

Visit us: www.frontiersin.org
Contact us: frontiersin.org/about/contact

REPRODUCIBILITY OF RESEARCH
Support open data and methods to enhance research reproducibility

DIGITAL PUBLISHING
Articles designed for optimal readership across devices

FOLLOW US
@frontiersin

IMPACT METRICS
Advanced article metrics track visibility across digital media

EXTENSIVE PROMOTION
Marketing and promotion of impactful research

LOOP RESEARCH NETWORK
Our network increases your article's readership